FORMATION DAMAGE ARISING

FROM

BARIUM SULPHATE SCALE PRECIPITATION

by

Philip S. Goulding

Thesis submitted for the Degree of

Doctor of Philosophy

Department of Petroleum Engineering

Heriot-Watt University

Edinburgh

November 1987

TABLE OF CONTENTS

LIST OF TABLES

LIST OF FIGURES

ACKNOWLEDGEMENTS

I wish to express my gratitude to my supervisor, Dr A. C. Todd, for his continued support throughout many difficult times in this project. Also amongst the academic staff of this Department I wish to thank Dr J. L. Jensen for his advice and opinion in several areas of the analysis of results and compilation of this thesis.

I would like to thank all my colleagues for their help and good humour. In particular my thanks go to Ian Simm for his competent introduction to laboratory core studies, Neil Turnbull for many useful discussions and the long hours of transducer calibration, John Somerville for tutoring me on the network model and putting up with endless questions on its operation and Yuan Ming-Dong for his valuable assistance in the later stages of the experimental work.

I wish to acknowledge Design Officer George Pratt, without whose skill and initiative the experimental work may not have begun at all. Alan Brown and his workshop team are also thanked for taking-on many tedious tasks, especially during the development of the distribution face and for "pulling out all the stops" when it mattered most. Lab technicians Elaine Blackie and Angela Nelson are thanked for their general support in the lab and for the weeks of battling with the mercury penetration porosimeter for results.

Cliff Ogle is to be thanked for his skillful and reliable work with the scanning electron microscope and advice on matters geological. On the same theme, I wish to make a special thanks to Dr Roy Gill and the staff of Edinburgh University Dept. of Geology for their willing advice and encouragement, which steered me in the right direction for the crystallographic study.

I wish to express my sincere gratitude to Alastair Reid both for his friendly assistance in many laboratory and computing problems and

for his tremendous support during the compilation of this thesis.

I should like to give special thanks to all those people in and around Edinburgh who have amused me "out of hours" thereby assuring "in hours" success. Their contribution is immeasurable. I specially wish to thank Helen Cruickshank for her assistance with some of the most boring tasks in thesis compilation. Special thanks also go to secretaries Heather Rigg and Sue Walters for their help and support in the printing of this thesis.

BP Sunbury Research Centre is acknowledged for sponsoring this project and my thanks go to its staff for their help and advice during the course of the work. I also wish to thank the SERC for my student grant.

Finally, I would like to thank Helen for believing in me for so long and being so patient.

ABSTRACT

Formation of scale in oilfield pipework has long been a problem. It is also likely that scale might form in the near well-bore region of the reservoir. This thesis examines the simulation of the formation damage possible due to scale, supported by experiments involving mixing brines in sandstone cores.

Simulation was performed using a network model to represent the sandstone. The model was "damaged" using precipitation theory and observations on the damage caused to experimental cores.

Experiments were performed, using quarried sandstone, to provide data for tuning and matching the model. The experiments used a pressure-tapped core holder to provide more detailed information on the scaling process and a new, two fluid, injection system for better control over mixing of the brines.

The experiments demonstrated that permeability loss would be most rapid in the initial stages of scaling. The rate of permeability loss decreased with decreasing supersaturation of the brine mix and increasing distance from the point of mixing. Characterisation of the permeability decline demonstrated a linear correlation between the damage rate and the initial permeability. Some effects on permeability damage due to morphology of the scale crystals were noted. The crystal morphology was shown to be mainly dependant on the solution composition rather than its supersaturation.

Results from the model indicated a great sensitivity to the "poro-perm" characteristics of the network model representing the sandstone. No matching of results to experiments was achieved, but the trends with relation to the permeability change were modelled successfully.

NOMENCLATURE

Many of the symbols used in this thesis are defined at the point they are first used for the convenience of the reader. This nomenclature table has been provided to cover those symbols which have not been defined elsewhere and to provide a master reference list for all the symbols used.

A = Debye-Huckel coefficient defined by theory

a = Ionic strength - pressure correlation coefficient

$a_{0,1,2}$ = Correlation coefficients

B = Debye-Huckel correlation coefficient

b = Ionic strength - pressure correlation coefficient

C = Debye-Huckel correlation coefficient

C_{node} = Number of node with coordinates i, j, k

$[C]$ = Concentration of ion C

$[C]_i$ = Concentration of ion C at any time i

$[C]_o$ = Concentration of ion C at saturation

c_a = Concentration of anion

c_a^* = Concentration of anion at saturation

c_{ex} = Anion concentration less cation concentration

c_m = Concentration of cation

c_m^* = Concentration of cation at saturation

c_{mi} = Concentration of cation at capillary inlet

c_{mo} = Concentration of cation at capillary outlet

D = Debye-Huckel correlation coefficient

D_a = Weighting factor for section a of capillary

D_{max} = Diameter of largest capillary throat in network

D_{thr} = Capillary throat diameter

d = Difference between sulphate and metal ion concentrations (Section 3.2)

d = Diameter of flow path (Section 3.3)

F_a = Fraction of scale in capillary assigned to section a of capillary

I = Ionic strength

i = Coordinate of node under consideration

i_{max} = Length of network along i axis

j = Coordinate of node under consideration

j_{max} = Breadth of network along j axis

K = Debye-Huckel correlation coefficient

K_{ai} = Combination of parameters describing flow supporting properties of section a of capillary i

K_i = Combination of parameters describing flow supporting properties for whole of capillary i

k = Reaction rate constant (Chapters 3 and 6)

k = Coordinate of node under consideration (Appendix A6.2)

k_{max} = Height of network along k axis

L_{cap} = Capillary or internodal length

L_{thr} = Capillary throat length

l = Length of flow path

l_a = Length of section a of capillary

M_v = Molar volume of scaling salt

m_x = Concentration of ion x

N_{cap} = Number of capillaries in network

N_{node} = Number of nodes in network

n = Order of reaction (Section 3.4)

n = Number of data points used (Section 3.2)

P = Pressure

ΔP = Pressure drop across flow path

P_d = Downstream pressure for capillary

P_{in} = Inlet pressure to section of capillary concerned

P_{out} = Outlet pressure from section of capillary concerned

P_r = Reference pressure for solubility correlation

P_u = Upstream pressure for capillary

Q = Solubility product

Q_e = Experimentally determined solubility product

Q_p = Solubility product predicted by model

Q_r = Solubility product at reference pressure

q = Flowrate

q_i = Flowrate through capillary i

q_{inlet} = Flowrate through capillary leading from inlet node

q_t = Total flowrate through network

R = Universal gas constant

S = Supersaturation

$S_{a,b,c}$ = Outlet supersaturations from pores leading into a node

S_b = Supersaturation at the beginning of a time period

S_e = Sulphate ion excess

S_f = Supersaturation at the end of a time period

S_{in} = Supersaturation at capillary/core inlet

S_{out} = Supersaturation at capillary/core outlet

S_x = Supersaturation at node x

s = "Surface area" term

T = Absolute temperature

t = Time

Δt = Length of time period associated with S_b and S_f

t_c = Residence time of fluids in core

t_p = Time for a packet of fluid to pass through a capillary

V = Volume

$\Delta V°$ = Standard state volume change

V_a = Volume of scale assigned to section a of a capillary

$V_{a,b,c}$ = Volume flowrates from pores leading into a node

V_s = Volume of scale assigned to a capillary

α = Interaction factor

$\alpha_{1,2,3}$ = Interaction factors

μ = Fluid viscosity

CHAPTER 1

INTRODUCTION

In the recovery of oil various techniques are used to maintain reservoir pressure and to sweep the oil towards the production wells. Amongst these techniques are inert gas injection, re-injection of produced gas and methods of enhanced oil recovery. One of the most common techniques is water injection. Waterflooding is widely used because the viscosity characteristics of the water in relation to the oil make it an efficient sweeping medium. Typically 15,000 to 20,000 barrels of water per day are required to be injected, so waterflooding also tends to be more economical than the use of special gases and chemicals. As the quantities of water required for injection are high, the water supply must be local to the injection point. This is of particular significance in offshore field exploitation as the only practical water supply is the sea water itself.

Injection of water from any source can lead to difficulties associated with the materials dissolved or suspended in the water. Suspended materials can plug the pores in the formation around the injection well and so must be removed by filtration. The level of filtration required is an economic factor which must be matched with the capacity of injection pumps to overcome permeability damage around the injection well due to suspended particles plugging the formation. As the temperature rises on the passage of the fluid down to the reservoir, dissolved material can precipitate to form a scale in injection pipework or on the sand face of the reservoir. This precipitation will depend upon how the solubility of the dissolved material changes with temperature.

Depending on its composition, injected water can be incompatible with the reservoir rocks themselves. Cation exchange between the injected water and clay materials in the reservoir can cause the clays to swell up by adsorption of water. This swelling reduces the size of pores and so reduces the permeability of the reservoir.

Restrictions on the supply of water for injection can often result in the need to inject water that is incompatible with the reservoir fluids. Upon mixing of an incompatible water with reservoir fluids a reaction occurs which precipitates an inorganic solid known as scale. The flow of fluids around an injection well are unlikely to lead to any significant mixing of injected and reservoir fluids. As injection water passes into the formation a narrow mixed front forms which continuously moves deeper into the reservoir. The potential scale that could be produced from this limited mixing is small and because the front is moving, no significant build-up of scale in any zone can occur. Scaling is not, therefore, expected to cause any significant damage to well injectivity. Some companies[1,10,27] prefer to take precautions, by the use of scale inhibitors during the initial stages of injection, to prevent any damage to the crucial near-well-bore zone.

Heterogeneities in the permeability of reservoirs can cause injected water to sweep rapidly through a high permeability sandstone layer and so result in early "breakthrough" of injected water in the production zone. After injection water breakthrough, water produced from the rapidly swept layers of the reservoir will mix in the production tubing with formation water produced from other zones. Mixing of the incompatible waters in the tubing creates the potential for scale deposition at any point downstream of the mixing zone.

Scaling of tubing is a well-known problem resulting in loss of oil production and the need for expensive treatments. Most of the common scales may be removed by a chemical treatment, however one common

scale, barium sulphate, is so insoluble that even specially developed dissolvers can be ineffective against it. Barium sulphate scales in general are removed mechanically, usually requiring removal of the pipework from the well. As oilfield scales are often radioactive, removal of the scale may require a special licence for disposal[43].

The converging flow patterns around a production well increase the likelyhood of injected water mixing with reservoir fluids and so increase the risk of scale within the reservoir itself. Scale precipitation in the reservoir formation has been a subject of controversy for some time. This controversy surrounds both the questions of whether scale within the reservoir exists and if it exists, whether it can cause any measurable damage to reservoir producibility. Certainly if scale were to form within the reservoir it would be very difficult to remove, as the reduction in permeability it causes would discourage the flow of any treatment through scaled regions. Thus, the only effective action that might be taken against scale formation within the reservoir is inhibition. Scale growth inhibitor treatments are already commonly used to control scaling of tubulars, but there is a great variation of opinion on how large treatments should be and how often they should be made. Before any questions as to how vital such treatments are for control of reservoir scale more information on the possible effects of such scale is required.

This thesis is the second of an on-going project investigating the extent and severity of oilfield scaling. The first work by Pucknell[35] covered most aspects of oilfield scale but concentrated more on scaling of production pipework. This thesis starts from the viewpoint that given the near irreversibility of scale deposition in the formation and the risk that scale could form close to production wells, the possible effects of scale on reservoir permeability should be investigated further. Because of the low solubility of barium sulphate and the

nature of the scale it produces, described further in chapter 2, this thesis concentrates specifically on barium sulphate scale.

Much data exists on the scaling of production tubing and "topsides"[12,49,51]. Very little has been published on the possible occurrence of scale within the reservoir formation. This is hardly surprising as scale in pipework can be easily observed, whereas scaling of the formation, at best, can only be inferred from careful monitoring of the composition of produced water. In a worst case scenario, a typical North Sea production well has the potential to produce 4 tonnes of barium sulphate scale per year. The nature of the barium sulphate precipitation reaction is such that it can precipitate very rapidly. Thus, it seems reasonable to expect that some scale will form in the formation. Some take the view that scale due to mixing of incompatible waters will not cause any noticible damage to reservoir producibility[26,32,51]. This thesis demonstrates that if scale were to form close to a production well its effects could be very serious. This possibility should not be neglected.

The results of scale deposition in the reservoir formation are difficult to assess in any simple manner. The reduction in permeability of one region of a reservoir due to scale will cause a change in the flow patterns that lead to the scale. Thus, it would require a reservoir simulator capable of modelling flows of various waters and the effects of any scale deposited, to judge whether formation scale is truly a risk to production. The work of this thesis is aimed at providing one part of such a simulator, that which predicts the effect on permeability of any scale formed.

The procedure followed in this work is to try to develop a model, which requires only what is known, or can be discovered about the fluids in the reservoir, to make its predictions. Experiments are performed with mixing incompatible waters in sandstone cores to assess how severely scale can damage permeability. The model is then used to

match experimental results to validate its operation. From this it is hoped that a larger model can be developed that will be applicable to a suitable reservoir simulator.

Chapter 2 of this thesis explains more of the nature of barium sulphate scale and discusses what other workers have achieved towards the aims of this work. In chapter 3 the theoretical basis of the preliminary model developed is described. The development of experimental equipment for providing the data required to run and match the model is described in chapter 4. This discussion includes details of the development of a new, two fluid injection system to provide greater control over mixing of the two waters in the experimental cores. The experimental work itself is described in chapter 5 where the results are analysed and discussed. In chapter 6 the sensitivity and behaviour of the model is discussed along with its simulation abilities. Proposals for extending the work are put in chapter 7 and the main conclusions presented in chapter 8. Some implications of the results of this work of direct applicability to oilfield and geothermal operations are also suggested in chapter 8.

CHAPTER 2

REVIEW OF THE OCCURRENCE AND STUDY OF BARIUM SULPHATE SCALE

2.1 INTRODUCTION

In the first thesis on this project[35], one of the objectives achieved by Pucknell was to gather together all relevant and published literature in the English language on the subject of oilfield scale. Consequently, the literature review in his thesis was very thorough and examined all aspects of scale considered in the available literature. Pucknell stated that because of the originality of his work in setting up a theoretical basis for the study of oilfield scale, as opposed to the try-it-and-see or troubleshooting approach used by many oil company researchers, his thesis was very broad-based. He pointed out that future work on this project would be more specific to one of the areas he considered. This is the case with this work, which considers the potential risk of scaling in the reservoir formation in greater depth.

As Pucknell's review was so thorough, discussion in this thesis will be limited to recently available literature and literature of direct relevance to the work described herein. There has been very little published recently that is of any great significance in this field.

2.2 THE PROBLEM OF SCALE

2.2.1 The Occurrence of Scale

Scale can occur at or downstream of any point in the production system, at which supersaturation is generated. Supersaturation can be generated in a single water by changing the pressure and temperature conditions or by mixing two incompatible waters.

Calcium carbonate scale generally forms because of a sharp reduction in pressure such as that which exists between the formation and the well bore and across any constriction in the production tubing, eg chokes and safety valves. The reduction in pressure liberates carbon dioxide into the gas phase leaving a solution supersaturated in calcium carbonate.

The various forms of calcium sulphate scale: gypsum; anhydrite and hemihydrate, can form due to an increase in temperature, since the solubility of calcium sulphate decreases with increasing temperature. Temperature increases occur as water passes down an injection well. Calcium sulphate can also form as a result of mixing incompatible brines in the formation or in the production pipework.

Barium sulphate has a decreasing solubility with decreasing temperature and so is likely to form as fluids cool on passage up a production well. However, because of its low solubility only small volumes of barium sulphate can be precipitated from a single water. Of greater risk is formation of barium sulphate from mixing two incompatible waters, which can lead to large supersaturations and hence large volumes of scale.

Once supersaturation has been created scale may not precipitate immediately. Supersaturated solutions can remain in a metastable condition for some time[30]. However, in an oilfield environment this is

unlikely to happen as there are many nucleation sites available. Precipitation may occur in the solution, the particles of scale being carried along until some change in the flow pattern causes them to be deposited. This deposition usually occurs at changes in pipe diameter or pipe direction. Thus, scale may by deposited a great distance from where it is generated.

Of all the scales, barium sulphate has been singled out for study in this thesis for several reasons:

i) it has the lowest solubility of all the common oilfield scales.

ii) it forms a hard scale that cannot easily be removed by chemical treatment.

iii) it is certain that many North Sea fields are likely to suffer from barium sulphate scale deposition during their lifetime.

Barium sulphate can precipitate very rapidly once supersaturation has been created. If the creation of supersaturation occurs deep in the reservoir the resultant precipitation and consequent permeability damage are unlikely to be of any risk to production. Indeed, it may even be of assistance by blocking off high permeability layers[22]. Such, useful, occurrence of scale can only be identified by a reservoir simulator. Creation of supersaturation near to the well-bore as separate flows of water converge, can cause problems in production by reducing near well-bore permeability[5,6].

2.2.2 The Nature of Barium Sulphate Scale

Composition

Barium sulphate scale is a crystalline deposit that is very adherent to many surfaces. It is composed mainly of barium and sulphate ions, but when deposited from complex polymetallic solutions can contain traces of many other ions. Barium sulphate often co-precipitates with strontium sulphate with which it is known to form a solid solution. Additionally, on precipitation from oilfield fluids, it can contain small amounts of wax, rust and silt.

Morphology

Both in this study and those of other workers[5,21,37,42] barium sulphate has been found to produce a large variety of crystal habits. Pucknell[35] put the change of crystal habit down to changes in solution supersaturation. However, this work shows that the habit is more dependant on the solution composition.

Obviously the crystal habit produced in any scaling situation will affect the possible permeability damage that the scale could cause. For the same quantity of scale being deposited, thin, flat crystals with high surface area to volume ratios will interfere with flow more than block-like crystals with low surface area to volume ratios. Special agents have been employed to try to change the habit of scale crystals to less damaging forms[22].

Growth sites

For scaling within the formation, which is under examination here, obviously the point at which scale crystals choose to grow will

be of importance to the permeability damage they can cause. It is very difficult to assess the location of scale with respect to the flows through a porous medium since all methods of observing the scale have a two dimensional viewpoint.

Pucknell[35] used micrographs of thin sections of scaled sandstones to demonstrate scale growth in pore throats. In this case the absence of the third dimension makes the identification of a pore throat somewhat subjective. Possibly the best technique for three dimensional visualisation of scale in place is stereoscopic imaging using a scanning electron microscope. Even this technique is difficult to interpret as the depth of field is limited to the depth of the surface pores and part of the structure has to be removed to gain access.

Growth of scale in the narrow channels that link pores will cause greater damage than would the same crystal growing in a wide pore body. Any preferred substrate for crystal growth could also influence the pattern of permeability damage in a rock containing several different minerals. Past evidence indicates that scale will grow all all substrates available in the reservoir rock[42].

2.3 REVIEW OF RELEVANT SCALE LITERATURE

As was mentioned earlier, the review of literature pertaining to barium sulphate precipitation and barium sulphate scale performed by Pucknell[85] was very thorough. There has been very little published in the field since he completed his review. In this thesis, much of the discussion of the contributions of other workers is presented within the discussion of the particular subject. A small discussion follows on relevant literature not described elsewhere in this thesis.

2.3.1 The Precipitation Reaction

Solubility models

In order to make any prediction as to the amount of precipitation that will occur, the level of supersaturation of barium sulphate in any given water system must be known. As described in chapter 3 the supersaturation is a key factor in the precipitation reaction. The supersaturation is a measure of how much of a salt is present in a solution above the amount that the solution can support. In order to assess the supersaturation the amount of salt the solution will support (ie the solubility, expressed as the solubility product) must be quantified. Such information can be obtained experimentally, but this is time consuming and becomes impractical when the solubility for many solutions of different compositions and under changing conditions are required. Thus, a quick and reliable method of predicting solubilities is required. With the general availability of high speed digital computers, a computer based model would seem to be the best approach.

Few of the models that have been developed for predicting solubilities of salts in reservoir type waters have been published. One, developed by Pucknell[35], is described in chapter 3 and makes solubility predictions for a single mineral in a given solution. Another model described by Vetter[52] goes a step further and considers which mineral will precipitate first from a given solution as the conditions change. In Vetter's model the solution compositions are then adjusted accordingly for making predictions on later precipitations. Vetter used his model to consider the whole cycle of oilfield water injection, passage through the reservoir and subsequent production, taking into account temperature and pressure changes and any assumed mixing. In this manner he claimed to predict problem zones for scale formation. This model comes a step closer to the model envisaged in chapter 1. However, it assumes a steady state condition of scale formation and does not allow for mixing patterns to change due to changing permeability. Also, any mixing it does allow for is assumed to result in complete removal of any supersaturation created by precipitation. No kinetic effects on precipitation were taken account of.

Another model for simulating the equilibrium condition of mixed oilfield waters was described more recently by Bertero, Chierici et al[4].

A major problem with using such predictive models for oilfield scales is in supplying the model with correct data on the scales concerned. Both Vetter[52] and others[34] have recognised that treatment of water samples from oilfields are seldom given the care required for a reliable analysis. For the case of scaling within the reservoir formation obtaining a relevant sample of brine is impossible anyway. In passing through a reservoir a brine can undergo many changes. Precipitations may occur due to changing pressure and temperature conditions or mixing of waters. Dissolution of the rock matrix may

also take place increasing the concentration of salts in the brine. Dissolution of indigeneous barium sulphate deposits in this way has been put foreward by Vetter[51] as a possible mechanism for scaling of production wells. Brine compositions may also be altered by cation exchange with clay minerals in the reservoir.

Barium sulphate precipitation

The barium sulphate precipitation reaction has always been of considerable interest to the world of analytical chemistry. The very low solubility of barium sulphate makes it of great use for determining the end point of titrations. Because of this, interest has been focussed on the rate of precipitation of barium sulphate. One of the most consistent workers in the field of sparingly soluble salts has been Nancollas, who, along with several different co-workers, has produced several papers covering barium sulphate precipitation over a range of temperatures[15,29,30].

In 1963 Nancollas and Purdie[30] demonstrated that the barium sulphate precipitation reaction followed second order kinetics and that confusion amongst other workers was probably due to an initial surge in precipitation, caused by nucleation processes. The rate equation proposed was modified in 1975 by Nancollas and Liu[29], when the surface area available for growth was also taken into account. It was demonstrated at this time that differing crystal morphologies had different densities of active growth sites on their surfaces. The work was extended to higher temperatures by Gardner and Nancollas[15] in 1983.

2.3.2 Crystal Morphology

The possible importance of crystal morphology in the permeability damage caused to reservoir rocks by scale was noted in section 2.2.2. As part of the interest in barium sulphate generated by analytical chemistry, some studies of barium sulphate crystal morphology have been performed[13,14,33,46,48].

Because of the size of crystals produced by spontaneous precipitation of barium sulphate, electron microscopy techniques are best suited for analysing the morphology of the crystals. One of the earliest studies was performed by Fischer[13] in 1951, who studied changes in crystal morphology due to aging. He also noticed that surface irregularities occurred in the crystals when grown in the presence of a foreign electrolyte. This work was followed up by Fischer and Rhinehammer[14] in 1953 with a study on the effect of various solution conditions on the crystals. Changes in the lattice ion concentration ratio, solution pH and temperature were all studied as well as the addition of some foreign ions.

In 1954 Suito and Takiyama published a paper[46] studying the effects of lattice ion concentration on the crystal morphology, which amounted to a study on changing solution supersaturation. Takiyama[48] followed this work in 1959 with a study of morphology changes on dissolution of barium sulphate. Okada and Magari[33] published work on barium sulphate crystal morphology for crystals produced from highly supersaturated solutions.

As part of work on the effects of crystal morphology on the kinetics of barium sulphate precipitation, Liu, Nancollas and Gasiecki[24] published electron photomicrographs of barium sulphate crystals grown under various conditions of solution composition and agitation. Additionally, several workers studying the effects of barium sulphate precipitation on permeability of various porous media

have published photomicrographs of the crystals they have produced[5,21,37,42].

2.4 OUTLINE OF STUDY

This study aims to investigate the nature of barium sulphate precipitate in a sandstone environment to discover its possible effect upon the permeability of the sandstone and to identify what factors control the nature of the scale. The information on the nature and effect of scale is gained experimentally by flooding sandstone cores with incompatible brines. The experimental data is used to develop and validate a model for predicting the permeability damage caused by scale.

The model is intended to provide a link between what is known or can be assumed about brines in an oil reservoir, the experimentally determined nature of barium sulphate scale and the observed pattern of permeability damage that can result from scale precipitation in a reservoir-type sandstone. Such a model could then be used in conjunction with a reservoir simulator for providing improved modelling of the potential hazards or uses of oilfield scale.

CHAPTER 3

DEVELOPMENT OF A MODEL TO SIMULATE THE EFFECT OF SCALE FORMATION IN A POROUS MEDIUM

3.1 INTRODUCTION

Over the last few years oil reservoir simulators have advanced to such a state where they can now map the movement of several different fluids through the reservoir. To utilise this feature the simulator might be given the existing formation brine and the injected brine to follow as well as the oil and gas movements. This, then, could provide information as to where the two brines mix and hence where scale formation is likely to be of concern. What it cannot tell is to what extent this scale growth will damage the permeability of the reservoir for a given brine mix and set of reservoir conditions.

Part of the aims of this project were to identify what factors affected the level of damage scale growth would cause to reservoir producibility and to what extent this damage might be expected to occur. This chapter describes the development of a model, which attempted to simulate these factors and their effects. The model provided a facility to discover what combination of simulated effects caused similar damage in a model to that observed in a real sandstone. This was seen as a first step towards filling the gap that existed in current simulators as far as formation of scale within the reservoir was concerned.

Several basic tools were required to perform this modelling. Firstly, it is a chemical principle that no scaling will occur without the creation of supersaturation. Thus, a model capable of predicting

the solubility of the scaling mineral in the brines in question and at the reservoir conditions was necessary to assess the level of supersaturation in the system. Secondly, in order to study the scale growth and its effect in a very complex medium like a reservoir sandstone, a model that could simulate the actual nature of the rock and the flows within it was required. Finally, and where this study most concerned itself, a means of linking these two models was required. That is, a model that could take into account the various factors involved in scaling and impliment them upon the reservoir rock model in a manner which would simulate the effect a real brine would have on a real reservoir rock.

3.2 SOLUBILITY PREDICTION

A variety of solubility prediction models have been described[4,35,52] that are suitable for the common oil reservoir scaling minerals. These are improving all the time, both in their accuracy and in the range of conditions over which predictions can be made. One of these models[35] was the work of a previous worker on this project, who elected to develop his own model as those which were generally available at the time did not cover the situation of reservoir brines adequately. This model was also used in this work for the reasons that it was readily available and its accuracy was adequate for the purposes of this work. This model is briefly described below.

3.2.1 Introduction to the Solubility Prediction Model

The solubility prediction model developed by Pucknell[35] was far more empirical than many of its peers and often reflected the hurried nature of its creation. Nevertheless, its predictions have been shown to be quite successful. It was based upon a correlation of a mass of experimental data using some theoretical equations, but mostly just polynomial curve fitting. The experimental data was gathered from a great many papers on the solubility of the scale-forming minerals as well as many standard data books. The data were sifted to remove data of dubious quality due to poor experimental technique or occasionally because of wide variations between data offered by different authors. The remaining data was grouped according to the ionic strength of the solution, the temperature, pressure and according to what other ions were present in the solution.

3.2.2 Making the Correlations

The correlation of the selected and grouped data was made in several stages.

The basic solubility, ionic strength and temperature correlation

The main base of the correlation was made from data for solubilities of barium sulphate in sodium chloride solutions or distilled water at a variety of temperatures. At each temperature the available data was fitted to a modified version of the Debye-Hückel equation (equation 3.1) to give a set of coefficients, K, B, C and D. These four coefficients were then correlated with temperature by a polynomial equation (equation 3.2).

$$\ln Q = K + \frac{AI^{1/2}}{(1 + BI^{1/2})} + CI + DI^2 \quad \ldots\ldots\ldots (3.1)$$

$$K, B, C, D = a_0 + a_1T + a_2T^2 \quad \ldots\ldots\ldots\ldots (3.2)$$

where: Q = solubility product

I = ionic strength

T = absolute temperature

A = Debye-Hückel coefficient defined by theory

K,B,C,D = Debye-Hückel coefficients from correlation

a_0, a_1, a_2 = temperature correlation coefficients

Most data in the literature were for barium sulphate in distilled water or in sodium chloride solution at atmospheric pressure. Significantly less data were available at higher pressures or for solutions containing other ions. Thus, the basic correlation using the

Debye-Hückel equation was made for atmospheric pressure, with higher ionic strengths created by the presence of sodium chloride only.

The pressure correlation

The rest of the correlation for data available at different pressures and including other ions in the solution, such as calcium and magnesium, was made in such a way as to provide a correction to the solubility calculated from equation 3.1. The reason for this was that to perform a full correlation for pressure and the presence of other ions would require considerably more data than was available. In order to correlate data from other pressures a correction term based on the pressure integral of volume change (the difference between the partial molal volumes of the ions and the molal volume of the mineral they constituted) was used.

$$\ln Q = \ln Q_r - \frac{1}{RT} \int_{P_r}^{P} \Delta V \, dP \quad \ldots\ldots\ldots\ldots\ldots (3.3)$$

where: Q = solubility product

Q_r = reference solubility product calculated at the reference pressure

P_r = reference pressure

P = pressure

ΔV = volume change

R = gas constant

T = absolute temperature

To use this equation the pressure integral was related to the standard state volume change by an empirical relationship with ionic strength. The resulting equation is given in equation 3.4. Using

equation 3.4 the standard state volume change (i.e. that at infinate dilution) was integrated with respect to pressure and then corrected for the ionic strength of the solution. This integrated equation was used for correlating solubility data at higher pressures. Coefficients a and b were calculated from this correlation for each mineral for which predictions were required. The standard state volume change was calculated from a set of theoretical and empirical equations given in Pucknell's thesis[35].

$$\ln Q = \ln Q_r - \frac{1}{RT} \int_{P_r}^{P} \Delta V^\circ \, dP \exp(aI^{1/2} + bI) \quad \ldots\ldots \quad (3.4)$$

where: ΔV° = standard state volume change considered to be independant of pressure.

Correlation of the effects of other ions

Wholly theoretically based models can take into account many ion interactions such as ion pairing and the common ion theories. These interactions generally tend to enhance solubility. For this model, based on experimental data, corrections to the solubility calculated from the basic correlation, equation 3.1, could only be made for those effects for which there were sufficient experimental data. This limited this model to corrections for calcium, magnesium and sulphate ions only.

The correction for sulphate ions refered to there being an excess of sulphate ions over metal ions, in the solution, for the mineral concerned. The correction was correlated for calcium sulphate with the consideration that the magnitude of the correction would be the same for barium sulphate. The correlation was made via an equation containing an interaction coefficient, α, for a term expressing the

sulphate excess, S_e, as shown in equation 3.5.

$$\ln Q = \ln Q_r + \alpha S_e \quad \ldots\ldots\ldots\ldots (3.5)$$

where: $$S_e = \sqrt{d^2 + 4Q} - 2\sqrt{Q_r} \quad \ldots\ldots\ldots (3.6)$$

$$d = |m_{Ca} - m_{SO_4}|$$

m_x = concentration of ion x

The ionic strength dependance of the interaction factor was allowed for by correlating it with the log of the ionic strength.

$$\alpha = a_1 + a_2 \ln I + a_3(\ln I)^2 \quad \ldots\ldots (3.7)$$

For calcium ions the correction used was a simple product of an interaction coefficient with the concentration of the calcium ions. Again the interaction coefficient was correlated with the log of the ionic strength as in equation 3.7 above.

$$\ln Q = \ln Q_r + \alpha\, m_{Ca} \quad \ldots\ldots\ldots\ldots (3.8)$$

The data for the magnesium correction suggested that its effect was combined with that for the sulphate excess. Thus, an empirical equation was used to combine the two terms. As before each of the interaction coefficients (α) was correlated with ionic strength as in equation 3.7.

$$\ln Q = \ln Q_r + (\alpha_1 - \alpha_2\, m_{Mg})\, S_e + \alpha_3\, m_{Mg} \quad \ldots\ldots (3.9)$$

As the data for the ion corrections was quite sparse a full

temperature correlation could not be made. Instead the data was correlated in temperature ranges to provide a set of coefficients for each range.

3.2.3 Accuracy of the Model

The result of all these correlations was a large set of coefficients. The model merely selected the correct coefficients for the conditions and substituted them into the relevant equations to make its predictions. The technique was quite successful, Pucknell reported a 90% success rate in predicting the type of scale likely to be present in over 50 different cases from around the World. This success was achieved, however, by predicting the level of supersaturation for each of the common oilfield scales and declaring them likely to form if any prediction of supersaturation was greater than 1.

For assessing the accuracy of the solubility prediction, Pucknell used his model to predict the solubility measurements used in the correlations. He produced statistics and plots of deviations based on a comparison of the predictions with the experimental data used for the correlation. For barium sulphate he reported a relative standard deviation (defined in equation 3.10) of 21.3% for the 248 data points used in the barium sulphate correlation. Of these points 3.6% were over-predicted by more than 20% and 6.8% were under-predicted by more than 20%.

$$\text{Relative standard deviation} = \sqrt{\frac{1}{n} \sum \left[\frac{Q_e - Q_p}{Q_p}\right]^2} \quad \ldots (3.10)$$

By far the larger proportion of the points in the plots of percentage deviations Pucknell presented, lay within ±15% of their predicted value. Thus, a prediction of barium sulphate solubility from

this model could be considered to be of an accuracy within 20%. Advanced theoretically based models can give more accurate results than this[4]. However, they have long run times, take a great deal of expense to develop and thus are not generally available.

3.2.4 Using the Model

All the coefficient selection and calculations involved in making solubility predictions and supersaturation calculations in the Pucknell model were handled by computer, which made the model very simple to use. It did have some drawbacks though.

The model would only ever be as good as the data that was used in the correlation. In his selection of data Pucknell had tried to avoid using data that appeared to be obviously erroneous when plotted against other data, which was often justified by a consideration of the experimental procedure used to make the solubility measurement. In some cases, though, his judgement was questionable. Even so, if a large number of data were used, the presence of some not-so-good data would be almost unnoticible.

The problem of the quantity of data used for the correlation raised the question of increasing the size of the data set used. In the Pucknell model this would be a very lengthy task, which, although also computerised, would involve a lot of visual judgement of how well curves fitted to data and generally shunting data about from one programme to another. Thus, it would only be worth while remaking the correlation by this means if a large amount of new data became available. A search of recent literature showed that almost no new data on barium sulphate solubility had been published since Pucknell completed his model. It seemed unlikely that the accuracy of this model would ever be improved without reassessing the whole of the data

set as to what was "good" or "bad" data or increasing the theoretical basis of the model.

3.3 POROUS MEDIA MODELLING

3.3.1 Choice of Model

Required properties of the model

There were a variety of types of model that could be used to represent a porous medium such as a reservoir sandstone. These differed widely in their accuracy of modelling the chosen medium, ease of computation and ability to support modifications required to simulate permeability damage to the medium. Before a type of model could be chosen, it was necessary to consider the ideal properties the model should possess for the task in hand.

Firstly, the model should be capable of producing a reasonable relationship between porosity and permeability for the material concerned. Earlier scale growth experiments[42] have shown that a great deal of permeability damage can result with only a small loss in porosity of the sandstone. This result should be reflected by the model.

Secondly, the mathematics involved should be fairly simple and readily understood. This requirement was specified so that different techniques of simulating growth of scale in the model could be readily programmed. Also, as the work of this study was of a somewhat pioneering nature, the model had to be suitable for being used and manipulated by later workers of many different disciplines.

Thirdly, as much development work would be required, the computation time required to run the model should not be excessive, especially as the porous media model would need to be run many times during a simulation of scale growth.

Types of model

Suitable models could be split into three main groups: i) those that consider relationships between porosity and permeability and do not attempt to model pore space; ii) capillaric models that consider the pore space to be a system of discrete tubes and iii) network models which simulate the medium by a lattice of interconnected tubes

In his study of dissolution of calcareous sandstones by carbonated brines, Scott-Will[40] performed a useful review of most of these types of models and their suitability for modelling oilfield sandstones. The system he was modelling was different in that he was considering pore space increasing in size whereas in this study the pore space would be decreasing in size. His general requirements for the model were broadly similar though.

Suitability of the models

Models based solely on porosity-permeability relationships were considered not to be useful due to their inability to simulate the sandstone with any degree of reliability. Scott-Will eventually elected to use a capillaric model as the difficulty of the increasing pore space was more easily handled. This was not a problem in this study. Of more concern here was that capillaric models did not allow for any cross-flow between channels. Through the use of pore size disributions and lithology factors, capillaric models could produce good porosity-permeability relationships. However, in a scaling environment the small tubes would be quickly closed at their entrance end, which would remove all contribution to permeability from small pores very early on in the simulation.

In a network model, with its ability to allow cross-flow

between channels, the large and small pores would be distributed randomly throughout the model. Thus the closing of any small pores would not necessarily close off flow to similar pores deeper into the network.

In his review Scott-Will admitted that the network model, once supplied with a pore size distribution, could produce accurate results for permeability and porosity without resort to a lithology factor. These results tended to be better for sandstones with narrow pore size distributions, such as Clashach sandstone, than for those calcareous sandstones with wider distributions that he was working with. The experimental work in this study was performed wholly with Clashach sandstone. Apart from the problem of growing pore space, Scott-Will also cited large computing times as a major reason for not using a network model. As this project had access to considerable computing power this objection was considered not relevant in this case.

From the discussion above it is clear that the network model was the most suitable porous media simulator available for use in this project.

3.3.2 Structure of the Network Model

The network model used in this study was of the square lattice type. The reason for this was that it was developed as part of a parallel study on the quality of injected water with respect to suspended particles[44,45,50] and so was readily available in working form to this project.

The model consisted of a square lattice of capillaries (pores), as shown in figure 3.1. The points where the capillaries meet, or for the inlet and outlet faces where they end, are referred to as nodes. Each capillary consisted of three sections (see figure 3.2). At either end

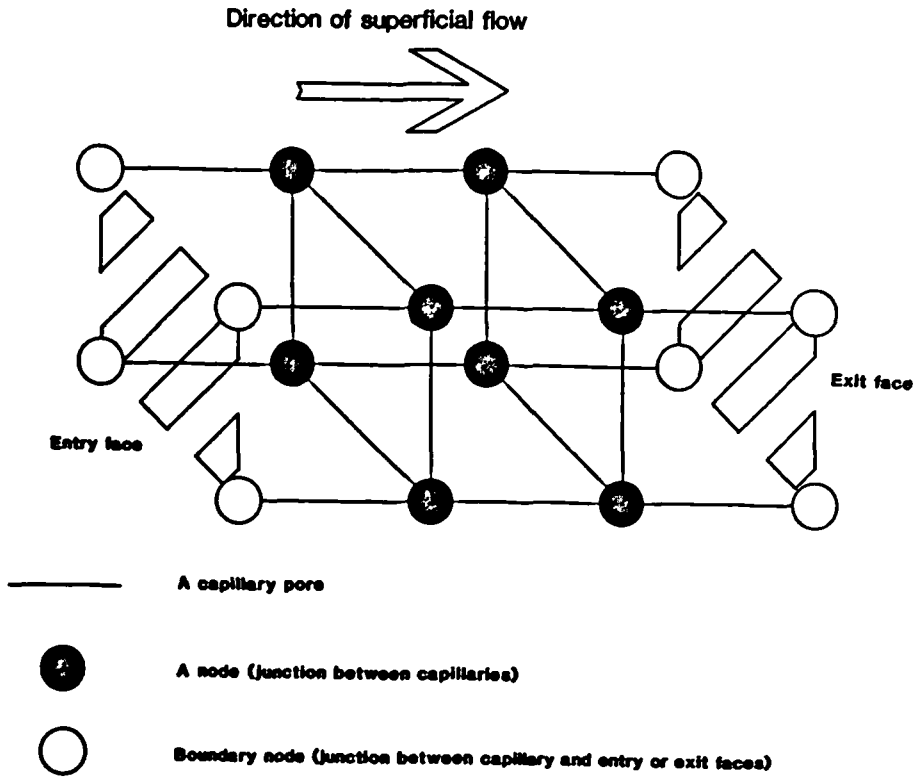

Figure 3.1 Square lattice structure of network model

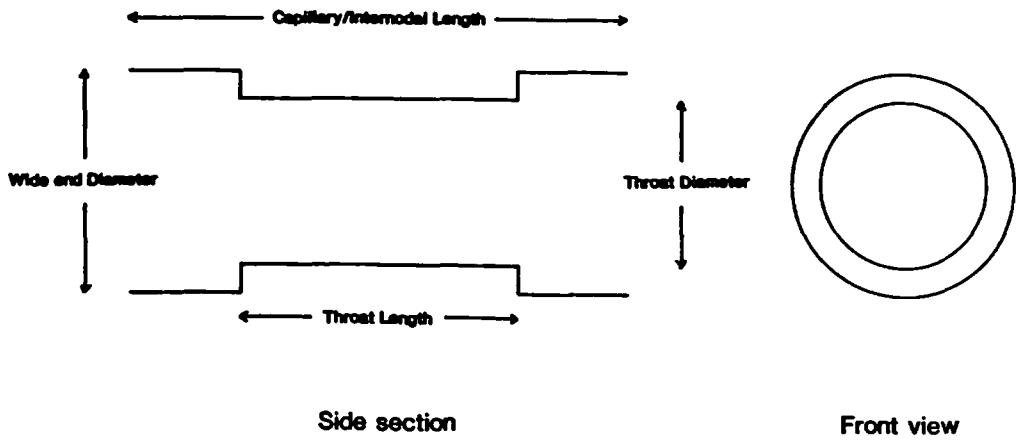

Figure 3.2 Structure of capillaries used in network model

the capillary had a fixed "wide-end" diameter which was the same for all capillaries in the network. Linking the two wide-ends was a narrower "throat". The total length of a capillary or inter-nodal length was fixed when the network was set up. The throat length was determined from a reciprocal relationship with the throat diameter, shown in equation 3.11, but was constrained to a maximum length equal to the inter-nodal length.

$$L_{thr} = \frac{L_{cap}}{2} \frac{D_{max}}{D_{thr}} \quad \ldots\ldots\ldots\ldots (3.11)$$

where: L_{thr} = throat length

L_{cap} = capillary or inter-nodal length

D_{max} = diameter of largest throat in the network

D_{thr} = throat diameter

The nodes themselves had no physical existence and could be considered to consist of the wide-ends of the pores that meet at the nodes. Figure 3.3 shows a 3-dimensional schematic diagram of a stochastic network. This is for visualisation purposes only and should in no way be compared to the structure of the pore space in a real piece of sandstone.

3.3.3 Description of Flow in the Network Model

The basic flow equation

The flow in the capillaries of the model was assumed to be laminar. Thus, the relationship between flowrate and pressure drop could be described by the Hagen-Poiseuille equation for laminar flow in

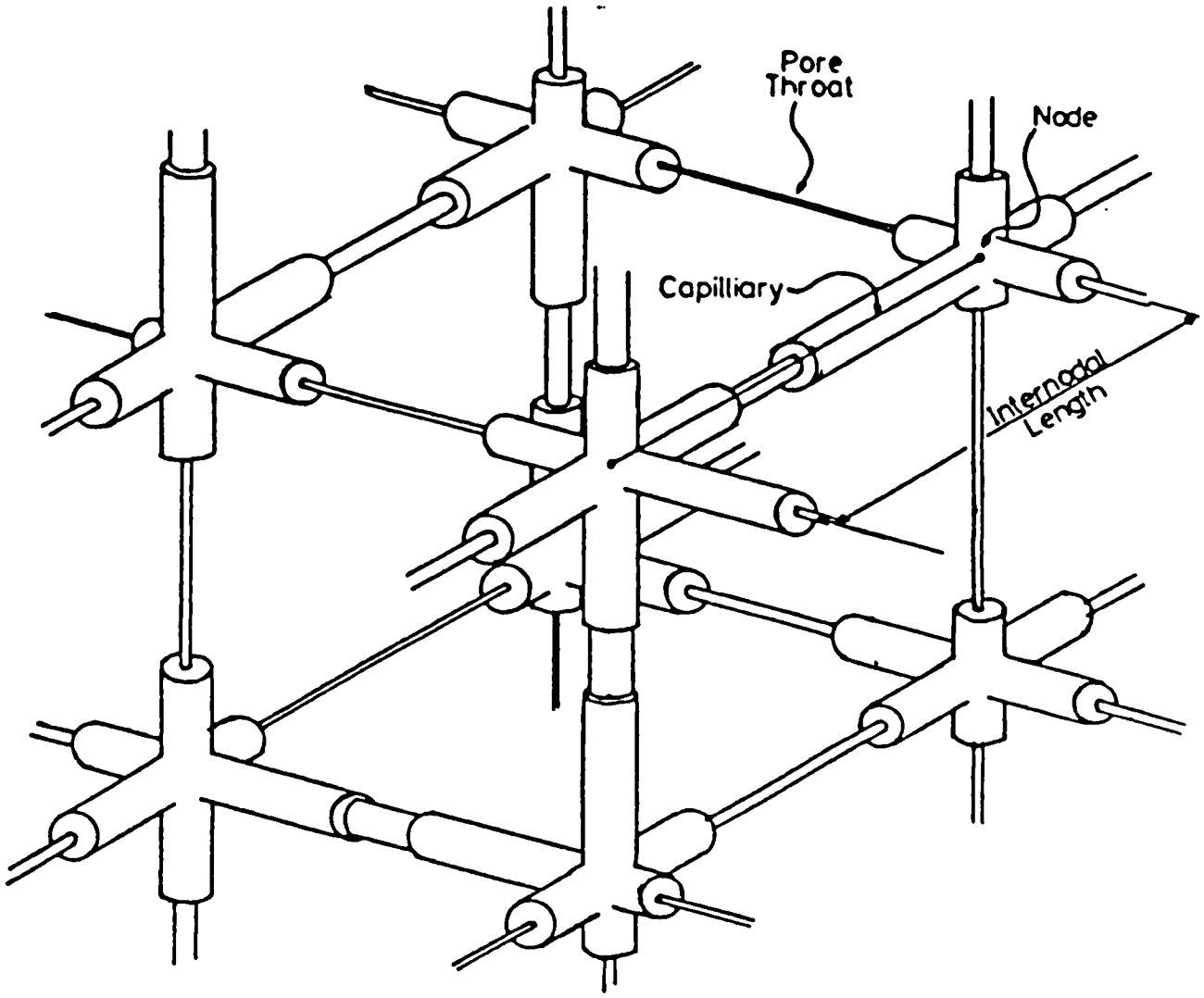

Figure 3.3 Three-dimensional representation of stochastic network model (after Scott-Will)

a pipe, equation 3.12.

$$q = \frac{\pi d^4}{128 \mu} \frac{\Delta P}{l} \qquad \ldots\ldots\ldots\ldots (3.12)$$

where: q = capillary flowrate

d = diameter of flow path

ΔP = pressure drop across flow length

l = flow length

μ = fluid viscosity

Taking account of the capillary wide ends

In the original model the flow length considered was just the throat length. However, for the purposes of studying scaling damage it was considered necessary to take account of the effect of the wide-ends of the capillaries as well. It will be described later how the majority of scale tended to form in the wide "bodies" of pores in the rock. Even though scale growth in the bodies of pores would have a much smaller effect on flow than scale growth at the constrictions between pores, it could still occur to such an extent that its contribution towards limiting flow through the rock became important. Thus, it was necessary that the model should be able to take account of scale growing in the wide-ends of the capillaries as these, for the model, represented the wide "bodies" of pores seen in the rock.

To take into account the wide ends of the capillaries each capillary was split into three flow lengths and equation 3.12, in the form of equation 3.13, was written for each.

$$q_i = K_{ai} (P_{in} - P_{out}) \quad \ldots\ldots\ldots\ldots (3.13)$$

where: $$K_{ai} = \frac{\pi d_a^4}{128 \mu l_a}$$

P_{in}, P_{out} = inlet and outlet pressures for flow length a of capillary i.

As the flowrate through the capillary as a whole was fixed, it could be used to equate the three flow length equations together to give a combined equation for the capillary, equation 3.14.

$$q_i = K_i (P_u - P_d) \quad \ldots\ldots\ldots\ldots (3.14)$$

where: $$K_i = \frac{1}{\frac{1}{K_{ai}} + \frac{1}{K_{bi}} + \frac{1}{K_{ci}}}$$

P_u, P_d = upstream and downstream pressures for the capillary

Equation 3.14 was written for every capillary in the network to express the capillary flowrate in terms of the pressure at either end and the dimensions of the capillary.

Solving the flow equations

Using a convention that flow into a node was positive, a materials balance on a node, assuming no accumulation, yielded equation 3.15.

$$\Sigma q_i = 0 \quad \ldots\ldots\ldots\ldots\ldots\ldots (3.15)$$

Writing this equation for every node within the network, ie not for nodes in the inlet and outlet faces, resulted in a set of simultaneous equations in the nodal pressures. These could be represented in matrix form as shown in figure 3.4. All that was now required to solve this system was a boundary condition.

Constant pressure drop boundary condition

There were two boundary conditions available in the model. The first was for a constant pressure drop across the network, for which the pressures at the nodes on the inlet and outlet faces were specified.

Each row of the matrix in figure 3.4 represented a nodal summation equation (equation 3.15). The inlet and outlet face nodes had only one flow associated with each node, thus there was only one term in the nodal summation equation, which appeared on the leading diagonal. As the solution to such an equation was trivial the leading diagonal term was equal to 1. The modification to the matrix system for a constant flowrate boundary condition is shown in figure 3.5.

Constant flowrate boundary condition

The second boundary condition that could be applied to the model was for constant flowrate. If the total flowrate was fixed then the sum of the flows in the capillaries leading from the inlet face would be equal to the total flowrate, as in equation 3.16.

$$\Sigma q_{inlet} = q_t \qquad \ldots\ldots\ldots\ldots \quad (3.16)$$

Substituting into equation 3.16 from equation 3.14 and noting that all the pressures of the front face nodes would be equal, lead to

$$
\begin{bmatrix}
0 & 0 & 0 & 0 & 0 & 0 & 0 & 0 & 0 & 0 & 0 & 0 & 0 & 0 & 0 & 0 \\
0 & 0 & 0 & 0 & 0 & 0 & 0 & 0 & 0 & 0 & 0 & 0 & 0 & 0 & 0 & 0 \\
0 & 0 & 0 & 0 & 0 & 0 & 0 & 0 & 0 & 0 & 0 & 0 & 0 & 0 & 0 & 0 \\
0 & 0 & 0 & 0 & 0 & 0 & 0 & 0 & 0 & 0 & 0 & 0 & 0 & 0 & 0 & 0 \\
K_A & 0 & 0 & 0 & \Sigma_5 & K_E & K_F & 0 & K_I & 0 & 0 & 0 & 0 & 0 & 0 & 0 \\
0 & K_B & 0 & 0 & K_E & \Sigma_6 & 0 & K_G & 0 & K_J & 0 & 0 & 0 & 0 & 0 & 0 \\
0 & 0 & K_C & 0 & K_F & 0 & \Sigma_7 & K_H & 0 & 0 & K_K & 0 & 0 & 0 & 0 & 0 \\
0 & 0 & 0 & K_D & 0 & K_G & K_H & \Sigma_8 & 0 & 0 & 0 & K_L & 0 & 0 & 0 & 0 \\
0 & 0 & 0 & 0 & K_I & 0 & 0 & 0 & \Sigma_9 & K_M & K_N & 0 & K_Q & 0 & 0 & 0 \\
0 & 0 & 0 & 0 & 0 & K_J & 0 & 0 & K_M & \Sigma_{10} & 0 & K_O & 0 & K_R & 0 & 0 \\
0 & 0 & 0 & 0 & 0 & 0 & K_K & 0 & K_N & 0 & \Sigma_{11} & K_P & 0 & 0 & K_S & 0 \\
0 & 0 & 0 & 0 & 0 & 0 & 0 & K_L & 0 & K_O & K_P & \Sigma_{12} & 0 & 0 & 0 & K_T \\
0 & 0 & 0 & 0 & 0 & 0 & 0 & 0 & 0 & 0 & 0 & 0 & 0 & 0 & 0 & 0 \\
0 & 0 & 0 & 0 & 0 & 0 & 0 & 0 & 0 & 0 & 0 & 0 & 0 & 0 & 0 & 0 \\
0 & 0 & 0 & 0 & 0 & 0 & 0 & 0 & 0 & 0 & 0 & 0 & 0 & 0 & 0 & 0 \\
0 & 0 & 0 & 0 & 0 & 0 & 0 & 0 & 0 & 0 & 0 & 0 & 0 & 0 & 0 & 0
\end{bmatrix}
\times
\begin{bmatrix} P_1 \\ P_2 \\ P_3 \\ P_4 \\ P_5 \\ P_6 \\ P_7 \\ P_8 \\ P_9 \\ P_{10} \\ P_{11} \\ P_{12} \\ P_{13} \\ P_{14} \\ P_{15} \\ P_{16} \end{bmatrix}
=
\begin{bmatrix} 0 \\ 0 \\ 0 \\ 0 \\ 0 \\ 0 \\ 0 \\ 0 \\ 0 \\ 0 \\ 0 \\ 0 \\ 0 \\ 0 \\ 0 \\ 0 \end{bmatrix}
$$

K_x = "K"-factor for capillary x

Σ_i = Negative sum of "K"-factors for capillaries connecting with node i

P_i = Pressure at node i

Figure 3.4 System of flow equations for main body of network shown in figure 3.1

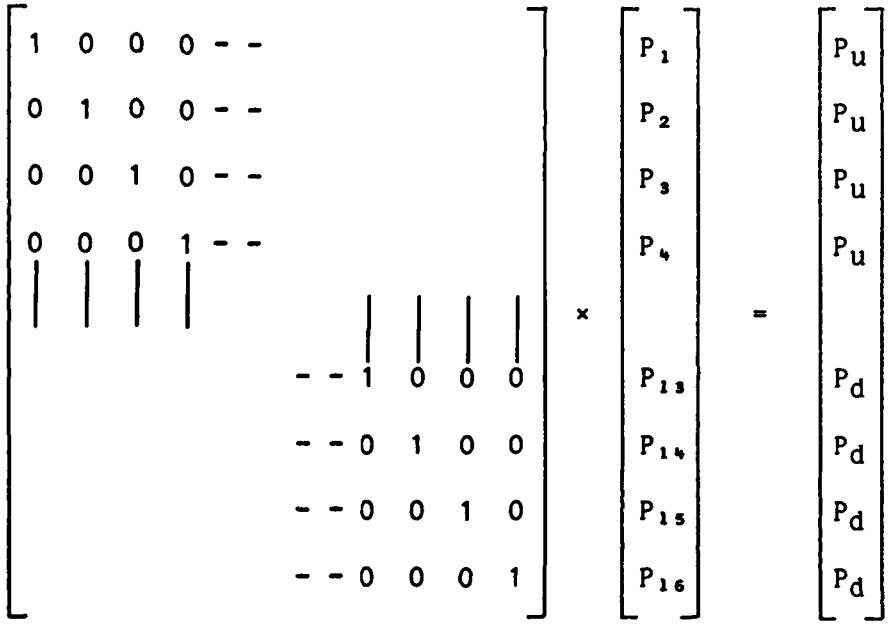

P_u = Pressure at entry face of network

P_d = Pressure at exit face of network

Figure 3.5 Modification of flow equation matrices for constant pressure drop boundary condition

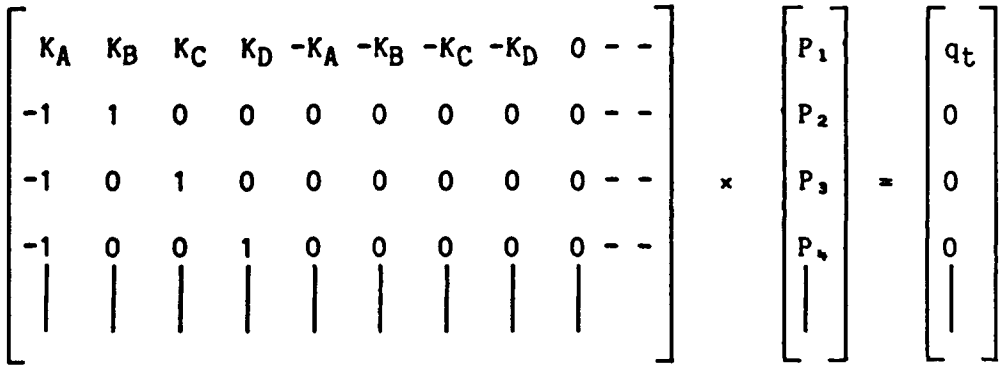

q_t = Total flowrate through network

Figure 3.6 Modification of flow equation matrices for constant flowrate boundary condition

the modification to the matrix system shown in figure 3.6. The outlet face condition was specified in the same manner as for the constant pressure drop case.

Performing the solution

This, then, was the manner in which the flow equations for the model were set up. The matrix of K factors (see equation 3.14) was a square matrix of an order equal to the number of nodes in the network. As there were only seven elements per row, the matrix equation was emminently suited to sparse matrix solution techniques.

Once solved to give either the total flowrate or the pressure drop, depending upon which boundary condition was used, this information could be used along with the external dimensions of the network in the Darcy equation to calculate the permeability of the network model.

3.3.4 Setting up the Network Model

The method by which the network was generated, ie the sizing of the pore throat diameters, was designed to give a close match with an experimentally derived pore size distribution and associated porosity.

Assigning the pore throat sizes

For each capillary in the network a random number generator was used to obtain a saturation value. The corresponding pore throat diameter was then found from a capillary pressure curve generated by mercury penetration porosimetry on a sample of the rock to be simulated.

Matching porosity

Once all the throat sizes had been assigned the porosity was calculated based on external dimensions of the network and the sum of the volumes of all the capillaries. The porosity was then matched to the experimental porosity by adjusting the overall dimensions of the network through increasing or decreasing the internodal length.

This technique should always give a close match of porosity. Obviously, due to the random technique of applying pore throat sizes, the matching of pore size distributions would improve as the total number of pores in the network increased.

Validity of permeability results

The permeability of the network was found by performing the calculation described at the end of subsection 3.3.3. As no matching was performed, the permeability was dependant upon how well the network was set up. It has been shown that this model, although giving good general agreement with experimentally derived permeabilities, did tend to overpredict permeability especially in the lower permeability range[50]. This was considered to be due to an unrepresentatively low proportion of small pores being generated.

3.3.5 Usability of the Network Model

Evidence suggested[11,16,50] that the network model was a very capable simulator of a porous medium given that: i) a sufficient number of pores were used in the network and ii) the techniques involved in generating the network could be further enhanced to give

better permeability matching. On the first point Golshan[16] considered there was little reason in increasing the number of capillaries above 3000.

It was not within the scope of this project to develop or improve the accuracy of porous media simulators other than those modifications required to suit the modelling of scale growth. It was considered that the accuracy of the current network model, described above, was sufficient for the purposes of this work, to identify means by which scale damage to porous sandstones may be simulated.

3.4 MODELLING PRECIPITATION

3.4.1 Scope of the Model

It was stated earlier that the aims of this project were to identify the factors involved in the creation of the many different forms of scale that have been observed[5,21,35,37,42] and the means by which the damage caused by this scale could be modelled. In view of this several constraints were placed on the scope of the precipitation modelling to enable these aims to be achieved within the time span of the project. These constraints were:-

i) the computing time required to carry out the precipitation part of the modelling should be equivalent to and preferably much less than, that for solving the porous media model. This condition was made to keep the run time of the model within sensible limits for a development tool and to conserve the limited resources of high power computing time available in order to maximise testing of the abilities of the model.

ii) the model should produce a satisfactory comparison with experimental results for the changing relationships between pore size distribution, porosity and permeability.

iii) the model should be based on parameters that could be easily adjusted to change the response of the model to the physical conditions it was subjected to. This was so that the model could be tuned to simulate real systems before being used in a predictive role.

The principle of modelling

When developing a computer model it should always be bourne in mind that the aim is not necessarily to come up with a close digital representation of the physical process under study. The principle of modelling is to simulate, with the required degree of accuracy, the system to be studied and the response of that system to changes in the conditions placed upon it. For example, in the model of a sandstone core and the process of scaling occuring within it being considered here, the manner in which the model makes its calculations is of no consequence provided the changes in permeability that the model predicts, which is the required result, reflect the results from a real core for the same conditions of supersaturation, flowrate etc.

If the development time of the model and the speed at which it produces its results are of any importance, then the simplest model that can fulfill the principle of modelling, described above, will be the best to use. Obviously if, at any time, the need for greater accuracy arose, then the model would have to be enhanced to go into greater detail of the process. The need for this would have to be set against the increased computational time necessary to produce results from the model.

Restrictions of computing power

As computing power and speed were expected to continue to increase in the future it might be possible to improve the model without significant increase in the computing time required. At the time of writing it was felt that the development of a model to try to simulate the "macro" effects of pressure drop and permeability loss in a small, experimental, sandstone core was all that could be reasonably expected, given the conditions above and the computing power

available.

Obviously it would be desirable to model the flow of brines through the network in terms of their component ions. Starting with the two brines separate and entering from different areas of the inlet face of the network, the flow of the brines' components could be mapped and new compositions calculated from the mixing of different flows at the nodes. In order to calculate the scaling tendancy for precipitation in the pores it would be necessary to run the solubility prediction model for every node in the network. Even compared to the considerable time required to solve the flow matrix for the network model, the time to perform this sort of modelling would be long. This sort of model was regarded as a much later development to what was required for this study.

The rest of this section describes the techniques used to extend the porous media network model to simulate the effects of scale formation in the porous medium. The results of testing this model and its ability to simulate the scaling process are discussed in chapter 6.

3.4.2 Background Theory

Control of the precipitation process

The question of how much scale can form is a problem for chemical thermodynamics. The question of how much scale will form is the domain of chemical kinetics. The former problem was answered using the solubility prediction model. From a knowledge of the solubility of a salt in a given solution, the supersaturation, being a measure of the excess salt present in the solution above the limit described by the

solubility, could be calculated. Thus, the potential amount of salt that could precipitate from the solution could be found. The thermodynamics relating to this exercise for the solubility prediction model used in this study may be found in the work where this model was developed[35].

The level of supersaturation provided a measure of the driving force behind the precipitation process, however, this was not the only factor involved. Solutions can sustain quite a high level of supersaturation without any precipitation at all[30]. The key to whether precipitation occurs was in the onset of nucleation. Without nucleii to grow on, the salt would remain in solution. The subject of how, when and at what rate nucleii form is extensively covered in many standard crystallization texts and was also covered in Pucknell's work[35].

Nucleation

In the environment of a reservoir sandstone there is a large specific surface attributable to the surface of the grains of which the rock is composed. There is also a large quantity of fine particulates drifting about which could easily act as nucleii for any precipitating salt. Thus, the mode of nucleation for a supersaturated brine flowing through this medium was considered almost certainly to be heterogeneous. Any contribution from homogeneous nucleation would be small owing to the high supersaturation required before homogeneous nucleation would occur to any significant extent[25,31]. Thus, for the case in question the mode of nucleation was expected to be heterogeneous and because of the large amount of heterogeneous nucleation sites available and the possible levels of supersaturation, was likely to be almost instantaneous[34].

Crystal growth

With no effect expected from the need to form nuclei, the problem reduced to one of how quickly would the scale grow on these immature crystals. Once again standard texts detail all the popular theories on rates of growth being limited by diffusion of ions through the solution, reactions on the surfaces of crystals and the like. Although theory can shed some light on the processes involved, it can never predict what the actual rate of growth of a crystal will be. The rate of precipitation can only be determined by experimental measurements.

3.4.3 Development of an Expression for the Amount of Scale in a Pore

The precipitation rate equation

The work of Nancollas and co-workers[15,24,29,30] on seeded crystal growth techniques in bulk supersaturated solutions showed that, after a growth surge on adding the crystals, the growth followed a rate law of the type shown in equation 3.17.

$$\frac{d[C]}{dt} = - k s S^n \quad \ldots\ldots\ldots\ldots\ldots (3.17)$$

where: [C] = concentration of ion C

t = time

S = supersaturation

k = rate constant

s = "surface area" term

n = order of reaction

Nancollas et al found that for the bulk of an experiment the order term, n, would have a value of 2 while in the initial growth surge a value between 3 and 4 could be expected. The initial growth surge was explained as being the result of there being insufficient growth sites on the seed crystals for the level of supersaturation in the solution. This was verified by the disappearance of the the surge period on reducing the supersaturation or increasing the number of seed crystals.

The arguments in subsection 3.4.2 suggested that there would be no shortage of nucleation/growth sites in a sandstone core. Therefore equation 3.17 could be used, with n equal to 2, to express the change in solution concentration of the scaling minerals with time.

Integration of the rate equation

Expressing the supersaturation as in equation 3.18, allowed equation 3.17 to be integrated to give equation 3.19, assuming the rate constant and surface area term were independant of time. This assumption was reasonable for the rate constant. The implications of the surface area term will be discussed later.

$$S = \frac{[C]_i - [C]_o}{[C]_o} = \frac{[C]_i}{[C]_o} - 1 \quad \ldots\ldots (3.18)$$

where: $[C]_i$ = concentration of scaling ion (ie barium) at any time t_i

$[C]_o$ = concentration of scaling ion at equilibrium (ie saturation)

$$\frac{1}{S_f} - \frac{1}{S_b} = \frac{k\ s\ \Delta t}{[C]_o} \quad \ldots\ldots\ldots (3.19)$$

where: S_b = supersaturation at beginning of time period

S_f = supersaturation at end of time period

Δt = length of time period

Equation 3.18 expresses supersaturation as the relative supersaturation. The relative supersaturation has the advantage of being equal to zero when the brine is just saturated, which was easier to handle mathematically. Supersaturation is usually expressed as the fractional supersaturation, which is the ratio of $[C]_i$ and $[C]_o$. The fractional supersaturation has a value of 1 at saturation.

Application of precipitation equation to flowing brines

Equation 3.19 related to the change in supersaturation, over a given time period, of a non-flowing bulk solution. The network model, however, considered a flowing solution. To make use of equation 3.19 the flow through the capillaries of the network model was likened to a series of small packets of fluid that had no significant mixing with the packets of fluid in front or behind them. This assumption was considered reasonable as the flow in the capillaries was laminar at the flowrates used in the model.

By setting S_b to the supersaturation at the inlet end of a capillary and Δt to the time for a packet of fluid to pass through the capillary, equation 3.19 could be applied to calculate the level of supersaturation in the packets of fluid leaving the capillary. In this case equation 3.19 was more appropriately written as equation 3.20.

$$\frac{1}{S_{out}} - \frac{1}{S_{in}} = \frac{k\ s\ t_p}{[C]_o} \qquad \ldots\ldots\ldots (3.20)$$

where: S_{in} = supersaturation at pore inlet

S_{out} = supersaturation at pore outlet

t_p = time to cross pore

Calculation of the nodal supersaturations

By writing equation 3.20 for every capillary in the network all the outlet supersaturations could be calculated if the inlet supersaturations were known. The inlet supersaturation to any pore was considered to be that of the node from which flow entered the pore. The supersaturation at the node would be a function of the flows entering it.

For the purposes of modelling it was useful to consider the nodal supersaturation to be the result of perfect mixing of all the flows entering it. Thus, the nodal supersaturation was given by equation 3.21, which is an average of supersaturations entering the node, weighted according to flowrate.

$$S_x = \frac{V_a S_a + V_b S_b + V_c S_c + \ldots}{V_a + V_b + V_c + \ldots} \qquad \ldots\ldots\ldots (3.21)$$

where: S_x = supersaturation at node x

$S_{a,b,c}$ = outlet supersaturations of pores leading into node x

$V_{a,b,c}$ = volume flowrates from pores leading into node x

As the outlet supersaturation appeared in both equations 3.20 and 3.21 an iterative technique was required to solve the system. In the model a method of successive substitutions was used. To begin with

all nodal supersaturations were assumed to be equal to the inlet supersaturation of the network. Each node was considered in turn and the outlet supersaturations flowing into it calculated using equation 3.20. From these the supersaturation at the node could be obtained from equation 3.21. This value was then used in any subsequent calculations with equation 3.20 to speed convergence to a solution. The end point was detected when the change in supersaturation at any node between iteration steps was below a given value.

The number of iteration steps to solution varied with the size of the network, which was expected given the starting point. It was considered likely that this could be improved by introducing a supersaturation gradient along the network as a starting point for the iteration. The final result of the iteration was that the supersaturation at every node in the network had been calculated.

Calculating the quantity of scale deposited

Supersaturation is usually calculated by using the geometric average of the concentrations for the constituent ions of the salt in question. The usual formulae are given in equations 3.22 and 3.23.

$$\text{Fractional supersaturation} = \frac{\sqrt{c_m c_a}}{\sqrt{c_m^* c_a^*}} \quad \ldots\ldots (3.22)$$

$$\text{Relative supersaturation} = \frac{\sqrt{c_m c_a} - \sqrt{c_m^* c_a^*}}{\sqrt{c_m^* c_a^*}} \quad \ldots (3.23)$$

where: c_m = concentration of cation in solution

c_a = concentration of anion in solution

c_m^* = concentration of cation at saturation

c_a^* = concentration of anion at saturation

The form of equation 3.23 could be compared with that of equation 3.18, the two being exactly equivalent when the cation and anion concentrations were equal. Equation 3.18 was used in the integration as it greatly simplified the mathematics.

By knowing the supersaturation at the inlet and outlet of a pore and obtaining the solubility product from the solubility prediction model, the concentration of the scaling mineral could be calculated at either end of the pore by substituting equation 3.24 into equation 3.23. This lead to an expression for the cation concentration, equation 3.25, which was the positive root of a quadratic equation (the negative root would have given a negative concentration).

$$c_a = c_m + c_{ex} \qquad \ldots\ldots\ldots\ldots (3.24)$$

$$c_m = \sqrt{\frac{c_{ex}^2}{4} + c_m^* c_a^* (S+1)^2} - \frac{c_{ex}}{2} \qquad \ldots (3.25)$$

where: c_{ex} = the difference in cation and anion concentrations

Thus, the drop in the concentration of the scaling mineral as the solution passed through a pore could be calculated. Combining this with the volume flowrate through the pore, as in equation 3.26, gave the quantity of scale deposited in the pore. As was pointed out in the earlier discussion on crystal shape, the manner in which this volume of scale was distributed within the pore could have a large effect on the flow through the pore.

$$V_s = (c_{mi} - c_{mo})\, q\, M_v\, t \quad \ldots\ldots\ldots (3.26)$$

where: V_s = volume of scale formed in pore

c_{mi} = concentration of cation at inlet to pore

c_{mo} = concentration of cation at outlet from pore

q = volume flowrate of solution through pore

M_v = molar volume of scaling salt

t = time

3.4.4 Distribution of Scale Within the Pores

The distribution of scale within the pores was considered a most important aspect of the model as it controlled the increase in the pressure gradient across a pore that occurred due to scale growth. The increasing pressure drops in each pore taken over the whole model resulted in a decrease in permeability of the network, which was the "macro" effect of scale growth that the model was intended to simulate.

Experimental evidence for scale distribution

Evidence from SEM photomicrographs of scale grown in cores (see section 5.4) showed that the majority of scale formed in the "bodies" of pores rather than in the throats between pores. This conclusion was supported by physical evidence. If all the scale formed were to grow only or mostly in pore throats, the cores used in the experiments described in chapter 5 would have become virtually impermeable in a few minutes.

In the network model of the pore structure, the "bodies" of

the pores were represented by the wide ends of the capillaries. In the distribution of scale, the major part of the scale in a single capillary must obviously be assigned to the wide end regions. However, there were difficulties involved here arising out of the way in which the lengths of the wide ends were generated.

Calculation of scale distribution between capillary sections

Referring back to figure 3.2 and equation 3.11, the throat length of each pore had an inverse relationship to the throat diameter up to a maximum constrained by the inter-nodal length. This meant that wide pores would have long wide ends, thinner pores would have short wide ends and very thin pores would have no wide ends at all. Thus, wide end volumes could vary greatly in size, which had to be taken into account when assigning the calculated volume of scale to the various regions of the pore.

Distribution of the scale within each capillary was achieved in the model by using a weighted fraction based on the lengths of each section of the capillary, equation 3.27. The volume of scale in each section was calculated from equation 3.28.

$$F_a = \frac{D_a\, l_a}{\Sigma D_a l_a} \qquad \ldots\ldots\ldots\ldots (3.27)$$

$$V_a = F_a\, V_s \qquad \ldots\ldots\ldots\ldots (3.28)$$

where: F_a = fraction of scale volume for whole pore assigned to section a

V_a = volume of scale assigned to section a

l_a = length of section a

D_a = weighting factor for section a

Distribution of scale within capillary sections

Once the scale within a pore had been allotted to the various sections of the pore, the question arose of how to distibute it within the sections. There were several possibilities here. The most simple was to allow the scale to form an annulus around the inner walls of the pore. A further step would be to confine the scale to discrete geometric shapes. A full modelling of the process would attempt to simulate the growth pattern and morphology of real crystals. This last case would have lead to a very complex model indeed.

Scale crystals growing in sandstone cores have been shown to have many varied shapes which were mostly very complex[5,21,35,37,42]. Simulating this sort of growth, even in a very simplified form would require very large computing resources to run a model in a sensible length of time. The second suggestion above, for modelling discrete growth was simpler in that it did not require to consider growth directions and which faces of the crystals were growing fastest. However, it did require questions of how many crystals, where to locate them and what happens when they reach a size when they overlap, to be answered. While not insurmountable, again a very time-expensive model would have resulted.

In the spirit of the principle of modelling the first suggestion for the distribution of scale within a section of a pore was considered the wisest to follow in a first model. If the type of damage seen could be satisfactorily modelled by the simple pore-lining technique then there would be no need to use the far more complicated options. This choice of technique also satisfied the modelling criterion that the scaling of the pores in the network should take no more time than the computation of the pressures and flows in the network.

Choosing the pore-lining type of distribution meant that the

effect of scale on pore flow was controlled by the weightings that decided the allotment of scale to each section within a pore. The distribution of scale within a pore was not the only way in which the effect of scale on the network as a whole could be controlled as will be described below.

3.4.5 Running and Tuning the Model

The procedures followed by the model to try to simulate the growth of scale with the passage of time, from a flow of supersaturated brine through the network, are decribed in some detail in section 6.2.

The purpose of tuning the model was to try to evaluate the factors, such as the rate constant and distribution weightings, that, when applied to the model, lead to satisfactory simulation of the permeability change expected due to scaling. A tuned model could then be used in a predictive role. As explained in subsection 3.4.2, factors relating to chemical kinetics can only be evaluated by experimentation. However, the "surface area" term might be evaluted by some theoretical considerations.

Evaluating the "surface area" term

The "surface area" term could be regarded as the surface area available for growth. For the purposes of the model it also encompassed the effects of surface nuleation, concentration of growth sites and other processes involved in the surface reaction of incorporating ions into the barium sulphate crystal lattice.

Nancollas et al[15,29] used the specific surface of their seed crystals, measured before adding them to the supersaturated solution, as the value for this term. This enabled them to separate a reaction

constant from the gradient of their plots of equation 3.19.

For the simple model proposed above, the surface area for growth could be made equal to the surface area of the interior of the capillaries. The surface area calculated in this manner would decrease as scaling progressed, which is the reverse of what was expected to be the case for real crystals.

Real crystals growing in a core would have continually expanding faces, but the surface area for growth would not necessarily expand at the same rate. Crystal growth theory[29] suggests that not all the available surface area is suitable for growth. In the same manner that crystals themselves must be nucleated, so must the growth of a new layer of atoms on the surface of a crystal. Even so, a decreasing "surface area"term would probably be unrepresentative of what occurs for a single real crystal. However, as described above, the "surface area" term takes account of many processes not specifically simulated in the model. Only experimentation with the model would indicate whether this simple evaluation of the "surface area" term is valid for the purposes of the model.

The rate constant

The rate constant and order of reaction were established by Nancollas et al[15,29], though, as was mentioned earlier, whether this data would be valid in a reservoir sandstone was open to question. Nevertheless, it served as a starting point from which to begin trying to model the effect of scale growth on a sandstone.

Scale distribution weightings

It was considered that the section weightings, as well as modelling the distribution of scale, might also be used to simulate the

effect of different shape crystals. This is not to say that shape would be linked to distribution in any way, but that the effect of crystals, which had more potential to disrupt the liquid flow through a pore by virtue of their shape, might be simulated by, for instance, locating more of the scale in the model in the pore throats where it would have a larger effect on the flow. Values for the weightings could only be ascertained by comparison of results from the model with the permeability change of experimental cores.

The response of the model to changes in its control factors and how well model results compare with experimental results is dicussed in chapter 6. The next chapter describes the development of experimental equipment to provide data of use for tuning the model.

CHAPTER 4

DESIGN OF EXPERIMENTS AND THE DEVELOPMENT OF THE EXPERIMENTAL APPARATUS

4.1 INTRODUCTION

The last chapter described the development of a model, which might be used to predict the effect of scale growth within a porous medium. It was pointed out that this model could only be as good as the data upon which it was founded. The model also had several variable parameters in it, whose values could only be justified by a comparison of what the model predicted with what damage would actually occur in a porous medium such as a reservoir sandstone.

This chapter reviews methods by which the data required to validate the model might be obtained. Few of these methods, in the form they have been used in the past, were able to supply the type of data required by the model described in chapter 3. In this chapter the experimental technique of core flooding is developed to supply more information on what is taking place within the core by the use of pressure tappings along the side of the core. The design and testing of the specialised equipment developed to carry out this function are also described here. In chapter 5 the experiments performed using this equipment are described along with how the results have been interpreted to try to derive the information required by the model.

4.2 TYPES OF EXPERIMENT

The problem of scale formation is almost as old as the oil industry itself. All of the common types of scale were reported in some of the earliest wells produced in America[7]. During the life of the oil industry various tests have evolved to assess compatibility of brines and to provide information on rate of growth and likely effects of scale. These tests can be divided into three main groups:

i) beaker or static precipitation tests - these consist of mixing a sample of each brine in a beaker or equivalent vessel and observing the precipitation that occurs.

ii) tube tests - this involves mixing the two brines at the entrance to a tube to study precipitation under dynamic conditions.

iii) core floods - these are performed by mixing brines within the pore-space of a core of similar material to that of the reservoir in order to observe the effect of precipitation on the flow properties of the core.

This section explores the suitability of these tests for providing the sort of data required, both to investigate whether that data might already be available and to provide a basis around which to design further experiments.

4.2.1 The Beaker Test

The beaker test is the oldest and simplest test for scaling known

to the industry. In its most basic form it consists of merely mixing a sample of each brine in a bottle to see if a precipitate forms. This type of beaker test was used in the early days of water injection as a secondary recovery method, to test various sources of water for incompatibility with the formation brine. It was considered then to be very bad practice to inject an incompatible brine. Nowadays the beaker test is more commonly used as a means of evaluating inhibitor efficiency. These tests must be conducted very carefully to produce any degree of repeatability and reliability. The test is most sensitive to the procedure by which it is performed. Glassware must be scrupulously clean.

In recent years Nancollas and co-workers[15,29,30] have developed the basic beaker test to a very powerful tool for measuring precipitation rates. In their system the "beaker" was an autoclave, which could be maintained at a given temperature, containing a supersaturated brine mix. Seed crystals were introduced into the autoclave to initiate growth. The change in solution concentration was monitored conductimetrically. In a later version of this technique[28], as growth proceded on the seed crystals the supersaturation was maintained by addition of solution from automatic burettes coupled to ion-selective electrodes. The precipitation rate was calculated from the amounts of solution added with time. The results of this constant-composition technique are especially useful as they were measured at a steady supersaturation. This made the test somewhat akin to dynamic tube tests as there was a constant supply of precipitating ions. The constant composition technique has also been used for assessing inhibitor effectiveness.

Modern technology has allowed the development of turbidity measurement as a method for evaluating scaling tendancy[19]. For this type of test a sample of brine is pumped through a turbidity cell from a continuously stirred tank of supersaturated brine. The turbidity

cell measures the size frequency distribution of the growing crystals by analysis of laser light scattered by the crystals. It is not possible to produce precipitation rate data as accurate as that from the constant-composition technique, though the results are useful and easier to produce for analysis of inhibitor performance.

4.2.2 The Tube Test

The tube test is essentially aimed at evaluating scaling tendancy in a flowing system such as oilfield production tubulars. It differs from the basic beaker test in that there is a constant supply of ions to the growing crystals. The general form of the test involves flowing the brines along the tube until the pressure drop across the tube reaches a predetermined level. The test is greatly infuenced by the manner in which the tube is set up. Having the tube horizontal, vertical or coiled can all give different results. The diameter of tube used affects the length of the test, some workers[36] recommend $^{1}/_{16}$ inch tube while others have used $^{1}/_{4}$ inch tube[21]. In any event the test is usually quite lengthy and has not shown itself to be very repeatable. It is useful for investigating the use of different tube coatings as a means of preventing scale adhesion.

4.2.3 The Core Test

As the only test capable of showing what can happen in a porous structure the core test is obviously of great value in the investigation of scaling. It has been used both to indicate whether scaling will happen within the reservoir formation and to show what effect it will have if it does. Bernard[2,3] was an early worker on the

problem of whether scale will form as a result of mixing between injected and interstitial waters at or around an injection well. He performed tests using consecutive flow, ie flooding the core with one brine and then washing it out with another, and using simultaneous flow of brines, ie flooding one longitudinal half of the core with one brine and the other half with another, incompatible brine. He concluded that no damaging scale would form as a result of injecting incompatible brines, though he did not publish his results for simultaneous flow of barium sulphate producing brines. Laird and Cogbill[23] performed similar simultaneous flow tests and concluded that damaging scale would form. Obviously core tests are as susceptible as any other to experimental procedure. More recent workers[5,21,37,42] have used the core test merely to study what damage to permeability can occur as a result of scaling as interest has now switched to the production end of the reservoir. No published study has, as yet, related damage to precipitation rate or obtained any precipitation rate data from core tests.

4.2.4 Choice of Test

It was clear from the descriptions above that the tube test would be of little value in an investigation of scale formation in a porous medium. Despite being a dynamic test the hydrodynamics and surface characteristics involved would be so different from those at work in a reservoir as to make the results wholly inapplicable.

Quite obviously the most suitable test to use would be the core test. As the increased surface area for heterogeneous nucleation and the manner of intermingling of the brines could not readily be simulated by any other means, no other test could really supply data as appropriate as that from a core test.

The seeded growth technique for determining precipitation rate is a very powerful one. It remains to be seen whether the same precipitation rate constant would apply in a porous medium. There seemed to be little point in performing further tests of this type unless the technique was extended to use higher supersaturation brines, which seemed unlikely given the nature of barium sulphate precipitation. With the popularity and simplicity of the basic beaker tests, it was considered worth performing some of these, especially from the point of view of studying the effect of crystal shape on the nature of damage. If crystal shape is an important factor in the level of damage caused by scale and if crystals grown in the beaker could be shown to have a similar morphology to those grown in the core, it would be much easier for an operator to use a beaker test to provide the crystal shape information for simulation purposes, than to run a core test.

For the purposes of this study it was considered that core tests were the most suitable experimental tool, backed up by beaker tests for comparison with a very popular assessment technique.

4.3 DESIGN OF EXPERIMENTS

The design of experiments used in a practical study such as the one proposed in this work, must be very carefully considered to ensure that the sort of data required can be measured. The experimental work in this project was largely a continuation of the earlier work performed in this Department by Pucknell[35], which was covered in his thesis.

4.3.1 Previous Work

The previous work in this area, described in Pucknell's thesis, was intended to be a preliminary study, as far as scaling in reservoir-type rock is concerned. The aim then was to establish whether a study of this type was possible and if so, how it might be carried out. The general conclusion for this target was that such a study was indeed feasible and that relevant data could be obtained if the short-comings of the core holder used in that study could be overcome.

Pucknell's experiments confirmed some basic relations, which with hindsight seem fairly obvious, but nevertheless should still be proven. These were that the rate of permeability decline, due to scale growth within a sandstone core, increased with increasing supersaturation of the brine mix and increasing flowrate of the brines through the core. There was little repeatability in his results, which showed a wide spread of permeability decline rates even for experiments performed under similar conditions. His analysis of the permeability change in the front and rear ends of his cores, measured before and after the experiment, demonstrated that more scale formed towards the front of the core.

Pucknell used scanning electron microscopy (SEM) to show that the crystals grown from his various brines had differing morphologies. He

offered an explanation for the different morphologies in terms of the supersaturation of the brine mix and the fastest growing faces of the crystals. This will be discussed further in a later section.

Pucknell stated that the aim of future work should be to establish unambiguous relationships between supersaturation, temperature, rate of precipitation and rate of permeability decline. He was also well aware of the limitations of his equipment and suggested the use of a multi-tapped core holder (ie one in which pressure measurements may be made at intervals along the core) to enable continuous measurement of the permeability of sections of the core.

4.3.2 A New Approach to the Study of Scale Formation

Experimental equipment

The equipment Pucknell[35] used was intended to be capable of monitoring the increase in differential pressure across the core with a view to converting it to a continuous permeability measurement. Because of the inadequacies of the distribution face (the part of the core holder responsible for introducing the brines into the core) a filter paper had to be placed on the front of the core to act as a sealing gasket to prevent the brines mixing prior to entering the core. The pressure drop created by the filter paper caused difficulty in assessing the true permeability of the core. It was therefore considered that Pucknell's results were only useful for indicating trends.

Because of the design of the distribution face used in those experiments, very high flowrates were required in order to obtain good mixing in a short length of core. Those flowrates were unrepresentatively high even when compared to near-wellbore flowrates

through the reservoir formation. Thus, there were obviously major improvements to be made in the design of the distribution face to remove the need for a gasket and to improve the mixing at lower flowrates. The improvements made are discussed in section 4.4.

The importance of crystal morphology

The objectives identified by Pucknell, mentioned in the last subsection, were largely quite sound. The process of scale growth leading to permeability decline is a very complex one and so must be broken down to simpler relationships. Pucknell's objectives were lacking in one point, that of the infuence of crystal morphology.

Pucknell considered the morphology to be a function of supersaturation, a view which probably stemmed from the compositions of the brines he used. These brines contained barium sulphate in a sodium chloride solution in two groups of supersaturation: 19.0 to 20.5 and 7.0 to 10.5. Crystals grown from the two groups showed two different morphologies. However, the change in supersaturation was brought about by changing the concentration of the sodium chloride and not that of the barium sulphate. Even though Pucknell appreciated that the presence of other ions could influence the crystal structure, possibly by becoming included in the lattice, he appeared to have discounted this as a reason for the change in morphology. It was considered by the current author, that factors such as solution composition and ionic strength, could be just as important as supersaturation in controlling the change in crystal habit observed by Pucknell.

Such a viewpoint was supported by Pucknell's own work. He only reported one morphology associated with each supersaturation. He also reported that most scale formed towards the front of the core, which would presumably have caused a drop in supersaturation of the flowing brine towards the end of the core. If morphology was controlled by

supersaturation alone then different morphologies should have been observed between crystals at the front of the core and those at the rear. A possible reason why this was not observed lies in the mixing pattern produced by the distribution face used. The distribution face properties are discussed further in the next section.

Given the possible importance of morphology in the rate of permeability decline, it was proposed that relationships between the following should be investigated: supersaturation; crystal morphology; solution composition; temperature; pressure; rate of precipitation and rate of permeability decline. These were to be investigated with a view to developing relationships that would be of use in the simulation model described in chapter 3.

4.3.3 Requirements for Design of Experimental Equipment

Following from the discussion above, the experimental equipment used for this study had to have two basic properties. It had to be able to generate supersaturation and scale growth within a sandstone core in a controlled manner and make measurements that reliably reflected the effect this growth had upon the flow properties of the core. It should be remembered that these experiments were intended to study the growth and effect of scale formation in a porous environment under reservoir conditions. Unlike the experiments of Bernard[2,3] and Laird and Cogbill[23] they were not studying whether permeability damage could occur due to the co-mingling of interstitial and injected brines in the reservoir.

Reduction of permeability could have two measurable effects on the flow through a core. For a constant injection pressure the flowrate would drop or for a contant flowrate the pressure would rise. With modern pressure transducer technology the latter of these was by far

the easier to monitor continuously. Also if pressure tappings along the side of the core were used, they would give larger, more easily measured pressure changes for the constant flowrate system than for the constant injection pressure system.

For the pressure tappings to give meaningful information the scale formation within the core had to be spread as evenly as possible across any cross-section of the core. This was so that by-passing of scaled areas did not give spurious increases of supersaturation and scaling later in the core. Also, as the tapping was made at the edge of the core, this condition was required to encourage the pressure profile to be fairly even across any cross-section of the core to ensure that any pressure measurement made was representative of that cross-section.

Some measurements, required to give a full picture of what was taking place within the core, could not be made continuously during the experiment e.g. porosity. Thus it was a necessary condition that these measurements could be made before the experiment and that the core could be recovered for comparable measurements to be made after the experiment.

Summarising, the requirements of the experimental equipment were as follows:

i) that the brines were introduced to the core in such a way that they did not mix before entering the core, but were mixed intimately and evenly across the whole cross-section of the core shortly after entering it.

ii) that the brines were pumped into the core at a constant flowrate so that any change in permeability could be monitored by recording changes in pressure.

iii) that pressure tappings could be made along the side of the

core to monitor permeability changes in different regions of the core

iv) that the core was mounted in such a way that it was available both before and after the experiment for measurements to be made of its flow supporting properties.

v) that it was possible to subject the core and the flow through it to reservoir conditions of temperature and pressure.

The first of these conditions was provided to satisfy the requirement for controlled creation of supersaturation, the following three to cover the requirements for monitoring the effect of scale growth. The final condition was made to ensure that the results would be relevant to oilfield conditions.

4.4 DESIGN OF EXPERIMENTAL APPARATUS

This section describes the design of experimental equipment to fulfill the requirements laid down in the previous section. The design of the components that were specially developed for this work is covered in some detail. The most important piece of equipment was the core holder, which had two newly developed features, its distribution face and its pressure tapping system. The rest of the equipment was fairly typical of core flood apparatus and so is only described in brief. A subsection is also included on the important aspect of the gathering and accuracy of the experimental data.

4.4.1 Development of the Distribution Face.

Requirements of the distribution face

The distribution face had the task of controlling the introduction of brines into the core. To fulfill this task, as laid down in the general requirements for the experimental equipment, it had to perform three functions:

i) to ensure that both brines were evenly distributed across the injection face of the core.

ii) to introduce the brines in such a way as to cause complete mixing within a short length of core.

iii) to prevent the brines mixing until after they had entered the core.

It was also a basic requirement that these three functions were performed adequately at all flowrates likely to be used and also for all mixing ratios to be used.

Before developing a completely new distribution face, the possibilty that an existing face might be able to perform these functions was explored. If one could not be identified as likely to achieve the ideal described above then an analysis of the performance of an existing face might provide valuble insights into how a face might be designed to approach the ideal more closely.

Types of distribution system

Two general types of injection system have been used for introducing incompatible brines into cores: axial and radial. The radial injection system was first used by Boyle and Mitchell[5] and has since been copied by other workers[37]. It consisted of a number of injection points spaced around the circumference of the front end of the core and pointing towards the axis of the core as shown in figure 4.1. An axial system introduces the brines onto the face parallel to the axis of the core. Pucknell's[35] distribution face, shown in figure 4.2, was of the axial type.

The axial system had many advantages over the radial system. Firstly the brines could be distributed over the face in many different ways. Pucknell's was just one example, shown in figure 4.2. Another rather clever means of distributing the brines separately over the face was used more recently by Bertero, Chierici et al[4], shown in figure 4.3, and was similar to that used by Pucknell. Secondly, there was far less plumbing required for an axial system and it was also essentially independant of the method used to confine the core. The radial system, on the other hand, was fixed in the pattern of injection it used except for increasing or decreasing the number of injectors used. The radial

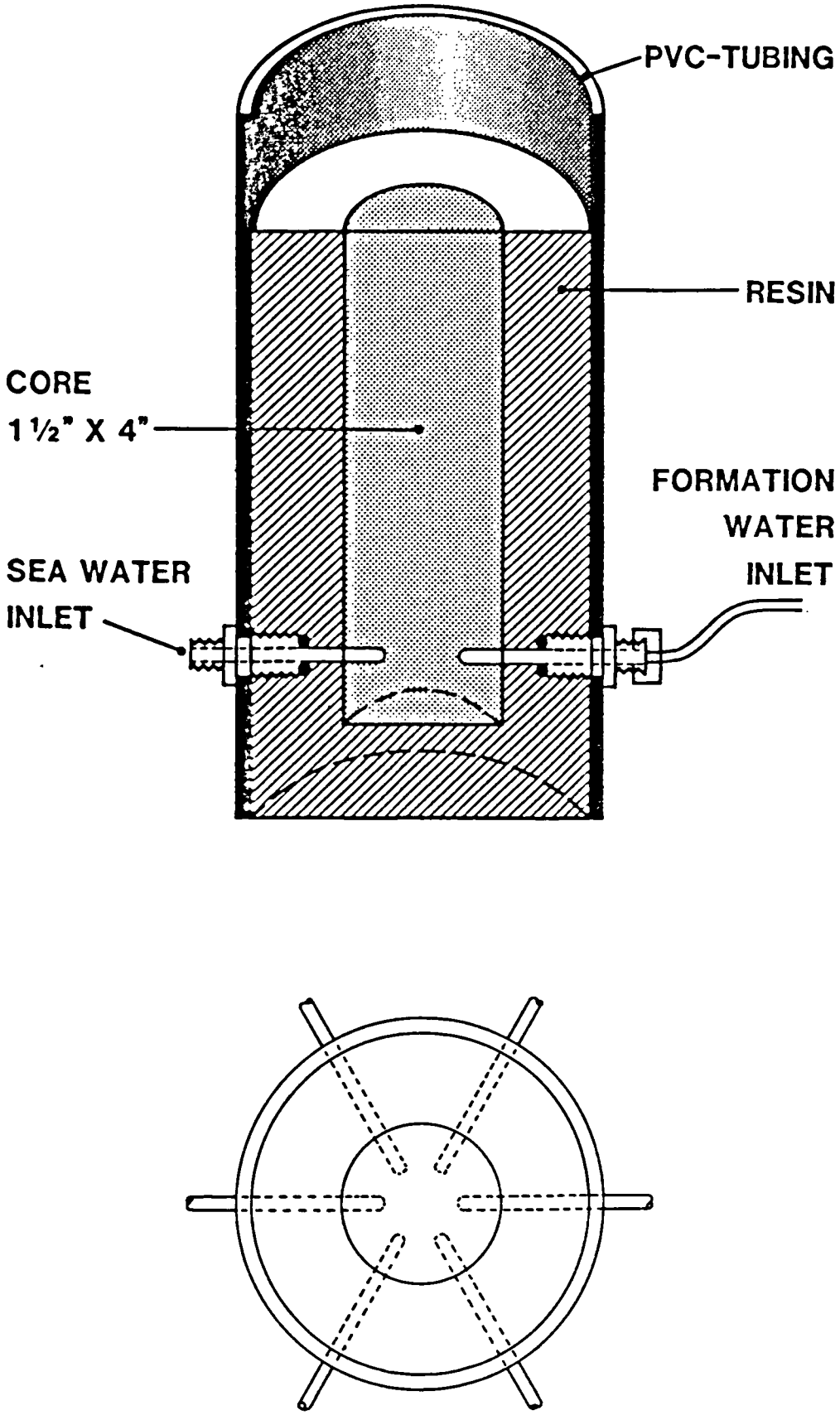

Figure 4.1 Boyle and Mitchell radial injection system

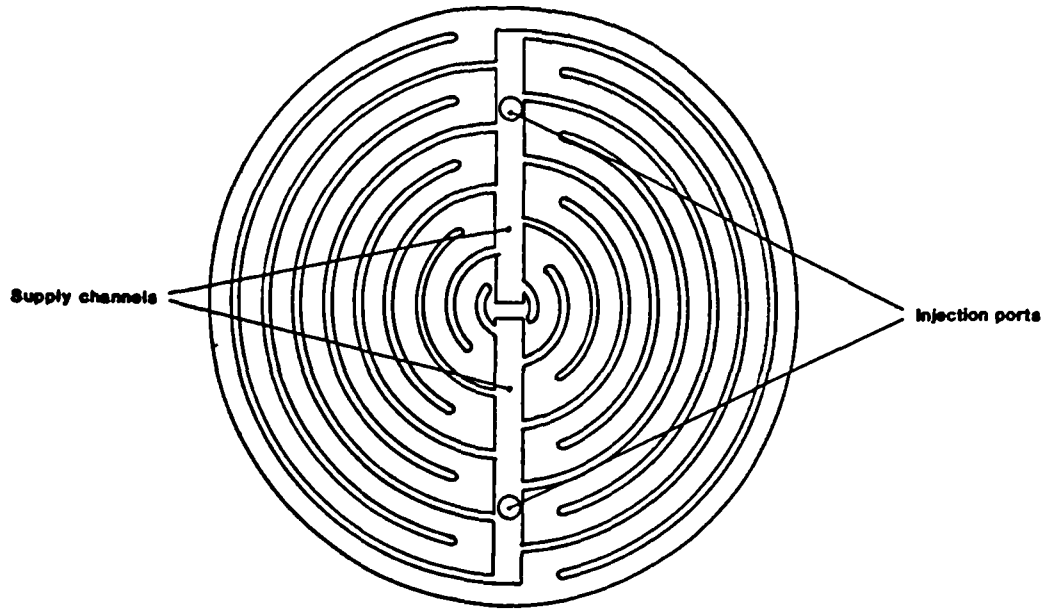

Figure 4.2 Distribution face used by Pucknell[35]

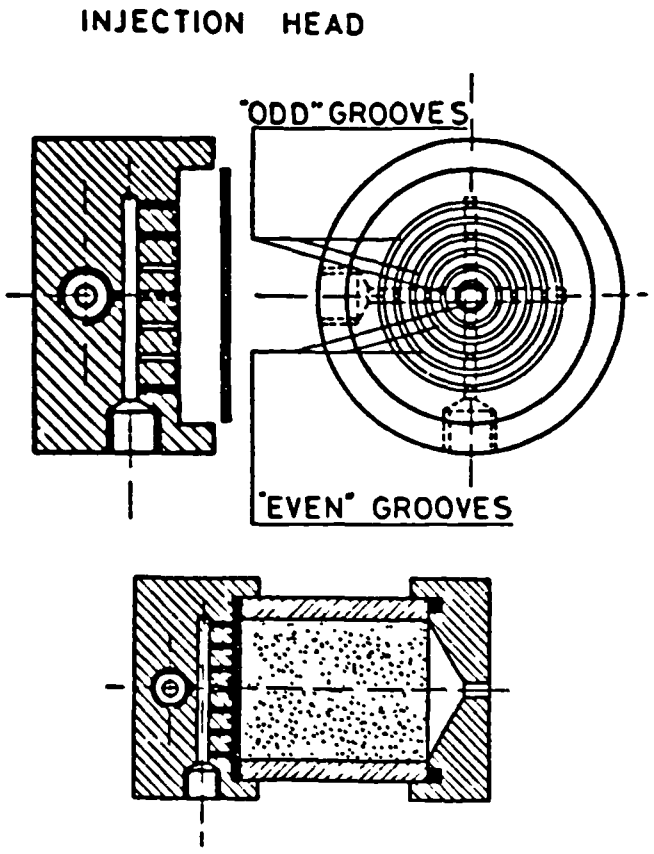

Figure 4.3 Distribution face used by Bertero, Chierici et al

system of Boyle and Mitchell relied on the core being bonded in resin. There will be further discussion on confining cores in the next section.

As no information was available from the papers describing the distribution systems mentioned above, as to how well they would perform the required functions described earlier, this had to be inferred from a study of the properties of a distribution face that was available. That used by Pucknell.

Analysis of the mixing pattern produced by an axial flow distribution face

The procedure, by which the study was performed, is described in appendix A4.1. It was carried out using two techniques. The first involved injecting a blue dye into one port of the distribution face, while injecting clear water into the other. In the second test two components of a dye were injected, one into either port. The two components remained clear until they mixed, thereby showing the areas of the core where mixing had occurred. This mixing dye test was used to confirm the conclusions from earlier, blue dye tests.

The distribution face used by Pucknell, shown in figure 4.2, consisted of a system of interlocking, concentric grooves. These grooves were fed from two, deeper, supply channels, which lay along a diameter of the face. The ports supplying the brines from the pump opened into these channels.

The results from one of the blue dye tests, shown in figures 4.4 and 4.5, demonstrated very clearly two main features of the mixing pattern produced by this distribution face. The first of these features, most easily seen in the "sectioned" core in figure 4.4, was a clear, and therefore unmixed, streak that persisted along the whole length of the core corresponding to the position of the supply channel

Figure 4.4 Sectioned core from blue dye test using Pucknell's distribution face

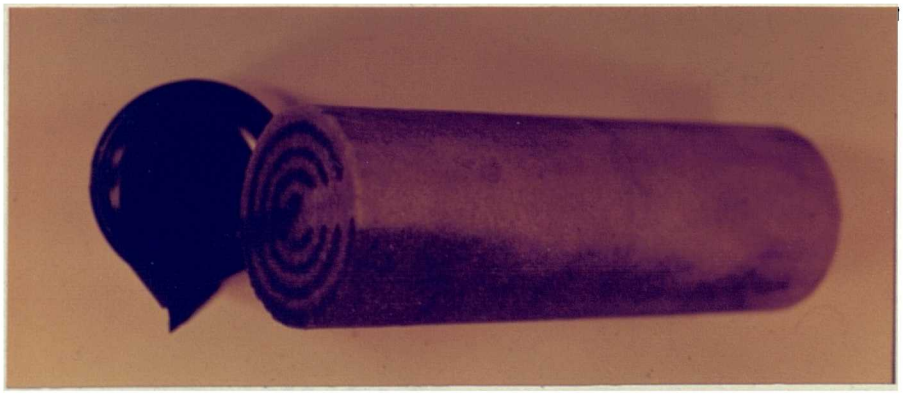

Figure 4.5 Side aspect of core from blue dye test using Pucknell's distribution face

on the distribution face. The second feature was most obvious on the view of the outside of the core, figure 4.5. This shows that the outside of the half of the core, where the outermost groove was connected to the blue dye supply channel, was a very deep blue. Meanwhile, on the other half, where the outermost groove was connected to the clean water channel, the outside of the core was almost completely clear of any blue dye. This showed that no mixing was occurring on the outer circumference of the core.

The results of the mixing dye test were not so clearly apparent as the dye was not so intense, but they supported this interpretation of the mixing pattern produced by this distribution face.

From these results a map of the cross-section of the core showing where mixing was occurring was drawn up and is shown in figure 4.6. This mixing pattern appeared to persist along the length of the core with little invasion into the unmixed areas.

This result had some implications for experiments conducted using this distribution face. The unmixed zones could maintain a supply of ions along the length of the core, supporting higher levels of supersaturation further into the core. As the unmixed zones continued to the end of the core, flow through them created new supersaturation in the outlet pipework and caused barium levels in the effluent to be unrepresentative of scaling in the core. Also, as scaling in the mixed zones would cause more flow to pass through the higher permeability, unmixed zones, the likelyhood of scaling the outlet pipework increased as the experiment progressed.

Evidence to support the likely scaling pattern produced by this face, ie corresponding to the mixing zones, was discovered by Simm[42] while trying to flood a scaled core with dissolver. He noticed that the parts of the core the dissolver had reached took on a darker shade. This darker shading formed a ring around the outside edge of

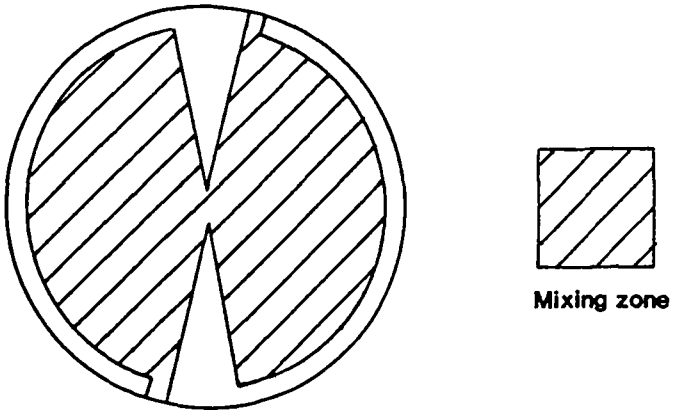

Figure 4.6 Map of mixing pattern produced by Pucknoll's distribution face

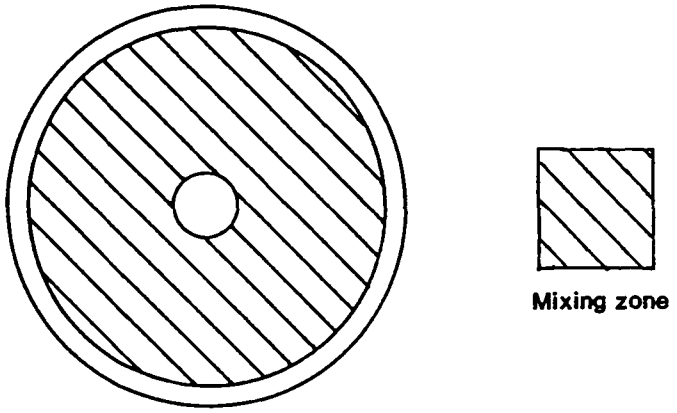

Figure 4.7 Map of mixing pattern expected to be produced by Bertero, Chiorici et al distribution face

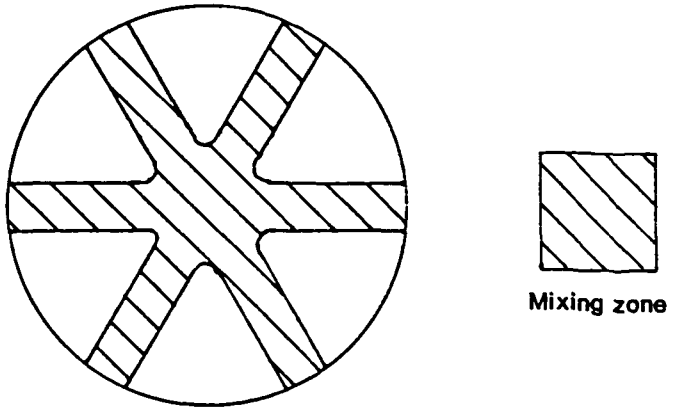

Figure 4.8 Map of mixing pattern expected to be produced by Boyle and Mitchell distribution face

the core. Obviously the dissolver had followed the higher permeability path through the unscaled outer areas of the core, leaving the scaled central region untouched.

A simple rule for mixing

From the study above, a simple "rule of thumb" was identified governing the degree of mixing in any distribution system. Where flow of one water from the distribution face was closely surrounded on two or more sides by flow of the other water then good mixing occurred. If this was not the case then there would be only a limited degree of mixing. For the case of the two outer halves of the cores in the blue dye tests there was flow of the opposite water on one side only of the flow of the water from the outermost groove. At the streaks from the supply channels, flow of the opposite water was not close enough for mixing to penetrate right across the flow into the core from the supply channels.

Likely mixing patterns produced by other distribution systems

From the analysis above it was possible to make inferences about what the likely mixing patterns produced by other distribution systems would be. These followed purely from applying the simple rule described above.

The axial flow type face of Bertero, Chierici et al[4] was quite similar to that of Pucknell[35]. Provided the circular grooves were deep enough to allow fluid to pass easily around the groove there should have been no effect from the ports supplying each groove. Mixing should have been good across the region of the core between the most central groove and the outermost groove. Outside the outermost groove and inside of the innermost groove no mixing would occur for similar

reasons as were identified for the unmixed areas of the Pucknell system. The mixing pattern expected to be produced by this distribution face is shown in figure 4.7.

The six injector, radial flow system of Boyle and Mitchell[5] was likely to create six segments in the core supporting alternate brines. Mixing would occur only on the boundaries of these segments and would probably lead eventually to the segregation of each segment by low permeability, scaled regions along the segment boundaries. Applying the rule for mixing this system could be improved by bringing the injectors closer together and using more of them. This would be restricted by the physical limitations of placing the injectors and supplying them. The probable mixing pattern for this injection system is shown in figure 4.8.

Specification for a new distribution system

The rule for mixing described above was applied to specify a new system for efficiently mixing the brines after they had entered the core. What the rule implied was that all channels providing flow of one brine from the distribution face should be surrounded on two or more sides by channels supporting flow of the opposite brine, sited as close as was physically possible.

The two concentric groove systems, described above came quite close to this ideal. They were let down mostly by the outermost groove, which could not have another flow source outside of it. This long run of unsurrounded flow had to be broken up to improve on this system, which could be best achieved by a system of radial grooves. A radial groove system, with alternate grooves supplying alternate brines, would leave only short zones on the outer circumference of the core that were not well served by both brines. Such a system of grooves had one major problem. The obvious place from which to supply

a system of radial grooves with brine was the centre of the face. However, this was not physically possible for two sets of grooves without breaking the requirement that the brines did not mix until after entering the core.

A means of overcoming this difficulty is shown in figure 4.9. Here the radial pattern was used but one set of grooves was replaced by a series of holes, which were supplied from the back of the distribution face. The remaining grooves were supplied from a central port on the front of the face. This system was the basis for the development of a new distribution face aimed at overcoming the problems associated with other systems described above.

After much testing of successively more complicated designs, a system that could satisfactorily mix the two brines across the whole cross-section of the core within about 5mm of the front of the core was discovered. The final pattern of holes and grooves used is shown in figure 4.10. This pattern still suffered a little from difficulties in balancing the brine flow between the centre of the core and its cicumference, especially when the flowrates of each brine were not equal. Balancing of the distribution was achieved by adjusting the depths of the grooves to match the mixing requirements. The cross-sections of the distribution head, shown in figure 4.10, indicate the groove depths used for mixing brines at flow ratios of 50:50, 60:40 and 70:30. For unequal flow ratios the brine with the lowest flowrate was injected into the holes as these had a lower surface area in contact with the core than did the grooves.

Figure 4.11 shows the results of using the new distribution system for a 50:50 flow ratio. It can be seen that good mixing could be expected within 5mm of the front face of the core. Figure 4.12 shows similar results for using a 70:30 flow ratio. In this case complete mixing can be seen to have taken a little longer.

The distribution heads were manufactured from PTFE bar and,

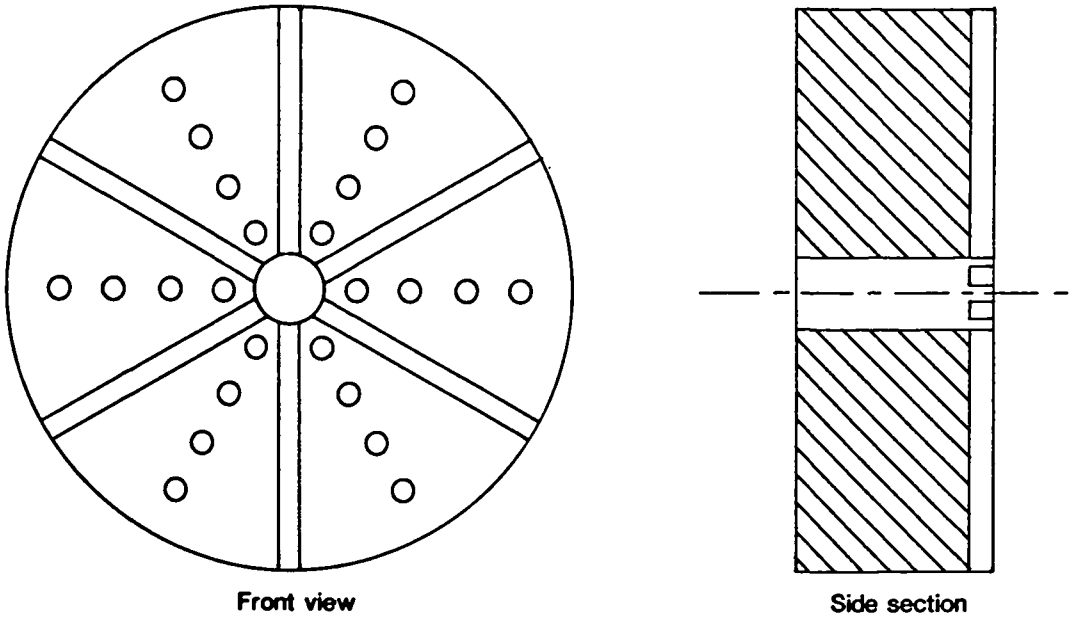

Figure 4.9 Initial concept of a two fluid radial pattern distribution face

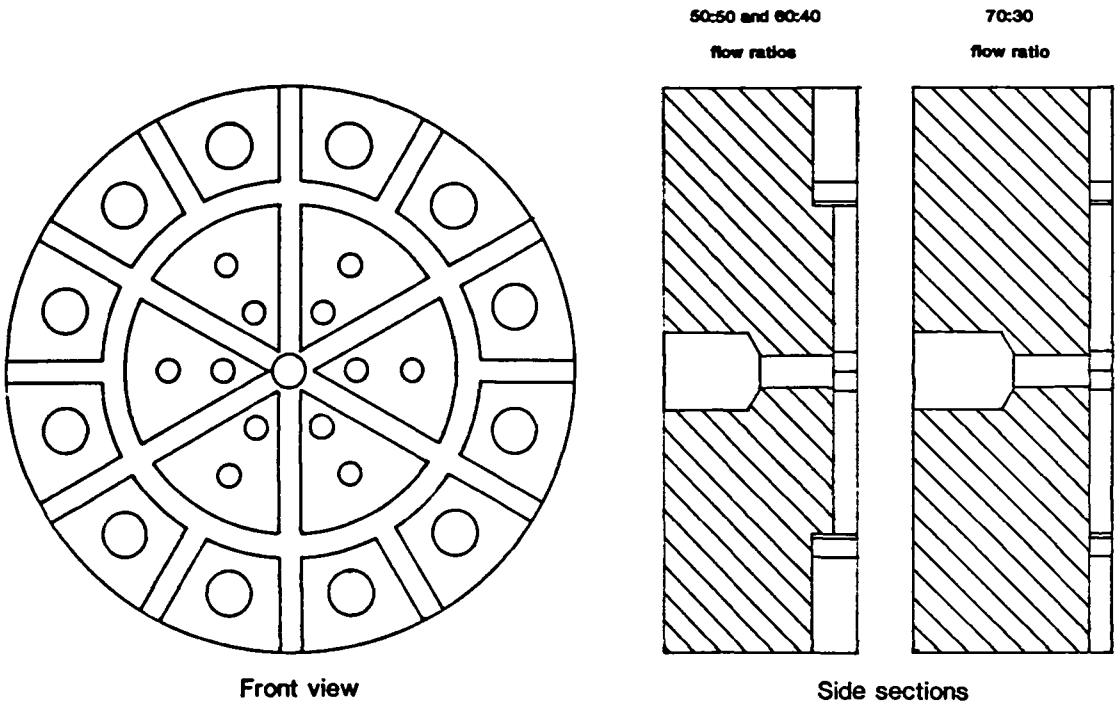

Figure 4.10 Final design of two fluid distribution face

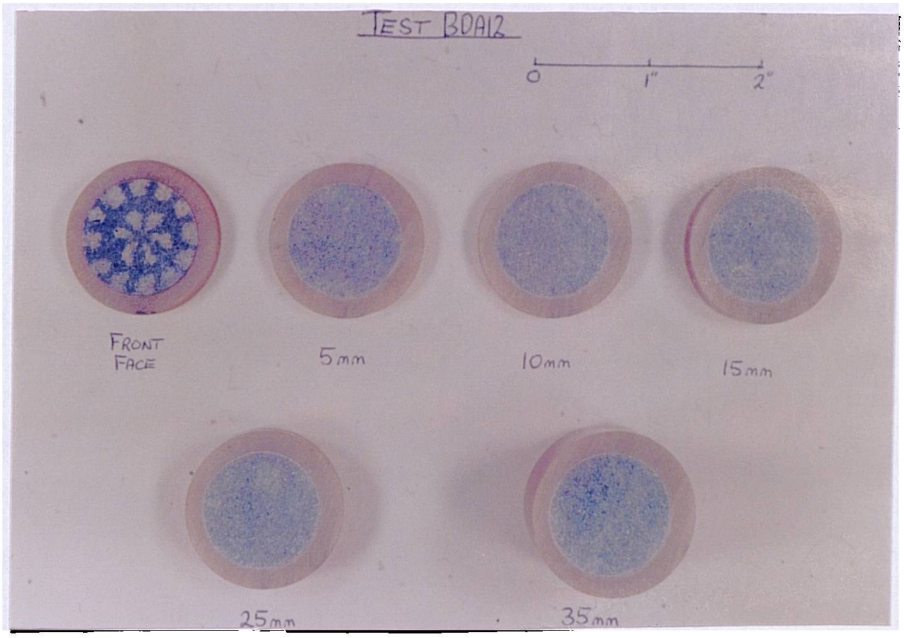

Figure 4.11 Results of using new two fluid distribution face with a 50:50 flow ratio

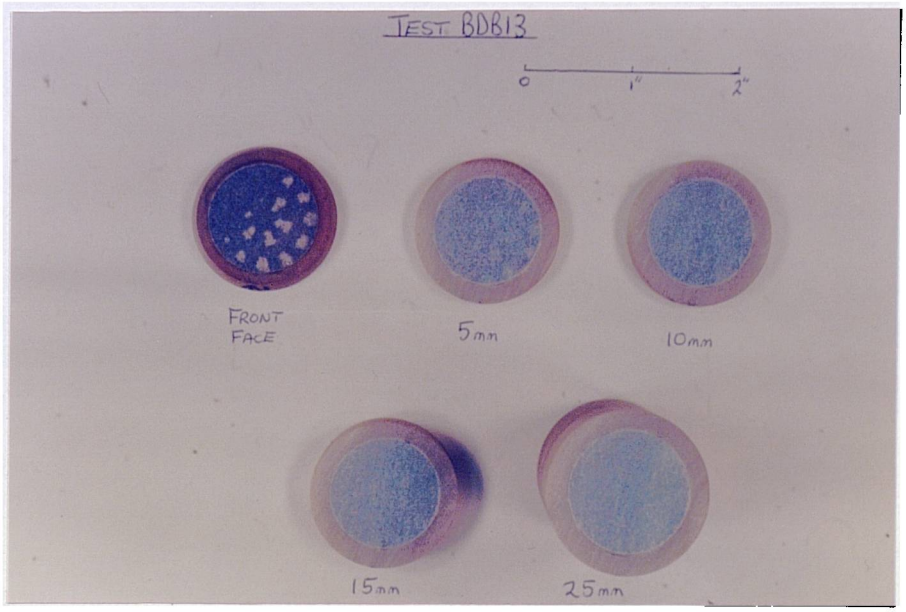

Figure 4.12 Results of using new two fluid distribution face with a 70:30 flow ratio

for the experiments described in this work, were mounted against the core using a clamp-type core holder, as shown in figure 4.14. The PTFE was soft enough to deform against the face of the core to provide a good seal between the holes and the grooves, which obviated the need to use a gasket between the head and the core as required by the Pucknell system. The PTFE could also be accurately machined to the intricate patterns shown in figure 4.10 and, on paper at least, should retain its strength up to the highest working temperature of the equipment described in this chapter of 120-150°C. How such distribution heads will behave under the stress of any applied confining pressure has yet to be tested.

4.4.2 A Core Holder with Multi Pressure Tappings

The idea of using pressure tappings along the side of a core in core flood experiments was not a new one. Bernard[2] used water manometers bonded into the resin coating on his cores. What was required in this work was something a little more substantial, capable of withstanding much higher pressures and temperatures.

The requirements for the core confining and tapping system have already been discussed in section 4.3.3. Various methods of confining the core and fixing tappings are discussed below and their strengths and weaknesses assessed. Unfortunately, some difficulties, not wholly technical, arose in the development work of the system considered most suitable for this study, causing the development time to be far longer than anticipated. Therefore a "fall-back" position had to be adopted to obtain a working system in time to carry out an experimental study. The design of this system obviously had slightly different criteria to the design originally intended. The results of development work on both of these systems is described below.

Core confining and tapping techniques

The aim of confining the core for core flood experiments was to seal the cylindrical, or longitudinal, faces to flow. This left an inlet face and an outlet face. The seal between the confining medium and the core had to be good enough to prevent fluids seeping along the sides of the core, which would corrupt any measurements made that assumed all flow was passing through the core. Tappings made through the confining seal had to break the seal only at the point the tapping was made. There needed to be no communication between the tapping points. The various techniques described below were assessed in terms of the practical aspects of their use and the requirements noted above.

1 Resin bonding: This involves moulding resin around the outside of the core. The resin is supplied as a viscous resin with a liquid hardener which must be mixed in the correct proportions before pouring into the mould. The seal obtained between resin and core is very good though care must be taken to avoid the resin being absorbed into the pores of the core. This is usually achieved by coating the core with a thin layer of a quick setting resin before moulding. Tappings can be made by drilling through the resin to the core and making a seal on the surface of the resin or by bonding or screwing a fitting into the resin. Working pressures of 500 psi have been used with this type of confining[9]. Higher pressures may be possible by using the core in a pressure vessel and supporting the resin with high pressure water, but there may still be a tendancy for the resin to crack. Working at elevated temperatures is not really possible as the resin loses strength and tends to creep. High temperature resins are available but their short curing times make them very difficult to work with in this application. Apart from this, this system has two major drawbacks. It

is very messy and time consuming to manufacture the moulded cores and the core is not readily available for analysis, either before or after experimentation, in the form in which it is actually used, unless equipment is specially modified to use resin bonded cores. All things considered, this method was not at all suitable for the intended study, but it has been used very successfully for low temperature, multi-tapped core flood experiments for some time[50].

2 Perspex bonding: By placing a core in a specially made perspex sleeve and subjecting it to high pressures in a hot oil bath a reasonable seal can be made between perspex and core. Tappings can be applied in a similar manner to the resin bonded core. Doubt exists as to whether this method provides a good enough seal against the core. Little is known of what working pressures may be used, though they are probably similar to the resin system. As this method was likely to suffer most of the drawbacks of the resin system, it too was unsuitable for the intended study.

3 Solder: The outside of the core can be sealed with solder by using a fairly close-fitting pressure vessel and filling the gap between the core and the wall of the vessel with molten solder while the whole core holder sits in a special heater. Evidence suggests that the seal obtained is very good and the working pressure is only limited by the pressure vessel used[53]. Tappings can be made by setting the fittings in place against the core before pouring the solder. Higher working temperatures should be possible by using higher melting point solder. The core can be recovered for analysis after experimentation by reheating the core holder and allowing the solder to drain out. Preparing a core for experimentation is still a lengthy task and the equipment used must be carefully designed to avoid flaws in the solder coat. It can also be a very unpleasant task as obnoxious fumes are

produced by the molten solder. If the practical problems can be overcome (or tolerated) this was considered an excellent system for the task. However, if overburden loading were to be considered important to the experimental study, this technique would be inappropriate as no loading of the core is possible.

4 Rubber sleeve: This method of confining cores is in common use in many core holders and was used by Pucknell[35] in his core holder. He pointed out that such a system is very attractive if the technical difficulties of fixing the tappings can be overcome. This does not appear too difficult to achieve as the automotive industry regularly obtains structural bonds between metal and rubber. Rubbers that can withstand high temperatures and chemical attack are readily available. The seal between core and rubber is made by applying water pressure on the outside of the sleeve, normally to a level of approximately twice that of the fluids within the core. By this technique overburden pressures can be applied to the core. The core is readily available for analysis by sliding it out of the sleeve and is easily loaded by the reverse process.

From the point of view of ease of preparation for experimentation and simplicity of disassembly afterwards, the rubber sleeve system was by far the most attractive. This alone recommended its use. Added to this, its ability to take in all the variables of pressure, temperature and overburden made it very suitable. All that was required was to overcome the problem of making the tappings. A system was designed to achieve this to make a comprehensive operational unit. This is described below. The only failing in its development was a failure to obtain a satisfactory bond between the rubber and the metal.

Design of a multi-tapped rubber sleeve

The sleeve described here used discrete tapping units spaced along the sleeve rather than a metal strip along most of the length of the sleeve as was being tested by other workers[38]. This was for two reasons: i) to reduce stress on the metal-rubber bond caused by the difference in the thermal expansion of the two materials when the sleeve was heated and ii) as the rubber had a lower coefficient of thermal expansion than the metal, the discrete tapping method would have a smaller shift in tapping positioning at high temperatures. The design for the sleeve and tapping pieces is shown in figure 4.13.

The tapping pieces were manufactured from a semi-circular metal plate cut from a tube of suitable internal diameter to give space for a thin layer of rubber between the surface of the core and the tapping piece. A "Nutsert" was crimped onto the centre of this plate. This is a device for fixing a thread behind a plate when no access can be gained to the rear of the plate to use a conventional nut. The required number of these tapping pieces were then buried in the rubber, at the appropriate spacings, leaving just the top of the Nutsert showing at the surface of the rubber. A communication hole was drilled below the Nutsert. An axially drilled M6 screw was used to fix a threaded adaptor to the tapping piece. A small o-ring provided a seal between the adaptor and the top of the Nutsert. A standard conversion fitting could then be used with the BSP threaded adaptor. A Dowty seal was used to make the seal between the fitting and the adaptor.

This system relied on a good seal being obtained between the tapping piece and the rubber. To facilitate this the tapping piece had quite a large surface area. The curved plate eased positioning in manufacture and stability and ruggedness in service as the holes in it allowed rubber to flow through the plate, "pinning" it in place.

Sealing at the ends of the sleeve employed an o-ring. The

End Sealing Ring

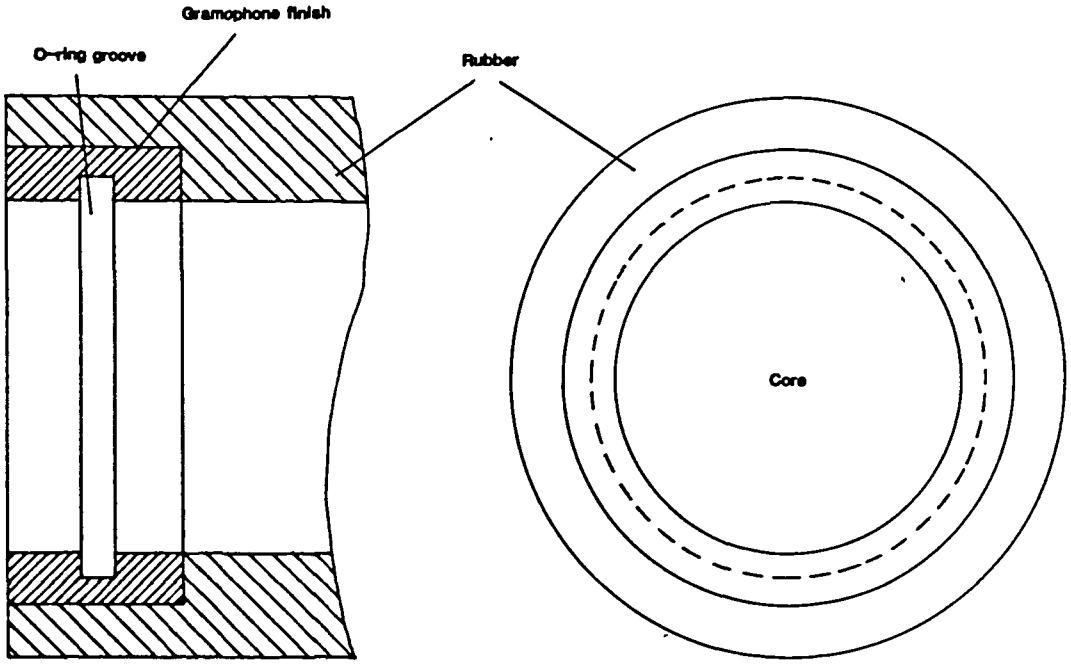

Tapping Piece

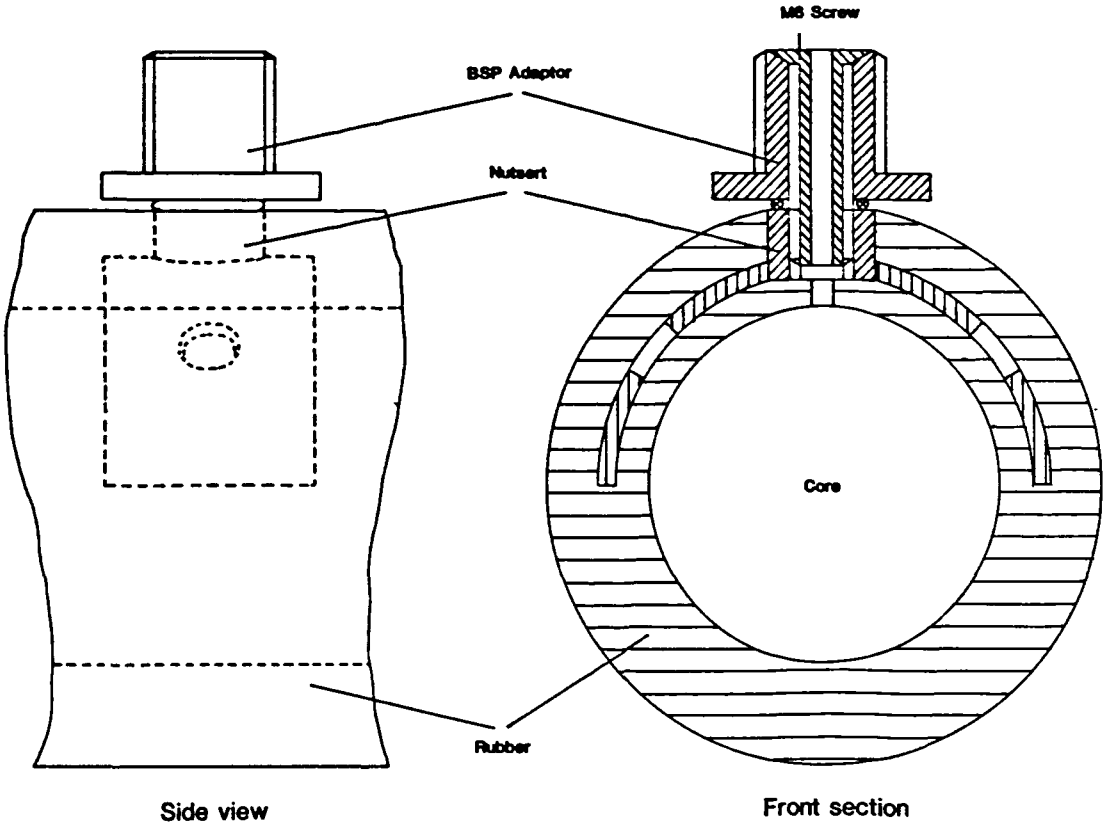

Figure 4.13 Design of components for proposed rubber sleeve

o-ring was housed in specially manufactured, steel rings bonded into the ends of the sleeve. Sealing between metal and rubber here was improved by using a gramophone finish on the outside of the steel ring. The use of an o-ring gave an "high-confidence" seal that did not rely on external pressure from the confining fluid to ensure sealing. Even in the event of loss of some confining pressure, fluid should not be lost from inside the sleeve. This system also had the ability to take up any differences in the expansions of the core, the sleeve and the core holder when the whole unit was raised to temperature, by the o-rings sliding along the outer faces of the inlet and outlet heads that would protrude through the o-rings to seat against the core.

No working core-holder for this sleeve was designed as at the point where development work stopped the sleeve was still suffering from leaks between the rubber and the Nutsert bodies. This was believed to be a factor of the manufacturing process, which was largely outside the control of the author, and not due to any fault in the design.

Design of a low pressure, low temperature, resin-bonded, multi-tapped core-holder

As mentioned earlier, the development time for the rubber sleeve was far longer than anticipated. The system chosen to fill the gap in order to get on with the experimental study was a modification of the resin-bonded system used for earlier testing of distribution faces. The design of the multi-tapped version of this system is shown in figure 4.14. Figure 4.15 shows the core holder in use and the components of the core holder when disassembled.

This core holder compromised the design criteria for the required multi-tapped core holder in several ways. The experiments could not be conducted at reservoir temperature and pressure, in fact

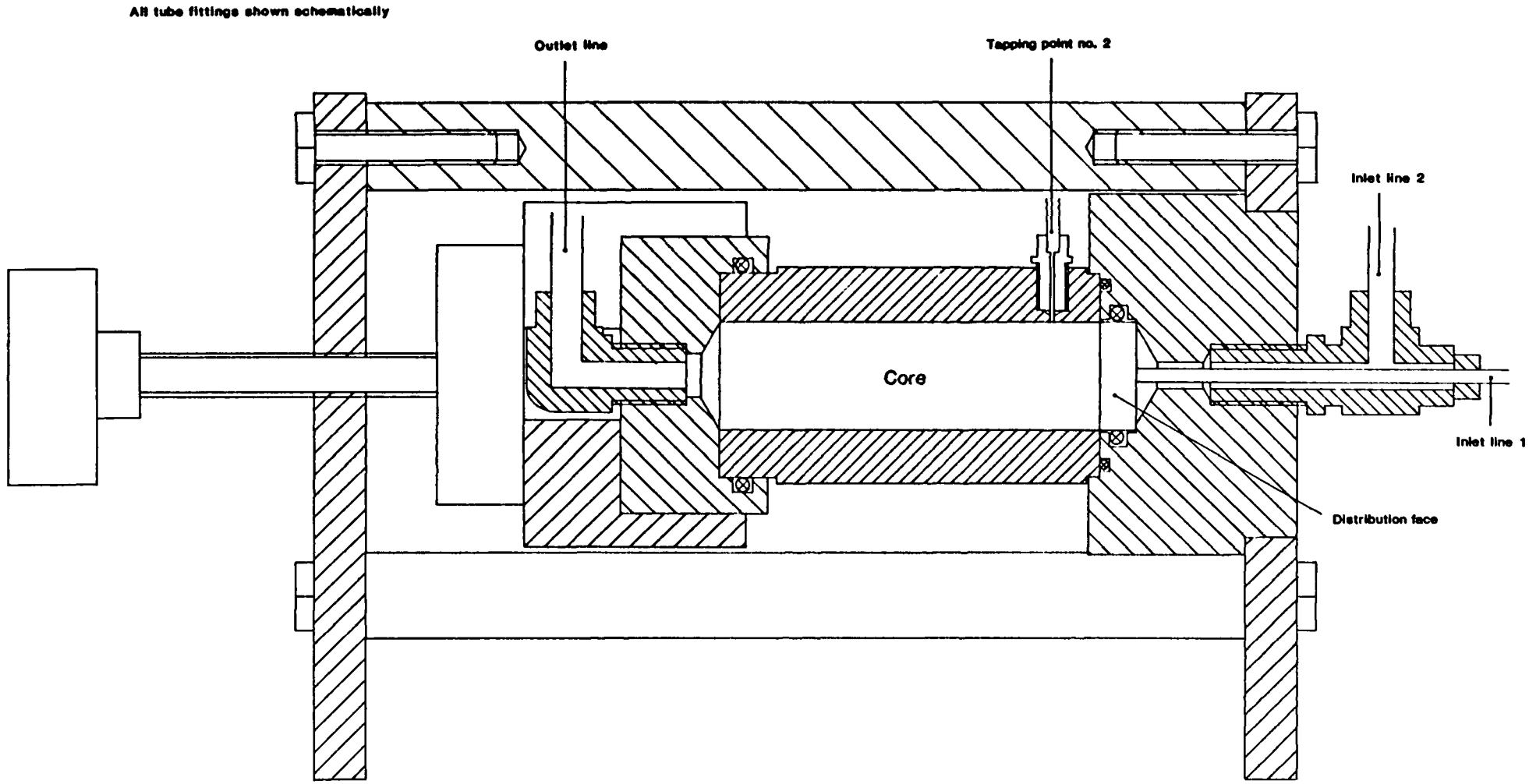

Figure 4.14 Sectioned drawing of clamp core holder

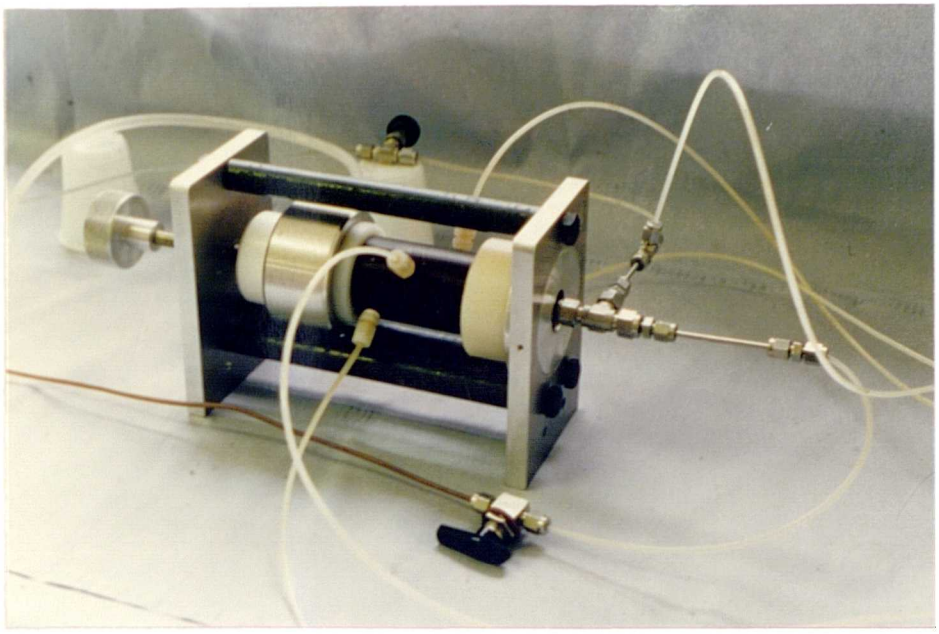

Figure 4.15a Clamp core holder in use

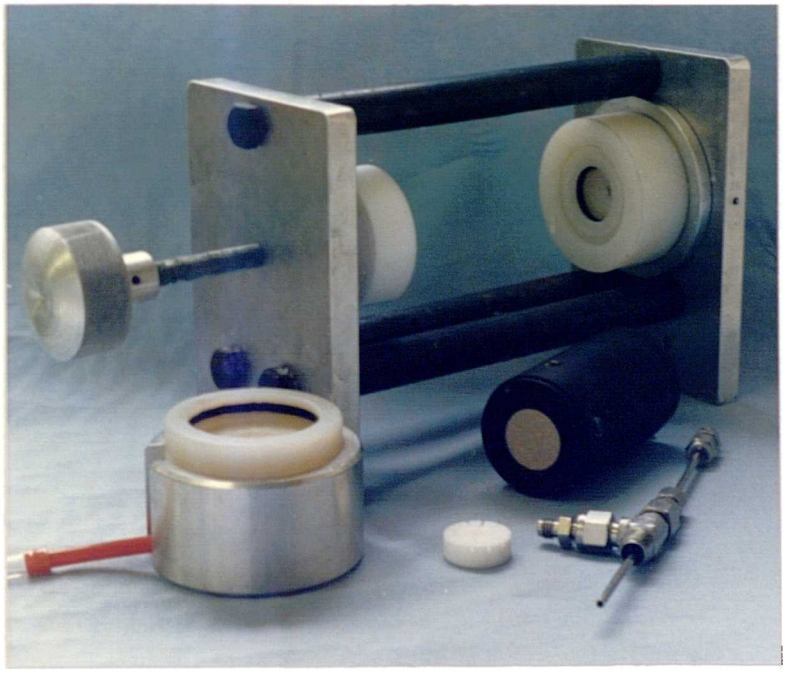

Figure 4.15b Components of clamp core holder disassembled

the temperature could not be raised much above room temperature and the pressure was limited to about 500 psi from previous experience with resin-bonded cores. Also, the core was not readily available for analysis before or after experimentation in the same form as it was when the experiment was performed. On top of this, preparation of the cores was very messy and time consuming. Nevertheless, this technique had a proven record under these limiting conditions[39,50] and so development time to a working system was very short.

To make the tappings the resin thickness was increased to about 12mm. The resin was drilled and tapped to take $^{1}/_{16}$" NPT conversion fittings. To avoid damaging the delicate resin threads nylon fittings were used to improve sealing of the threads without having to tighten the fitting too much. The tappings were spaced radially around the core as well as along its length to increase the amount of resin between the tappings.

The clamp core holder was modified from its earlier form used for testing distribution faces[17] to accept the larger cores and was strengthened to withstand the higher working pressures. The sealing arrangement at the front face was changed from a circumferential seal to a face seal to enable the first tapping to be placed as close to the front face as possible.

This system was very sucessful in service. Apart from the manufacturing of the cores it was very easy to work with. The core holder could be quickly dismantled and reloaded between experiments and was quite robust, great care only being required in fitting the tappings due to the delicate resin threads. There were no experimental failures due to tapping failure or leaking seals.

4.4.3 Data Collection

The manner in which data is collected and recorded from an experiment is as important as any other part of experimentation. If carried out improperly the data becomes invalid and so the experiment is wasted.

In view of the likely amount of data to be gathered for each experiment, several tapping points to be measured at frequent intervals over several hours, it was desirable to have some degree of automation in the collection of the data. This was easily achieved by the use of a computer based data logging system. It was also considered advantageous to strive for the greatest accuracy reasonably possible (cost being the biggest factor here). For any measurement system, accuracy is largely a function of calibration as well as the properties of the measuring device.

The data collection system to be used for recording pressures at the tappings in the proposed experimental study is described below. Attention is drawn to the fact that the method of application of the system can have a large effect on the accuracy and reliability of the data gathered.

General description of equipment used

The intended layout for transducer connections is shown in figure 4.16. It will be shown later that this layout was not concurrent with obtaining the greatest accuracy from the transducers and an alternative layout will be proposed. Differential pressure transducers were used as these should give consistent accuracy at any working pressure used in the core. As the amount of permeability damage due to scale that was likely to occur in any section of the core could only be guessed prior to the experimental study, the pressure

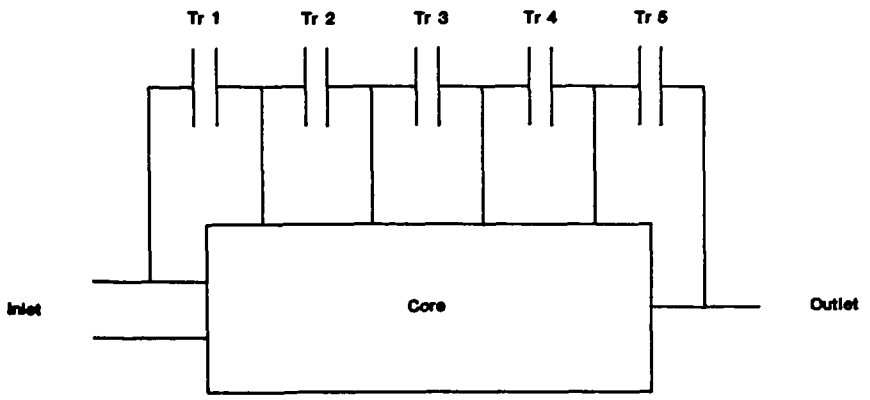

Figure 4.16 Intended layout of tapping transducer connections

Figure 4.17 Transducer Calibration Results
Transducer 1 (0-1000psi): Change in Response With Line Pressure

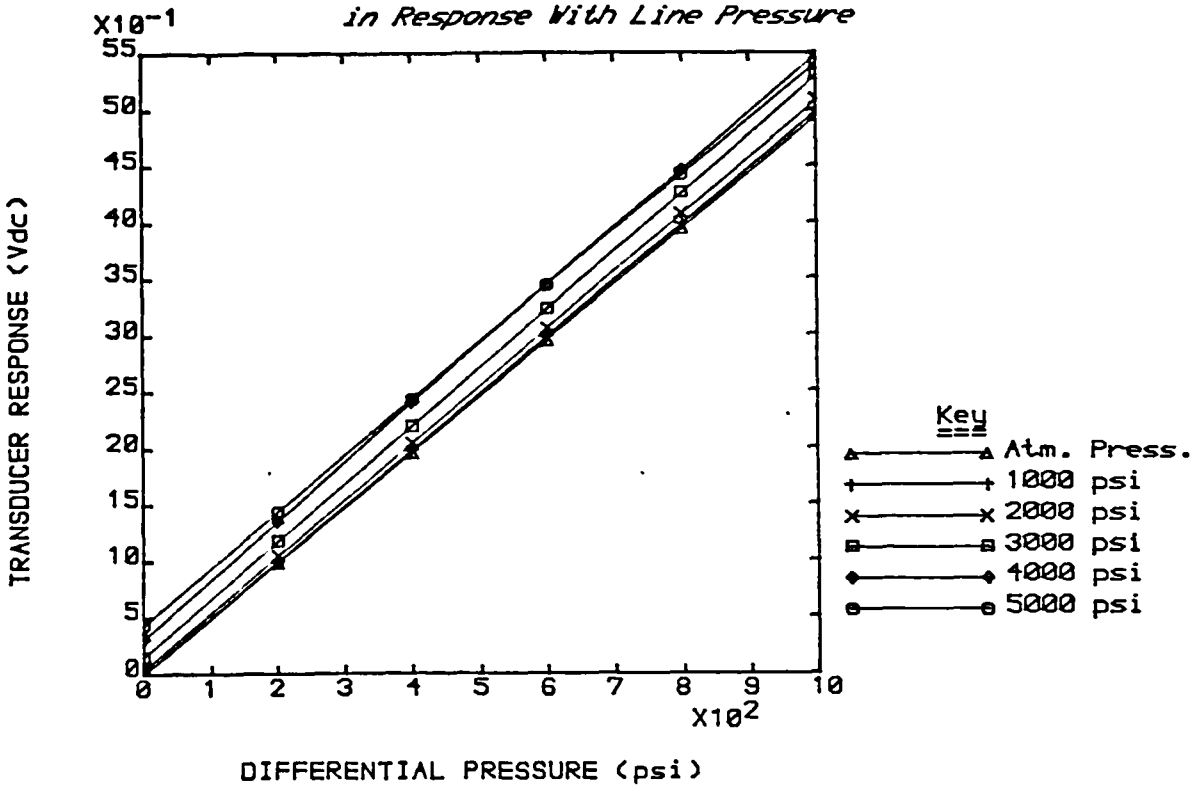

range over which each transducer was required to operate was unknown. From the point of view of obtaining the greatest accuracy it was advantageous to be able to tailor the range of each transducer to suit its position on the core as experience grew of the likely pressure drop it would be measuring. Thus, the requirements for the pressure transducers were that they had a variable pressure range and were capable of working up to reservoir pressures.

Of the systems available to satisfy these requirements, the Thorn-EMI, SE Labs SE-1150 transducer was chosen for use, as much on the reputation of SE Labs transducers as on the paper specification. The SE-1150 was a variable reluctance transducer with a quickly inter-changable diaphragm to vary the pressure range. The accuracy was specified as a linearity to within 1% of range.

These transducers were driven by an SE-1050 rack system containing one SE-1053 ac signal conditioning module for each transducer and an SE-1051 monitor module to ease setting-up of the system. The SE-1050 system considerably increased the flexibility of the transducers by allowing them to be calibrated to a range within the range of the diaphragm fitted, without loss of accuracy. It also made zeroing and calibrating the transducers a fairly simple procedure.

Each SE-1053 module sent a dc signal to the computer logging system, which comprised a Hewlett-Packard HP-85 laboratory computer coupled by an HP-IB interface bus to an HP-3421A data acquisition and control unit. The HP-3421A was configured with 18 data channels and 2 actuating channels. For the range in which the transducers operated it had a measuring accuracy of 10^{-4}Vdc. The HP-85 was supplied with comprehensive software enabling it to make measurements on all data channels at any frequency up to once per minute. It recorded the data on tape using its internal tape drive.

Transducer calibration

While attempting to calibrate the transducers and verify the claimed accuracy, problems were encountered which have great implications for any work that uses variable reluctance type differential pressure transducers.

Figure 4.17 shows a typical set of results from the calibration of one of the pressure transducers. This was produced by measuring the response of the transducer at eleven set points across its range and at line pressure increments of 1000 psi. For any single line pressure the linearity of the transducer was well within the specified 1%.

An attempt was made to convert these readings into a single equation for pressure in terms of transducer response and line pressure. With the number of points shown in figure 4.17 in the calibration it was difficult to get better than 7% accuracy for any one transducer. To bring this anywhere close to the specified accuracy would require a substantial increase in the amount of data to about 500 calibration points, which was totally impractical. Therefore, to achieve reasonable accuracy the transducers were limited to working only with a limited range of downstream pressure. This sort of behaviour was apparently typical of variable reluctance type transducers[18] and made them unsuitable for use with widely varying line pressures.

For the intended application this posed great difficulties for the accuracy of the readings. In the layout shown in figure 4.16 the first four transducers had their downstream legs at unknown pressures, which would further reduce accuracy as the only known pressure would be at the end of the core. Clearly the only way to obtain reasonable accuracy out of the transducer system was to have the downstream legs at known pressures and the transducers calibrated to suit this line

pressure. A layout which fulfilled this requirement is shown in figure 4.18. This layout has lost the benefits of having the tranducers closely tailored to specific tapping points, but this was considered minor in comparison to overcoming the accuracy problems of the transducers when used at fluctuating line pressures. In this layout all the transducers were calibrated to suit a single line pressure, the back-pressure on the core, and so each had the full specified accuracy. To ensure that this line pressure was maintained a gauge pressure transducer was to be fitted to the outflow line from the core for any higher pressure work.

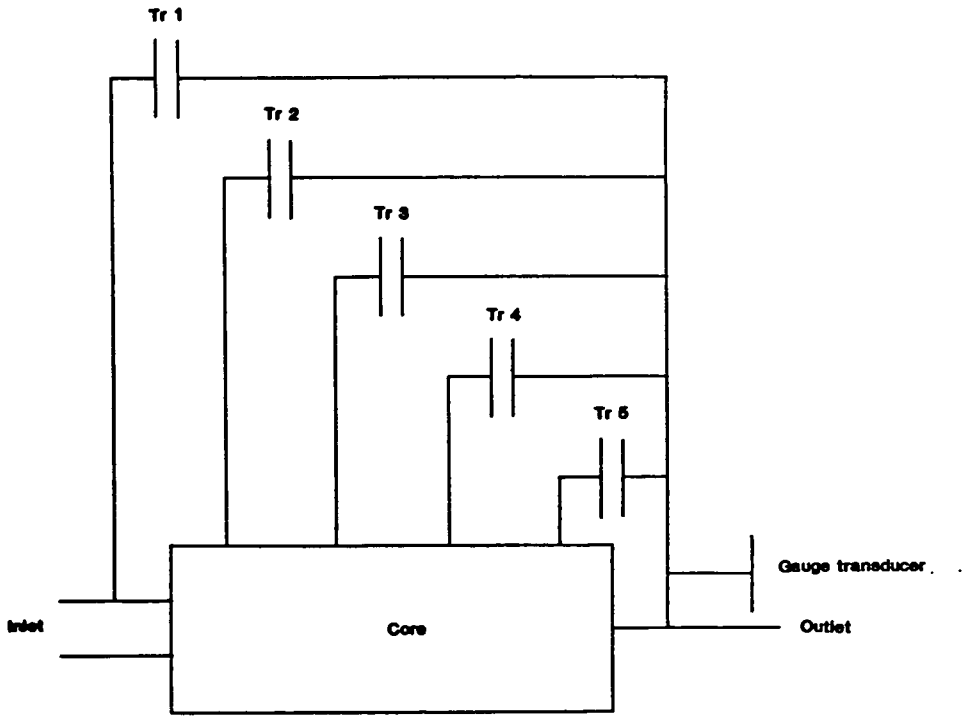

Figure 4.18 Layout of tapping transducer connections used to achieve the best accuracy from the transducers

4.5 THE SCALING PERMEAMETER

The rest of the equipment used in the experimental study for this work was broadly an upgraded version of that used by Pucknell[35] and later improved by Simm[41]. The general layout and equipment used were improved to ease operation and give better reliablility. Adoption of a modular design made the equipment highly adaptable so enabling many different types of experiment to be performed in the future.

The main criteria for the design of the permeameter were for it to be able to simulate reservoir temperature and pressure conditions, whilst maintaining safety and ease of use, and the ability to run for long periods unattended. The added requirements for mobility and versatility were easily achieved through modular design. The schematic plans for the permeameter are shown in figures 4.19 to 4.21 and the permeameter itself is shown in figure 4.22. The major points of each of the modules are described below.

4.5.1 The Tank Module

The tank module carried five tanks, four of 20 litre capacity and one of 1 litre capacity. The 20 litre tanks supplied the two lines to the pump through various switching valves. The 1 litre tank by-passed the pump system to feed directly into the core for saturation purposes prior to pumped flooding. All the tanks were independantly served by vacuum, for filling and deaerating the solution in the tanks, and nitrogen, for blanketing and to increase the pressure head for the pump. There was also a facility for draining each tank. A service line from the tank module vacuum system was provided for supplying vacuum to other modules and experiments.

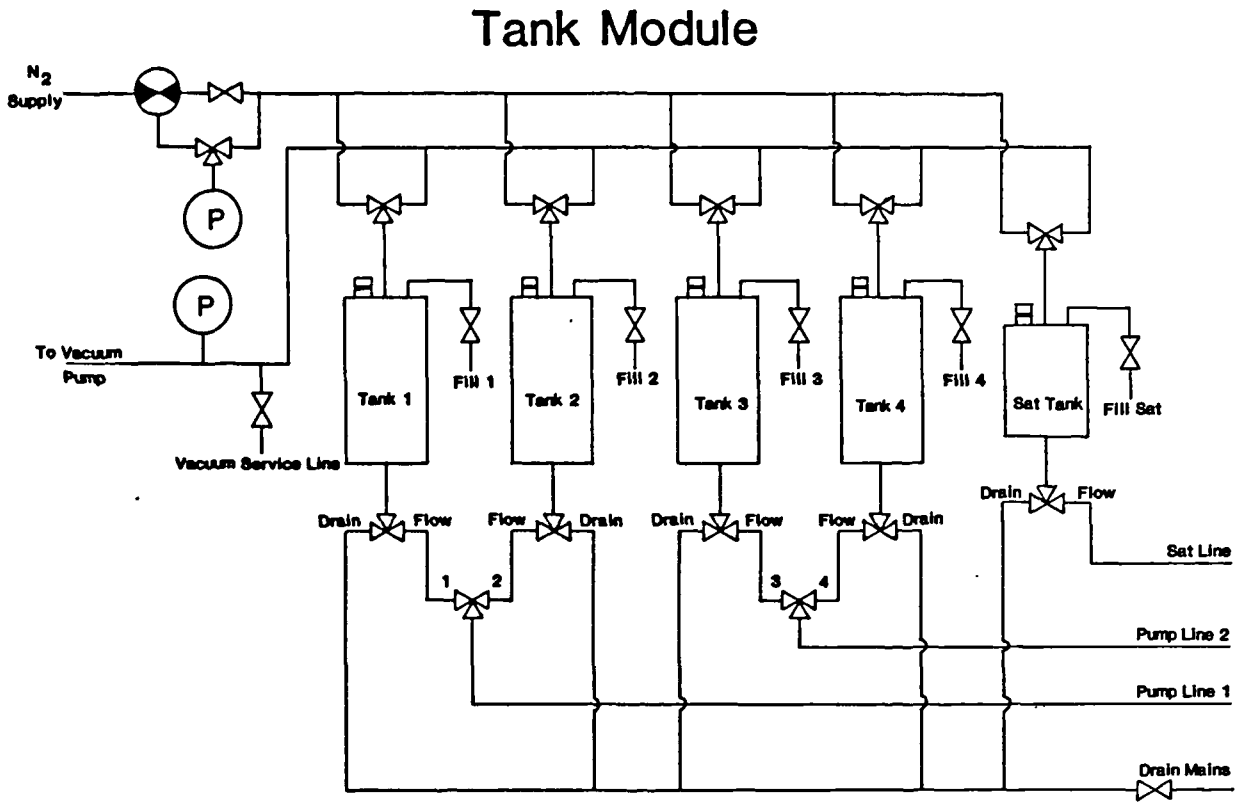

Figure 4.19 Flowscheme for tank module

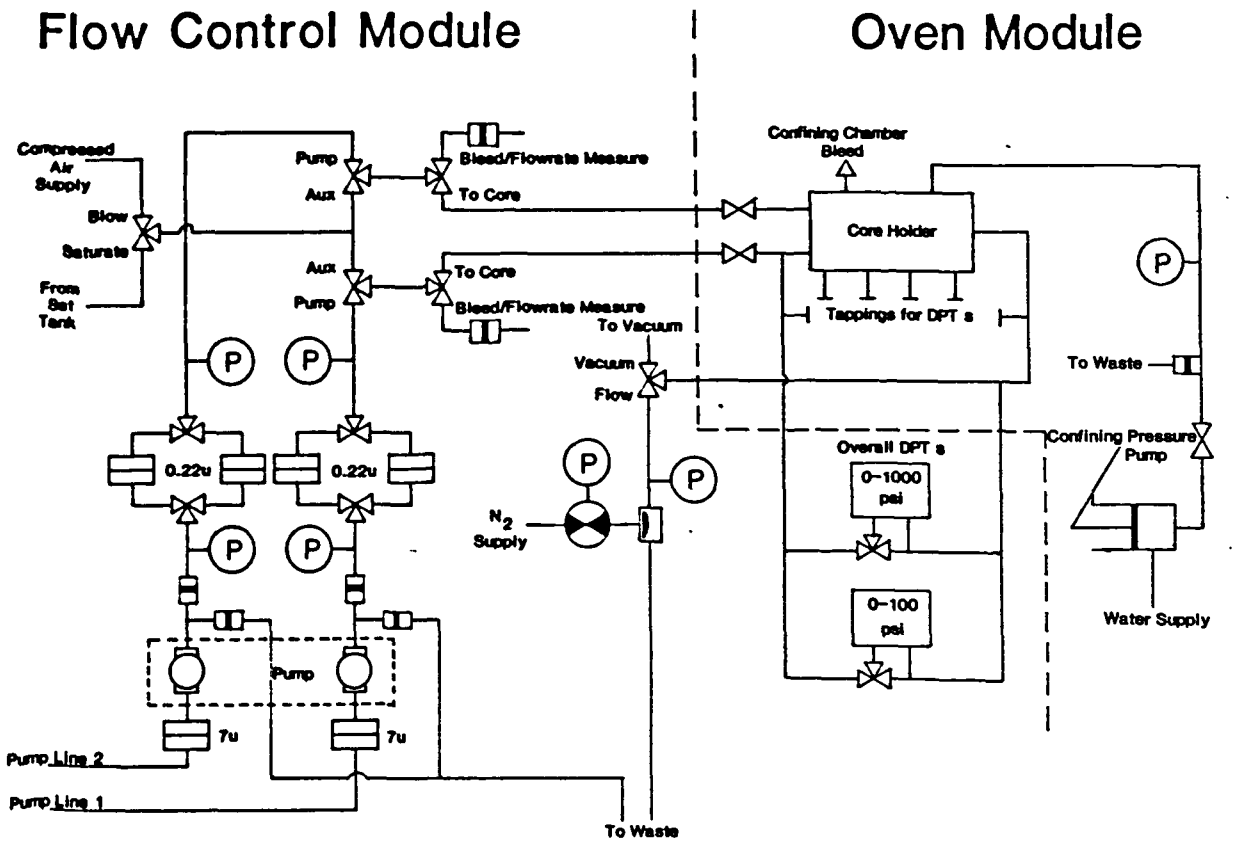

Figure 4.20 Flowscheme for flow control and oven modules

Key to symbols used in figures 4.19 and 4.20

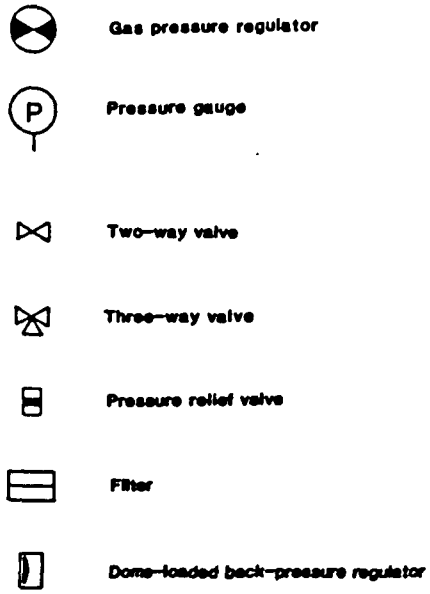

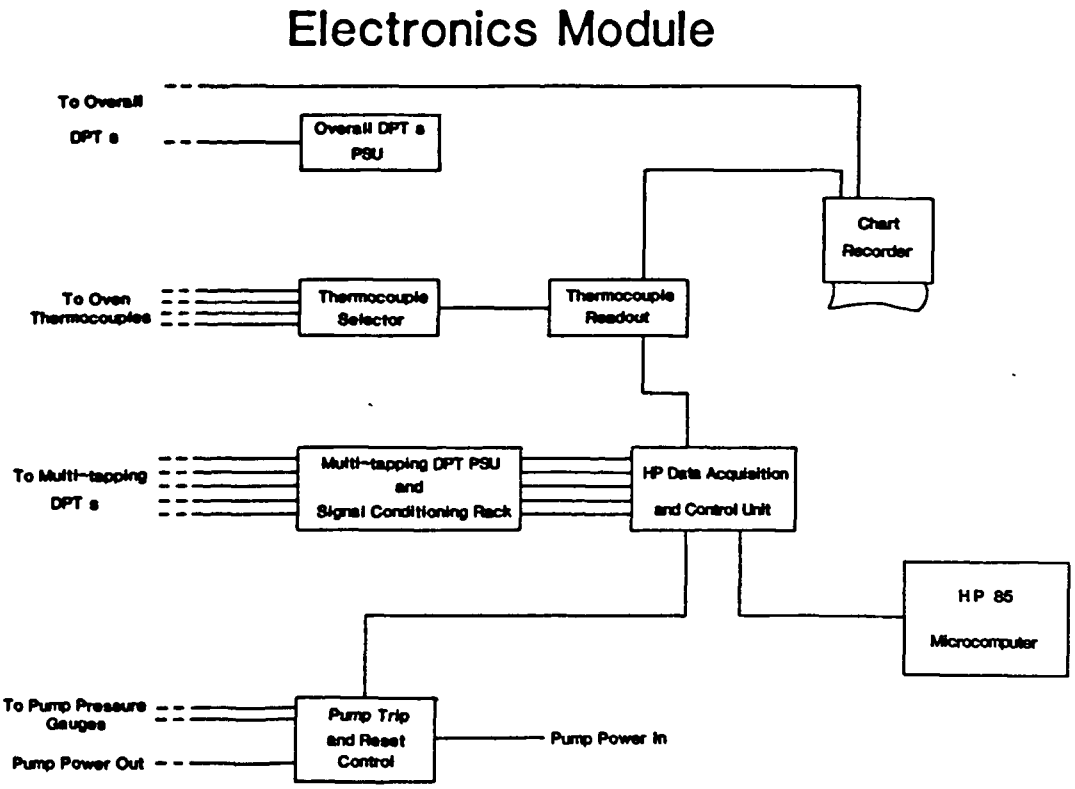

Figure 4.21 Schematic layout of electronics module

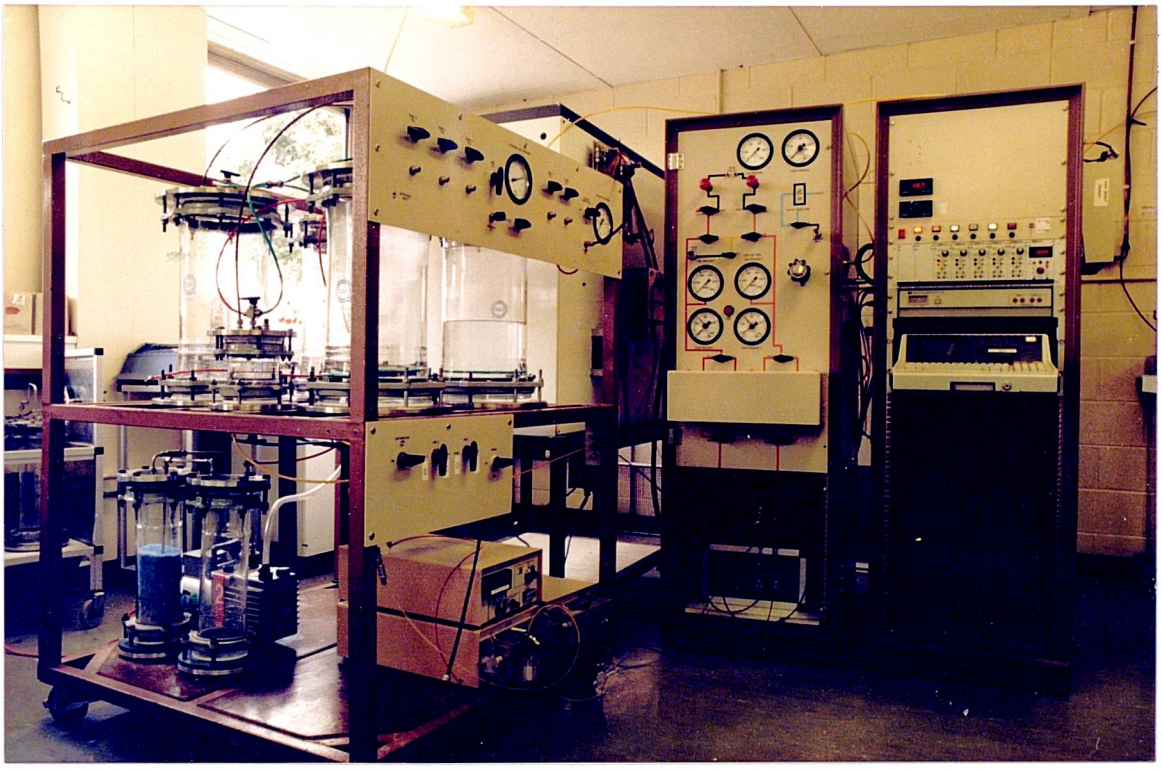

Figure 4.22 Front view of scaling permeameter with both pumping systems used in place

4.5.2 The Flow Control Module

The flow control module was fairly typical of high pressure core flood equipment, the main difference being that the flow lines were doubled-up to keep the two brines separate until they reached the core. The flow in the two lines from the tank module was filtered to 7μm before reaching the pump heads. The pumped flow was then filtered to 0.22μm before entering the core. This level of filtration was used to remove any chance of damaging the core by particle invasion.

Before switching the flow to the core or at any time during the experiment the flowrate could be measured or pressure bled off through externally adjustable pressure relief valves. These allowed the flowrate to be measured at pressure or the pressure in the lines to be released gradually. Any air getting into the system during an experiment, through the need to break fittings for any reason, could be bled out through this facility. This was important as any air reaching the distribution face could seriously affect its mixing performance.

Flow returning from the core passed through a back-pressure regulator, which could be used to increase the line pressure at the exit end of the core. Because of the low pressure rating of the core holder used for the experiments in this study this facility was not used.

Pump pressure, line pressure and back-pressure in the liquid lines were monitored on pressure gauges. The pump pressure gauges were fitted with adjustable make-on-rise electrical contacts to provide a signal to the electronics module should the pressure rise to a preset limit. All components in the flow lines from pump to core were rated for 6000psi working pressure.

Two pumps were used with this equipment during the course of the experimental study. The first was an Applied Chromatography Systems Model 400H laboratory pump fitted with 0-30ml/min "prep" heads for low

pressure work and 0-10ml/min "analytical" heads for high pressure work. This pump became prone to flowrate fluctuations and flow cessation and was thus unreliable for long unattended core-flooding experiments. This pump was replaced by Lab Data Control Constametric I and II pumps, which had a maximum flowrate of 10ml/min each.

The flow control module also carried two SE-Labs SE 21/V differential pressure transducers with protective plumbing, one of 0-1000psi and one of 0-100psi. These transducers were intended to provide overall differential pressure readings across the core on a continuous basis as their output was routed to a chart recorder on the electronics module.

4.5.3 The Oven Module

The oven module was the "business end" of the permeameter. It carried the core holder, the tapping transducers and the confining system. The core holder was housed within a thermostated enclosure (a Baird and Tatlock Unitemp oven), which raised the temperature of the whole system to slightly above that required to simulate the reservoir condition. The flows from the flow control module were taken through lengths of coiled pipe so that by the time they reached the core they had been raised to the experimental temperature.

The differential pressure transducers, used for measuring pressure at the tappings on the core, were mounted on the back of the oven. Although these transducers were rated for the temperatures to be used, operating them inside the oven would have caused additional complications in calibration and a further reduction in accuracy.

Due to the risk of stress corrosion cracking in high pressure, high temperature, high salinity systems using ordinary 316 stainless steel tube, for working at high pressure all brine-wetted tubing was to be

replaced by alloy 825 tubing. This alloy is very resistive to chemical attack under severe conditions of temperature and pressure.

4.5.4 The Electronics Module

The electronics module performed the collection and storage of data from the experiment and was also the heart of the system that enabled the apparatus to operate unattended. Data on temperature and pressure at various points of the system was recorded and displayed. This information could be used to stop the experiment if necessary due to overstepping of the limits of the equipment.

At the centre of the module was the HP-85 experimental logging computer and HP-3421A data acquisition and control unit. This unit was connected to the tapping transducers, the line pressure, gauge transducer and a set of five type K thermocouples used for measuring the temperature of various flow lines in the oven module.

The key to the unattended operation of the apparatus lay in the pump control circuitry. The power to the pump was controlled by a relay which could be tripped to the off position by the contacts on the pump line pressure gauges or by the computer if either i) one of the pressure transducers was overpressured or ii) a preprogrammed time limit for the experiment was reached.

4.5.5 Use and Limitations of Scaling Permeameter

As the core holder described in sub-section 4.4.2 was not available in time for the experimental study performed for this work, none of the high pressure and high temperature facilities of this equipment could be put to use because of the limitations of the clamp core holder

discussed at the end of sub-section 4.4.2. The equipment could still inject considerable variety into the experiments as it allowed different flowrates to be used and rapid changes of the brines being pumped. The next chapter describes how these available factors were brought together for the study of scale formation in sanstone cores.

CHAPTER 5

EXPERIMENTAL INVESTIGATION OF THE NATURE OF SCALING IN SANDSTONE CORES

5.1 INTRODUCTION

The model proposed in chapter 3 required the support of experimental data both to run it and to justify any results it produced. The choice of technique and design of equipment that might provide the necessary experimental data from the flooding of sandstone cores was discussed in chapter 4. In this chapter the experimental work is described and the results generated are analysed and discussed both as general data on scale formation and as a database for matching with the model.

The experimental study was based on how the solution composition and supersaturation, with respect to barium sulphate, affected the morphology of barium sulphate crystals grown both in static bulk solutions and under conditions of continuous flow in sandstone cores. Through this study, the effect of solution composition, supersaturation and flowrate on the flow supporting properties of the cores could be observed. The study of crystal morphology was not only useful in its own right, but also provided valuble clues to understanding the nature of the permeability decline and porosity change of the sandstone due to scale growth within it.

Several theories are proposed to explain the pattern of permeability damage observed. These theories are investigated separately and one is adopted and used with success to explain most of the results generated by the experimental work. The relationships produced in the light of this theory are expected to be of direct use

in fields where scale formation is a problem, such as secondary recovery of oil by water drive and geothermal energy, as well as for the purposes of developing a model of the scaling process. The experimental results are also analysed using the precipitation rate equation (equation 3.17) upon which the model discussed in chapter 3 was based. This latter analysis was carried out in an attempt to find a direct relation between the core experiments and the model.

5.2 THE PROGRAMME OF EXPERIMENTAL STUDY

5.2.1 Purpose of the Experimental Study

The purpose of performing the experimental study described below was to provide more detailed information than was previously available on the nature and extent of damage to the flow supporting properties of sandstone cores due to scale formation. This information was to assist in generating and validating a model of the scaling process. The experimental work was also aimed at improving knowledge as to the degree of damage to permeability possible and what factors influence its severity.

5.2.2 Aims of the Experimental Study

General aims

The experimental work had two general aims. Firstly to identify the general pattern of a scaling process in a porous sandstone environment as seen through its effect on the permeability of the sandstone. These overall patterns were to serve as a coarse tuning device that would indicate whether or not the model was capable of producing more quantitative information. Secondly, quantitative data was required in the form of permeability decline rates, porosity changes, etc., for fine tuning the model and, if the data was good enough, for evaluating terms such as the reaction constant in the precipitation rate equation (equation 3.17). The data for the latter of these aims obviously reflected the inherent variability of the natural sandstone that was used for the study, though every effort was

made to keep this variability to a minimum.

Investigation of effects of scale on the permeability and porosity of the cores

The permeability decline of a core and the quantity of scale involved in causing the decline were considered to be most important to the tuning of a model. In work related to this study Simm[42] had already shown that large permeability damage could occur for very small changes in porosity. This study, then, was to investigate the relationship between the permeability and porosity and attempt to identify what affects the rate, nature and extent of the permeability decline.

A vital factor in the relationship between the permeability and porosity changes was thought to be the effect that differing crystal morphologies might have upon the rate of permeability decline as was discussed in subsection 4.3.2. It was also considered useful to attempt to discover what controls the morphology of the crystals and therefore their influence on the permeability of the core.

An investigation of the effects of flowrate and supersaturation of the brines was performed by Pucknell[35]. This was also to be included as part of this, more detailed study especially as supersaturation not only controls the rate of precipitation, according to the precipitation rate equation (equation 3.17), but could have an effect upon the crystal morphology.

Use of a multi-tapped core holder

Unlike previous studies, a multi-pressure-tapped core holder was used in this work. This enabled the processes occuring within the core during the flow of scaling brines to be observed in greater detail

by studying the permeability changes in each section rather than in the core as a whole. This provided improved information on what happened after mixing of the incompatible brines. The aim of this part of the investigation was to see if there were any time factors involved, such as might be attributed to an induction period for nucleation, though the likelyhood of this has already been dismissed in section 3.4.1. The consequences of long term flooding with a mixture of incompatible brines could also be studied to see whether the permeability damage caused would remain localised or would spread downstream.

Summary of experimental aims

In summary, the aims of the experimental study can be largely expressed by the four points below:

i) to study the rate, nature and extent of permeability changes in a sandstone core due to the formation of barium sulphate scale under flowing conditions both as a function of time after mixing and of the duration of the flow.

ii) to investigate the effect on the characteristics of the permeability decline of the core of differing supersaturations and flowrates of the brine flowing through the core.

iii) to quantify the amount of scale formed that lead to the observed permeability changes.

iv) to investigate what factors influenced barium sulphate crystal morphology and whether the morphology had any effect upon the characteristics of the permeability decline.

5.2.3 The Programme for Experimental Work

Basis of the programme

The morphology of the crystals grown in the sandstone cores was considered as likely to be of great significance to the nature of the permeability damage caused. Thus, the study of crystal morphology was chosen as the basis of an experimental programme designed to satisfy the aims outlined above. As the crystal morphology was considered so important to the nature of permeability change its study was expected to automatically cover the main aim of the work, to investigate what influences the nature of permeability change. Factors not expected to affect morphology, such as flowrate of the brines flowing through the core, were also included to complete the study of permeability decline due to scale formation.

Factors affecting crystal morphology

The programme for experimentation was mainly devised from factors expected to influence the crystal morphology. Pucknell[35] cites supersaturation as the major factor affecting morphology. The discussion in subsection 4.3.2 analyses Pucknell's view and suggests that the solution composition might be just as significant as the supersaturation to the crystal morphology. Both of these factors were investigated in the experimental work as a greater dependance of the crystal morphology on either one of them could have significant implications for industrial water-flooding operations.

A study on the effect of unequal concentrations of the mineral forming ions was also included. It is most unlikely that equal ion concentrations would be present if scale were forming in a natural sandstone formation, so any effect of unequal concentrations on

morphology should be noted in order to be able to relate the results of the experimental study to a real situation.

Summary of the experimental programme

The principle points of the experimental programme followed to try to achieve the aims of the experimental work described earlier are set out below:

i) a study of ion ratio effect by successively reducing the concentration of one mineral ion with respect to the other from an initial ratio of 1:1 whilst maintaining a level supersaturation.

ii) a study of the effect of supersaturation starting with a supersaturation equivalent to one of the highest known in the North Sea (approx. 70) and reducing the supersaturation in steps until equivalent to one of the lowest known in the North Sea (approx. 8), mineral ion concentrations being kept equal throughout.

iii) a study of the effect of ionic strength by choosing a middling supersaturation (approx. 20) and using a higher background concentration of sodium chloride than for the supersaturation study, raising the scaling ion concentrations accordingly.

iv) a study of the effects of the presence of other interfering ions by adding strontium, magnesium and calcium in quantities typical for North Sea fields.

All these experiments were performed at room temperature and

pressure due to the limitations of the clamp core holder. Temperature was also expected to have an influence on morphology as the mobility of the ions would be increased and any surface reactions involved would be faster as the temperature was raised. Unfortunately, investigation of this effect must be left to later workers. Limitations in the control of the pump flowrates meant that the flowrate was only adjusted occasionally and no detailed study of its effect was performed.

5.2.4 Specification of the Brines Used in the Experimental Work

Table 1 gives the compositions of the brines used in the experimental work. Each brine system, designated by a letter of the alphabet, consisted of two brines, one rich in barium ions the other rich in sulphate ions, which were kept separate until after they had entered the core as described in section 4.4. For example the first pair of brines in table 1 constituted brine system A. A certain "background" concentration of sodium chloride was used in all the brines to provide a means of controlling the ionic strength of the brines independant of the barium and sulphate concentrations. Sodium chloride was used as sodium and chloride ions are generally the most abundant ions in natural sea and formation waters.

A supersaturation value for each brine system is also given in table 1. Brine system A had a supersaturation of 70. This is the fractional supersaturation (see equation 3.22) for a 1:1 mix of the two brines that form each brine system and was calculated by the solubility prediction programme described in chapter 3.

The specification of the brines used for each of the four studies detailed above is described below.

Table 1. Brine compositions

BRINE	SALT CONCENTRATION (molar) NaCl	$BaCl_2$	Na_2SO_4	$MgCl_2$	SQ. RT. SOLUBILITY PRODUCT (molal)	FRCTNL S-SATN FOR 1:1 MIX
Barium A	0.1	0.005			3.62×10^{-5}	70.0
Sulphate A	0.1		0.005			
Barium B	0.1	0.01			3.74×10^{-5}	67.0
Sulphate B	0.1		0.0025			
Barium C	0.1	0.02			3.96×10^{-5}	63.0
Sulphate C	0.1		0.00125			
Barium D	0.1	0.0025			3.59×10^{-5}	35.0
Sulphate D	0.1		0.0025			
Barium E	0.1	0.00125			3.57×10^{-5}	17.5
Sulphate E	0.1		0.00125			
Barium F	0.1	0.0006			3.56×10^{-5}	8.4
Sulphate F	0.1		0.0006			
Barium G	1.0	0.00179			1.02×10^{-4}	19.0
Sulphate G	1.0		0.00845			
Barium H	1.0	0.004			1.02×10^{-4}	19.0
Sulphate H	1.0		0.004			
Barium I	1.0	0.004			1.02×10^{-4}	19.0
Sulphate I	1.0		0.004	0.004		

Table 1. Continued

BRINE	SALT CONCENTRATION (molar)					SQ. RT. SOLUBILITY PRODUCT (molal)	FRCTNL S-SATN FOR 1:1 MIX
	NaCl	$BaCl_2$	Na_2SO_4	$SrCl_2$	$CaCl_2$		
Barium J	1.0	0.004		0.004		1.02×10^{-4}	19.0
Sulphate J	1.0		0.004				
Barium K	1.0	0.004			0.05	1.07×10^{-4}	18.5
Sulphate K	1.0		0.004				

Brines for the ion ratio study

The first three brine systems in table 1, brine systems A, B and C, were used in the study of the effects of changing the ratio of the concentrations of the scale forming ions to each other at constant supersaturation. The concentration of the sulphate ion was successively halved while that of the barium ion was raised to maintain the ionic concentration product. Table 1 shows that a slight decrease in supersaturation occurred which was due to the slight increase in ionic strength of the mixed brines.

Brines for the supersaturation study

Brine systems A, D, E and F in table 1 were used in the study of the effects of changing the supersaturation. As shown in table 1, the supersaturation was halved in successive brine systems. Note that the change in supersaturation was brought about by changing the concentrations of the scale forming ions only.

Brines with higher ionic strength

Two brines of higher ionic strength were used to study the effect of the change. The first, brine system G, was a copy of Pucknell's type C brines and was included to demonstrate whether the new distribution face, described in chapter 4, would produce similar crystals to those produced by Pucknell. The second higher ionic strength brine, brine system H, had the same supersaturation as brine system G but with equal concentrations of the scale forming ions. As shown in table 1, the supersaturation of these two brine systems was a little above that for brine system E, but the background sodium chloride concentration was ten times higher.

Addition of other metal ions

The last three brine systems in table 1, brine systems I, J and K, had magnesium, strontium and calcium ions added to them respectively. The composition of these brines was based on brine system H with the extra ions added at a concentration considered representative of the concentration of those ions in North Sea oilfield waters. Again table 1 shows that the slight increase in the ionic strength of brine system K caused a reduction in the calculated supersaturation.

5.2.5 Analyses Performed in the Experimental Work

Techniques employed

Plasma emission spectroscopy was used to analyse samples of brine for their barium content. Samples were taken from the stock solutions and the effluent stream from the core to provide data on the quantity of barium (and hence scale) remaining in the core. Helium gas porosimetry of the scaled cores provided another measure of the quantity of scale deposited. The morphology of crystals grown in the cores was observed by using scanning electron microscopy (SEM) to produce photomicrographs of the crystals on the rock grains. Mercury penetration porosimetry provided capillary pressure curves for both scaled and unscaled samples of sandstone.

Difficulties encountered with the analyses

For the analyses by mercury penetration porosimetry and helium gas porosimetry, comparison of results from before and after scaling

for the same sandstone sample was not possible. In the case of mercury penetration porosimetry, this was because the analysis was destructive. For helium gas porosimetry, because of the method of preparation of the cores for flooding, described in appendix A5.1, and the limitations of the helium gas porosimeter, mentioned in appendix A5.2, to carry out helium gas porosimetry on the cores prior to scaling would have resulted in a core length little over 2". A core of this length was considered unsuitable for the study intended. To provide data for these analyses on the pre-scaled condition of the cores, sample cores from each sandstone block used were analysed to try to characterise the block. For various reasons few cores were available for this sort of analysis and so only limited comparisons between scaled and unscaled data could be made.

The analysis of effluent samples by plasma emission spectroscopy was delayed for reasons outside the control of the author. Additionally, some time was lost in identifying an adequate level of dilution for the samples. The problem here was that the lower level of detection of the spectrometer was not far below the upper level of solubility of the barium in the low ionic strength brines used. This left only a small concentration range available to try to dilute the sample, of unknown concentration, into. As a result effluent data was only available for the later experiments.

5.2.6 The Core Material Used in the Experimental Work

Description of the sandstone

The core material for this study was the largest source of variability in the experiments. The sandstone used was wholly of the Clashach variety, which was quarried in the Elgin area of Scotland.

This sandstone had been extensively used in the past both in this Department and other core laboratories as it had proven itself to be a very suitable material for the reasons described below.

Clashach sandstone had a very low clay content with some feldspars and micas, but for the most part consisted of well cemented grains of quartz. These were fairly well sorted which gave rise to beds of roughly even permeability. Thus, it had little or no reaction to being flooded with aqueous solutions, was easy to cut to size and was available in a permeability range suitable for giving sensible pressure drops at the chosen flowrates. After the sandstone was laid down some of the faces of the grains reformed to give smooth quartz crystal faces known to the geologist as quartz overgrowths. This created a varied environment, for use in the experiments, for the growth of scale. There were some smooth quartz surfaces, some broken quartz grains and some very rough feldspars. Examples of these surfaces may be seen in the SEM photomicrographs later in this chapter.

Difficulties encountered with the sandstone

Unfortunately, recent samples of Clashach sandstone did not quite live up to the description above. Many of the cores used in this work had large quantities of fine material washed out of them on commencement of flooding. In some cases the fines did not all wash out and reduced the permeability of the core to the extent where it was unusable. Almost all of the cores used showed a reaction to distilled water flow after flooding with the scaling brines. Whilst this was not a threat to the data provided by the experiment, which had already been gathered by that time, it did indicate a change in the characteristics of the sandstone. These problems were attributed to a different area of the quarry being worked at the time the blocks used were cut. In

this area fines had probably been washed into the sandstone formation by movement of ground waters. Also the feldspars in the rock had begun to degrade to clays to give the sensitivity to distilled water mentioned above after having been activated by ions in the scaling brines. These problems were, fortunately, at worst an annoyance and as no substitute was available the study was performed using Clashach sandstone.

Most of the cores used in the study were taken from one of two blocks, numbered 22 and 24. Due to availability and difficulties of the types described above a few cores from other blocks (7, 14, 16, 23 and 26) were also used.

The problems of the cores' reaction to flooding described above caused difficulties, when performing experiments, in establishing the initial permeability of the core. To be certain this was identified correctly most experiments were preceded by a lengthy flood of distilled water which continued until the observed pressures stabilised. To back this up and to demonstrate that the cores would not then react to the commencement of a saline flood, some control experiments were performed in which the scaling ions were ommitted from the brines used.

5.3 EXPERIMENTAL TECHNIQUE AND RESULTS

5.3.1 Procedure Used for a Core Flooding Experiment

Preparing a sandstone core for brine flooding

The preparation of the sandstone cores for use with the clamp core holder, which was used throughout this study, is described in appendix A5.1. The prepared core was mounted in the core holder as shown in figure 4.14. With all the inlet pipework connected, but closed to flow, the outlet pipe was connected to the vacuum service line from the tank module and a vacuum applied. This was to aid and improve complete saturation of the dry core with liquid. When a good level of vacuum was indicated by all the tapping transducers, usually after about 30 minutes, both inlet lines were opened to flow from the saturation tank, which normally contained distilled water. When the outlet line from the core was filled with liquid the vacuum was disconnected and the transducer lines bled of any trapped gases using the pressure provided by the nitrogen blanketing of the saturation tank.

Flooding the core

With saturation completed the core inlet lines were switched to pumped flow on the flow control module and the pump switched on. Initially the pump took its supply from tanks containing non-scale forming solutions, usually distilled water. The flowrate through the core was checked and corrected, if necessary, before activating the data logging system. Flow of the non-scale forming solutions was continued until the tapping pressures had stabilised.

The pump supply was then switched to the scale forming solutions. The flowrate through the core was checked before and after flow switching and at regular intervals throughout the experiment to ensure that the pump was performing correctly. During unattended operation the core inlet pressure was logged continuously on the chart recorder to indicate if any fluctuations in flowrate occurred.

Effluent sampling

Effluent samples were taken 5-10 minutes after flow switching and at half-hourly or hourly intervals thereafter. Effluent samples were made by first measuring out the quantity of distilled water required for dilution. The flowrate through the core was then measured and either half a minute or one minute's flow timed directly into the diluting water. This procedure was used to reduce to a minimum any time between production of the effluent sample and its dilution. The sampling was followed immediately by another measurement of flowrate to confirm flow stability during the sampling period. Approximately 15cc of each sample were stored in a sealed test tube for later analysis.

Ending the experiment

The end point of the experiment was decided upon either by running it for a prescribed time, or because the automatic systems on the experimental equipment had detected that the core holder or one of the transducers had reached its pressure limit. At the end of the experiment the pump supplies were switched to distilled water and flooding continued for about 10 minutes. This was to remove all salt forming ions from the core, whose presence could confuse later analyses.

After the experiment the equipment was dismantled cleaned and

dried ready for the next experiment. The core was labelled and dried in an humidity oven for 48 hours before storing ready for analysis.

Reducing the flowrate during a core flood

In some experiments the flowrate was reduced during the experiment in order to observe whether this had any effect on the pattern of permeability change. To achieve this the pumped flow was switched from the core to the bleed outlets on the flow control module (see figure 4.20). The pump flowrates were then adjusted as quickly as possible before returning flow to the core so as to minimise any effect of keeping stagnant solution in the core. The resulting gap in the logged data was later edited out during reprocessing.

Treatment of tapping pressure data

The logged data stored on the internal tape drive of the HP-85 experimental logging computer was transferred to a GEC 4180 mini-computer to take advantage of the larger storage and processing capacity of the GEC. This transfer was performed by interfacing the two computers through a Tektronix 4052 micro-computer running specially written interpretation software. Specially written transmitting and recieving programmes were used on the HP-85 and GEC 4180 respectively.

Analysis of the core

The porosity of the dried cores was measured using an helium gas expansion porosimeter with a 3 × 1.5 inch sample chamber. The procedure for preparing the cores for this analysis is described in appendix A5.2. After this selected cores were cut into the sections defined by the tapping points for analysis by SEM or mercury

penetration porosimetry. SEM work was performed on a Cambridge Stereoscan machine fitted with a sensing head for energy dispersive x-ray analysis (EDAX) of the elemental constituents of the crystals formed. The mercury penetration porosimetry work was carried out on a Micromeritics model 910 mercury penetration porosimeter.

5.3.2 Procedure Followed for a Beaker Test

For the study of the morphology of crystals grown in bulk solutions scrupulously clean glassware was prepared. 50ml of each of the two brines to be mixed were measured out into beakers and then quickly mixed together. The mixed brines were allowed to stand for 24 hours. The crystals formed were filtered off, using Millipore vacuum filtration equipment and 0.22μm filters, and washed with distilled water. The filters and crystals were dried for 24 hours in an humidity oven before being prepared for SEM analysis.

5.3.3 Results from Core Flooding Experiments

All the results arising directly from the experiments and the analyses of scaled and unscaled cores, with the exception of the SEM photomicrographs, are presented in appendix A5.4. Each experiment performed is referred to by a special identification code. The identification system is described in appendix A5.3 and enables the reader to see, at a glance, the core material, flowrates and brines used in any experiment. The system of identification was designed to ease comparison of data presented in tables by removing the need to refer to other tables to discover the conditions under which the experiment was performed.

Pressure tapping data

By far the largest quantity of information from the experiments relates to the measurements of pressure at the five tapping points along the cores, logged, mostly, at one minute intervals throughout each experiment. The logged pressures were processed by computer to produce plots of the permeability of each section of the cores against the time since the start of the experiment. An example of one of these plots is shown in figure 5.1. The rest of the plots for each experiment are presented in appendix A5.4 preceded by table A1, which lists the initial and final permeabilities for each section of the cores and for each core as a whole. Table A1 also includes information on the length of each experiment and the total flowrate of the brines measured during each experiment.

It is normal practise, in presenting permeability data with respect to core floods, to plot the permeability changes against the pore volumes of brine pumped through the core. This practise is intended to normalise the data to allow for the difference in porosity between cores. The main reason that this convention was not followed here was because of the unreliability of the initial porosity data for the cores used.

Helium gas porosity data

Final porosities of the cores, as measured by helium gas porosimetry, are presented in table A1 in appendix A5.4. Because of the scheduling of the SEM analysis and delay in preparing the helium gas porosimeter, some gas porosities of earlier cores were not available.

Figure 5.1 EXPERIMENT C141515AA-4
SECTION PERMEABILITIES

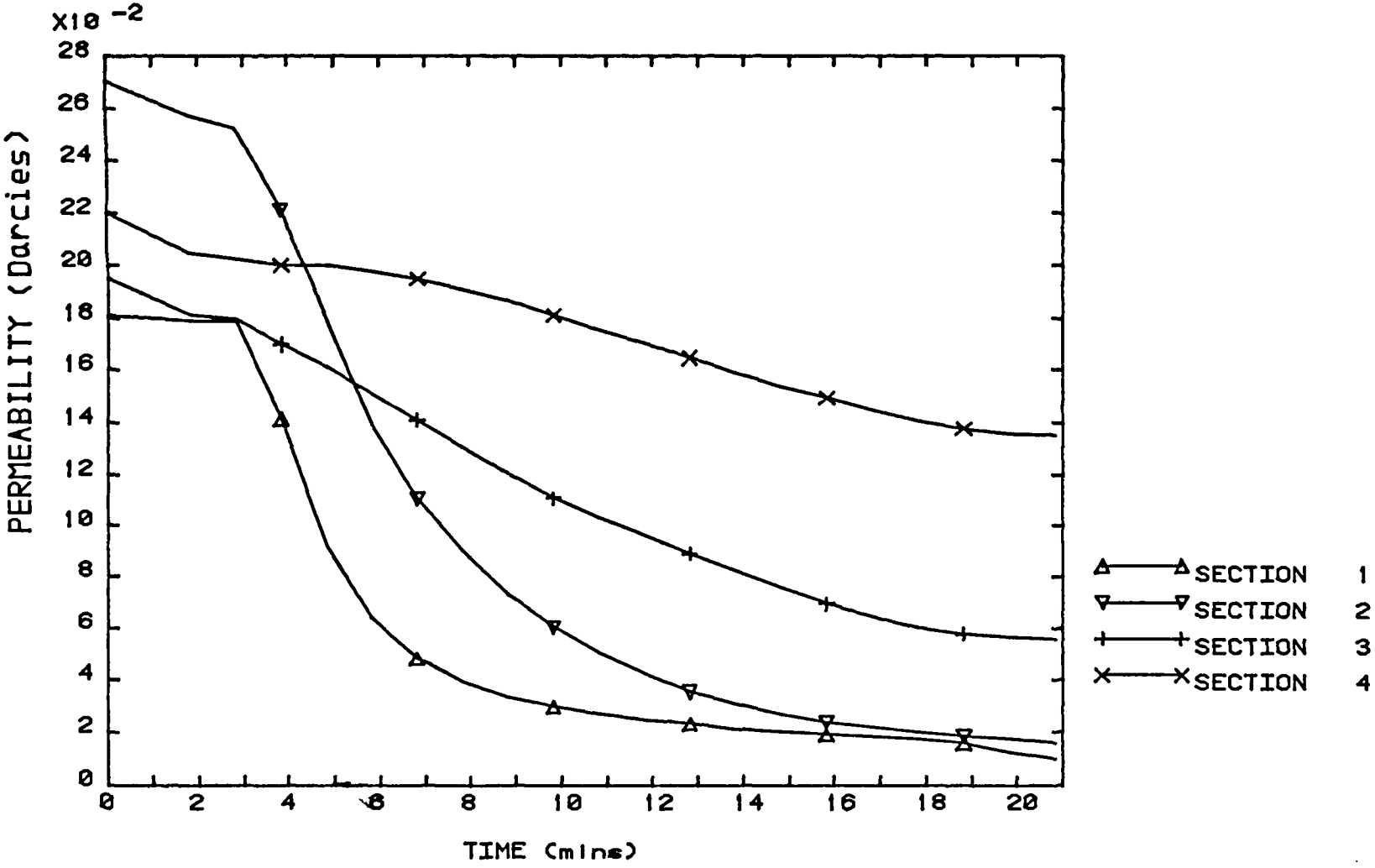

Mercury penetration porosimetry data

The results of the mercury penetration porosimetry study were also processed by computer and are presented in tabular form in tables A4 to A36 in appendix A5.4. Because of the length of time required for each analysis only two sections of each core chosen for mercury penetration porosimetry were analysed. The two sections were generally sections 1 and 4, which were chosen as representative of heavily and lightly scale damaged regions respectively. The information in some of the mercury penetration porosimetry results tables was plotted to show the "s"-shaped capillary pressure curve typical for sandstone specimens. These plots appear with the discussion on the mercury penetration porosimetry results in section 5.7.

Effluent analysis data

The results of the analyses for the barium ion concentration of samples of effluent from the cores are presented in table A2 in appendix A5.4. These analyses were performed by plasma emission spectroscopy and are listed with the times at which each sample was taken. For reasons of cost not all effluent samples were analysed. Also presented in table A2 are the analyses for the barium ion concentration in the barium rich brines before injection into the core. As experiments with brine systems A, B and C were run prior to this form of analysis being implimented no data exists for these brines.

Results of SEM analysis

The SEM study was performed in a similar manner to the mercury penetratration porosimetry study by choosing sections 1 and 4 of the cores as representative of heavily and lightly scaled regions

respectively. The crystals formed in the beaker experiments were also studied using SEM. The photomicrographs resulting from these studies are presented with the discussion on crystallography in section 5.4. The results of using the EDAX facility of the scanning electron microscope to identify the elemental constituents of the crystals produced in the beaker study are listed in table A3 of appendix A5.4.

5.4 CRYSTALLOGRAPHIC ANALYSIS FOR THE MORPHOLOGICAL STUDY

5.4.1 Introduction

Barium sulphate crystals grown as part of this study and by other workers have shown great diversity in the apparent variety of morphologies this mineral can produce. The purpose of performing crystallographic analysis was to try to uncover some common threads that link the many crystal habits observed to what must be, within the limits of normal crystal distortions, a fixed lattice structure of barium and sulphate ions, which was known to be orthorhombic[9]. Establishing similarities between crystals would, at the same time, allow their differences to be qualified scientifically. These differences could then be related to the growth conditions that lead to them.

This crystallographic study was based on information from SEM photomicrographs. In the majority of cases SEM was performed on sections 1 and 4 of the cores chosen for analysis. These sections were considered to be representative of the regions of the core that showed sharply concave permeability decline curves and those regions that showed more gently concave curves respectively. In one case, for a core flooded with brine system A, SEM was performed on all sections of the core. This complete analysis was intended to provide a full picture of the changes in crystal morpholgy that might be expected along a core which would put into perspective the other analyses of just two sections of the core. Because time on the microscope was limited it was not possible to perform full analyses for all cores.

In preparation for analysis the sections of core were broken longitudinally to provide a largely undisturbed profile of the type of crystal produced along the section. Although the mixing efficiency of

the distribution face should have prevented any variation of crystal habit across any cross-section of the core, this possibility could also be investigated using the longitudinal breaking technique.

Over 300 photomicrographs were produced as a result of the SEM study. The comments and observations made below were a result of a consideration of all of them, though for obvious reasons of space not all of the photomicrographs could be presented here. The ones that are presented were chosen to illustrate the discussion in the text and may be considered as representative of the morphologies and populations of the crystals described. Comments on the population of crystals within the core were made with reservation. The comments were based on photomicrographs and, more importantly, on the observations of the analyst as to the general pattern of distribution of growth in the core, which could not be sensibly quantified. Interpretations of SEM photomicrographs had to be made with great care. No information could be obtained about the spread of crystals, or even which were the most commonly occurring types, from photomicrographs alone. Amongst the reasons for this were that only one plane through any section of the core was studied, which may have been a low or high permeability streak and, of course, photomicrographs were only taken where scale occured, not where it did not occur.

Another criterion used in selecting photomicrographs for presentation in this work, was that they should be of a similar level of magnification to ease direct comparison. Unfortunately it was not always possible to follow this policy so when examining the photomicrographs, reference should always be made to the bar at the bottom left of the picture, which indicates the linear dimensions in the frame.

The terminology, such as "form" and "habit", used in the discussion below is concurrent with standard crystallographic usage. Definitions of these terms may be found in most crystallographic texts. It should

be noted that the author had no geological training and so only the most basic techniques were employed here. All the same, it was felt that this simple analysis could throw considerable light on how barium sulphate crystals could be affected by their environment. The technique used here was simply to try to identify the crystal faces and forms observed in the different habits by use of the Miller indexing system and comparison with standard crytallographic works such as those of Dana[8] and Deer, Howie and Zussman[9]. The method of analysis was purely by inspection of the SEM photomicrographs of the crystals and comparison with the analyses of naturally occurring minerals as reported in the standard works mentioned above. Identification of crystal faces can be performed more accurately by using special equipment for measuring the angles between them. This was not considered necessary for this study.

5.4.2 Crystals Formed From Static Bulk Solutions

The most well-formed crystals produced in this work came from the beaker tests. In the bulk solution of a beaker the hydrodynamics of supply of ions was stable and constant. The crystals were not constrained by growing in small spaces, though their growth was limited by the rapidly falling supply of ions as they were included into crystals. The greater regularity of crystals formed in the beaker study made them a good point at which to start the analysis of morphology. For the discussion below the crystals grown were first considered in relation to each other from a crystallographic point of view and later with respect to the four main areas of the morphological study, as detailed in subsection 5.2.3.

General description of crystals formed

Samples of the types of crystal formed by each brine system when mixed in a beaker are shown in figures 5.2 to 5.13. These photomicrographs are examples of the most commonly occurring crystal habits produced by each brine system and were chosen to indicate morphological trends. Other distortions of these habits were observed in many cases, but it would add or detract little in the discussion here to make a full presentation of crystals observed and so for reasons of space this was limited to those shown.

The crystals produced by brine systems A, B and C (figures 5.2 to 5.4), which comprised the study on the change of the ratio of the scaling ions, were broadly similar and could be interpreted in two ways. Either they were single crystals, which had two pairs of parallel sides which were fast growing faces and had grown most rapidly in the central region of each face as shown in figure 5.14a. Alternatively they could have been a group of four crystals growing out from a central point like leaves of a four-leaf clover as shown in figure 5.14b. Examples of this latter form have been reported by Liu, Nancollas and Gasiecki[24] and Okada and Magari[33] when using highly supersaturated solutions. At a supersaturation of 70, brines A, B and C were quite highly supersaturated.

Crystals from brine system D (figure 5.5), at half the supersaturation of brine system A, appeared similar to those mentioned above, but were beginning to show some definate faces at their edges. These faces were starting to form on one pair of roughly parallel edges only, which gave the type D crystals something in common with crystals from brine system E (half the supersaturation of brine system D), shown in figure 5.6, where these faces were very definate. None of the crystals from brine systems A to E had any faces sufficiently developed for independant identification using Miller indexing, though some

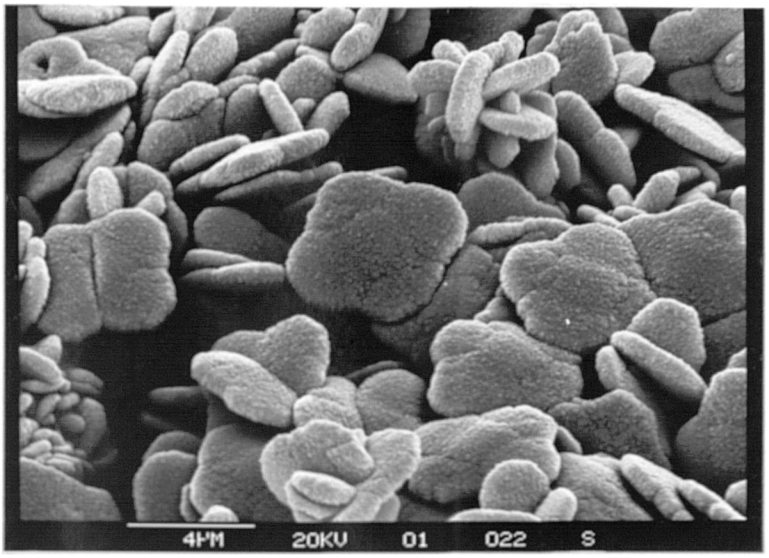

Figure 5.2 Beaker test - brine system A

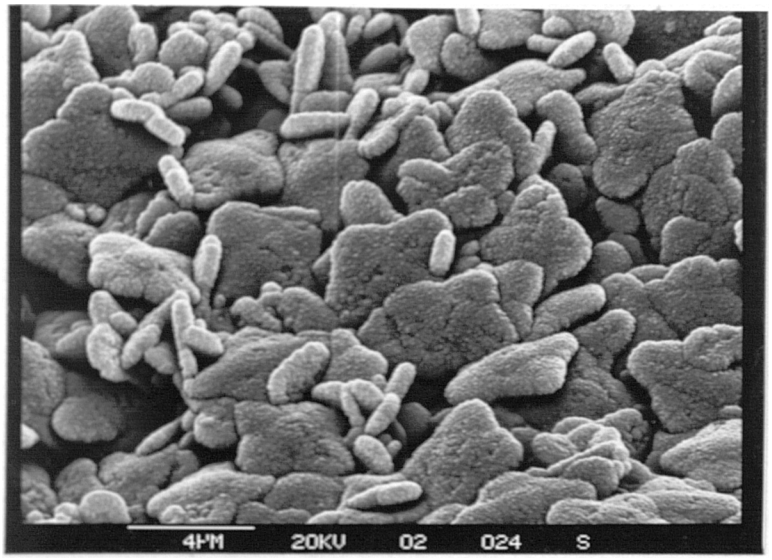

Figure 5.3 Beaker test - brine system B

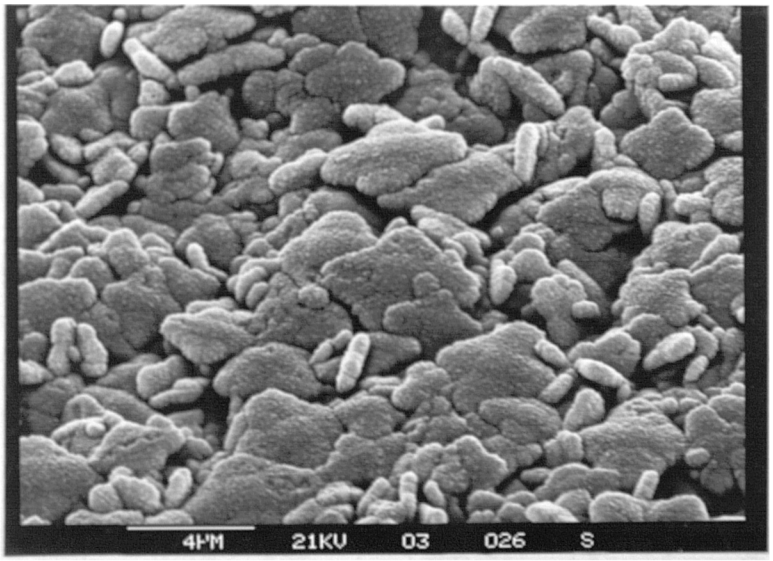

Figure 5.4 Beaker test - brine system C

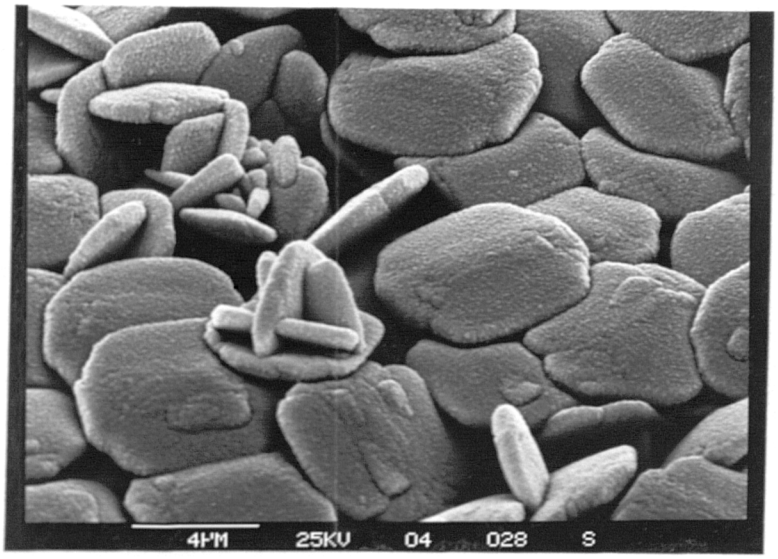

Figure 5.5 Beaker test - brine system D

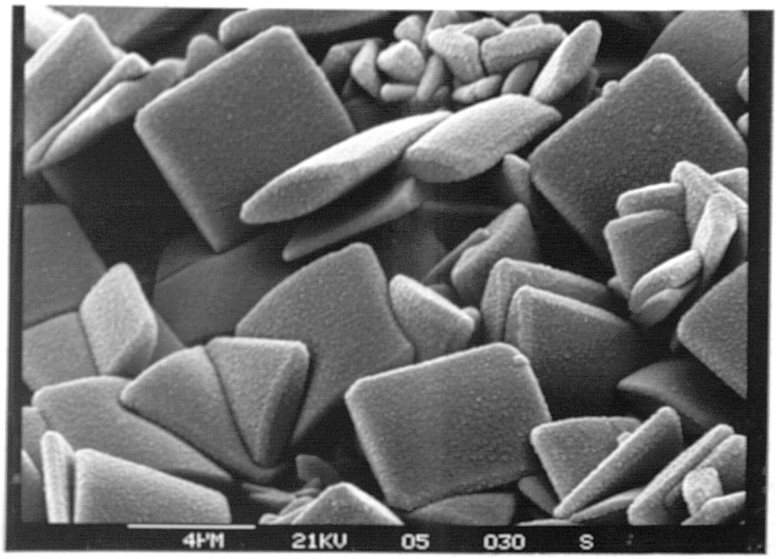

Figure 5.6 Beaker test - brine system E

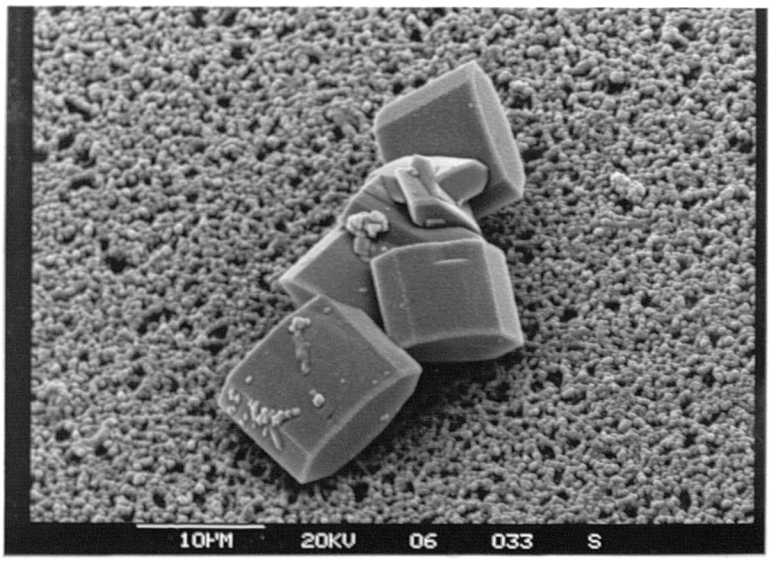

Figure 5.7 Beaker test - brine system F

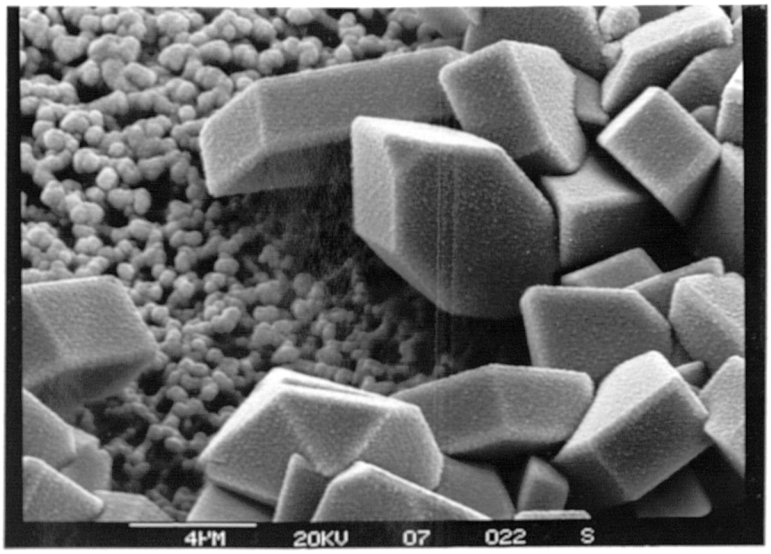

Figure 5.8 Beaker test - brine system G

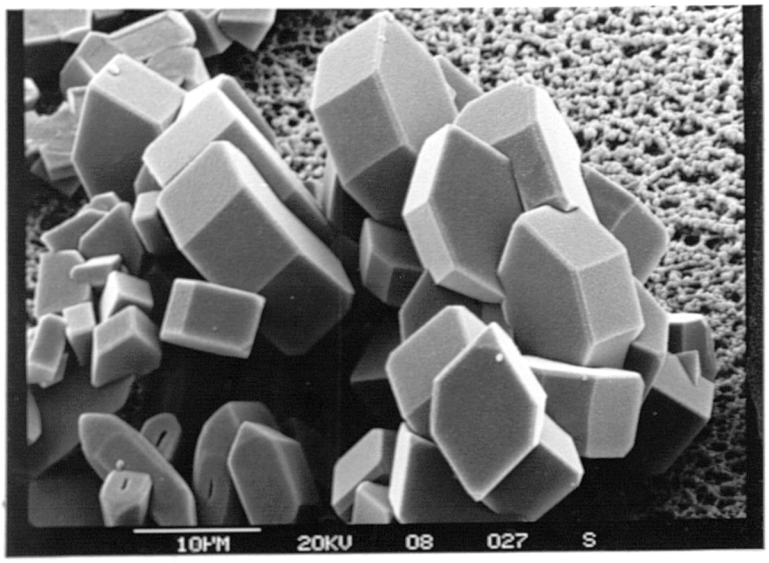

Figure 5.9 Beaker test - brine system H

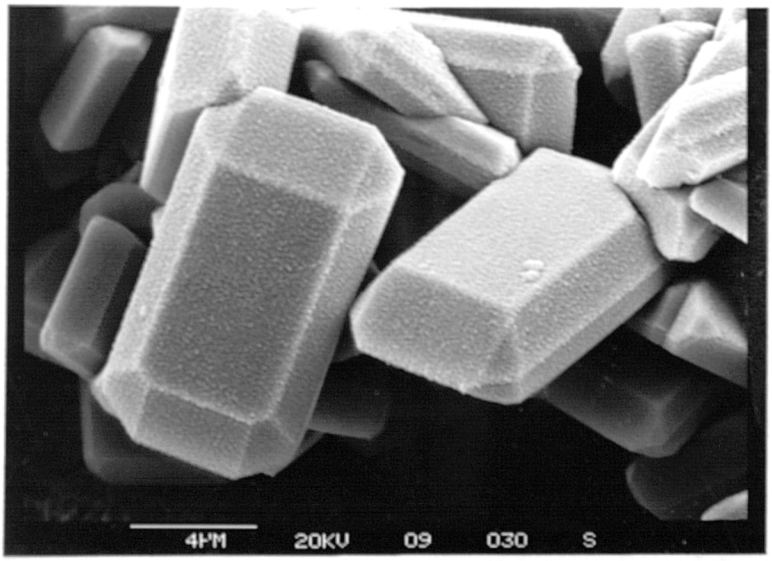

Figure 5.10 Beaker test - brine system I

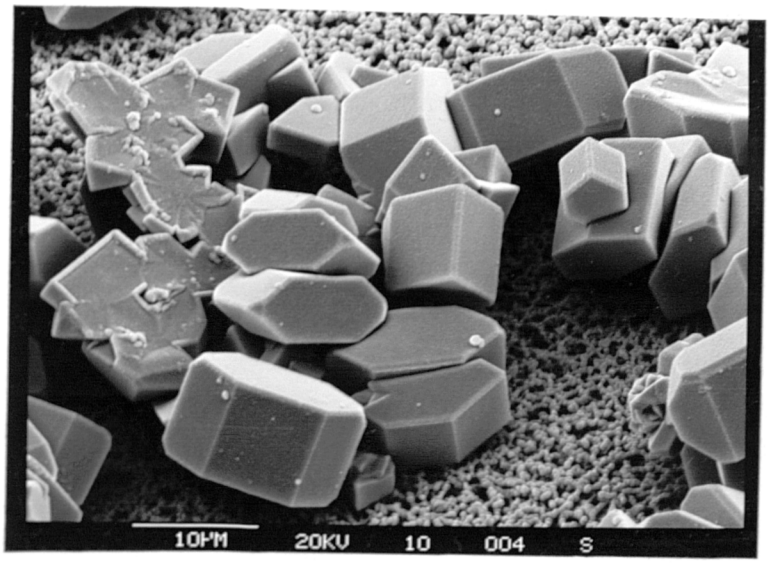

Figure 5.11 Beaker test - brine system J

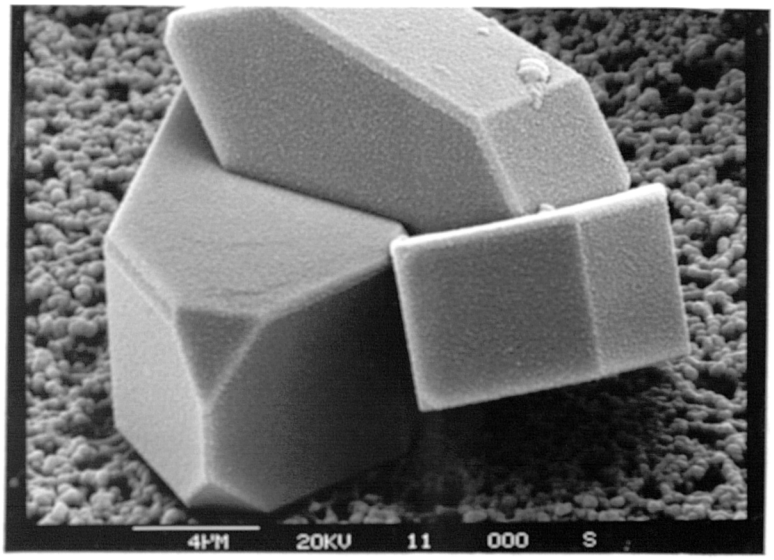

Figure 5.12 Beaker test - brine system K
(commonly observed)

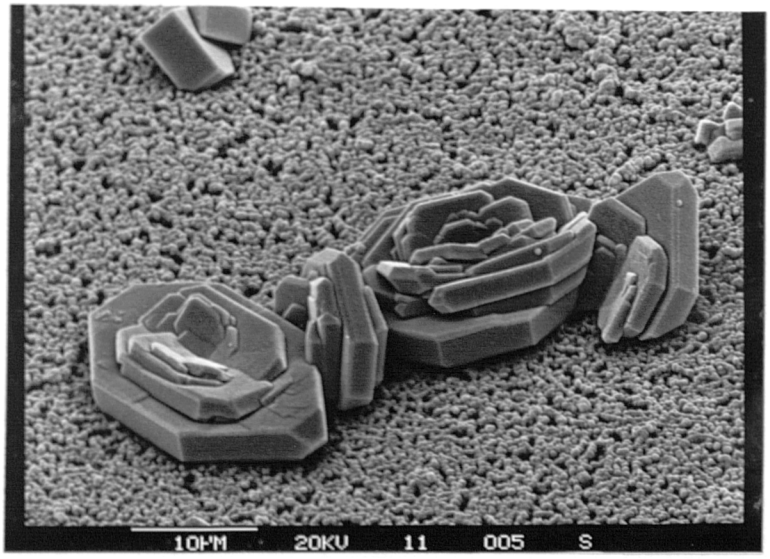

Figure 5.13 Beaker test - brine system K
(occasionally observed)

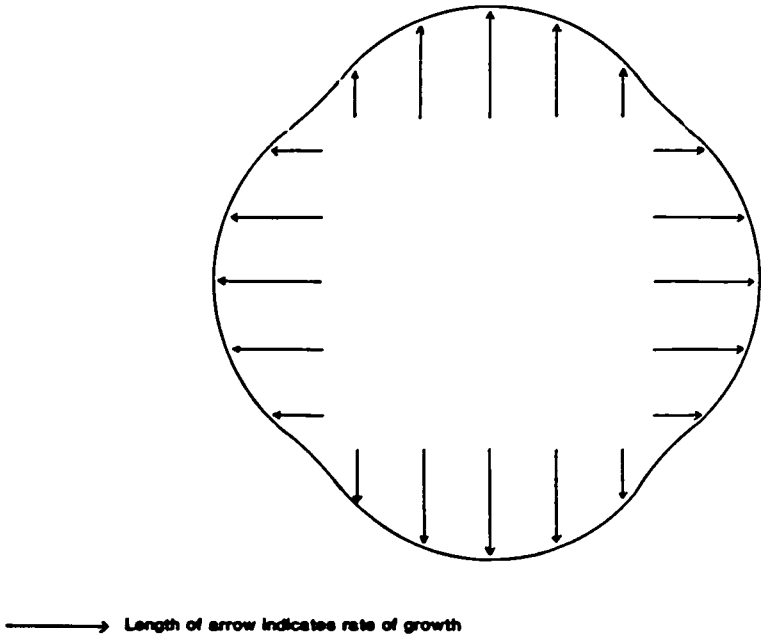

a) Fast-growing face mechanism

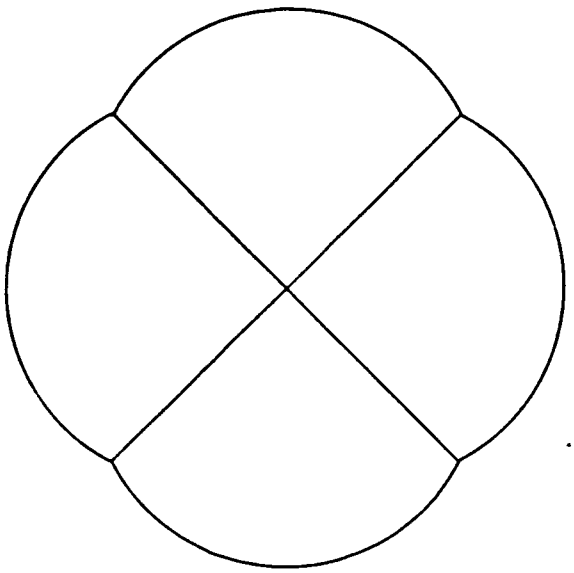

b) Four-crystal cluster (clover leaf)

Figure 5.14 Possible growth mechanisms for crystal types A, B, C and D

identification could be inferred for type E crystals by comparison with some of the others as is described later.

Crystals from brine system F (with the lowest supersaturation of 8, about half that of brine system E), shown in figure 5.7, were showing a basic morphology that could be seen reflected in the crystals from the remainder of the beaker study, shown in figures 5.8 to 5.13, and, indeed, in many of the crystals found in cores. One notable exception in the beaker study was the type of crystal produced from brine system I, figure 5.10, which had a higher ionic strength and added magnesium ions. These crystals appeared to be quite different from the basic shape reflected in the type F crystals. However, the discussion of face and form identification below will show that this habit was related to all the others observed in the beaker study.

Identification of faces using Miller indexing

Figure 5.15 shows simplified and regularised drawings of the main crystal habits observed in the beaker study. These drawings have been labelled with the crystal forms, that were inferred for them by the methods described at the end of subsection 5.4.1, according to the system of Dana[8]. The corresponding Miller indices for the forms are given in table 2. The orientation of the crystal to the axes used by Dana was decided by identifying the form c as being the most commonly occurring large face in Dana's examples, along with a consideration of the relation of form c to the forms d and m. When this idendification of forms was applied to the crystals generated in this study, the forms turned out as shown in figure 5.15 and appeared sensible in comparison with those determined by Dana. The letters beside the drawings in figure 5.15 indicate what brine system produced that habit. Many crystals showed slight bevels around some of their edges. It was difficult to say whether or not this was another face developing, but

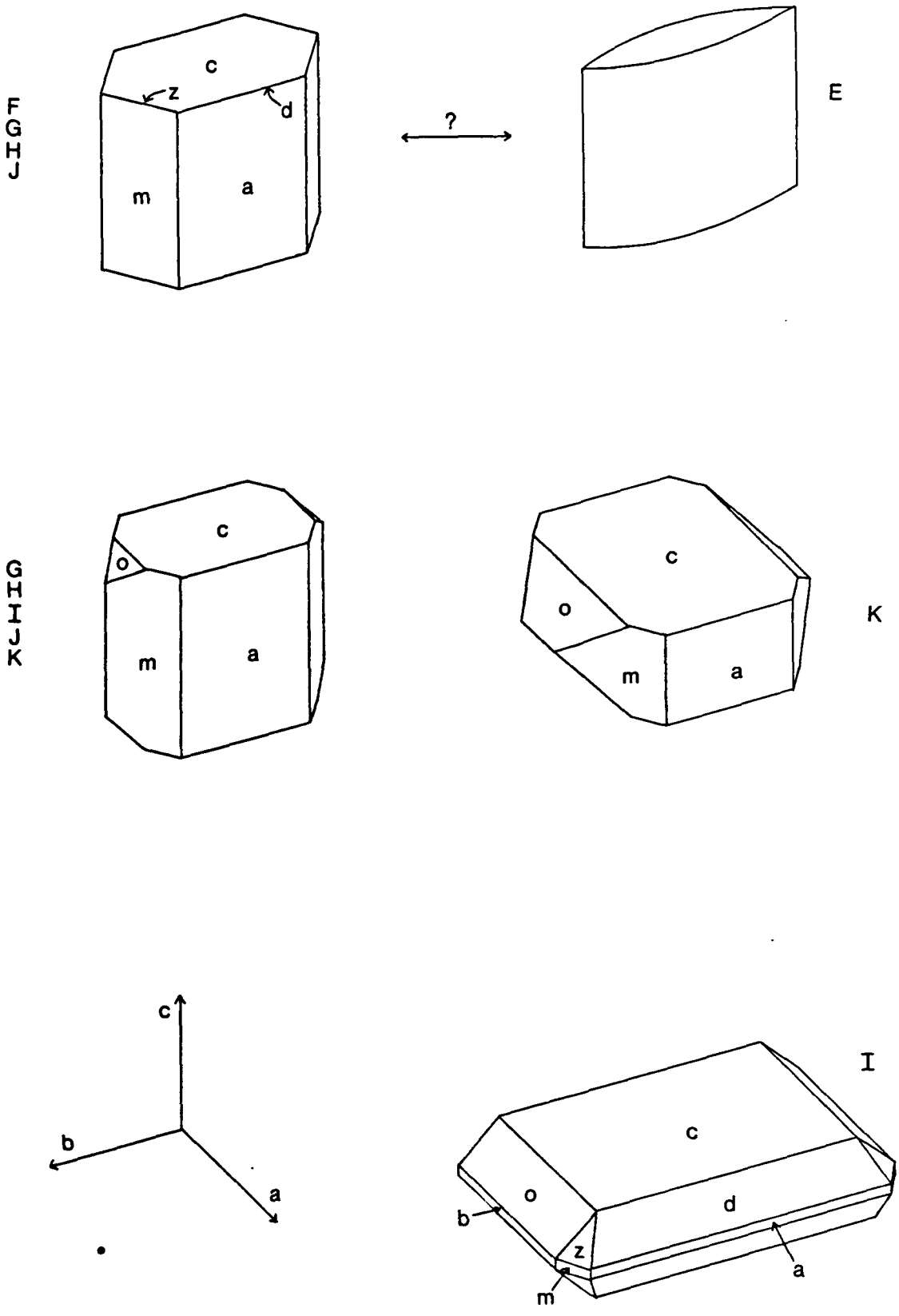

Figure 5.15 Morphology of crystals and identification of forms

Table 2. Crystal forms and associated Miller indices for crystal faces shown in figure 5.15

FORM	MILLER INDICES
a	100
b	010
c	001
d	102
m	110
o	011
z	111

if this was the case the likely form of the face has been shown in figure 5.15 by labelling the edge of the crystal where the bevel occurred. Bevels have not been shown on the drawings.

From a consideration of the forms given in figure 5.15 it could be seen that these crystals were all related through the types of faces they exhibited. The different habits were brought about by the level of development of each type of face. Some faces could be so large that they dominated the crystal, whilst others might not have developed at all. The crystals from the higher ionic strength brine systems G, H and J (see table 1 for exact compositions), shown in figures 5.8, 5.9 and 5.11 respectively, and those commonly found from brine system K, figure 5.12, all showed small intrusions of new faces into the basic habit exhibited by type F crystals described above. With type I crystals, figure 5.10, and rarer type K crystals, figure 5.13, the development of other faces completely altered the habit of the crystal. The type K crystals in figure 5.13 also showed another habit common in barium sulphate crytals, that of a group of diverging crystals having one axis in common. Although Dana did not illustrate crystals of this type he did mention their regular occurrence stating that the common axis was the b axis, which was the case with these crystals, according to the identification of forms presented here.

Effect of mineral ion ratio on morphology

A comparison of figures 5.2, 5.3 and 5.4, which show crystals from the three brine systems that formed the study on the effect of changing the mineral ion ratio, revealed no sigificant dissimilarities between them. The crystals in the latter two figures appeared to have more ragged edges than those in the first figure, but this could just as easily have been a factor of which group of crystals was photographed as anything else. The crystals were all of a similar size

range with some large "plates" along with smaller aggregated crystals.

Effect of supersaturation on morphology

In the study of the effect of supersaturation on morphology, using brine systems A, D, E and F whose crystals are shown in figures 5.2, 5.5, 5.6 and 5.7 respectively, the possible relation between crystals of type D (supersaturation 35) and those of type E (supersaturation 17.5) through the development of edge faces has already been described. Crystal types A (supersaturation 70) and D appeared similar but for the very small edge faces on the type D crystals. The likely relation between crystal types E (supersaturation 17.5) and F (supersaturation 8.4) was indicated in figure 5.15. Thus, the progressive increase in supersaturation of the mixed brine systems from brine system F (supersaturation 8.4) to brine system A (supersaturation 70) was considered to lead to less and less well-formed crystals, which essentially possessed the same habit. Of course it was also possible, as described earlier and shown in figure 5.14, that crystals of type A and possibly those of type D had a completely different habit altogether. There was insufficient evidence here to support either claim, though the study of crystals formed in cores might offer further evidence in one direction or another.

Effect of ionic strength on morphology

The increase in ionic strength clearly affected the crystal habit. Based on the idea that supersaturation controls morphology, crystals of types G and H (supersaturation 19), figures 5.8 and 5.9, should have appeared something like those of types D or E (supersaturations 35 and 17.5), shown in figures 5.5 and 5.6. In fact crystals of types G and H were much more well-formed with extra faces

appearing and the 001 face, form c, beginning to dominate the crystal. It was beyond the scope of this work and the abilities of its author to explain why this was so, but it appeared that the increased concentration of sodium chloride interfered with, or poisoned the growth of some faces, leaving others to develop freely.

Effect of additional cations on morphology

The presence of calcium or magnesium ions also appeared to have a marked effect on the crystal habit as was seen in crystal types I (added magnesium ions) and K (added calcium ions), figures 5.10, 5.12 and 5.13. This could also have been a poisoning mechanism of the faces on the a and b axes as the c form again increased its dominance of the crystal habit. Alternatively the inclusion of a few "foreign" ions in the lattice could have been distorting it into other forms.

Strontium ions did not appear to have had any effect in the beaker test as crystals of type J (added strontium ions), figure 5.11, were much the same as those of type H (no added ions), figure 5.9. Strontium is known to form a continuous solid solution with barium[9]. The ease of substitution of strontium ions for barium ions in the crystal lattice could have been the reason that added strontium ions had no apparent effect on the morphology. Alternatively, strontium ions might have no influence on barium sulphate crystal morphology.

EDAX analysis of crystals from the beaker tests

In order to identify what elements were present in the crystals, that might explain some of the changes of habit, energy dispersive X-ray analysis (EDAX) was performed on the crystals from the beaker tests. The results of this analysis are presented in table A3 in appendix A5.4. The figures presented in table A3 refer to the

percentage intensity of the X-rays emitted by the crystal when irradiated in the scanning electron microscope. They reflected the relative quantities of each element present, but without a lengthy calibration procedure it was not possible to convert these to molar ratios.

All the EDAX results indicated some small quantity of iodide present in the crystals. This iodide came into the solutions in very small concentrations with the reagent grade sodium chloride used to make the solutions. The iodide appeared to have concentrated itself in the crystals.

For the study on the effect of added ions the EDAX could not detect any amount of magnesium ion in the crystals from brine system I. Therefore, it was condidered that any effect of magnesium ion on the crystal habit was limited to interfering with the surface reactions. Both strontium and calcium ions could be detected in the crystals from brine systems J and K respectively. Strontium was present to a higher level than calcium despite having been at a much lower concentration in the "mother" solutions, which was understandable given the ease with which strontium can substitute into the barium sulphate lattice. It was, therefore, possible for strontium and calcium to have influenced the crystal habit from within the crystal structure in addition to affecting surface reactions.

5.4.3 Crystals Formed Under Continuous Flowing Conditions in Sandstone Cores

Growth of barium sulphate crystals in the core experiments used in this study took place under a very different environment from the beaker experiments. The growing crytals had a constant supply of ions, a variety of substrates and were confined by the walls of the pores.

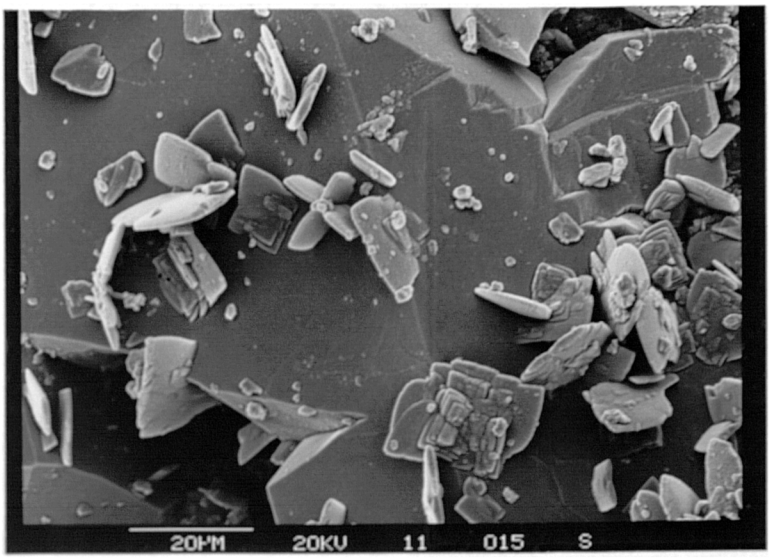

Figure 5.16 Expt. C141515AA-2
5mm from front face of the core

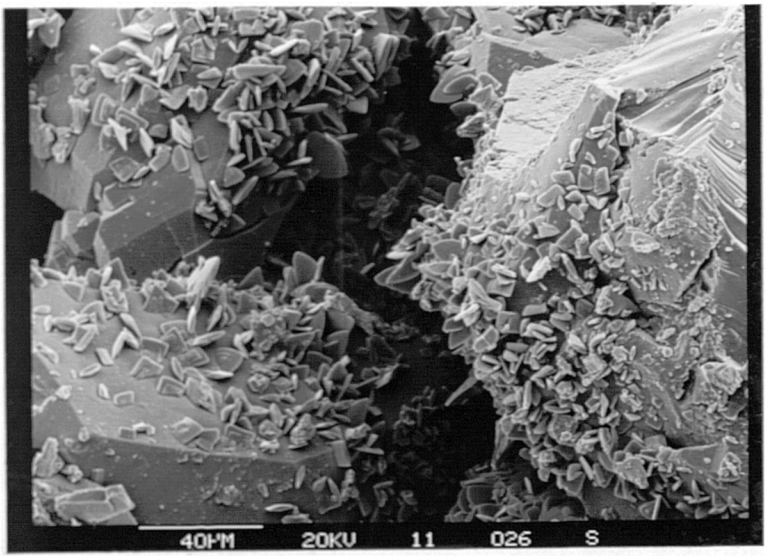

Figure 5.17 Expt. C141515AA-2
5mm from front face of the core

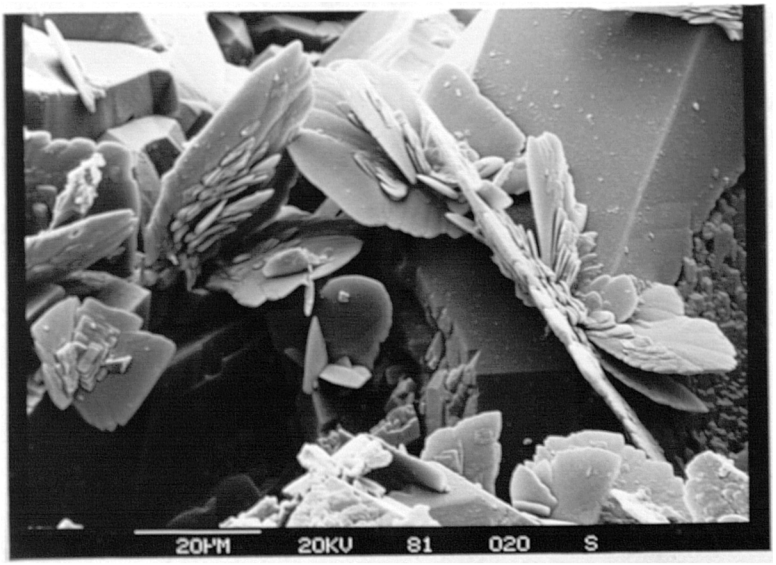

Figure 5.18 Expt. C181515AA-8
Section 1

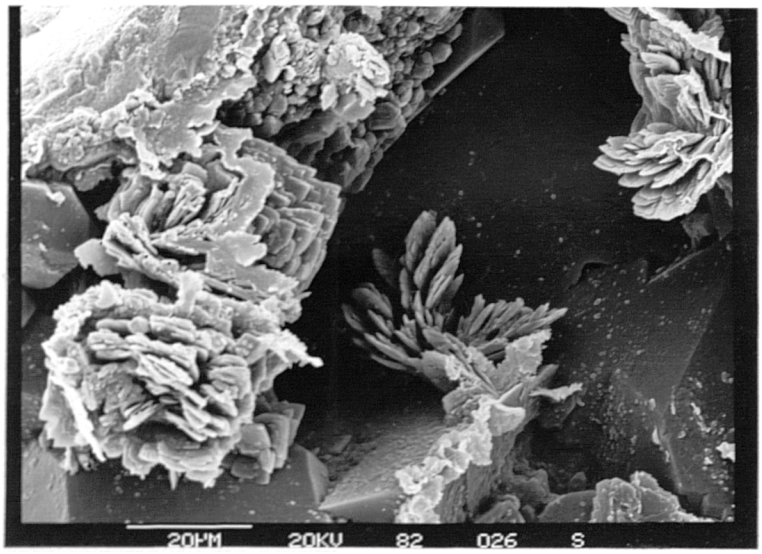

Figure 5.19 Expt. C181515AA-8
Section 2

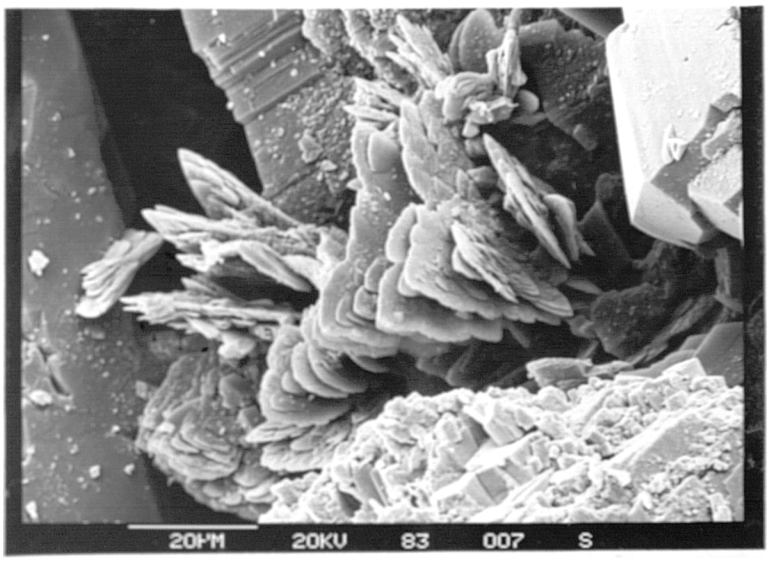

Figure 5.20 Expt. C181515AA-8
Section 3

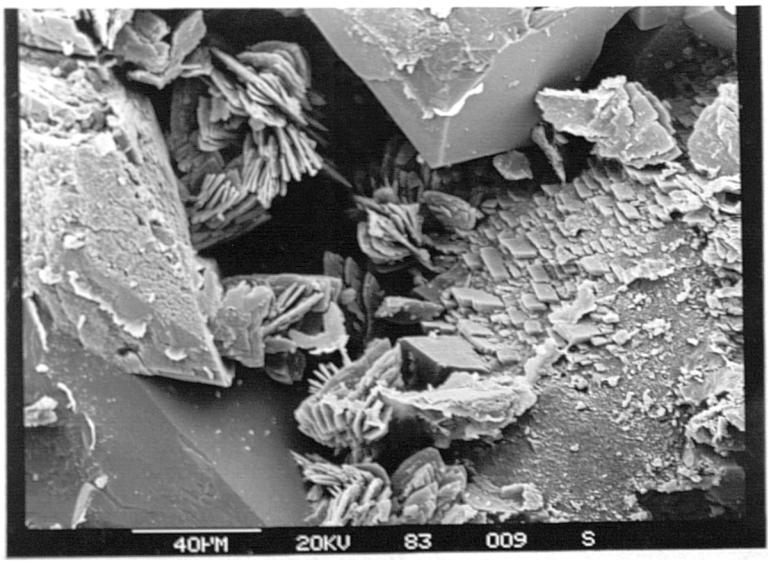

Figure 5.21 Expt. C181515AA-8
Section 3

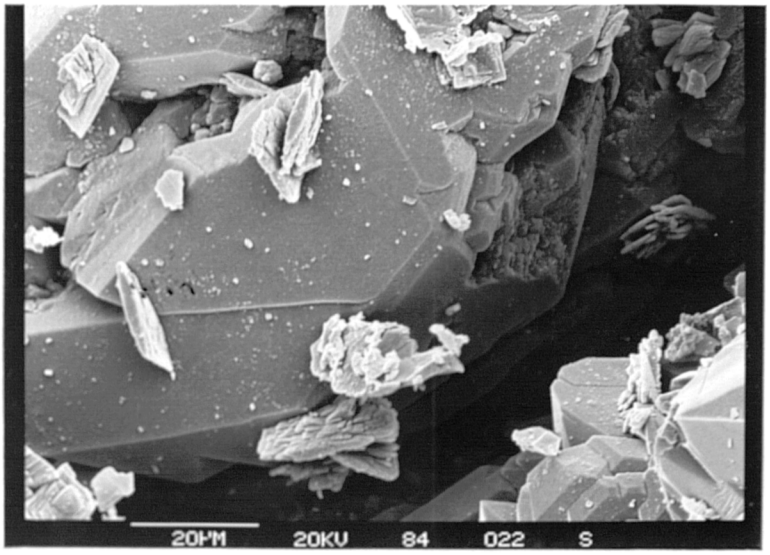

Figure 5.22 Expt. C181515AA-8
Section 4

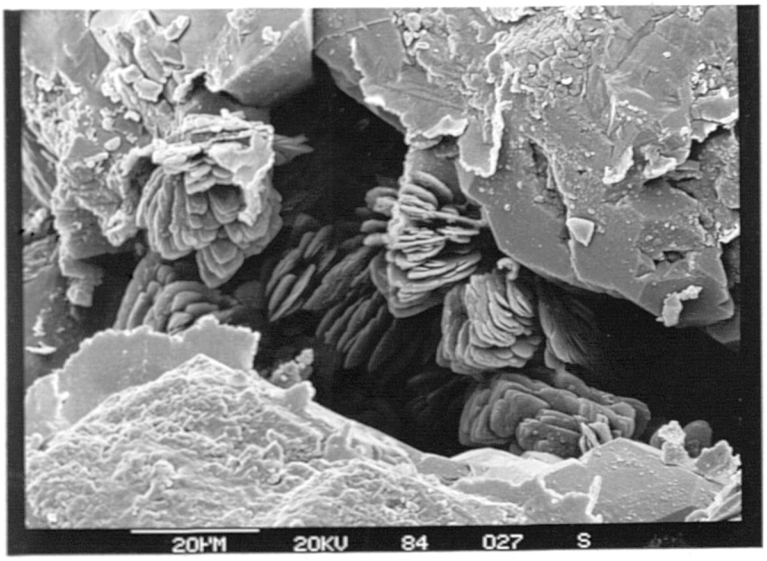

Figure 5.23 Expt. C181515AA-8
Section 4

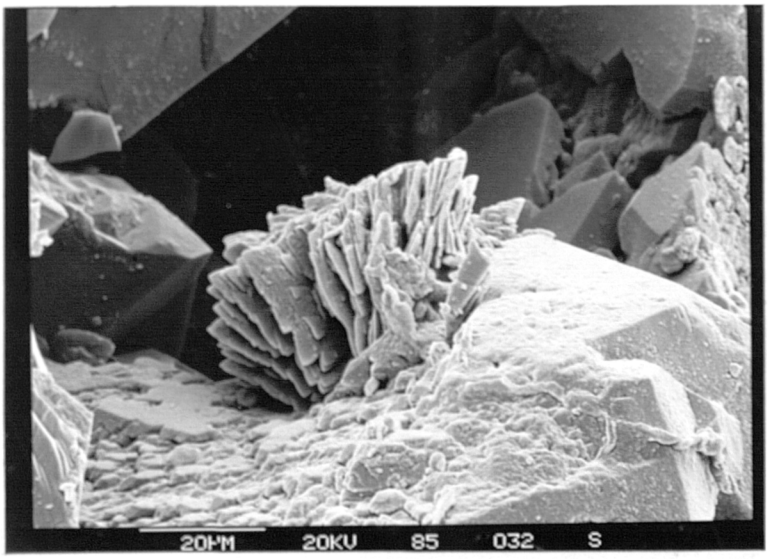

Figure 5.24 Expt. C181515AA-8
Section 5

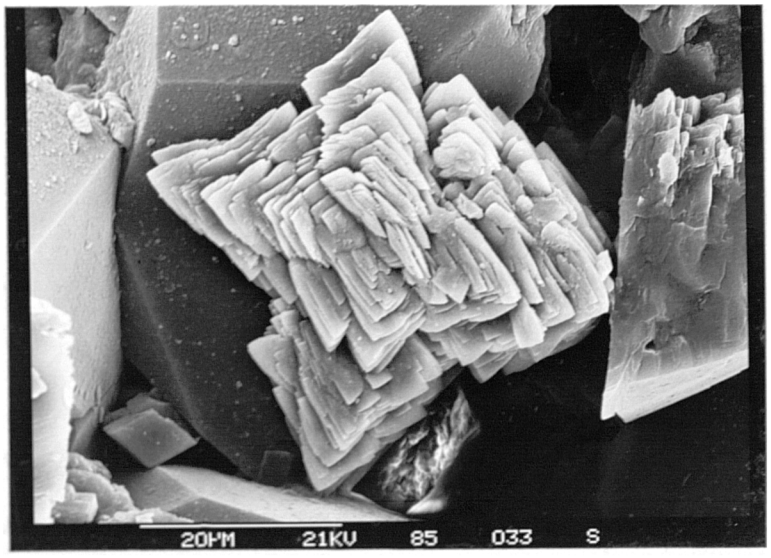

Figure 5.25 Expt. C181515AA-8
Section 5

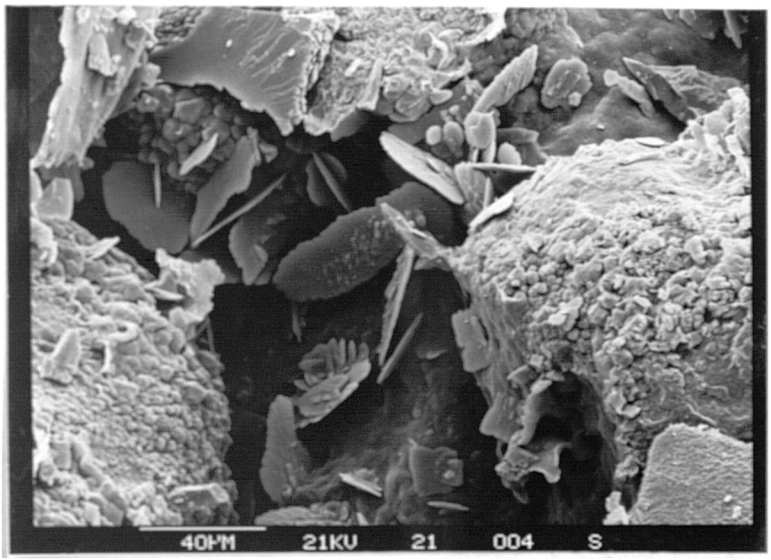

Figure 5.26 Expt. C181515BB-2
Front of section 1

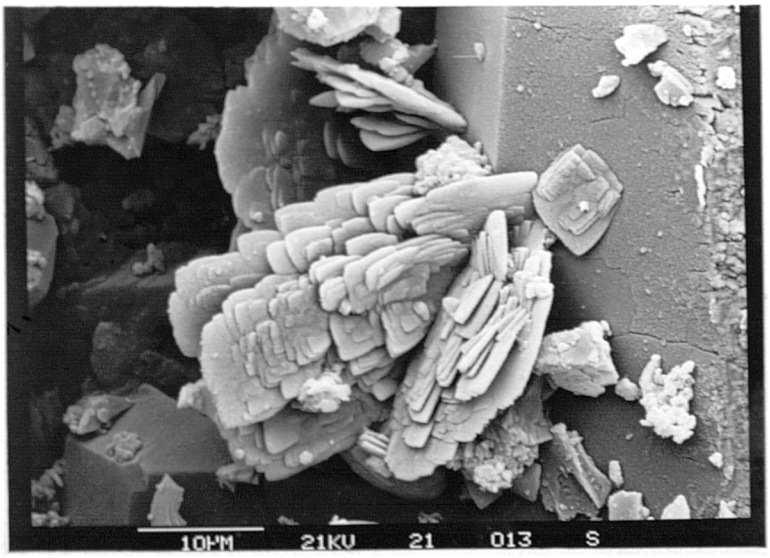

Figure 5.27 Expt. C181515BB-2
Back of section 1

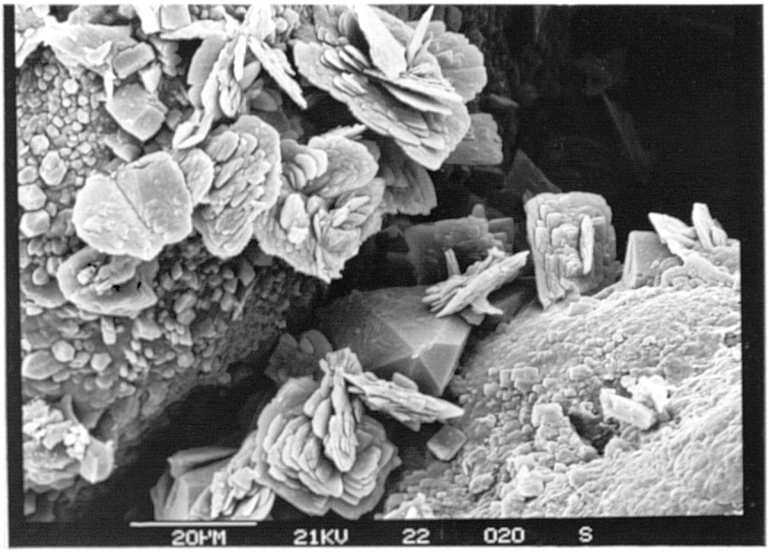

Figure 5.28 Expt. C181515BB-2
Back of section 2

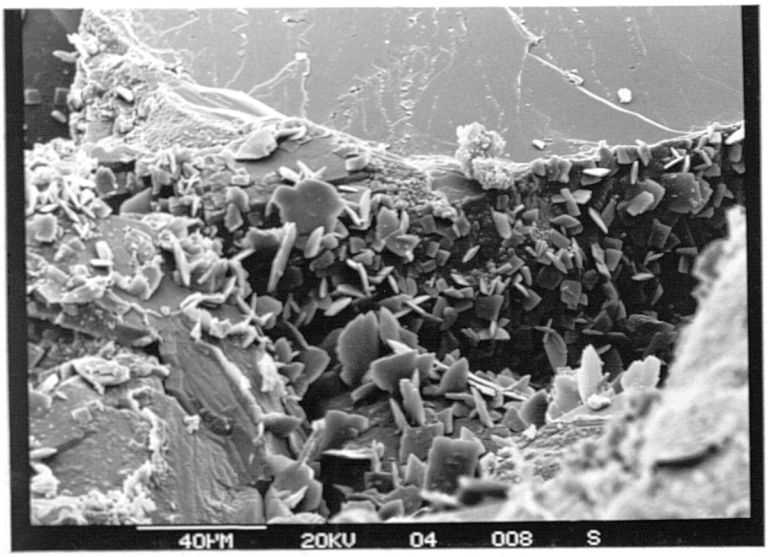

Figure 5.29 Expt. C221515CC-4
Front of section 1

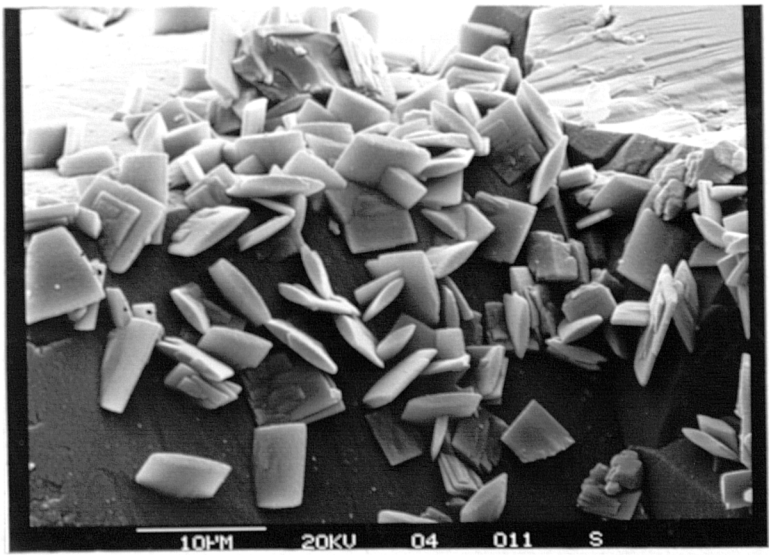

Figure 5.30 Expt. C221515CC-4
Section 1

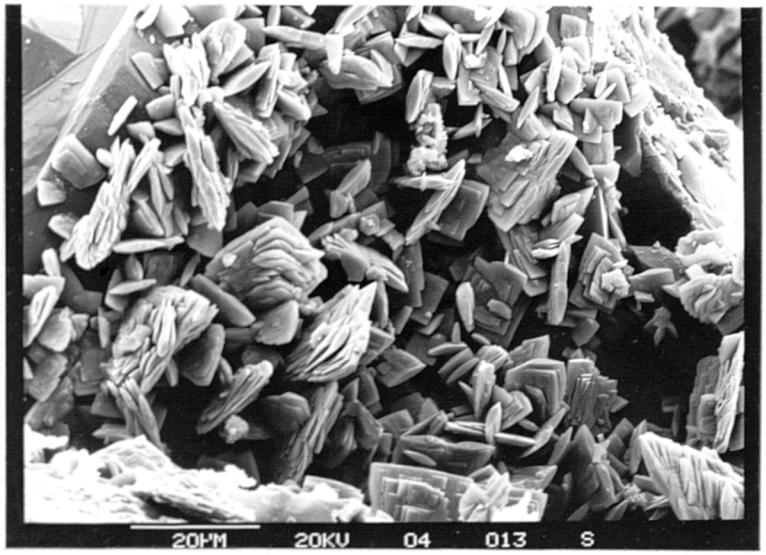

Figure 5.31 Expt. C221515CC-4
Back of section 1

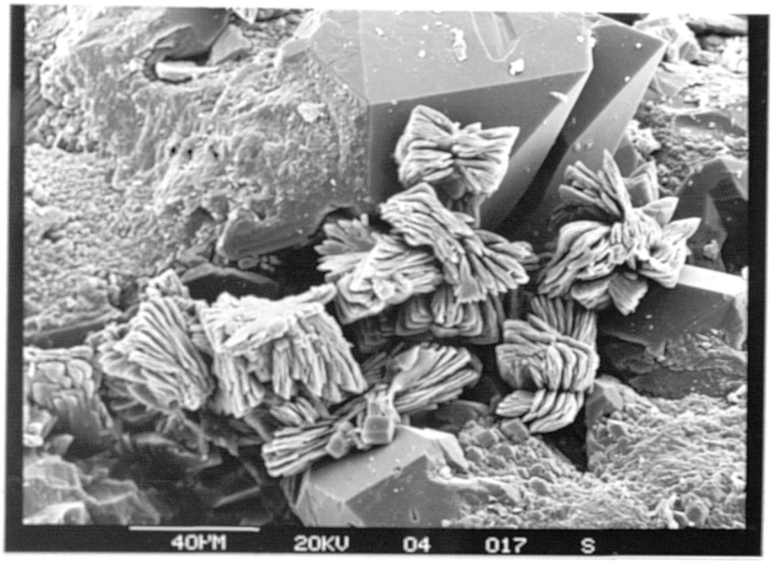

Figure 5.32 Expt. C221515CC-4
Front of section 4

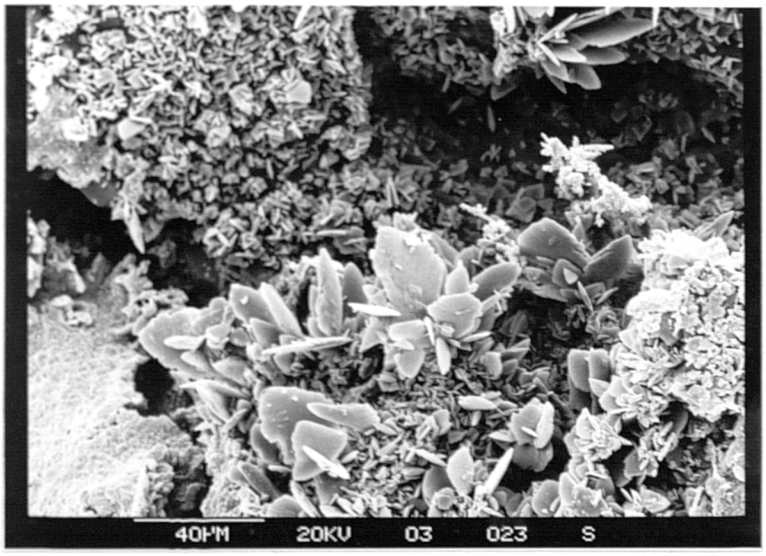

Figure 5.33 Expt. C221515DD-3
Front of section 1

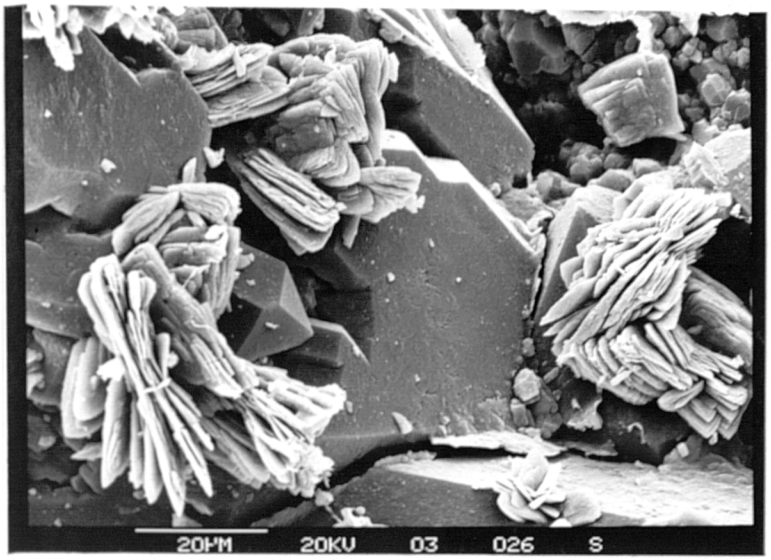

Figure 5.34 Expt. C221515DD-3
Back of section 1

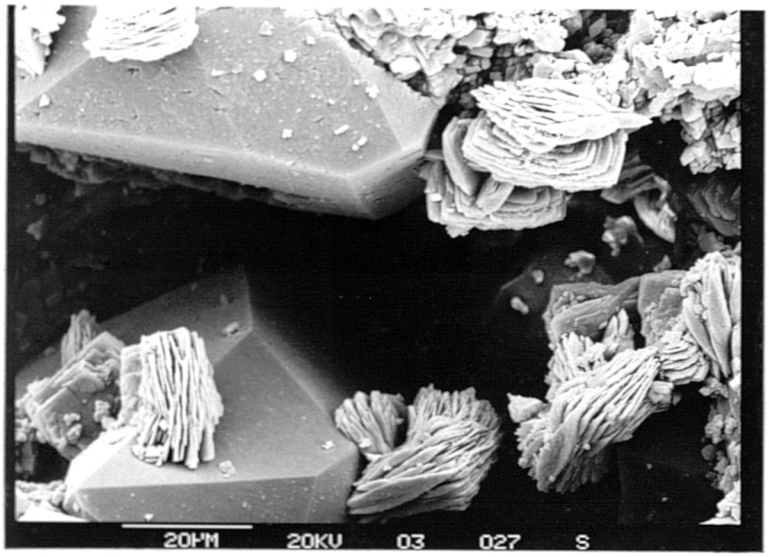

Figure 5.35 Expt. C221515DD-3
Front of section 4

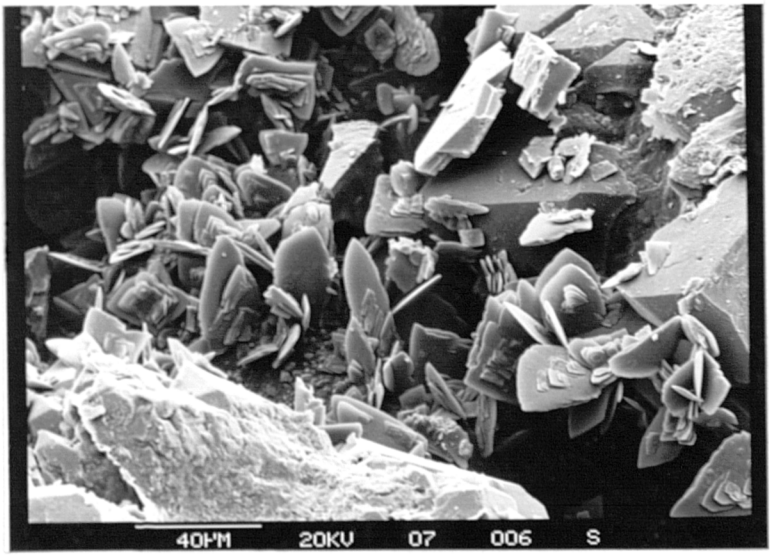

Figure 5.36 Expt. C221515DD-7S
Middle of section 1

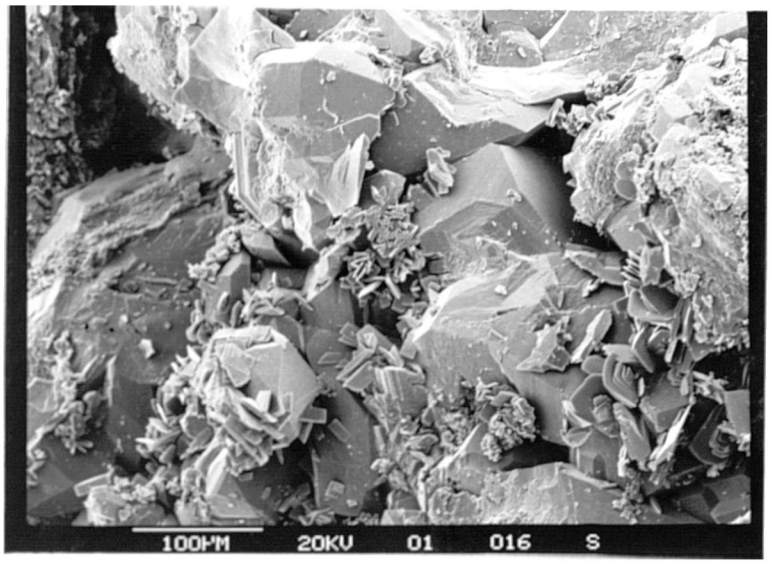

Figure 5.40 Expt. C237.57.5FF-1S
Front of section 1

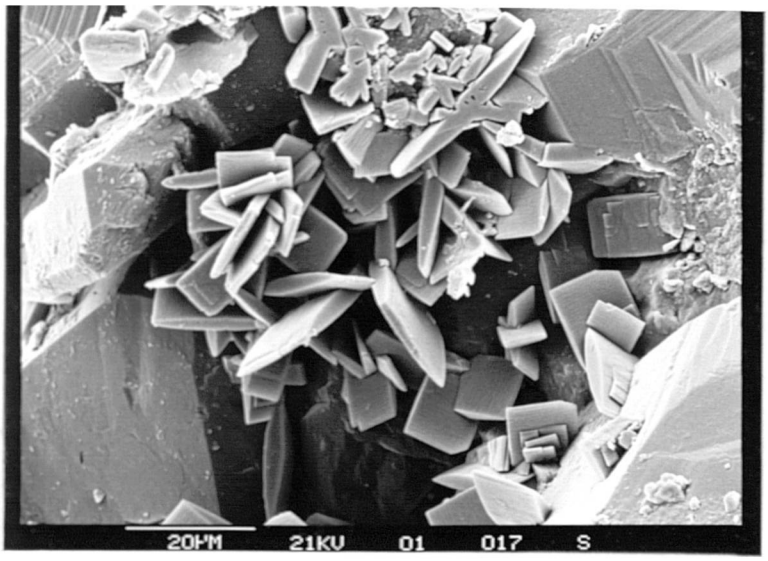

Figure 5.41 Expt. C237.57.5FF-1S
Front of section 1

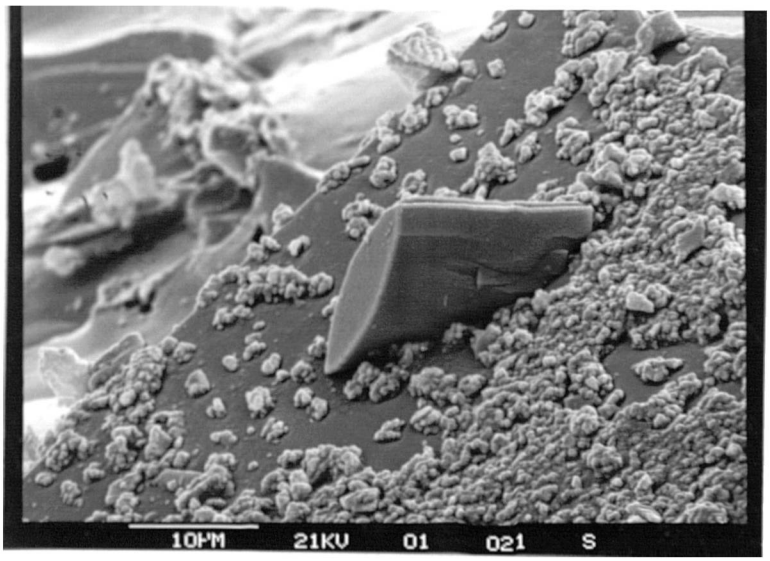

Figure 5.42 Expt. C237.57.5FF-1S
Section 4

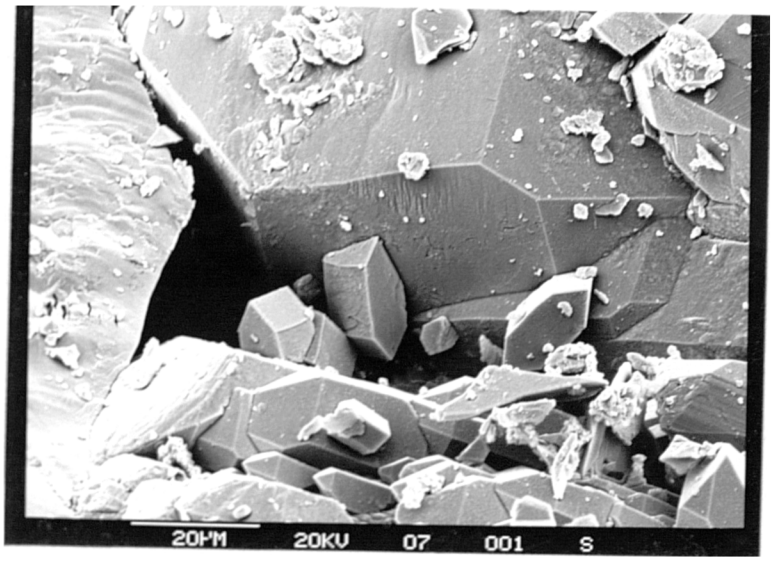

Figure 5.43 Expt. C237.57.5GG-1
Section 3

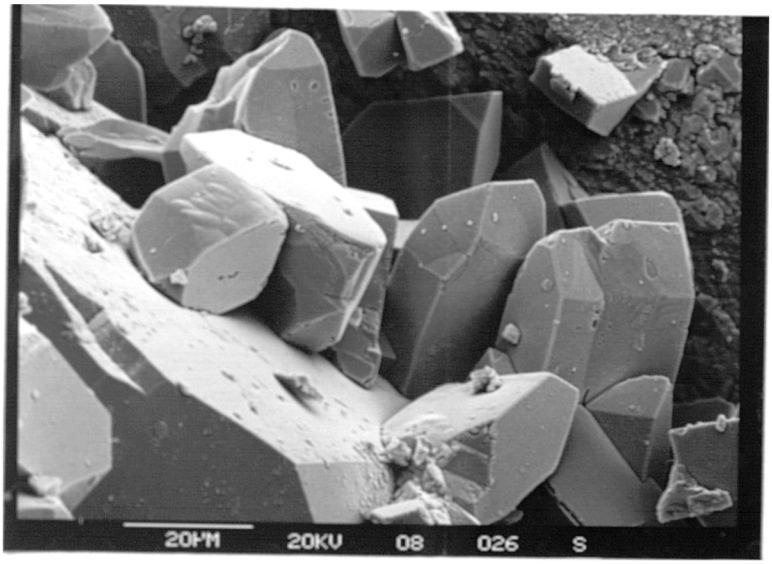

Figure 5.44 Expt. C247.57.5HH-2
Front of Section 1

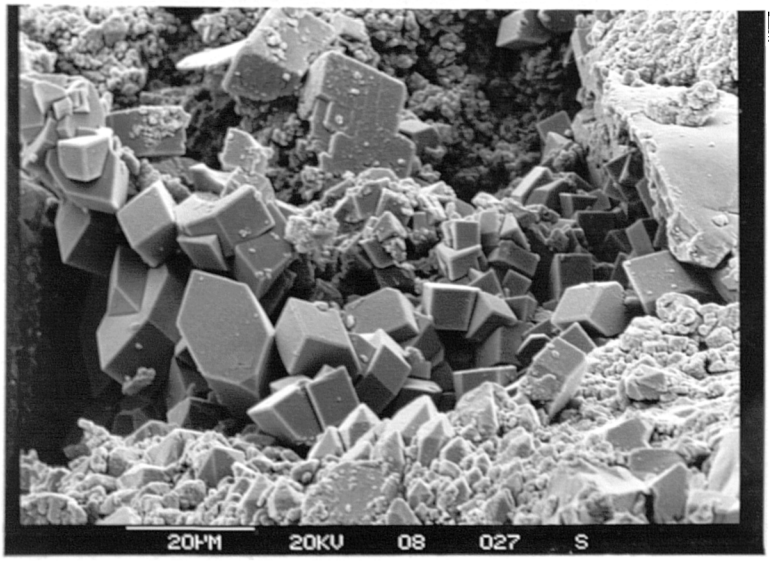

Figure 5.45 Expt. C247.57.5HH-2
Front of section 1

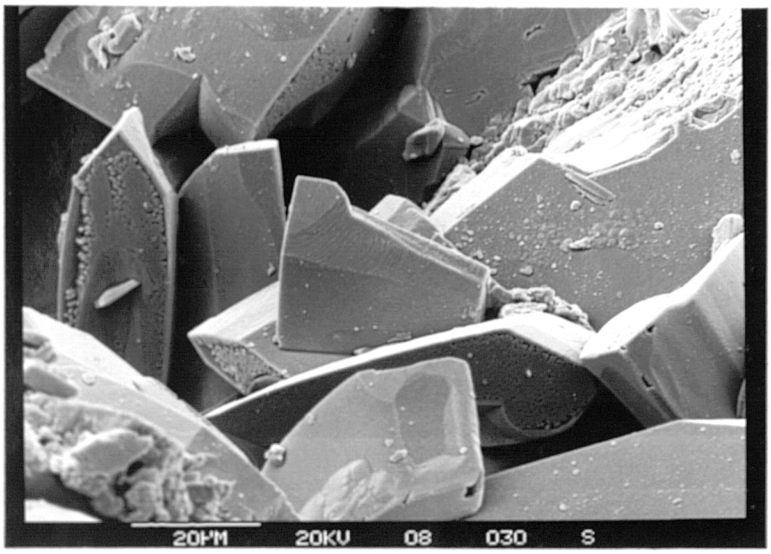

Figure 5.46 Expt. C247.57.5HH-2
Back of section 1

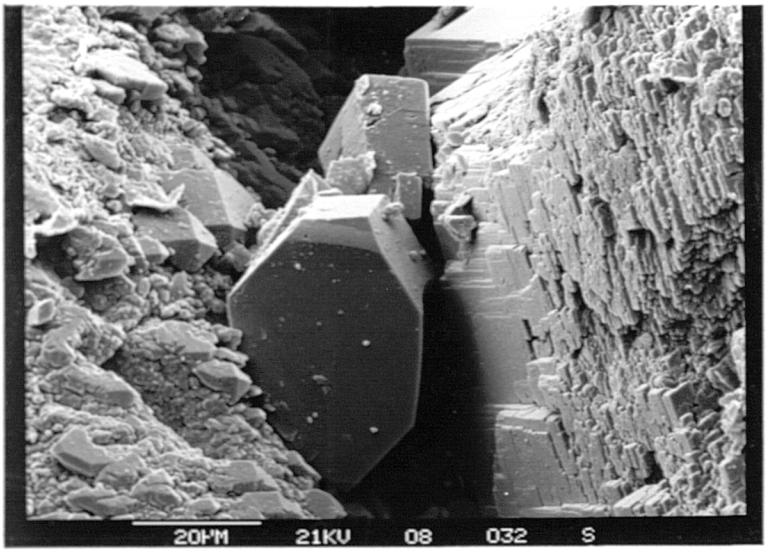

Figure 5.47 Expt. C247.57.5HH-2
Front of section 4

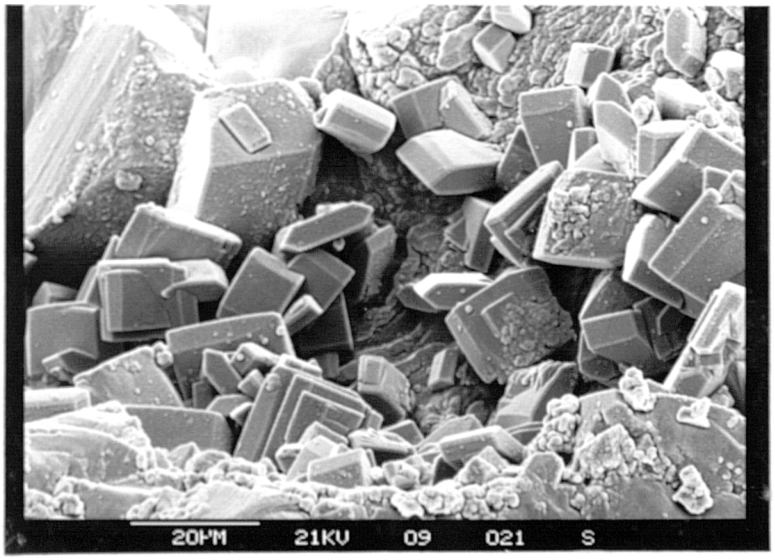

Figure 5.48 Expt. C247.57.5II-2S
Front of section 1

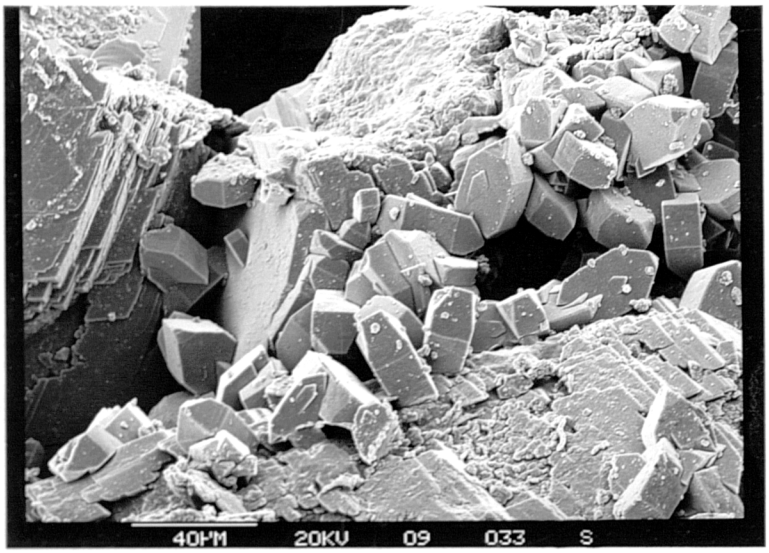

Figure 5.49 Expt. C247.57.5 II-2S
Back of section 4

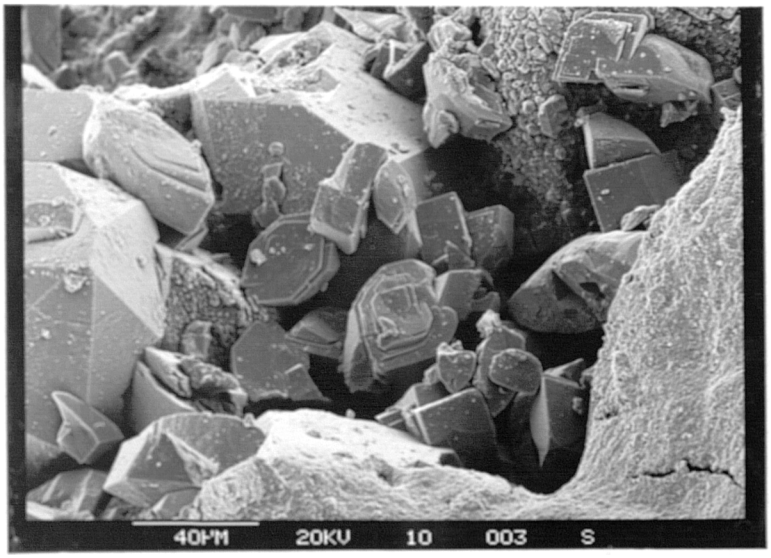

Figure 5.50 Expt. C247.57.5JJ-1S
Section 1

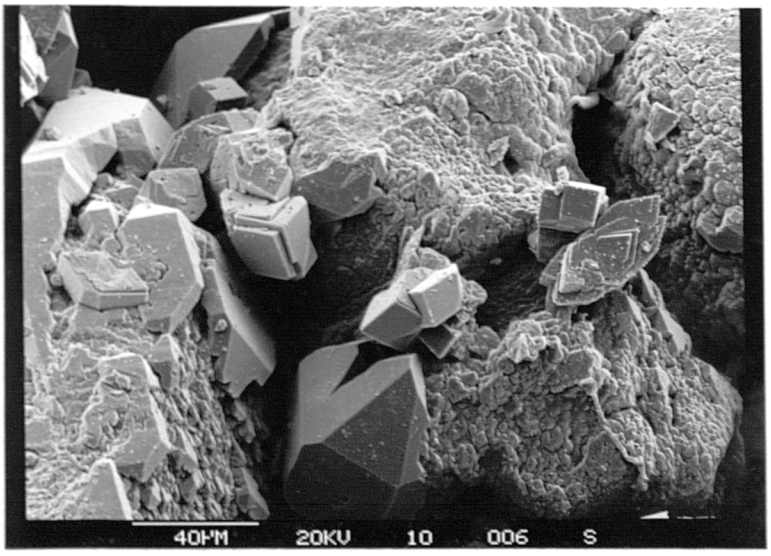

Figure 5.51 Expt. C247.57.5JJ-1S
Front of section 4

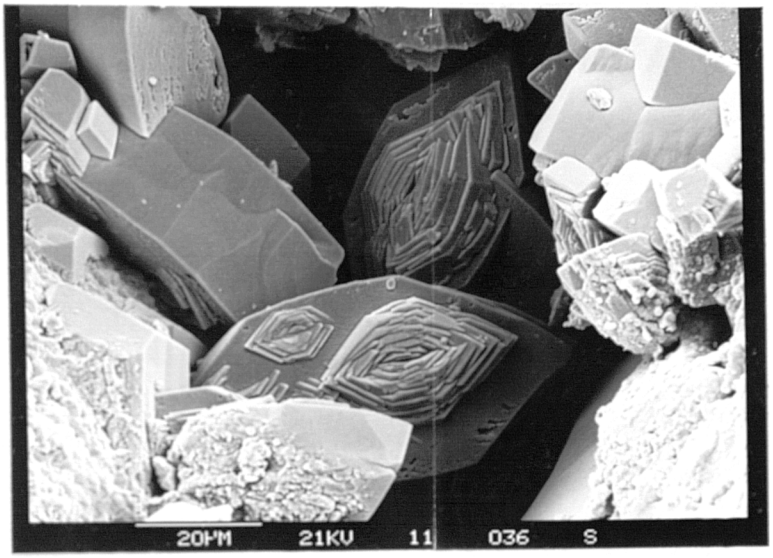

Figure 5.52 Expt. C247.57.5KK-1
Front of section 1

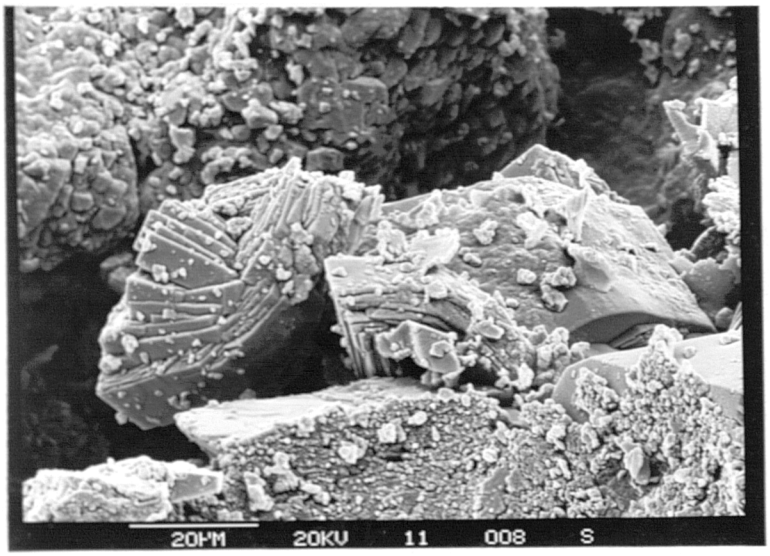

Figure 5.53 Expt. C247.57.5KK-1
Front of section 4

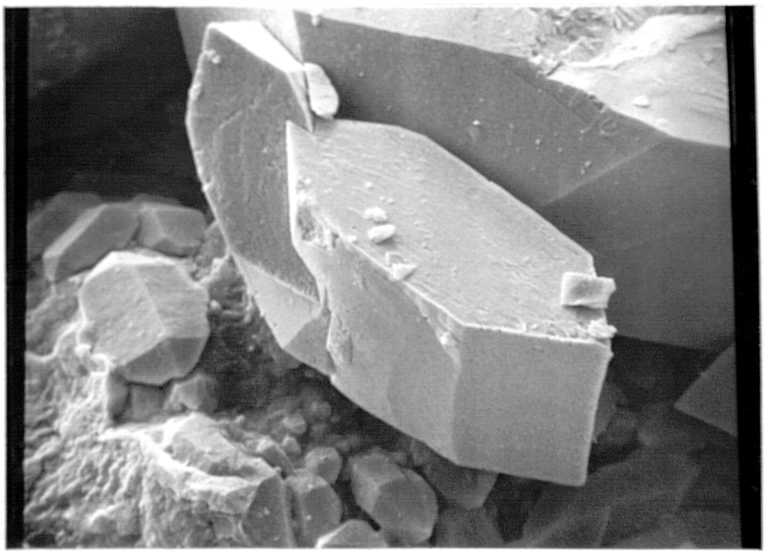

Figure 5.54 Crystals produced by Pucknell's type C brine. Magnification 620×

As the amount of precipitation occurring upstream of any particular crystal was unlikely to have varied by any large amount (this is discussed further later), growth would have been taking place at more or less constant supersaturation.

A benefit of the improved distribution face used in this work (see chapter 4) was that the level of supersaturation of the mixed brines would have fallen due to precipitation as they moved along the core and should not have been replenished by unmixed brines reaching deep into the core. The manner in which the SEM study was performed to exploit this effect was described in subsection 5.4.1. Other aspects of the SEM study were also described there. A selection of the photomicrographs generated by this study is presented in figures 5.16 to 5.53. It can be seen from these photomicrographs that the crystals grew on all the types of substrate present in the cores. No tendancy for crystals to grow on one substrate in preference to another was observed.

General description of crystals formed

Crystals grown from brine systems A to D, figures 5.16 to 5.37, showed fairly similar habits to each other when grown in the core as they did in the beaker tests. The dominant morphology in the cores, though, was a roughly triangular, flat plate with curved edges leading up to the point which was furthest from the flat base, anchored to the substrate. Typical examples of single crystals exhibiting this habit appear in figure 5.17.

The single crystals were usually accompanied by parallel and diverging growths, which had a common base axis with the main crystal, as appear in figure 5.18. In some cases the growth was characterised by the main crystal, as in figure 5.18, and in others by the parallel and diverging growths, as in figure 5.24.

Some structures akin to the "desert rose" reported by other workers[9,20] could be seen, eg figure 5.25. These appeared to be formed from the common parallel and diverging growth structure, but based on the "four-leaf clover" multi-crystal shown in figure 5.14b. The lozenge-shaped end face, first seen in the beaker study with brine system E (figure 5.6), could be seen occasionally in the core study for brine systems A to D, which have a much higher supersaturation. Figure 5.30 shows a group of these type of crystals formed from brine system C (supersaturation 63).

Crystals produced by brine system E, at half the supersaturation of brine system D, still showed the roughly triangular form described above, as shown in figure 5.38, but the lozenge-shaped end face crystal was much more prolific and also appeared with associated parallel growths, figure 5.39. Brine system F (half the supersaturation of brine system E) produced similar results, figures 5.40 and 5.41 and also produced a crystal similar to those seen in the equivalent beaker tests (compare figures 5.7 and 5.42).

As in the beaker study, the higher ionic strength brine systems G to K produced crystals whose orthorhombic axes' lengths were of a more similar size to each other (figures 5.43 to 5.53). This gave them an appearance more of blocks than of plates. Crystal habits and faces produced were similar to those for the same brine system in the beaker study (figures 5.8 to 5.13), but in the main, they were far less regular. Although similar faces appeared, the crystals lacked the symmetry seen in those produced in the beaker. The faces were often curved or distorted, e.g. crystals from brine system H in figure 5.44.

Brine system I (added magnesium ions) was exceptional in that the crystals produced in the core, figures 5.48 and 5.49, were similar to those of brine system H (no added ions), figures 5.44 to 5.47, and showed little of the complexity of face development of those produced in the beaker, figure 5.10. Crystals from brine system J (added

strontium ions), shown in figures 5.50 and 5.51, were akin to those of type H, but they often exhibited parallel twinning as shown in figure 5.51. A slight tendancy for type J crystals to have parallel growths on them was also apparent, which was only observed with type K crystals in the beaker study (figure 5.13). The crystals from brine system K (added calcium ions), shown in figures 5.52 and 5.53, followed both the patterns seen for this brine system in the beaker study (figures 5.12 and 5.13), producing a roughly regular type H crystal topped by parallel growths, as shown in figure 5.53. In addition to these type crystals, brine system K also produced many crystals without the parallel growths.

Effect of mineral ion ratio on morphology

Again in the core-flooding study there was little difference to be seen between the crystals formed by brine systems A, B and C as the ratio of the scale forming ions was altered. Thus, it was concluded that changing the mineral ion ratio within the limits used in this work had no detectable effect on the crystal morphology.

Effect of supersaturation on morphology

There were two methods of observing the effects of supersaturation changes in this study. There was the decreasing initial supersaturations of brine systems A, D, E and F (supersaturations 70, 35, 17.5 and 8.4 respectively) and the falling supersaturation of the brine as it moved along the core. Only one full SEM study of all five sections in a core was performed, on a core scaled by brine system A, figures 5.18 to 5.25. For other cores only sections 1 and 4 were examined as described in subsection 5.4.1. The similarities between the crystals formed by all of these brine systems

has already been noted above as well as their relation to those produced by the beaker study.

Crystals at the very front of the core often showed a pattern of larger flat plates surrounded by smaller crystals, eg figure 5.33. This was less pronounced in cores flooded with the E and F brine systems. There were some comparisons to be made between crystals growing from the lower supersaturation brine systems (E and F) and those growing later in the core, flooded with brine system A, where a full SEM study was made. With a study of this nature where only a small number of the crystal population was observed it was not possible to state anything conclusive about this sort of inter-experiment comparison.

Within each experimental core a pattern could be seen. Early in the core the crystals tended to be dominated by the central "plate", eg figure 5.18, whereas further along the core the parallel and diverging growths became just as significant causing the crystals to resemble the leaves of a book, eg figure 5.35. Later crystals also tended to be smaller. With brine systems A and D the increasing importance of the secondary growths lead to more complex crystals later in the core, e.g. figure 5.23. This pattern was less apparent with brine systems E and F, partly because there were very few crystals in the later part of the core and partly because the starting supersaturation for brine systems E and F did not seem to have the same potential for causing parallel growths.

Changing the supersaturation at the ionic strength used appeared only to affect the morphology of the crystals in a minimal fashion. Higher supersaturations in the continuous flow environment of the cores appeared to encourage more complicated crystals with parallel and diverging growths. The simpler crystals observed at the front of the cores had probably grown more slowly as a result of being within the 5mm zone required for complete mixing of the brines flowing from

the distribution face.

Effect of ionic strength on morphology

When the ionic strength was increased a similar change in the crystals could be observed to that seen with the beaker study. The type of crystals produced by brine system G, shown in figure 5.43, were comparable to those produced by Pucknell[35] for the same brine mix, figure 5.54. This confirmed that the changes that Pucknell put down to a change in supersaturation were more a result of changes in the brine composition. Brine system H, which had equal concentrations of the scaling ions, produced similar crystals, eg figure 5.44, but many were distorted and unsymmetrical. Whether this was due to there being a continuous supply of ions or some other aspect of their environment was difficult to say and it was not part of this work to explore the reasons for this. These crystals showed little change later in the core other than in size and prevalence, eg figure 5.47, further supporting the case that ionic strength and solution composition were the major factors controlling their habit.

Effect of added cations on morphology

Crystals from brine system I (added magnesium ions), figures 5.48 and 5.49, showed little tendancy towards the morphology of their counterparts grown in a beaker, figure 5.10. This suggested that the effect of the added magnesium ion was negated by the environment in the core. The magnesium ion could have been removed by some reaction with the core, especially the feldspars and small clay content. This removal must have continued long enough for the crystal habit to become established.

With crystals grown from brine system J (added strontium

ions), figures 5.50 and 5.51, there appeared to be some slight modification to the crystal habit. Parallel twinning of crystals and parallel growths on what corresponds to the c form in figure 5.15 were common. However this may have been a factor of the core environment as many of the other crystal types showed parallel growths when grown in a core, when they did not when grown in a beaker.

The modification associated with the calcium ion in the beaker study also appeared in the core grown crystals from brine system K, figures 5.52 and 5.53. Again the crystals were more irregularly formed, but the presence of extra growths on what again corresponded to the c form were clear. It should be noted that the calcium ion concentration in brine system K was far higher than the magnesium ion concentration in brine system I. If the lack of any effect on morphology due to the magnesium ions in brine system I, discussed above, were due to the magnesium ions being adsorbed by core materials, then this was overcome by the higher concentration of calcium in brine system K.

5.4.4 Relation of Crystals to Naturally Occurring Barytes

The barium sulphate crystals produced in this study all precipitated from simple brines. They did, however, possess a great similarity with geological hand specimens of naturally formed barytes from different localities, in many cases the difference being in size alone.

Of special interest are Kuroko type barite deposits[54]. These deposits were formed by subsea erruption of hot polymetallic waters associated with magma, which mixed with the sea-water to produce stratiform mineral deposits, amongst which are thick layers of barytes.

In the waterflooding of oil reservoirs similarly polymetallic brine is injected into the complex formation brine, which will result in mixing, sometimes producing a barite precipitate. Given that the crytals grown in this work showed similarities to naturally ocurring crystals and that naturally occurring crystals could have formed from processes that were similar to the way in which waters might mix in a water flooded sandstone formation, it is possible that barium sulphate crystals produced in this work could bear some resemblance to those that might be formed in a water-driven oil reservoir.

5.5 THE PATTERN OF PERMEABILITY CHANGE

The change of permeability and the pattern it follows were the most significant pieces of information to be gained from the experimental study, as testified by the linear relation between flowrate and permeability in the Darcy equation for flow through a porous medium. The flowrate a sandstone can support for a given pressure drop is important in all aspects of waterflooding of natural sandstone formations.

5.5.1 Proposal of Theories as to the General Shape of the Permeability Decline Curves

The most striking thing about all the permeability plots shown in appendix A5.4 was that all the curves were concave, some most sharply so, especially the curves for the front sections of the cores. This was most significant as it implied that permeability loss would be fastest in the early stages of scaling. Several theories as to why the plots were curved in this way are discussed below. It was considered unlikely that any one of them could be shown to be solely responsible for the shape of the curves. Most probably they all made some contribution, whether large or small.

Theory of increasing velocity of the flow through the pores

The first theory considered for explaining the shape of the permeability curves was that the narrowing of the channels in the core due to scaling increased the flow velocity through the channels and so decreased the time available for precipitation to occur in any one

section of the core. Hence, the rate of precipitation in the section would decrease and the rate of loss of permeability would fall.

One interpretation of this theory was that reducing the superficial flowrate through the core would reduce the pore flow velocities and restore the permeability decline rate by allowing more time for precipitation to occur in each section. This was the basis of those experiments in which the flowrate was reduced part way through. Only one of these experiments, performed with brine system C at an initial flowrate for each brine of 15cc/min (experiment C221515CC-3R) for which the permeability curves are shown in figure 5.55, showed any sign of an increase in gradient of the permeability curve. A careful inspection of the curves for this experiment revealed that this increase actually began before the change of flowrate.

A consequence of this flow velocity effect would be to increase the supersaturation later in the core. Increased supersaturation would increase the precipitation rate later in the core also, which might show up as an increase in the rate of permeability loss of later sections corresponding to decreasing rates in the front sections. Little evidence for this could be seen in the permeability plots. If this effect was occurring and forcing higher levels of supersaturation deeper into the core it might be detected in the effluent analysis results as a steadily increasing concentration of barium ion. The results of the effluent analysis are presented in table A2 in appendix A5.4, but again they provided no real evidence to support this theory. The absence of evidence for the theory did not totally discount its validity, but it did mean that it was not the major factor involved in bringing about the shape of the permeability decline curves.

Figure 5.55 EXPERIMENT C221515CC-3R
SECTION PERMEABILITIES SUPERSATURATION = 63.0

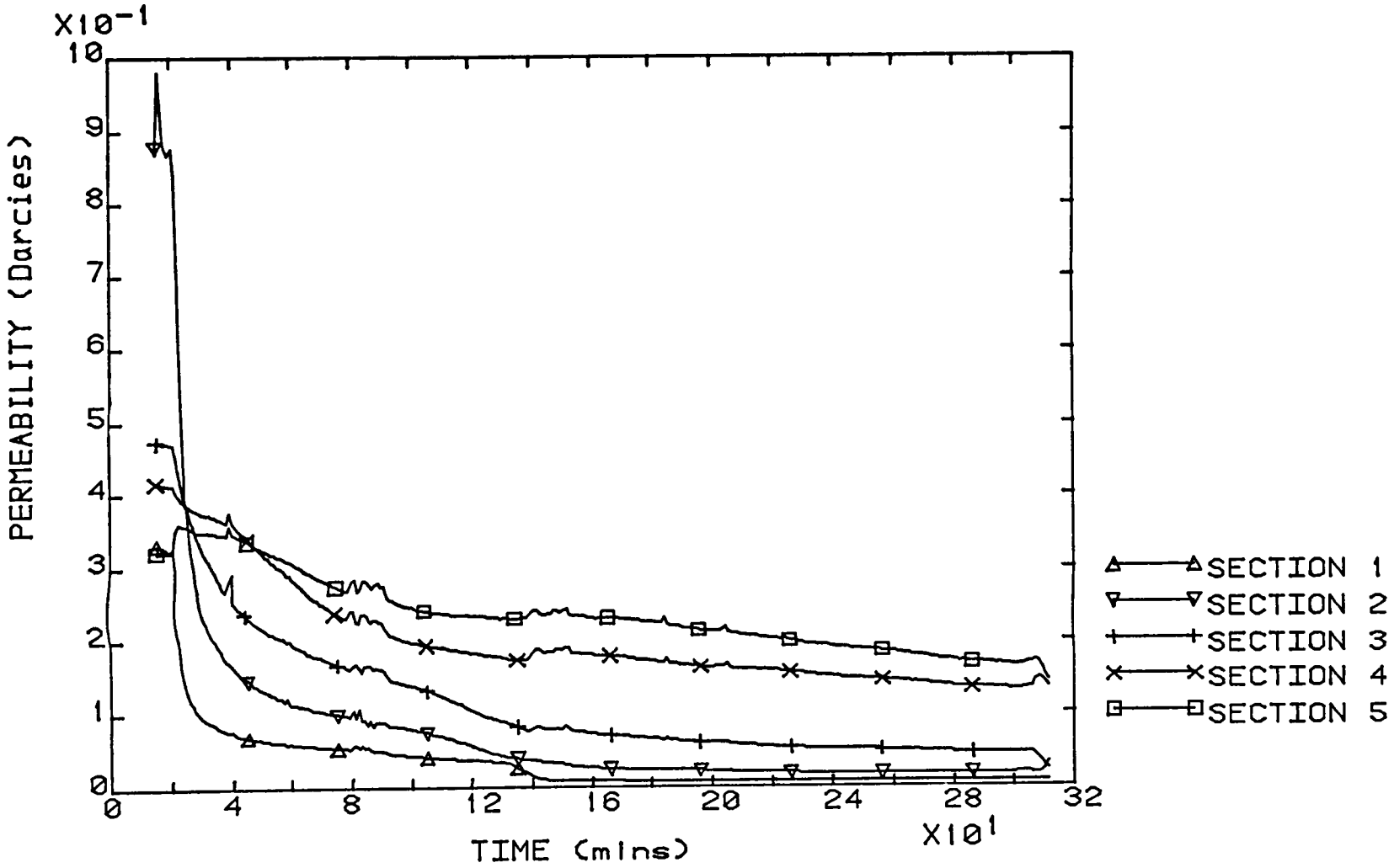

Rapid initial precipitation theory

In the work of Nancollas et al[15,29,30] on the precipitation rate of barium sulphate using a seeded crystal growth technique, a similar curve shape was produced, except that in that case the curve was for the decreasing barium content of the brines with time. It was shown that those experiments had an initial period of very rapid precipitation that did not fit in with the second order rate equation that was demonstrated to apply for the rest of the experiment. The rapid precipitation was attributed to a period of nucleation to provide the extra growth sites that the level of supersaturation of the brines appeared to demand. In the experiments involving precipitation of barium sulphate in sandstone cores, performed in this study, there were no seed crystals and so a similar period of nucleation might be responsible for the change in the rate of loss of permeability observed as these experiments progressed.

In table 3 measurements of the times for the gradients of the permeability curves to reach half their initial slope are presented. These times showed that as the supersaturation of the brines decreased through brine systems A (supersaturation 70), D (35), E (17.5) and F (8.4), the length of the initial period of rapid loss of permeability increased. This was the reverse of the trend for the initial periods of rapid precipitation observed in the experiments of Nancollas et al. Thus, an initial nucleation period, if one existed, was discounted as having been a significant factor in the initial rapid loss of permeability observed in the experiments in this work.

Crystal growth pattern theory

A theory was devised concerning the changing pattern of crystal growth with time. This theory was based on observations of SEM

photomicrographs. As was described in section 5.4, barium sulphate crystals tended to grow as a large mono-crystal often surrounded by subsidiary crystals. A photomicrograph, shown in figure 5.36, from an experiment that was stopped near where the permeability curve began to level out, demonstrated that the central blade of the crystals was well-developed early on in the experiment. This suggested that these multi-crystals grew by first forming the central crystal until growth of this crystal became restricted by hydrodynamic or physical contraints. The secondary crystals, that were growing alongside the main crystal, then increased their growth rate.

The rapid initial growth of the central blade would cause significant restriction of the flow channels in the core for a small quantity of scale. Later growth, tending to favour the secondary crystals alongside the central blade, would not have the same capacity for interfering with the flow as the early growth. Thus, even if the rate of precipitation at any one point remained the same throughout the experiment, the pattern of crystal growth, suggested above, would lead to the change of rate of permeability damage observed in the experiments performed in this study.

This crystal growth pattern theory was fine for the multi-crystal type growths produced by low ionic strength brine systems A to F, yet the discrete, well-formed crystals produced by the higher ionic strength brines also lead to concave permeability curves. For these well-formed crystals the principle of the theory was essentially the same though the mechanism was slightly different. Growth of these crystals would have been more evenly distributed about their faces, which was what lead to the different habits they exhibited. Initial growth of the crystals was on small faces, which would have caused a rapid change of the linear dimensions of the crystal. In later growth the faces were much larger and so for the same precipitation rate the rate of change of the linear dimensions of the crystal would have been

slower.

In general, the crystal growth pattern theory presented here was similar in principle to that proposed by Pucknell[35] for the growth of hard scale in tubulars. Early growth produces crystals of rapidly changing dimensions. Later growth tended to fill in the porosity created by these crystals leading to hard scale in a tube and decreasing damage rates in a porous environment.

Application of the crystal growth pattern theory to later sections of the cores

The photomicrographs for the one experiment for which a complete SEM study was performed, shown in figures 5.18 to 5.25, showed that the dominance of the central blade of the crystal clusters diminished further into the core. This matched the change of gradient of the permeability curves becoming more gradual further into the core, as the growth pattern theory would have predicted because of the greater spread of growth at the crystal site.

The permeability of the last two sections of the core changed much more gradually as a result of there being far less scale formed towards the end of the core. The curves for the last two sections were mostly concave and sometimes straight, following the pattern of the curves for the earlier sections but over a much longer timespan. This demonstrated that the same processes governing permeability loss in the front sections of the core were probably also controlling the permeability damage at the end of the core. It was not possible to study the further development of the permeability curves for the last two sections of the cores by extending the time of the experiments owing to the pressure limitations of the clamp core holder used in the study.

5.5.2 Numerical Characterisation of the Permeability Decline Curves

Initial and final permeability damage rates

The pattern of the permeability changes in the core could be characterised by quantifying the rates of permeability damage. Most of the permeability curves presented in this work showed two stages. The first stage covered the concave section of the curve with its initial high slope, which gradually decreased into the second stage, a period of constant slope (damage rate) which continued up until the end of the experiment. In table 3 the initial damage rates, evaluated for each section of the core are presented. Where the curve could be seen to have reached the second stage of constant slope this final, steady, damage rate was also evaluated.

The data presented in table 3 for the initial damage rates of the sections showed clearly the seriousness of the permeability loss that might be expected to occur around the point of mixing of two incompatible brines. Even the final, steady rates suggested, in most cases, that considerable permeability damage would occur if the flow was allowed to continue over long periods of time.

The pattern of initial damage rates and their correlation with initial permeability

There was little pattern to be seen in the damage rates alone, even for brines of the same type. In general there was a trend for lower supersaturation brine mixes to cause smaller initial damage rates, which was to be expected from a consideration of the precipitation rate equation (equation 3.17) and following from the work of Pucknell.

The wide variation in initial damage rates for brines of the

Table 3. Experimental permeability damage rates and curve characterisation times

EXPERIMENT IDENTITY	PERMEABILITY DAMAGE RATES (mD/min) Initial rate above steady rate					CHARACTERISATION TIMES		
	SECTION					SECTION		
	1	2	3	4	5	1	2	3
C141515AA-2	25 1	36 1.2	19 -	5 -	- -	4.0	5.0	8.0
C071515AA-3	35 0.0	74 0.0	21 0.2	2 0.8	- -	4.4	6.4	16
C141515AA-4	28 -	32 -	10 -	2.2 -	- -	4.0	5.0	14
C071515AA-5	79 -	53 -	18 1.2	13 1.5	- -	3.4	5.0	14
C141515AA-6	21 -	15 -	6.2 -	1.6 -	- -	3.8	8.0	10
C181515AA-8	41 0.5	84 0.5	16 -	12 3.0	- -	4.0	6.0	18
C181515AA-11	26 -	45 -	15 -	10 7.0	7.2 4.4	4.0	6.0	11
C181515BB-2	32 -	42 -	8.0 -	1.6 -	0.6 -	4.0	6.0	-
C221515BB-4	40 -	64 -	11 -	3.4 -	1.8 2.4	4.0	8.0	13
C221515BB-5	40 1.1	83 0.8	15 1.1	2.8 2.6	0.4 -	4.3	6.8	21
C221515BB-6	49 -	- -	22 -	8.5 -	4.4 -	3.6	-	9.8
C221515BB-7	65 0.5	96 0.2	36 0.1	12 0.5	8.0 0.5	4.4	8.0	12

Table 3. Continued

EXPERIMENT IDENTITY	PERMEABILITY DAMAGE RATES (mD/min) Initial rate above steady rate					CHARACTERISATION TIMES		
	SECTION					SECTION		
	1	2	3	4	5	1	2	3
C221515CC-1	123 0.4	134 0.3	18 0.1	0.8 0.2	0.4 0.2	3.7	5.8	20
C221515CC-2	23 0.0	25 0.1	6.2 0.1	2.4 -	0.0 -	5.0	11	29
C221515CC-3R	55 0.0	123 0.0	19 0.1	3.2 -	0.0 -	3.0	4.0	9.0
C221515CC-4R	28 0.0	19 0.0	4.4 0.0	1.2 -	0.0 -	4.2	10	37
C221515CC-5R	24 0.2	19 0.7	5.2 1.1	1.4 0.5	1.4 0.0	6.0	13	-
C221515DD-1S	29 0.4	36 0.4	14 0.4	11 -	2.5 -	5.2	9.0	9.0
C221515DD-2S	29 0.3	35 0.2	14 0.4	9.4 -	3.8 -	7.0	9.0	17
C221515DD-3S	19 0.3	43 0.3	9.4 0.8	4.6 0.6	2.0 0.5	6.0	9.0	15
C221515DD-5R	24 0.1	46 0.1	10 0.2	4.8 0.5	2.6 0.3	6.0	12	25
C221515DD-7S	36 -	173 -	2.8 1.6	3.8 1.6	0.8 0.4	6.0	7.0	-
C221515DD-8S	33 -	160 -	6.2 -	1.5 -	0.5 -	6.0	-	35
C227.57.5DD-10S	11 -	11 -	- -	- -	- -	12	20	-

Table 3. Continued

EXPERIMENT IDENTITY	PERMEABILITY DAMAGE RATES (mD/min) Initial rate above steady rate					CHARACTERISATION TIMES		
	SECTION					SECTION		
	1	2	3	4	5	1	2	3
C221515EE-1	9.2 0.0	9.8 0.2	3.0 0.3	5.2 0.8	2.3 0.3	27	27	-
C231515EE-3	7.8 -	3.6 -	2.2 -	0.0 -	- -	20	24	-
C277.57.5EE-10	6.2 -	5.2 -	0.6 -	0.4 0.3	0.8 0.1	34	48	120
C167.57.5EE-11	2.4 -	4.1 -	0.9 -	0.8 -	0.2 -	42	37	58
C1644EE-12	1.0 -	0.7 -	0.1 -	0.0 -	0.0 -	38	26	-
C237.57.5FF-1S	0.1 0.0	0.7 -	0.2 0.1	0.1 0.1	0.0 0.0	407	153	-
C167.57.5FF-2S	0.3 -	0.5 -	0.1 0.0	- -	0.1 0.0	100	120	-
C167.57.5FF-4	0.3 -	0.6 -	0.1 0.2	0.2 0.1	0.0 0.0	100	120	-
C267.57.5HH-1S	21 1.2	13 0.1	2.0 0.0	0.6 0.0	0.1 0.0	31	55	273
C247.57.5HH-2	23 0.1	33 0.2	1.0 0.3	0.1 0.5	0.2 0.1	111	50	-
C247.57.5II-1S	29 -	73 -	1.1 0.1	0.2 0.2	0.2 0.2	20	26	98
C247.57.5II-2S	9.4 0.1	96 0.3	1.2 0.3	1.0 0.2	0.6 0.2	20	72	255

Table 3. Continued

EXPERIMENT IDENTITY	PERMEABILITY DAMAGE RATES (mD/min) Initial rate above steady rate					CHARACTERISATION TIMES		
	SECTION					SECTION		
	1	2	3	4	5	1	2	3
C247.57.5JJ-1S	7.5 -	6.3 -	- -	- -	- -	-	-	-
C247.57.5JJ-2S	9.3 0.0	7.8 0.0	0.4 0.0	0.1 0.1	0.1 0.1	28	62	270
C247.57.5KK-1S	6.2 0.2	3.8 0.3	0.5 -	0.3 0.6	0.2 0.4	32	79	419
C247.57.5KK-2S	162 0.5	2.6 0.6	2.0 1.6	0.4 1.5	0.6 1.3	21	131	282

same type was probably brought about by the range of initial permeability of the cores, with which the damage rates appeared to have some correlation. In figures 5.56 and 5.57 the initial damage rates for the first two sections, which were both roughly at the point of mixing, have been plotted against the initial permeability of the sections. Figure 5.56 was based on the data for the higher supersaturation brine systems A, B, C (all supersaturation 70) and D (supersaturation 35). A best fit straight line through this data had a gradient of 8.4×10^{-2} min^{-1}. Figure 5.57 was based on data for the lower supersaturation brine systems E (supersaturation 17.5), F (supersaturation 8.4), H, I, J and K (all supersaturation 19). All but two of these experiments were run at a lower flowrate than those shown in figure 5.56. A best fit straight line through the data in figure 5.57, ignoring the two higher flowrate experiments, had a gradient of 3.3×10^{-2} min^{-1}.

Figures 5.56 and 5.57 showed two patterns. Higher initial permeabilities had higher initial damage rates with a reasonable correlation between the two. Comparison of the two correlation line gradients, even taking into account the differences in flowrates, showed that higher supersaturations caused higher initial damage rates, as was concluded from comparing the damage rate data alone. A lower flowrate would also contribute to a lower damage rate as demonstrated by Pucknell[35].

Characterisation of the permeability curves using the crystal growth pattern theory

The growth pattern theory was applied to consider the effect of the crystal growth on the permeability. It was realised that the permeability damage rate would start to decrease when the initial, most flow-disrupting growth began to slow down, due to physical or

Figure 5.56 Damage Rate Correlation For Brines A, B, C and D. First two sections of each core only

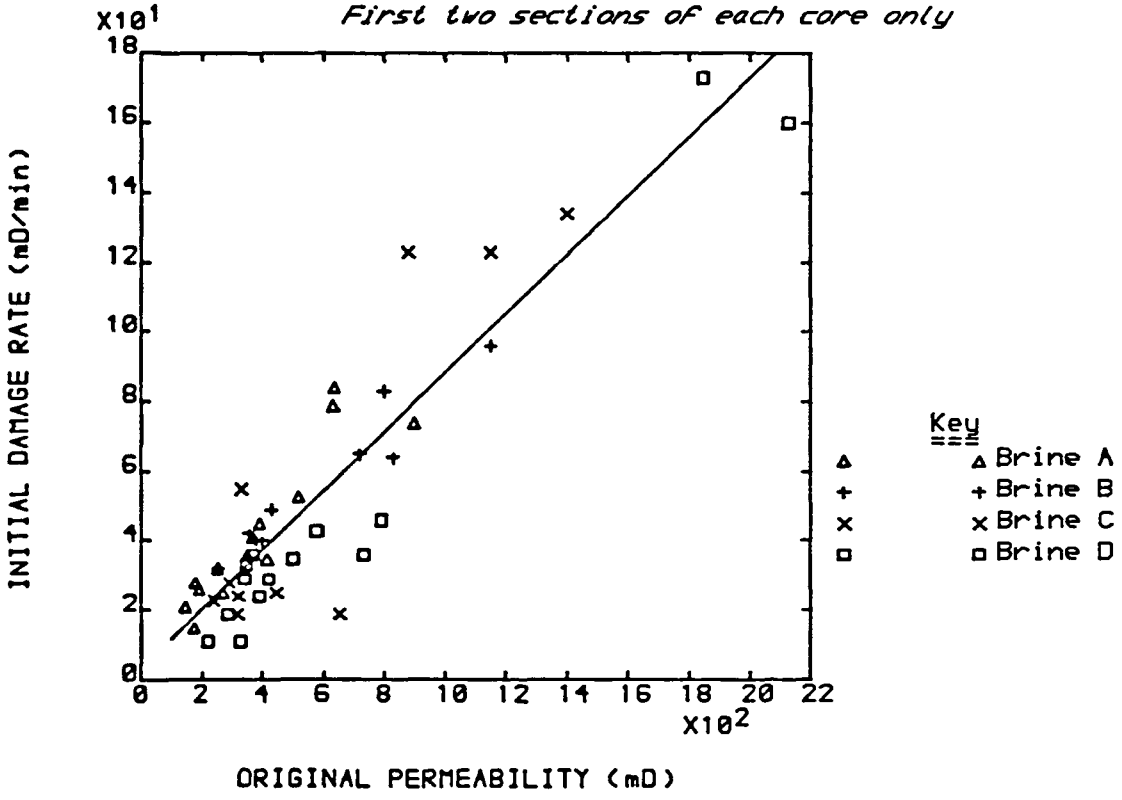

Figure 5.57a Damage Rate Correlation For Brines E, F, H, I, J and K First two sections of each core

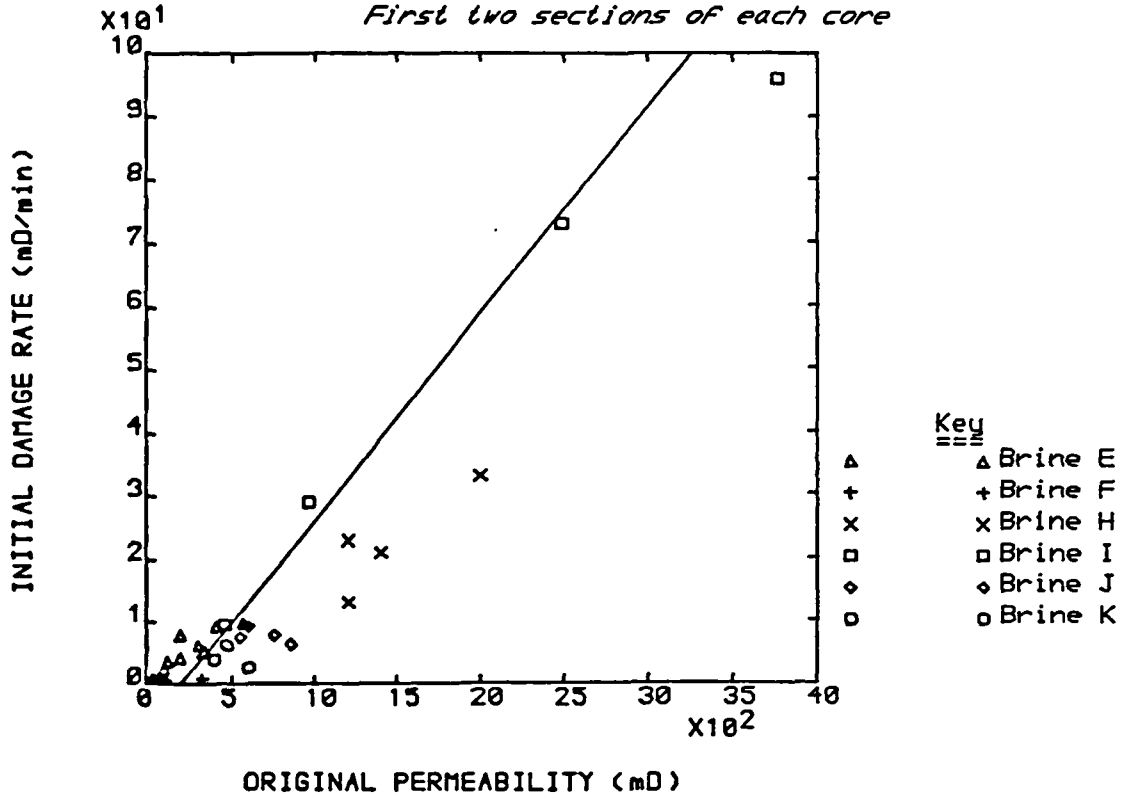

Figure 5.57b Damage Rate Correlation Enlargement of lower left corner of Figure 5.57a

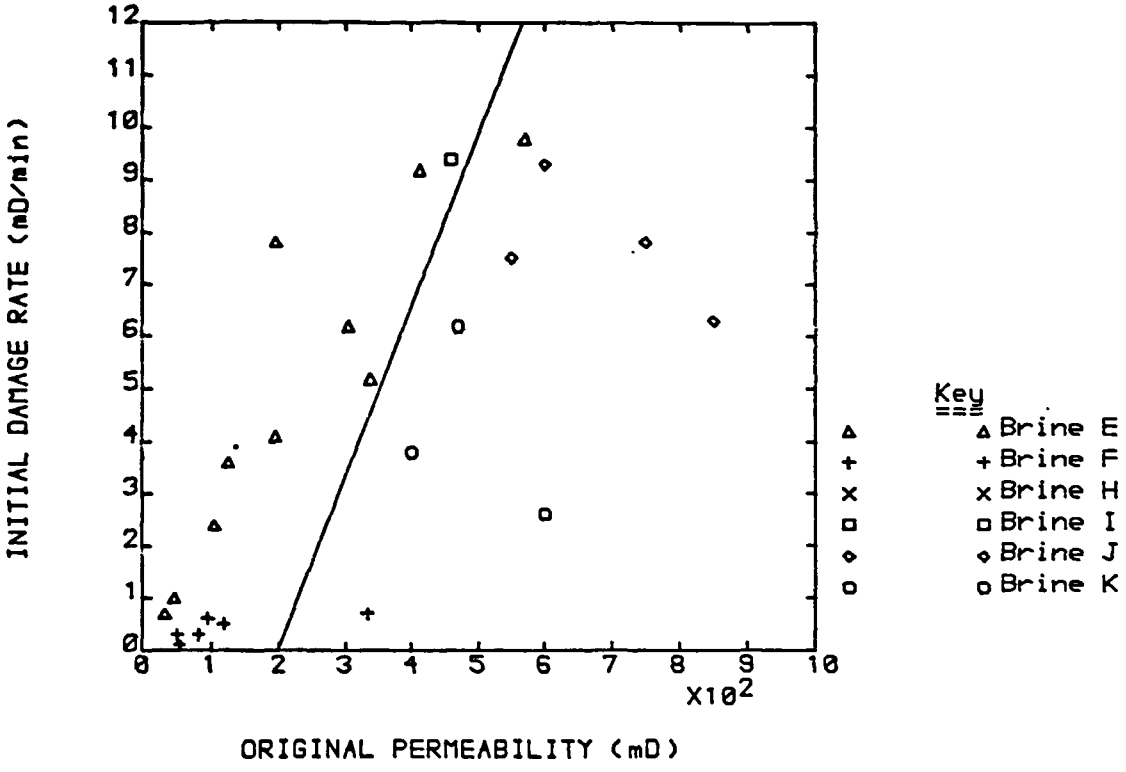

hydrodynamic restrictions, to be replaced by less disrupting growth. The time required for crystals to reach the point of shift in their growth pattern would depend upon three main factors: i) the rate of precipitation, governed mainly by the supersaturation of the brines; ii) the habit of the crystal and iii) the size and shape of the pores in the sandstone. Thus, the growth pattern theory suggested that by looking for the point where the growth pattern shifted the initial high slope phase of the permeability curves might be characterised independant of the magnitude of the permeability.

With so many crystals and different pore sizes in the core there was obviously no sudden change in the permeability curve that could be identified with the shift in growth pattern. Rather, the whole of the curve from the initial slope to the final steady gradient represented this change occurring at different times for the range of pore sizes and crystal locations in the core. To characterise this overall gradual change it was decided to choose the point at which the gradient of the permeability curve was half the initial gradient and to measure the time taken to reach this point from the onset of the permeability decline, as shown in figure 5.58. These characterisation times, for which the curve was at its steepest, were measured for the first three sections of the cores and are presented alongside the damage rate data in table 3. In some cases the permeability curve for section 3 did not reach half its initial gradient by the end of the experiment.

In general the characterisation times for section 1 were shorter than those for section 2, which in turn were shorter than those for section 3. Such a comparison was not so readily made based on the initial damage rate data alone, where section 2 damage rates were often higher than those for section 1. This characterisation technique appeared to have largely removed the effects of the considerable variation in initial permeability, whilst emphasising the differences

Figure 5.58 Example of evaluation of characterisation time for a permeability decline curve

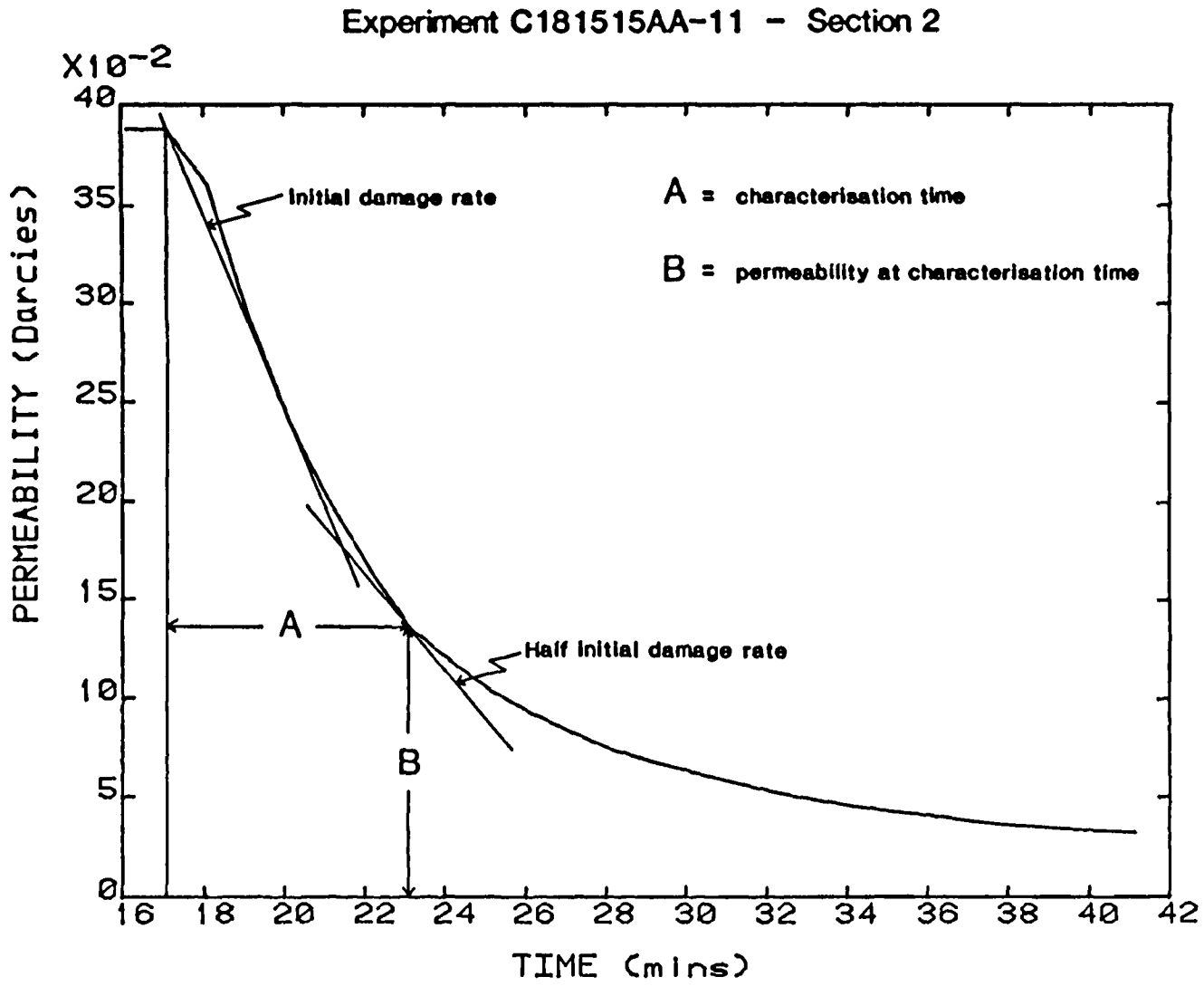

resulting from changing supersaturation both between experiments and between sections of the same core. Thus, this technique was considered to be a useful tool in gauging the effect of supersaturation in the process of permeability loss due to scaling.

There were four experiments where the characterisation time for section 2 was shorter than that for section 1. No reason for this could be discovered in the data for those experiments. It could only be supposed that something about the nature of the particular sandstone cores used in those experiments had reduced the efficacy of the distribution face causing the point of complete mixing to move deeper into the core.

5.5.3 Effect of Mineral Ion Ratio on the Pattern of Permeability Change

In the ion ratio study, using brine systems A, B and C (all of supersaturation around 70), there was very good repeatability in the characterisation times, given in table 3, for section 1 of the cores, which all tended to fall around 4 minutes. Characterisation times for section 2 of the cores for brine systems A (mineral ion ratio 1:1) and B (ion ratio 4:1) were about 6-8 minutes, but section 2 times for brine system C (ion ratio 16:1) tended to be a little longer. Again with section 3 the times for brine system C were generally longer than for brine systems A and B.

The increasing characterisation times deeper into the core for experiments where the mineral ion concentrations were very dissimilar demonstrated an effect that the crystallographic study could not show. Because of the manner in which supersaturation was calculated, see equation 3.22, supersaturation would drop faster due to precipitation in a brine with an unequal ion ratio than in an equivalent brine with

an equal ion ratio. In the first section of the cores, the newly generated supersaturation of the three brine systems A, B and C was roughly equal. It was only in the later sections of the core that the more rapid drop in supersaturation became noticible for brine system C (ion ratio 16:1), identified by the crystal growth pattern theory characterisation technique.

The effect of changing the mineral ion ratio, demonstrated here, suggested that for brines with widely differing concentrations of the mineral ions, any permeability damage due to scaling would be more localised to the point of mixing than for brines with more equal ion concentrations.

5.5.4 Effect of Supersaturation on the Pattern of Permeability Change

In the supersaturation study performed with brine systems A (supersaturation 70), D (35), E (17.5) and F (8.4), the characterisation times, given in table 3, were increasing with decreasing supersaturation. This result was expected according to the crystal growth pattern theory outlined in subsection 5.5.2. Repeatability of the results was good for brine systems A and D, but appeared to worsen as the initial supersaturation was progressively decreased. Reduced repeatability of characterisation times was also apparent in section 3 of the cores, where the supersaturation could be expected to have fallen well below the initial value. The reduced repeatability with falling supersaturation was considered indicative of other aspects of scale growth beginning to have a greater significance at lower levels of supersaturation, eg crystal nucleation rate.

Comparison of the magnitudes of the characterisation times for brine systems A, D, E and F, presented in table 3, showed that the times for brine system D (supersaturation 35) were roughly 1.5-2 times

longer than the equivalent times for brine system A (supersaturation 70). The factor relating the characterisation times for brine system E (supersaturation 17.5) to those of brine system D was somewhat larger. The differences in flowrate used in the experiments with brine system F (supersaturation 8.4) made comparisons with the characterisation times for these experiments difficult. The relationship between supersaturation and the characterisation time, therefore, did not appear to be a linear one. There were insufficient results available for the lower supersaturation brines to ascertain what the relationship might be.

5.5.5 Effect of Crystal Morphology on the Pattern of Permeability Change

The higher ionic strength brine systems H, I, J and K, were demonstrated in section 5.4 to produce crystals of a different, though related, morphology to the crystals produced by the lower ionic strength brine systems A to F. The supersaturation of brine systems H to K was about 19, which put it a little above that for brine system E (supersaturation 17.5). Concurrent with the observations of the effect of changing supersaturation, the characterisation times for brine systems H to K were generally a little shorter than those for brine system E, for section 1 at least. This implied that if morphology had any effect on permeability loss then there was a greater similarity between morphologies of crystals produced by brine systems E, H, I, J and K, from a permeability loss point of view, than the SEM study suggested.

As with the ion ratio study the effect of the change in brine composition was more noticible in later sections of the core. In experiments with brine systems H to K the characterisation times for

section 2 of the cores were generally longer than times for section 2 of cores flooded with brine system E. The characterisation times for section 3 were also longer. This increase in the characterisation times between brine system E and brine systems H to K was the reverse of what the supersaturation relationship, described above, indicated and was almost certainly due to the change in crystal morphology.

5.5.6 Growth Pattern Theory and the Relative Magnitude of Permeability Change

The technique of measuring a characterisation time for the change of the crystal growth pattern, derived from the crystal growth pattern theory, has been demonstrated to be a useful one for comparing the effects of changing conditions. For practical purposes, though, it is the magnitude of the change in permeability that is important.

To relate the characterisation time to permeability damage, the permeability for each section of core at the characterisation time was measured, as shown in figure 5.58. Using the initial permeability of each section, given in table A1 in appendix A5.4, the percentage permeability damage at the characterisation time of each section was calculated. This damage data is presented in table 4. The permeability damage percentages are shown as frequency histograms in figures 5.59, 5.60 and 5.61, corresponding to sections 1, 2 and 3 of the experimental cores respectively. The arithmetic means of the permeability damage percentages for sections 1, 2 and 3 were 52.4%, 54.4% and 47.4% respectively with an overall mean of 51.7%. The spread of percentages is shown by the histograms.

Thus, the characterisation times calculated for the experiments performed in this work were shown to be associated with approximately 50% permeability damage.

Table 4. Permeabilities at curve characterisation times

EXPERIMENT IDENTITY	PERMEABILITY AT CHARACTERISATION TIME (mD)			PERCENTAGE OF ORIGINAL PERMEABILITY AT CHARACTERISATION TIME		
	SECTION			SECTION		
	1	2	3	1	2	3
C141515AA-2	169	183	146	63	52	62
C071515AA-3	229	431	298	55	48	51
C141515AA-4	50	86	65	28	34	36
C071515AA-5	282	252	232	45	49	51
C141515AA-6	48	54	67	33	31	56
C181515AA-8	178	190	203	49	30	46
C181515AA-11	74	139	113	39	36	44
C181515BB-2	109	120	-	43	34	-
C221515BB-4	188	388	285	47	47	62
C221515BB-5	168	279	161	44	35	36
C221515BB-6	255	-	231	59	-	54
C221515BB-7	355	640	477	49	56	64
C221515CC-1	564	786	282	49	56	56
C221515CC-2	132	227	209	55	51	60
C221515CC-3R	162	434	336	49	49	71
C221515CC-4R	151	178	200	52	56	67
C221515CC-5R	187	463	-	58	71	-
C221515DD-1S	172	388	279	51	53	71
C221515DD-2S	228	240	337	54	48	59
C221515DD-3S	168	256	202	59	44	65
C221515DD-5R	238	343	258	61	43	61
C221515DD-7S	186	676	-	50	37	-
C221515DD-8S	201	-	162	58	-	49
C227.57.5DD-10S	126	167	-	57	51	-

Table 4. Continued

EXPERIMENT IDENTITY	PERMEABILITY AT CHARACTERISATION TIME (mD)			PERCENTAGE OF ORIGINAL PERMEABILITY AT CHARACTERISATION TIME		
	SECTION			SECTION		
	1	2	3	1	2	3
C221515EE-1	213	360	-	52	63	-
C231515EE-3	71	50	-	36	40	-
C277.57.5EE-10	106	133	30	35	39	42
C167.57.5EE-11	27	76	80	26	39	67
C1644EE-12	11	17	-	24	53	-
C237.57.5FF-1S	15	-	-	27	-	-
C167.57.5FF-2S	42	46	-	51	39	-
C167.57.5FF-4	25	34	-	49	36	-
C267.57.5HH-1S	714	514	251	51	43	26
C247.57.5HH-2S	397	894	-	33	45	-
C247.57.5II-1S	552	930	87	58	37	49
C247.57.5II-2S	311	1700	138	68	45	35
C247.57.5JJ-2S	294	287	83	49	38	39
C247.57.5KK-1S	198	217	88	42	54	30
C247.57.5KK-2S	976	272	499	38	45	59

Figure 5.59 Frequency of Permeability Damage Percentages For Section 1 of Experimental Cores

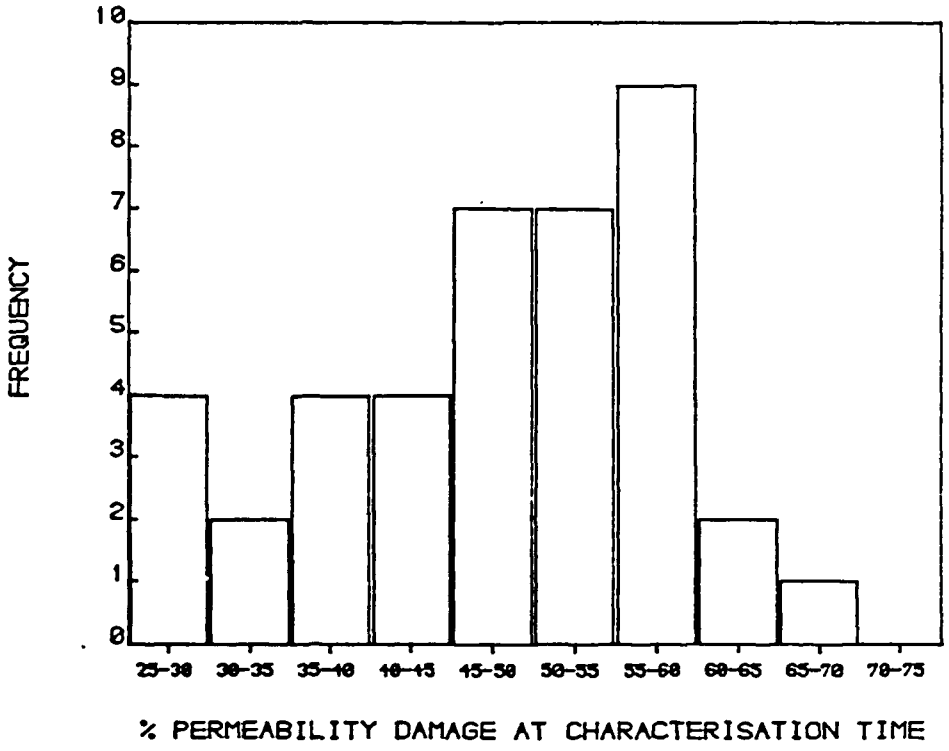

Figure 5.60 Frequency of Permeability Damage Percentages For Section 2 of Experimental Cores

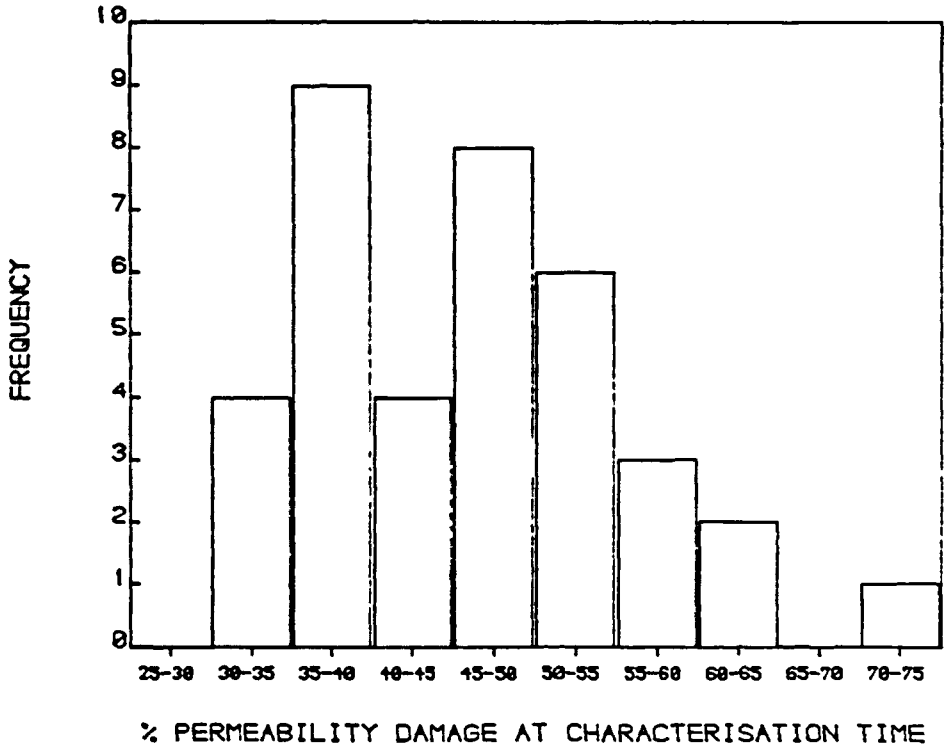

Figure 5.61 Frequency of Permeability Damage Percentages For Section 3 of Experimental Cores

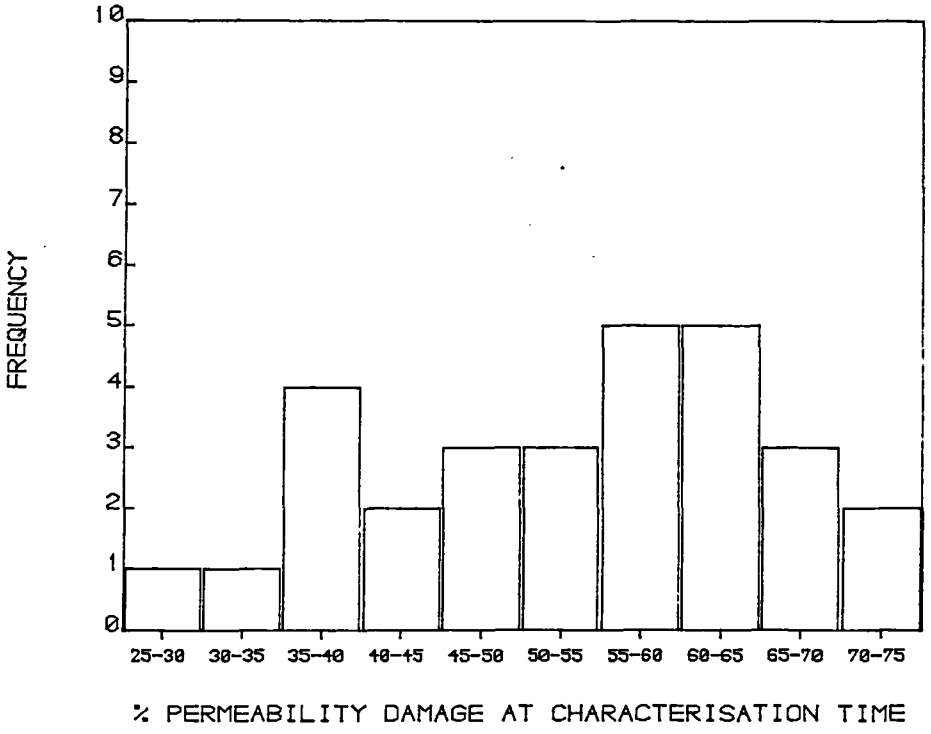

5.5.7 Summary of Section 5.5

The pattern of permeability change in a porous sandstone due to continuous scaling was characterised by a concave curve formed by a steep initial permeability decline which gradually decreased to a low, but often significant, constant damage rate. The initial steepness of this curve generally decreased with increasing distance from the point of mixing of the incompatible brines. The shape of the curve was related to a change in the pattern of growth of the scale crystals.

The theory of the crystal growth pattern was used to characterise the curves by calculating a time corresponding to the change from one growth pattern to another. This characterisation time was then used to compare the results of experiments run under different conditions.

The supersaturation was shown to be the major factor controlling the rate of damage at the point of mixing with morphological factors having a secondary effect. Further from the point of mixing, crystal morphology and the ratio of the mineral ions in the brine had an increased effect upon the damage rate. The characterisation time for each section of the cores was concurrent with that section having suffered approximately 50% permeability damage.

5.6 POROSITY DAMAGE AND THE QUANTITY OF SCALE FORMED

5.6.1 Introduction

The possibility of large permeability damage about the point of mixing of two incompatible brines in a porous sandstone was made clear in the last section. Of equal importance to reservoir modellers and reservoir engineers is the quantity of scale that caused the loss of permeability.

5.6.2 Calculation of Porosity Changes and Scale Volumes

From the data gathered in this experimental study there were two methods of assessing the amount of scale formed in the core, the porosities of the cores measured after the experiments and the measurements of the concentration of barium ion in the effluent stream from the core. Both these methods were subject to difficulties for the purposes of calculating the quantity of scale deposited in the core.

Calculations based on gas porosities

The problems of assessing the change in porosity due to the unreliability of the estimate of initial porosity and the errors in measuring the final porosity were discussed in subsection 5.2.5. The final gas porosities of the cores are given in table A1 in appendix A5.4 and the estimates of the initial porosities of the cores are given in table A4 also in appendix A5.4. The porosity damage percentages calculated from these measurements are presented in table 5. Using the bulk volume of the whole core, the volume of scale deposited in the

Table 5. Porosity damage and volume of scale formed for experimental cores

H indicates that calculated value was based on the highest measurement of initial porosity on unscaled cores (given in table A4) as opposed to the average measurement, which was too low for use with the particular experimental data.

Equations for the calculation of the various terms in this table are presented at the bottom of the table.

EXPERIMENT IDENTITY	PERMEABILITY DAMAGE (%)	GAS POROSITY DERIVED DATA		EFFLUENT CONCENTRATION DERIVED DATA	
		POROSITY DAMAGE %	VOLUME OF SCALE cm^3	POROSITY DAMAGE %	VOLUME OF SCALE cm^3
C221515CC-1	83.3	0.3	0.03		
C221515CC-4R	78.8	4.6	0.38		
C221515CC-5R	76.1	5.5^H	0.48^H		
C221515DD-1S	89.9	12.7	1.05		
C221515DD-2S	95.7	5.3	0.44	7.0	0.57
C221515DD-3S	91.1	9.8	0.81		
C221515DD-5R	76.4	20.0	1.6		
C221515DD-7S	48.5	4.5	0.55		
C221515DD-8S	47.2	4.8^H	0.43^H	2.1	0.15
C227.57.5DD-9S	46.3	2.2	0.02		
C227.57.DD-10S	-	3.8	0.31	1.5	0.11
C221515EE-1	73.8	11.5	0.94		
C231515EE-3	82.0	17.5	1.1		
C167.57.5EE-11	89.1	9.2	0.48	1.8	0.08
C1644EE-12	70.1	8.3	0.43		
C237.57.5FF-1S	64.3	38.0	2.53	3.1	0.22
C167.57.5FF-2S	40.9	8.1	0.42	2.7	0.12
C167.57.5FF-4	38.8	12.1	0.63		
C247.57.5HH-2	53.3	10.8	1.0		
C247.57.5II-1S	82.7	14.3	1.4	14.4	1.4
C247.57.5II-2S	75.0	35.9	3.4	17.7	1.7

Table 5. Continued

EXPERIMENT IDENTITY	PERMEABILITY DAMAGE (%)	GAS POROSITY DERIVED DATA		EFFLUENT CONCENTRATION DERIVED DATA	
		POROSITY DAMAGE %	VOLUME OF SCALE cm^3	POROSITY DAMAGE %	VOLUME OF SCALE cm^3
C247.57.5JJ-1S	64.0	25.2	2.4	12.1	1.2
C247.57.5JJ-2S	81.3	16.7	1.6		
C247.57.5KK-1S	63.0	10.4	0.80	14.4	1.4
C247.57.5KK-2S	68.7	14.0	1.3	15.8	1.5

For porosity data

$$\text{Porosity Damage} = \frac{\text{Initial Porosity} - \text{Final Porosity}}{\text{Initial Porosity}}$$

$$\text{Volume of Scale Formed} = \left[\text{Initial Porosity} - \text{Final Porosity}\right] \text{Bulk Volume}$$

$$\text{Bulk Volume} = 44.6 cm^3$$

For effluent data

$$\text{Volume of Scale} = \frac{\left[\text{Inlet Conc.} - \text{Effl. Conc.}\right]\left[\text{Flow rate}\right]\left[\text{Duration of Expt.}\right]\left[\text{Molar Volume of Scale}\right]}{\text{Atomic Weight Ba}}$$

$$\text{Porosity Damage} = \frac{\text{Volume of Scale}}{\text{Bulk Volume} \cdot \text{Initial Porosity}}$$

core was estimated from the calculated porosity change. The results of this estimation also appear in table 5.

Calculations based on effluent data

The difficulty with the effluent concentration data, presented in table A2 in appendix A5.4, was that it was often inconsistent, sometimes varying by an order of magnitude. The volume of scale formed was calculated using the flowrate measured during the experiment and the time for which the brines were flowing through the core. The volumes were recalculated to give an estimated porosity change for the cores based on the bulk volume of the cores and their estimated initial porosity. The results of these calculations are presented in table 5. The effluent barium ion concentration used for the calculations was either a mean or median value of the data in table A2. The initial barium ion concentrations of the brines, as measured by plasma emission spectroscopy, is also given in table A2 in appendix A5.4.

5.6.3 Comparison of Porosity and Scale Volume Results

Apart from the problem of accuracy, both methods suffered from the same problem that the calculations of scale volumes deposited made by them related to the core as a whole. The SEM study showed that the scale was not evenly distributed along the length of the core but was heavily biased towards the inlet end, so interpreting the results of scale quantity calculations was not possible in respect of specific sections of the core.

Comparing the figures in table 5 for the two methods of calculation it was noticed that neither method gave results consistently higher or lower than the other. This suggested that results of both methods were

equally valid. There also appeared to be no correlation between the porosity damage calculated from porosity measurements being lower than that calculated from effluent concentrations and those experiments which were preceded by fine material being washed out of the core. This indicated that either this fine material was of little consequence to the porosity or that its effect was insignificant compared to the errors in the calculations described above.

5.6.4 The Relationship Between Porosity and Permeability Damage

As the porosity damage data calculated above was related to the core as a whole, for comparison purposes, the percentage permeability damage for the cores was calculated from the overall permeability data given in table A1 in appendix A5.4. The overall permeability damage percentages calculated are given in table 5.

The percentage porosity damage was plotted against the percentage permeability damage in figure 5.62 for the data calculated from porosity measurements and in figure 5.63 for the data calculated from effluent concentrations. These figures showed there was no obvious, direct relationship between porosity and permeability changes for either method of calculation. Porosity damage of the cores flooded with higher ionic strength brines (brine systems H-K) was consistently higher than for the cores flooded with the lower ionic strength brines (brine systems A-F). This higher porosity damage over a range of permeability damages supported the view that the lower profile crystal habit observed for the higher ionic strength brines, as described in section 5.4, was less damaging to the flow through the core. Thus, greater volumes of scale were required to be deposited to cause permeability damage equivalent to that caused by the lower ionic strength brines.

Figure 5.62 Relationship Between Porosity and Permeability Damage Based on Gas Porosity Data

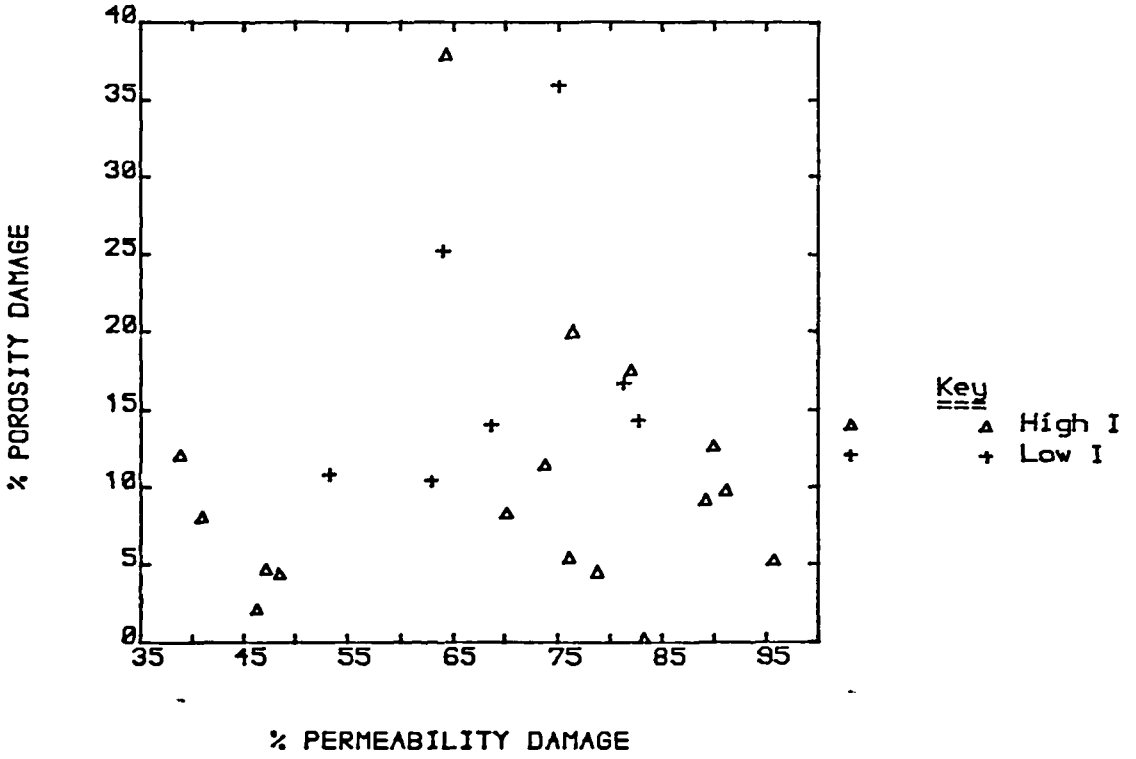

Figure 5.63 Relationship Between Porosity and Permeability Damage Based on Effluent Data

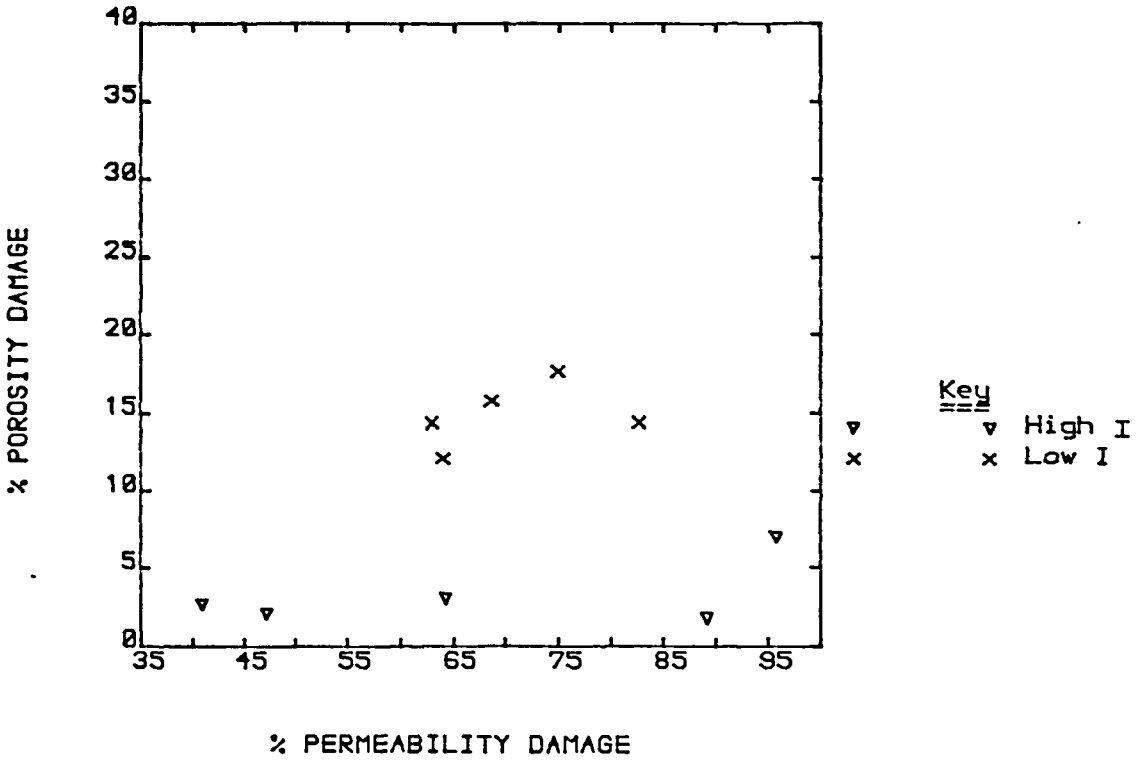

5.7 ANALYSIS OF MERCURY PENETRATION POROSIMETRY RESULTS

5.7.1 Introduction

The results of the mercury penetration porosimetry study are presented in tables A5 to A36 in appendix A5.4. These tables give the relative saturation of the sandstone sample with mercury for the absolute pressure applied. The relative saturation given is the percentage fraction of the total pore space that the space occupied by the mercury represented at each pressure, based on the volume of mercury impregnated into the sandstone sample at the end of the test. These results were used to draw capillary pressure curves by plotting the relative saturation against the log of the absolute pressure. In figures 5.65 to 5.71 the results for both sections analysed of several cores have been plotted together with a sample result for an unscaled specimen of the same core material.

The capillary pressure curve is a means of representing the structure of the pore space in the sandstone, but interpreting it required a little thought about how the pore space in the sandstone was created and how the mercury filled this pore space.

5.7.2 Structure of the Pore Space of Sandstone and the Capillary Pressure Curve

Porosity occurred in the sandstone because the grains that made up the sandstone did not fit together perfectly. As the grains in the rock were irregularly shaped the pore space they created was also irregular. Figure 5.64 shows a two-dimensional representation of the pore space that could be created by four grains in a sandstone. The

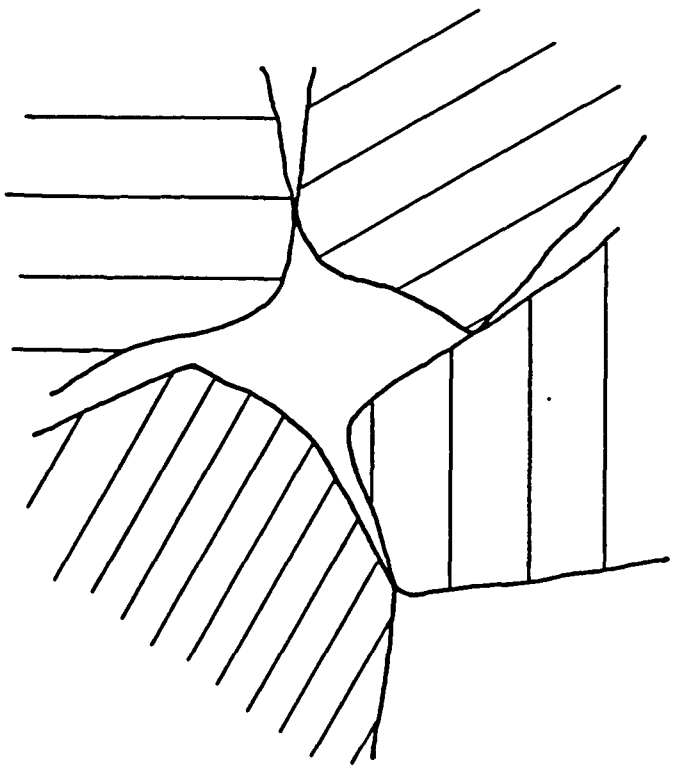

Figure 5.64 Two-dimensional representation of a pore

pore shown is made up of a large body which narrows rapidly towards where the grains rest against each other. In the plane shown this pore has only one communication channel with another pore, but would have connections with other pores in different planes.

During mercury penetration porosimetry, mercury would first enter a pore when either a) the pressure applied to the mercury was sufficient to overcome the surface tension forces involved in pushing mercury into a capillary of diameter roughly equivalent to that of the largest circle that can be drawn inside the pore; or b) when the pressure was sufficient to overcome the forces involved in pushing the mercury through the largest channel leading to this pore. For most pores in a core case b) would apply. Case a) would only apply for pores on the surface of the sandstone specimen.

When it first entered the pore the mercury would occupy the large body of the pore, but its pressure would not be sufficient to force it into the tapering edges of the pore. As the pressure was increased the mercury would be forced further into the edges of the pore. The additional volume of mercury required to progressively fill the edges of the pore would become less and less. This pattern of filling the pore space is reflected in the typical "s"-shape of the capillary pressure curve. Pressure changes at the lower pressures required to fill the pore bodies are associated with large volume changes, while at high pressures increasing pressure results in a much smaller volume change.

In the capillary pressure curves presented in this section the pressure axis was rescaled to give the equivalent capillary diameter that the mercury could enter at the corresponding pressure, assuming a 130° contact angle. The relative saturation axis was labelled in terms of the volume percentage of the pore space that had an equivalent capillary diameter greater than that indicated on the pore diameter axis.

5.7.3 Relation of the Capillary Pressure Curve to Permeability Change

Assessing permeability from the capillary pressure curve

As with simple flow through pipes, the flow of fluid through a sandstone core is governed by the dimensions of the flow channels or pores. Therefore, from a knowledge of these pore dimensions, as provided by the capillary pressure curve, it should be possible to infer the magnitude of the permeability of the sandstone. Swanson[47] proposed that the permeability was controlled by the smallest equivalent pore diameter necessary to connect all the flowing porosity of the sandstone. He identified this pore diameter with the turning point of a capillary pressure curve based on bulk saturations, rather than the relative saturations, on which the curves presented in this section were based. For assessing permeability the lower turning point of the capillary pressure curve was ignored. At the turning point the rate of increase of the volume of mercury impregnated into the sample with increasing pressure, began to fall suggesting that the mercury had reached all the pore bodies and had begun to fill the lower volume edges of the pores. Thus, the pore size indicated at the turning point was the minimum pore size that contributed to the permeability of the core.

Although the turning point could not easily be accurately located in the plots presented in this section, its location for comparison purposes was clear. By plotting the capillary pressure curve using relative saturation data it was hoped to remove the differences due to differing permeabilities of the sections of the core so as to concentrate on the relative changes in permeability.

Effect of permeability changes on the capillary pressure curve

A shift in the turning point of the capillary pressure curves to the right would demonstrate that the equivalent pore diameters that control the permeability had been reduced, resulting in a lower permeability. Thus, by Swanson's theory, the permeability of the sandstone was controlled by the pore sizes indicated by the lower portion of the curve up to the turning point. Any permeability damage to the sandstone should result in a shift of the lower portion of the curve to the right. As the capillary pressure curves plotted in this section are based on relative saturation data, equal shifts should relate to equal relative changes in permeability.

The relative changes in permeability for each scaled sandstone sample plotted in figures 5.65 to 5.71 are given in the key to each figure. The relative changes in permeability, expressed as the percentage permeability damage, were calculated from the data given in table A1 in appendix A5.4.

Comparison of capillary pressure curves with the permeability data

The curves plotted in figure 5.65 related to a core from Clashach block 7 that was flooded with brine system A at a fairly high flowrate (experiment C071515AA-5). The two curves, in figure 5.65, relating to the damaged samples more or less overlay each other, which concurred with their nearly equal permeability damages. For an experiment in which Clashach block 22 was flooded with brine system C at a similar flowrate (experiment C221515CC-3), figure 5.66, section 1 had a much larger permeability damage than section 4. This difference in the damages was reflected in the curve for section 1 being shifted far more to the right than that for section 4.

The curve for section 4 in figure 5.66 had a turning point

SAMPLE IDENTIFICATION _____ DATE _____

BY _____

PORE DIAMETER (μm) for 130° Contact Angle

Fold to Here - - - -

PENETRATION VOLUME (cc/g)

PERCENT OF PORES GREATER THAN INDICATED DIAMETER

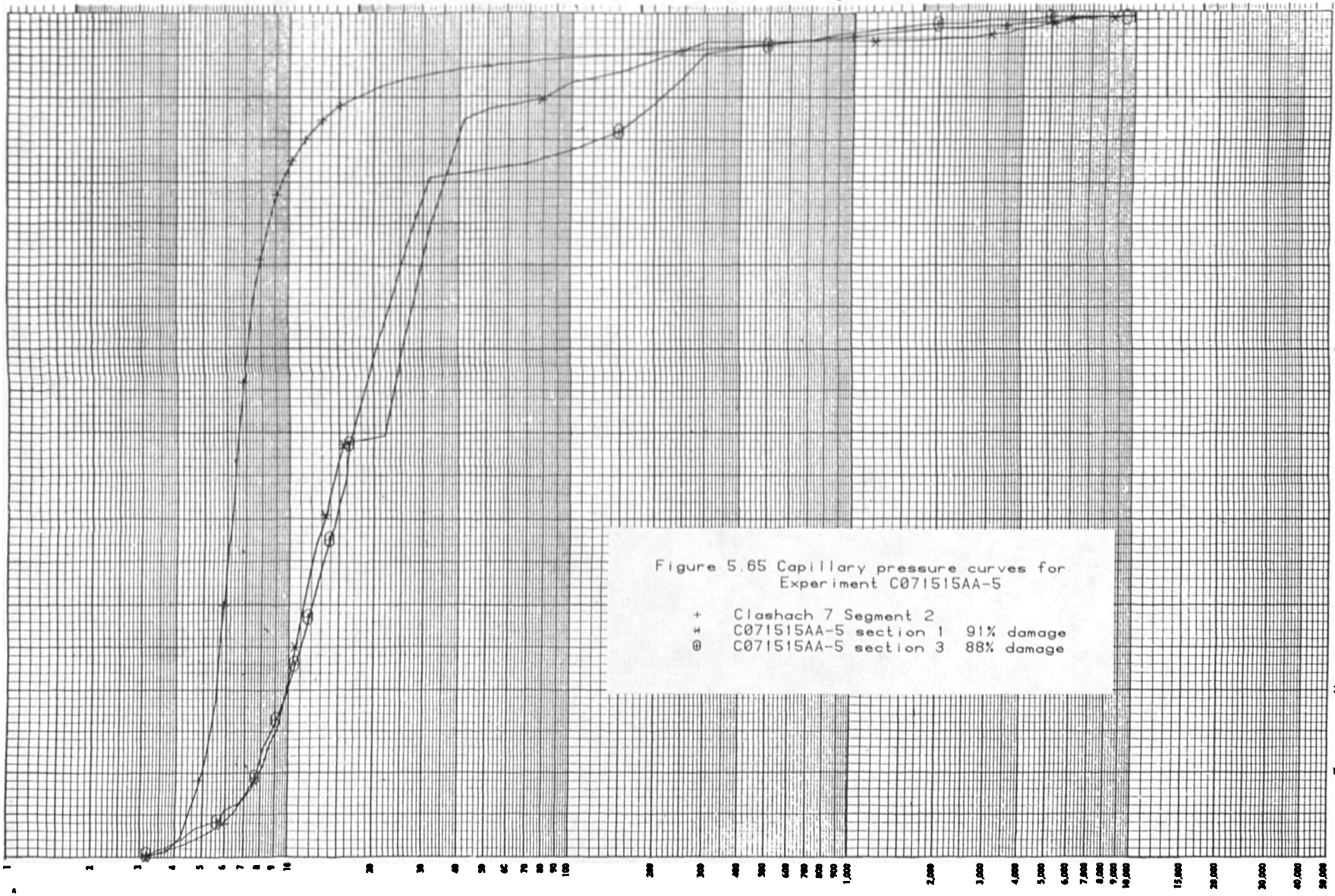

Figure 5.65 Capillary pressure curves for Experiment C071515AA-5

+ Clashach 7 Segment 2
H C071515AA-5 section 1 91% damage
@ C071515AA-5 section 3 88% damage

ABSOLUTE PRESSURE (psia)

micromeritics instrument corporation

Form 900/42704/00

SAMPLE IDENTIFICATION _____ DATE _____

BY _____

PORE DIAMETER (μm) for 130° Contact Angle

Fold to Here - - - -

PENETRATION VOLUME (cc/g)

PERCENT OF PORES GREATER THAN INDICATED DIAMETER

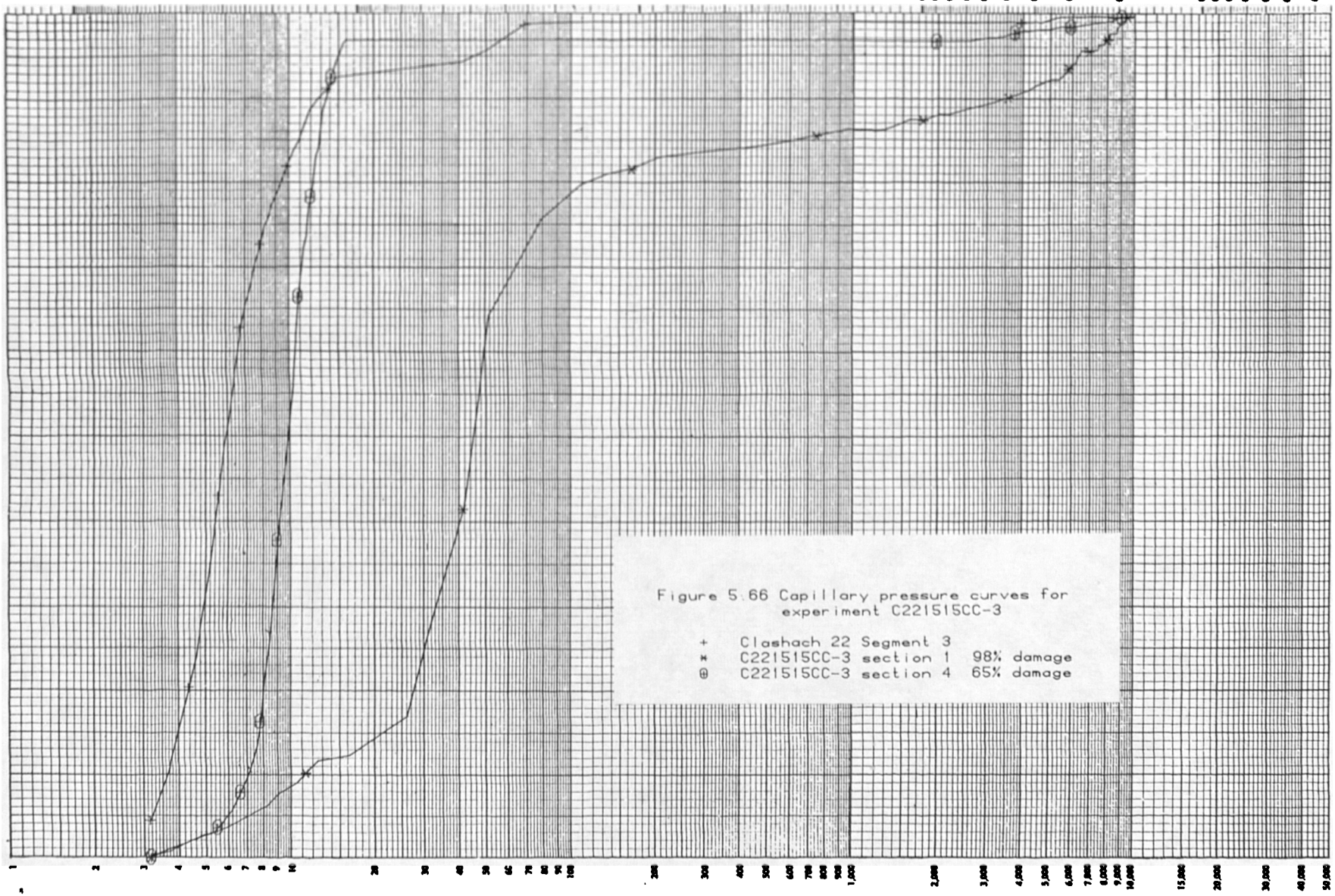

Figure 5.66 Capillary pressure curves for experiment C221515CC-3

+ Clashach 22 Segment 3
* C221515CC-3 section 1 98% damage
⊕ C221515CC-3 section 4 65% damage

ABSOLUTE PRESSURE (psia)

micromeritics instrument corporation

Form 900/42704/00

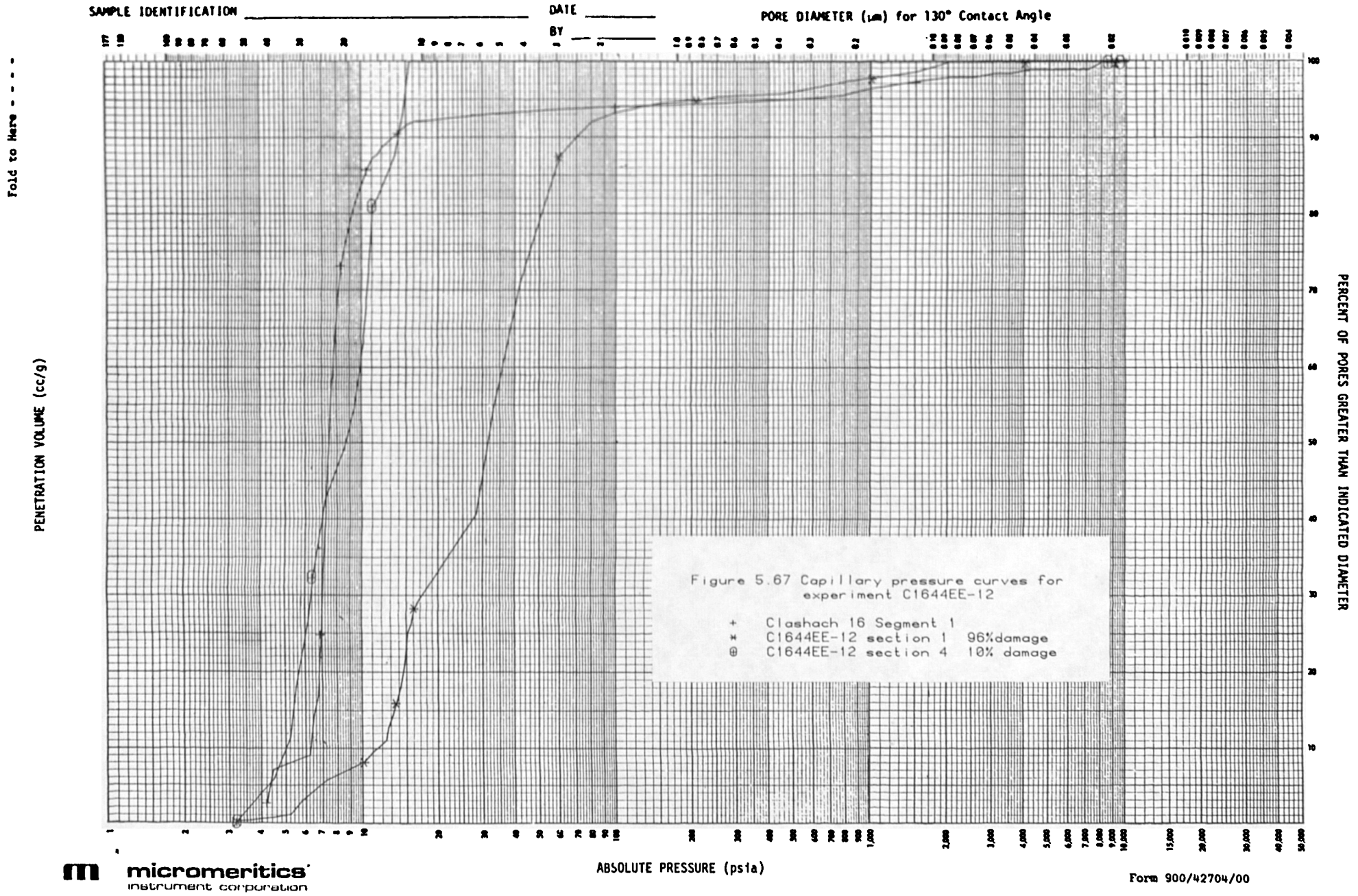
SAMPLE IDENTIFICATION
DATE
BY
PORE DIAMETER (μm) for 130° Contact Angle
Fold to Here - - - -
PENETRATION VOLUME (cc/g)
PERCENT OF PORES GREATER THAN INDICATED DIAMETER
ABSOLUTE PRESSURE (psia)
Figure 5.67 Capillary pressure curves for experiment C1644EE-12
+ Clashach 16 Segment 1
* C1644EE-12 section 1 96%damage
⊕ C1644EE-12 section 4 10% damage
micromeritics
instrument corporation
Form 900/42704/00

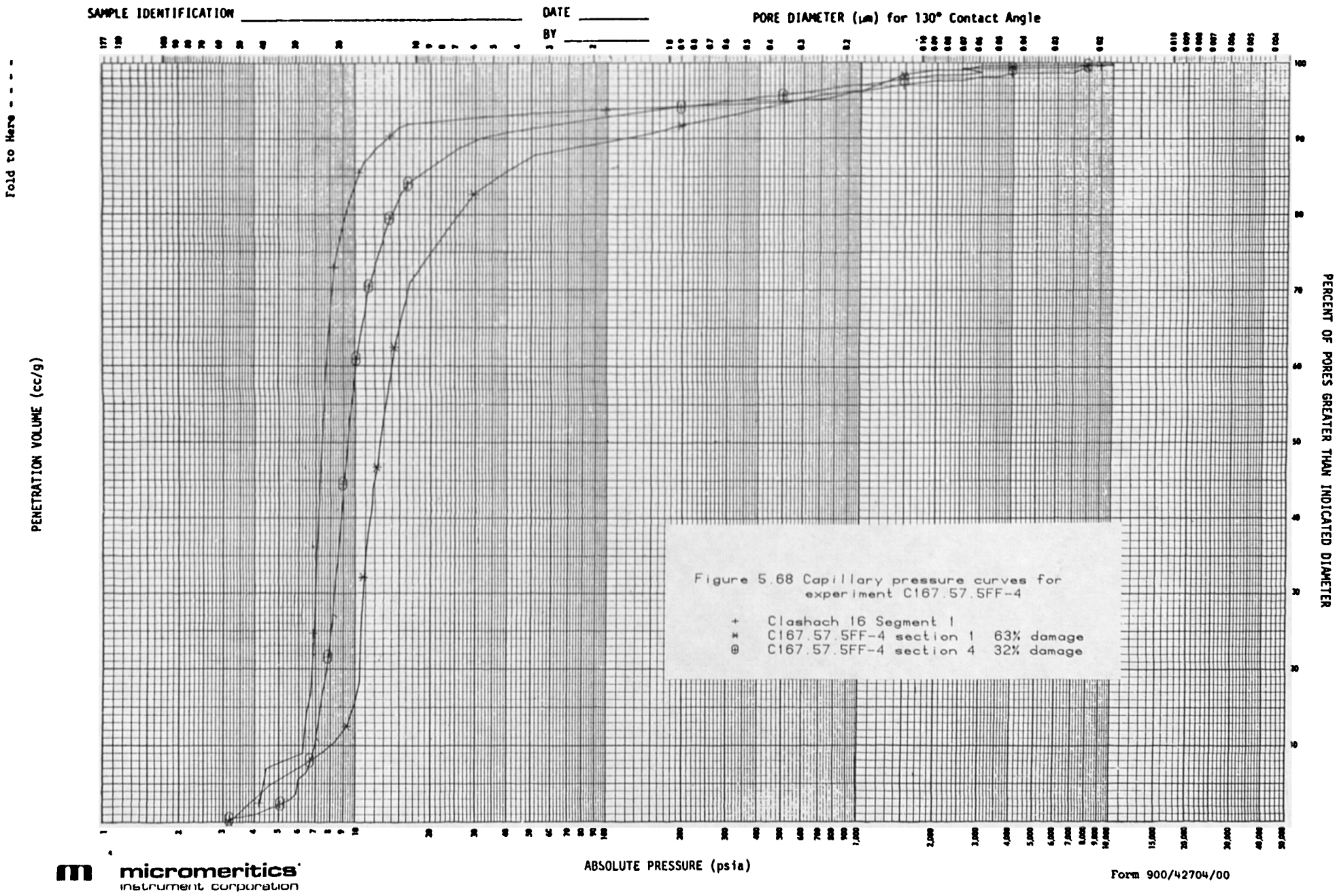
SAMPLE IDENTIFICATION
DATE
BY
PORE DIAMETER (μm) for 130° Contact Angle
Fold to Here - - - -
PENETRATION VOLUME (cc/g)
PERCENT OF PORES GREATER THAN INDICATED DIAMETER
ABSOLUTE PRESSURE (psia)
Figure 5.68 Capillary pressure curves for experiment C167.57.5FF-4
+ Clashach 16 Segment 1
* C167.57.5FF-4 section 1 63% damage
⊕ C167.57.5FF-4 section 4 32% damage
micromeritics
instrument corporation
Form 900/42704/00

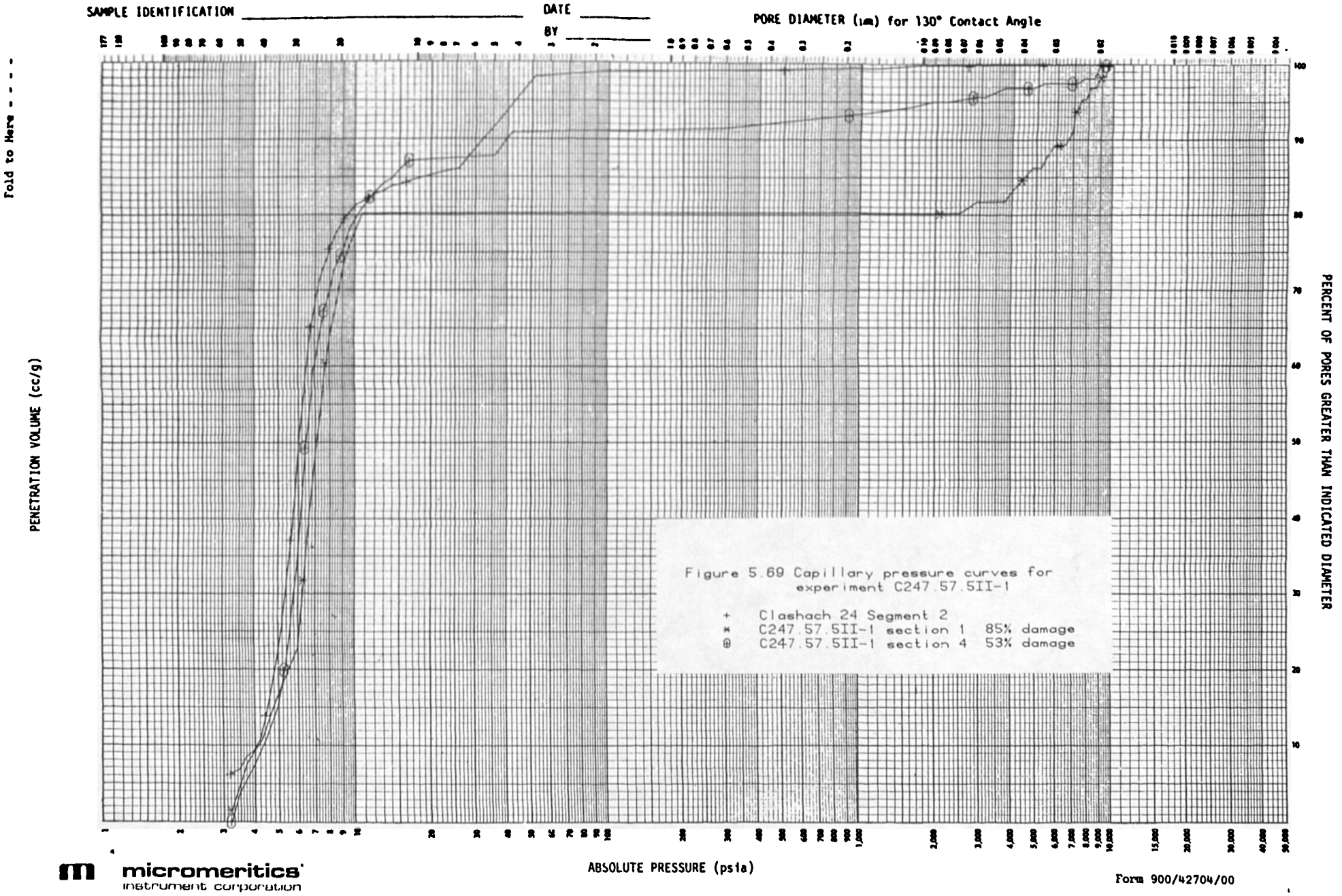
SAMPLE IDENTIFICATION
DATE
BY
PORE DIAMETER (μm) for 130° Contact Angle
Fold to Here - - - -
PENETRATION VOLUME (cc/g)
PERCENT OF PORES GREATER THAN INDICATED DIAMETER
ABSOLUTE PRESSURE (psia)
Figure 5.69 Capillary pressure curves for experiment C247.57.5II-1
+ Clashach 24 Segment 2
* C247.57.5II-1 section 1 85% damage
⊕ C247.57.5II-1 section 4 53% damage
micromeritics
instrument corporation
Form 900/42704/00

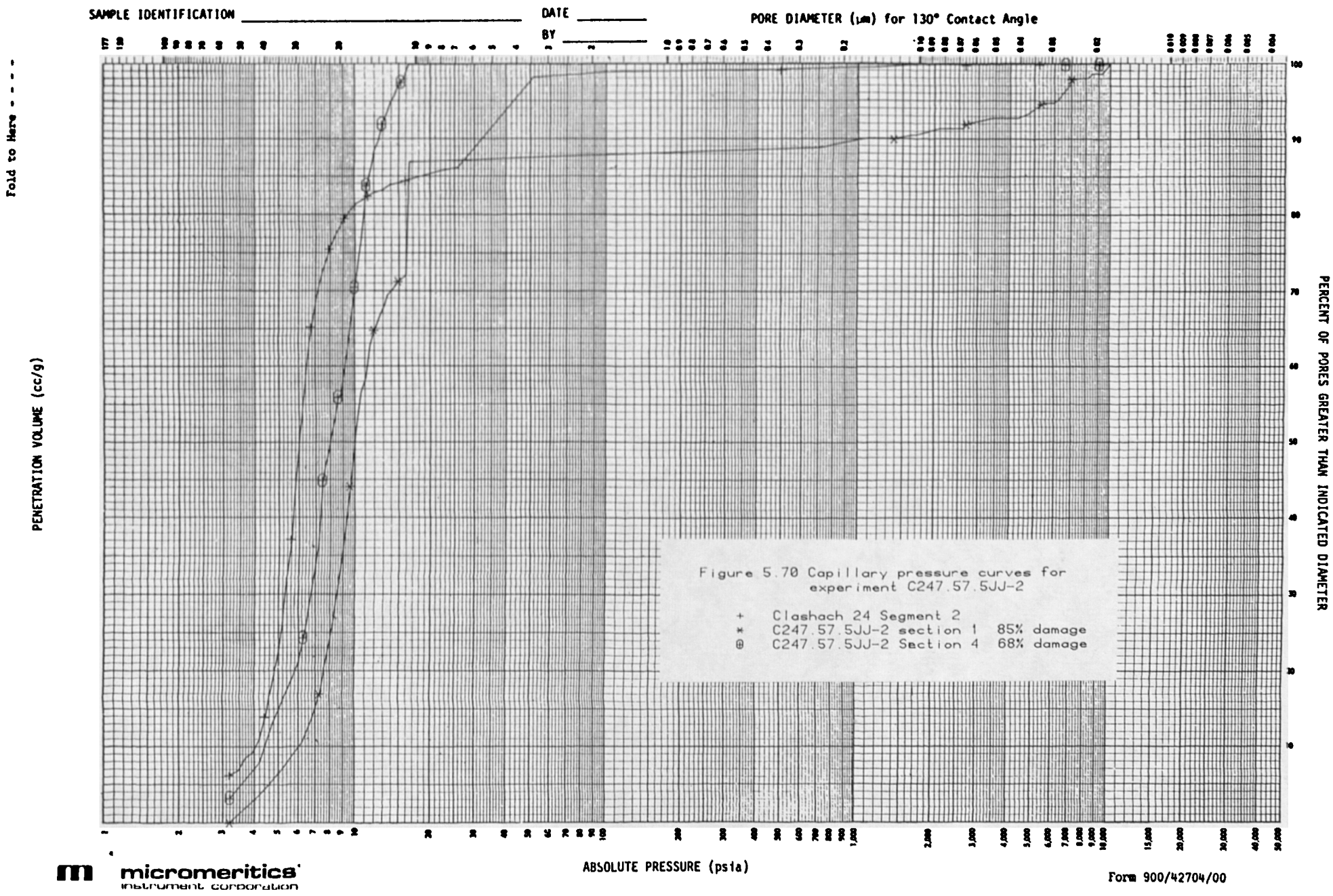
SAMPLE IDENTIFICATION
DATE
BY
PORE DIAMETER (μm) for 130° Contact Angle
Fold to Here - - - -
PENETRATION VOLUME (cc/g)
PERCENT OF PORES GREATER THAN INDICATED DIAMETER
ABSOLUTE PRESSURE (psia)
Figure 5.70 Capillary pressure curves for experiment C247.57.5JJ-2
+ Clashach 24 Segment 2
* C247.57.5JJ-2 section 1 85% damage
⊕ C247.57.5JJ-2 Section 4 68% damage
micromeritics
instrument corporation
Form 900/42704/00

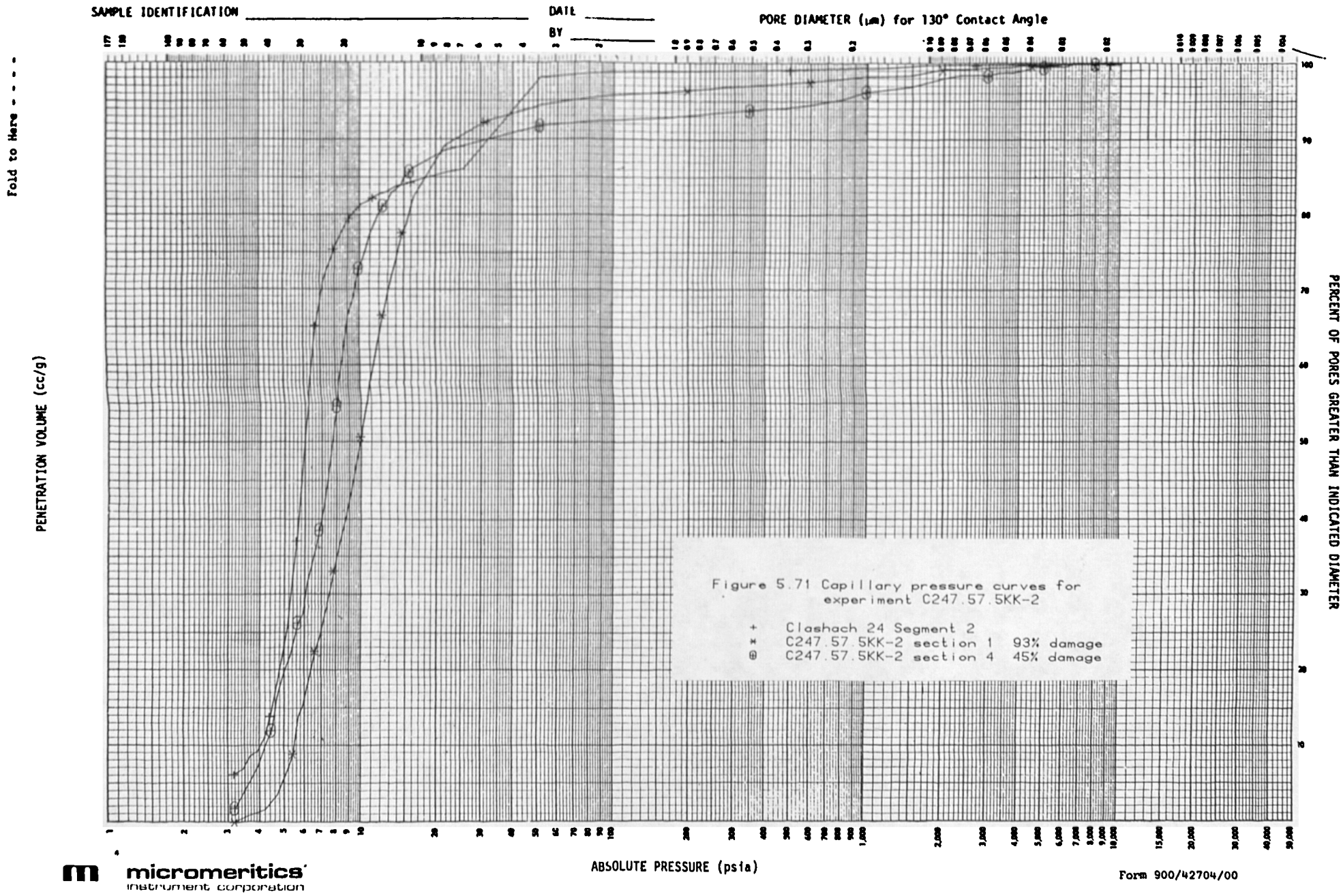
SAMPLE IDENTIFICATION
DATE
BY
PORE DIAMETER (μm) for 130° Contact Angle
Fold to Here - - - -
PENETRATION VOLUME (cc/g)
PERCENT OF PORES GREATER THAN INDICATED DIAMETER
ABSOLUTE PRESSURE (psia)
Figure 5.71 Capillary pressure curves for experiment C247.57.5KK-2
+ Clashach 24 Segment 2
* C247.57.5KK-2 section 1 93% damage
⊕ C247.57.5KK-2 section 4 45% damage
micromeritics
instrument corporation
Form 900/42704/00

fairly close to that for the unscaled sandstone yet it had suffered permeability damage of 65%. The closeness of the turning points could have been due to errors in the analytical technique or a poor match of scaled and unscaled specimens, ie the unscaled specimen was not representative of the structure of the scaled specimen prior to scaling. However, the two curves did illustrate the importance of all the lower portion of the capillary pressure curve. Even though the turning points of the curves lay close together, the difference at the lower ends of the curves was marked. This suggested that in section 4 of this core those pores which contributed most to the permeability suffered most scale growth.

Figure 5.67 illustrated another point for an experiment performed by flooding a core from Clashach block 16 with brine system E at a very low flowrate (experiment C1644EE-12). In this experiment section 4 of the core suffered very little damage, which was reflected in the curve for section 4 nearly overlying the curve for the unscaled sandstone. Again, this example supported Swanson's theory[47] and the extension of its use to consider relative changes in permeability. Similar patterns to those described above could be seen in all the curves presented in figures 5.65 to 5.71.

Scale growth in small pores

The capillary pressure curves presented in this section generally supported Swanson's[47] theory of relating permeability to the turning point of the curve. The shift to the right of the lower portion of the curve demonstrated that the pores that contributed most to the permeability were being constricted by scale growth. However, it was difficult to conclude anything about the growth of scale in the pore space that corresponded to lower equivalent pore diameters, ie the narrow edges of the pores, which was of no particular consequence to

the permeability of the core. Firstly, because the volumes involved were small, any changes in volume caused by scaling would be too small to distinguish from the errors present in the analysis. Secondly, as the larger pores were damaged, their remaining volume would begin to contribute to the volume attributed by the analysis to smaller pores, further confusing the issue.

The latter of these two observations was the likely process that caused the large shift in the upper portion of the curve, shown in figure 5.66, for section 1 of the core. The large amount of damage, that occurred in the larger pores for this section, caused such a quantity of smaller pores to be created, that the small pores began to collectively represent a significant portion of the remaining pore space.

As smaller pore sizes, initially, only had small volumes associated with them, it was considered that the majority of the scale was forming in the larger pores, that contributed most to the permeability of the sandstone.

5.7.4 Crystal Morphology Effects on the Capillary Pressure Curve

The shift downwards in the upper portion of the capillary pressure curve, visible in many of the curves in figures 5.65 to 5.71, indicated an increase in the number and hence volume, of the pores of the diameter indicated on the upper axis. The increase in the volume of smaller size pores probably occurred because of the size of the spaces left by scale crystals formed in larger pores. As different shaped crystals lead to different sized spaces between them, the shift in the upper portion of the capillary pressure curve reflected these differences.

The curves for two experiments where cores from Clashach block 24

were flooded with brine system I and brine system J (experiments C247.57.5II-1 and C247.57.5JJ-2 respectively) are shown in figures 5.69 and 5.70 respectively. These exhibited larger shifts downwards of the upper portions of the curves, for a comparatively small shift to the right of the lower portion of the curves, than was common in the rest of the capillary pressure curves presented in this section. The higher ionic strength brine systems I and J were demonstrated, in section 5.4, to lead to different crystal habits from the lower ionic strength brine systems A to F. The large shift in the upper portion of the capillary pressure curves in figures 5.69 and 5.70, suggested that the crystal habits associated with brine systems I and J lead to a more porous scale than was produced by brine systems A to F. A conclusion of this type was supported by the evidence presented in section 5.5, which showed damage by brine systems I and J to be equivalent to their position in a supersaturation range, despite the morphology of the crystals suggesting that less permeability damage should occur. If the crystal habit lead to a more porous scale this would counteract the effect of lower profile crystals being produced.

The capillary pressure curve for a core flooded with brine system K, shown in figure 5.71, which lead to a crystal habit similar to that from brine systems I and J, did not show any marked shift downwards of the upper portion of the curve. This experiment did not support the conclusion that the crystal morphology associated with the higher ionic strength brine systems lead to a more porous scale.

The conclusions made in the whole of section 5.7 were of a very general nature, because very few sets of capillary pressure curves were available for inspection. Owing to the inherent variabilities in the nature of the sandstone used for the experiments, a much larger number of curves must be considered to reach firm conclusions.

5.8 INTERPRETING THE EXPERIMENTAL RESULTS FOR THE PURPOSES OF MODELLING

5.8.1 Experimental Results of Direct Use to a Scaling Model

This subsection considers which experimental results may be used as input data for scaling the porous media model, described in chapter 3, and which experimental results would be the yardsticks against which the performance of the model could be judged. Further treatment of the experimental results to try to provide data for the model are discussed in the next subsection.

Data for setting-up the porous media model

For the initial generation of the tube sizes in the network that constituted the porous media model, the data from the mercury penetration porosimetry and helium gas porosimetry analyses, described in this chapter, were required. As described in subsection 3.3.1 the capillary pressure curve, showing mercury saturation versus pore size, generated by mercury penetration porosimetry was used as a constraint to the random process of assigning pore throat diameters in the model. The corresponding helium gas porosity was used as the test figure when adjusting the overall size of the network so that its porosity matches that of the specimen for which the capillary pressure curve was generated.

Data for controlling damaging strategies in the model

Evidence from SEM photomicrographs could provide input data for the model, however, the information from these photomicrographs was

considered more likely to be of use in a more advanced model than the one used in this work. More advanced models would consider the location and size of discrete crystals in the network. Information from SEM photomicrographs was only of use in the current model in deciding the relative magnitudes of the weighting factors for each section of the capillaries in the network model (see equation 3.27).

The only other parameters that affect the scaling behaviour of the model and which might have values inferred for them from the experimental results, are the precipitation reaction rate constant and the order of the precipitation reaction (k and n respectively in equation 3.17). Evaluation of k and n from experimental results is discussed in subsection 5.8.2.

Experimental results for judging the performance of the model

All other data relating to the experimental work and presented in this chapter could only be utilised for comparison purposes as far as modelling was concerned. The first objective for the model was for it to be able to simulate the pattern of permeability change in the experimental cores, observed in the concave nature of the permeability decline curves. If this could be achieved then the rates of permeability damage, quantities of scale formed and levels of supersaturation at the outlet of the experimental cores were all to be used as the basis for fine tuning the model. As the model could perform a crude simulation of mercury penetration porosimetry, matching simulated and experimental capillary pressure curves was also possible.

5.8.2 Estimation of the ks Product from Experimental Data

Sensitivity of terms in the precipitation rate equation

There were three terms in the precipitation rate equation (equation 3.17) which had to be supplied before the equation could be solved by the techniques used in the model. These terms were the reaction rate constant, k, the order of the reaction, n and the surface area for precipitation, s. As all these terms relate to the kinetics of the reaction they could only really be evaluated by experimentation. Both k and n were evaluated by Nancollas et al[15,29] for crystals growing in bulk solutions, but whether these values were applicable to crystals growing in a porous medium was open to question.

It was considered unlikely that the value of the order of the reaction, n, would change for solutions in a porous media environment. The work of Nancollas et al identified variations in this parameter with the initial nucleation phase of crystal growth required to produce sufficient growth sites for the level of supersaturation of the brines. In a sandstone core any nucleation period was expected to be extremely short owing to the enormous number of heterogeneous nucleation sites available. Thus, crystal growth in a core should rapidly settle into the second order kinetics demonstrated by Nancollas et al to apply for the barium sulphate precipitation reaction.

The reaction rate constant, k, did not appear to be nearly so predictable. The results of Nancollas and co-workers[15,29] suggested that the rate constant had a considerable dependance on the temperature and ionic strength of the solutions. It was considered possible that this term might also be sensitive to the hydrodynamics or some other property of the flow within the pore structure of a sandstone core.

For the purposes of the model used in this work, the surface area for precipitation, s, was calculated from the internal surface

area of the capillaries in the network. As will be discussed further in chapter 7, this was not a wholly satisfactory technique. A method for estimating a value for the product of the rate constant and surface area term, ks, is discussed below

Calculation of values for the ks product

If the rate constant, k, order of reaction, n and surface area for precipitation, s, were all treated as unknown variables it would be impossible, because of their relationship in the precipitation rate equation (equation 3.17), to use the results from the experimental work, described in this chapter, to approximate any of them. If, however, the order of reaction, n, was fixed as being equal to 2, as was considered likely, it became possible to calculate a value for the product of the rate constant, k and the surface area for precipitation, s, from the experimental results.

By using the estimated porosities for the unscaled cores and the flowrates measured during the experiment the residence time of solution in the core could be calculated. Actual, experimental inlet and oulet supersaturations were calculated from the plasma emission analysis of the stock solutions and core effluent solutions, using an estimate of the square root of the solubility product from the solubility prediction programme, described in chapter 3. The residence time, inlet and oulet supersaturations and estimate of the square root of the solubility product were all used in equation 3.20 to calculate a value for the product of k and s, treating the core as though it were a single pore.

$$\frac{1}{S_{out}} - \frac{1}{S_{in}} = \frac{k\ s\ t_c}{[C]_o} \quad \ldots\ldots\ldots (3.20)$$

where: S_{in} = supersaturation at core inlet

S_{out} = supersaturation at core outlet

t_c = residence time in core

The results of these calculations are shown in table 6 for the experiments for which all the necessary data were available. It should be noted that the supersaturations calculated in this table were not relative supersaturations as defined by equation 3.18, but were fractional supersaturations. The fractional supersaturation used was the ratio of the concentration of the scaling ion in the solution under consideration to its concentration in the same solution at saturation or $[C]_i/[C]_o$ in the terminology used for equation 3.18. The fractional supersaturation was used in the calculations in table 6 as some of the effluents were subsaturated, which would have caused complications in the calculation if relative supersaturations had been used.

Possible factors affecting the value of the ks product

Without a separate means of estimating the surface area for growth, s, it was not possible to get any closer to an estimate of the rate constant, k, using these results. A consideration of the values calculated for the product of k and s might give some clues as to what factors they were influenced by.

For cores cut from the same block the magnitudes of the ks product, calculated in table 6, were of the same order, though there were differences between different blocks. Assuming that there was no effect on the rate constant due to the precipitation reaction occurring in a porous medium, these differences could easily be put down to

Table 6. Calculation of the ks product from experimental data

EXPERIMENT IDENTITY	t_c (min)	FRACTIONAL SUPERSATURATION		$[C]_o$ $\times 10^{-5}$ molal	ks $\times 10^{-6}$ mol/ls
		INLET	OUTLET		
C221515DD-2S	0.27	29.5	1.3	3.59	1.6
C221515DD-8S	0.27	29.5	1.9	3.59	1.1
C227.57.5DD-10S	0.56	29.5	0.9	3.59	1.2
C221515EE-5S	0.27	17.1	1.2	3.57	1.7
C167.57.5EE-11	0.34	17.1	3.0	3.57	0.4
C237.57.5FF-1S	0.46	8.1	2.0	3.56	0.4
C167.57.5FF-2S	0.36	8.1	2.3	3.56	0.5
C247.57.5II-1S	0.60	19.3	0.4	10.2	6.9
C247.57.5II-2S	0.60	19.3	0.3	10.2	9.3
C247.57.5JJ-1S	0.64	20.5	1.9	10.2	1.3
C247.57.5JJ-2S	0.64	20.5	1.5	10.2	1.7
C247.57.5KK-1S	0.64	19.4	1.6	10.7	1.6
C247.57.5KK-2S	0.62	19.4	1.8	10.7	1.5

$$ks = \frac{1}{S_{out}} - \frac{1}{S_{in}} \frac{[C]_o}{t_c}$$

$$\text{Residence time } (t_c) = \frac{\text{Bulk volume . Porosity}}{\text{Flowrate}}$$

Porosity and flowrate may be found in table A1

differing surface areas available for precipitation. Fluctuations in the rate constant could not be discounted, especially as in some cases there were large changes in the ionic strengths of the solutions. As mentioned above, ionic strength appeared to influence the value of the rate constants calculated by Nancollas et al. The ks values calculated for cores from Clashach blocks 22 and 24 were of similar magnitude, but the brines used with them were of differing ionic stengths suggesting that the change in s between the blocks was matched by an opposite change in k between the brines.

The two experiments in which cores from Clashach block 24 were flooded with brine system I (experiments C247.57.5II-1 and C247.57.5II-2) appeared to be exceptional. The ks values calculated for these experiments were well above the values calculated for other cores from block 24. This difference between brine system I and the similar brine systems H, J and K suggested that in the case of brine system I the precipitation reaction was being catalysed to some extent. The most likely candidate for this catalyst was the magnesium ions, which were added to brine system I alone.

CHAPTER 6

ASSESSMENT OF THE SCALE GROWTH SIMULATION MODEL

6.1 INTRODUCTION

The experimental work identified many interesting characteristics of how the flow-supporting properties of sandstone change under a scaling environment. The remaining task was to investigate whether the computer model discussed in chapter 3 was capable of simulating, to any degree, the sort of changes observed in the experimental cores due to the deposition of scale.

There were many problems involved in comparing the results of the model with those of the experiments. The model was based on macroscopic, ie large scale, theories, such as the precipitation rate equation which applied to precipitation in bulk solutions. These theories were applied to the model in a microscopic manner, by considering what was occurring in each capillary. This produced results for a simulated core which was still microscopic in relation to the real, experimental core. Thus, a model based on macroscopic principles applied in a microscopic way was to be compared with the macroscopic results of the experiments, ie measurements of permeability and porosity. The difficulties in making this comparison are clearer if one considers comparing the results of the relatively microscopic experimental cores with what occurs in a macroscopic oil reservoir.

Some microscopic information was available from the experimental work in the form of SEM photomicrographs and mercury injection porosimetry curves. Unfortunately, at the time of writing only the latter of these had been implimented into the model. The model, then,

was only at a very early stage of development and the work described in this chapter must be considered as being only of a preliminary nature. It was hoped that this work would serve to identify the areas where major improvements could be made.

In this chapter the workings of the current model will be described in greater detail in order to clarify what is being discussed thereafter. In the final section of this chapter the response of the model to various changes in its operating conditions is discussed and comparisons made with the experimental work. This discussion is concluded with a review of how closely the model could simulate what occurred in the experimental cores. Improving and extending the model is discussed in chapter 7.

6.2 THE MODELLING PROGRAMME

In chapter 3 the theoretical equations and principles employed in developing the model for simulating damage to a porous medium due to scale formation were discussed. In this section the manner in which these equations were brought together to carry out the simulation is described in greater detail. The aim of this section is to familiarise the reader with what processes occurred or could be made to occur during the running of the model so that a greater understanding of what effect changes in the input parameters would have on the behaviour of the model might be gained.

6.2.1 The Network Model of a Porous Medium

Structure of the model

The key to understanding the manner of operation of the network model lies in the system of coordinates used to refer to the locations of capillaries and nodes within the network. This coordinate system is described in appendix A6.1. The coordinates of each capillary were used to store the data relevant to that capillary, such as throat diameter, throat length and flowrate, in three-dimensional arrays. The maximum dimensions of these arrays were set to the maximum size of network that the programme was set up to use, based on the capacity of the computer used to run the model.

The phenomena that the network model could be used to simulate were usually, as in this case, varying mainly with the length of the model. In order to extend the length of the model to simulate the phenomenon of interest further, the modelling programme was structured

so that several networks could be strung together with the status at the end of one network becoming the status at the start of the next. Thus, the capabilities of the model could be extended beyond the capacity of the computer supporting it by making each network exploit the full capacity of the computer. The model was run for each network or section in turn, the data for each being stored before recalling the data relevant to the next section. Figure 6.1 shows a flowchart which covers the main tasks performed by the model for a single network.

Calculation of flows in the network

Once the capillary sizes of the first network had been set up, as described in subsection 3.3.1, the flow equations were solved using a sparse matrix technique and a constant pressure drop boundary condition. This lead to a calculation of the superficial flowrate through the first section. Successive networks were solved using a constant flowrate boundary condition so that the same flowrate was preserved right along the simulated core.

Collecting data on the network

The network model had within it a facility for gathering data on the network. This system counted the capillaries that fell in certain size ranges to provide a pore size frequency distribution. Within each size range the volume of the capillaries was calculated as a fraction of the total pore space in the network. These fractions were then recalculated to give a cumulative sum at each size range working from the largest to the smallest. This cummulative sum was akin to the saturation values produced for each pore size in mercury penetration porosimetry, described in section 5.7. In the network model all capillaries were available to the calculation, which

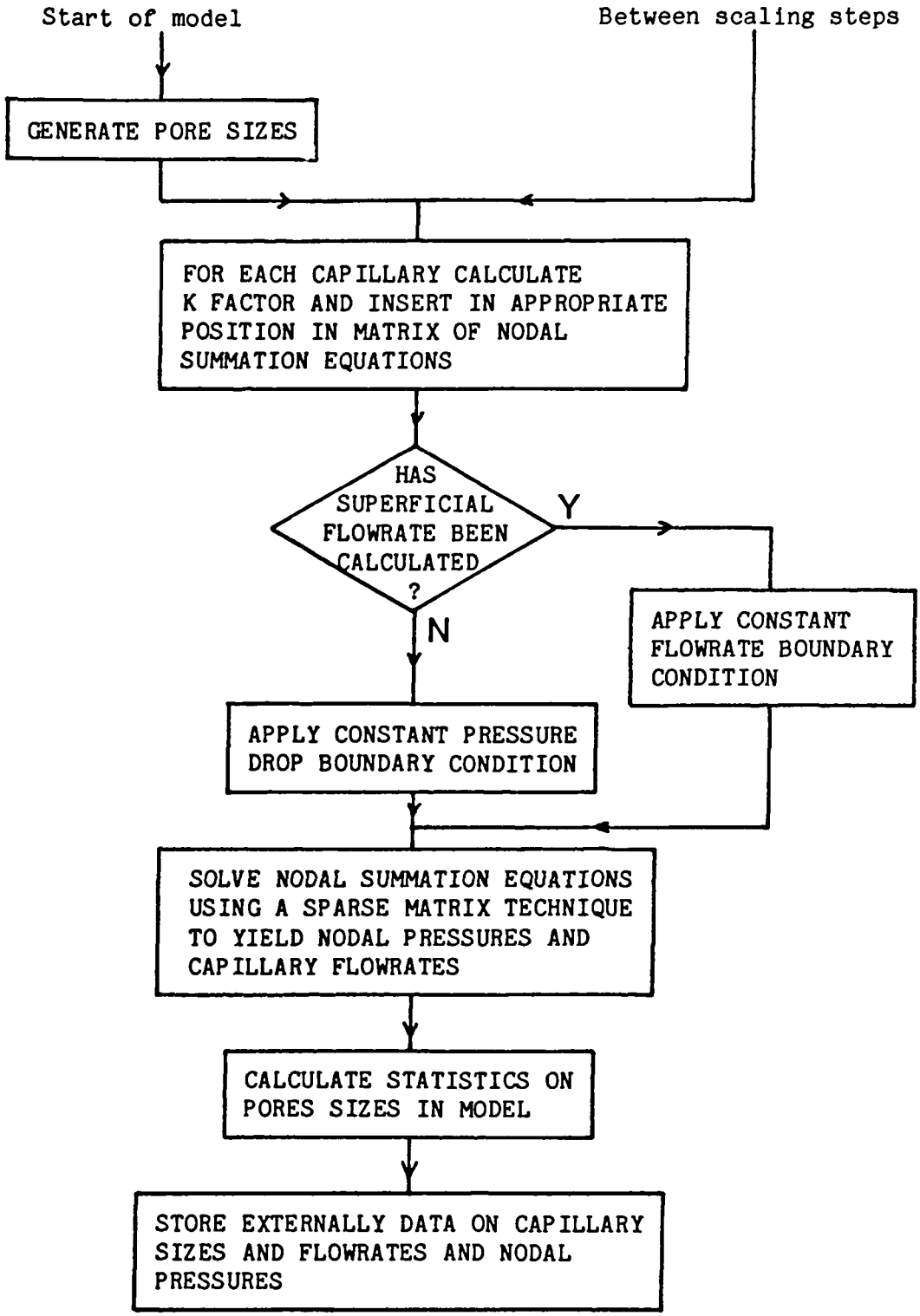

Figure 6.1 Flowchart for network model

therefore became an ideallised version of its experimental counterpart.

6.2.2 Assessing the Quantity of Scale in Each Capillary

Calculation of nodal supersaturations

Once the pressures at all the nodes and the flowrates in all the capillaries of the newly generated network had been calculated the simulation of scale growth could begin. Figure 6.2 shows a flowchart of the steps followed by the model in calculating the nodal supersaturations. The model was based on a knowledge of supersaturation at the network nodes and initially these were set to whatever the inlet supersaturation for the section of the simulated core had been decided or calculated to be. Most models were made up of three to five network sections strung together to extend the simulated length of the model.

Equations 3.20 and 3.21 were solved iteratively for each capillary in the network by a method of successive substitutions to produce a value for the level of supersaturation at every node in the network.

$$\frac{1}{S_{out}} - \frac{1}{S_{in}} = \frac{k\ s\ t_p}{[C]_o} \qquad \ldots\ldots (3.20)$$

where: S_{in} = supersaturation at pore inlet

S_{out} = supersaturation at pore outlet

t_p = time to cross pore

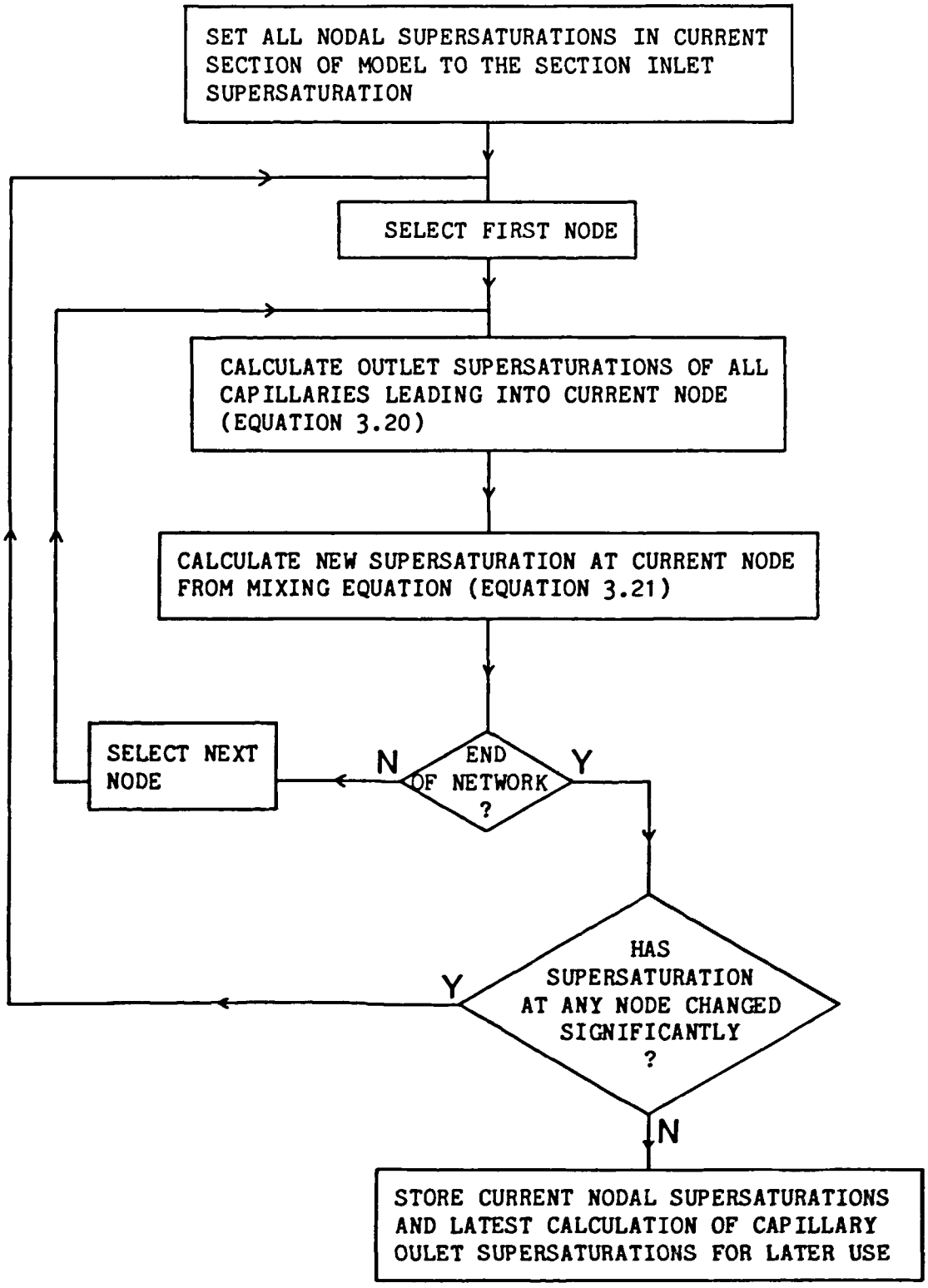

Figure 6.2 Flowchart for calculation of nodal supersaturations

$$S_x = \frac{V_a S_a + V_b S_b + V_c S_c + \ldots}{V_a + V_b + V_c + \ldots} \quad \ldots\ldots (3.21)$$

where: S_x = supersaturation at node x

$S_{a,b,c}$ = outlet supersaturations of pores leading into node x

$V_{a,b,c}$ = volume flowrates from pores leading into node x

It was at this stage that complications could arise due to the way in which the drop in supersaturation across a pore was calculated. The calculation was based on the time taken for a packet of fluid to pass through a capillary. If the flowrate in a capillary was very low an excessively high passage time could result, which in the mathematics of the model could eventually lead to an increase in supersaturation across certain capillaries. A long passage time would mean that the fluid in the capillary would have ample time to precipitate most of its excess load of scale. Using this principle the problem of high capillary passage times was circumvented by setting the outlet supersaturation for all capillaries whose passage times were above a certain level, to a value close to saturation.

Calculation of the volume of scale in a capillary

For the calculation of scale volumes the capillary coordinate system for storing data relevant to each capillary was dispensed with as it was extremely wasteful of memory space and so constrained the maximum size of model that it was possible to run on any particular computer system. Instead, the coordinates were used to calculate the number of the capillary or node according to a specific numbering sequence, described in appendix A6.1. Data was stored according to the number of the capillary or node and thus, only as many storage

locations were required as there were capillaries and nodes. In the calculation of supersaturation, described above, the outlet supersaturation from each capillary was stored in addition to the supersaturations at the nodes, for use in calculating the volume of scale deposited.

Figure 6.3 shows a flowchart of the steps taken by the model in calculating scale volumes. To calculate the volume of scale deposited, equation 3.25 was used first, to calculate the concentration of the cation at the inlet and outlet of each capillary from the inlet and outlet supersaturations.

$$c_m = \sqrt{\frac{c_{ex}^2}{4} + c_m^* c_a^* (S+1)^2} - \frac{c_{ex}}{2} \quad \ldots (3.25)$$

where: S = relative supersaturation

c_m = cation concentration

c_a = anion concentration

c_{ex} = the difference in cation and anion concentrations

The difference in concentrations was equivalent to the amount of scale deposited in the capillary in molal units. This concentration difference was converted to molar units and adjusted for the flowrate through the capillary and the length of time this flow was assumed to have been passing, according to the time-stepping of the model described in subsection 6.2.4. The resulting number of moles of barium sulphate deposited in each capillary was converted to a volume and stored for the next stage of the model.

The volume of scale formed in each section of the model was added up after each time step and summed for the amount of scale formed in the section since the start of the simulation and the amount of

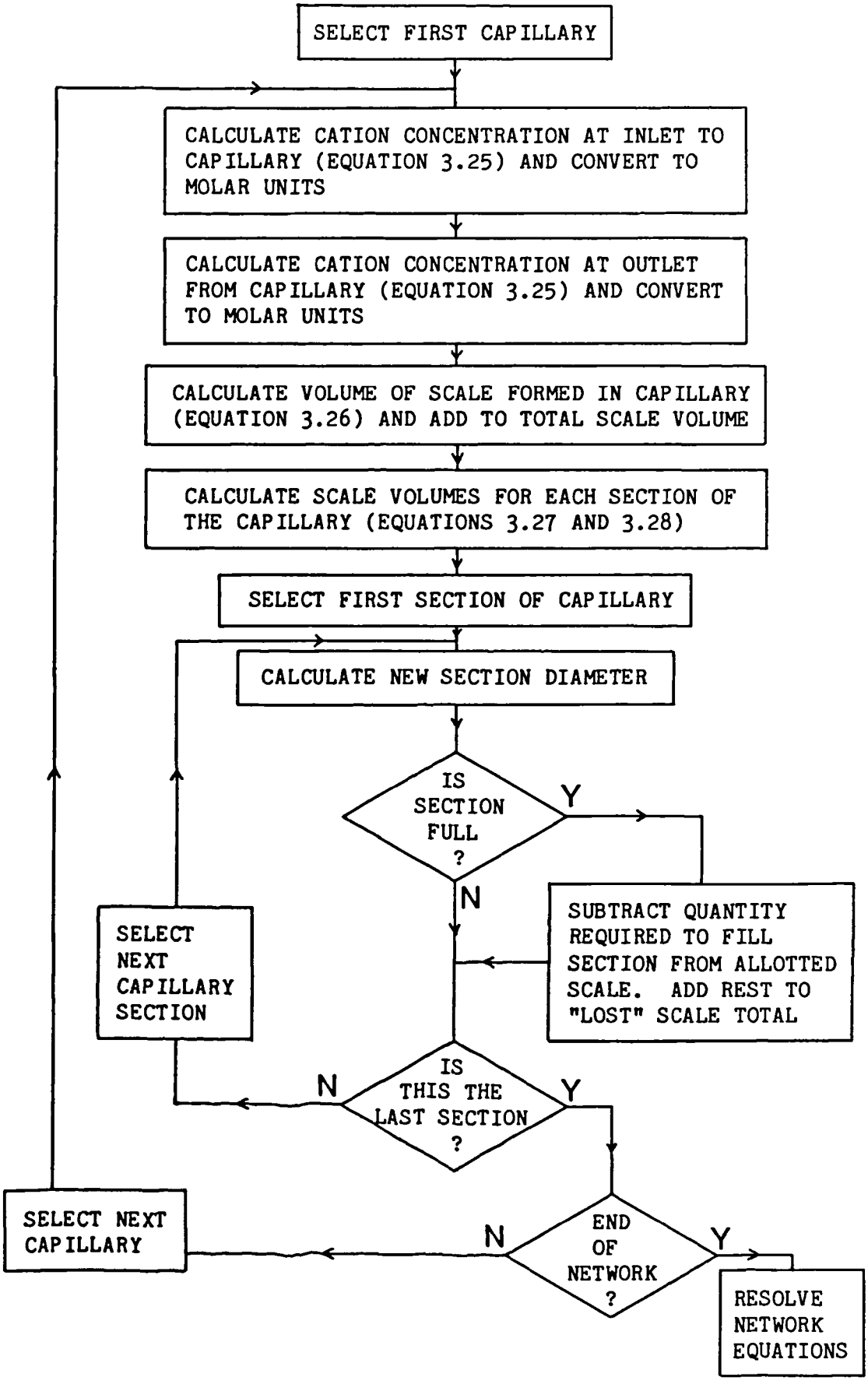

Figure 6.3 Flowchart for calculation and distribution of scale volumes

scale formed in the simulated core as a whole.

6.2.3 Distributing the Scale Within the Capillary

When the quantity of scale in all the capillaries had been calculated the problem of the distribution of the scale within the capillaries was addressed. The scale could be located in either of the wide ends of the capillary or in the narrower throat section. The volumes assigned to each section of the capillary were decided by the weighting factors, given in the input data to the programme, and the relative lengths of the sections of the capillary according to equations 3.27 and 3.28. Assigning the scale in this way avoided the problem of either of the wide ends being of zero length, which often occurred with narrow capillaries because of the inverse relationship between throat diameter and throat length, described in subsection 3.3.2.

$$F_a = \frac{D_a\, l_a}{\Sigma D_a l_a} \qquad \ldots\ldots\ldots\ldots (3.27)$$

$$V_a = F_a\, V_s \qquad \ldots\ldots\ldots\ldots (3.28)$$

where: F_a = fraction of scale volume for whole pore assigned to section a

V_a = volume of scale assigned to section a

l_a = length of section a

D_a = weighting factor for section a

The scale assigned to each section of the capillary was assumed to form a layer of even thickness all around the curved surfaces of the

capillary. A new radius was calculated for each section of the capillary and the storage arrays of capillary diameters were updated.

Problems arose in the calculation of new diameters if the amount of scale assigned to a section of the capillary had a greater volume than the remaining volume in that section. If this occurred, the diameter of that section of the capillary was given a very small value and a message was printed to the effect that the capillary was closed. The quantity of scale required to close the section of the capillary was calculated and subtracted from the amount of scale assigned. The remainder of the assigned scale was added to a total of "lost scale" and had no further involvement in the model. All these steps are shown in the flowchart in figure 6.3.

Overfilling of capillaries in this manner occurred more frequently for long time steps. This was because the model could not continuously adjust itself as pores gradually closed and because long time steps caused larger batches of scale to be deposited.

6.2.4 Modelling the Passage of Time

The passage of time in the model was a batch process, the length of the time steps being set in the input data for the programme. The conditions of inlet and outlet supersaturation calculated for the start of a time period were considered to stand for the whole of that period. At the end of a time period, when all of the capillary diameters had been recalculated to take into account the volumes of scale assigned to them, the network model was used again to calculate a new set of flowrates and pressures in the network corresponding to the new capillary sizes. For this calculation the constant flowrate boundary condition was used for every section of the model. The steps involved in modelling the passage of time are shown in the flowchart in figure

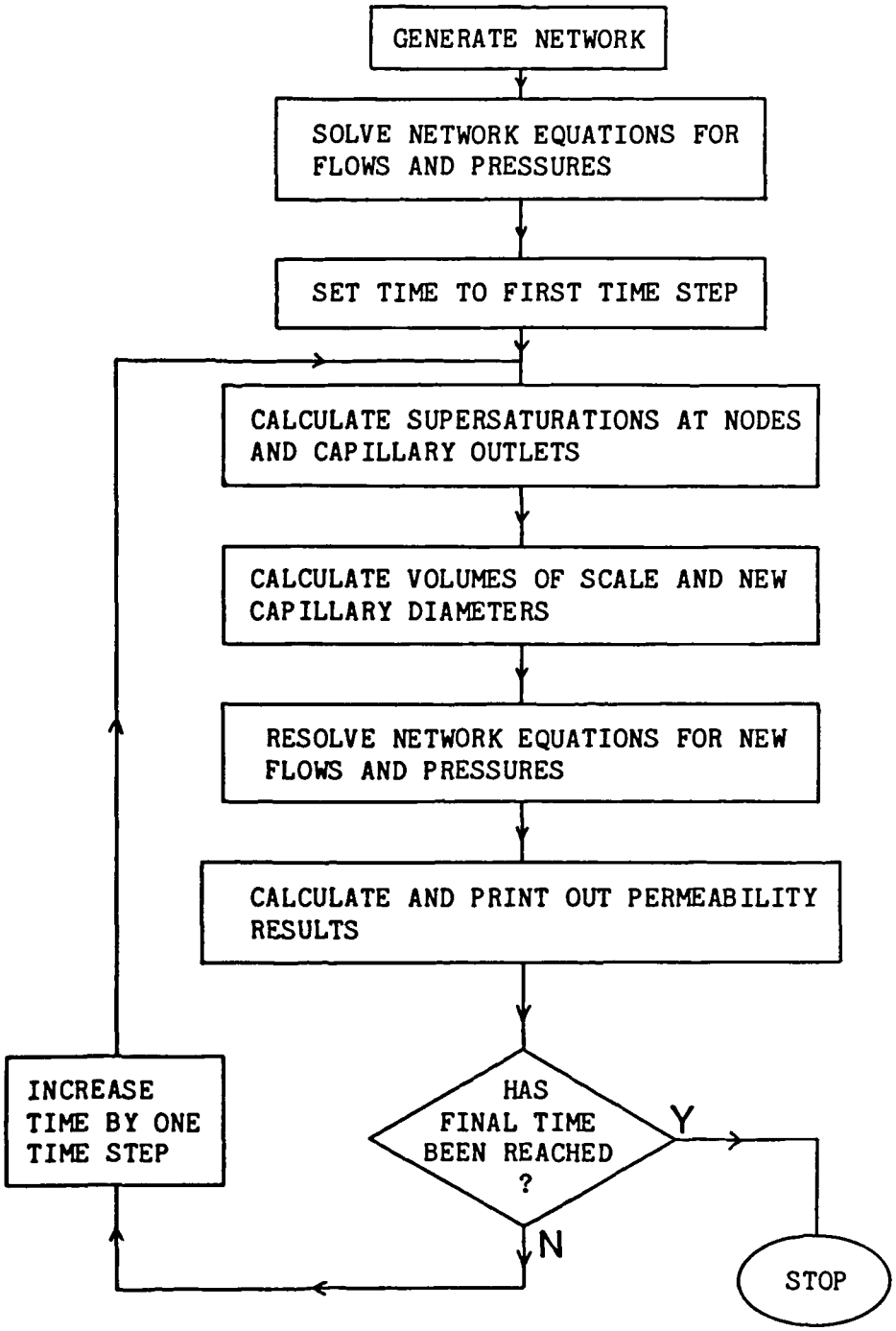

Figure 6.4 Flowchart for modelling the passage of time

6.4.

In this manner the model was able to adjust the flows within itself to suit the pattern of scale formation. As a capillary was reduced in size the flowrate through it should have decreased so reducing the volume of scale formed in that capillary in the future. This process was opposed by the lower flowrate leading to a longer passage time through the capillary, which would create an increase in the drop in supersaturation across the capillary.

As mentioned above, when the time periods between reassessing the flow patterns in the network were long, adjustments to flows to compensate for the formation of scale took place less often. This could lead to overlarge volumes of scale being calculated for capillaries and a consequent increase in the amount of scale "lost" to the model. Running the model, therefore, was a process of optimising between long time steps leading to larger amounts of scale being "lost" and more frequent solution of the network flow equations requiring greater use of computer time to simulate a given real time.

6.2.5 Data Required and Data Produced by the Model

Data required to run the model

Physical data of relevance to the precipitation reaction was supplied to the model in its input data. Many of the options built into the model, that controlled its pattern of behaviour, could be selected by setting the values of control variables for these options in the input data to the programme. These options and their use is described in appendix A6.2. This subsection only considers factors relevant to the precipitation reaction.

For calculating the supersaturation levels throughout the

network values for the precipitation reaction rate constant and the inlet supersaturation were required. The inlet supersaturation could either be specified directly or calculated from the compositions of the two brines involved using the solubility prediction model. For the purposes of the model the brines were considered to be perfectly mixed, in whatever proportions were chosen, prior to entering the network. Thus, the whole inlet face of the network had the same level of supersaturation.

The flowrate through the model was calculated by first specifying the pressure drop over the first section of the model. The first solution of the network flow equations was performed with a constant pressure drop boundary condition using the supplied pressure drop. The results of this first solution provided the individual flowrates of all the capillaries, from which, the overall flowrate through the network was calculated.

The length of the time periods between successive assessments of the flows in the network was set in the input data and was used in the calculation of the quantity of scale formed in each capillary. The distribution of this scale was controlled by weighting factors for each section of the capillary, which were also supplied in the input data to the programme.

Data produced by the model

The model could produce data on almost every aspect of what was happening within it. For general purposes most of this was not required, so the data available was split into several levels of data of successively greater detail. The choice of level of data provided was controlled by an option set in the input data. Details of what was available at each level are given in appendix A6.2.

Outside this structure the model produced a basic level of

information. The permeabilities and pressure drops for each section of the model were reported for each time step, as were the quantities of scale deposited and "lost". Messages were printed if any capillaries were closed. Optionally, the model would print a table of pore size frequencies and simulated mercury saturation values for each section of the model and for the simulated core as a whole.

6.3 RESULTS OF SIMULATION WITH THE MODEL

6.3.1 Introduction

Section 6.2 completed the description of the workings of the model that was begun in chapter 3, where the model's development was discussed. This section describes how the model responded to changes in the criteria it was supplied with and discusses how well this response simulated what happened in the experimental work.

The importance of permeability changes

The most important objective of the model was to satisfactorily simulate permeability changes as a result of scale deposition. Change in permeability is the factor that is most likely to affect the movement of groundwaters and hydrocarbon liquids around a wellbore in a natural sandstone formation. The sensitivity and simulation ability of the model was, therefore, assessed through its calculations of permeability. The factors considered in judging the model were the pattern of permeability damage, ie the shape of the permeability decline curve; the initial rate of permeability damage and the overall damage at the end of the simulation. All these were analagous to the techniques used for comparing results in the experimental work.

The time for the permeability decline curve to reach half its initial gradient (ie the characterisation time used for the experimental curves) was not a practical measure in the stepwise environment of the model. As this statistic was identified with approximately 50% permeability damage in the experimental work it could be approached from a different angle and expressed as the time for the

network to reach half its initial permeability.

Significance of porosity changes

Of lesser importance than the permeability changes, but still of great significance, is the quantity of scale that leads to the calculated permeabilty damage. The usefulness of scale quantity data as a tool for tuning and assessing the model was severely reduced by the poor quality of the experimental data in this area. Even so, a knowledge of how the scale was distributed throughout the model was a helpful measure of the efficacy of the damaging strategies applied in the model. The outlet supersaturations from the various sections of the model provided a similarly useful measure of the movement of scaling potential within the model.

Calculation of equivalent flowrate

In order to ease comparisons between the model and the experimental work and to overcome the problems associated with sizing the model (discussed in subsection 6.3.2), an equivalent flowrate was calculated for each model. This was the flowrate that would be supported by an experimental core with the same properties as and under similar conditions to the model core. The calculation of the equivalent flowrate was based on the assumption that one model would exhibit the same lengthwise properties as would many models side-by-side or one model of much larger cross section.

The calculation was made by first calculating a length for a real core, supporting a flowrate of 30cc/min, which had a pressure drop and permeability equivalent to the model. The flowrate of 30cc/min was then adjusted in the proportion of the actual length of the model to the length calculated for a 30cc/min flowrate.

Factors controlling the model

The factors that might be used to control the response of the model could be split into three main groups:

i) Factors affecting the set-up and control of the porous media model. These were the overall dimensions of the model, the pore size distribution curve used in generating the network, the porosity given to correspond with this distribution and, to a lesser extent, which of the options on passage of fluids between sections of the model was adopted.

ii) Factors affecting the quantity of scale formed. The largest factors here were expected to be the supersaturation and the length of the time steps. The magnitude of the reaction rate constant and the way in which the surface area term for each capillary was evaluated could also have major influences as would the flowrate through the network.

iii) Factors affecting the distribution of scale. At the time of writing the only control in this area was through the weighting factors for each section of the capillaries.

The factors above were split into groups according to the areas in which they had most influence. This does not mean that their influence was restricted to the group in which they were placed. In such a complex model it was difficult to isolate any factor to only affecting one of the areas mentioned above. For example, almost any change to the model would have some influence on the distribution of scale throughout the model as a whole which could accumulate over several time steps into noticable shifts in the pattern of permeability

damage.

In the rest of this section each of the main groups of factors mentioned above is discussed in terms of how the model responded to changes in the control factors and how well the model could be expected to simulate the effects deduced from the experimental results.

6.3.2 Factors Affecting the Porous Media Model

Sizing the model

The level of damage caused by scale growth in a porous medium due to the mixing of incompatible brines was largely dependant on the distance from the point of mixing. In the model the mixing point of the brines was assumed to be at the front face of the network. To maximise the study of the effect of distance from the point of mixing it was therefore desirable to have a long network. Within the restrictions of computer capacity, extending the length of the network could only be achieved at the expense of cutting down on the cross-sectional area. However, provided sufficient cross-sectional area was available to satisfy the simulation of cross-mixing, cutting down the cross-sectional area was not expected to cause any problems.

In order to judge what was the minimum cross-sectional area required for the satisfactory simulation of cross-mixing, a series of models were run with gradually increasing cross-sectional area and constant length. The results of these tests are shown in table 7, which gives a range of parameters that may be used to compare the results of the models. The relevance of the dimensions of the network to the number of capillaries used is explained in appendix A6.1.

The initial permeability in the tests detailed in table 7 can

Table 7. Results of changing the cross-sectional area of the network model for an inlet supersaturation of 20

MODEL SIZE (L,B,H)		13,15,15	13,17,17	13,21,21	13,23,23	13,25,25	13,29,29	13,33,33
PERMEA-BILITY (mD)	INITIAL	580	653	643	612	586	613	596
	AFTER 10 MINS SCALING	530	596	587	561	538	563	-
	AFTER 20 MINS SCALING	485	546	537	516	495	519	-
POROSITY (%)	INITIAL	0.223	0.223	0.222	0.222	0.223	0.223	0.223
PRESSURE DROP ACROSS MODEL (PSI)	INITIAL	0.294	0.294	0.294	0.294	0.294	0.294	0.294
	AFTER 10 MINS SCALING	0.322	0.322	0.322	0.320	0.320	0.320	-
	AFTER 20 MINS SCALING	0.352	0.351	0.352	0.349	0.348	0.348	-
SUPER-SATURATION AT OUTLET	AFTER 10 MINS SCALING	18.946	19.139	19.002	19.059	18.923	19.005	19.059
	AFTER 20 MINS SCALING	19.025	19.202	19.054	19.171	19.024	19.086	19.171

be seen to have varied by up to 11% as the cross-sectional area of the model was altered. This was mainly due to the manner in which porosity matching of the network was performed. In order to make the network porosity equivalent to an experimental porosity the capillary length was adjusted as described in section 3.3.4. As all the models used in the tests in table 7 were adjusted for porosity to different extents their physical cross-sectional areas were no longer comparable in the way the coordinate dimensions suggested that they should be. As the physical cross-sectional area was used in the calculation of permeability, differences were bound to arise.

Instead of permeability, the pressure drop across the network was used as a more reliable means of comparing what the effective permeability of the model was, independant of the cross-sectional area. There was very little difference to be seen in these pressure drops for any of the models in table 7. The same similarity could also be seen in the outlet supersaturation figures supporting a view that, as far as the pattern of scaling was concerned, any model of size greater than 15×15 in cross-section would produce similar results. Thus, a cross-section of 17×17 was chosen for use in all further work with this model.

For the rest of the models described in this chapter a section length of 27 was used with either three or five sections being used to make up the model core. Depending on the adjustments made by the porosity matching technique, for the models mentioned in this chapter a 27×17×17 network could have physical dimensions between 3.16 × 1.58 × 1.58mm and 1.44 × 0.72 × 0.72mm, with the overall length of the model being three or five times the individual network section lengths. This was clearly still very small in comparison to an experimental core. At best the length of the model was only that of the first section of the experimental cores. The matter of the physical size of the model and how it could be extended will be discussed later.

Pore size distributions

Pore size distributions, in the form of experimental capillary pressure curves from mercury penetration porosimetry, were supplied to the model to enable it to simulate the pore structure of a particular specimen of rock. As described in subsection 3.3.4, after using the pore size distribution to assign sizes to all the capillaries in the network, the model adjusted the dimensions of the network so that its porosity matched the experimental porosity of the original rock specimen. However, as described below, small errors in the porosity and slight changes in the pore size distributions could significantly affect the resultant permeability of the model.

Using a pore size distribution for Clashach block 22, which was used in many of the experiments, and an average porosity of 22.3%, the model predicted a permeability of 1.86 Darcies, which only occurred in a few core samples and then, only in one section of the core. To obtain the more normal permeability level for Clashach 22 of 500-600mD, a porosity of 6.8% was used. This demonstrated a marked sensitivity of the network model to porosity changes.

The effect of slight changes in the pore size distribution can be seen table 8. Each of the three models in table 8 consisted of more than one network section. Successive sections of the same model were generated from the same pore size distribution, but using a different set of randomly generated pore sizes. The differences between the distributions for the different network sections was only very slight yet the difference between the initial permeabilities could be as much as 10%. Figures 6.5 to 6.7 show simulated mercury penetration porosimetry curves for the three network sections of the Clashach 22i model shown in table 8. The calculated initial permeabilities of these three sections were 601, 585 and 581mD respectively. Comparing the curves there were very slight differences to be seen at the large pore

Table 8. Results showing effect of changing the model's pore size distribution

PORE SIZE DISTRIBUTION		CLASHACH 7	CLASHACH 22i	CLASHACH 22ii
EQUIVALENT FLOWRATE (cc/min)		51.9	11.5	47.7
CROSS-SECTIONAL AREA (mm^2)		0.72	1.58	0.75
PERMEABILITIES (mD) Initial above final	OVERALL	903 263	585 146	1152 298
	SECTION 1	901 161	601 39	1167 140
	SECTION 2	898 323	585 385	1136 320
	SECTION 3	909 474	581 519	1153 577
INITIAL DAMAGE RATES (mD/min)	SECTION 1	12.3	11.0	19.8
	SECTION 2	7.1	0.7	9.7
	SECTION 3	4.1	0.4	5.5
TIME TO HALVE INITIAL PERMEABILITY (mins)	OVERALL	61.2	59.0	57.2
	SECTION 1	42.7	26.4	37.0
	SECTION 2	72.1	-	70.1
	SECTION 3	-	-	-

Figure 6.5 Simulated capillary pressure curve for model based on Clashach 221 pore size distribution

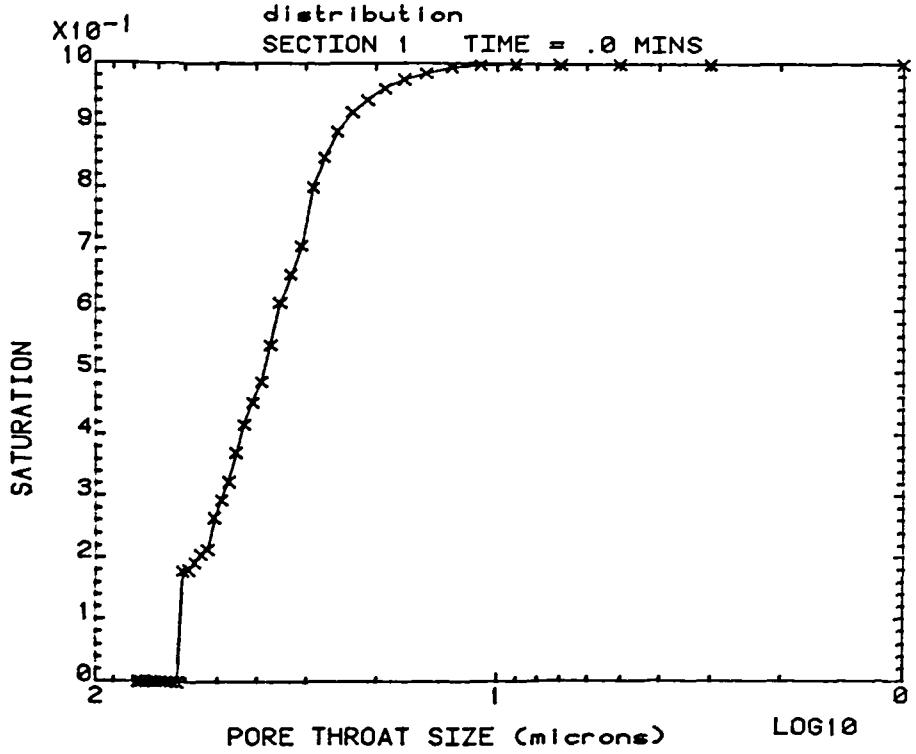

Figure 6.6 Simulated capillary pressure curve for model based on Clashach 221 pore size distribution

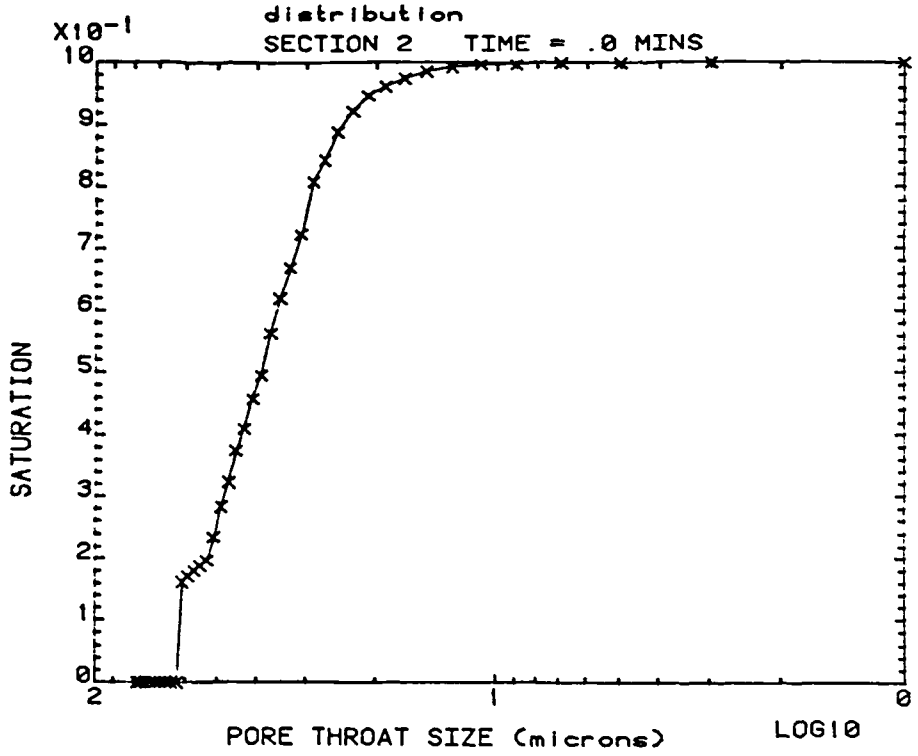

Figure 6.7 Simulated capillary pressure curve for model based on Cashach 221 pore size distribution

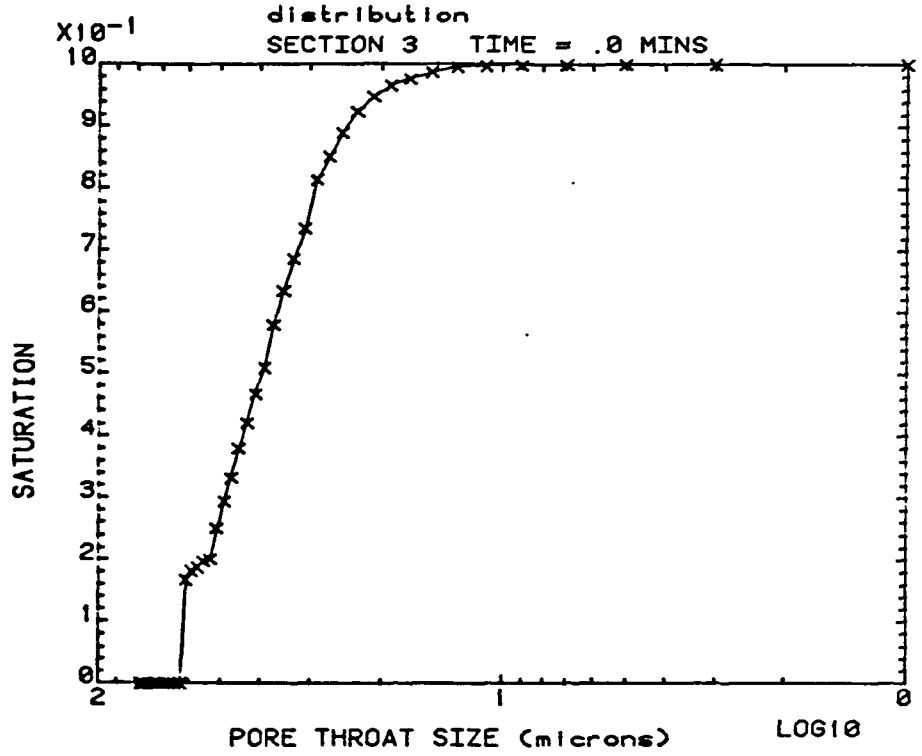

throat size end demonstrating that at the dimensions of 27×17×17 the model was still sensitive to a slight increase in the number of large pores in the network.

Clearly the setting up of the network model to exactly simulate a given sandstone required great care involving the manipulation of parameters not discussed in the brief description of the model presented in this work. It was not part of this project to investigate and develop the network model's ability to simulate porous sandstones. Further information may be found in the work of other authors[11,16].

The change in the permeability of models, generated using different pore size distributions, due to scale formation was of interest to this work. Table 8 shows results from three models that differed in their initial set-up, leading to different initial permeabilities. It can be seen from the initial rates of damage, given in table 8, that higher initial permeabilities lead to higher rates of damage. Also with higher initial permeabilities, higher rates of damage persisted further into the model core.

This relation of damage pattern to initial permeability compared favourably with the experimental results, most notably one experiment performed with brine system H at low flowrate (C267.57.5HH-1). The damage rates for this experiment, given in table 3, show that there were comparatively high damage rates in the first two sections for the level of supersaturation (about 19) and that higher levels of damage continued into section 3, which had a higher initial damage rate than the same section in comparable experiments.

Intersection mixing option

The intersection mixing option, described in appendix A6.2, allowed the flows of brine leaving one network section of the model to

be either passed directly to equivalent inlet nodes on the next section or to be mixed to provide a uniform level of supersaturation for entry to the next section. Obviously the former of these options was the most realistic.

Table 9 shows that direct linking of outlet and inlet nodes resulted in a slight lessening of damage to all sections after the first section when compared to the results of using mixing between sections. This suggested that sizable differences in supersaturation level were generated across the network in the passage through a single section. It was not possible to tell from the experimental work whether such a degree of supersaturation variability across the cross-section of the network was representative of what occurred in a real sandstone flooding situation.

Although in microscopic terms the direct linking of exit and entry nodes between sections was probably the most realistic, the intersection mixing option provided the facility to reduce the supersaturation variability across the cross-section if a greater degree of cross-mixing was expected than the model appeared to have been providing. This option may go some way towards compensating for the reduced cross-mixing in the model because of its small cross-sectional area in comparison to an experimental core.

Summary

The size of the cross-sectional area of the model appeared to have little effect on the prediction of permeability above a grid size of 15 × 15. The maximum coordinates used for the models in this work were therefore set to 27 × 17 × 17 (length, breadth, height). The physical size of the model was very small in comparison to the experimental cores.

The model's calculations of permeability were very sensitive

Table 9. Results of using different intersection mixing options

		NO MIXING BETWEEN SECTIONS	INTERSECTION MIXING OPTION USED
PERMEABILITIES (mD) Initial above final	OVERALL	585 147	585 146
	SECTION 1	601 39	601 39
	SECTION 2	585 400	585 385
	SECTION 3	581 529	581 519
INITIAL DAMAGE RATE (mD/min)	SECTION 1	11.0	11.0
	SECTION 2	0.6	0.7
	SECTION 3	0.3	0.4
TIME TO HALVE INITIAL PERMEABILITY (mins)	OVERALL	59.2	59.0
	SECTION 1	26.4	26.4
	SECTION 2	-	-
	SECTION 3	-	-
QUANTITY OF SCALE FORMED ($10^6 \mu m^3$)	SECTION 1	262	262
	SECTION 2	83.6	89.0
	SECTION 3	26.1	31.2

to slight changes in the pore size distribution and porosity used to generate the model. The effect of different initial permeabilities on the pattern of permeability damage was well modelled, with higher initial permeabilities leading to higher initial damage rates.

6.3.3 Factors Affecting the Quantity of Scale Formed

In subsection 6.3.1 there were five factors considered likely to directly influence the amount of scale formed at any particular location in the network. These were not the only factors that could affect how much scale was deposited. Through the complexities of the model the effect other changes made to the model had on the flow patterns within the model could also result in shifts in the pattern of scale deposition.

Length of time steps

For the self-integrity of the model it was important that similar results should be arrived at, from the point of view of permeability change, for the same period of simulated time even though the time steps used to reach that time were of differing lengths. It was not expected that an exact comparison would result, since, as described in subsection 6.2.4, depositing scale in larger batches would cause the flows through the network to be modified in a different manner to when smaller batches were deposited. Also, large batches of scale were more likely to result in scale being "lost" to the model through overfilling of capillaries. This increase in "lost" scale could exaggerate the other differences occurring due to longer time steps being used.

A series of tests was performed with the model to examine what

differences might result from differing lengths of time periods between reassessing flows in the model. Some results of these tests of particular interest are presented in table 10. In this case the initial damage rates of the first three sections were the most useful in making the comparisons.

As the length of the time steps was increased the pores that contributed most to the permeability and hence had the highest flowrates, were more and more severely damaged. Thus, the initial damage rates for the first section increased as the length of time step was increased. A time step of 30 minutes appeared to represent a limit in this process as the initial damage rate, given in table 10, for a time step of 40 minutes dropped to a level close to that for 20 minute time steps. After the 30 minute time step limit it was likely that the secondary factor of scale "loss" had started to take effect resulting in less damage per minute than might have been expected.

In figure 6.8 the permeability decline curves for the first section of each of the four models run for this time step study have been plotted. This figure shows the effects of different time steps over longer periods of simulated time. When all the models had had several chances to adjust their flows, the magnitudes of the permeabilities were not too dissimilar, but the relative differences in permeability were considerable.

The damage pattern for sections 2 and 3 of the models in table 10 showed a similar trend to the pattern for section 1, but with a much smaller effect from changing the length of the time step. This was probably due to there being less scale deposited in these sections.

Obviously the models with shorter time steps must be considered to be more accurate as they were closer to the ideal of flows being continuously adjusted for scale deposition. In order to maintain the degree of time resolution in the model, when factors such as flowrate and supersaturation, which affect the quantity of scale

Table 10. Results of using different lengths of time steps

TIME STEP LENGTH (mins)		10	20	30	40
INITIAL DAMAGE RATE (mD/min)	SECTION 1	11.0	14.1	15.8	14.2
	SECTION 2	0.7	1.2	1.2	1.3
	SECTION 3	0.4	0.5	0.4	0.5
TIME TO HALVE INITIAL PERMEABILITY (mins)	OVERALL	59.0	52.4	37.1	26.1
	SECTION 1	26.4	22.3	19.0	21.2
	SECTION 2	-	143	150	207
	SECTION 3	-	-	-	-
QUANTITY OF SCALE FORMED ($10^6 \mu m^3$)	SECTION 1	262	348	379	381
	SECTION 2	89.0	182	219	223
	SECTION 3	31.2	80.1	110	125

Figure 6.8 Permeability decline curves for section 1 of model showing effect of changing time steps

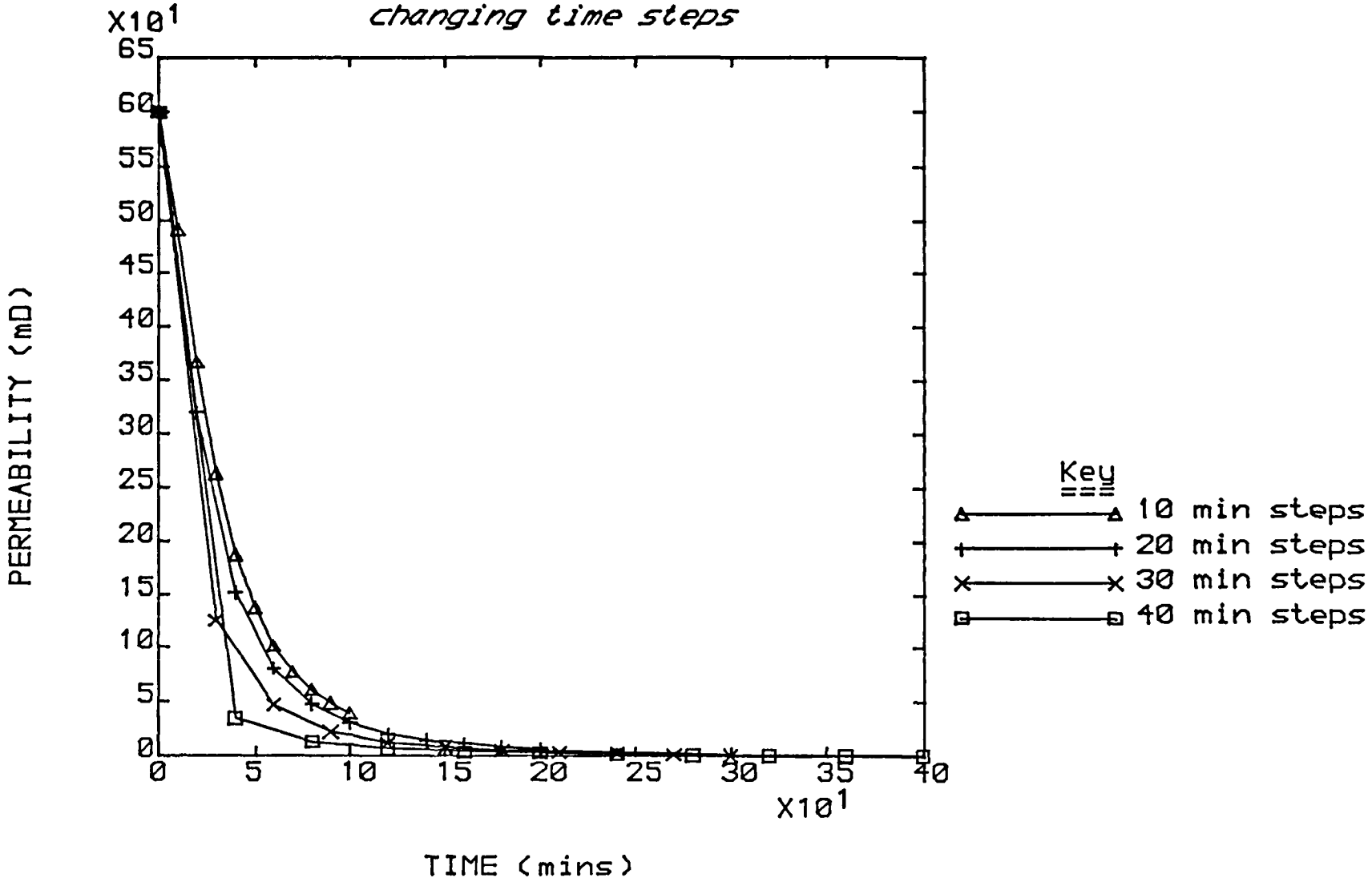

being deposited, are adjusted, the length of time step should be adjusted to suit.

Supersaturation

Changing the initial supersaturation of the brine in the model could also lead to larger volumes of scale being deposited and so could increase the chances of scale being "lost". Consequently, higher supersaturation models should be run with shorter time steps. The effect of different initial supersaturations on the permeability changes in the model is shown in table 11. This table gives the results for four supersaturations roughly equivalent to those used in the experimental work. The permeability decline curves for the first three sections of the models in table 11 are presented in figures 6.9 to 6.12.

As was expected, increasing the supersaturation increased the damage to the permeability of the network. An anomaly was observed in table 11 for the final permeabilities after 100 minutes for sections 2 and 3 of the model run with an initial supersaturation of 70. These final permeabilities were higher than the equivalent values when the initial supersaturation was only 35. These differences were thought to be due to the severe damage that had occurred in the first section of the model with an initial supersaturation of 70, which took the model beyond the bounds of its ability to sensibly simulate the scaling process. The figures for the initial damage rate and time to reach 50% of initial permeability in table 11 show the trends more reliably.

The initial rates of damage and consequently the time for the permeability to fall to 50% of its initial value showed a trend in keeping with the rate of precipitation being dependant upon the square of the supersaturation, the relationship upon which the model was based. Unfortunately, the relationship between the times to 50% damage

Table 11. Results of changing inlet supersaturation to model

INITIAL SUPERSATURATION		10	20	35	70
PERMEABILITIES (mD) Initial above final	OVERALL	903 674	903 263	903 41	903 1
	SECTION 1	901 596	901 161	901 19	901 0
	SECTION 2	898 684	898 323	898 71	898 75
	SECTION 3	909 763	909 474	909 186	909 218
INITIAL DAMAGE RATE (mD/min)	SECTION 1	2.2	12.3	35.3	88.6
	SECTION 2	2.5	7.1	15.3	32.5
	SECTION 3	1.7	4.1	7.3	15.1
TIME TO HALVE INITIAL PERMEABILITY (mins)	OVERALL	-	61.2	21.4	5.2
	SECTION 1	-	42.7	14.1	5.1
	SECTION 2	-	72.1	28.5	15.7
	SECTION 3	-	-	47.2	40.6
QUANTITY OF SCALE FORMED ($10^6 \mu m^3$)	SECTION 1	25.1	67.3	96.5	116
	SECTION 2	16.6	48.7	82.5	80.3
	SECTION 3	11.5	36.0	65.8	62.1

Figure 6.9 Permeability decline curves for model with initial supersaturation of 10

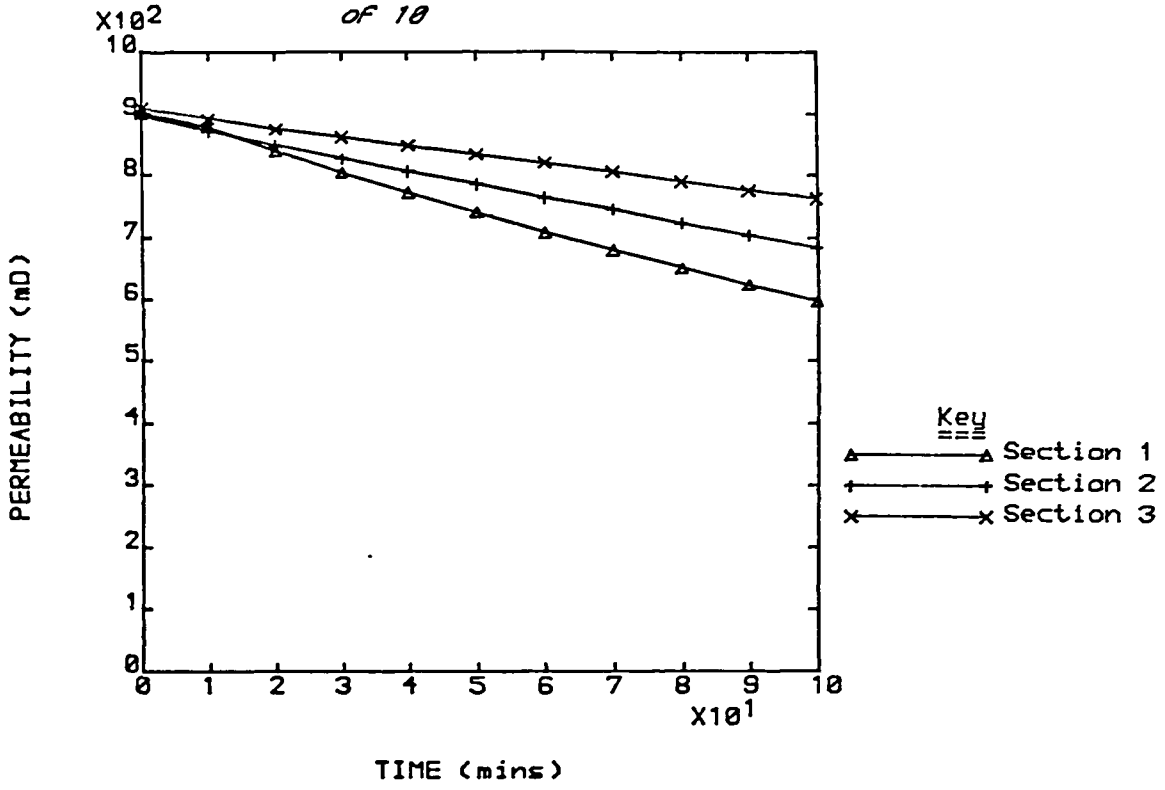

Figure 6.10 Permeability decline curves for model with initial supersaturation of 20

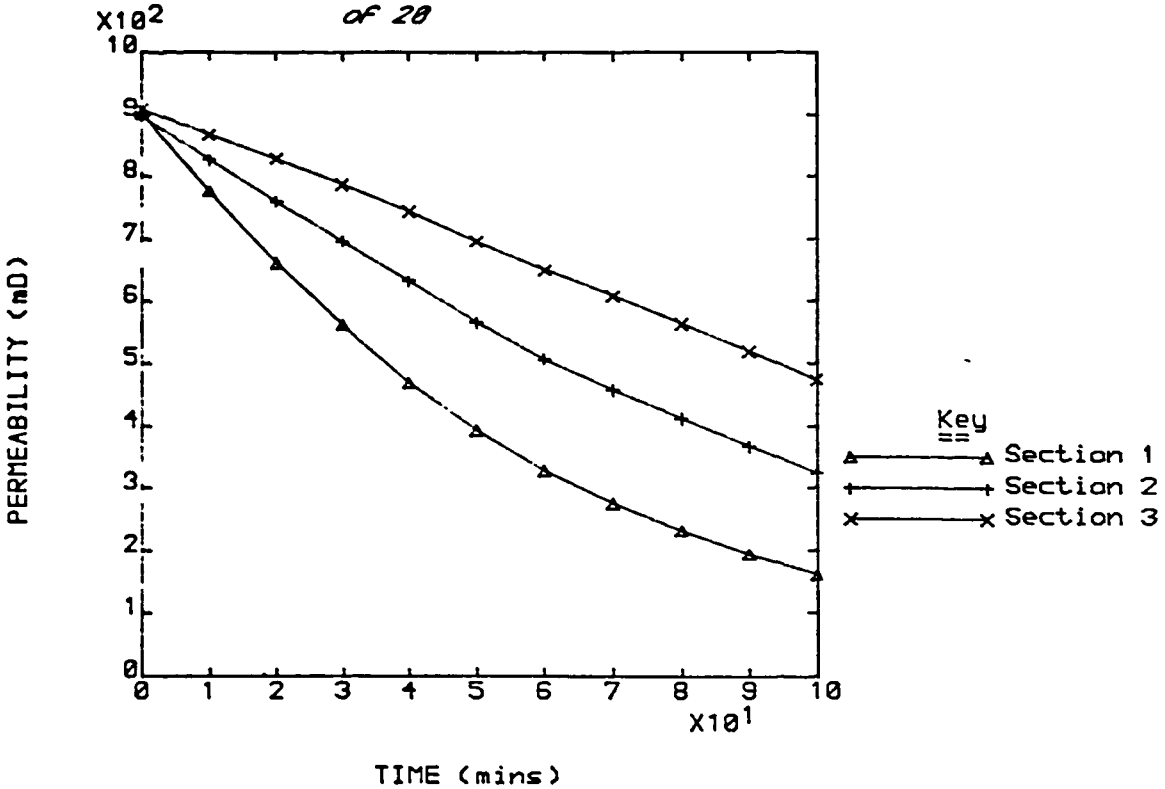

Figure 6.11 Permeability decline curves for model with initial supersaturation of 35

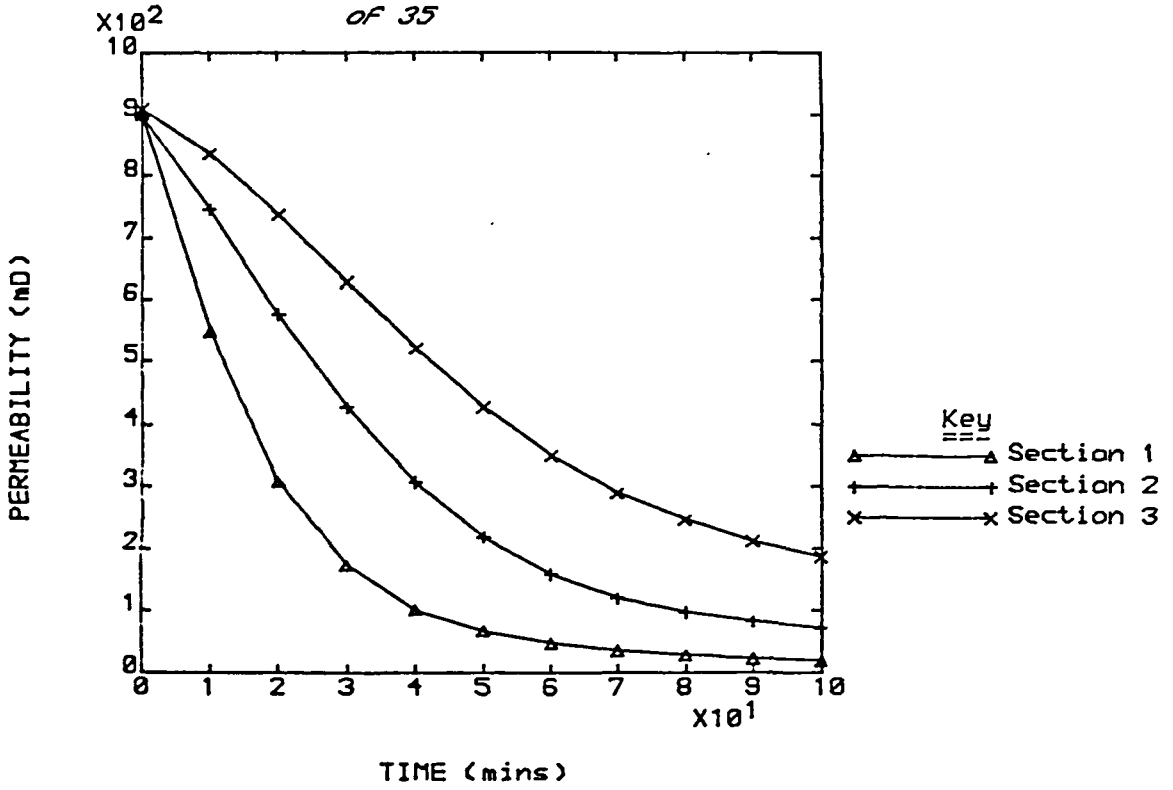

Figure 6.12 Permeability decline curves for model with initial supersaturation of 70

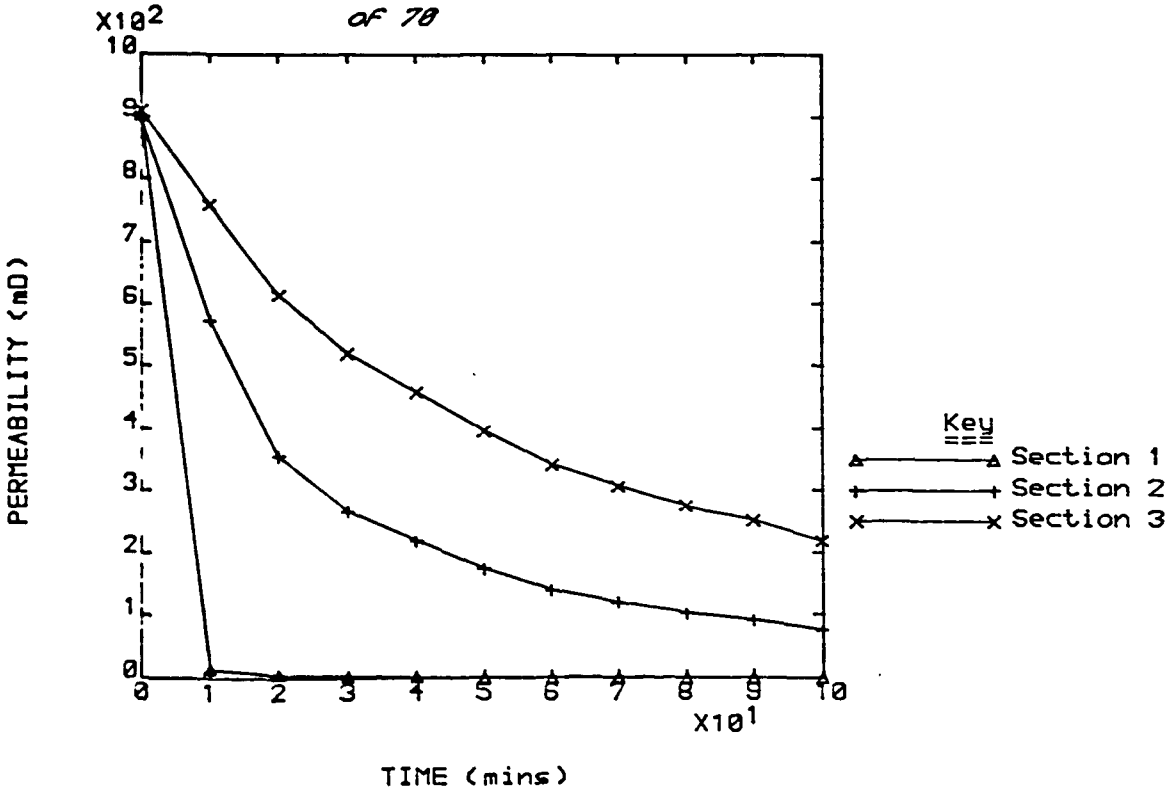

did not compare well with the relationship between the equivalent measures for the experimental cores. The equivalent flowrates for the models in table 11 were over 70% higher than for any of the experiments with real cores. Even so, the times to reach 50% of initial permeability were all much higher than the times for their experimental counterparts, shown in table 3, even taking section 2 of the experimental cores into account. The time to halve initial permeability for the model with initial supersaturation 70 would have been a reasonable match if it were not for the large equivalent flowrate.

These results suggested that the model was not performing well. However, the models in table 11 were only run as sensitivity tests and no attempt was made to ring the changes in the rest of the model to try to achieve a match.

Reaction rate constant and surface area term

The reaction rate constant, k, and the surface area for precipitation term, s, were linked to each other through the equation for supersaturation change across a capillary, equation 3.19. Any change in either of these parameters would have had the same effect as an equivalent change in the other, as far as the model was concerned. Thus, any consequences of adjusting the values of these parameters could be investigated simultaneously.

$$\frac{1}{S_f} - \frac{1}{S_b} = \frac{k\ s\ \Delta t}{[C]_o} \qquad \ldots\ldots (3.19)$$

where: S_b = supersaturation at beginning of time period

S_f = supersaturation at end of time period

Δt = length of time period

Figure 6.13 shows the change in permeability for each section of the model for a model with 10 minute time steps and distribution weightings of 5, 3, 4. It will be noticed that the first section suffered a far greater degree of damage than the other sections. A few tests were performed to investigate what effect the ks product might have on this pattern. It was expected that by reducing the ks product the quantity of scale formed in the first section could be reduced and so, deposited further along the model. Results of these tests, in the form of permeability decline curves, are given in figures 6.14 to 6.16 for models where the ks product was reduced by factors of 4, 8 and 20.

A reduction in precipitation in the first section of the model would leave a higher supersaturation, which should have lead to greater precipitation in later sections. However, figures 6.14 to 6.16 show that the influence of the ks product, which applied equally throughout the model, had a greater effect than the increased supersaturation and so reduced precipitation in the later sections also. Thus, the dispropotionately high precipitation in the first section remained more or less intact, though the magnitude of the permeability changes were reduced with the fall in the ks product.

In the experimental work, k and s were inseparable for the same reasons as they interact in the model. As described in section 5.8, there were very few experiments, for which a value for the ks product could be calculated. Thus, direct comparisons between the model and experiments on this account were inadvisable.

Flowrate

The results of changing the flowrate of the brine in the model are presented in table 12. For the models in table 12 the flowrate was progressively halved. The initial rates of damage for section 1 of each model showed what was almost a square relationship with the

Figure 6.13 Permeability decline curves for model based on Clashach 22i. ks product unchanged

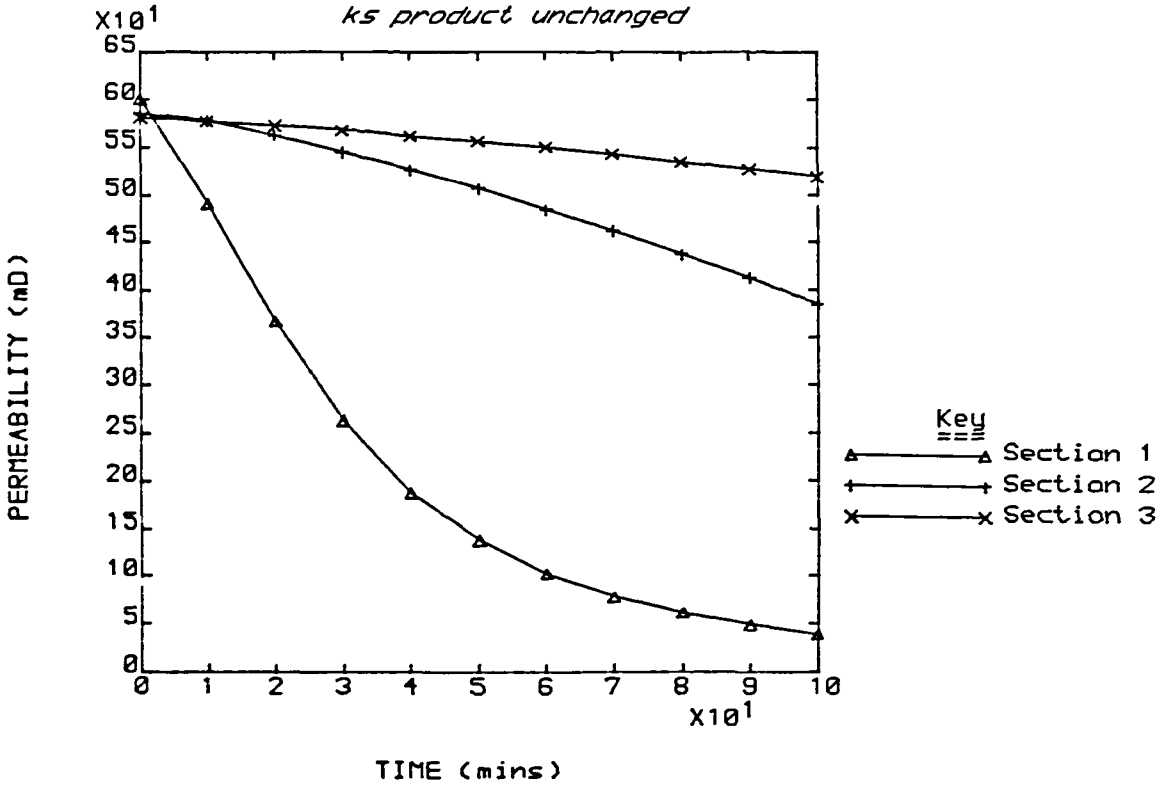

Figure 6.14 Permeability decline curves for model based on Clashach 22i. ks product divided by 4

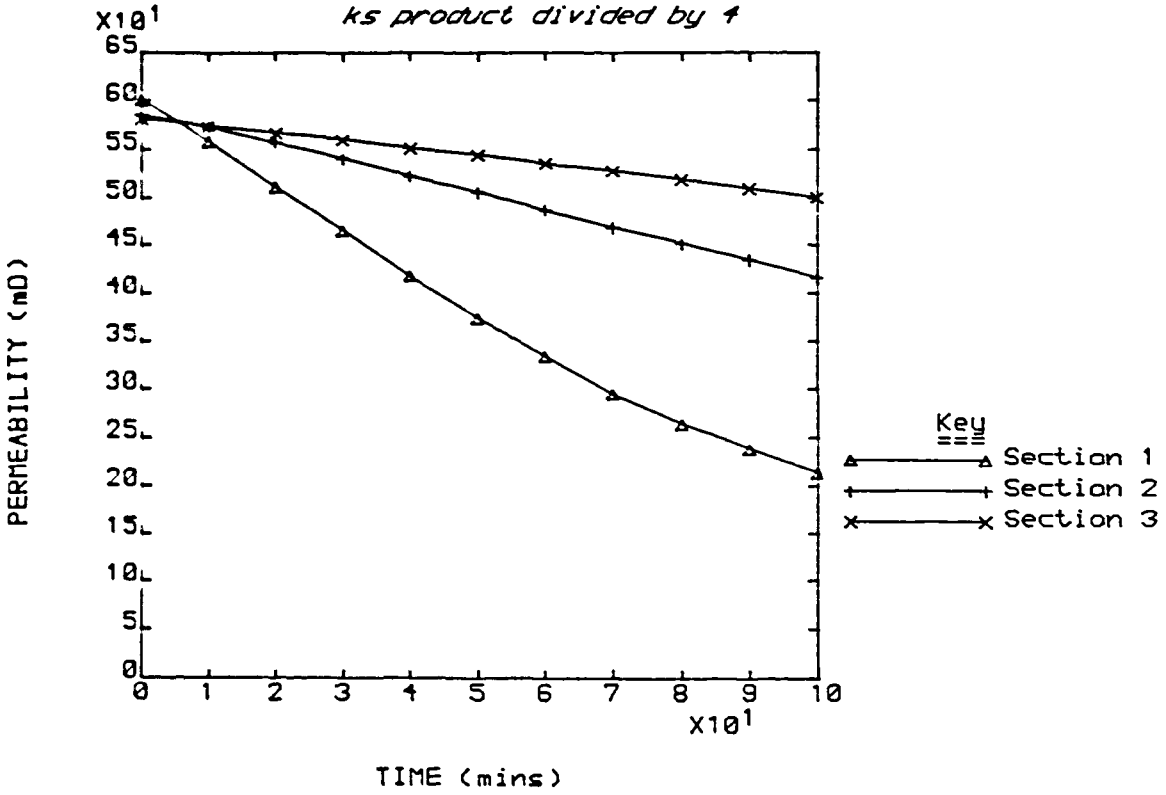

Figure 6.15 Permeability decline curves for model based on Clashach 22i. ks product divided by 8

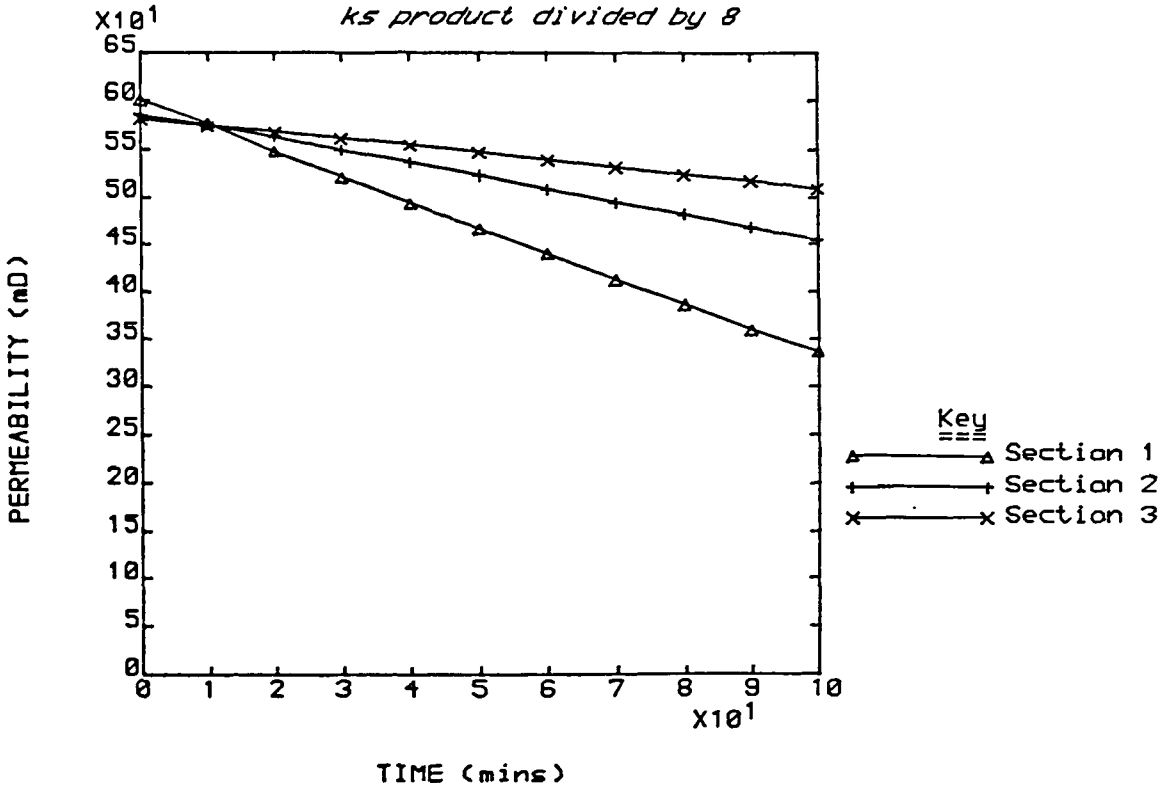

Figure 6.16 Permeability decline curves for model based on Clashach 22i. ks product divided by 20

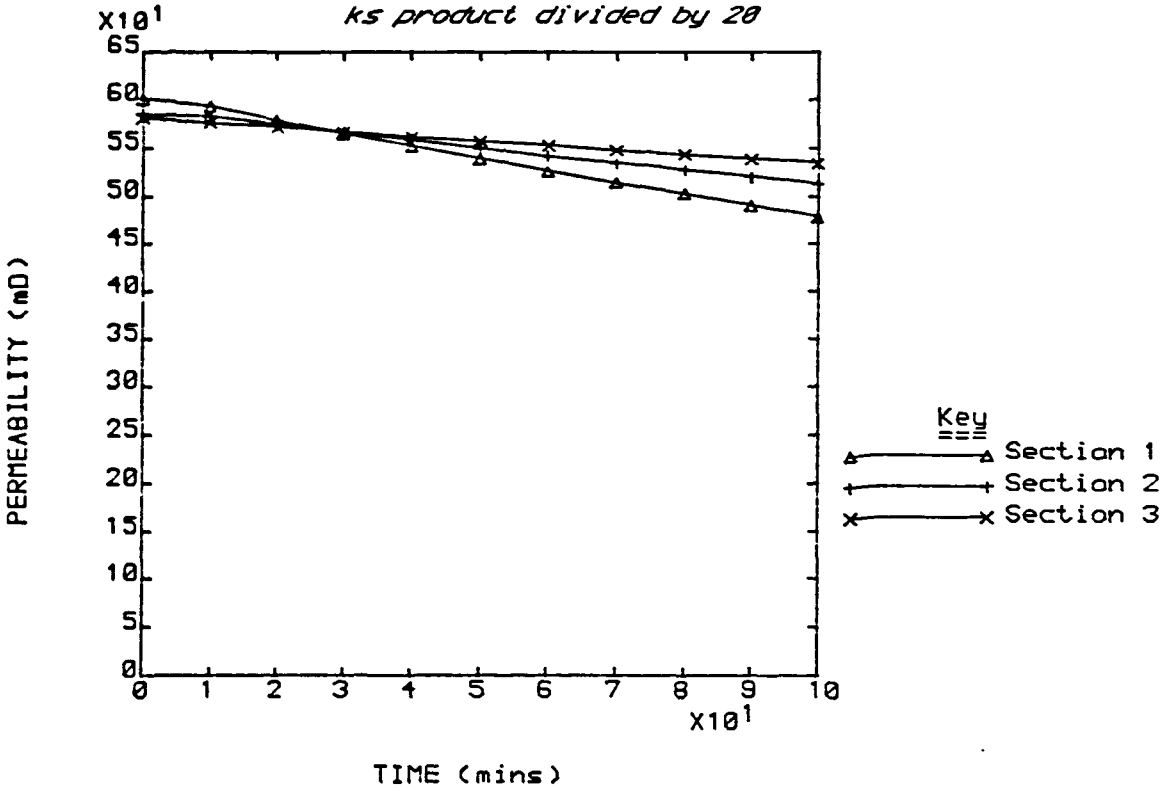

Table 12. Results of changing flowrate through model

EQUIVALENT FLOWRATE (cc/min)		51.9	26.2	13.1
PERMEABILITIES Initial above final	OVERALL	903 263	903 374	903 519
	SECTION 1	901 161	901 215	901 310
	SECTION 2	898 323	898 512	898 725
	SECTION 3	909 474	909 705	909 850
INITIAL DAMAGE RATE (mD/min)	SECTION 1	12.3	9.5	6.2
	SECTION 2	7.1	3.7	1.5
	SECTION 3	4.1	1.6	0.5
TIME TO HALVE INITIAL PERMEABILITY (mins)	OVERALL	61.2	83.4	-
	SECTION 1	42.7	52.1	69.2
	SECTION 2	72.1	-	-
	SECTION 3	-	-	-
QUANTITY OF SCALE FORMED ($10^6 \mu m^3$)	SECTION 1	67.3	56.5	40.6
	SECTION 2	48.7	29.7	12.2
	SECTION 3	36.0	15.5	4.4

flowrate, ie the flowrate had to be increased four times to achieve a doubling of the damage rate. This relationship did not apply to the other sections.

Table 12 shows that in section 1 of the model lowering the flowrate resulted in a larger supersaturation drop, which was probably caused by the longer residence time. This increase in precipitation counteracted, to some extent, the effect of the reduced flowrate. However, in successive sections the effect of the increased precipitation in section 1 was to reduce the supersaturation entering the later sections and so decrease the likely precipitation. Thus, later sections suffered a combined effect of lower precipitation and lower flowrate. As the reverse of this scenario was also true, it could be stated that for the model, high flowrates caused damage to penetrate deeper into the model whilst lower flowrates tended to concentrate the damage at the front face of the model. This view was reflected in the initial damage rates and quantities of scale formed given in table 12. The trend for damage to concentrate itself towards the front of the model is also evident in figures 6.17 to 6.19, which show the permeability decline curves for the first three sections of the models in table 12.

There was only one set of experiments which had sufficiently clear results for comparable experiments with different flowrates. These were the experiments performed with brine system E, which were run at three different flowrates. The results for these experiments, given in table 3, showed no sign of the damage being concentrated towards the front of the core as the flowrate was progressively lowered. These few experiments, then, did not support the model's predictions that damage at the front of the core would become relatively more significant as the flowrate was reduced. This lack of support may have been due to the point of mixing in the experimental cores not being so well defined as it was in the model. There were also

Figure 6.17 Permeability decline curves for model based on Clashach 7 with equivalent flowrate 51.9 cc/min

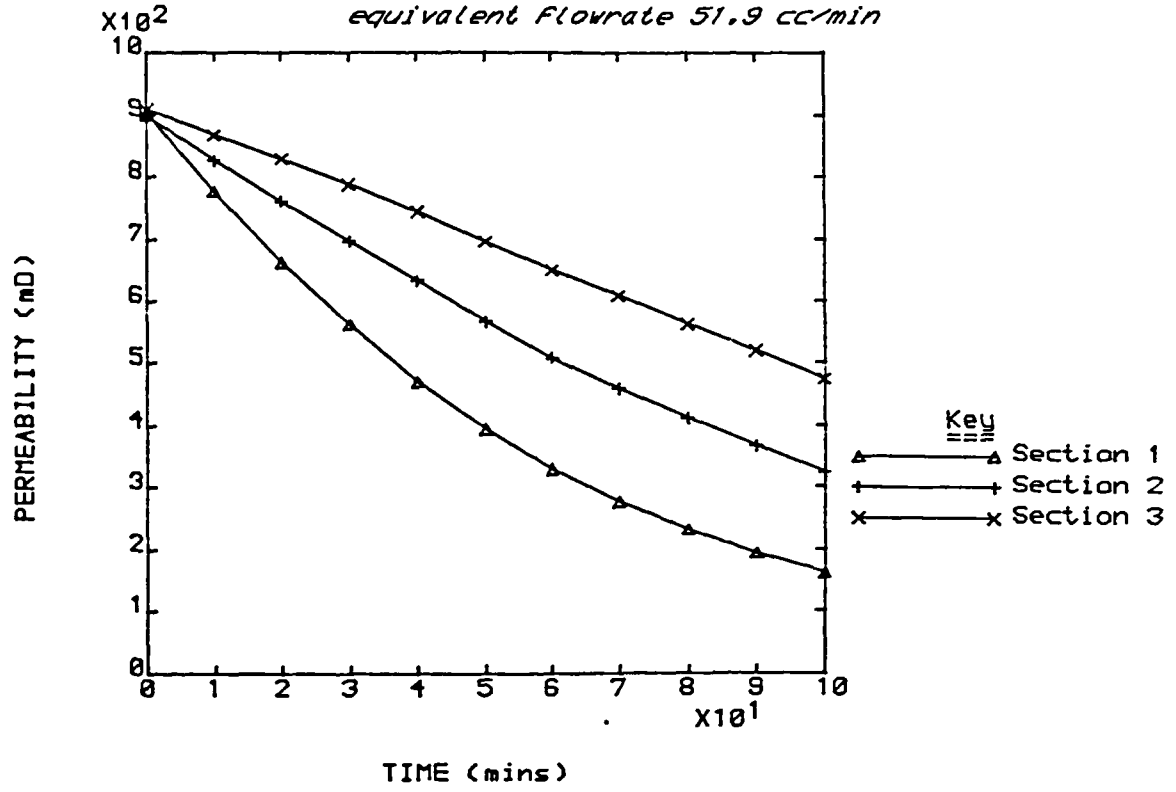

Figure 6.18 Permeability decline curves for model based on Clashach 7 with equivalent flowrate 26.2 cc/min

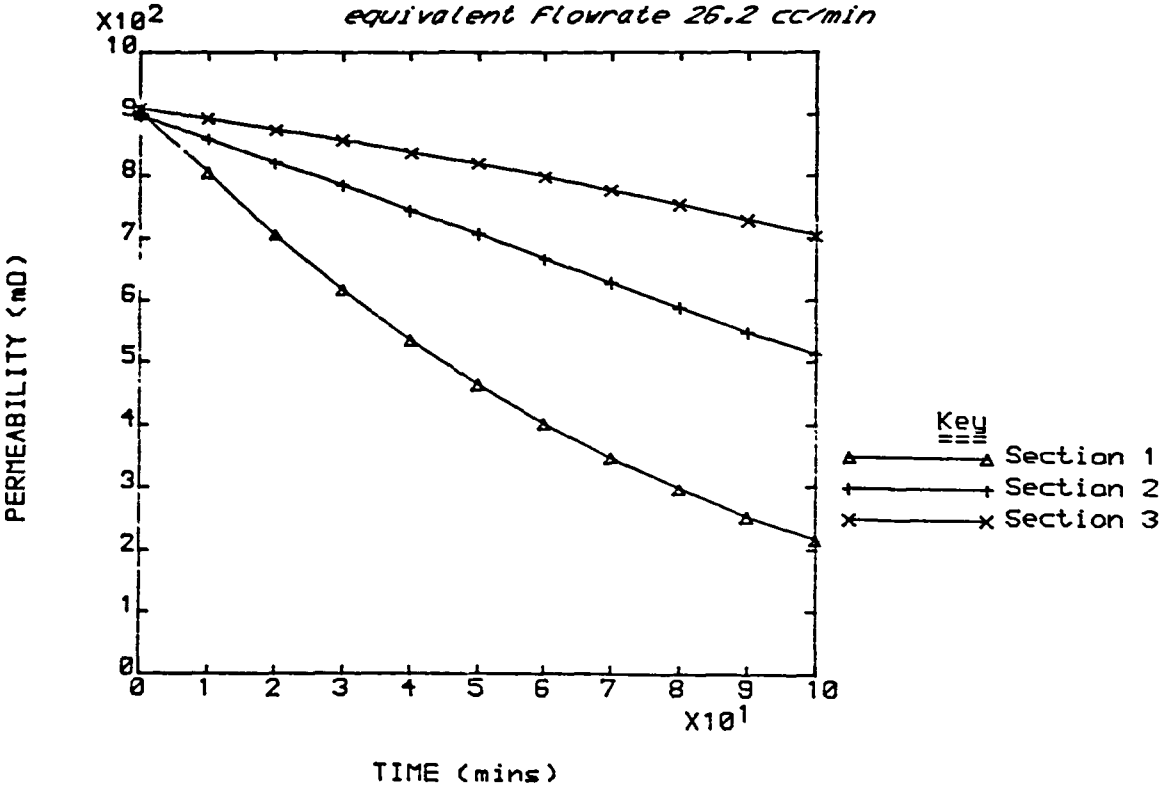

Figure 6.19 Permeability decline curves for model based on Clashach 7 with equivalent Flowrate 13.1 cc/min

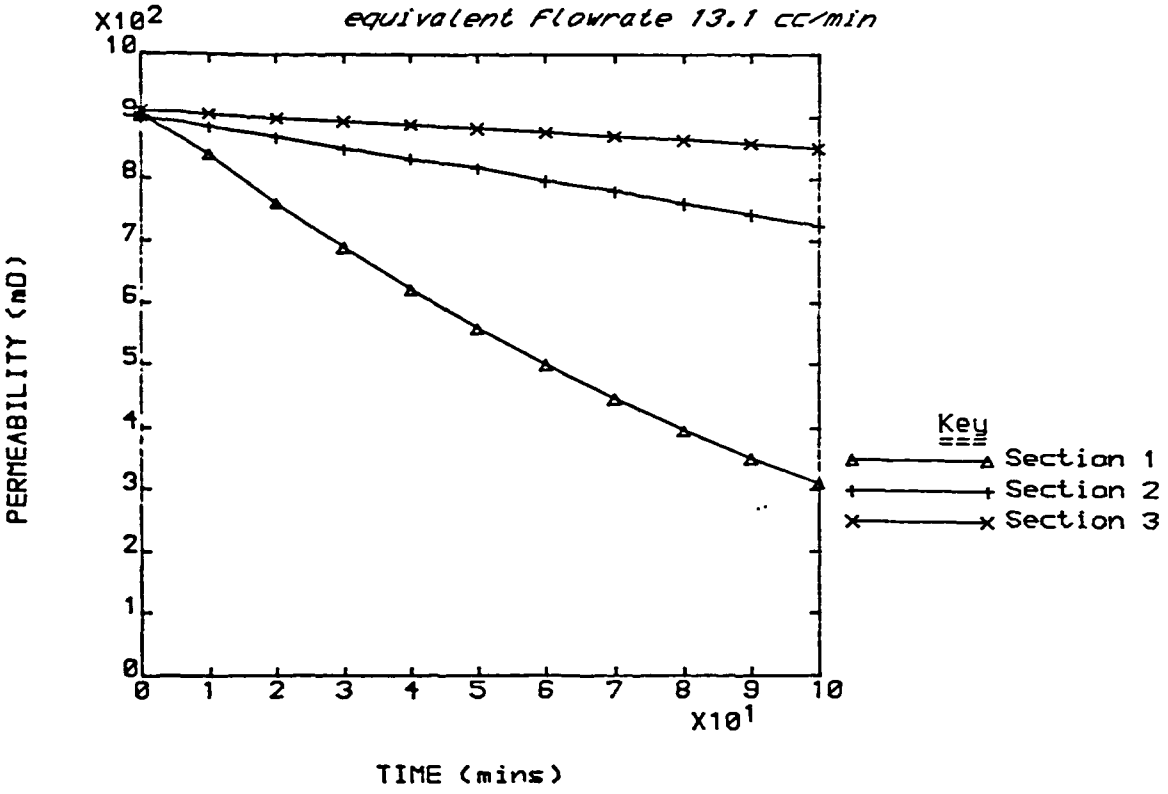

too few results to say whether the model's predictions of the change in magnitude of the damage for section 1 of the model, as flowrate changed, were reasonable.

Summary

The model was not overly sensitive to the length of time step used. However, it would be advisable to keep the time step as short as practically possible and to take it into account when changing such factors as the initial supersaturation and the flowrate of the brines.

For changes in initial supersaturation the model responded as expected with increasing permeability damage as the supersaturation increased. However, without other refinements to the model, experimental relationships between supersaturation and permeability damage were not well simulated. Permeability damage to the model appeared to be roughly proportional with changes in the ks product.

The model predicted that flowrate reduction would increase the localization of damage to the point of mixing. Insufficient experimental evidence was available to confirm or defeat this prediction.

6.3.4 Factors Affecting the Distribution of Scale Within the Capillaries

In the model used in this study there was only one means of adjusting the manner in which scale assigned to a capillary was distributed within that capillary, which was through the weighting factors for the three sections of the capillary. The weighting factors were used to calculate the fraction of scale allotted to the capillary that was presumed to be deposited in each capillary section according

to equations 3.27 and 3.28.

$$F_a = \frac{D_a l_a}{\Sigma D_a l_a} \qquad \ldots\ldots\ldots\ldots (3.27)$$

$$V_a = F_a V_s \qquad \ldots\ldots\ldots\ldots (3.28)$$

where: F_a = fraction of scale volume for whole pore assigned to section a

V_a = volume of scale assigned to section a

l_a = length of section a

D_a = weighting factor for section a

The three weighting factors applied to every capillary in the model and were intended to simulate the spread of scale between the wide bodies of pores and the narrow throats between pores. It was also hoped that they could compensate for the lack of any specific attempt to simulate crystal morphology in this model as described in subsection 3.4.3.

Assessment of the effect of the weighting factors through numerical data and permeability decline curves

To examine the sensitivity of the model to the weighting factors four cases were chosen: the two extreme cases; the centre case and the slightly off-centre case that was used for all the other models described in this chapter.

The extreme cases were when all the scale was deposited in the capillary throat and when all the scale was deposited in the capillary wide ends. The latter of these two could not be fully implimented as many of the capillaries did not have wide ends. Thus, a small possibility for scale to be deposited in the pore throat had to be

allowed to prevent large levels of "lost" scale. The values of the weighting factors in equation 3.27, in the order: entry wide end; throat; exit wide end, for the above two cases were 0, 1, 0 and 100, 0.1, 100 respectively. For the central case the weighting factors used were 1, 1, 1, which resulted in scale being deposited in each section of the capillary in proportion with the length of that section. All model tests thus far mentioned were run with weighting factors 5, 3, 4, which biased the scale deposition slightly towards the wide ends and to the inlet wide end more than the outlet wide end.

The results of testing the model with different distribution weightings are given in table 13. The results are presented in three groups, one for each of three pore size distributions that were supplied to the model. The initial rates of damage, final scale volumes and percentage permeability damage for three network sections are given for comparison purposes. In two cases, for various reasons, the model failed to complete its full set of ten 10 minute time steps.

In table 13 there are very few differences to note between the results for the central case (weightings 1, 1, 1) and those for the off centre case (weightings 5, 3, 4) in any of the three groups. The extreme case where all the scale was deposited in capillary throats (weightings 0, 1, 0), produced similar results to the two cases mentioned above in respect of the first section, but in the two later sections the level of damage and initial damage rate was higher than for any of the other cases. In the other extreme case, when the scale deposition was almost totally biased towards the wide ends (weightings 100, 0.1, 100), the initial damage caused to the network permeabilities was higher or equivalent to the other cases, but for much smaller volumes of scale being deposited, as demonstrated by the final scale volume figures in table 13.

Figures 6.20 to 6.23 show the permeability decline curves for the series of models based on a pore size distribution derived from

Table 13. Results of using different distribution weightings with three pore size distributions

PSD	WEIGHTING FACTORS	FINAL TIME (mins)	% PERMEABILITY DAMAGE AT FINAL TIME			INITIAL DAMAGE RATE (mD/min)			FINAL VOLUME OF SCALE DEPOSITED (10^6 μm^3)		
			SECTION			SECTION			SECTION		
			1	2	3	1	2	3	1	2	3
C221	5 , 3 , 4	100	94	34	11	11.0	0.7	0.4	262	89.0	31.2
	1 , 1 , 1	60	82	18	6	10.8	0.8	0.4	204	50.2	16.1
	0 , 1 , 0	100	94	59	11	10.9	0.8	0.4	266	95.1	32.9
	100,0.1,10	100	95	59	17	23.6	1.7	0.4	202	71.4	25.5
C2211	5 , 3 , 4	100	85	66	49	19.8	9.7	5.5	82.3	58.9	42.2
	1 , 1 , 1	100	87	68	50	20.4	9.8	5.3	81.2	58.6	41.5
	0 , 1 , 0	100	88	72	57	22.1	10.8	6.1	72.6	54.1	40.2
	100,0.1,10	90	89	35	13	21.3	8.5	3.8	45.5	22.1	12.9
C7	5 , 3 , 4	100	82	64	48	12.3	7.1	4.1	67.3	48.7	36.0
	1 , 1 , 1	100	84	65	48	12.7	7.3	4.2	65.4	47.0	34.6
	0 , 1 , 0	100	86	71	58	14.0	8.1	4.5	58.5	45.2	34.7
	100,0.1,10	100	86	42	22	12.2	6.6	3.4	43.5	24.2	13.6

Figure 6.20 Permeability decline curves for model based on Clashach 7, scale distribution weightings 5, 3, 4

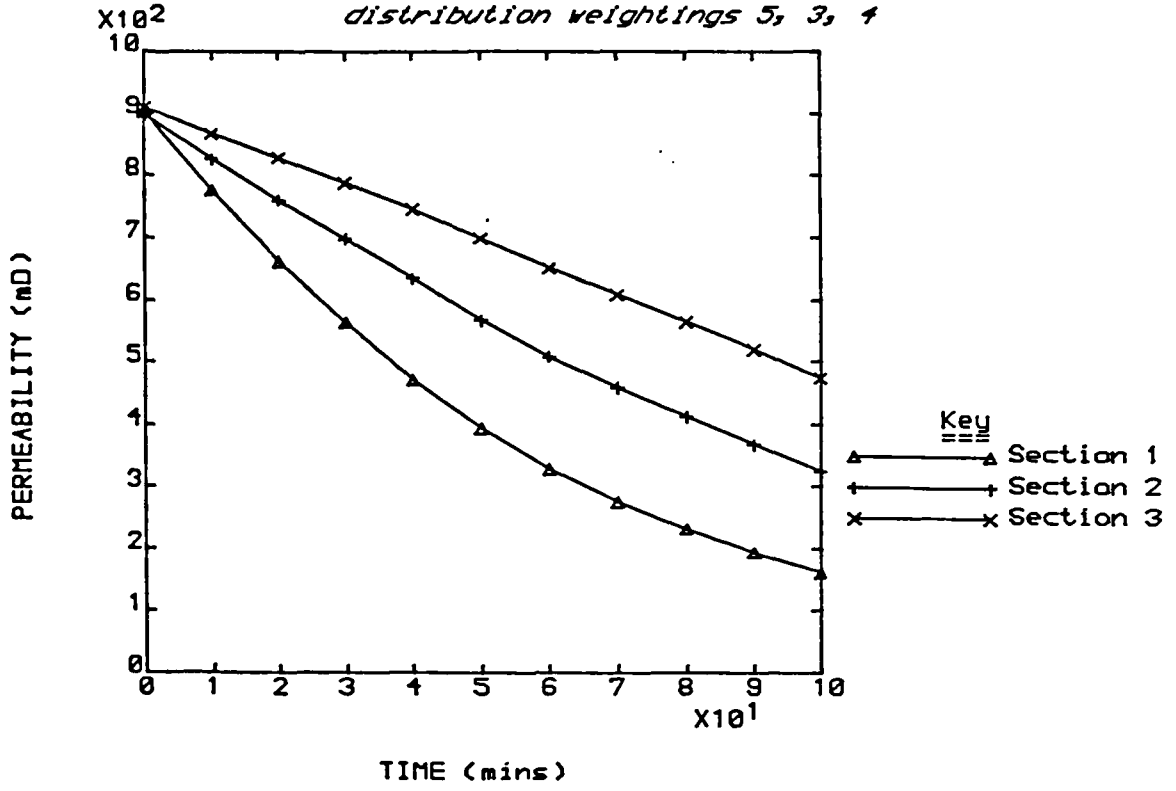

Figure 6.21 Permeability decline curves for model based on Clashach 7, scale distribution weightings 1, 1, 1

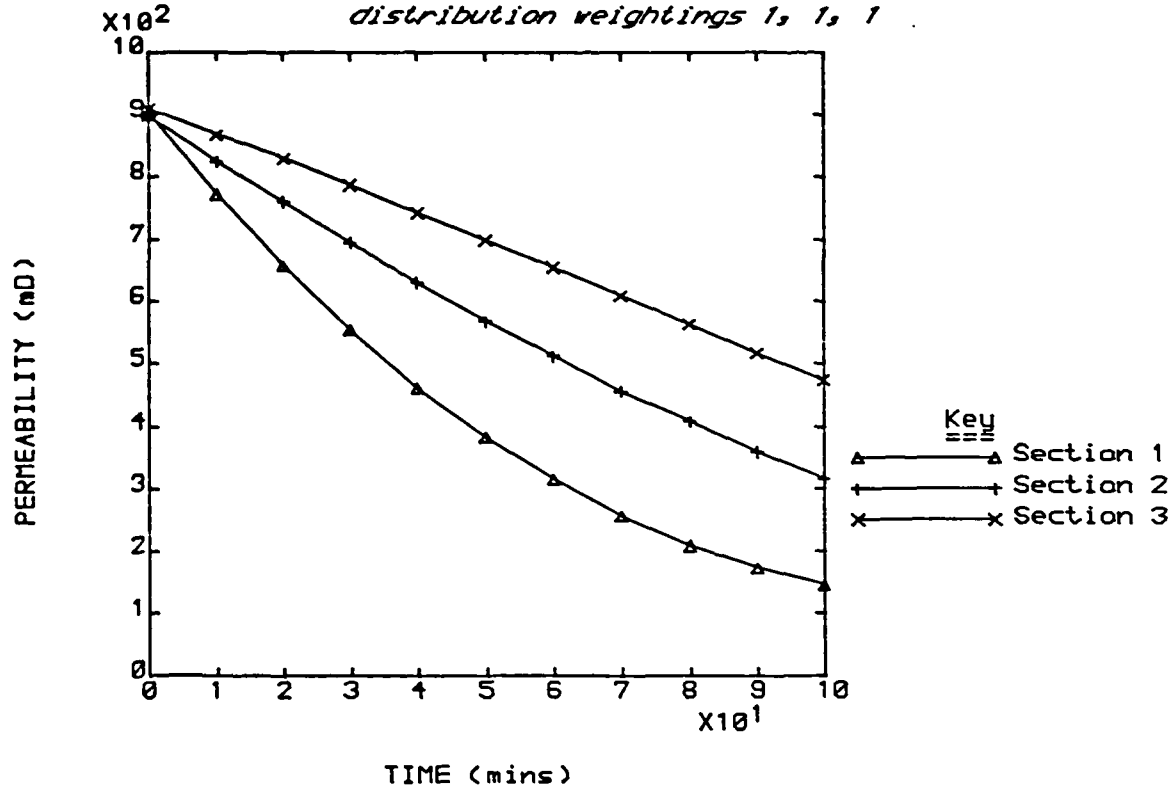

Figure 6.22 Permeability decline curves for model based on Clashach 7, scale distribution weightings 0, 1, 0

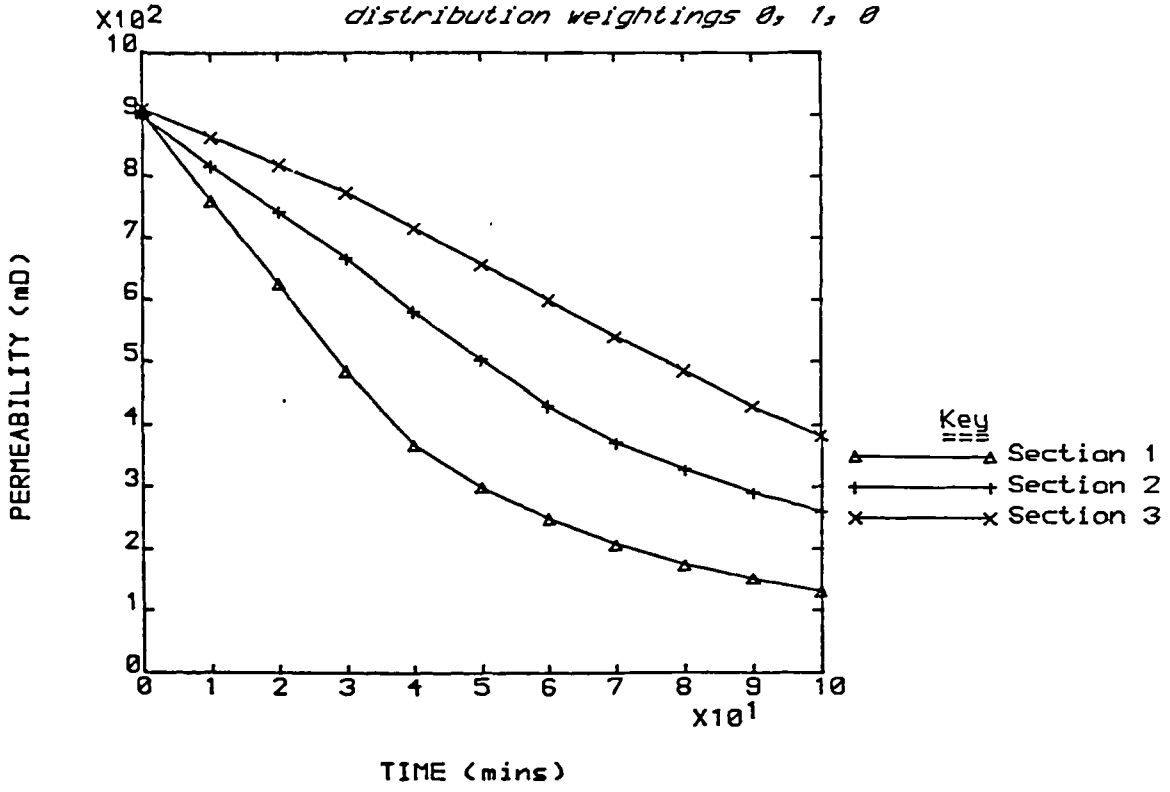

Figure 6.23 Permeability decline curves for model based on Clashach 7, scale distribution weightings 100, 0.1, 100

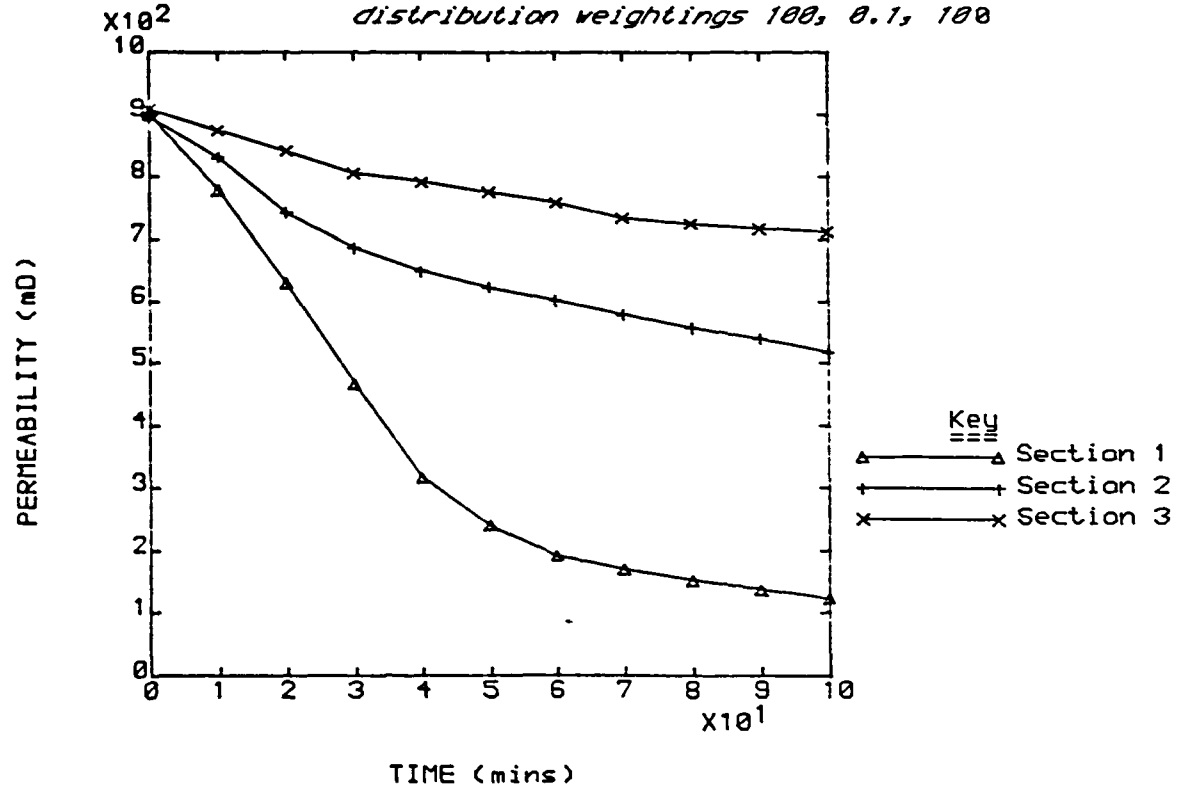

Clashach block 7. These demonstrate that although initial damage rates between the different weighting strategies were comparable, this is not necessarily the case with later scaling patterns. This difference was most noticable for the case when the scale was almost completely biased towards the wide ends (figure 6.23), when the last two sections had much lower final levels of damage than in the other models.

The good level of comparability between the centre case (weightings 1, 1, 1), the off-centre case (weightings 5, 3, 4) and the case when the scale was biased totally towards the pore throats (weightings 0, 1, 0) suggested that the only adjustment to the weightings that could have any significant effect on altering the behaviour of the model, as seen through the permeability, was to bias the scale heavily towards the wide ends.

The models in table 13 were run with a supersaturation of 20. The equivalent flowrates and the times to reach 50% of initial permeability were used to compare with the experimental results for supersaturations near 20, given in table 3. From this comparison it was seen that only the top group in table 13 had times close to the experimental values. This emphasised the importance of setting up the initial model to accurately reflect the properties of the sandstone being modelled.

The effect of the weightings on the simulated capillary pressure curve

The effect different weightings had on the way the pore size distribution changed as scaling progressed could be observed by plotting the simulated mercury penetration porosimetry capillary pressure curves from the data provided by the model. A set of these curves is presented in figures 6.25 to 6.32 for section 1 of the same Clashach 7 models discussed above. These all had the same initial pore

Figure 6.24 Simulated capillary pressure curve for undamaged model based on Clashach 7 pore size distribution

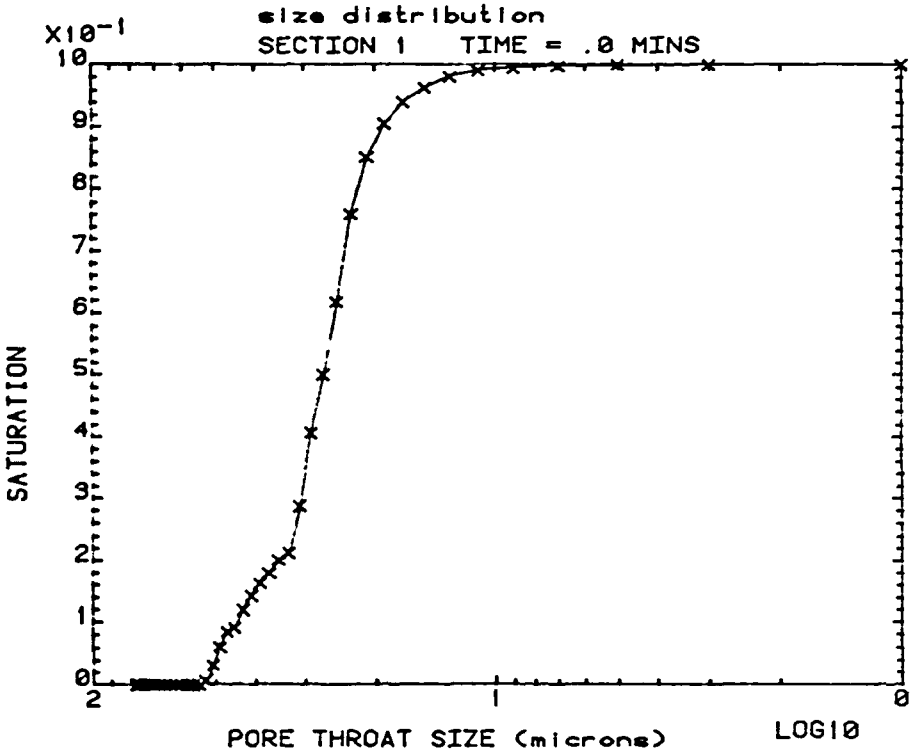

Figure 6.25 Simulated capillary pressure curve for damaged model with scale distribution weightings 5, 3, 4

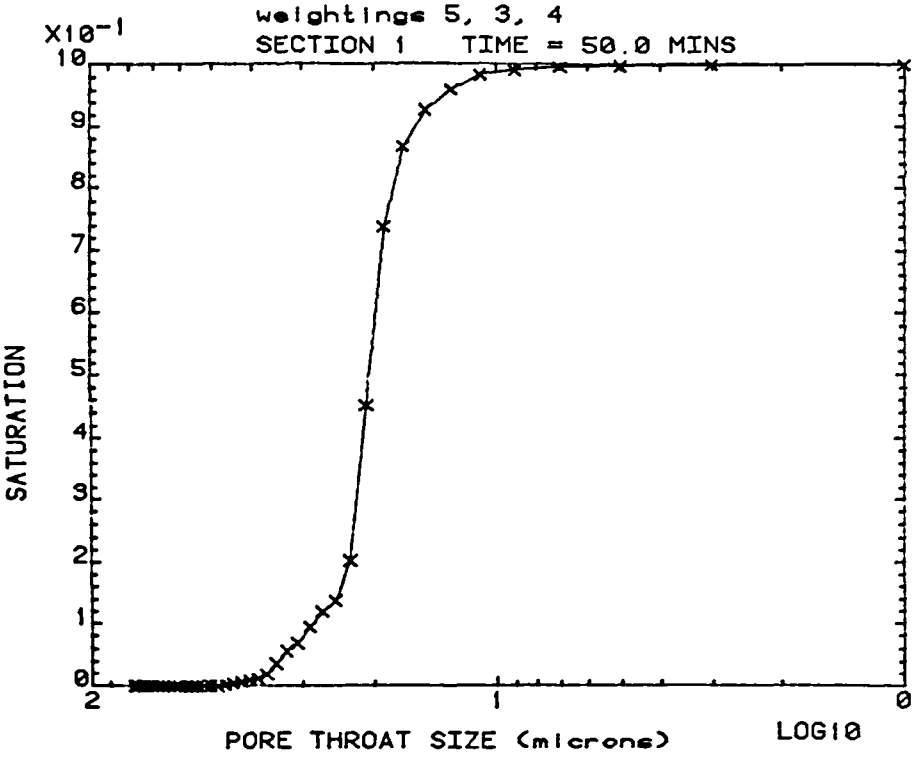

Figure 6.26 Simulated capillary pressure curve for damaged model with scale distribution weightings 5, 3, 4

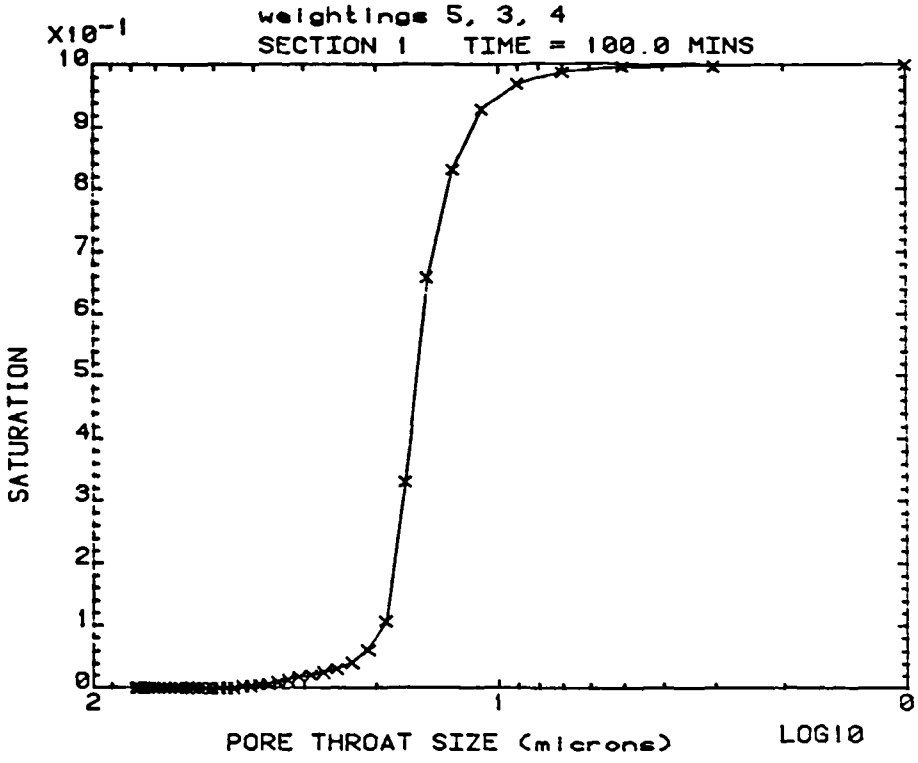

Figure 6.27 Simulated capillary pressure curve for damaged model with scale distribution weightings 1, 1, 1

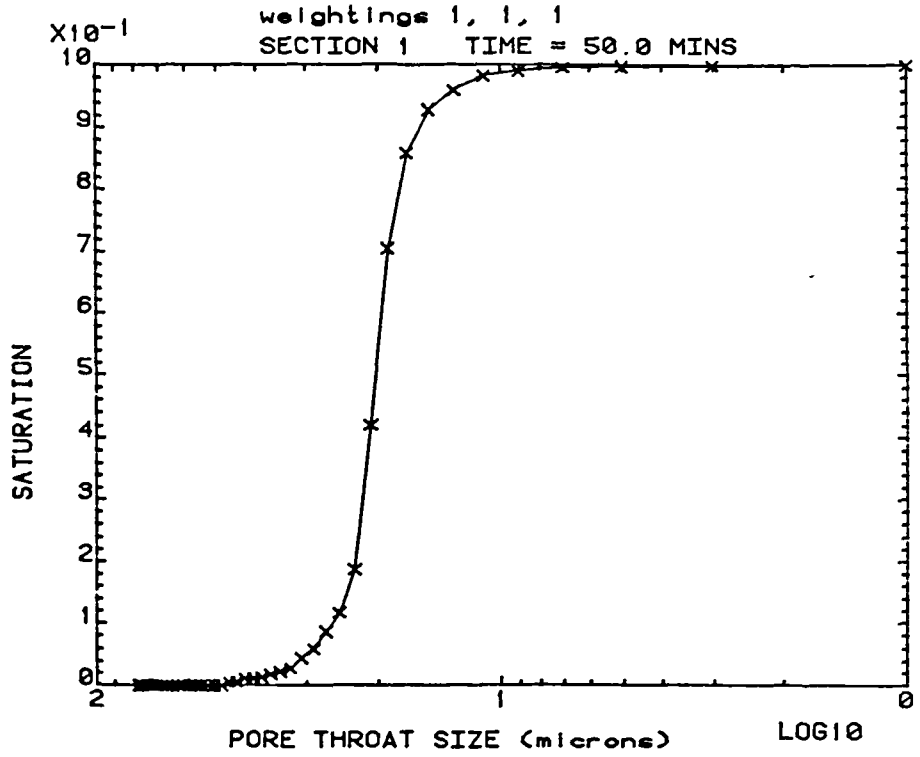

Figure 6.28 Simulated capillary pressure curve for damaged model with scale distribution weightings 1, 1, 1

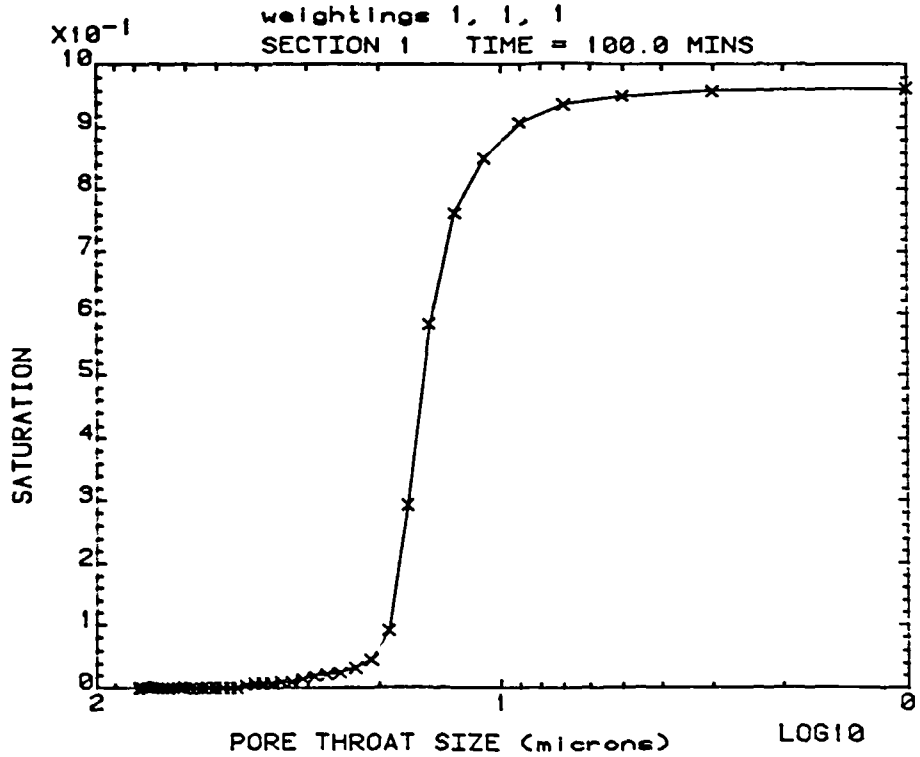

Figure 6.29 Simulated capillary pressure curve for damaged model with scale distribution weightings 0, 1, 0

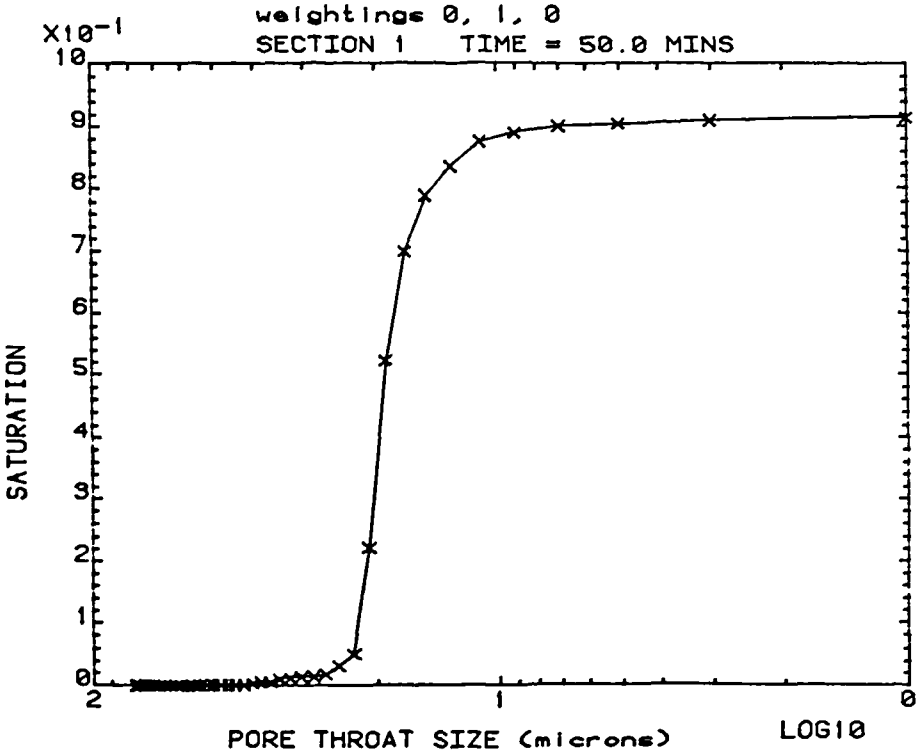

Figure 6.30 Simulated capillary pressure curve for damaged model with scale distribution weightings 0, 1, 0

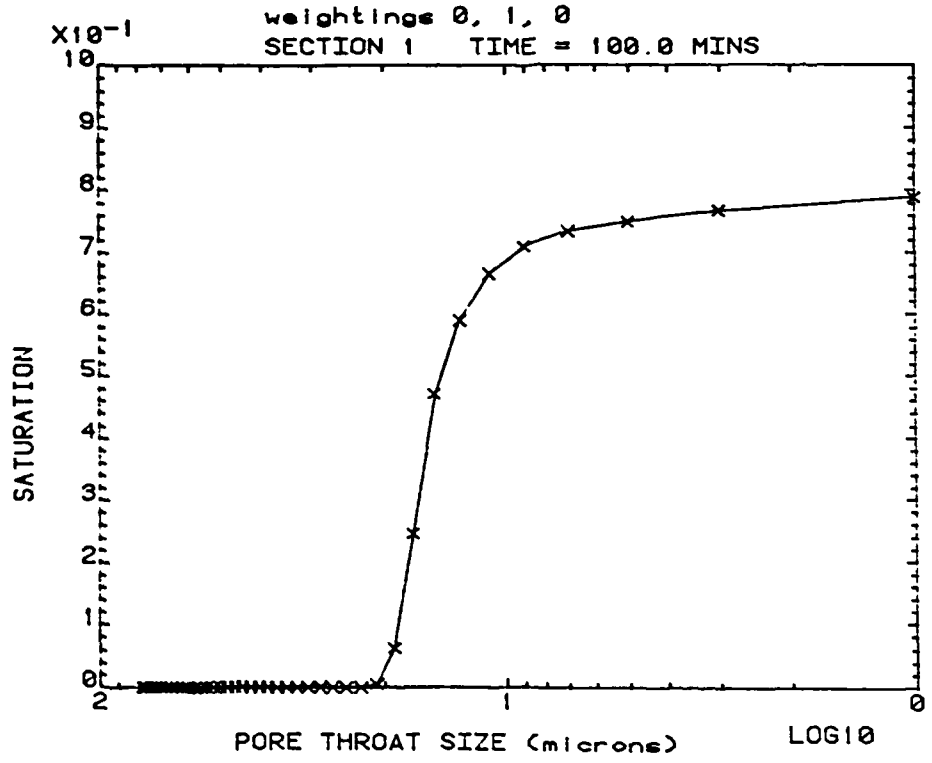

Figure 6.31 Simulated capillary pressure curve for damaged model with scale distribution weightings 100, 0.1, 100

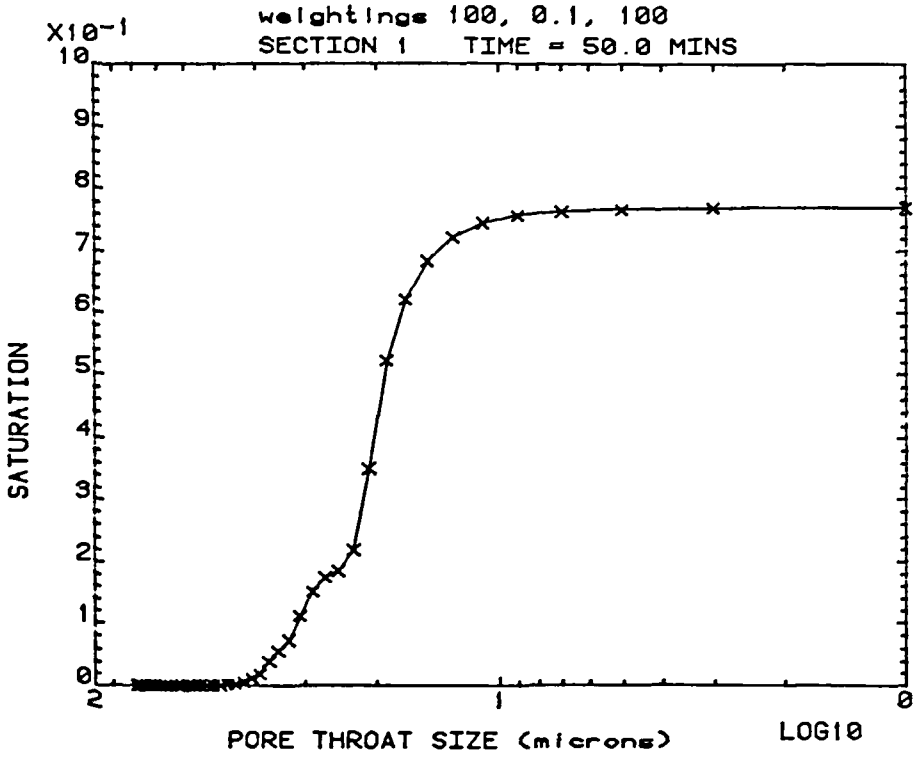

Figure 6.32 Simulated capillary pressure curve for damaged model with scale distribution weightings 100, 0.1, 100

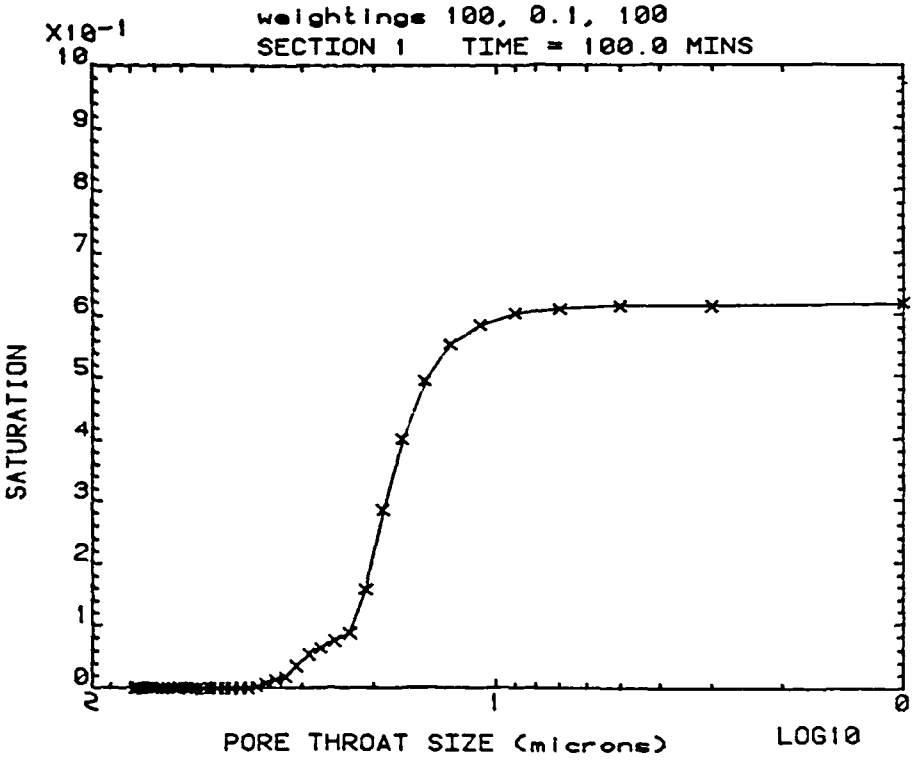

size distribution shown in figure 6.24. The rest of the figures show the pore size distributions after 50 and 100 minutes of simulated scaling for each of the four sets of weightings.

As with the permeability data, there were many similarities between the two central cases and the extreme case that only blocked pore throats (figures 6.25 to 6.30). These curves all showed that the larger size pores were severely damaged, though there were slight variations between the three cases.

In the other extreme case, where the scale was biased towards the wide ends (figures 6.31 and 6.32), the curves indicated a much lower level of damage to larger pores. This explained why this model had achieved similar levels of damage for smaller quantities of scale. The permeability change observed for this model was due to the severe damage of the smaller pores that linked the larger pores, which required smaller amounts of scale than damaging the large pores in the manner of the other models.

The shift of the upper portion of these curves away from the 100% saturation point was caused by the way in which the diameter of the capillaries was decided. In this model the diameter of a capillary was considered to be its smallest dimension. If the wide ends were severely damaged, the capillary size would be taken as being small, but the rest of the capillary might still have had a significant volume. Thus, the case of biasing the scale towards the wide ends had the largest shift of the upper portion of the curve.

6.3.5 Summary of the Simulating Abilities of the Model

The response of the model when subjected to scaling and how well it compared with experimental results appeared to depend, to a large extent, on how well the porous media model simulated the properties of

the sandstone to be modelled. The setting up of the porous media model to simulate the properties of a given sandstone required more than just the generation of a pore size distribution and associated porosity. Other factors not discussed in this work such as the sizing of the wide end diameter and even the relationship between the capillary throat diameter and the throat length may have needed adjusting to achieve this simulation.

Changing supersaturation in the model caused far greater changes in the pattern of damage, measured by the time to reach 50% of initial permeability, than the experimental evidence suggested. Experimental evidence on the effect of changing flowrate was limited, but tended not to support the model's predictions on the effect of flowrate changes on the pattern of permeability damage. Also due to lack of experimental data it was not possible to judge the results of the model with respect to the influence of changing the product of the reaction rate constant, k, and the surface area term, s.

The results presented in subsection 6.3.4 suggested that the weighting factors for the distribution of scale did not provide sufficient, controllable modification of the model's response to allow them to be used as a means of tuning the model. Clearly this system should be replaced with one that considers the process of scale deposition in greater detail, as discussed in section 3.4.4.

CHAPTER 7

FUTURE WORK

7.1 ACHIEVING THE MODELLING OBJECTIVE

As was discussed in chapter 3, the ultimate aim of the modelling work in this thesis was to provide a means by which scale damage in a sandstone formation could be predicted. The discussion in chapter 6 admitted that this objective was not achieved, but demonstrated that further development of the network modelling technique would be worthwhile. Section 6.1 pointed out the limitations of the network modelling technique for making predictions for a physical size of relevance to a real sandstone formation. Because the network model was based on microscopic intra-pore processes, it was not expected that these problems of size could be easily overcome.

It is suggested, therefore, that a better route to a usable model would be to use the results of the network model as the small scale data for a larger model, probably of a size relevant to the experimental cores. Data from such a model could then be used for an even larger model, either a radial model for simulating scale damage around a wellbore or a linear model for simulating scale formation deep within a reservoir. Both of these later models, when applied to a reservoir, would need to take into account changes that would have occurred in the brine composition prior to its reaching the zone of the reservoir being modelled. These changes can occur due to scale deposition, dissolution of rock matrix or cation exchange on passage of the brine through the reservoir.

An alternative route to these reservoir size models would be to take experimental core data and impliment it directly into a model. As a much larger experimental data base would be required to validate the smaller of the models described above, there should be sufficient experimental data available. However, such a model would be dependant upon producing experimental data in the future, whereas the earlier models described above could be used in a purely predictive mode.

To follow any of these routes both the experimental and modelling work described here must be improved upon. Such improvements are discussed below.

7.2 IMPROVEMENTS TO THE SCALING NETWORK MODEL

If the scaling network model were to be used as the base for a series of models, then its capabilities must be improved beyond the mere simulation of patterns of damage that were achieved by the model discussed in this work. The model must be able to make reasonable predictions of permeability damage rates and, if damage further downstream is to be modelled, it must correctly predict the change in brine compositions across the network. Two major changes to the model are suggested here for increasing both the accuracy and the applicability of the scaling network model.

7.2.1 Simulation of Mixing

In the scaling network model the two brines were considered to be mixed prior to entering the core. However, in the experimental cores the brines mixed in the first few millimetres of the core. This difference probably made a major contribution to the lack of comparison between the two sets of results Changing the model to simulate the mixing process might bring the two sets of results closer together and would also increase the usefulness of the model to simulating the effects of such mixing phenomena.

To perform the calculation of quantities of scale deposited for a mixing model the current supersaturation mapping system would have to be replaced by an ion concentration mapping system, ie the concentration drop of the scaling ions across each capillary would have to be calculated and supersaturation of the brines obtained from the solubility prediction model. This would make much greater use of the solubility prediction model and require more memory space for storing

concentration data.

7.2.2 Crystal Growth Modelling

The discussion in chapter 6 pointed out that the simple technique of lining pores with scale and controlling the balance of scale between the throats and wide ends of the capillaries was not a satifactory method of controlling the predictions of the model. Following the principle of modelling, a technique which mimics more closely the growth and intergrowth of scale crystals should be used.

7.3 IMPROVING EXPERIMENTAL DATA

The experimental data must be made more reliable if a model based on it or matched to it is to be of any use. The data for each experiment should also be extended and analysed further to confirm the pattern of damage identified in chapter 5.

The discussion in chapter 5 identified the characterisation time for the permeability decline curve (the time for the gradient of the curve to reach half its initial gradient) with approximately 50% permeability damage. This time could, therefore, be viewed as a form of half life of permeability. For a true half life relationship the permeability should again be reduced by half after another space of time equal to the characterisation time. Unfortunately, to do this by the graphical technique used in this work especially with the sort of data produced by the current equipment would not be easy. A much better technique would be to fit a curve to the experimental data and then test the half life relationship mathematically. To reliably fit a curve to the data the variability in the data must be reduced. The biggest factor causing variability in the data was the flowrate fluctuation of the pumps used. Thus, to test the extension of the half life theory a far more reliably stable pumping system should be employed.

The weakest point of the experimental data was in the assessment of the quantity of scale formed. This situation could easily be improved by completing the development of a rubber sleeve core holder, thereby making possible measurements of the porosity of experimental cores prior to scaling. It would also be worthwhile increasing the resolution of this technique by measuring the porosity of individual sections of the core after scaling. The effluent sampling technique of assessing scale quantity could be extended in the same manner by taking

samples of brine from the tapping points on the core. This sampling technique would also allow for the mapping of supersaturation change within the core, data that would also be of use to the model.

7.4 EXTENDING THE EXPERIMENTAL WORK

The experimental work described in this thesis was limited to low pressure and temperature. Obviously this reduced its applicability for modelling of oil reservoir scaling. Raising the temperature is expected to have a marked effect on the scaling of a sandstone. Although the solubility of barium sulphate increases with increasing temperature so too will the rate of the precipitation reaction. Pressure increase has little effect on the solubility of barium sulphate and is not expected to have any significant effects on the kinetics of precipitation. As little data has been published on scale formed at high pressures nothing about the influence of pressure can be stated with certainty.

In addition to studying any effects of pressure on the precipitation reaction, increasing the working pressure of the experimental equipment (ie the core holder) would allow a higher pressure drop across the core. A higher pressure drop would be required to overcome the severe damage at the front of a core in order to study the scaling potential of brines further from the mixing point. Thus, introducing the use of a high temperature, high pressure core holder should be a priority of future experimental work.

Further experimental work should also be aimed at confirming and consolidating the relationships discovered in this work. If the modelling work is to consider crystal growth more deeply then more experimental evidence on the pattern of damage associated with various crystal morphologies would be required. The study of the influence of ionic strength and solution composition on crystal habit could eventually lead to crystal habit prediction.

A large experimental data base is required to confirm the observations made in this work and to generate firm relationships

between the pattern of permeability damage and the solution supersaturation, flowrate, ionic strength etc.

CHAPTER 8

CONCLUSIONS AND SOME IMPLICATIONS

8.1 CONCLUSIONS

8.1.1 Modelling Work

The modelling performed in this work was of a preliminary nature to investigate the suitability of the network modelling technique for simulation of scale growth in a porous medium.

The model simulated, reasonably well, the pattern of permeability decline demonstrated by the experimental work. Permeability decline curves produced by the model were of a similar shape to those produced experimentally. The pattern of increased initial damage rates with higher initial permeabilities evident in the experimental work was also apparent in the results from the model.

Quantitatively, experimental results were not well matched by the model. Although damage predicted by the model increased with increasing flowrate and supersaturation of the brines, the magnitude of the change was not similar to that demonstrated by the experimental work. The model predicted that decreasing the flowrate of brines caused the permeability damage due to scale to become more localized to the point of mixing of the brines.

The technique used in this model for controlling the growth of scale within capillaries in the model did not appear to give sufficient control over the response of the model to enable it to be tuned more closely to quantitative experimental results. However, in view of the

good matching of general permeability damage patterns, it was considered that further development of this model would be worthwhile.

8.1.2 Experimental Work

The experimental work was originally intended to supply information for validating the model. Analysis of the results showed that they would be useful in their own right.

The change in permeability with time of a sandstone core when subjected to scale formation within it, was found to form a concave curve. The curve was initially very steep, but the gradient quickly decreased to a small, but significant permeability damage rate. The shape of this curve was explained through a theory as to the pattern of growth of the barium sulphate crystals.

The initial damage rate of the permeability decline curve, for regions of the core close to the mixing point, was found to have an approximately linear correlation with the initial permeability of the sandstone.

The permeability decline curves were characterised by measuring the time for the gradient of the curve to fall to half its initial gradient. This characterisation appeared to remove the variability attributed to differing initial permeability and allowed comparisons to be made between experiments run under the same conditions. The characterisation time varied with the initial supersaturation and with supersaturation decline due to precipitation, seen through the results for later sections of the cores. There was insufficient data generated to make a reasonable correlation between supersaturation and the characterisation times of the curves. Similarly there was insufficient data to draw any conclusions on the influence of changes in crystal morphology on the characterisation times.

The point at which the gradient of the permeability decline curve reached half its initial gradient was found to correspond to approximately 50% permeability damage. This suggested that the permeability decline might follow a "half-life" pattern. Insufficient data was available to test whether this pattern held for later scaling.

No relationship was discovered between the quantity of scale formed and the amount of permeability damage suffered by the cores.

The morphology of the barium sulphate crystals was found to be controlled more by the ionic strength and composition of the brines than by their supersaturation. Low ionic strength brines were found to form "plate" crystals while higher ionic strength brines formed "block" crystals. Addition of "foreign" ions, such as magnesium and calcium, was found to cause subtle changes in the crystal habit. Some evidence was found to suggest that the "block" crystals from the higher ionic strength brines formed more porous scales.

8.2 SOME IMPLICATIONS

The shape of the permeability decline curves is considered to be most important as it indicates that if barium sulphate scale does start to form within a reservoir, the initial stages of growth will cause the most damage. The characterisation times for the curves show, for the case of the experimental cores, how much time was required from the onset of damage for 50% damage to occur.

The linear correlation of the initial damage rate of the scale demonstrates that not even for high permeability formations can the risk of scale damage be ignored. The same characterisation time for the curves holds for high initial permeabilities as well as low ones.

The experimental results further from the point of mixing show that the precipitation of scale is a fairly rapid process and so the majority of damage should remain local to the mixing zone. However, under reservoir flow conditions it is likely that once one region begins to suffer permeability damage, the brines will find another, higher permeability path to follow. Thus, the extent of damage and its effects on the producibility of the reservoir can only really be predicted through the use of reservoir simulators.

To add to the difficulties of predicting the likely effects of barium sulphate scale formation, as brines move about the reservoir the composition of any mixed brine will change. The study of crystal morphology in this work showed that a change in composition is likely to cause a change in the crystal morphology. Although it could not be proven in this work, a change in crystal morphology is expected to cause a shift in the pattern of damage due to the scale.

APPENDIX A4.1 PROCEDURE USED IN DYE TESTS TO EVALUATE PERFORMANCE OF DISTRIBUTION FACES

Dyes Used for the Tests

For some of the tests a "mixing dye" was used. This was a dye made from two colourless liquids, which take on an intense colouration when mixed. The reasoning behind the use of such a dye was that only the areas of the core where mixing occurred would be coloured. The "mixing dye" used was a colourless indicator, phenanthroline hydrate, which turns blood red on mixing with ferrous chloride solution. For the 50:50 flow ratio tests performed the concentrations of the two solutions were 2.5g per litre phenanthroline hydrate and 1g per litre ferrous chloride.

Most of the dye tests were performed using methylene blue dye as one solution and distilled water as the other. This had a disadvantage compared to the mixing dye system in that it could only mark the course of one of the solutions. Thus, two tests had to be performed to infer a mixing pattern from the methylene blue dye technique. The reason most tests were performed by this technique was because the methylene blue dye was much more intense than the "mixing dye" and so the results were much easier to observe.

Preparing Cores for Dye Testing

The procedure used for dye tests was similar to that used for all other core flooding experiments. The cores were cast in $^{1}/_{4}$" thick tooling resin and mounted in a clamp-type core holder against the distribution face under test. With the flow lines into the core

closed, a vacuum was applied to the outlet line for approximately one hour.

Performing the Test

After evacuation, the core was saturated with distilled water followed by a pumped flood of distilled water. Distilled water flow was continued for half an hour to allow the flow patterns in the core to become established. The pump supply lines were then switched to the dye reservoirs and flooding continued until 2 minutes after dye was detected in the outlet from the core.

The core was then quickly removed from the core holder and cut into sections to observe the distribution of dye. This was carried out immediately to reduce any chance of the dye diffusing through the still wet core.

APPENDIX A5.1 PREPARATION OF SANDSTONE CORES FOR USE WITH CLAMP CORE HOLDER

Design of the Resin Bonded Cores

For use with the clamp core holder the core was coated with resin. The resin also supported the pressure tappings made at intervals along the core. As the tappings were made by screwing fittings into the resin, the resin had to be thick enough to accommodate the thread of the fitting. A resin thickness of about 12mm was used.

Because of the size of the fitting and the strength of the resin, the closest a tapping point could be placed to the front face of the core was discovered to be 11mm. This measure was used as the basis for the spacing of the other tappings so that the observed pressures were directly comparable. The second tapping point was placed 11mm further along the core from the first. The remaining two tapping points were spaced at 22mm intervals, leaving 22mm to the end of the core. Thus, the core was 88mm long in all.

Casting the Cores in Resin

To begin with, the cores were cut about 4.5" in length and trimmed so that one end was square to the sides. The cores were then dried in an humidity oven for 24 hours.

To prevent the resin fom being absorbed into the cores they were first coated all over with a rapid-setting epoxy resin. This resin was quite viscous and so only penetrated a few microns into the core before setting. The epoxy resin provided a good bond with the core to prevent fluid by-passing the core and was an excellent base on which to bond

the tooling resin.

The tooling resin used to provide the main resin coat on the cores was the three part Araldite D219 system manufactured by Ciba-Geigy. This consisted of a resin, hardener and accelerator and was mixed to a pouring consistency according to the manufacturer's recommendations. For some of the early cores, marble flour was added to the mix to strengthen the resin. Complete dipersal of the fine marble flour was found to be very difficult to achieve, resulting in pockets of unmixed flour which left holes in the cured resin. These holes caused problems when machining the vital sealing faces onto the resin and so the practise of adding marble flour was abandoned.

The resin was cast around the cores in specially made moulds. These moulds had a 5mm deep well at the bottom to hold the flat end of the core central in the mould. The other end of the core was held central by a special collar inserted after pouring the resin. The cast cores were left in the moulds for 24 hours at room temperature. The manufacturer's suggestion for using higher curing temperatures was found to cause air to force its way out of the core to create holes in the resin.

Machining of the Resin Bonded Cores

After removal from the moulds the resin coated cores were machined to a diameter of 50mm. The end of the core that was at the base of the mould was then carefully trimmed to be absolutely square to the sides of the core, usually removing about $^{1}/_{4}$" to $^{3}/_{8}$" off the core's length. The squareness of the trimmed end was most important as the seal at the front end of the core holder was made against the resin of this face. The other end of the core was trimmed to leave a final core length of 88mm.

In the final manufacturing process a 3mm locating rebate was machined around the edge of the front face and a longer rebate was machined at the other end for the circumferential seal. The positions of the tappings were then marked on the core. These had the longitudinal spacings described above and radial spacings of 80° to ensure a large amount of resin between tappings. The tappings were first drilled with a pilot drill of 1mm right down to the underlying core and were then opened out to the diameter and depth required to accommodate the thread of the fitting. Finally the tapping holes had a $^{1}/_{16}$" NPT thread cut in them. The finished resin bonded core is shown in figure A5.1.

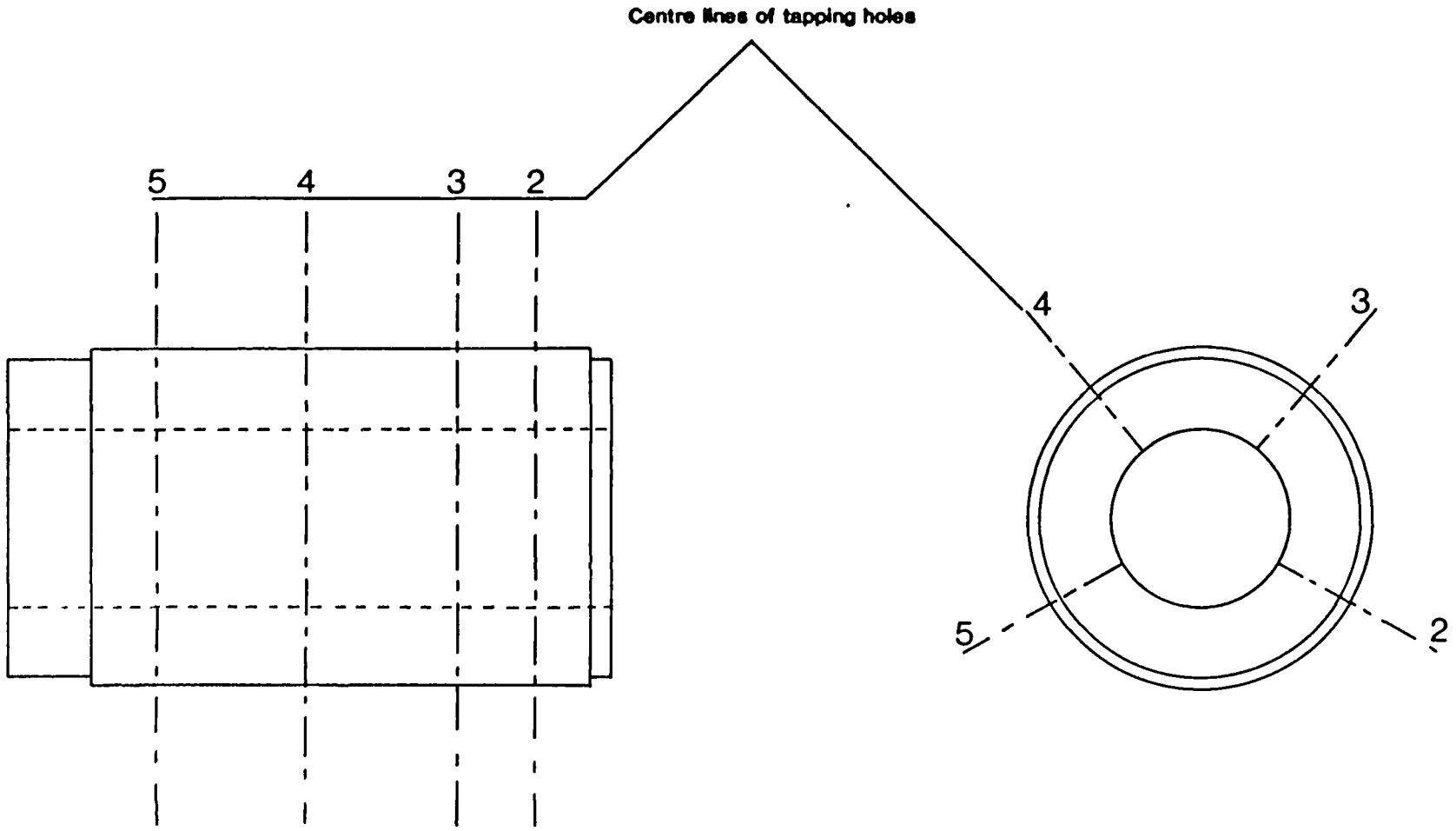

Figure A5.1 Design of a resin bonded core

APPENDIX A5.2 POROSITY MEASUREMENTS WITH RESIN BONDED CORES

Measuring the Porosity of the Resin Bonded Cores

The problems with the resin bonded cores, as far as porosity measurements by helium gas porosimetry is concerned, were many. The cores were too big to fit into the sample chamber of the porosimeter, which was 1.5" in diameter and 3" in length, both in length and diameter terms. The resin could not be removed and its volume was unknown. This appendix describes how these difficulties were overcome to obtain a measurement of porosity as accurate as was possible.

Firstly, to overcome the size problem, the resin bonded core was machined down to a diameter of 1.5" and the back end of the core was trimmed off to leave the core approximately 3" long. The experimental evidence shows that very little scale was formed at the end of the core so this adjustment in length should not unduly affect the results for the purposes of calculating the quantity of scale deposited in the core.

The porosity of the core and remaining resin could now be measured in the porosimeter.

Obtaining Porosity of the Core Alone

The porosity calculated for the resin bonded core reflected the volume of the pore space in the core and the volume of the tapping holes in the resin. In order to find the porosity of the core alone the volume of the tapping holes had to be measured.

To find the volume of the tapping holes dummy cores were manufactured in exactly the same manner as the real cores, but instead

of using a resin coated core the dummies were manufactured from solid bars of PVC. The dummy cores were machined down to 1.5" diameter and 3" length just as the real cores were. The porosity measurement on the dummy cores reflected the volume of the tapping holes alone. The volume of the holes on the dummy cores was used to correct the porosities measured on the real cores.

Sources of Error

There were several sources of error in this process in addition to the errors involved in measuring the porosity of the cores and their bulk volumes. Firstly, the pilot holes drilled in the dummy cores were not constrained by the position of the core itself and so were all drilled to the same depth, that at which the core should lie. With the real cores, however, the depth of these holes could vary slightly as the core was not always exactly central.

The second source of error was in the correction calculation on the measured porosity of the real resin-bonded core. For this calculation the bulk volume of the core alone was required. For calculating the bulk volume the average diameter of the cores cut was used, thereby assuming that the depth of penetration of the rapid-epoxy resin was minimal, which was not necessarily the case.

Finally, the removal of the last $^1/_2$" of the core could only increase the error when values of porosity change are compared with other "whole core" measurements such as the amount of scale formed in the core calculated from effluent analysis data.

An analysis of the measurement errors involved in measuring the porosity of the resin coated core showed that an error of ±20% was possible. This figure does not take into account the sources of error described above, which were difficult to quantify. However, the

measurement error alone demonstrates the poor reliability of scale quantity calculations from the available porosity data.

APPENDIX A5.3 THE EXPERIMENT IDENTIFICATION SYSTEM

The identification system for the experiments was designed to give, at a glance, all the necessary information on the conditions under which the experiment was run. Two, fully explained examples are given at the end of this appendix.

Type of Core Material

The first three characters indicate the type and identification of the core material used. For all the cores used in this work the type designation is C for Clashach followed by the number of the block from which the core was taken. This eases making comparisons between results from cores of the same block. Comparing results for cores from the same block can be important as large differences in core characteristics were observed between cores from different blocks.

Brines and Flowrates Used

The rest of the identity upto the hyphen refers to the brines used and is split into two parts. Taking the second part first, the two letters just before the hyphen relate to the brine systems used (see subsection 5.2.4 in chapter 5). Normally the two letters are the same as both parts of the brine system were in use, but the identification system also allowed for brines from two different systems to be used or alternatively other methods of designating brines. The first of the two letters refers to the barium rich or formation brine used and the second to the sulphate rich or injection brine.

Between the core designation and the brines used are two numbers. These are the volumetric flowrates (cm^3/min) of the two brines used in

the same order as the brines are named. In all of the experiments in the study equal flowrates of the two brines are used so these numbers are always the same.

Experiment Number and Special Conditions

The first number after the hyphen is the experiment number for the particular combination of brines specified. Any letters following this refer to special conditions used for the experiment. Here, two letters have been used. The letter R refers to an experiment in which the flowrates were reduced at some time during its course. The letter S indicates that effluent sampling was performed during the experiment.

Examples

The experiment identity C221515CC-3R shows that a core from Clashach block 22 was used. The flowrate of each brine was 15cm^3/min and both brines were from the C system. This was the third experiment performed with both brines from the C system and the flowrate was deliberately reduced at some point during the experiment.

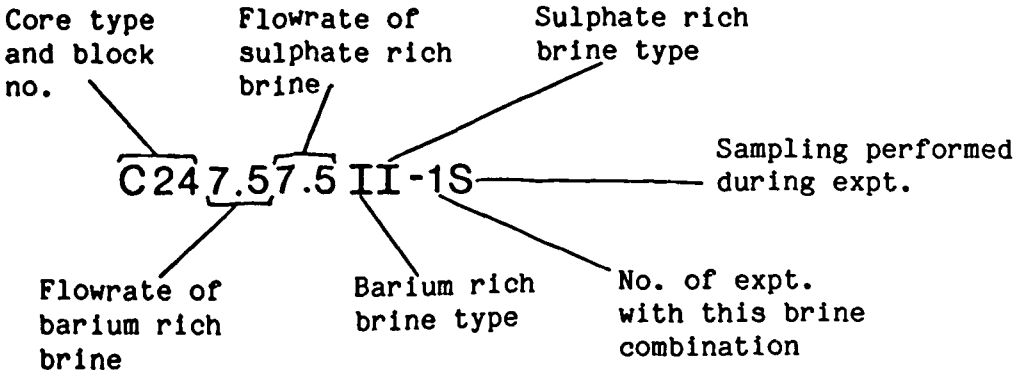

APPENDIX A5.4 EXPERIMENTAL RESULTS

Introduction

This appendix contains the data that arose directly from the experimental work. Almost all the data available for the successful experiments has been presented. The reason for this is so that any reader wishing to further analyse the data or apply these results to his or her own work has all the relevant information available.

Presentation of data

The majority of the data is presented in tabular form and so may easily be extracted for use. It was not practical to present the data relating to the pressure measurements at the tappings on the core in this way owing to the sheer quantity of information. Instead this information is presented as a set of permeability decline curves for each core.

In addition to the results presented in this appendix there are the results of the SEM analysis, which are presented in chapter 5. In this case, as described in section 5.4, the results presented have been selected to illustrate the type and quantity of crystals observed. Photomicrographs have been included to illustrate the crystals growing at the front of the core and much later in the core for all the brine systems used.

Contents of results tables

Table A1 contains data on the length of each experiment and the measured flowrate of brine used (as opposed to that intended as given

in the experiment identity). For experiments in which the flowrate was reduced part way through, the time and flowrates are given separately for each part of the experiment. Also in table A1 are the helium gas porosities for each core (where measured) after the core had been scaled. The rest of table A1 gives initial and final permeability data both for each section of the core and for the core as a whole.

Table A2 deals with the water analyses. The concentration of barium in each analysed effluent sample is presented along with the time since the start of the saline flood at which the sample was taken. The results of analyses of the barium containing stock solutions injected into the core are also given. Some data was available on the concentration of barium in the solution remaining from the beaker tests after the crystals had been filtered off. This is presented in the final column of table A2.

Table A3 contains the results of the use of EDAX to identify what elements are present in crystals from the beaker tests. Table A4 presents the data relating to the initial porosities of the cores from each of the Clashach sandstone blocks used.

Tables A5 to A36 contain the results of all the mercury penetration porosimetry carried out on various samples of scaled and unscaled sandstone. Some of this data is presented graphically in chapter 5. As discussed above a full set of results has been presented in this manner as they may be of use to other workers in any field where mercury penetration porosimetry of sandstones is used.

Graphical data

After the tables, the data generated by the tapping transducers is presented as permeability decline curves. Each figure consists of a set of curves for each section of the core and a separate curve for the overall permeability of the core. The latter curve has been included

so that this data may be compared with results from core flood experiments that do not have the facility for measuring pressure at intervals along the core.

Finally, the solubility and fractional supersaturation curves produced by the solubility prediction model described in chapter 3 have been included so that others may assess the validity of this model and for general completeness of the data.

Table A1. Experimental results: duration, flowrate, final gas porosity and initial and final permeabilities

EXPERIMENT IDENTITY	LENGTH OF EXPERIMENT (mins)	FLOWRATE (cm^3/min)	FINAL GAS POROSITY %	Initial values above final values					
				SECTION PERMEABILITIES (mD)					OVERALL PERMEABILITY (mD)
				SECTION					
				1	2	3	4	5	
C141515AA-2	25	30.0	-	270 60	350 40	235 55	185 70	- -	235 55
C071515AA-3	140	30.0	-	415 65	900 88	580 86	387 127	- -	500 85
C141515AA-4	17	30.0	-	178 12	252 17	180 57	202 135	- -	200 25
C071515AA-5	98	30.0	-	631 55	519 34	459 55	630 153	- -	550 60
C141515AA-6	16	30.0	-	145 10	172 35	119 65	108 75	- -	125 35
C181515AA-8	45	32.0	-	365 100	636 35	444 80	427 250	- -	450 80
C181515AA-11	29	30.0	14.9	191 34	390 34	257 60	403 210	321 200	300 65

Table A1. Continued

EXPERIMENT IDENTITY	LENGTH OF EXPERIMENT (mins)	FLOWRATE (cm^3/min)	FINAL GAS POROSITY %	Initial values above final values					
				SECTION PERMEABILITIES (mD)					OVERALL PERMEABILITY (mD)
				SECTION					
				1	2	3	4	5	
C181515BB-2	13	30.0	-	253 65	354 45	163 70	181 155	113 108	170 80
C221515BB-4	80	30.0	-	400 37	830 29	460 66	435 148	463 234	480 70
C221515BB-5	49	29.0	-	380 13	800 24	450 51	563 222	850 640	575 40
C221515BB-6	169	30.0	-	430 84	- -	430 30	520 60	590 130	555 60
C221515BB-7	278	30.0	-	720 100	1150 40	750 20	1000 120	1200 300	940 50
C221515CC-1	274	29.0	18.3	1150 139	1400 91	500 75	600 138	460 142	600 100
C221515CC-2	324	30.0	-	240 20	447 30	350 55	374 110	470 280	375 60

Table A1. Continued

EXPERIMENT IDENTITY	LENGTH OF EXPERIMENT (mins)	FLOWRATE (cm^3/min)	FINAL GAS POROSITY %	Initial values above final values					
				SECTION PERMEABILITIES (mD)					OVERALL PERMEABILITY (mD)
				SECTION					
				1	2	3	4	5	
C221515CC-3R	128	30.0	-	329	880	473	416	322	410
	159	14.5		7	18	50	146	185	30
C221515CC-4R	208	29.0	17.5	290	317	300	429	510	400
	79	14.0		38	37	85	262	450	85
C221515CC-5R	110	29.0	18.6	320	650	520	442	448	460
	130	15.0		24	111	187	332	291	110
C221515DD-1S	281	31.0	16.0	340	730	395	950	800	540
				22	30	32	215	435	55
C221515DD-2S	172	30.0	17.4	420	500	570	630	780	580
				22	6	42	236	426	25
C221515DD-3S	173	31.0	16.6	285	578	310	278	207	280
				18	18	25	85	90	25
C221515DD-5R	255	29.0	14.7	390	790	420	350	273	360
				84	75	65	85	160	85

Table A1. Continued

EXPERIMENT IDENTITY	LENGTH OF EXPERIMENT (mins)	FLOWRATE (cm^3/min)	FINAL GAS POROSITY %	Initial values above final values					
				SECTION PERMEABILITIES (mD)					OVERALL PERMEABILITY (mD)
				SECTION					
				1	2	3	4	5	
C221515DD-7S	36	31.0	17.6	370	1850	116	261	170	200
				75	203	60	195	150	103
C221515DD-8S	46	30.0	18.7	346	2130	334	146	261	265
				78	450	145	101	226	140
C227.57.5DD-9S	152	13.5	18.3	615	1400	250	520	360	430
				100	410	150	390	360	225
C227.57.5DD-10S	70	14.5	17.7	220	325	50	-	-	410
				70	70	60	210	145	220
C221515EE-1	319	32.0	16.3	413	570	320	550	310	400
				60	60	80	264	205	105
C231515EE-3	75	30.0	12.3	195	125	165	85	-	150
				8	15	50	97	112	27
C277.57.5EE-10	204	15.0	15.4	305	338	71	226	245	160
				7	23	21	162	210	25

Table A1. Continued

EXPERIMENT IDENTITY	LENGTH OF EXPERIMENT (mins)	FLOWRATE (cm^3/min)	FINAL GAS POROSITY %	Initial values above final values					
				SECTION PERMEABILITIES (mD)					OVERALL PERMEABILITY (mD)
				SECTION					
				1	2	3	4	5	
C167.57.5EE-11	98	15.0	10.5	105	195	120	130	80	110
				3	20	68	100	65	12
C1644EE-12	106	8.0	10.7	46	32	26	44	13	24
				2	8	16	40	12	7
C237.57.5FF-1S	579	14.5	9.3	55	333	182	180	145	140
				10	81	96	133	117	50
C167.57.5FF-2S	303	14.5	10.7	82	118	57	-	22	44
				22	24	44	-	16	26
C167.57.5FF-4	170	14.5	10.2	51	95	63	56	32	49
				19	28	38	38	28	30
C267.57.5HH-1S	790	15.0	19.1	1400	1200	950	900	700	1000
				296	132	130	420	420	220
C247.57.5HH-2	530	15.0	19.2	1200	2000	373	400	132	300
				263	147	136	270	85	140

Table A1. Continued

EXPERIMENT IDENTITY	LENGTH OF EXPERIMENT (mins)	FLOWRATE (cm^3/min)	FINAL GAS POROSITY %	Initial values above final values					
				SECTION PERMEABILITIES (mD)					OVERALL PERMEABILITY (mD)
				SECTION					
				1	2	3	4	5	
C247.57.5II-1S	415	16.0	18.4	960 140	2490 60	176 17	200 95	260 175	260 45
C247.57.5II-2S	525	16.0	13.8	460 100	3760 114	400 50	200 50	200 95	300 75
C247.57.5JJ-1S	373	15.0	16.1	550 80	850 100	400 80	200 80	170 100	250 90
C247.57.5JJ-2S	953	15.5	17.9	600 89	750 38	211 37	320 104	320 121	320 60
C247.57.5KK-1S	454	15.0	19.3	470 77	400 79	290 85	305 132	210 113	270 100
C247.57.5KK-2S	448	15.5	18.5	2600 173	600 113	850 233	811 450	556 308	750 235

Table A2. Results of effluent analyses and analyses of stock solutions and beaker test filtrate

Time of sample is the time from switching the pump supply to the scaling solutions. The beaker test results are for the solution in equilibrium with the crystals in the beaker, which was filtered-off and sampled as for the effluent samples.

BRINE SYSTEM	EXPERIMENT IDENTITY	TIME OF SAMPLE (mins)	CONC. OF Ba^{2+} IN SAMPLE (mg/l)	CONC. OF Ba^{2+} IN STOCK SOLN. (mg/l)	CONC. OF Ba^{2+} IN BEAKER SOLN. (mg/l)
D	C221515DD-2S	17	1.8	290	
		173	6.3		
	C221515DD-8S	5	16.5		
		45	2.4		
	C227.57.5DD10S	8	4.0		
		38	5.3		
E	C221515EE-5S	36	5.7	167	
		350	6.3		
	C167.57.5EE-11S	15	9.6		
		45	14.3		
		75	14.8		
F	C237.57.5FF-1S	42	9.8	79	12.1
		153	8.2		
		576	10.5		
	C167.57.5FF-2S	25	8.7		
		95	6.6		12.6
		297	14.7		
	C267.57.5FF-5S	508	14.1		
		647	14.2		
H	C267.57.5HH-1S	14	362	375	1.4
		55	284		
		175	278		
		425	137		
		787	19.9		
I	C247.57.5II-1S	69	6.2	538	18.4
		415	5.7		
	C247.57.5II-2S	11	4.7		
		515	4.2		

Table A2. Continued

BRINE SYSTEM	EXPERIMENT IDENTITY	TIME OF SAMPLE (mins)	CONC. OF Ba^{2+} IN SAMPLE (mg/l)	CONC. OF Ba^{2+} IN STOCK SOLN. (mg/l)	CONC. OF Ba^{2+} IN BEAKER SOLN. (mg/l)
J	C247.57.5JJ-1S	14	19.4	572	29.0
		46	28.2		
		181	23.7		
	C247.57.5JJ-2S	20	21.8		
		950	20.7		
K	C247.57.5KK-1S	21	24.2	570	
		96	23.0		
		453	23.8		
	C247.57.5KK-2S	20	26.0		
		447	25.2		

Table A3. Results of EDAX analysis on crystals from beaker tests

The figures in this table refer to the percentage intensity of the X-rays emitted by the crystal under electron bombardment. The crystals are identified by the brine system from which they originated and a sample number.

CRYSTAL	ELEMENT (% intensity)					
	Ba	S	Mg	Ca	Sr	I
A1	59.86	38.89				1.25
A2	57.27	40.82				1.91
F1	57.84	41.15				1.01
F2	53.60	45.28				1.12
I1	54.33	42.83				2.84
I2	52.42	44.66				2.08
I3	52.84	44.45				2.01
J1	49.21	46.70			2.84	1.19
J2	48.57	45.88			3.13	2.31
J3	49.28	45.97			4.07	0.58
J4	47.84	44.89			5.95	1.10
K1	59.14	36.74		2.54		0.99
K2	50.70	46.68		1.08		1.46
K3	50.87	44.95		1.51		1.35

Table A4. Unscaled core porosities for Clashach sandstone

BLOCK NO.	MEASURED POROSITIES (%)				AVERAGE POROSITY (%)
7	17.1	18.0			17.6
16	11.2	11.7	12.0		11.6
22	19.7	18.4	18.1	17.4	18.4
23	14.6	15.5	14.8		15.0
24	22.0	21.9	20.6		21.5

TABLE A5 MERCURY PENETRATION POROSIMETRY DATA FOR SAMPLE CLASHACH 7 SEGMENT 1

ABSOLUTE PRESSURE (PSIA)	RELATIVE SATURATION (%)	ABSOLUTE PRESSURE (PSIA)	RELATIVE SATURATION (%)
3.20	0.40	14.46	86.53
3.65	0.53	14.96	87.02
4.19	0.80	15.45	87.33
4.68	2.36	15.85	87.68
5.15	5.42	21.43	89.82
5.39	7.29	31.42	91.64
5.62	9.38	41.40	93.24
5.84	12.85	51.40	93.37
6.05	17.30	61.40	93.55
6.30	23.52	69.40	93.86
6.46	27.92	99.39	94.40
6.66	33.84	148.39	94.98
6.95	40.60	197.00	95.38
7.06	45.26	247.00	95.60
7.27	50.38	297.00	95.78
7.49	53.76	346.00	95.95
7.71	57.58	397.00	96.18
7.93	61.00	446.00	96.31
8.16	62.92	497.00	96.53
8.39	65.72	600.00	96.84
8.62	67.99	700.00	97.07
8.85	70.74	800.00	97.20
9.09	71.54	900.00	97.42
9.33	73.05	1000.00	97.51
9.57	74.21	1500.00	98.18
9.80	75.68	2000.00	98.62
10.04	76.75	2500.00	98.80
10.29	77.68	3000.00	98.89
10.53	78.57	3500.00	99.07
10.77	79.28	4000.00	99.24
11.02	80.08	4500.00	99.38
11.25	81.41	5000.00	99.51
11.50	81.55	5500.00	99.60
11.99	83.10	6000.00	99.78
12.48	84.17	6500.00	99.82
12.97	84.84	7000.00	99.87
13.47	85.37	8000.00	99.87
13.96	86.04	9000.00	99.96
14.46	86.53		

TABLE A6 MERCURY PENETRATION POROSIMETRY DATA FOR SAMPLE CLASHACH 7 SEGMENT 2

ABSOLUTE PRESSURE (PSIA)	RELATIVE SATURATION (%)	ABSOLUTE PRESSURE (PSIA)	RELATIVE SATURATION (%)
3.20	0.22	13.44	87.95
3.70	0.44	13.93	88.39
4.18	2.28	14.43	88.83
4.41	4.47	14.93	89.22
4.64	6.79	15.42	89.57
4.87	9.11	15.62	89.70
5.10	11.70	21.40	91.85
5.32	15.21	27.39	92.86
5.54	18.71	31.39	93.25
5.77	26.64	41.39	93.95
5.94	30.06	51.38	94.30
6.13	36.94	79.38	94.96
6.34	41.06	99.37	95.22
6.58	48.60	148.37	95.53
6.75	51.97	197.00	95.84
6.96	56.27	247.00	96.10
7.19	59.38	297.00	96.23
7.40	63.23	346.00	96.45
7.62	66.78	397.00	96.67
7.85	69.19	446.00	96.76
8.08	71.21	497.00	96.89
8.32	73.23	600.00	97.15
8.55	75.02	700.00	97.33
8.79	76.47	800.00	97.55
9.02	78.13	900.00	97.63
9.26	79.05	1000.00	97.85
9.50	80.19	1500.00	98.38
9.75	81.16	2000.00	98.73
9.99	81.68	2500.00	98.86
10.23	82.47	3000.00	98.95
10.48	83.09	3500.00	99.08
10.72	83.61	4000.00	99.26
10.97	84.27	4500.00	99.34
11.22	84.75	5000.00	99.34
11.46	85.19	5500.00	99.69
11.71	85.67	6000.00	99.87
11.95	86.06	6500.00	99.87
12.20	86.42	7000.00	99.96
12.45	86.72	8000.00	100.00
12.94	87.34	9000.00	100.00
13.44	87.95		

TABLE A7 MERCURY PENETRATION POROSIMETRY DATA FOR SAMPLE CLASHACH 7 SEGMENT 3

ABSOLUTE PRESSURE (PSIA)	RELATIVE SATURATION (%)	ABSOLUTE PRESSURE (PSIA)	RELATIVE SATURATION (%)
3.20	1.57	25.96	77.48
3.44	2.54	35.95	80.99
3.69	3.15	51.94	82.93
3.94	4.00	61.94	83.66
4.18	4.84	71.94	84.02
4.43	5.33	81.94	84.38
4.68	7.26	101.93	84.75
4.92	8.11	271.93	87.41
5.17	9.32	340.00	87.65
5.42	10.77	350.00	87.77
5.66	12.23	370.00	87.89
6.01	14.04	400.00	88.14
6.15	15.62	450.00	88.62
6.40	17.19	500.00	89.10
6.64	18.89	600.00	90.44
6.88	20.82	700.00	90.92
7.13	22.76	800.00	91.40
7.62	26.39	900.00	91.89
8.11	29.06	1000.00	92.25
8.60	31.84	1500.00	94.19
9.09	33.66	2000.00	95.28
9.59	36.32	2500.00	95.88
10.08	38.62	3000.00	96.61
10.57	40.68	3500.00	97.09
11.06	43.10	4000.00	97.46
11.55	46.49	4500.00	97.94
12.04	51.45	5000.00	98.43
12.53	54.24	5500.00	98.67
13.02	57.02	6000.00	98.79
13.51	59.93	6500.00	98.91
14.01	61.74	7000.00	99.15
14.50	63.56	7500.00	99.15
15.00	65.13	8000.00	99.39
15.49	66.34	8500.00	99.39
15.99	67.43	9000.00	99.64
16.09	68.40	9500.00	99.76
21.97	74.70	10000.00	100.00

TABLE A8 MERCURY PENETRATION POROSIMETRY DATA FOR SAMPLE CLASHACH 16 SEGMENT 1

ABSOLUTE PRESSURE (PSIA)	RELATIVE SATURATION (%)	ABSOLUTE PRESSURE (PSIA)	RELATIVE SATURATION (%)
4.20	2.43	15.13	91.75
4.44	6.80	16.53	92.23
6.19	8.74	32.13	93.20
6.44	14.08	52.13	93.69
6.69	16.50	100.13	94.17
6.93	24.76	249.13	94.66
7.17	37.86	497.00	95.15
7.41	48.54	750.00	95.63
7.66	56.80	1000.00	96.60
8.15	69.42	1500.00	97.57
8.39	73.30	2000.00	98.06
8.64	75.73	2500.00	98.06
9.14	79.13	3000.00	98.54
9.64	82.04	3500.00	98.54
10.13	83.98	4000.00	99.03
10.63	85.92	5000.00	99.03
11.13	87.38	6000.00	99.03
11.63	87.86	7000.00	99.03
12.13	88.83	8000.00	100.00
13.13	89.81	9000.00	100.00
14.13	90.78	10000.00	100.00

TABLE A9 MERCURY PENETRATION POROSIMETRY DATA FOR SAMPLE CLASHACH 16 SEGMENT 2

ABSOLUTE PRESSURE (PSIA)	RELATIVE SATURATION (%)	ABSOLUTE PRESSURE (PSIA)	RELATIVE SATURATION (%)
3.45	1.16	13.11	70.06
3.65	2.62	13.61	71.51
4.15	3.49	14.11	72.67
4.54	4.94	14.60	74.13
4.89	6.10	15.10	74.71
5.19	8.43	15.60	75.58
5.73	11.92	16.10	76.16
5.93	12.79	16.35	76.74
6.18	14.24	22.09	84.01
6.43	15.12	30.09	86.34
6.68	17.15	38.08	88.37
6.92	19.19	44.08	88.95
7.17	20.35	52.08	90.41
7.42	22.97	100.08	91.86
7.67	25.58	149.08	92.73
7.91	27.62	197.00	93.60
8.26	31.40	297.00	94.48
8.41	34.30	397.00	95.06
8.65	37.21	497.00	95.35
8.90	40.99	600.00	96.22
9.14	44.19	800.00	96.80
9.39	47.38	1000.00	97.38
9.64	49.13	1500.00	98.26
9.88	51.74	2000.00	99.13
10.13	54.36	2500.00	99.13
10.38	56.40	3000.00	99.13
10.62	58.14	3500.00	99.13
10.87	60.17	4000.00	99.42
11.12	62.21	5000.00	99.42
11.37	63.37	6000.00	99.42
11.62	64.24	7000.00	99.71
11.86	65.70	8000.00	100.00
12.11	66.28	9000.00	100.00
12.61	68.60	10000.00	100.00

TABLE A10 MERCURY PENETRATION POROSIMETRY DATA FOR SAMPLE CLASHACH 22 SEGMENT 1

ABSOLUTE PRESSURE (PSIA)	RELATIVE SATURATION (%)	ABSOLUTE PRESSURE (PSIA)	RELATIVE SATURATION (%)
3.20	0.16	13.38	88.53
3.45	0.33	13.87	89.10
3.69	0.57	14.37	89.59
3.94	0.73	14.86	90.00
4.19	0.90	15.36	90.73
4.44	1.22	15.65	90.81
4.78	1.80	21.33	93.06
4.97	3.14	25.32	94.24
5.15	5.72	31.32	94.90
5.41	9.84	51.30	96.24
5.56	14.58	61.30	96.45
5.81	20.17	69.30	96.61
6.00	26.87	79.30	96.77
6.15	32.09	89.30	96.86
6.43	39.53	99.29	97.26
6.55	42.71	148.29	97.47
6.76	47.69	227.00	97.51
6.96	52.27	247.00	97.55
7.17	56.51	277.00	97.67
7.43	60.80	317.00	97.75
7.62	62.76	346.00	97.84
7.88	66.15	387.00	97.88
8.16	68.60	417.00	97.96
8.30	70.23	468.00	98.08
8.52	72.60	600.00	98.20
8.76	74.11	800.00	98.29
8.99	75.87	1000.00	98.49
9.23	77.09	1500.00	98.65
9.47	78.64	2000.00	98.82
9.71	79.54	2500.00	99.02
9.95	80.73	3000.00	99.10
10.19	81.58	3500.00	99.18
10.43	82.48	4000.00	99.35
10.68	83.18	4500.00	99.47
10.92	84.20	5000.00	99.71
11.16	84.65	5500.00	99.92
11.65	85.59	6000.00	100.00
12.14	86.85	8500.00	100.00
12.39	87.18	9000.00	100.00
12.88	88.00	9500.00	100.00
13.38	88.53		

TABLE A11 MERCURY PENETRATION POROSIMETRY DATA FOR SAMPLE CLASHACH 22 SEGMENT 2

ABSOLUTE PRESSURE (PSIA)	RELATIVE SATURATION (%)	ABSOLUTE PRESSURE (PSIA)	RELATIVE SATURATION (%)
3.20	0.42	10.31	77.00
3.65	0.84	10.61	77.85
3.95	1.27	10.76	78.90
4.20	2.11	11.15	80.59
4.49	3.16	11.45	81.86
4.84	4.43	11.80	83.12
5.04	5.70	12.05	83.76
5.29	6.33	12.45	84.60
5.64	8.02	12.90	85.65
5.88	9.28	13.35	85.86
6.13	11.18	13.79	86.92
6.33	12.87	14.34	87.13
6.52	14.56	14.84	87.76
6.67	16.24	15.59	88.61
6.77	17.72	16.34	89.24
6.87	19.20	16.74	89.24
7.01	21.52	30.04	90.93
7.11	23.84	60.04	91.56
7.25	26.58	92.03	92.41
7.34	30.59	118.03	92.83
7.49	32.91	157.00	93.25
7.54	35.86	211.00	93.46
7.63	38.82	281.00	93.88
7.72	41.98	331.00	94.09
7.77	44.51	415.00	94.30
8.96	48.73	523.00	94.51
8.11	52.53	700.00	94.73
8.25	55.27	800.00	94.94
8.40	58.23	950.00	95.36
8.54	60.55	1300.00	95.57
8.69	62.45	1650.00	95.99
8.83	64.14	2050.00	95.99
8.98	65.82	2350.00	96.20
9.13	67.72	2850.00	99.37
9.28	68.78	4450.00	99.58
9.47	71.73	6050.00	99.58
9.72	73.63	7900.00	99.58
10.06	75.32	9600.00	100.00
10.31	77.00		

TABLE A12 MERCURY PENETRATION POROSIMETRY DATA FOR SAMPLE CLASHACH 22 SEGMENT 3

ABSOLUTE PRESSURE (PSIA)	RELATIVE SATURATION (%)	ABSOLUTE PRESSURE (PSIA)	RELATIVE SATURATION (%)
3.19	4.44	8.85	77.51
3.44	7.40	9.35	79.29
3.69	10.06	10.09	82.25
3.93	13.61	10.59	84.02
4.18	17.46	11.09	85.21
4.42	20.41	12.09	89.05
4.67	23.96	13.08	90.53
4.91	28.99	14.08	91.72
5.16	33.43	15.08	92.90
5.40	38.76	42.08	94.67
5.64	43.20	52.08	96.15
5.89	48.82	60.07	97.63
6.13	51.78	70.07	99.11
6.38	55.62	124.07	99.41
6.62	59.17	2550.00	99.41
6.87	63.02	3000.00	99.41
7.12	65.68	3500.00	99.41
7.36	67.46	4000.00	99.41
7.71	70.71	4700.00	99.41
7.91	71.89	5450.00	100.00
8.11	73.08	6300.00	100.00
8.35	75.15	7000.00	100.00
8.60	76.04	8500.00	100.00
8.85	77.51		

TABLE A13 MERCURY PENETRATION POROSIMETRY DATA FOR SAMPLE CLASHACH 24 SEGMENT 1

ABSOLUTE PRESSURE (PSIA)	RELATIVE SATURATION (%)	ABSOLUTE PRESSURE (PSIA)	RELATIVE SATURATION (%)
3.20	1.73	14.04	74.96
3.54	2.94	14.53	75.30
3.79	4.49	15.03	75.99
3.94	6.39	15.53	76.34
4.17	11.40	16.03	76.86
4.42	15.03	16.43	77.55
4.67	15.89	22.03	79.10
4.91	20.03	32.02	82.21
5.15	22.28	42.02	83.42
5.39	25.73	52.01	88.43
5.64	28.67	100.00	89.81
5.88	31.95	149.00	90.50
6.12	35.23	197.00	90.85
6.36	39.03	247.00	91.19
6.61	42.49	297.00	91.54
6.85	46.11	346.00	91.88
7.09	48.36	397.00	92.23
7.34	50.60	497.00	92.57
7.58	54.06	600.00	93.26
7.83	55.96	800.00	94.30
8.07	57.86	1000.00	94.99
8.32	59.59	1500.00	96.20
8.56	61.49	2000.00	97.06
8.81	62.69	2500.00	97.24
9.06	63.90	3500.00	97.93
9.31	64.25	4000.00	98.45
9.56	64.59	4300.00	98.79
10.05	66.49	4500.00	99.31
10.55	68.22	5000.00	99.31
11.05	69.26	5400.00	99.48
11.54	70.47	6000.00	99.48
12.04	71.68	7000.00	99.65
12.54	72.71	8000.00	99.83
13.04	73.75	9000.00	100.00
13.54	74.27	10000.00	100.00

TABLE A14 MERCURY PENETRATION POROSIMETRY DATA FOR SAMPLE CLASHACH 24 SEGMENT 2

ABSOLUTE PRESSURE (PSIA)	RELATIVE SATURATION (%)	ABSOLUTE PRESSURE (PSIA)	RELATIVE SATURATION (%)
3.19	6.16	10.27	81.51
3.44	6.68	11.02	82.02
3.68	8.39	11.52	82.53
3.93	9.08	12.02	82.88
4.18	10.79	13.02	83.22
4.42	13.87	14.01	83.90
4.66	17.64	15.41	84.25
4.90	21.23	16.31	84.59
5.14	25.68	22.01	85.79
5.38	31.85	26.01	86.30
5.62	37.16	51.98	98.29
5.85	44.69	99.98	98.97
6.09	51.71	498.98	99.32
6.32	56.51	800.00	99.49
6.56	61.47	1200.00	99.66
6.80	65.41	1700.00	100.00
7.05	68.66	2100.00	100.00
7.29	71.06	2700.00	100.00
7.54	72.95	3200.00	100.00
7.79	74.32	3700.00	100.00
8.03	75.68	4200.00	100.00
8.28	76.71	4900.00	100.00
8.53	77.74	5300.00	100.00
8.78	78.42	6300.00	100.00
9.02	79.28	7000.00	100.00
9.27	79.62	7800.00	100.00
9.52	80.31	8400.00	100.00
9.82	80.82	9200.00	100.00
10.27	81.51		

TABLE A15 MERCURY PENETRATION POROSIMETRY DATA FOR SAMPLE C071515AA-5 SECTION 1

ABSOLUTE PRESSURE (PSIA)	RELATIVE SATURATION (%)	ABSOLUTE PRESSURE (PSIA)	RELATIVE SATURATION (%)
3.20	0.00	22.12	49.88
3.70	0.73	32.08	75.06
4.20	1.21	42.06	87.89
4.70	1.94	52.06	89.10
5.20	2.66	80.06	90.31
5.94	3.87	100.06	92.25
6.19	4.60	149.05	93.46
6.44	5.08	197.00	94.92
6.69	6.05	297.00	97.09
7.44	7.99	1200.00	97.34
7.69	8.96	1650.00	97.34
8.18	10.90	1800.00	97.34
8.68	13.56	2200.00	97.58
9.18	15.01	2600.00	97.58
10.17	21.79	3100.00	98.06
10.66	25.18	3500.00	98.06
11.40	30.27	3800.00	98.55
12.15	34.62	4300.00	98.79
12.64	37.29	4750.00	99.03
13.14	38.74	5200.00	99.27
13.64	40.68	5800.00	99.52
14.13	42.86	6250.00	99.76
14.73	45.28	7000.00	99.76
15.13	46.73	7600.00	100.00
15.62	48.18	8500.00	100.00
15.87	48.91	9300.00	100.00

TABLE A16 MERCURY PENETRATION POROSIMETRY DATA FOR SAMPLE C071515AA-5 SECTION 3

ABSOLUTE PRESSURE (PSIA)	RELATIVE SATURATION (%)	ABSOLUTE PRESSURE (PSIA)	RELATIVE SATURATION (%)
3.20	0.36	14.12	37.72
3.70	1.07	14.62	39.32
4.20	1.96	15.11	41.46
4.69	3.20	15.61	43.06
5.44	3.91	16.10	44.66
5.69	4.09	16.60	48.93
5.94	5.34	28.04	75.09
6.69	6.23	32.03	80.96
7.08	7.30	70.02	82.56
7.43	8.54	100.02	84.16
7.68	9.43	149.02	86.48
8.17	12.81	197.00	89.68
8.42	13.70	247.00	92.70
8.67	14.59	297.00	95.73
8.92	15.48	397.00	96.44
9.17	16.37	497.00	96.80
9.41	17.44	700.00	97.33
9.91	19.57	900.00	98.04
10.16	20.64	1100.00	98.40
10.40	21.89	1500.00	98.93
10.65	23.13	2000.00	99.29
10.90	24.02	2500.00	99.29
11.15	25.27	3000.00	99.64
11.39	26.16	3500.00	99.64
11.64	27.22	4000.00	99.64
11.89	28.65	5000.00	100.00
12.14	29.72	6000.00	100.00
12.63	31.85	7000.00	100.00
13.13	34.16	8000.00	100.00
13.62	35.94	9000.00	100.00
14.12	37.72		

TABLE A17 MERCURY PENETRATION POROSIMETRY DATA FOR SAMPLE C181515AA-11 SECTION 1

ABSOLUTE PRESSURE (PSIA)	RELATIVE SATURATION (%)	ABSOLUTE PRESSURE (PSIA)	RELATIVE SATURATION (%)
3.20	1.09	16.60	55.56
4.45	1.74	22.08	69.72
5.45	2.18	32.06	82.35
5.95	2.83	42.05	86.06
6.69	3.49	120.04	90.85
7.19	4.79	147.00	91.50
7.69	6.10	197.00	92.16
8.18	10.24	247.00	92.59
8.43	10.89	267.00	95.21
8.68	11.55	356.00	95.64
8.93	12.64	476.00	96.51
9.18	13.07	700.00	96.95
9.42	14.38	800.00	97.60
9.67	15.25	900.00	98.26
9.92	15.69	1000.00	98.47
10.42	17.65	1500.00	98.91
10.67	19.17	2000.00	99.56
11.41	22.22	2500.00	99.56
11.66	23.97	3000.00	99.56
12.15	26.80	3500.00	99.56
12.65	30.50	4000.00	100.00
13.14	33.77	4500.00	100.00
13.64	37.25	5000.00	100.00
14.13	40.31	6000.00	100.00
14.63	42.92	7000.00	100.00
15.12	46.84	8000.00	100.00
15.61	49.46	9000.00	100.00
16.11	51.63	10000.00	100.00

TABLE A18 MERCURY PENETRATION POROSIMETRY DATA FOR SAMPLE C181515AA-11 SECTION 4

ABSOLUTE PRESSURE (PSIA)	RELATIVE SATURATION (%)	ABSOLUTE PRESSURE (PSIA)	RELATIVE SATURATION (%)
3.20	0.79	14.95	86.11
4.20	1.32	15.45	87.17
5.19	1.85	15.95	88.23
5.69	2.38	16.39	89.02
5.94	3.04	47.94	89.29
6.44	4.63	51.94	90.08
6.68	6.48	79.94	91.27
6.93	7.80	99.94	91.67
7.17	8.73	128.93	92.33
7.42	9.79	147.00	92.72
7.67	11.90	197.00	93.25
7.91	14.15	247.00	93.52
8.15	16.53	297.00	94.05
8.39	19.31	397.00	94.44
8.88	25.66	497.00	94.84
9.12	28.44	600.00	95.24
9.35	33.60	700.00	95.50
9.59	36.90	800.00	95.90
9.83	41.67	1000.00	96.30
10.07	46.03	1500.00	97.09
10.31	50.40	2000.00	97.62
10.55	53.84	2500.00	97.88
11.02	61.38	3000.00	98.15
11.27	63.62	3500.00	98.41
11.51	67.06	4000.00	98.54
11.75	69.05	4500.00	98.81
11.99	71.56	5000.00	98.81
12.24	73.28	5500.00	99.21
12.73	76.32	6000.00	99.34
12.97	78.84	6500.00	99.34
13.47	80.56	7000.00	99.60
13.96	82.80	8000.00	99.74
14.46	84.52	9000.00	99.87
14.95	86.11		

TABLE A19 MERCURY PENETRATION POROSIMETRY DATA FOR SAMPLE C221515BB-7 SECTION 1

ABSOLUTE PRESSURE (PSIA)	RELATIVE SATURATION (%)	ABSOLUTE PRESSURE (PSIA)	RELATIVE SATURATION (%)
3.20	0.00	14.16	44.66
3.70	1.15	14.65	46.56
4.20	1.91	15.15	47.71
4.70	3.05	15.65	49.24
5.20	4.58	16.15	51.15
5.69	6.49	16.65	52.67
6.19	8.40	22.15	54.58
6.69	11.07	32.13	67.18
7.19	12.98	42.12	80.15
7.68	15.65	52.11	93.51
8.18	17.56	60.10	95.80
8.68	20.99	100.10	97.33
9.18	23.28	199.10	98.47
9.43	24.81	1150.00	98.85
9.67	25.95	2000.00	98.85
9.92	27.10	2500.00	98.85
10.42	29.01	2800.00	98.85
10.67	29.77	3600.00	98.85
10.92	31.30	4400.00	98.85
11.17	32.44	5200.00	98.85
11.42	34.35	5800.00	98.85
11.66	35.88	6450.00	98.85
12.16	38.17	7050.00	98.85
12.66	39.69	7700.00	98.85
13.16	41.60	7150.00	100.00
13.66	43.13	8950.00	100.00
14.16	44.66		

TABLE A20 MERCURY PENETRATION POROSIMETRY DATA FOR SAMPLE C221515BB-7 SECTION 4

ABSOLUTE PRESSURE (PSIA)	RELATIVE SATURATION (%)	ABSOLUTE PRESSURE (PSIA)	RELATIVE SATURATION (%)
3.20	0.18	12.33	55.63
3.45	0.53	12.58	56.87
3.70	0.88	12.82	58.10
3.95	1.06	13.07	59.51
4.45	1.58	13.32	60.74
4.70	2.11	13.57	61.80
4.94	2.82	13.81	63.20
5.19	3.35	14.06	64.26
5.44	4.23	14.31	65.14
5.69	4.93	14.56	66.90
5.94	5.63	14.80	67.78
6.19	6.87	15.05	69.01
6.43	8.80	15.30	69.72
6.68	10.04	15.55	70.95
6.92	13.03	16.04	71.83
7.17	14.26	22.04	73.94
7.42	15.67	32.03	76.76
7.66	18.13	52.02	82.57
8.15	23.42	100.01	88.20
8.44	26.06	149.00	92.61
8.64	27.82	197.00	98.77
8.89	30.11	650.00	98.94
9.13	32.39	1100.00	99.30
9.37	34.86	1400.00	99.47
9.62	36.27	2000.00	99.65
9.87	39.26	2400.00	99.65
10.11	41.20	3300.00	99.82
10.36	43.13	3700.00	99.82
10.60	45.25	4500.00	99.82
10.85	46.83	5200.00	99.82
11.10	48.24	5900.00	100.00
11.34	49.82	6800.00	100.00
11.59	51.41	8000.00	100.00
12.08	54.40	9100.00	100.00
12.33	55.63		

TABLE A21 MERCURY PENETRATION POROSIMETRY DATA FOR SAMPLE C221515CC-3 SECTION 1

ABSOLUTE PRESSURE (PSIA)	RELATIVE SATURATION (%)	ABSOLUTE PRESSURE (PSIA)	RELATIVE SATURATION (%)
3.20	0.00	2050.00	88.59
5.95	3.36	2200.00	88.59
8.30	6.04	2600.00	89.26
9.00	7.38	3150.00	89.93
10.55	8.72	3600.00	90.60
11.49	10.07	4100.00	91.28
12.64	11.41	4500.00	91.95
16.34	12.08	5050.00	92.62
26.19	16.78	5400.00	92.62
32.18	28.19	5900.00	93.96
42.18	41.61	6000.00	93.96
52.16	64.43	6200.00	94.63
80.16	75.84	6300.00	95.30
110.15	79.87	6500.00	95.97
137.00	81.21	7000.00	95.97
167.00	81.88	7400.00	95.97
207.00	83.22	7500.00	96.64
297.00	83.89	7800.00	96.64
466.00	84.56	7900.00	97.32
600.00	85.23	8100.00	97.32
750.00	85.91	8200.00	97.99
950.00	86.58	8650.00	97.99
1300.00	86.58	8750.00	98.66
1450.00	87.25	9050.00	99.33
1600.00	87.92	9600.00	100.00
1800.00	87.92	9850.00	100.00

TABLE A22 MERCURY PENETRATION POROSIMETRY DATA FOR SAMPLE C221515CC-3 SECTION 4

ABSOLUTE PRESSURE (PSIA)	RELATIVE SATURATION (%)	ABSOLUTE PRESSURE (PSIA)	RELATIVE SATURATION (%)
3.20	0.00	11.78	73.85
3.70	0.49	12.02	77.30
3.95	0.99	12.27	78.62
4.79	2.30	12.76	83.55
5.34	2.80	13.01	84.21
5.54	3.45	13.49	88.98
5.69	3.78	13.99	90.79
5.94	4.77	14.49	92.93
6.19	5.43	14.98	94.57
6.43	6.58	15.48	95.56
6.68	7.73	15.98	96.88
6.93	9.05	16.28	97.20
7.18	10.20	2001.97	97.20
7.42	11.68	2200.00	97.20
7.67	13.32	2600.00	97.20
7.91	16.28	3000.00	97.53
8.15	21.05	3450.00	97.70
8.39	24.18	3800.00	98.19
8.64	27.96	4200.00	98.36
8.87	33.06	4600.00	98.52
9.11	37.83	5000.00	98.52
9.84	47.70	5500.00	98.85
10.08	50.82	6000.00	98.85
10.37	54.93	6500.00	99.01
10.57	57.89	7200.00	99.18
11.05	66.78	7800.00	99.34
11.29	69.90	8300.00	99.51
11.53	72.53	9100.00	100.00
11.78	73.85		

TABLE A23 MERCURY PENETRATION POROSIMETRY DATA FOR SAMPLE C221515DD-1 SECTION 1

ABSOLUTE PRESSURE (PSIA)	RELATIVE SATURATION (%)	ABSOLUTE PRESSURE (PSIA)	RELATIVE SATURATION (%)
3.20	0.00	217.00	92.58
5.20	0.97	247.00	93.23
7.95	1.94	297.00	93.87
8.60	3.23	397.00	94.52
9.19	5.16	497.00	94.84
9.69	6.77	600.00	95.48
10.69	10.00	700.00	96.13
11.94	11.29	800.00	96.45
13.18	19.03	1000.00	96.77
13.67	24.19	1500.00	97.74
14.17	26.77	2000.00	98.71
14.67	28.71	2500.00	98.71
15.16	31.61	3000.00	98.71
15.66	35.48	3500.00	98.71
16.15	38.71	4000.00	99.68
16.50	40.97	4500.00	99.68
24.13	56.13	5000.00	100.00
34.11	75.48	6000.00	100.00
42.10	82.90	7000.00	100.00
60.10	86.45	8000.00	100.00
110.09	90.00	9000.00	100.00
147.00	91.61	10000.00	100.00

TABLE A24 MERCURY PENETRATION POROSIMETRY DATA FOR SAMPLE C221515DD-1 SECTION 4

ABSOLUTE PRESSURE (PSIA)	RELATIVE SATURATION (%)	ABSOLUTE PRESSURE (PSIA)	RELATIVE SATURATION (%)
3.20	0.00	6.75	46.39
1.75	1.90	7.00	49.05
2.00	4.18	7.25	51.71
2.50	6.46	7.50	53.99
3.00	7.98	8.00	57.41
3.50	11.79	8.50	64.26
4.00	17.87	9.00	71.10
4.50	24.33	9.50	77.57
5.00	28.90	10.00	81.75
5.25	30.80	10.50	86.31
5.50	34.22	11.00	88.59
5.75	36.12	12.00	93.16
6.00	39.16	13.00	96.20
6.25	41.44	14.00	98.86
6.50	44.11	14.30	100.00

TABLE A25 MERCURY PENETRATION POROSIMETRY DATA FOR SAMPLE C221515EE-1 SECTION 1

ABSOLUTE PRESSURE (PSIA)	RELATIVE SATURATION (%)	ABSOLUTE PRESSURE (PSIA)	RELATIVE SATURATION (%)
3.20	0.00	15.14	43.79
3.70	0.89	15.64	46.15
4.20	1.78	16.24	50.00
4.70	2.66	22.13	52.66
5.85	3.55	32.10	77.22
6.19	4.44	42.09	86.98
6.44	5.03	100.08	91.12
6.79	5.62	149.08	92.01
6.94	6.21	197.00	92.90
7.19	6.80	247.00	93.49
7.44	7.69	347.00	94.08
7.69	8.58	446.00	94.38
7.94	9.47	600.00	94.67
8.29	10.65	700.00	95.27
8.49	11.24	900.00	95.56
8.68	12.72	1000.00	95.86
8.93	13.91	1500.00	96.45
9.18	14.79	2000.00	96.75
9.43	15.38	2500.00	97.04
9.68	17.16	3000.00	97.34
9.93	18.05	3500.00	97.34
10.43	19.23	4000.00	97.63
10.67	21.30	4500.00	97.93
11.37	25.15	5000.00	98.22
12.16	29.88	5500.00	98.52
12.66	32.54	6000.00	98.52
13.16	34.91	6500.00	98.52
13.75	37.87	7000.00	98.52
14.15	39.64	8000.00	99.41
14.75	42.01	9000.00	99.41
15.14	43.79		

TABLE A26 MERCURY PENETRATION POROSIMETRY DATA FOR SAMPLE C221515EE-1 SECTION 4

ABSOLUTE PRESSURE (PSIA)	RELATIVE SATURATION (%)	ABSOLUTE PRESSURE (PSIA)	RELATIVE SATURATION (%)
3.20	0.00	13.60	93.29
4.55	1.41	14.10	94.70
5.35	3.89	14.60	95.76
5.54	4.95	15.10	96.82
5.69	6.01	15.59	98.23
5.99	8.13	16.39	99.29
6.19	9.54	3502.09	99.29
6.44	11.66	3700.00	99.29
6.68	14.49	3800.00	99.29
6.98	18.02	4000.00	99.29
7.18	19.79	4400.00	99.29
7.42	23.67	4650.00	99.29
7.77	27.56	4900.00	99.29
8.01	33.92	5200.00	99.29
8.45	43.82	5500.00	99.29
8.65	47.70	5800.00	99.29
8.89	53.36	6100.00	99.29
9.14	57.60	6300.00	99.29
9.38	61.48	6600.00	99.29
9.73	66.43	6800.00	99.29
9.92	69.96	7300.00	99.29
10.12	72.08	7500.00	99.65
10.37	75.27	7900.00	99.65
10.62	77.03	8200.00	99.65
11.11	81.98	8600.00	99.65
11.61	85.16	8900.00	99.65
12.11	87.99	9300.00	99.65
12.60	90.11	9600.00	100.00
13.10	91.87	9800.00	100.00

TABLE A27 MERCURY PENETRATION POROSIMETRY DATA FOR SAMPLE C1644EE-12 SECTION 1

ABSOLUTE PRESSURE (PSIA)	RELATIVE SATURATION (%)	ABSOLUTE PRESSURE (PSIA)	RELATIVE SATURATION (%)
3.20	0.00	70.12	90.08
4.45	0.41	80.12	92.15
5.20	0.83	100.11	93.39
5.70	2.48	149.11	94.63
7.20	5.37	207.00	95.04
10.19	7.85	247.00	95.45
10.94	9.09	446.00	95.87
12.44	10.74	600.00	96.69
12.69	12.40	800.00	97.52
13.19	14.05	1000.00	97.93
13.69	15.70	1500.00	98.76
14.18	17.77	2000.00	100.00
14.68	20.66	2500.00	100.00
15.18	24.79	3000.00	100.00
15.68	26.03	4000.00	100.00
16.17	28.10	5000.00	100.00
16.67	28.93	6000.00	100.00
28.16	40.50	7000.00	100.00
32.15	52.07	8000.00	100.00
42.13	71.07	9000.00	100.00
60.12	87.60	10000.00	100.00

TABLE A28 MERCURY PENETRATION POROSIMETRY DATA FOR SAMPLE C1644EE-12 SECTION 4

ABSOLUTE PRESSURE (PSIA)	RELATIVE SATURATION (%)	ABSOLUTE PRESSURE (PSIA)	RELATIVE SATURATION (%)
3.20	0.00	11.67	82.22
4.45	5.56	13.67	87.78
5.20	11.11	14.77	93.33
5.49	17.78	15.67	100.00
6.19	26.67	8402.17	100.00
6.44	32.22	9500.00	100.00
7.19	42.22	9600.00	100.00
8.48	48.89	9700.00	100.00
9.43	54.44	9800.00	100.00
10.28	63.33	9900.00	100.00
11.17	81.11	10000.00	100.00

TABLE A29 MERCURY PENETRATION POROSIMETRY DATA FOR SAMPLE C167.57.5FF-4 SECTION 1

ABSOLUTE PRESSURE (PSIA)	RELATIVE SATURATION (%)	ABSOLUTE PRESSURE (PSIA)	RELATIVE SATURATION (%)
3.20	0.00	16.75	71.19
4.55	4.52	30.14	83.05
6.79	7.91	40.14	85.88
7.54	9.04	52.14	88.14
8.29	10.17	100.14	89.83
9.34	12.43	149.14	90.96
9.69	14.12	197.00	92.09
9.99	15.25	297.00	93.22
10.44	18.08	497.00	94.92
10.68	26.55	700.00	96.05
10.93	32.20	1000.00	96.61
11.18	35.59	1500.00	98.87
11.47	38.98	2000.00	99.44
11.67	40.68	2500.00	99.44
11.92	44.07	3000.00	100.00
12.42	46.89	3500.00	100.00
12.67	49.72	4000.00	100.00
13.16	53.67	4500.00	100.00
13.71	57.06	5000.00	100.00
14.16	59.32	6000.00	100.00
14.66	62.71	7000.00	100.00
15.16	64.97	8000.00	100.00
15.65	67.23	9000.00	100.00
16.15	68.93	10000.00	100.00

TABLE A30 MERCURY PENETRATION POROSIMETRY DATA FOR SAMPLE C167.57.5FF-4 SECTION 4

ABSOLUTE PRESSURE (PSIA)	RELATIVE SATURATION (%)	ABSOLUTE PRESSURE (PSIA)	RELATIVE SATURATION (%)
3.20	0.34	13.53	78.25
3.80	0.68	14.02	79.79
4.05	0.86	14.52	80.82
4.55	1.54	15.02	82.02
4.90	1.88	15.52	83.05
5.10	2.23	16.01	83.73
5.44	2.57	16.61	84.42
5.84	3.42	26.00	89.04
5.94	5.31	32.00	90.41
6.44	6.34	42.00	91.27
6.68	7.88	148.99	94.01
6.93	9.76	197.00	94.52
7.17	12.84	247.00	94.86
7.41	16.27	297.00	95.21
7.66	18.49	346.00	95.38
7.90	21.58	397.00	95.72
8.14	25.51	497.00	96.06
8.38	31.51	600.00	96.40
8.62	34.25	700.00	96.75
8.86	40.24	800.00	97.09
9.10	44.69	1000.00	97.43
9.34	47.60	1500.00	98.29
9.58	52.91	2000.00	98.80
9.83	55.82	2500.00	98.80
10.07	58.56	3000.00	99.14
10.31	61.13	2500.00	99.66
10.56	63.53	4000.00	99.66
10.80	65.41	4500.00	99.66
11.05	66.78	5000.00	99.66
11.30	69.35	6000.00	99.66
11.54	70.72	7000.00	99.66
12.04	72.77	8000.00	100.00
12.53	74.66	9000.00	100.00
13.03	76.54	10000.00	100.00

TABLE A31 MERCURY PENETRATION POROSIMETRY DATA FOR SAMPLE C247.57.5II-1 SECTION 1

ABSOLUTE PRESSURE (PSIA)	RELATIVE SATURATION (%)	ABSOLUTE PRESSURE (PSIA)	RELATIVE SATURATION (%)
3.20	1.52	4000.00	83.33
3.70	7.58	4400.00	84.85
4.25	10.61	4800.00	86.36
4.75	15.15	5200.00	86.36
5.94	22.73	5500.00	87.88
6.29	31.82	5900.00	89.39
6.44	36.36	6200.00	89.39
6.69	42.42	6500.00	89.39
6.94	46.97	6900.00	90.91
7.29	53.03	7000.00	92.42
7.78	60.61	7100.00	93.94
8.18	65.15	7200.00	93.94
8.68	69.70	7500.00	95.45
9.18	74.24	7800.00	95.45
10.78	80.30	8100.00	96.97
2102.18	80.30	8500.00	96.97
2500.00	80.30	9000.00	98.48
2900.00	81.82	9300.00	98.48
3700.00	81.82	9600.00	100.00
4000.00	83.33		

TABLE A32 MERCURY PENETRATION POROSIMETRY DATA FOR SAMPLE C247.57.5II-1 SECTION 4

ABSOLUTE PRESSURE (PSIA)	RELATIVE SATURATION (%)	ABSOLUTE PRESSURE (PSIA)	RELATIVE SATURATION (%)
3.20	0.00	14.15	84.94
3.45	3.61	15.15	86.14
3.95	7.23	16.74	87.35
4.44	10.84	36.14	87.95
4.94	15.06	42.14	90.96
5.29	19.88	279.14	91.57
5.53	24.70	600.00	92.77
5.68	28.92	900.00	93.37
5.93	33.73	1200.00	93.98
6.17	42.17	1600.00	94.58
6.42	49.40	1900.00	95.18
6.76	56.02	2200.00	95.18
6.91	59.64	2800.00	95.78
7.16	62.05	3100.00	95.78
7.41	65.06	3400.00	96.39
7.66	67.47	3700.00	96.99
7.91	69.28	4000.00	96.99
8.16	71.08	4600.00	96.99
8.40	72.89	4800.00	96.99
8.65	74.10	5300.00	97.59
8.90	74.70	5700.00	97.59
9.15	75.90	6500.00	97.59
9.65	78.31	6900.00	97.59
10.15	79.52	7200.00	97.59
10.65	80.72	7700.00	98.19
11.65	82.53	8400.00	98.19
12.15	83.13	8900.00	100.00
13.15	84.34	9600.00	100.00

TABLE A33 MERCURY PENETRATION POROSIMETRY DATA FOR SAMPLE C247.57.5JJ-2 SECTION 1

ABSOLUTE PRESSURE (PSIA)	RELATIVE SATURATION (%)	ABSOLUTE PRESSURE (PSIA)	RELATIVE SATURATION (%)
3.20	0.00	702.15	88.96
4.30	3.90	1100.00	90.26
5.20	7.14	1400.00	90.26
6.19	10.39	1800.00	90.91
6.79	13.64	2100.00	91.56
7.29	16.88	2300.00	91.56
7.69	21.43	2600.00	91.56
8.18	25.97	2700.00	92.21
8.68	31.82	3400.00	92.86
9.18	37.66	4000.00	92.86
9.67	44.16	4300.00	92.86
10.17	51.30	4750.00	93.51
10.67	56.49	5400.00	94.81
11.17	58.44	6000.00	94.81
11.66	62.99	6300.00	95.45
12.16	64.94	6500.00	96.10
12.76	66.88	7000.00	97.40
13.26	68.18	7100.00	98.05
13.66	69.48	8000.00	98.05
14.16	70.13	8200.00	98.05
15.16	71.43	8500.00	98.70
16.16	72.08	9300.00	98.70
16.75	87.01	10000.00	100.00

TABLE A34 MERCURY PENETRATION POROSIMETRY DATA FOR SAMPLE C247.57.5JJ-2 SECTION 4

ABSOLUTE PRESSURE (PSIA)	RELATIVE SATURATION (%)	ABSOLUTE PRESSURE (PSIA)	RELATIVE SATURATION (%)
3.20	3.21	11.13	82.11
4.19	7.80	11.38	83.94
4.69	12.84	11.63	85.32
5.19	16.06	11.88	86.70
5.93	20.64	12.13	88.53
6.28	24.31	12.63	89.91
6.48	26.61	13.12	92.20
6.68	29.36	13.62	93.58
6.97	33.03	14.12	94.95
7.17	36.24	14.62	95.87
7.51	44.95	15.12	97.25
7.66	46.79	15.62	97.71
7.91	48.62	16.12	98.62
8.16	51.38	16.62	100.00
8.41	53.21	5502.12	100.00
8.70	55.96	6100.00	100.00
8.90	56.42	6700.00	100.00
9.40	61.93	7200.00	100.00
9.65	64.68	7700.00	100.00
9.89	67.89	8100.00	100.00
10.14	70.64	8500.00	100.00
10.39	73.85	9100.00	100.00
10.74	77.06	9300.00	100.00
10.93	79.36	9700.00	100.00

TABLE A35 MERCURY PENETRATION POROSIMETRY DATA FOR SAMPLE C247.57.5KK-2 SECTION 1

ABSOLUTE PRESSURE (PSIA)	RELATIVE SATURATION (%)	ABSOLUTE PRESSURE (PSIA)	RELATIVE SATURATION (%)
3.20	0.00	15.54	78.81
3.70	0.74	16.04	80.67
4.20	1.49	16.58	82.53
4.69	3.35	22.02	89.41
5.19	6.88	32.01	92.57
5.43	8.74	42.01	93.68
5.67	13.75	52.01	94.61
5.92	15.24	100.00	95.91
6.16	17.66	149.00	96.28
6.41	20.07	197.00	96.65
6.65	22.49	247.00	96.84
6.90	24.35	267.00	97.03
7.15	26.39	356.00	97.21
7.39	28.62	489.00	97.58
7.64	30.86	600.00	97.77
7.88	33.09	700.00	97.96
8.42	37.55	800.00	98.14
8.72	39.78	1000.00	98.51
9.21	43.68	1500.00	98.70
9.60	46.84	2000.00	99.44
10.10	50.74	2500.00	99.44
10.59	54.46	3000.00	99.63
11.08	57.62	3500.00	99.63
11.58	60.97	4000.00	99.81
12.07	63.75	4500.00	99.81
12.56	66.73	5000.00	99.81
13.06	68.96	5500.00	99.81
13.55	71.56	6000.00	100.00
14.05	73.79	7000.00	100.00
14.54	76.02	8000.00	100.00
15.04	77.88	9000.00	100.00
15.54	78.81		

TABLE A36 MERCURY PENETRATION POROSIMETRY DATA FOR SAMPLE C247.57.5KK-2 SECTION 4

ABSOLUTE PRESSURE (PSIA)	RELATIVE SATURATION (%)	ABSOLUTE PRESSURE (PSIA)	RELATIVE SATURATION (%)
3.20	1.75	15.11	84.91
3.45	3.51	16.11	85.96
3.69	5.26	16.36	86.32
3.94	7.02	22.10	88.77
4.19	9.47	32.10	90.18
4.49	11.93	42.10	91.23
4.68	16.14	52.10	91.93
4.93	18.95	100.10	92.63
5.28	21.75	149.10	92.98
5.42	23.51	197.00	93.33
5.67	26.32	257.00	93.68
5.92	27.37	346.00	94.04
6.17	31.58	487.00	94.39
6.41	33.68	600.00	94.74
6.66	36.14	700.00	95.09
6.91	38.60	800.00	95.44
7.16	41.40	1000.00	96.49
7.40	44.56	1500.00	97.19
7.65	48.07	2000.00	98.25
7.89	51.93	2300.00	98.60
8.14	54.74	2600.00	98.60
8.39	58.60	3000.00	98.60
8.73	62.11	3300.00	98.95
9.13	66.67	3700.00	98.95
9.63	69.12	4200.00	99.30
10.12	72.98	4500.00	99.65
10.62	75.09	5000.00	99.65
11.12	77.54	5300.00	99.65
11.61	78.95	6000.00	99.65
12.11	80.35	6500.00	100.00
12.61	81.40	7000.00	100.00
13.11	82.11	8000.00	100.00
13.61	83.16	9000.00	100.00
14.86	84.21	10000.00	100.00

Figure A5.2a EXPERIMENT C141515AA-2
SECTION PERMEABILITIES SUPERSATURATION = 70.0

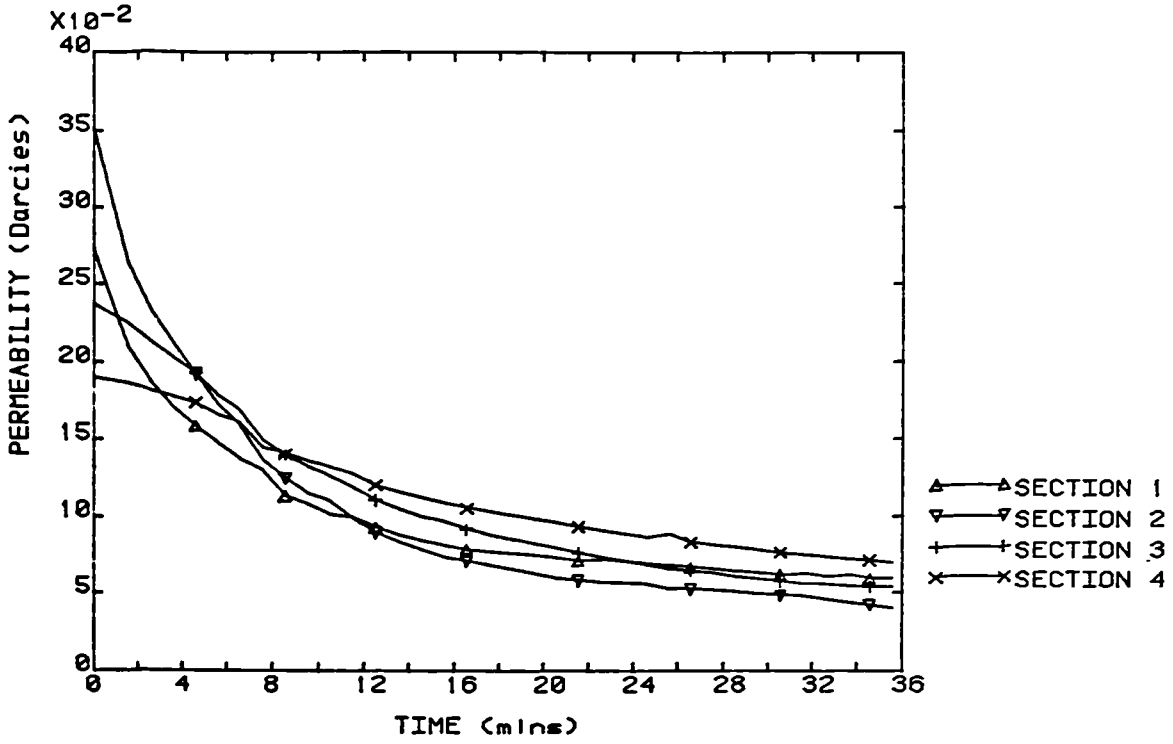

Figure A5.2b EXPERIMENT C141515AA-2
OVERALL PERMEABILITY SUPERSATURATION = 70.0

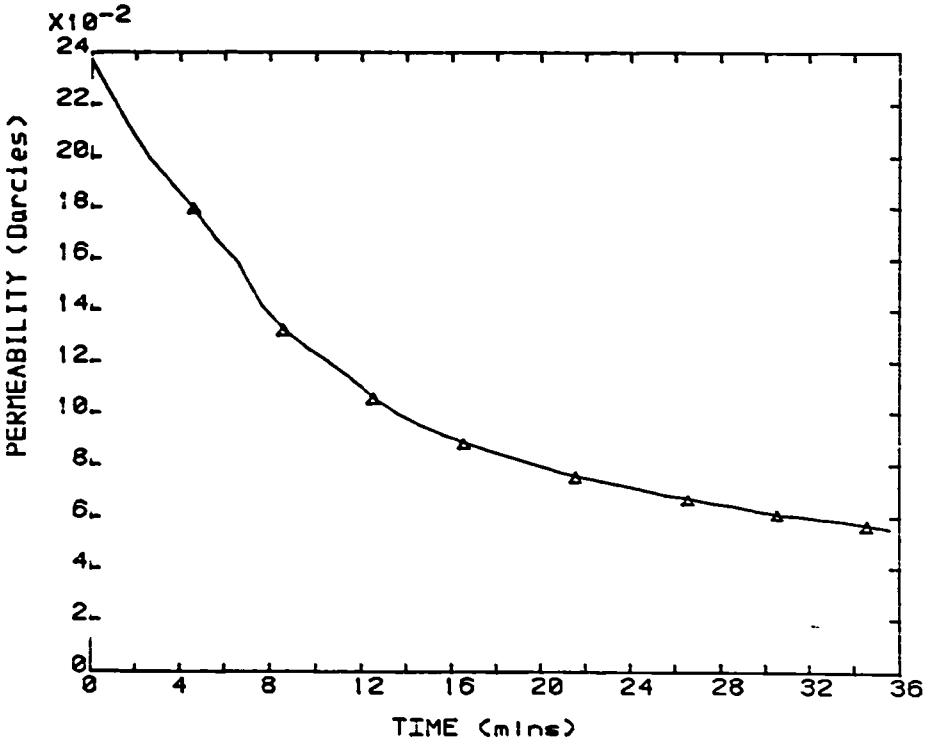

Figure A5.5a EXPERIMENT C071515AA-5
SECTION PERMEABILITIES SUPERSATURATION = 70.0

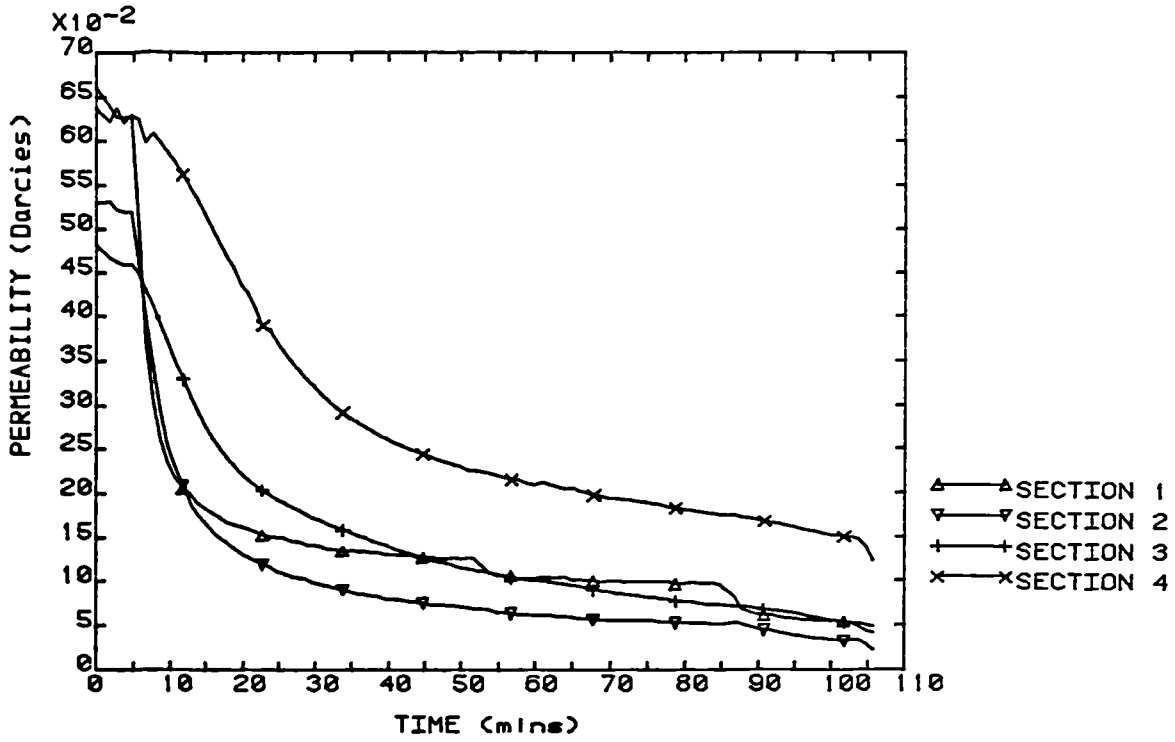

Figure A5.5b EXPERIMENT C071515AA-5
OVERALL PERMEABILITY SUPERSATURATION =70.0

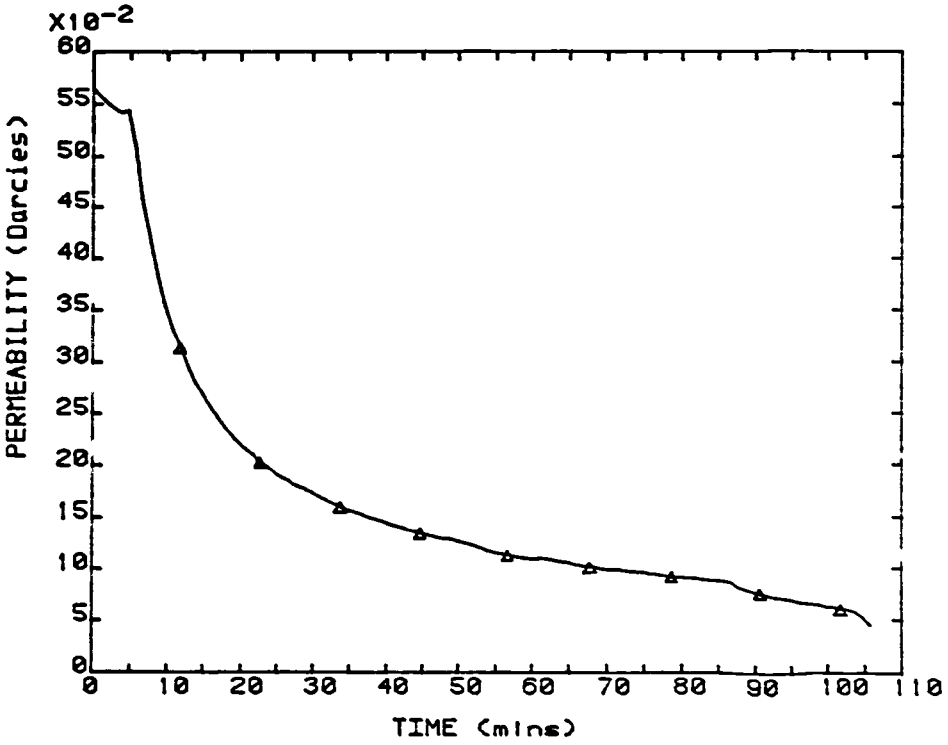

Figure A5.6a EXPERIMENT C141515AA-6
SECTION PERMEABILITIES SUPERSATURATION = 70.0

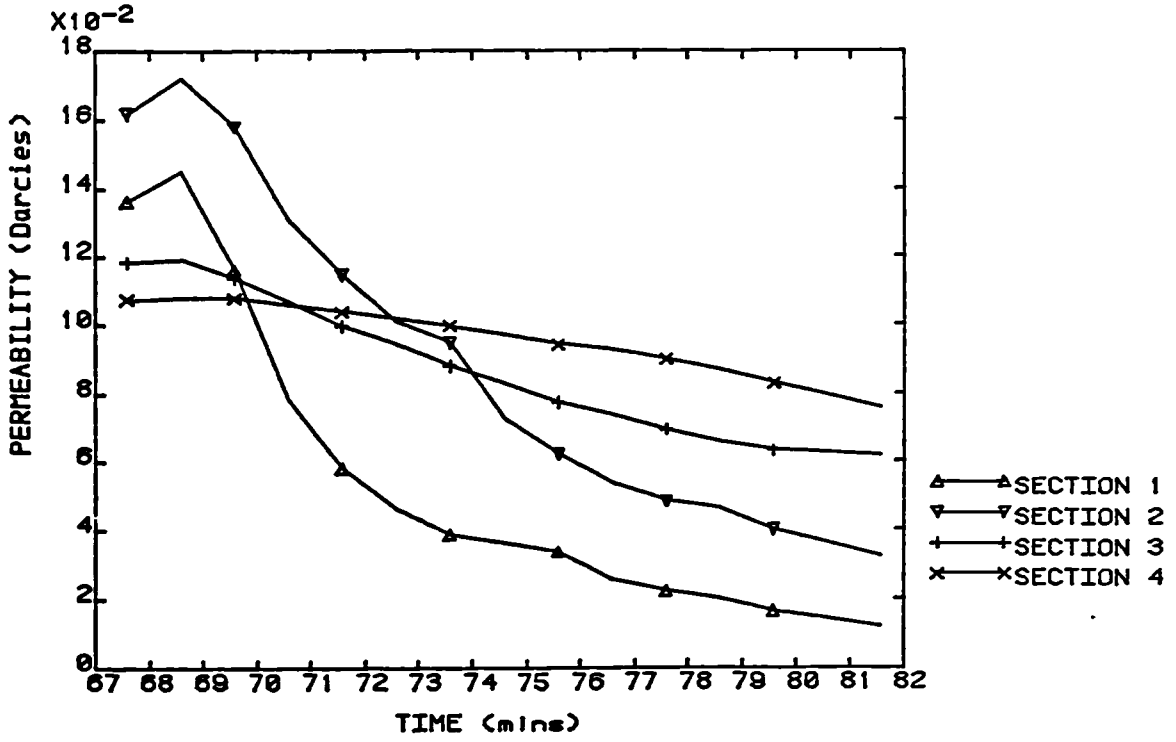

Figure A5.6b EXPERIMENT C141515AA-6
OVERALL PERMEABILITY SUPERSATURATION = 70.0

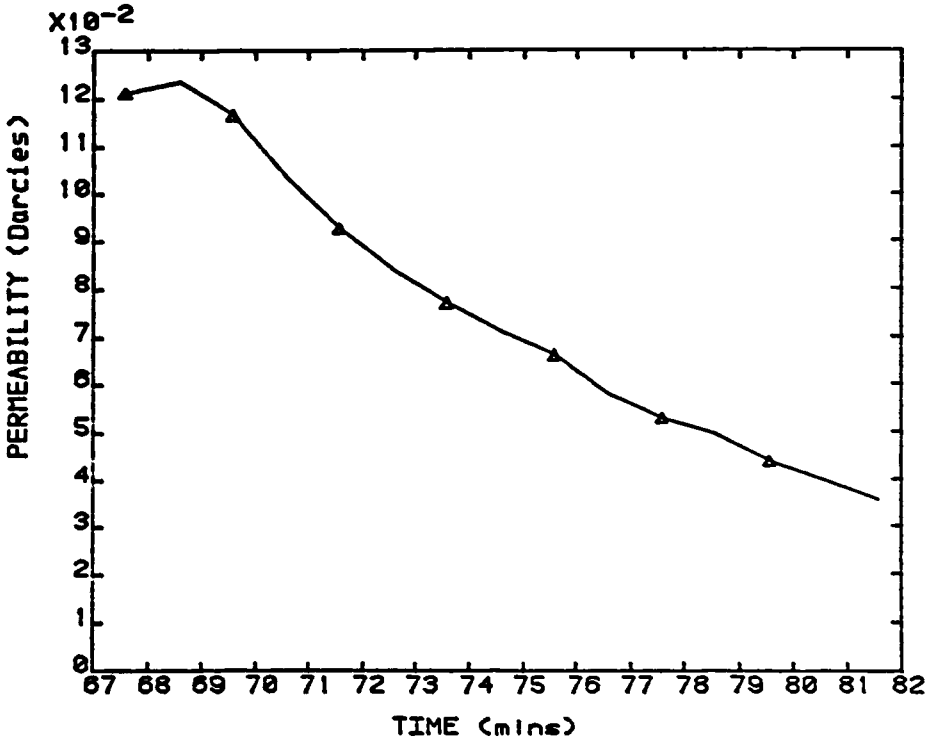

Figure A5.7a EXPERIMENT C181515AA-8
SECTION PERMEABILITIES SUPERSATURATION = 70.0

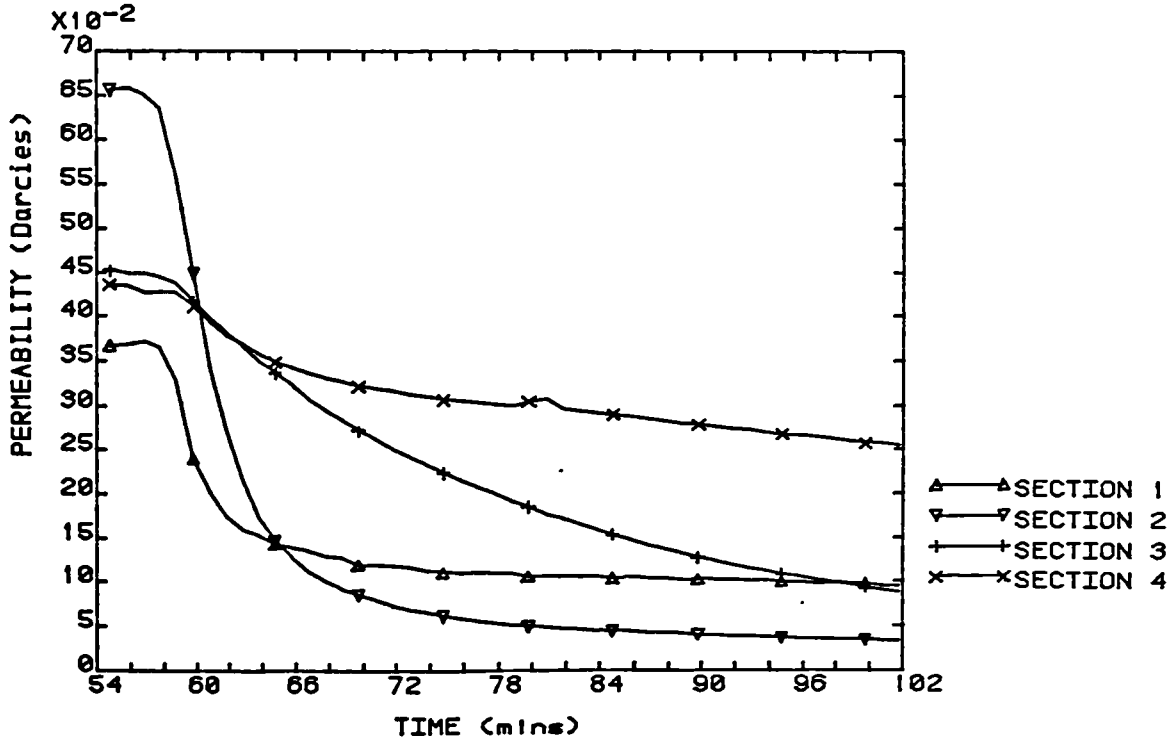

Figure A5.7b EXPERIMENT C181515AA-8
OVERALL PERMEABILITY SUPERSATURATION = 70.0

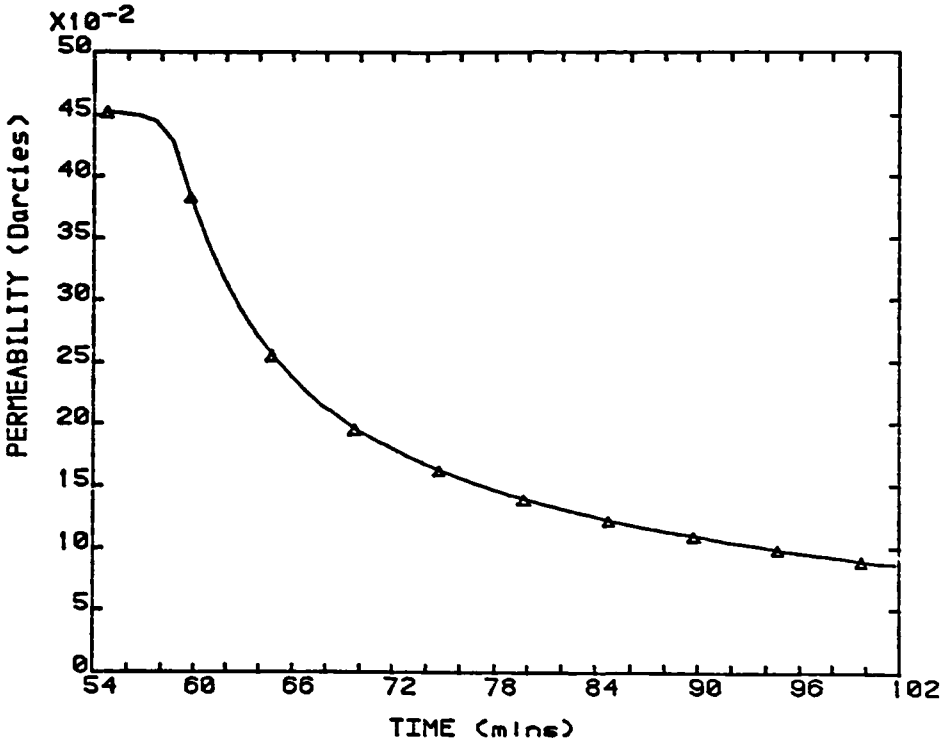

Figure A5.8a EXPERIMENT C181515AA-11
SECTION PERMEABILITIES SUPERSATURATION =70.0

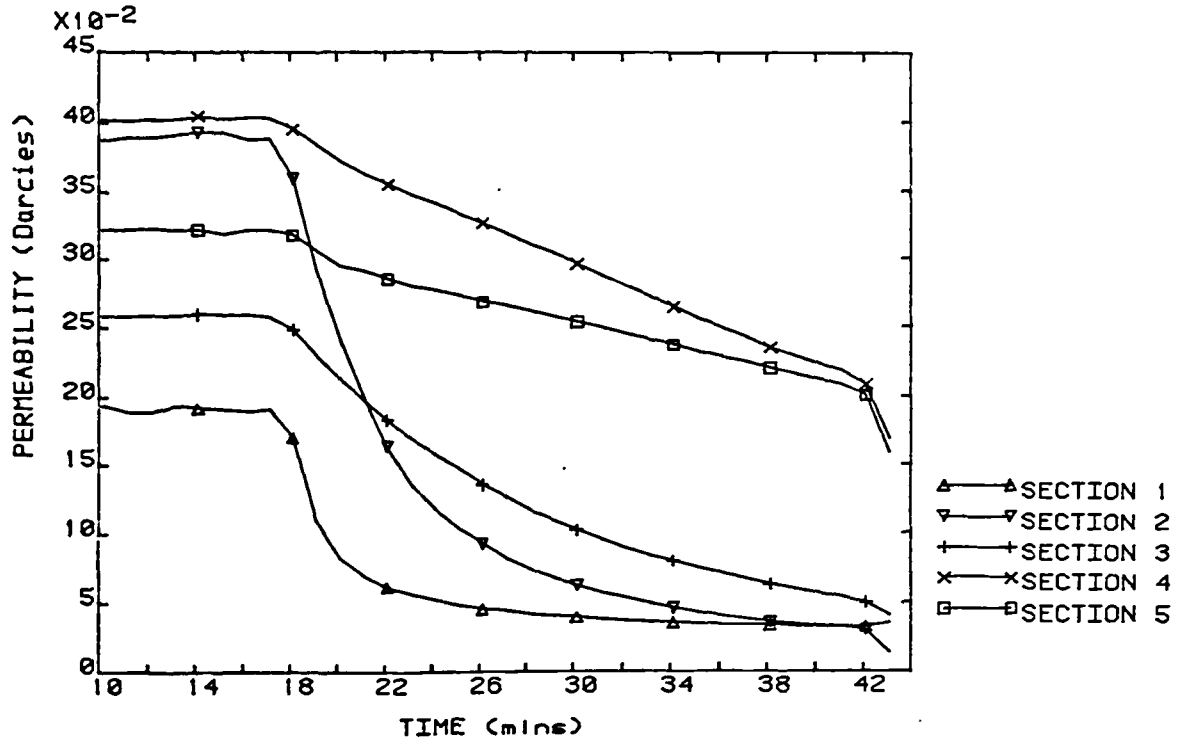

Figure A5.8b EXPERIMENT C181515AA-11
OVERALL PERMEABILITY SUPERSATURATION = 70.0

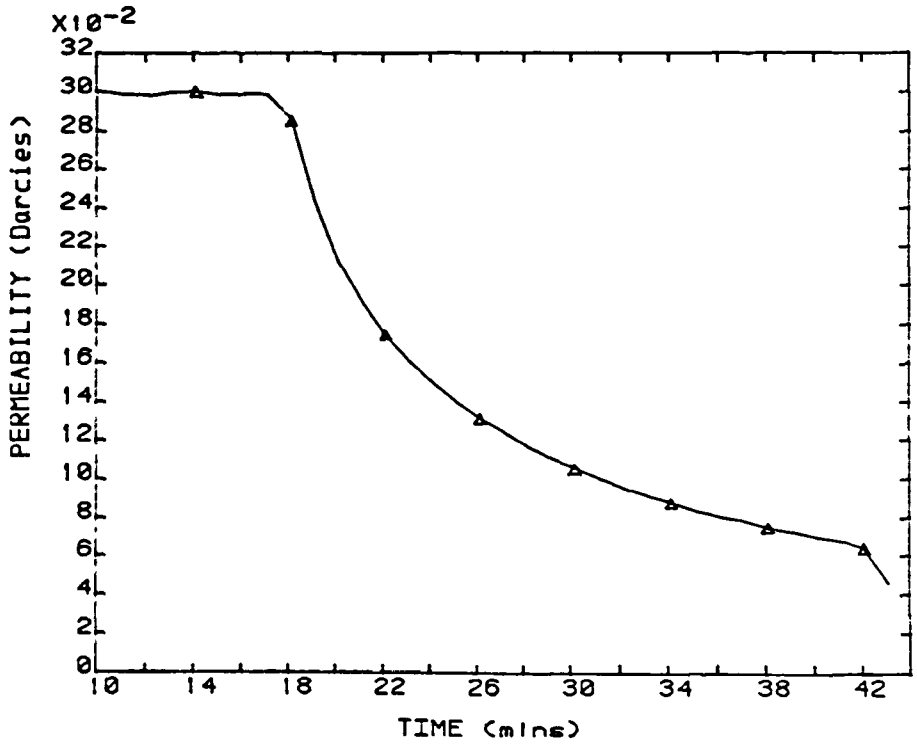

Figure A5.9a EXPERIMENT C181515BB-2
SECTION PERMEABILITIES SUPERSATURATION = 67.0

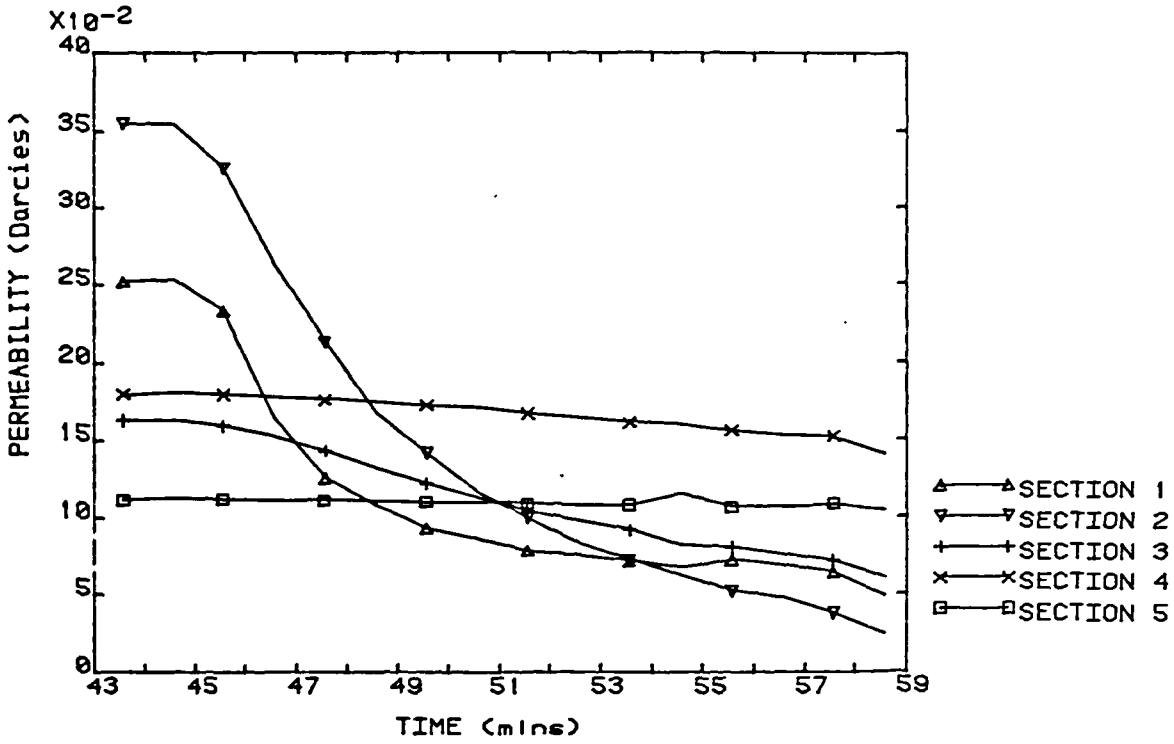

Figure A5.9b EXPERIMENT C181515BB-2
OVERALL PERMEABILITY SUPERSATURATION = 67.0

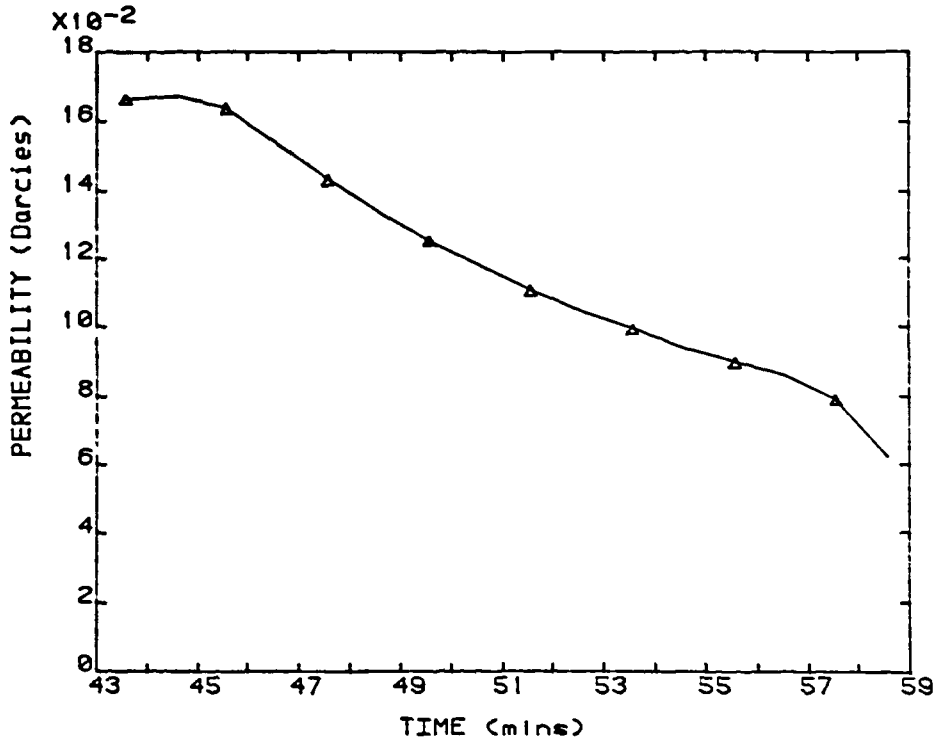

Figure A5.10a EXPERIMENT C221515BB-4
SECTION PERMEABILITIES SUPERSATURATION = 67.0

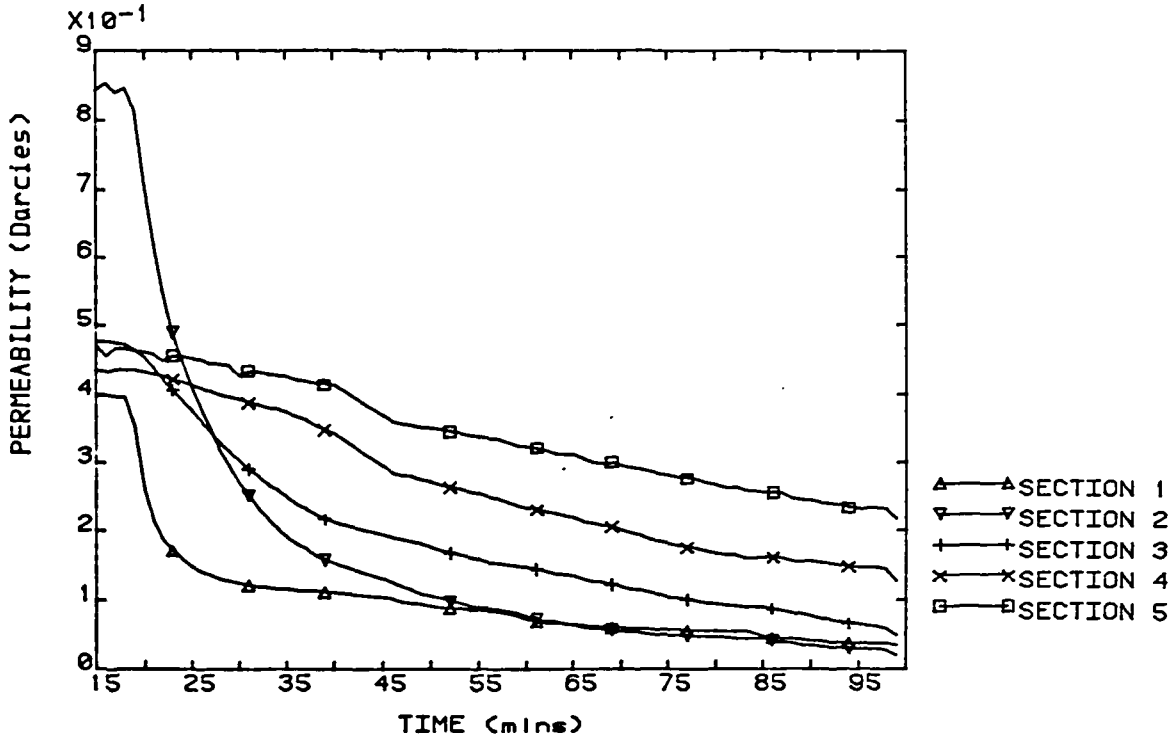

Figure A5.10b EXPERIMENT C221515BB-4
OVERALL PERMEABILITY SUPERSATURATION = 67.0

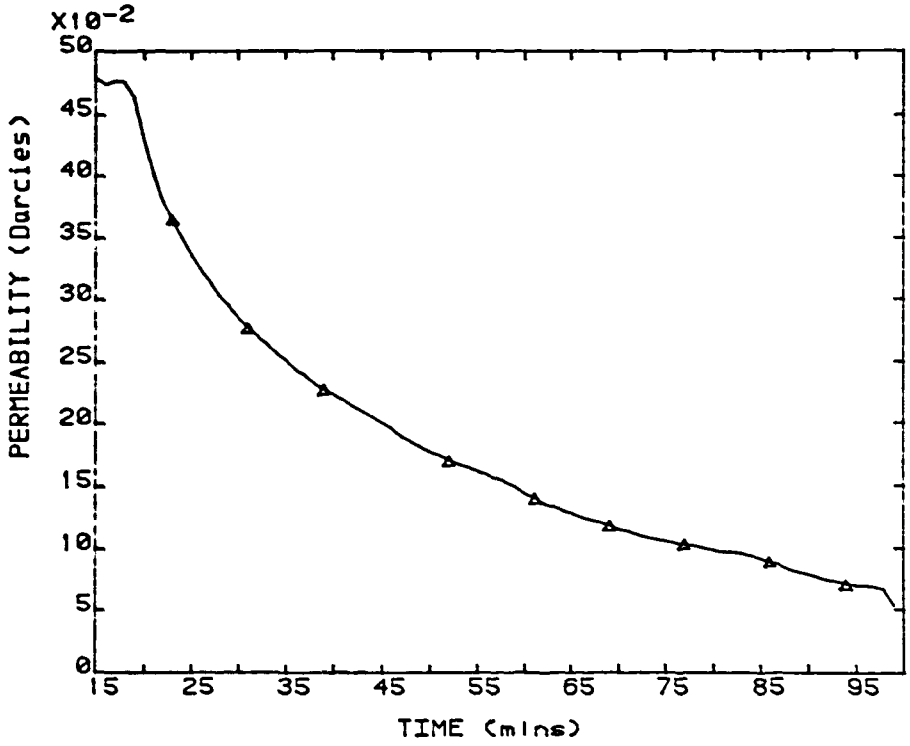

Figure A5.11a EXPERIMENT C221515BB-5
SECTION PERMEABILITIES SUPERSATURATION = 67.0

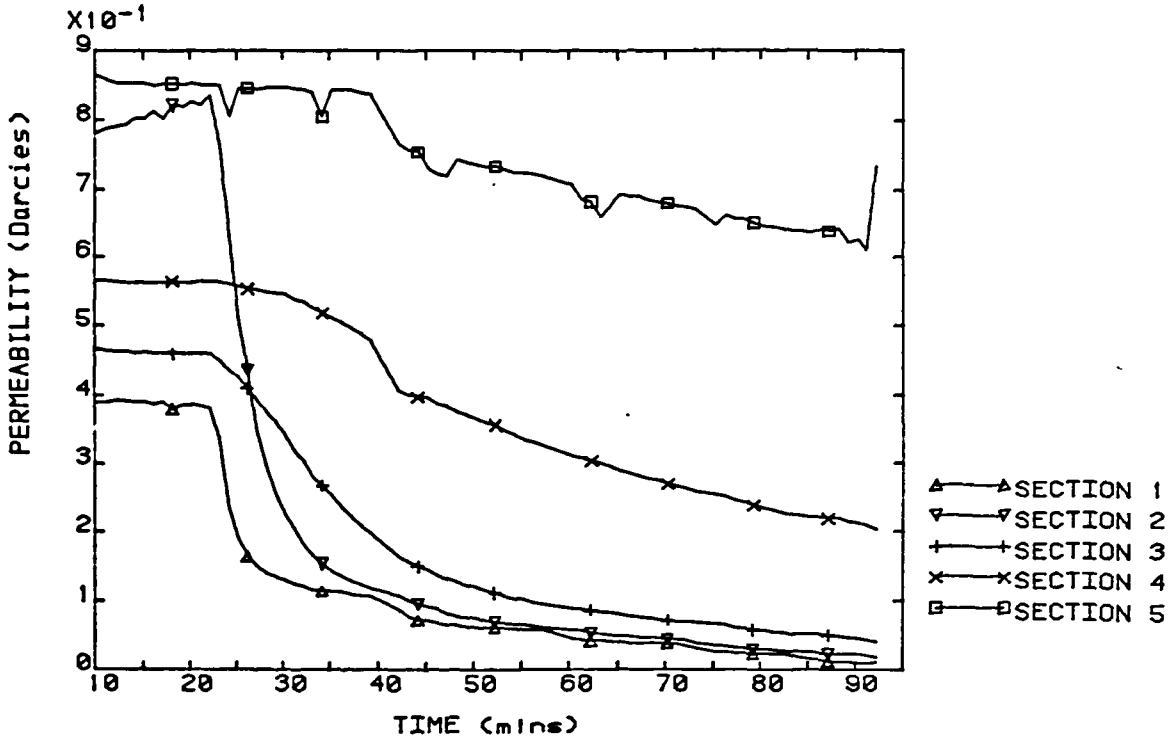

Figure A5.11b EXPERIMENT C221515BB-5
OVERALL PERMEABILITY SUPERSATURATION = 67.0

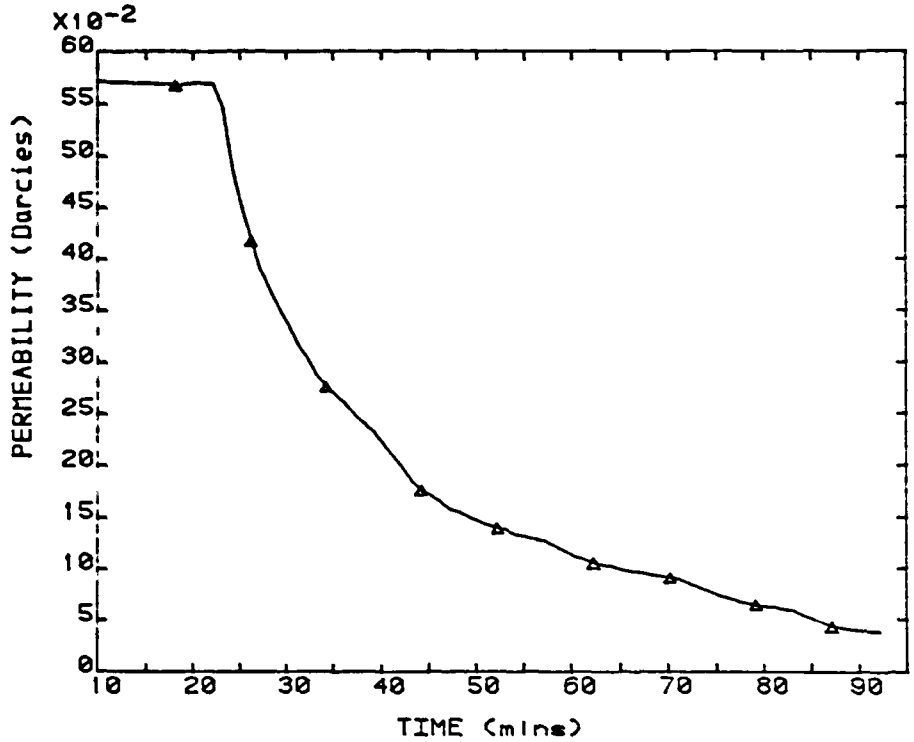

Figure A5.12a EXPERIMENT C221515BB-6
SECTION PERMEABILITIES SUPERSATURATION = 67.0

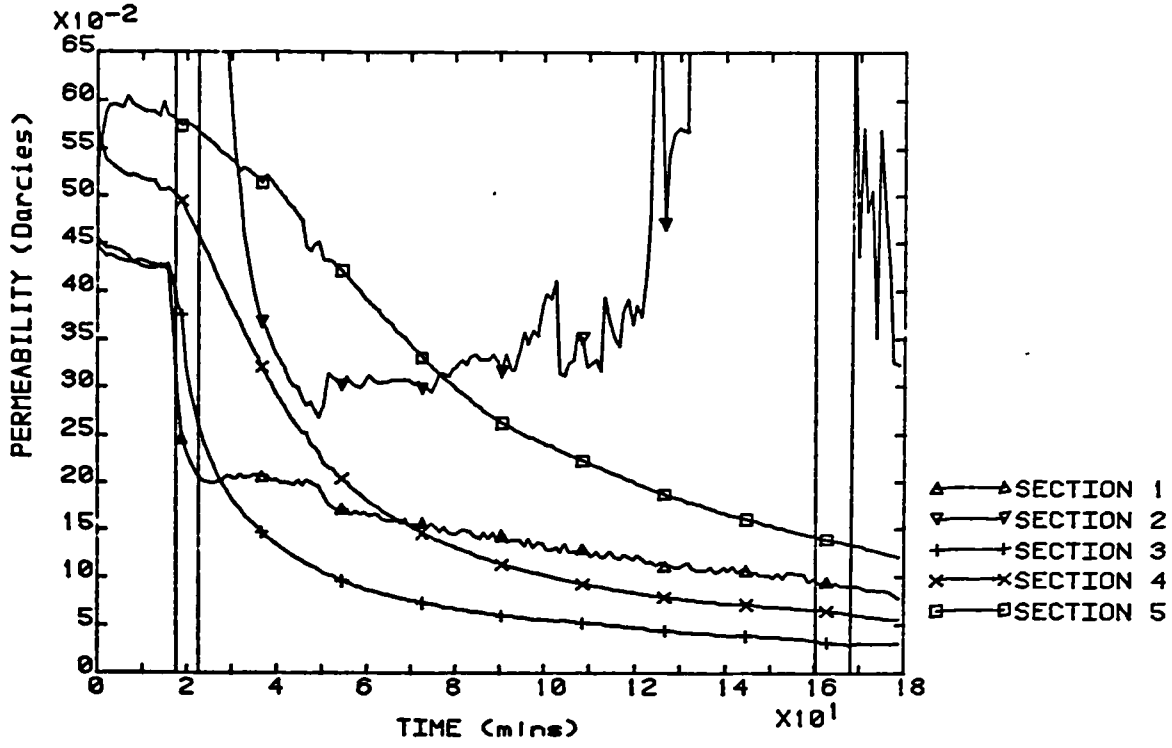

Figure A5.12b EXPERIMENT C221515BB-6
OVERALL PERMEABILITY SUPERSATURATION = 67.0

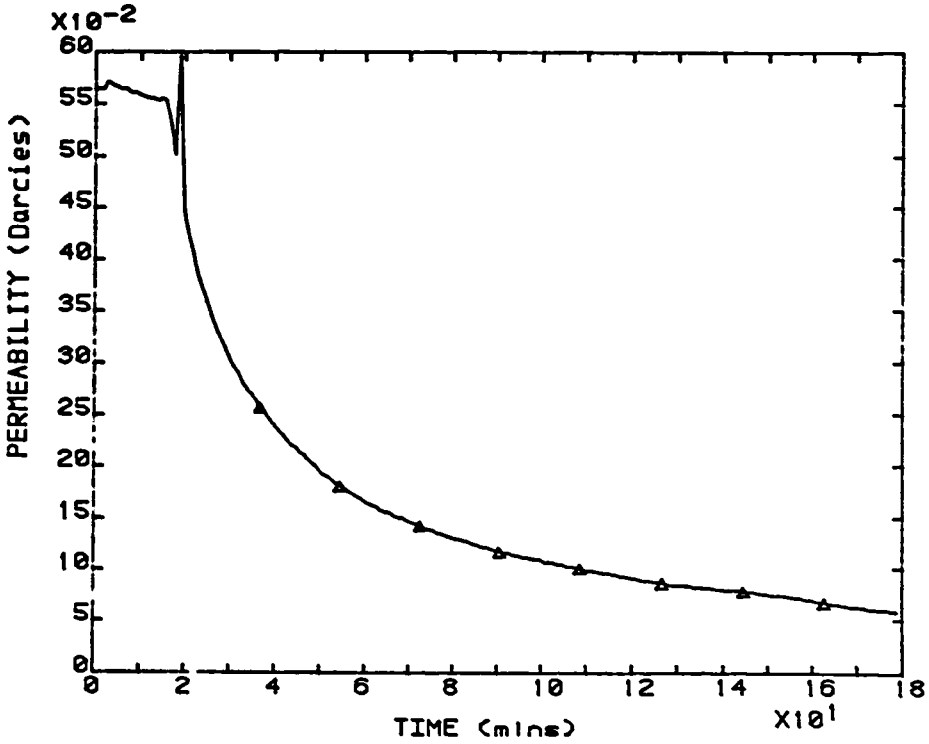

Figure A5.13a EXPERIMENT C221515BB-7
SECTION PERMEABILITIES SUPERSATURATION = 67.0

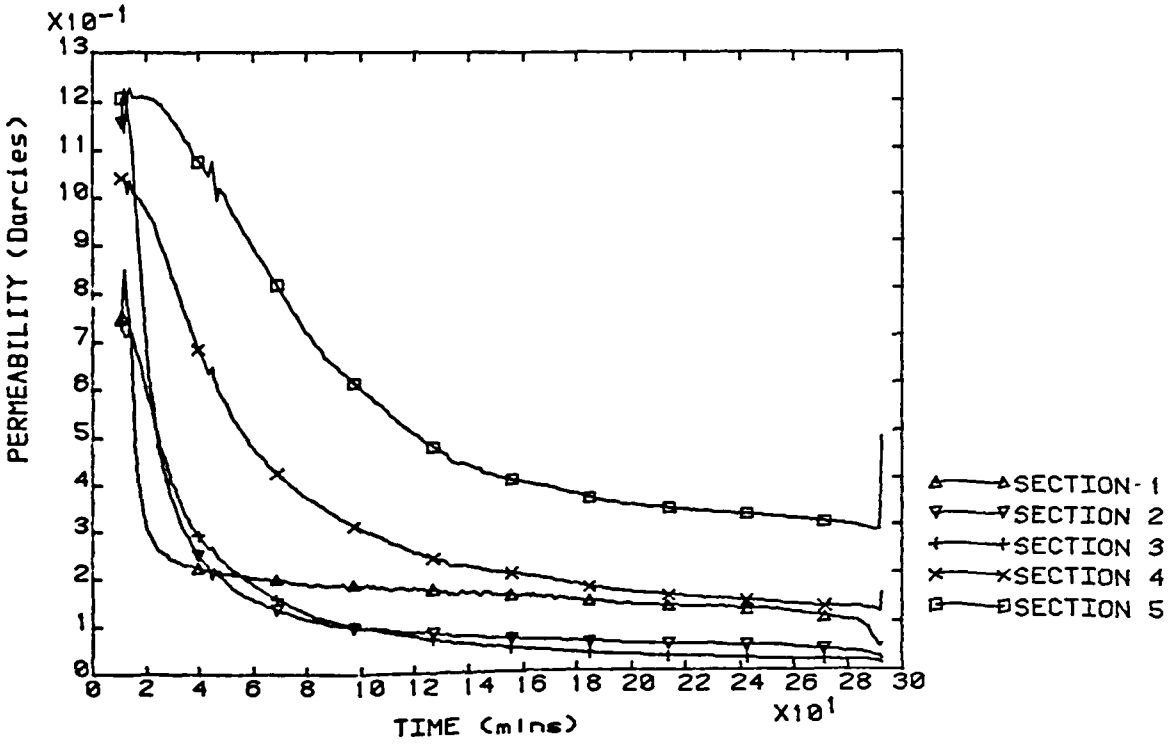

Figure A5.13b EXPERIMENT C221515BB-7
OVERALL PERMEABILITY SUPERSATURATION = 67.0

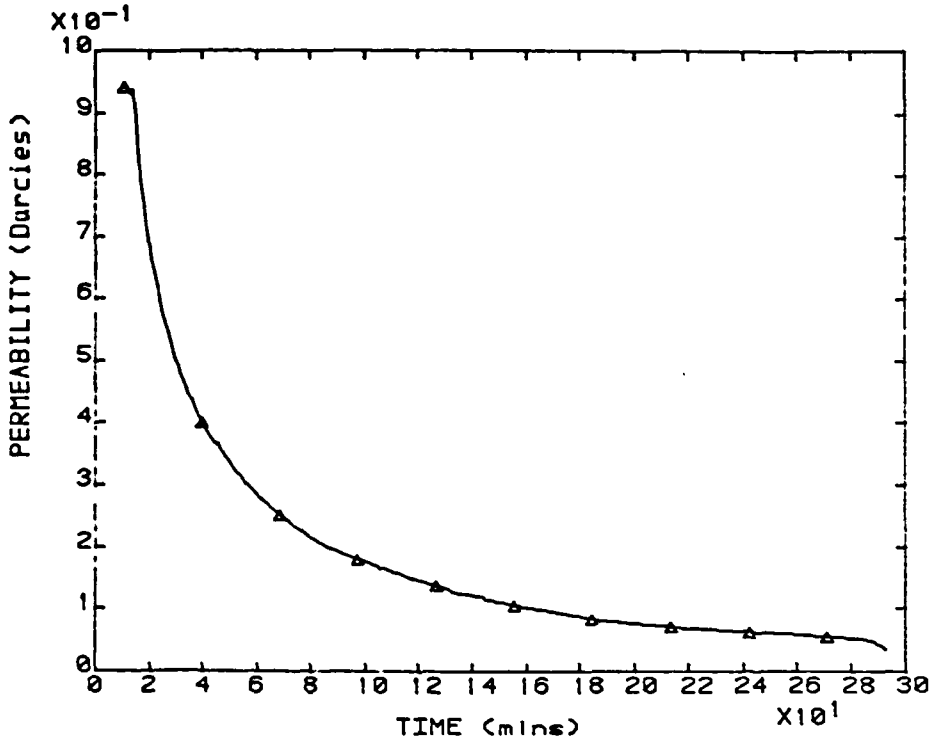

Figure A5.14a EXPERIMENT C221515CC-1
SECTION PERMEABILITIES SUPERSATURATION = 63.0

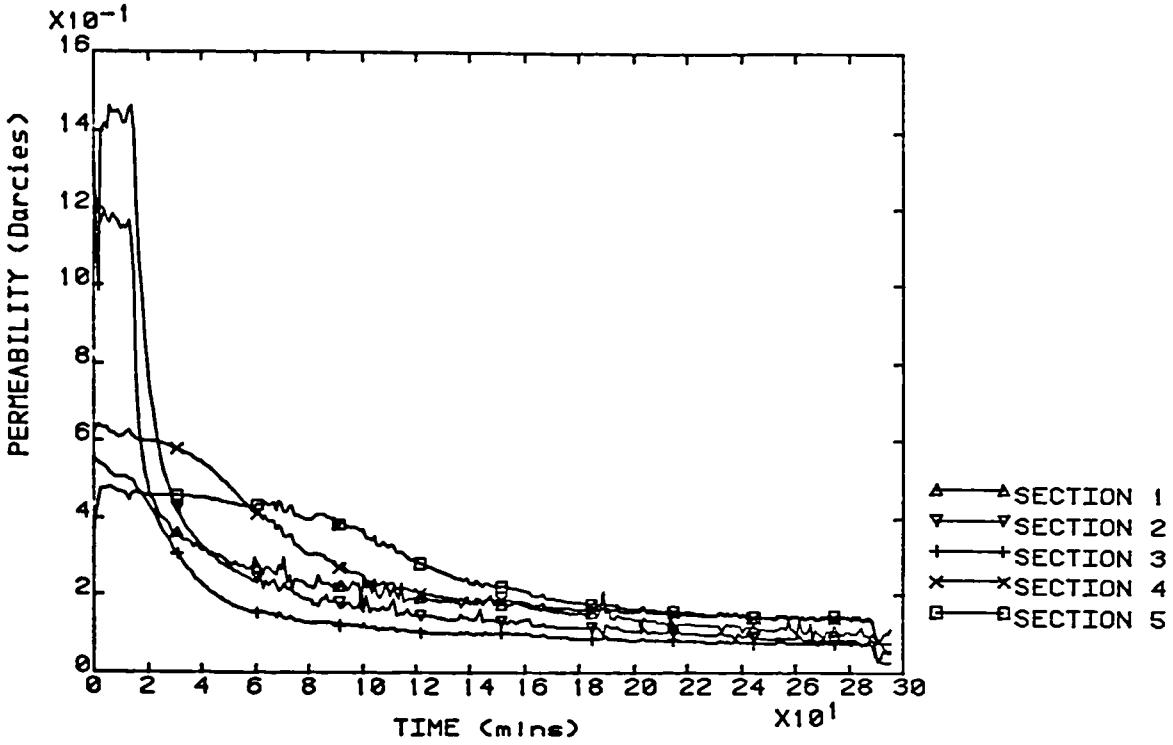

Figure A5.14b EXPERIMENT C221515CC-1
OVERALL PERMEABILITY SUPERSATURATION = 63.0

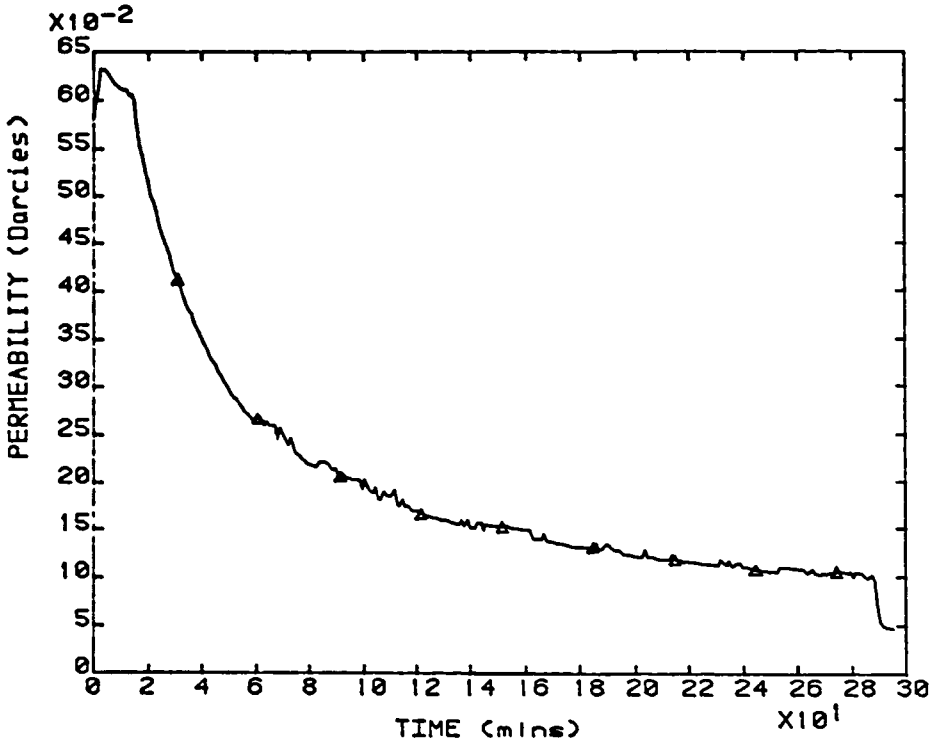

Figure A5.15a EXPERIMENT C221515CC-2
SECTION PERMEABILITIES SUPERSATURATION = 63.0

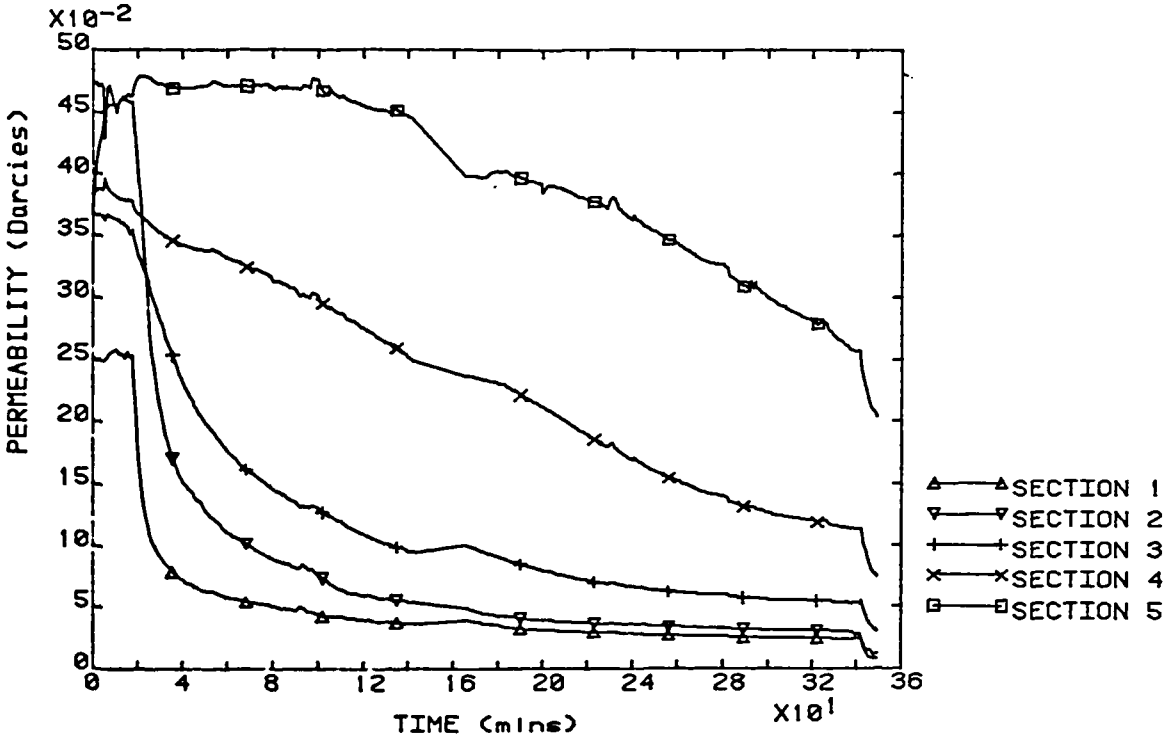

Figure A5.15b EXPERIMENT C221515CC-2
OVERALL PERMEABILITY SUPERSATURATION = 63.0

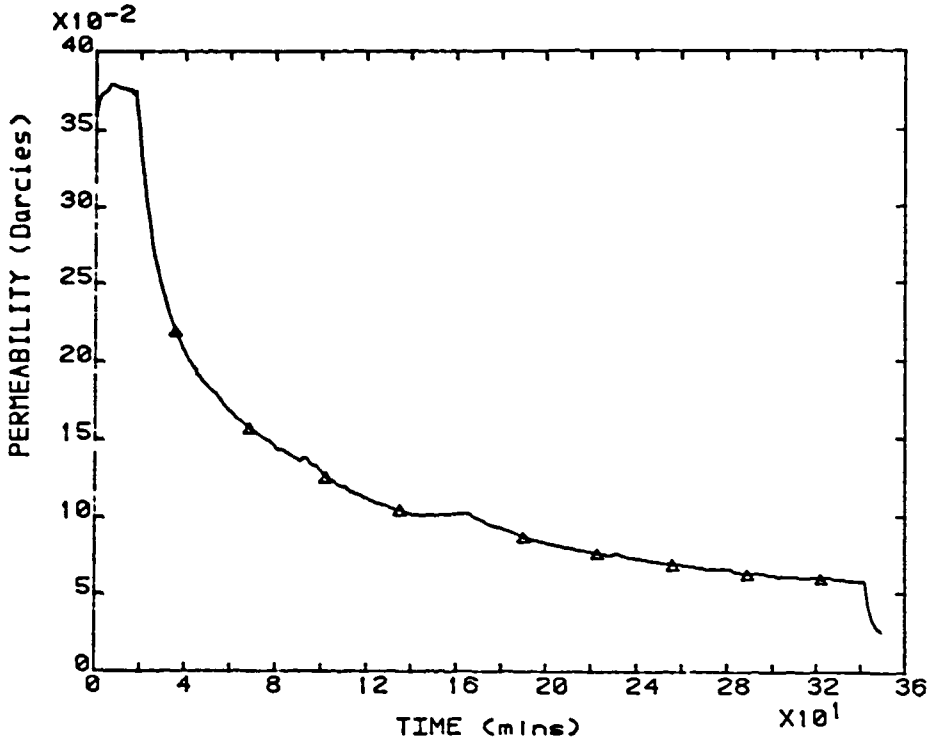

Figure A5.16a EXPERIMENT C221515CC-3R
SECTION PERMEABILITIES SUPERSATURATION = 63.0

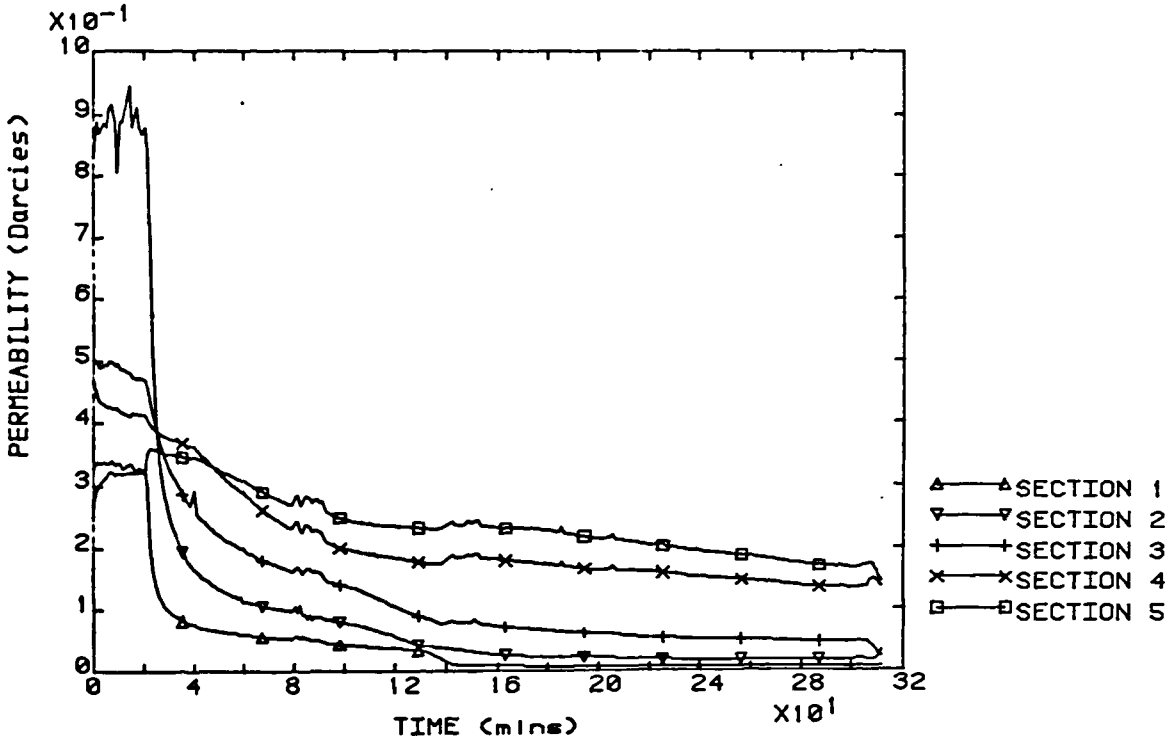

Figure A5.16b EXPERIMENT C221515CC-3R
OVERALL PERMEABILITY SUPERSATURATION = 63.0

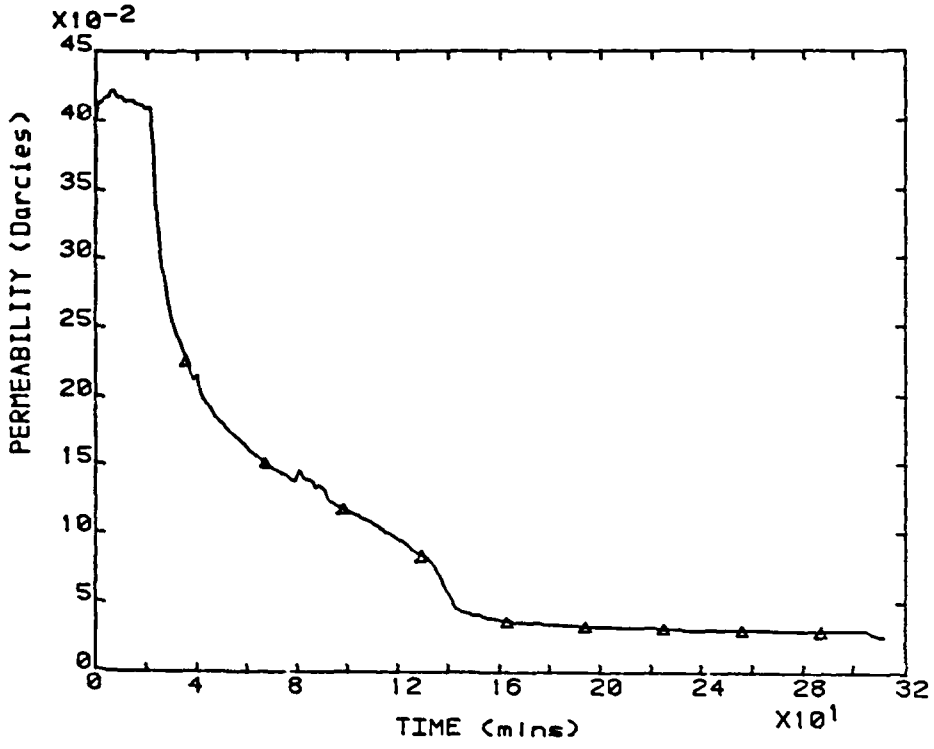

Figure A5.17a EXPERIMENT C221515CC-4R
SECTION PERMEABILITIES SUPERSATURATION = 63.0

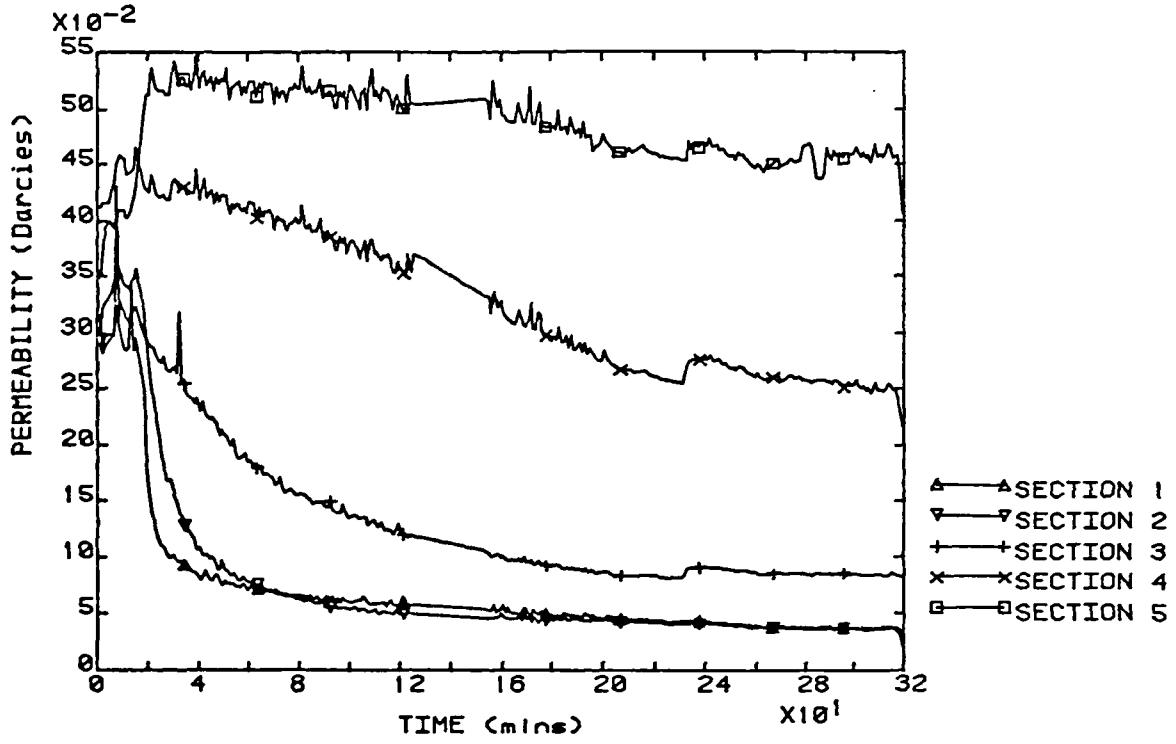

Figure A5.17b EXPERIMENT C221515CC-4R
OVERALL PERMEABILITY SUPERSATURATION = 63.0

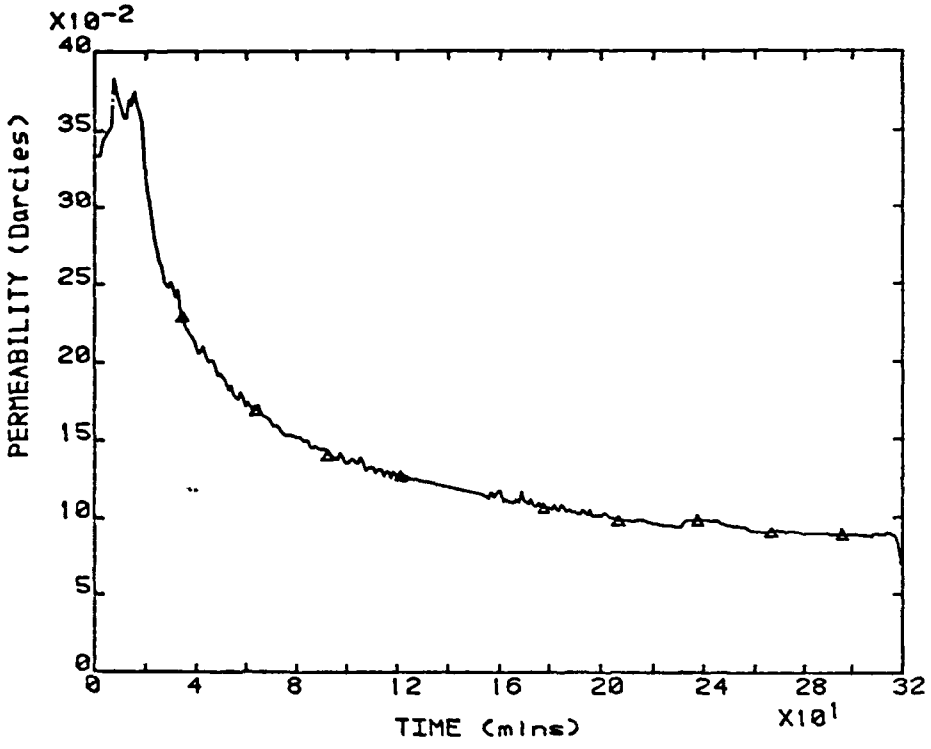

Figure A5.18a EXPERIMENT C221515CC-5R
SECTION PERMEABILITIES SUPERSATURATION = 63.0

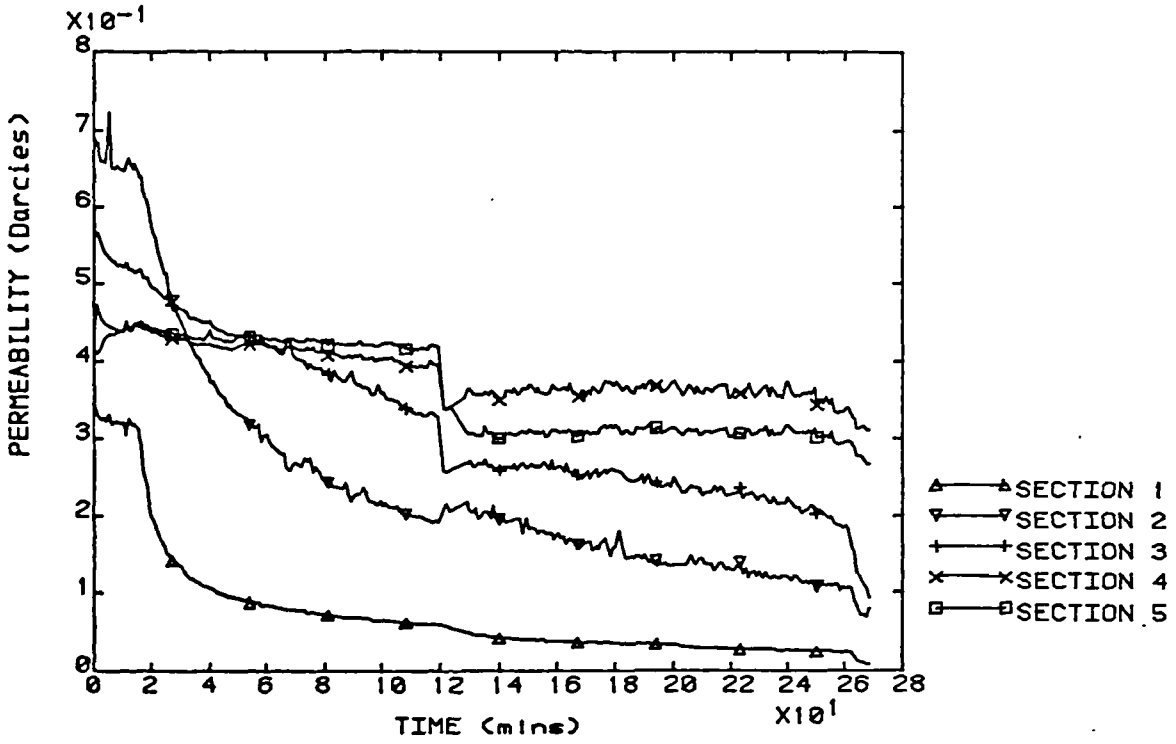

Figure A5.18b EXPERIMENT C221515CC-5R
OVERALL PERMEABILITY SUPERSATURATION = 63.0

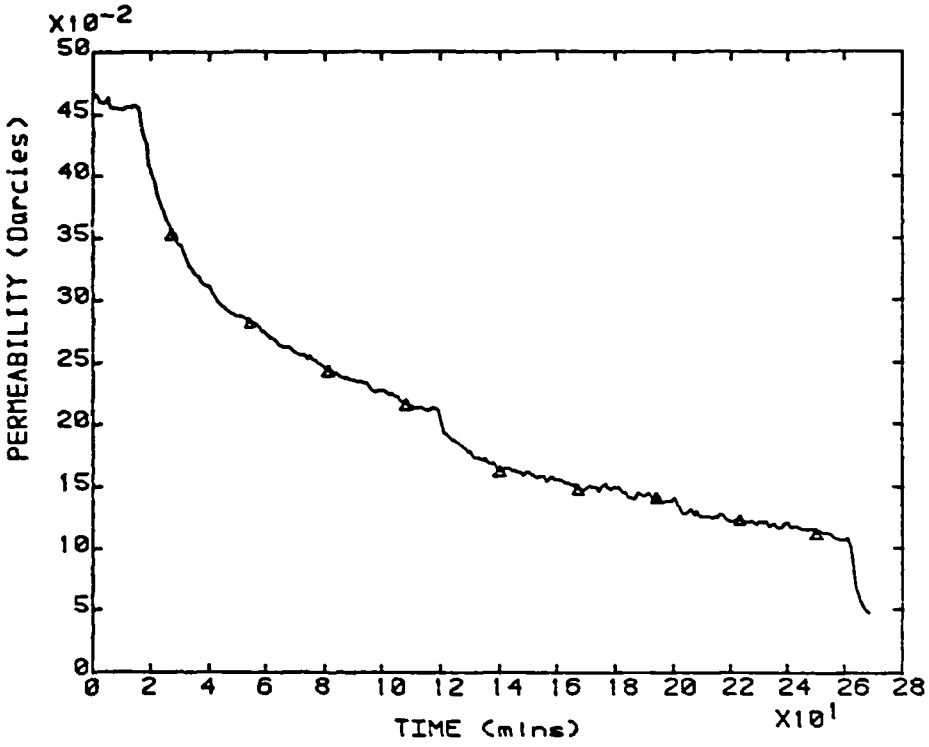

Figure A5.19a EXPERIMENT C221515DD-1
SECTION PERMEABILITIES SUPERSATURATION = 35.0

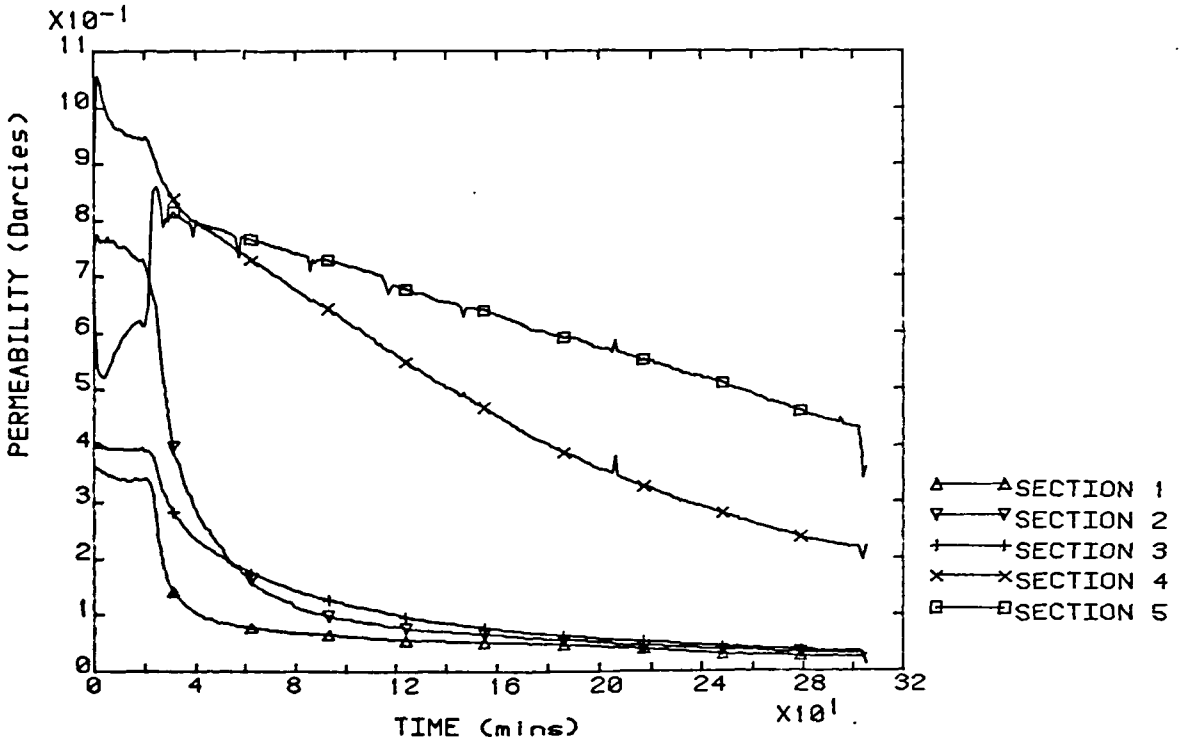

Figure A5.19b EXPERIMENT C221515DD-1
OVERALL PERMEABILITY SUPERSATURATION = 35.0

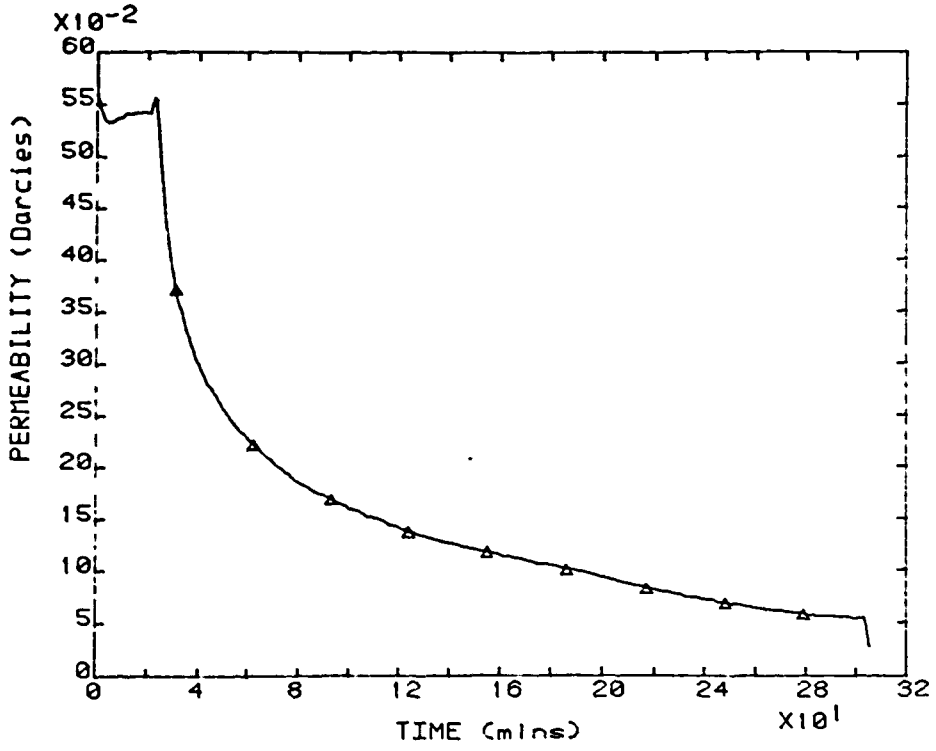

Figure A5.20a EXPERIMENT C221515DD-2
SECTION PERMEABILITIES SUPERSATURATION = 35.0

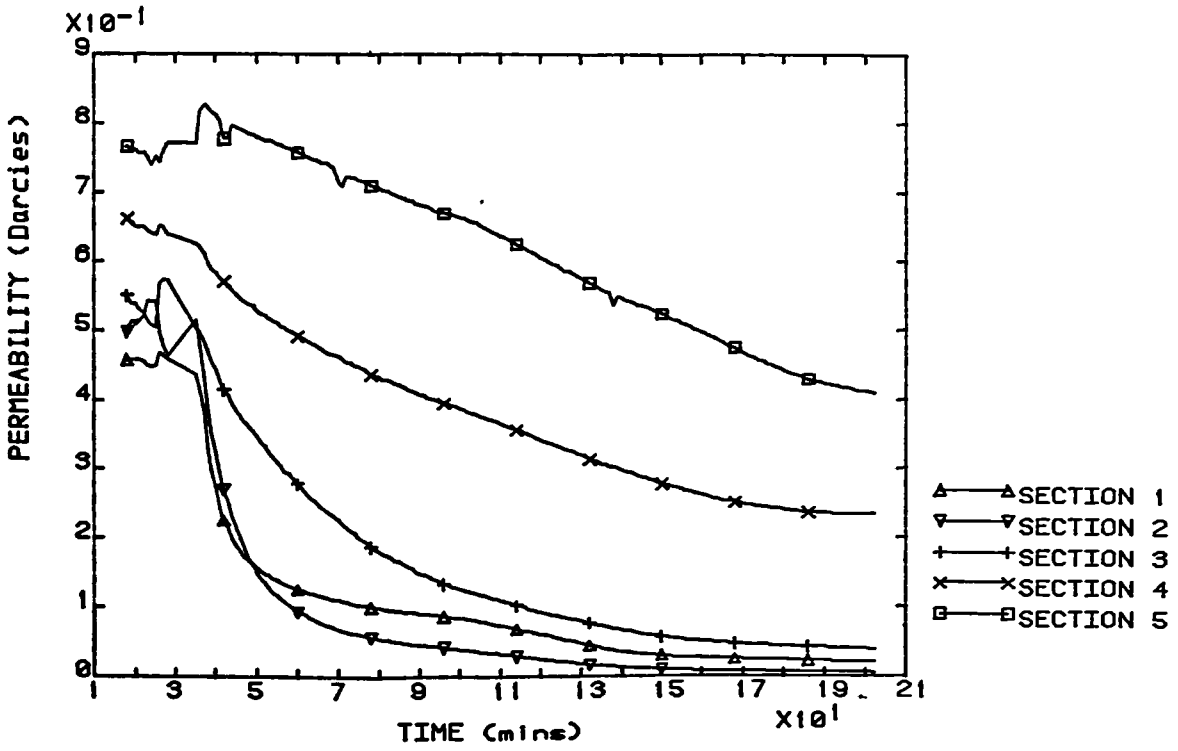

Figure A5.20b EXPERIMENT C221515DD-2
OVERALL PERMEABILITY SUPERSATURATION = 35.0

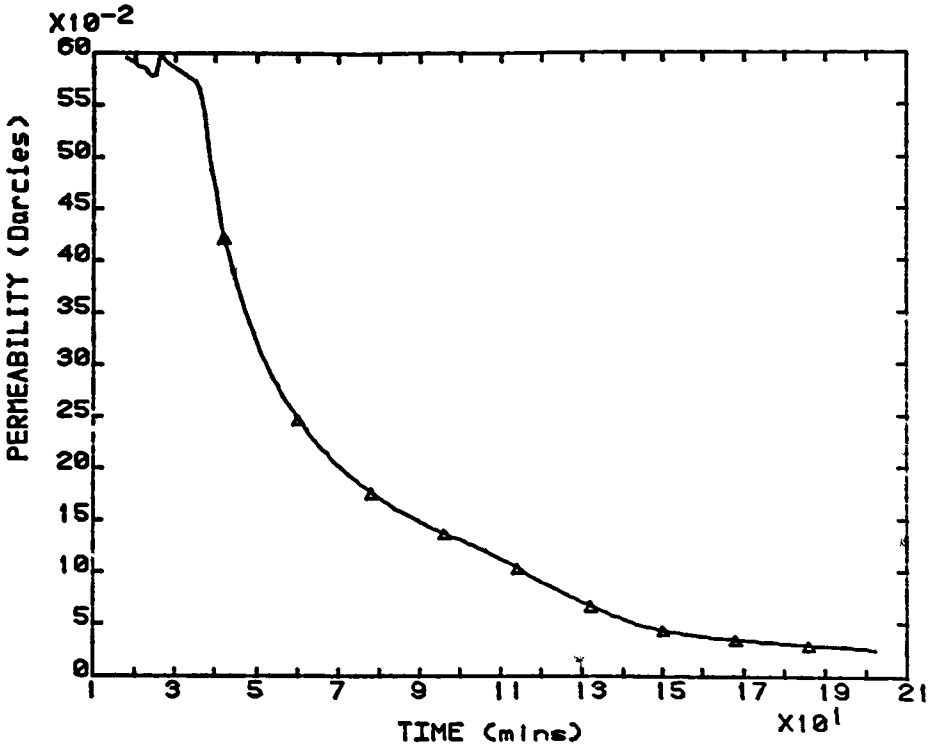

Figure A5.21a EXPERIMENT C221515DD-3
SECTION PERMEABILITIES SUPERSATURATION = 35.0

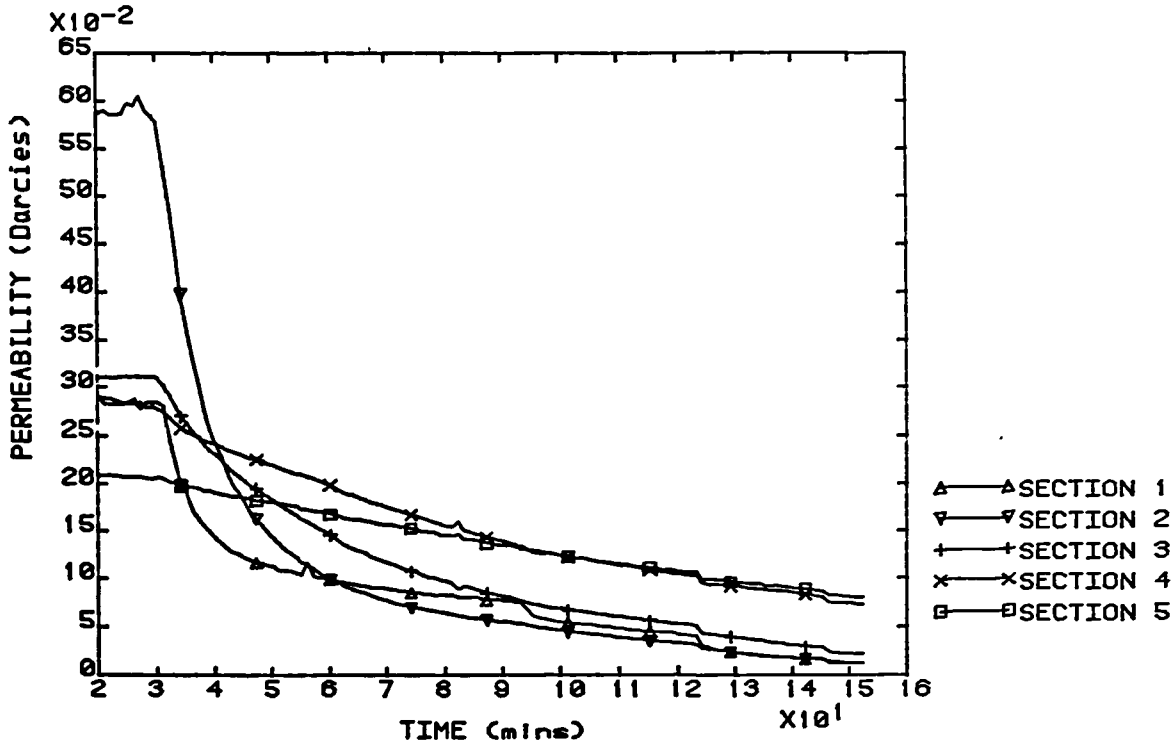

Figure A5.21b EXPERIMENT C221515DD-3
OVERALL PERMEABILITY SUPERSATURATION = 35.0

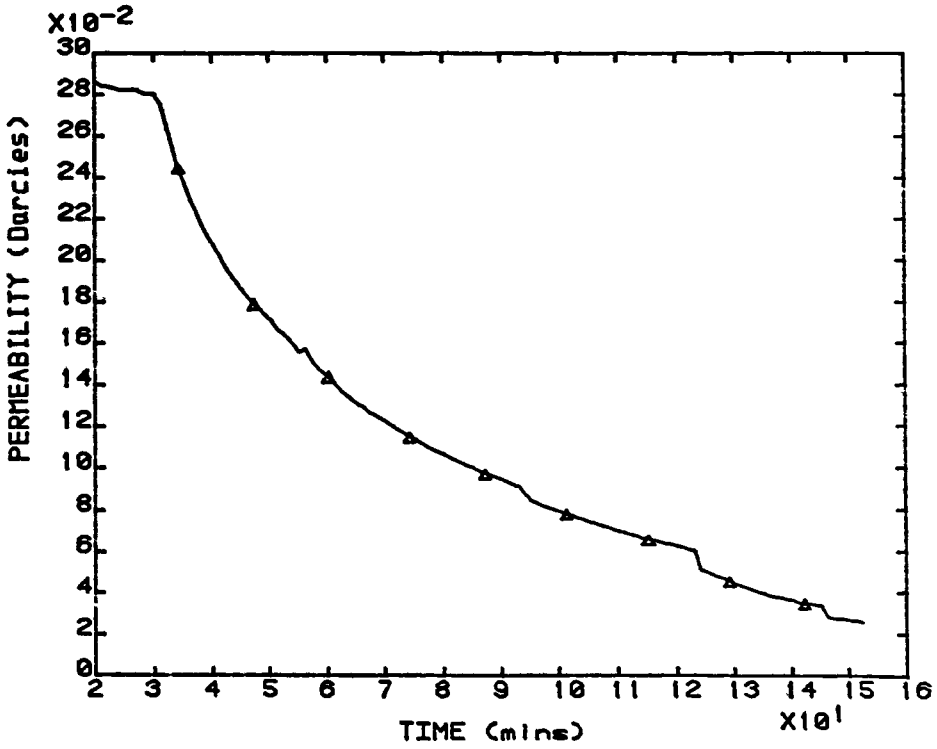

Figure A5.22a EXPERIMENT C221515DD-5R
SECTION PERMEABILITIES SUPERSATURATION = 35.0

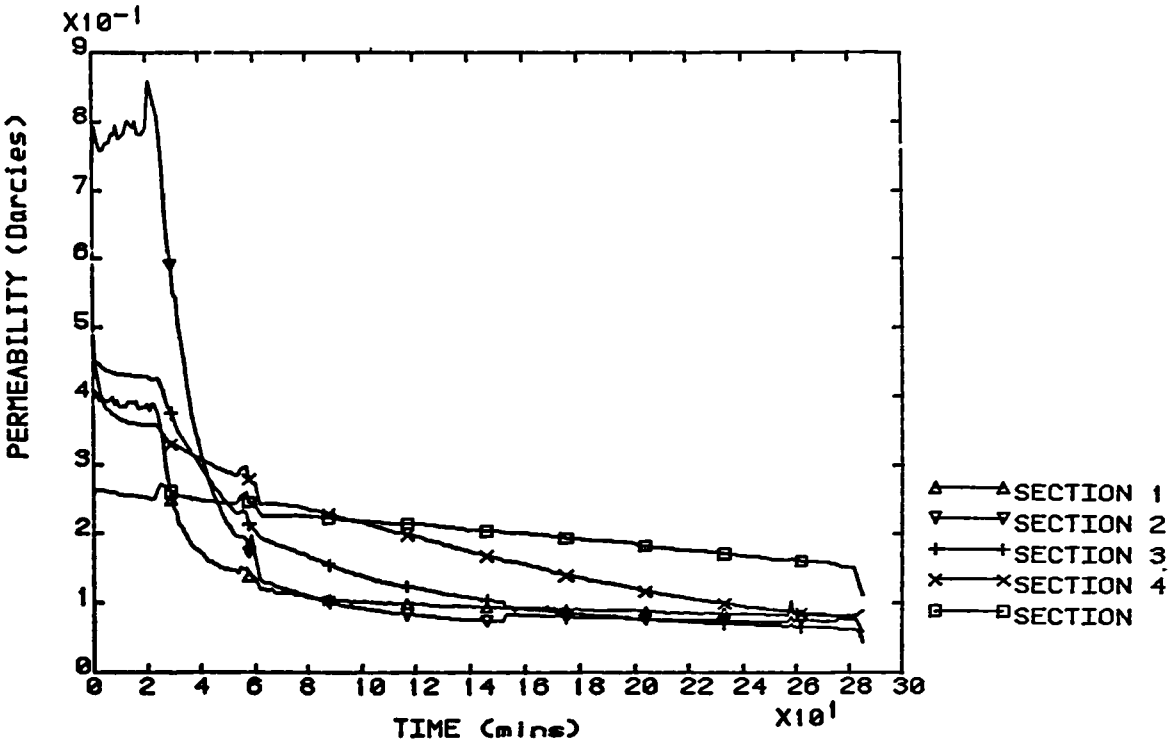

Figure A5.22b EXPERIMENT C221515DD-5R
OVERALL PERMEABILITY SUPERSATURATION = 35.0

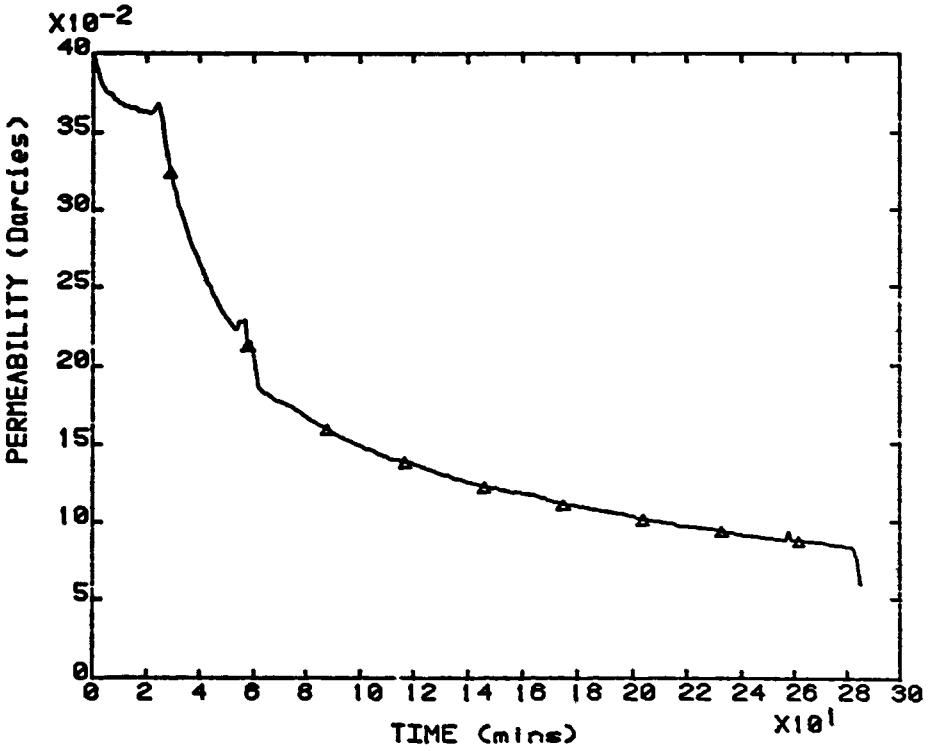

Figure A5.23a EXPERIMENT C221515DD-7
SECTION PERMEABILITIES SUPERSATURATION = 35.0

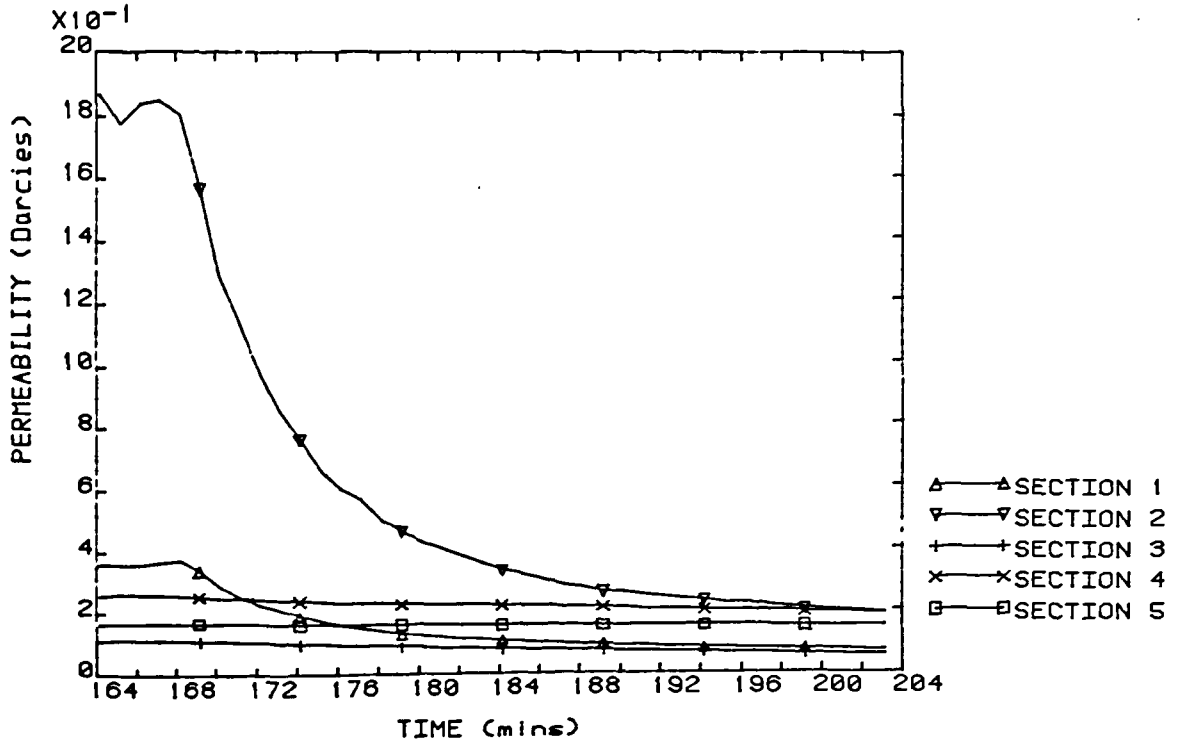

Figure A5.23b EXPERIMENT C221515DD-7
OVERALL PERMEABILITY SUPERSATURATION = 35.0

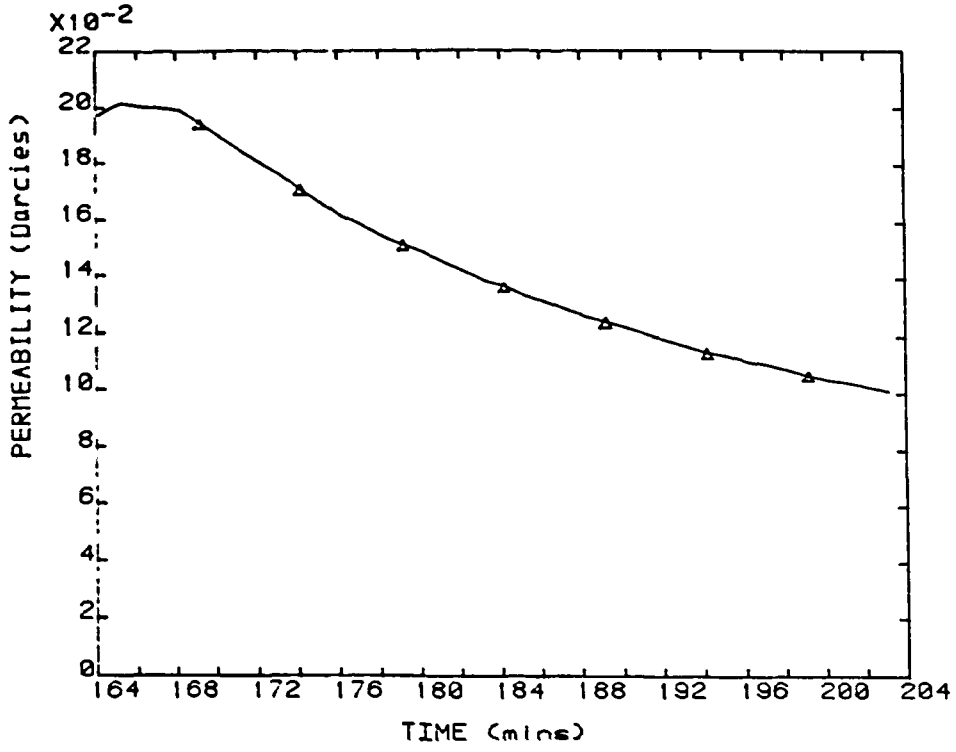

Figure A5.24a EXPERIMENT C221515DD-8S
SECTION PERMEABILITIES SUPERSATURATION = 35.0

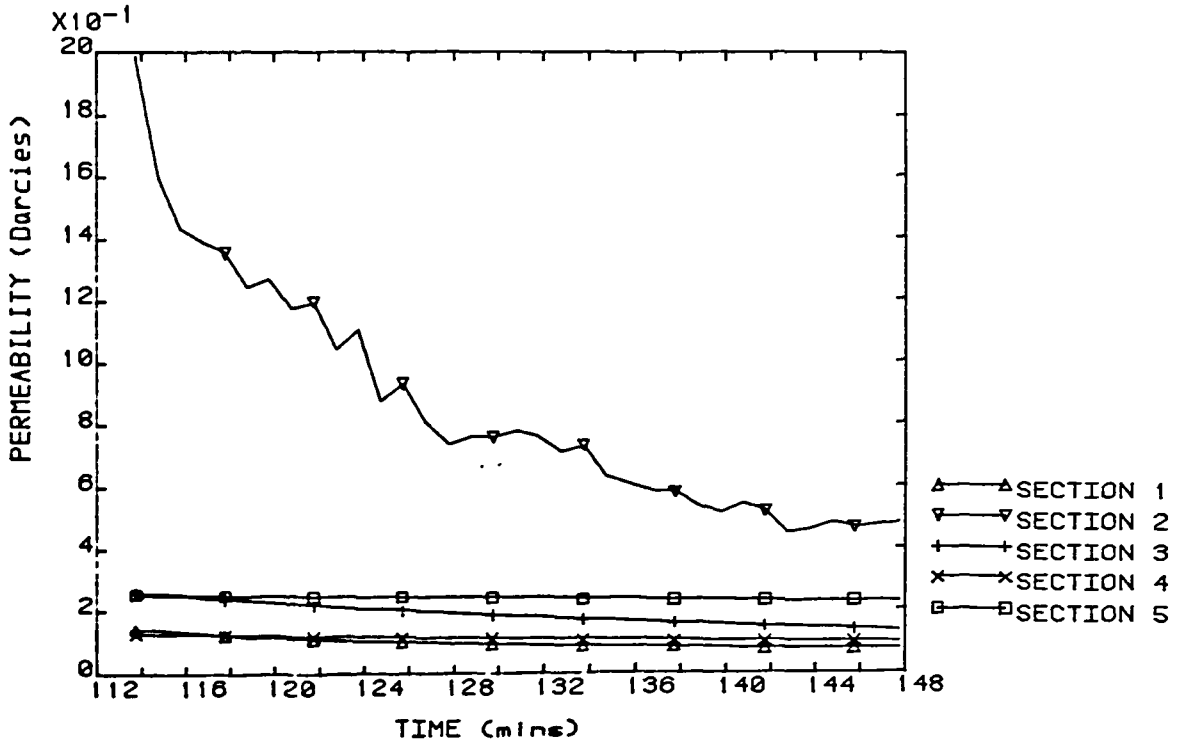

Figure A5.24b EXPERIMENT C221515DD-8S
OVERALL PERMEABILITY SUPERSATURATION = 35.0

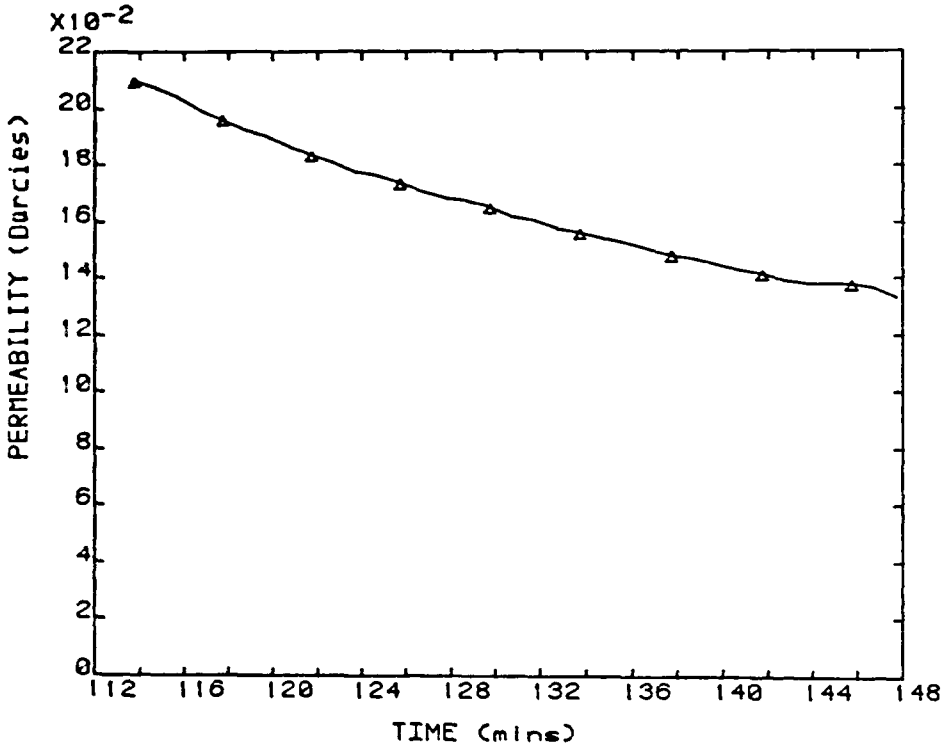

Figure A5.25a EXPERIMENT C227.57.5DD-9S
SECTION PERMEABILITIES SUPERSATURATION = 35.0

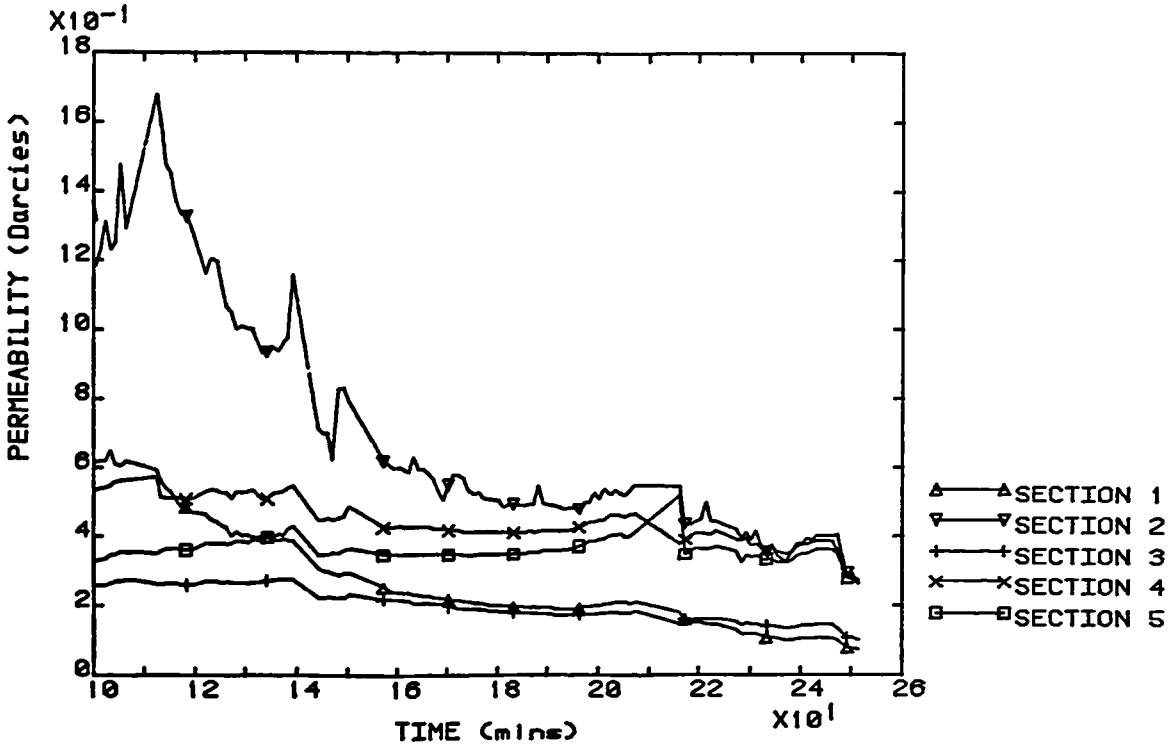

Figure A5.25b EXPERIMENT C227.57.5DD-9S
OVERALL PERMEABILITY SUPERSATURATION = 35.0

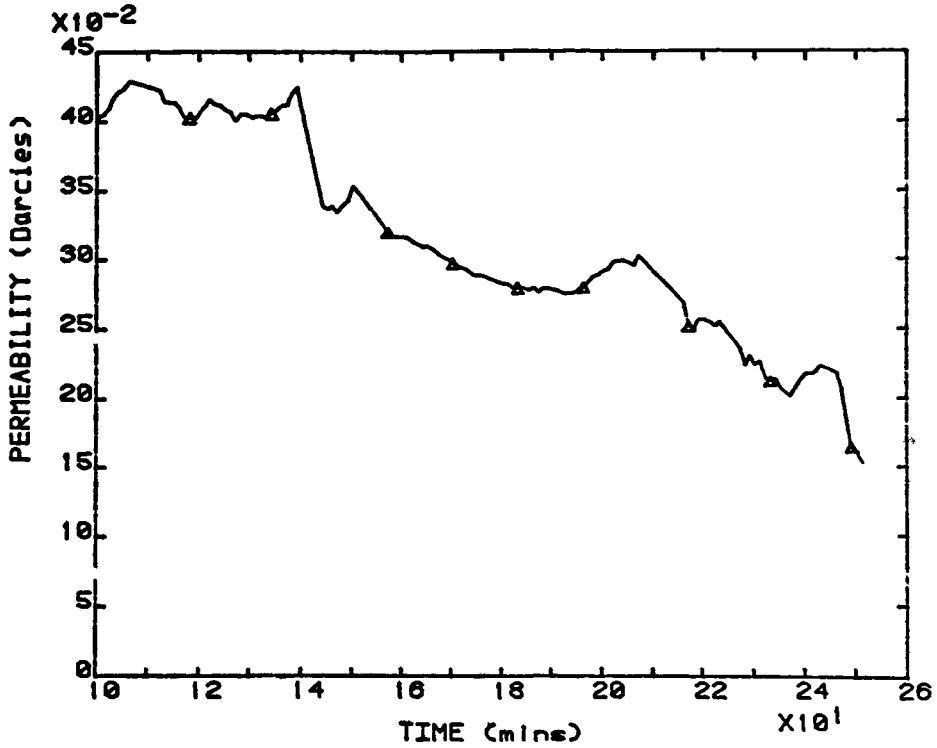

Figure A5.26a EXPERIMENT C227.57.5DD-10
SECTION PERMEABILITIES SUPERSATURATION = 35.0

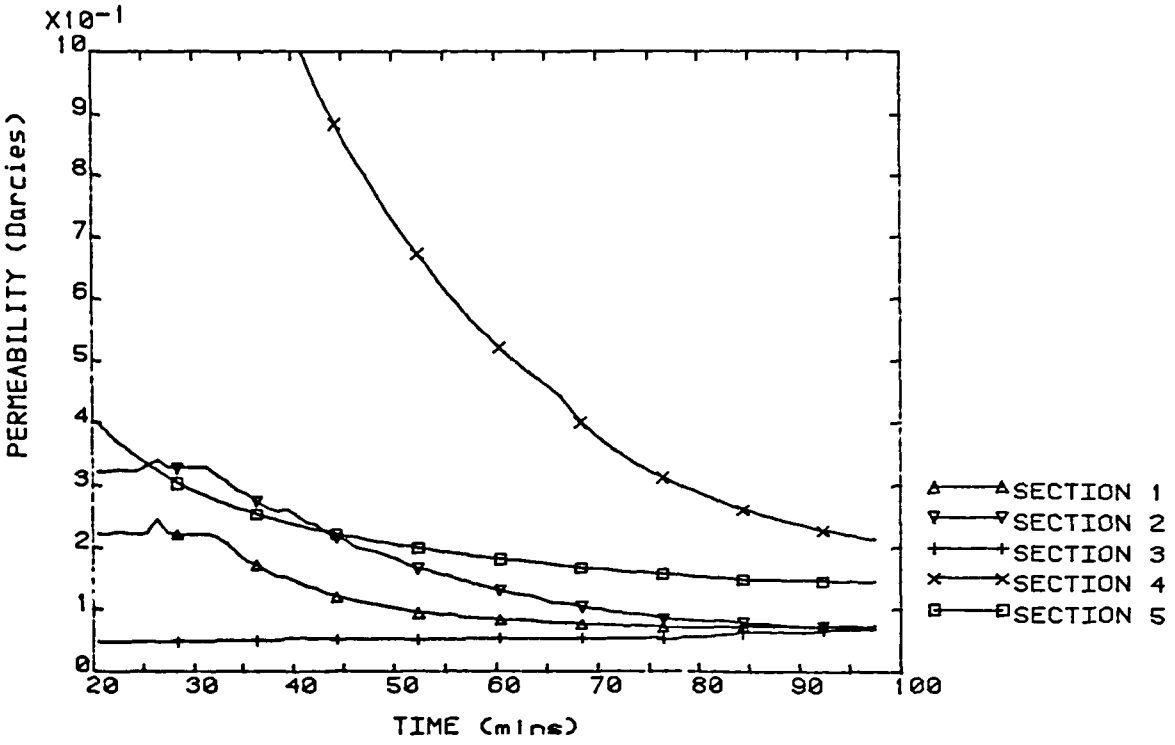

Figure A5.26b EXPERIMENT C227.57.5DD-10
OVERALL PERMEABILITY SUPERSATURATION = 35.0

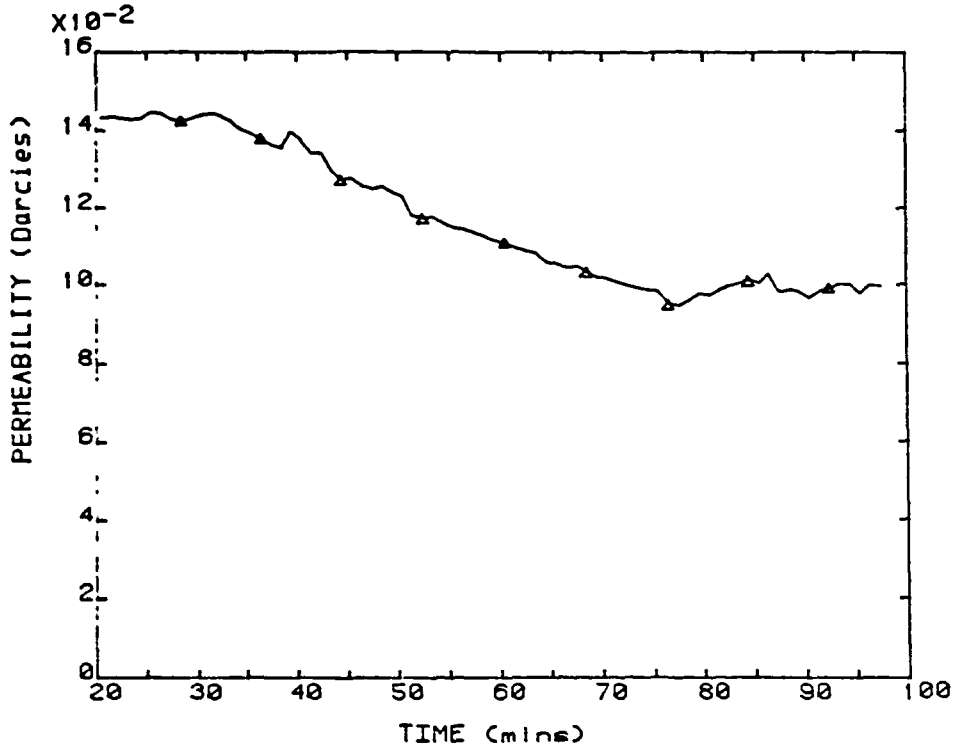

Figure A5.27a EXPERIMENT C221515EE-1
SECTION PERMEABILITIES SUPERSATURATION = 17.5

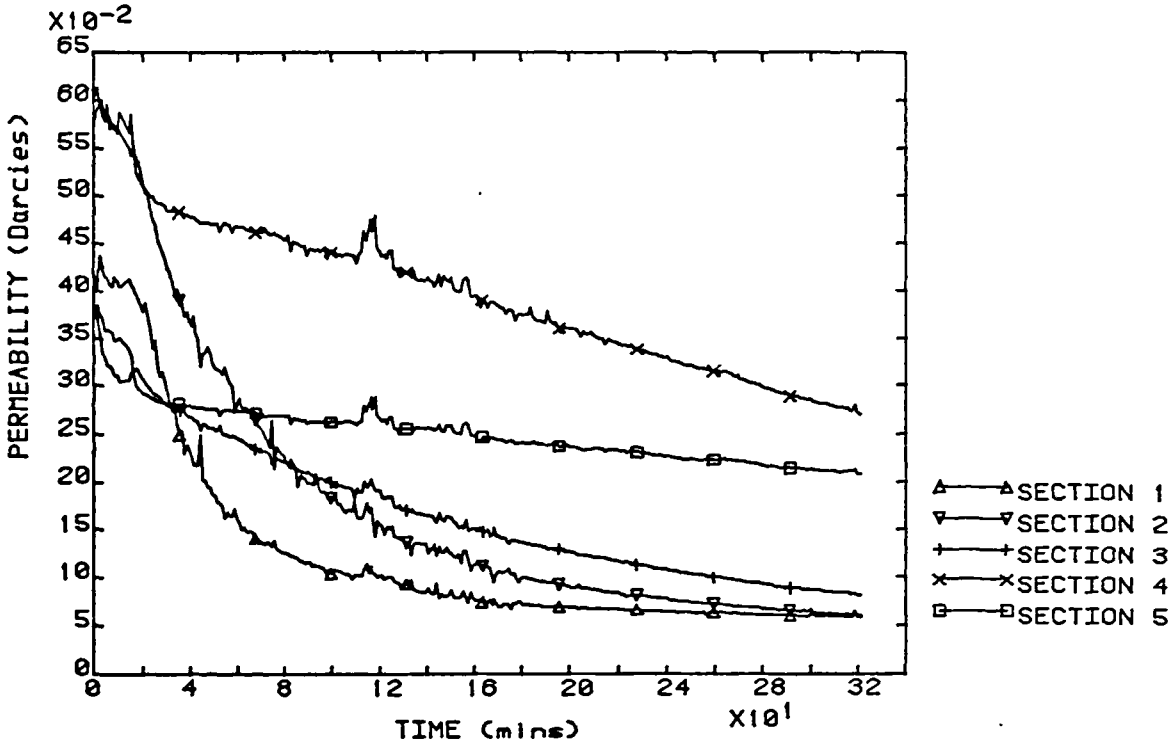

Figure A5.27b EXPERIMENT C221515EE-1
OVERALL PERMEABILITY SUPERSATURATION = 17.5

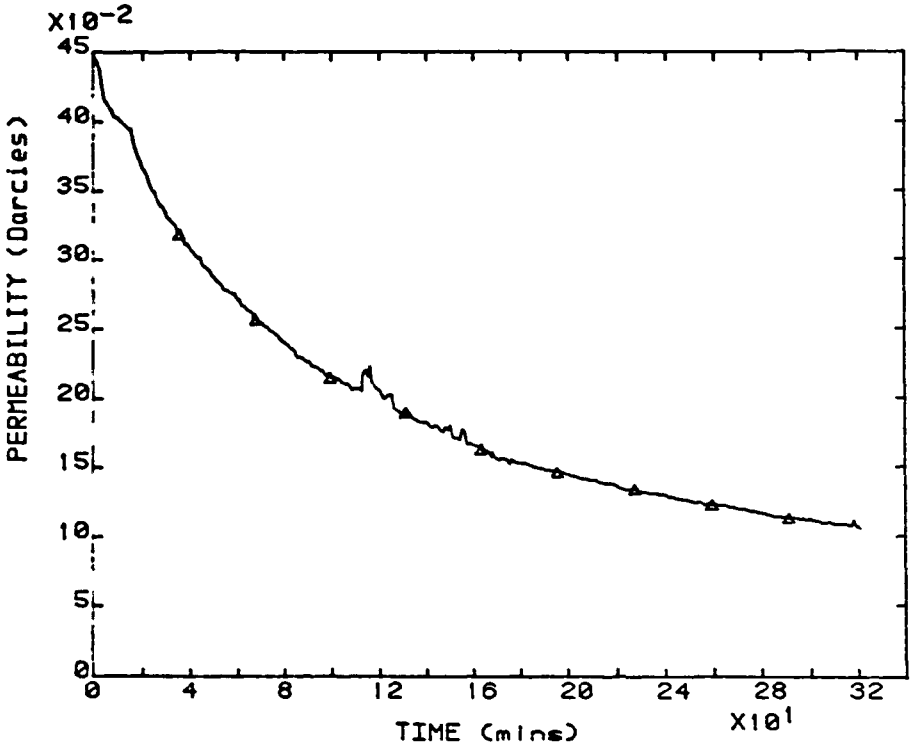

Figure A5.28a EXPERIMENT C231515EE-3
SECTION PERMEABILITIES SUPERSATURATION = 17.5

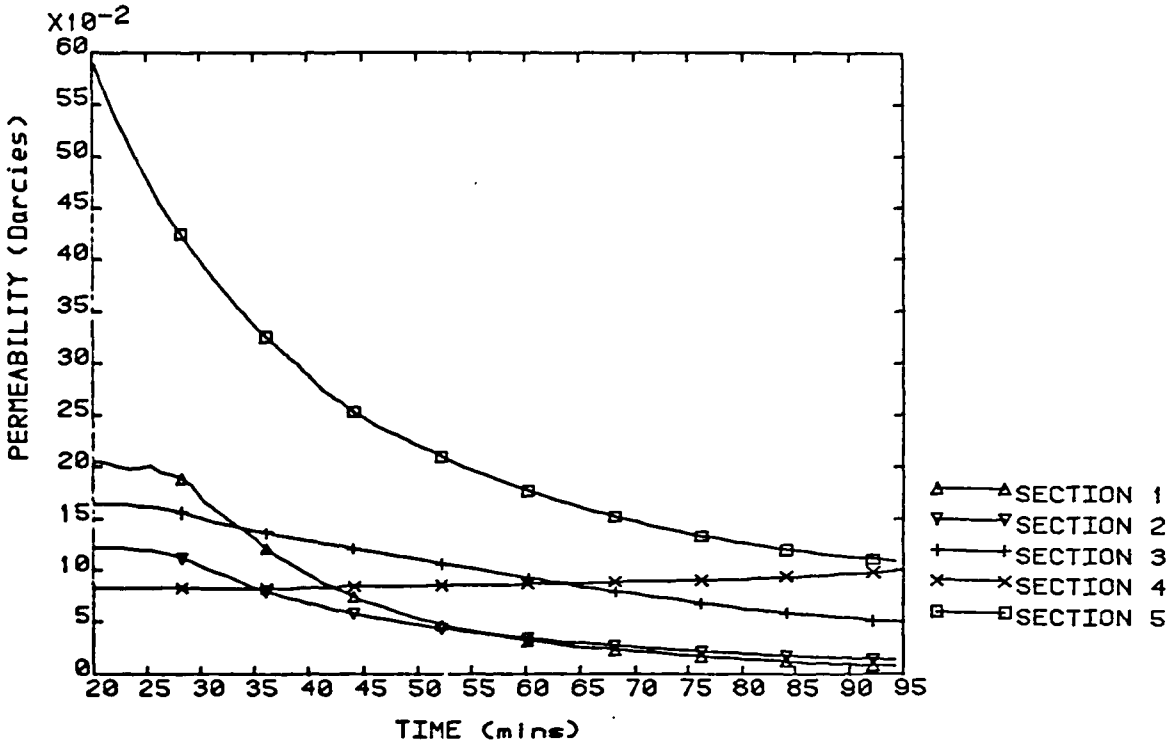

Figure A5.28b EXPERIMENT C231515EE-3
OVERALL PERMEABILITY SUPERSATURATION = 17.5

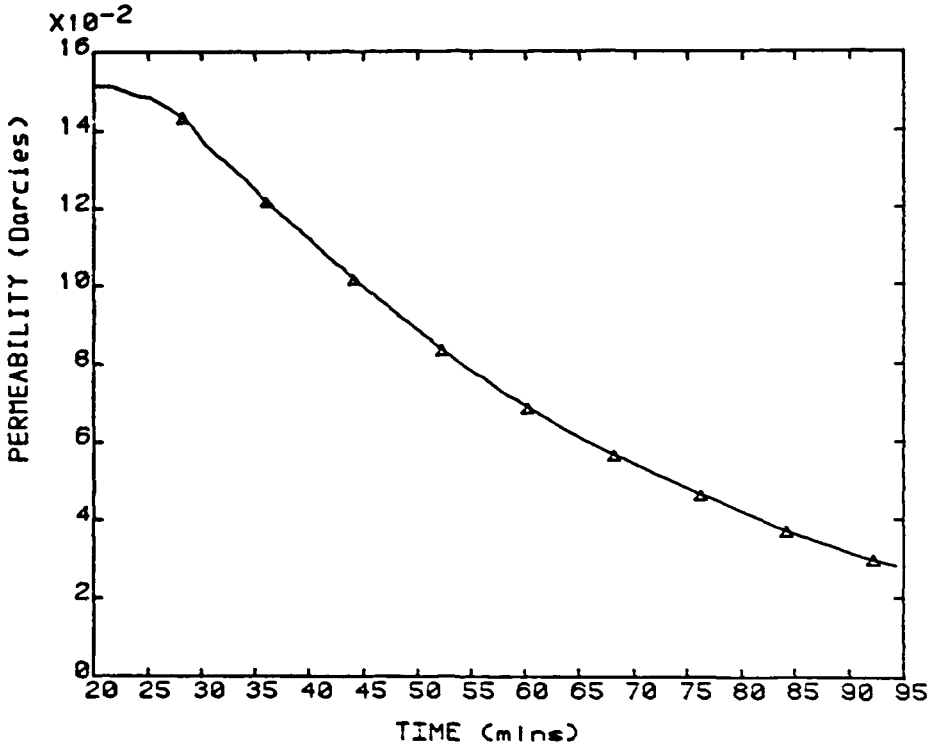

Figure A5.29a EXPERIMENT C277.57.5EE-10
SECTION PERMEABILITIES SUPERSATURATION = 17.5

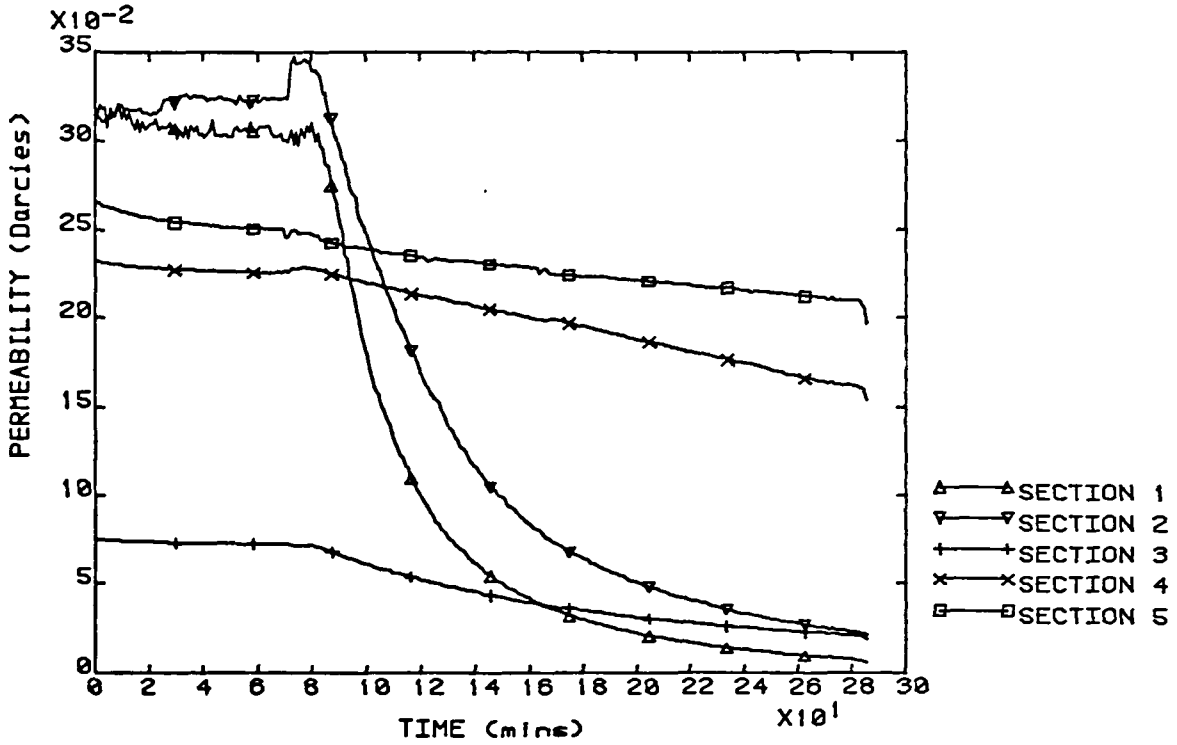

Figure A5.29b EXPERIMENT C277.57.5EE-10
OVERALL PERMEABILITY SUPERSATURATION = 17.5

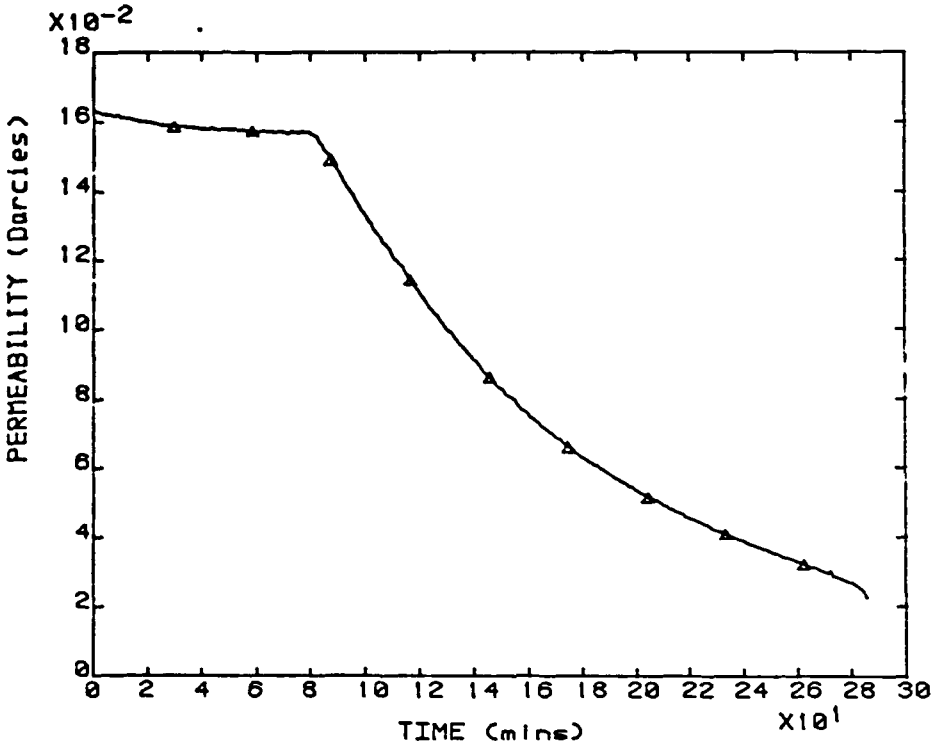

Figure A5.30a EXPERIMENT C167.57.5EE-11S
SECTION PERMEABILITIES SUPERSATURATION = 17.5

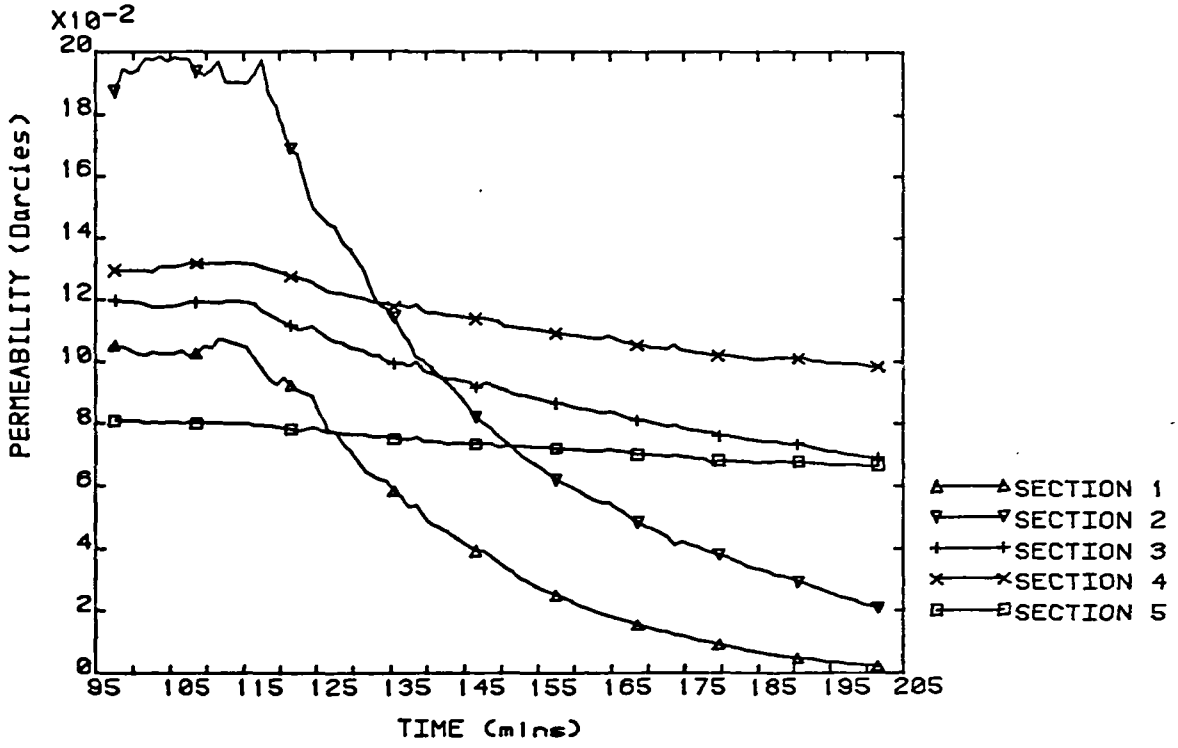

Figure A5.30b EXPERIMENT C167.57.5EE-11S
OVERALL PERMEABILITY SUPERSATURATION = 17.5

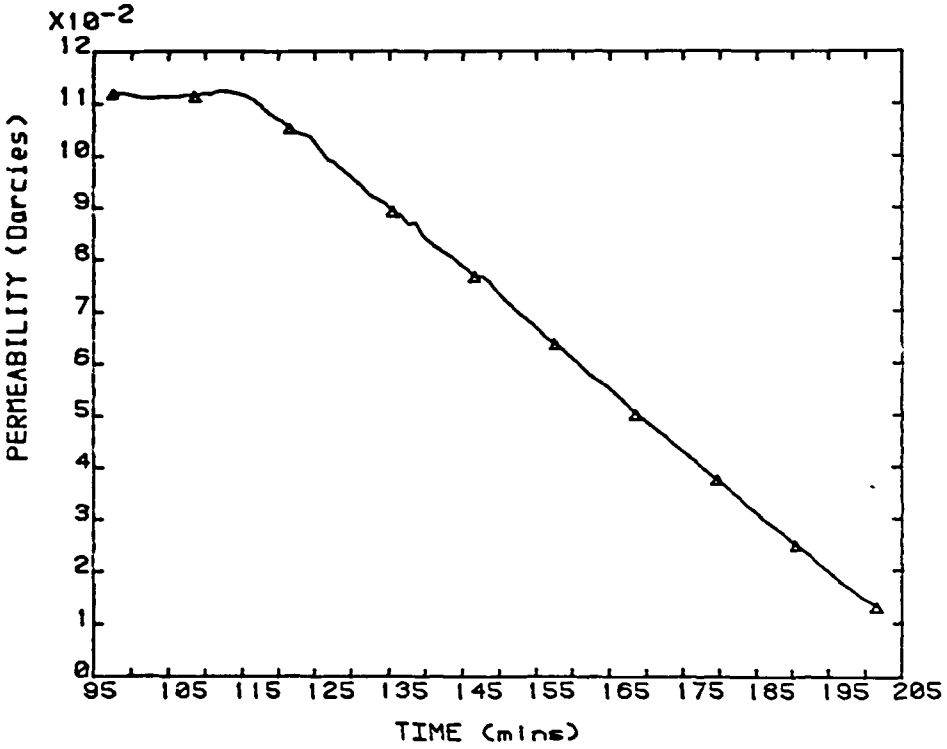

Figure A5.31a EXPERIMENT C1644EE-12
SECTION PERMEABILITIES SUPERSATURATION = 17.5

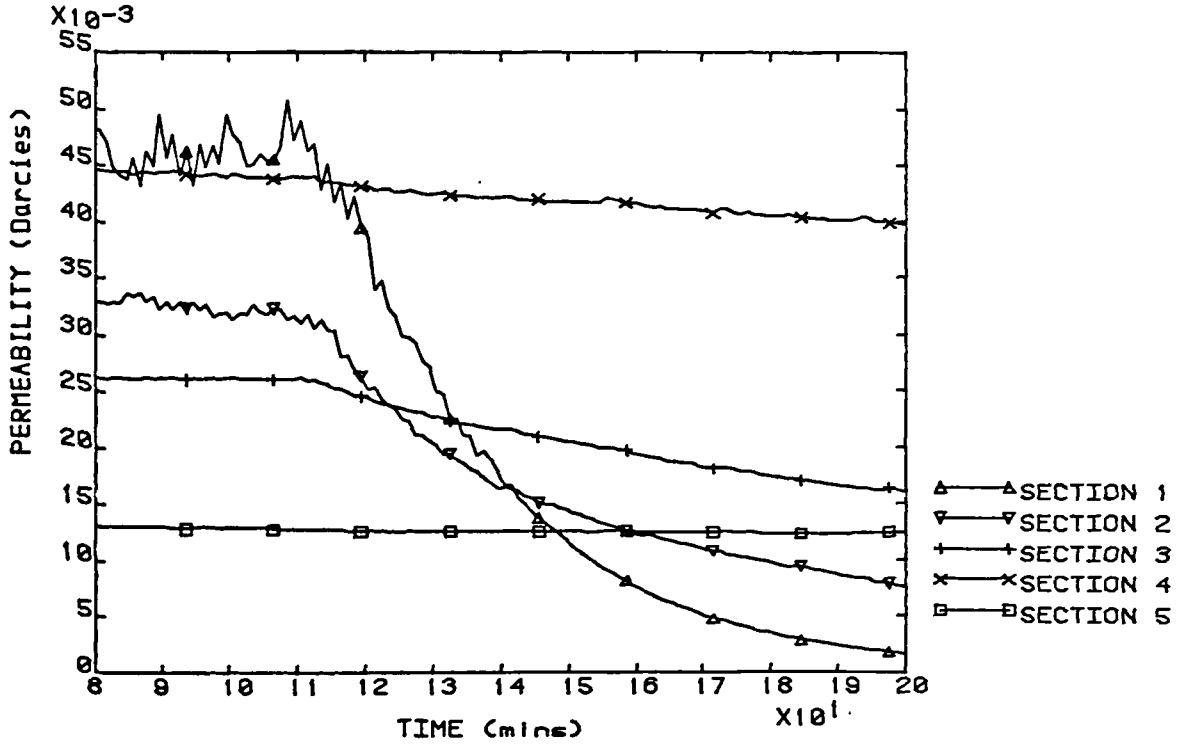

Figure A5.31b EXPERIMENT C1644EE-12
OVERALL PERMEABILITY SUPERSATURATION = 17.5

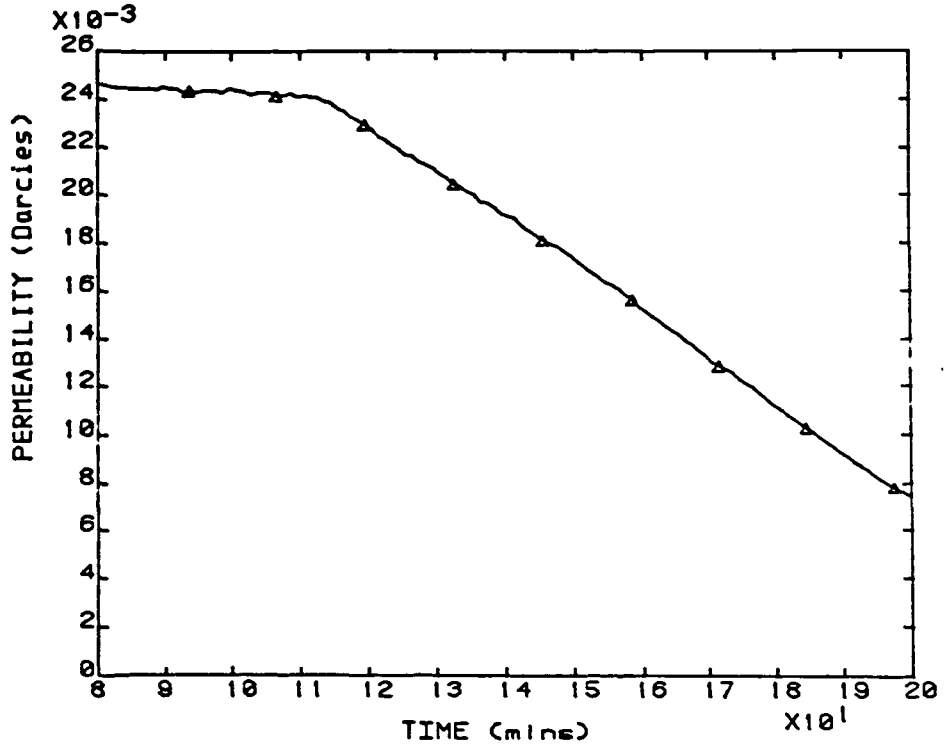

Figure A5.32a EXPERIMENT C237.57.5FF-1S
SECTION PERMEABILITIES SUPERSATURATION = 8.4

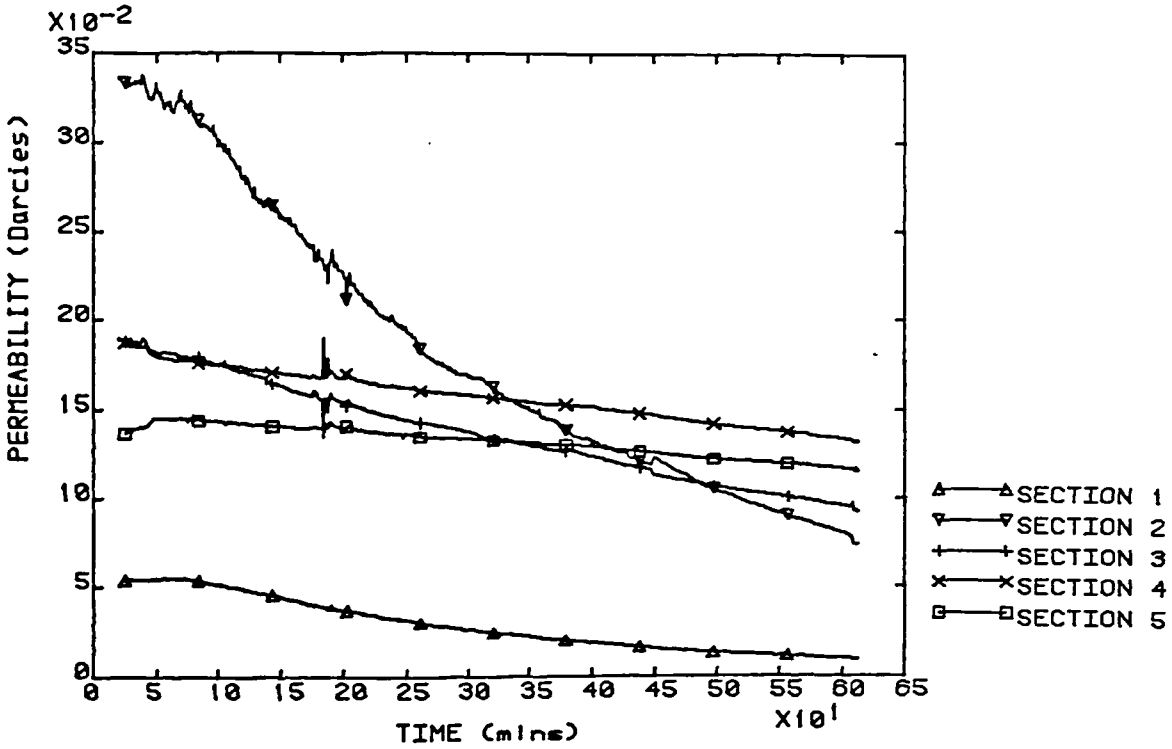

Figure A5.32b EXPERIMENT C237.57.5FF-1S
OVERALL PERMEABILITY SUPERSATURATION = 8.4

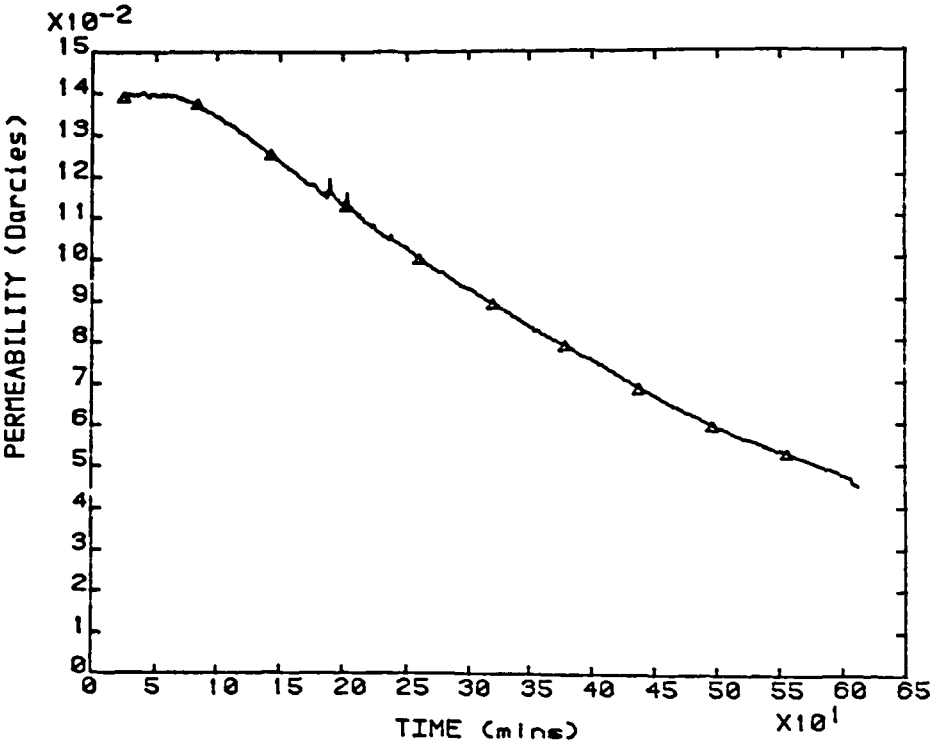

Figure A5.33a EXPERIMENT C167.57.5FF-2S
SECTION PERMEABILITIES SUPERSATURATION = 8.4

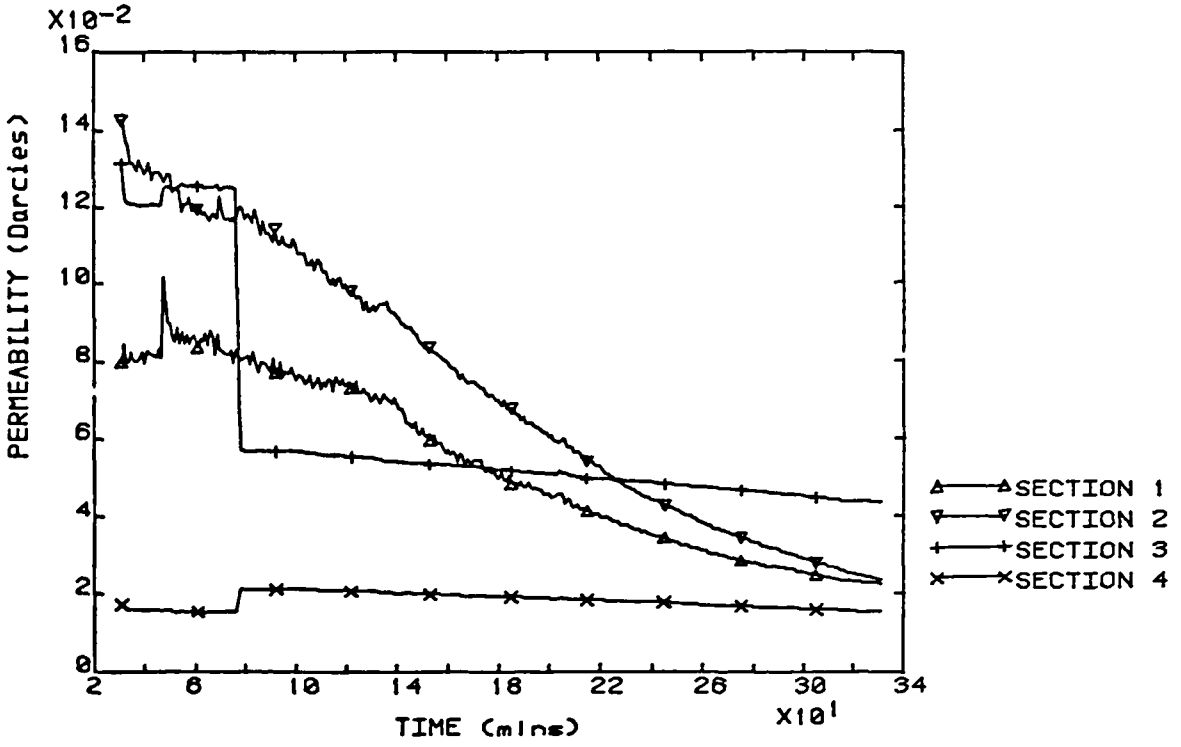

Figure A5.33b EXPERIMENT C167.57.5FF-2S
OVERALL PERMEABILITY SUPERSATURATION = 8.4

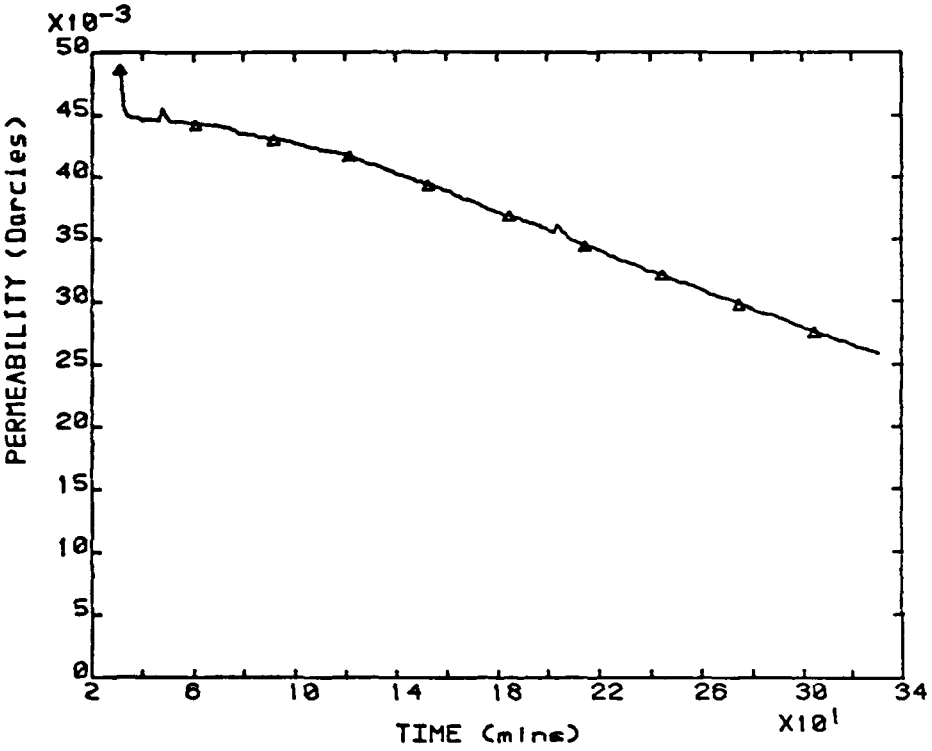

Figure A5.34a EXPERIMENT C167.57.5FF-4
SECTION PERMEABILITIES SUPERSATURATION = 8.4

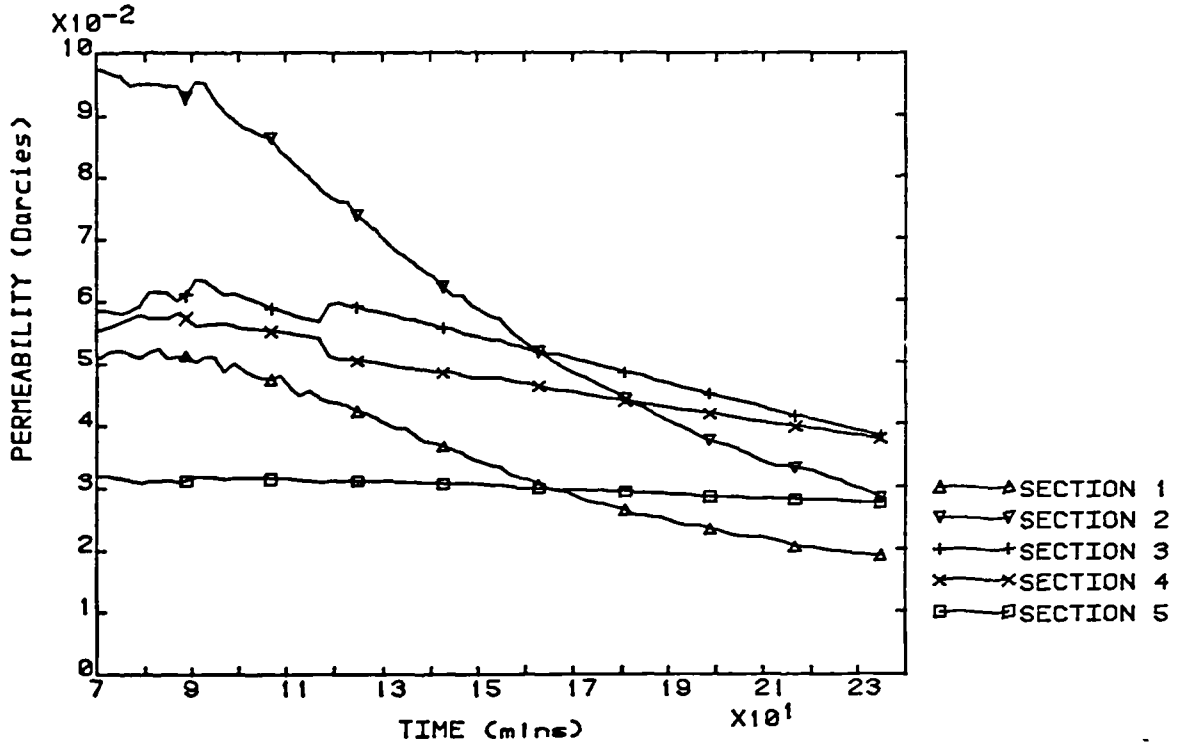

Figure A5.34b EXPERIMENT C167.57.5FF-4
OVERALL PERMEABILITY SUPERSATURATION = 8.4

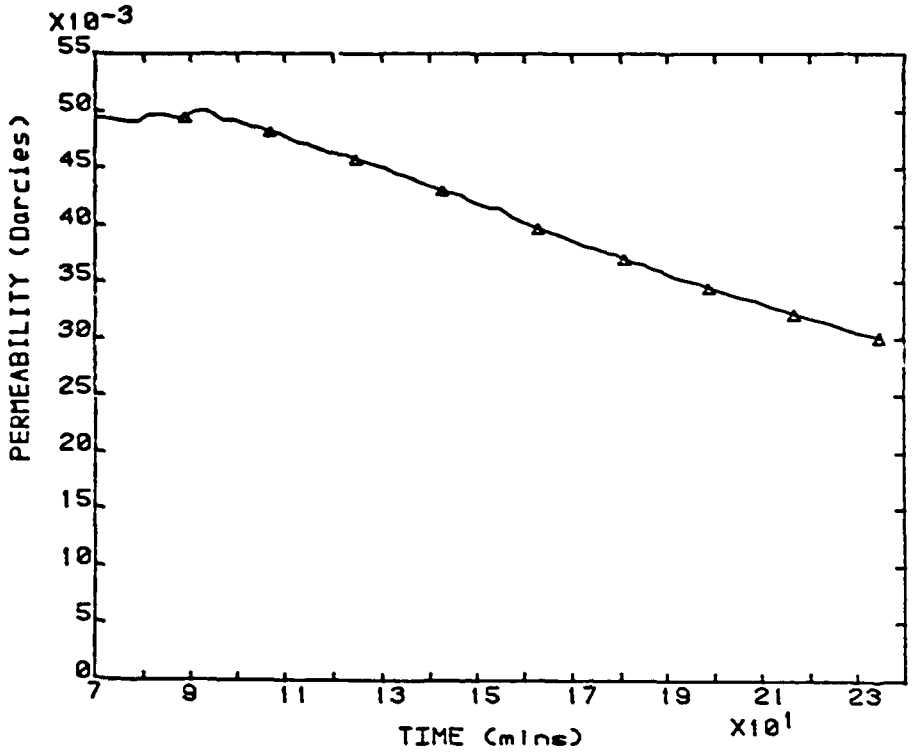

Figure A5.35a EXPERIMENT C267.57.5HH-1S
SECTION PERMEABILITIES SUPERSATURATION = 19.0

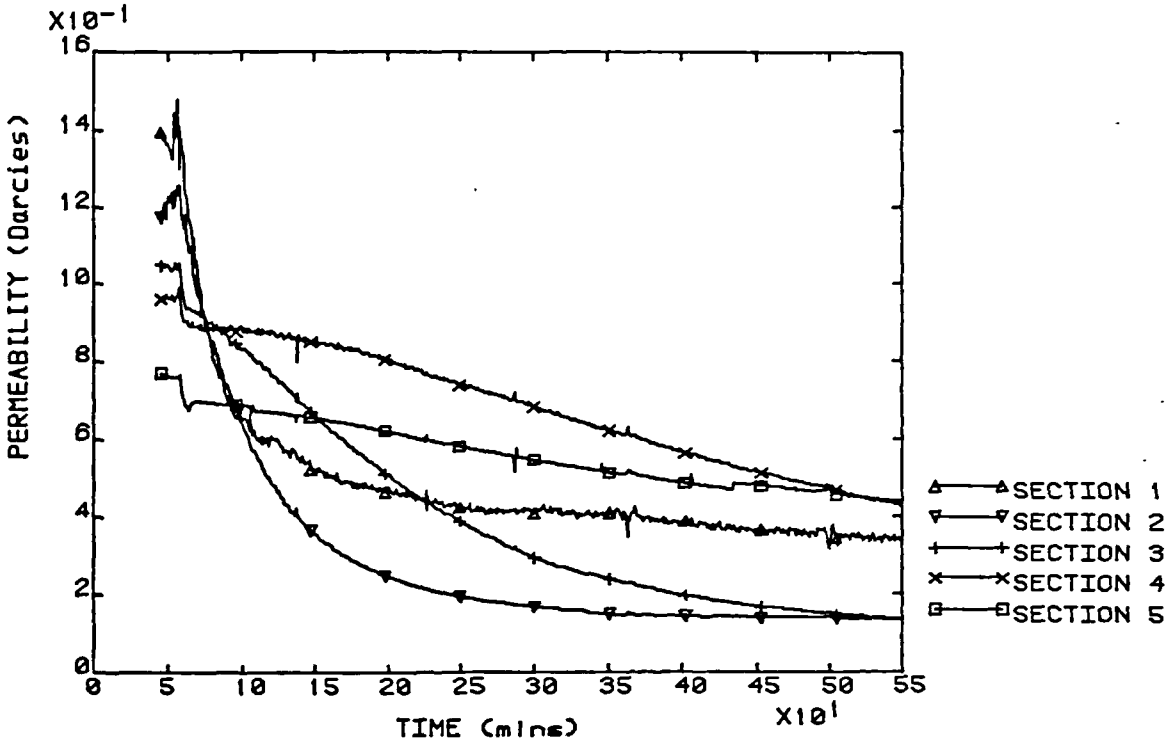

Figure A5.35b EXPERIMENT C267.57.5HH-1S
OVERALL PERMEABILITY SUPERSATURATION = 19.0

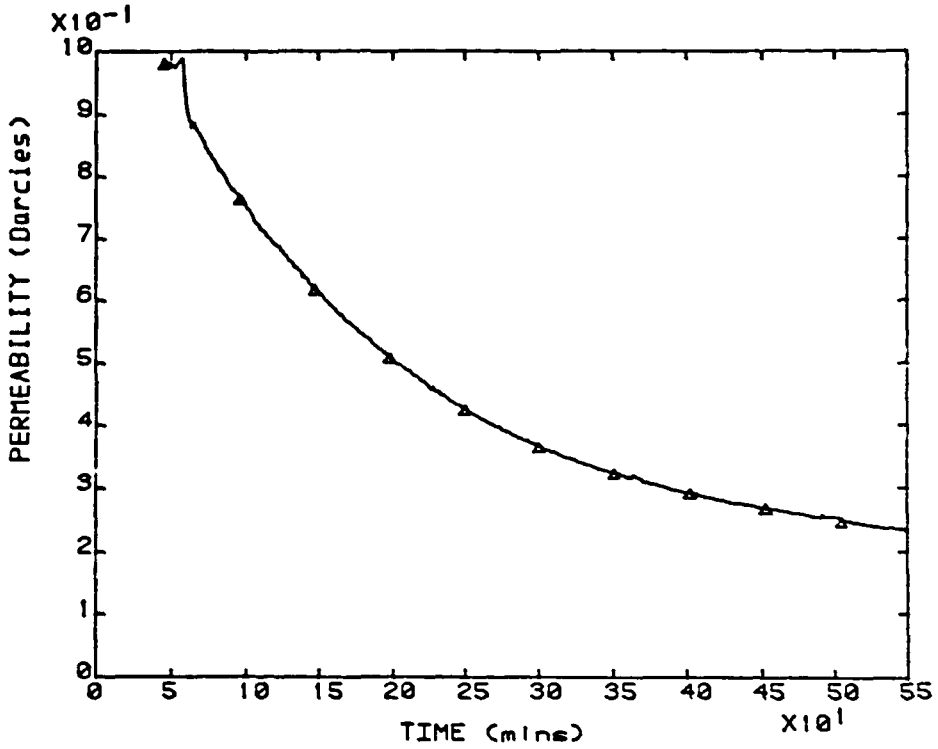

Figure A5.36a EXPERIMENT C247.57.5HH-2
SECTION PERMEABILITIES SUPERSATURATION = 19.0

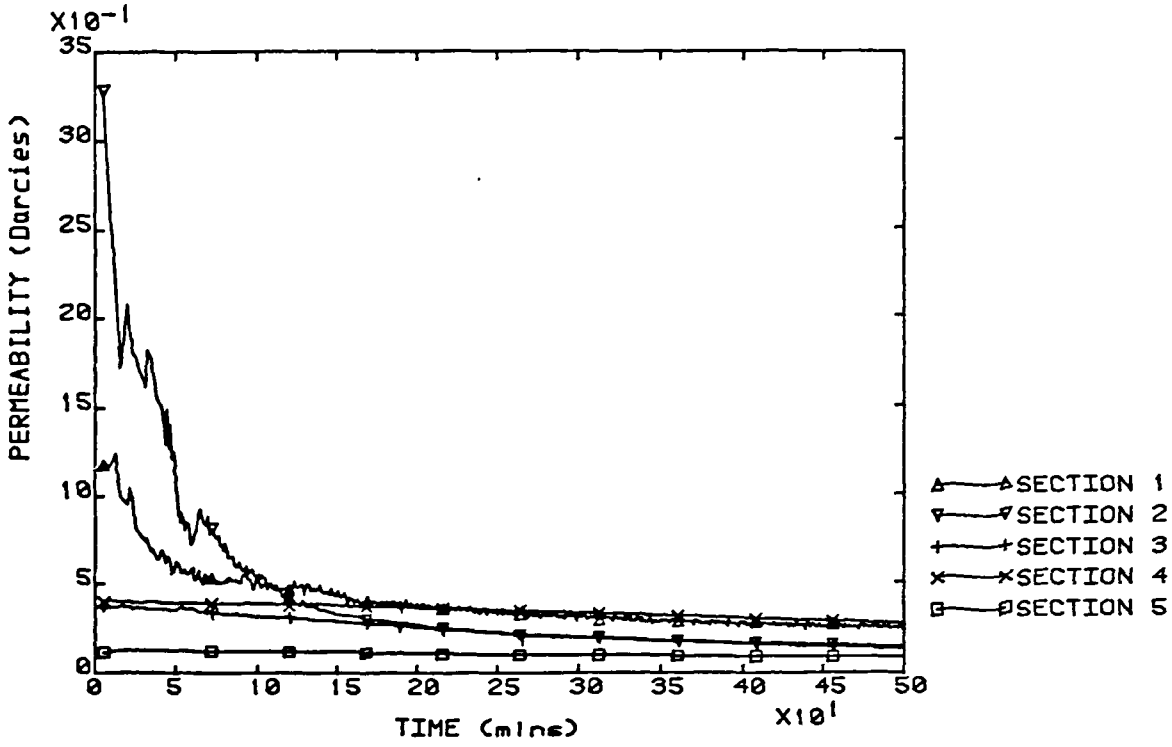

Figure A5.36b EXPERIMENT C247.57.5HH-2
OVERALL PERMEABILITY SUPERSATURATION = 19.0

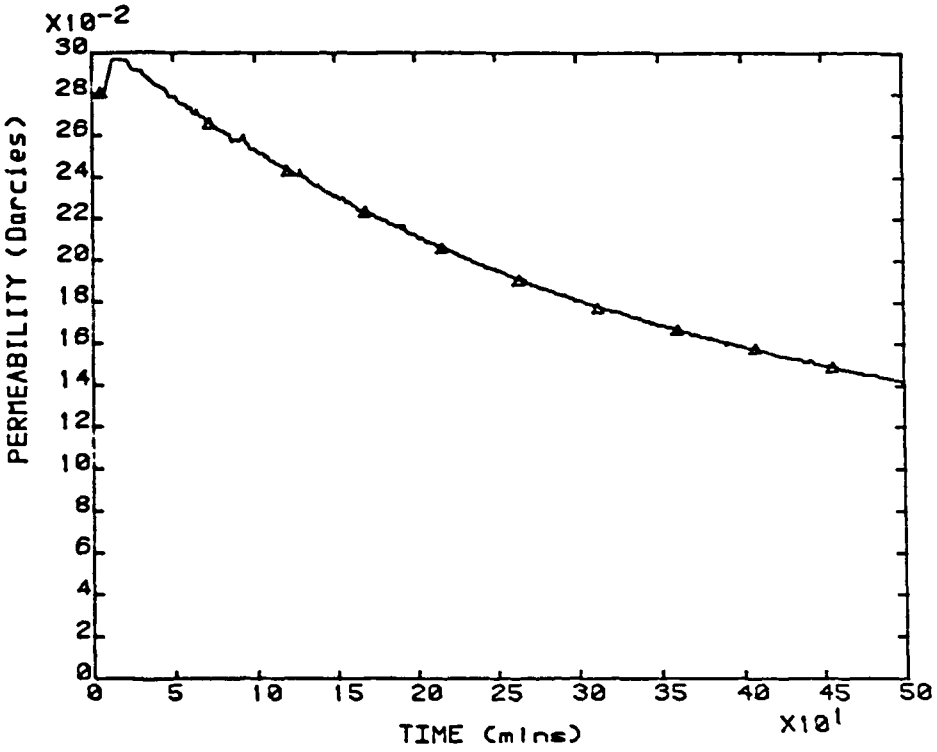

Figure A5.37a EXPERIMENT C247.57.5II-1S
SECTION PERMEABILITIES SUPERSATURATION = 19.0

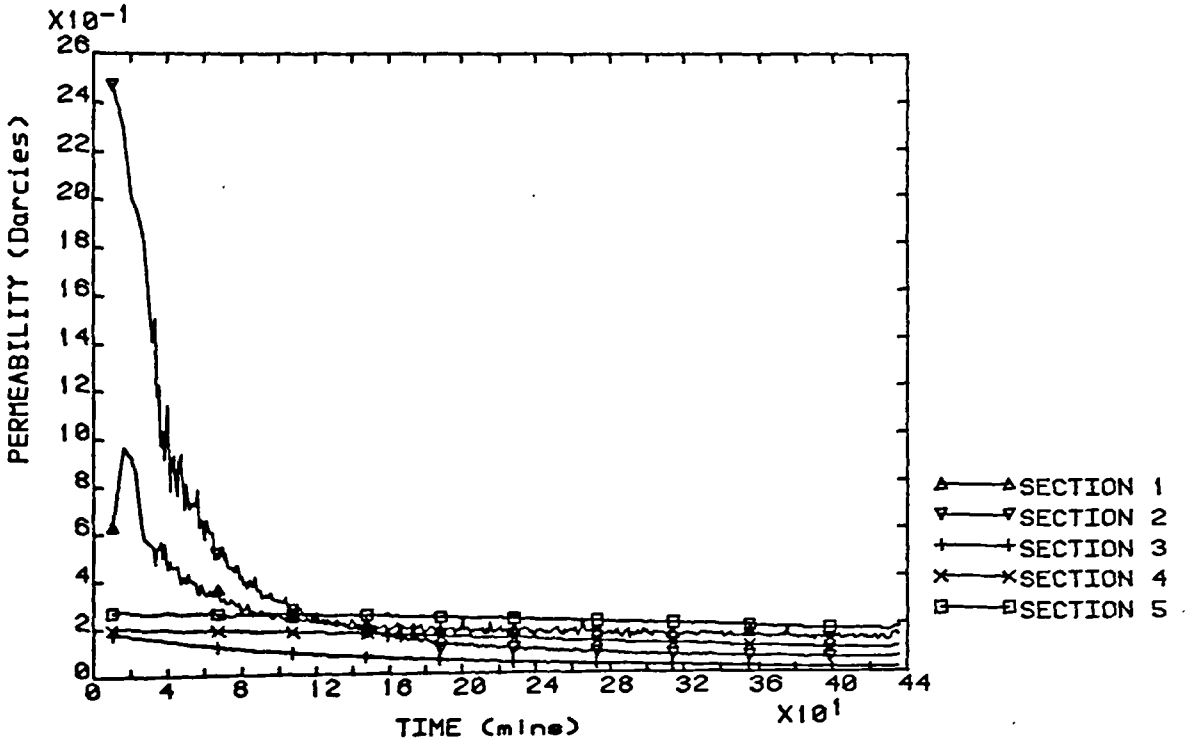

Figure A5.37b EXPERIMENT C247.57.5II-1S
OVERALL PERMEABILITY SUPERSATURATION = 19.0

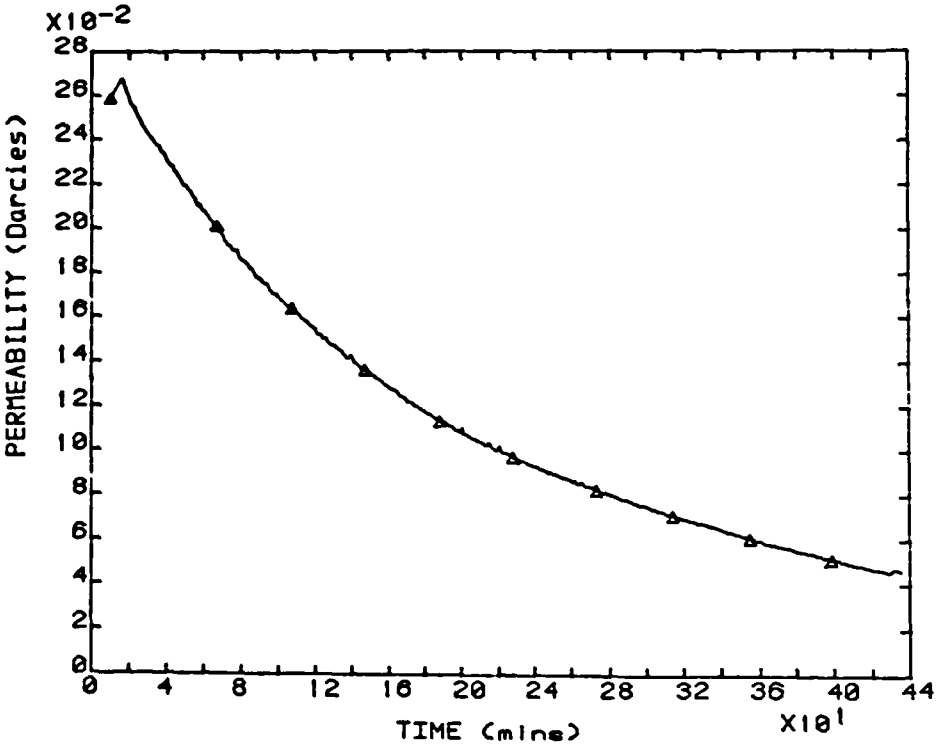

Figure A5.38a EXPERIMENT C247.57.5II-2S
SECTION PERMEABILITIES SUPERSATURATION = 19.0

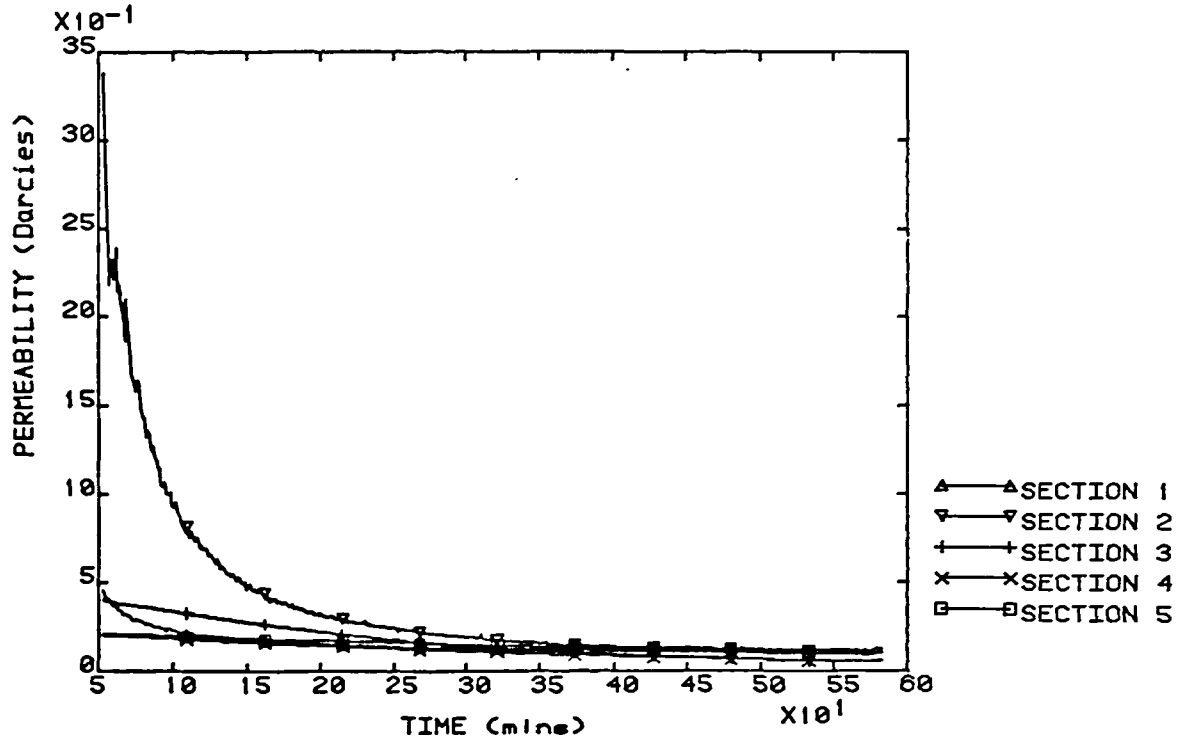

Figure A5.38b EXPERIMENT C247.57.5II-2S
OVERALL PERMEABILITY SUPERSATURATION = 19.0

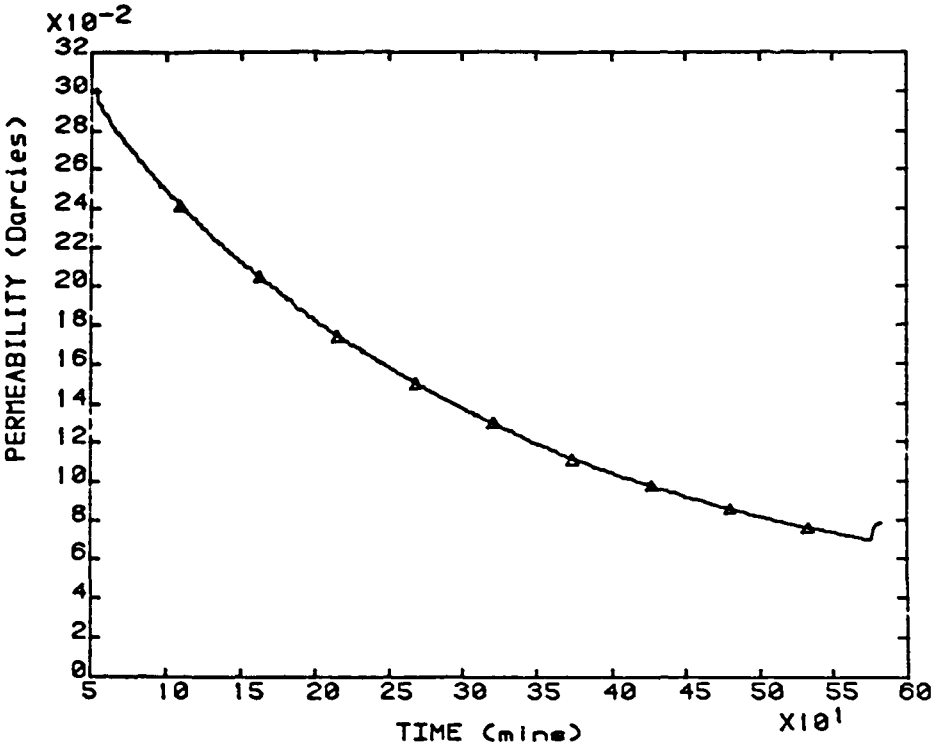

Figure A5.39a EXPERIMENT C247.57.5JJ-1S
SECTION PERMEABILITIES SUPERSATURATION = 19.0

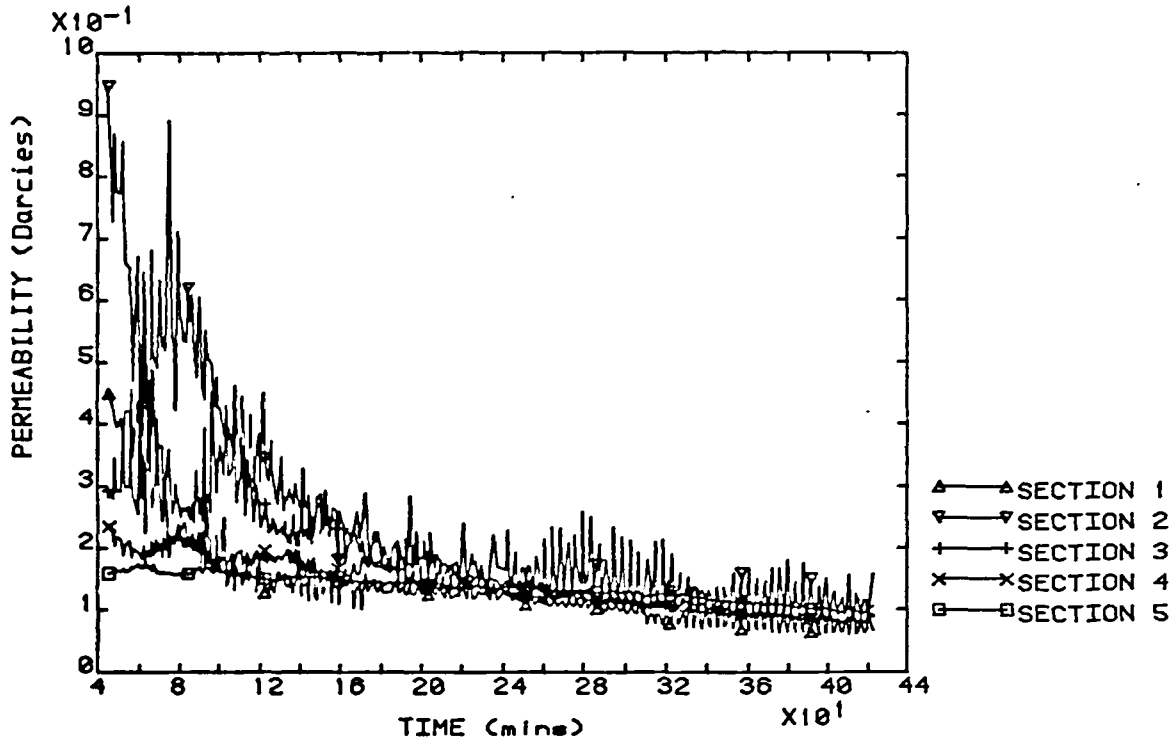

Figure A5.39b EXPERIMENT C247.57.5JJ-1S
OVERALL PERMEABILITY SUPERSATURATION = 19.0

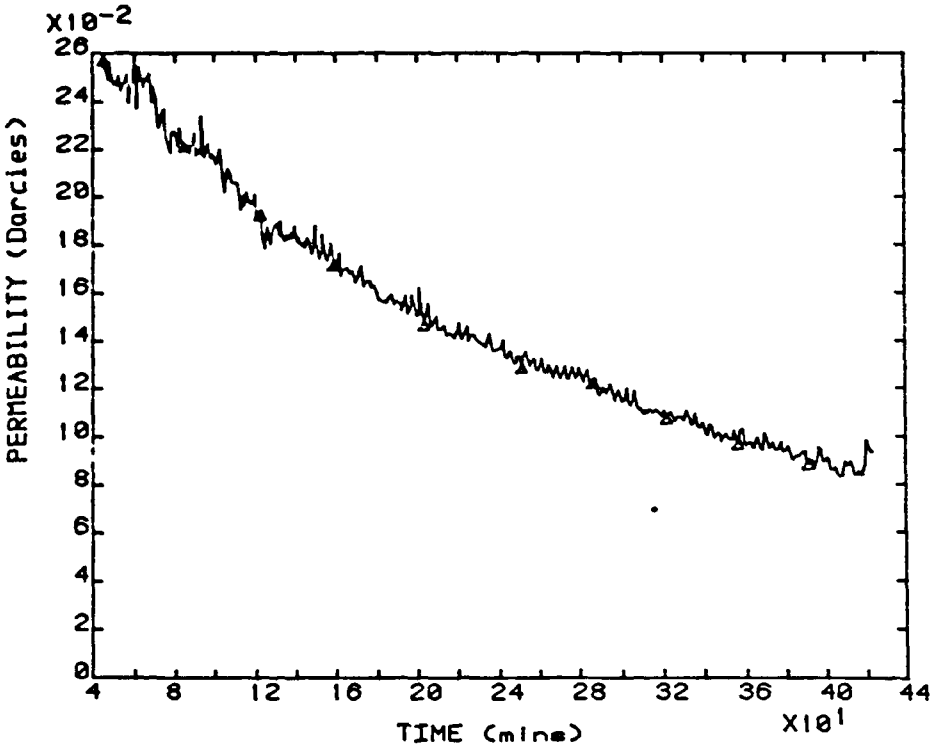

Figure A5.40a EXPERIMENT C247.57.5JJ-2S
SECTION PERMEABILITIES SUPERSATURATION = 19.0

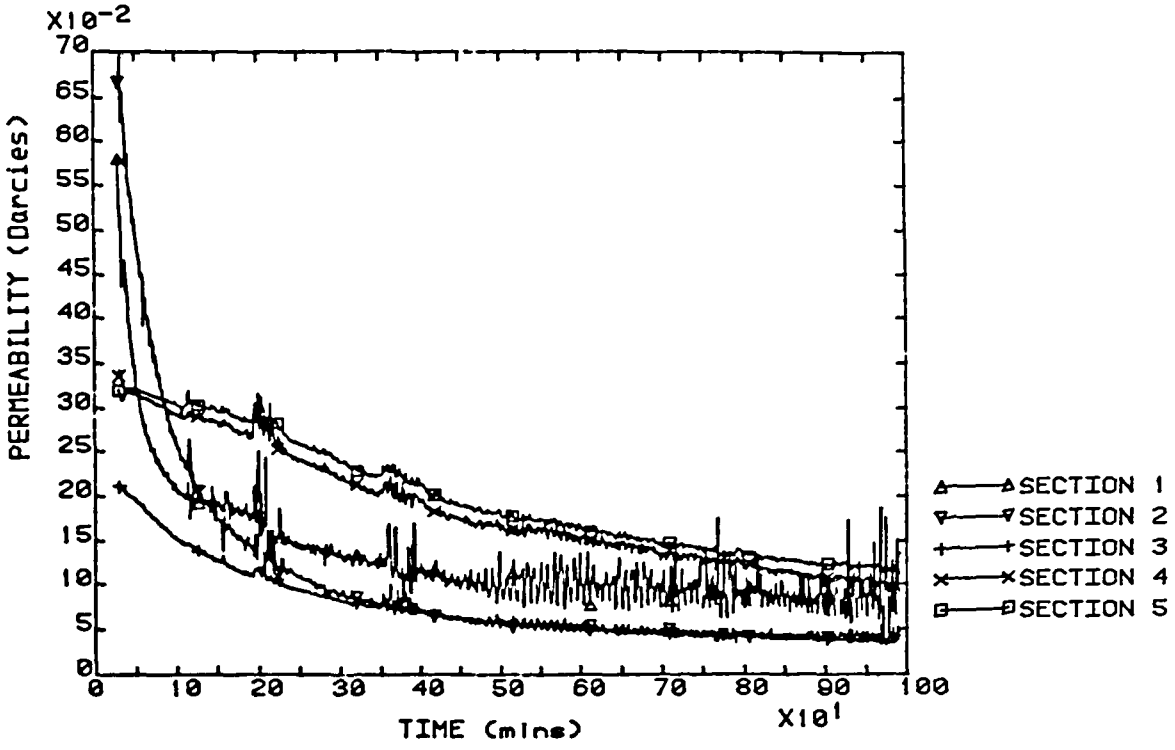

Figure A5.40b EXPERIMENT C247.57.5JJ-2S
OVERALL PERMEABILITY SUPERSATURATION = 19.0

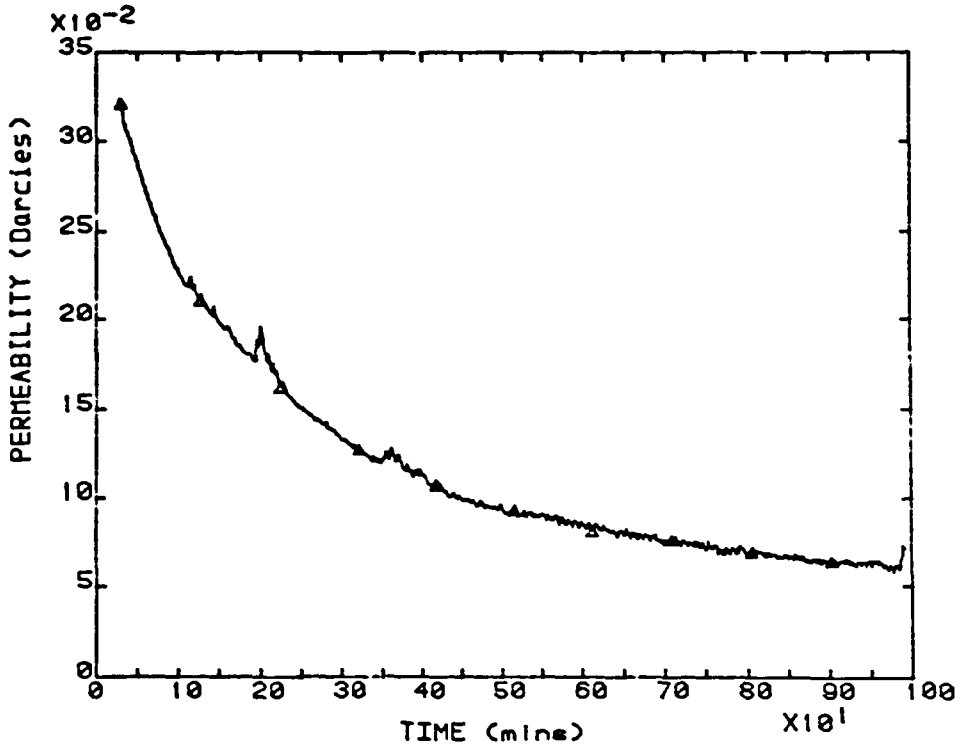

Figure A5.41a EXPERIMENT C247.57.5KK-1S
SECTION PERMEABILITIES SUPERSATURATION = 18.5

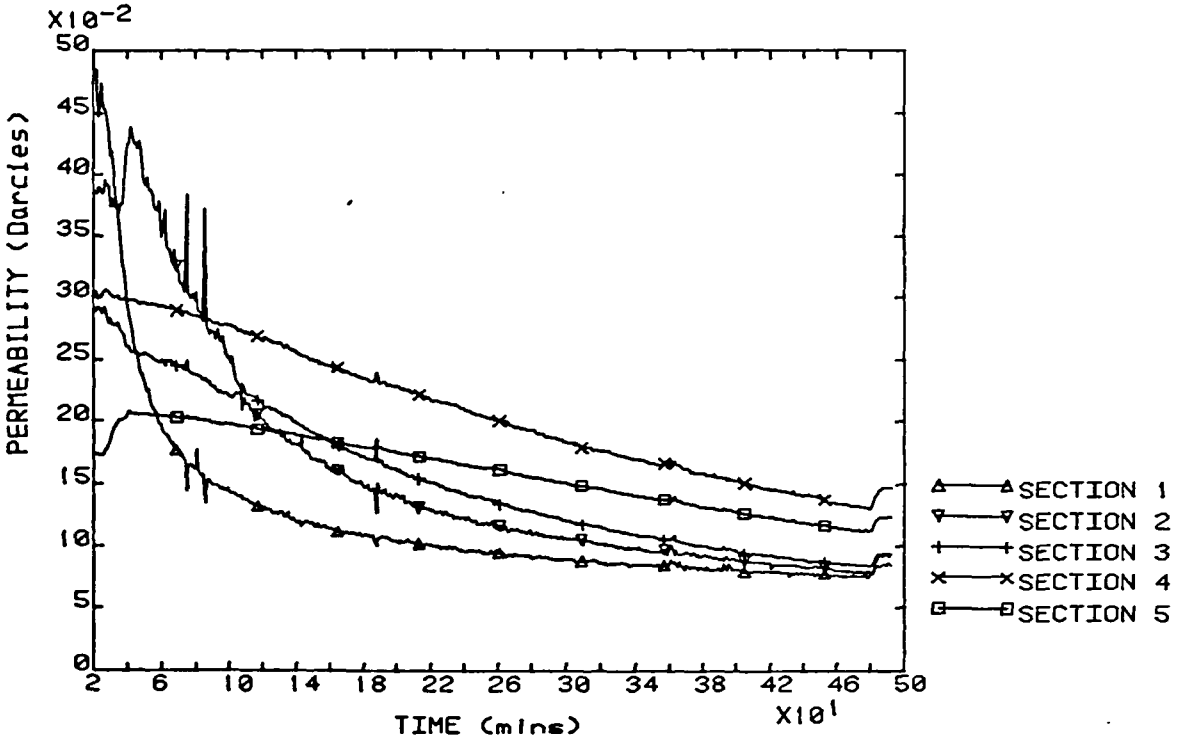

Figure A5.41b EXPERIMENT C247.57.5KK-1S
OVERALL PERMEABILITY SUPERSATURATION = 18.5

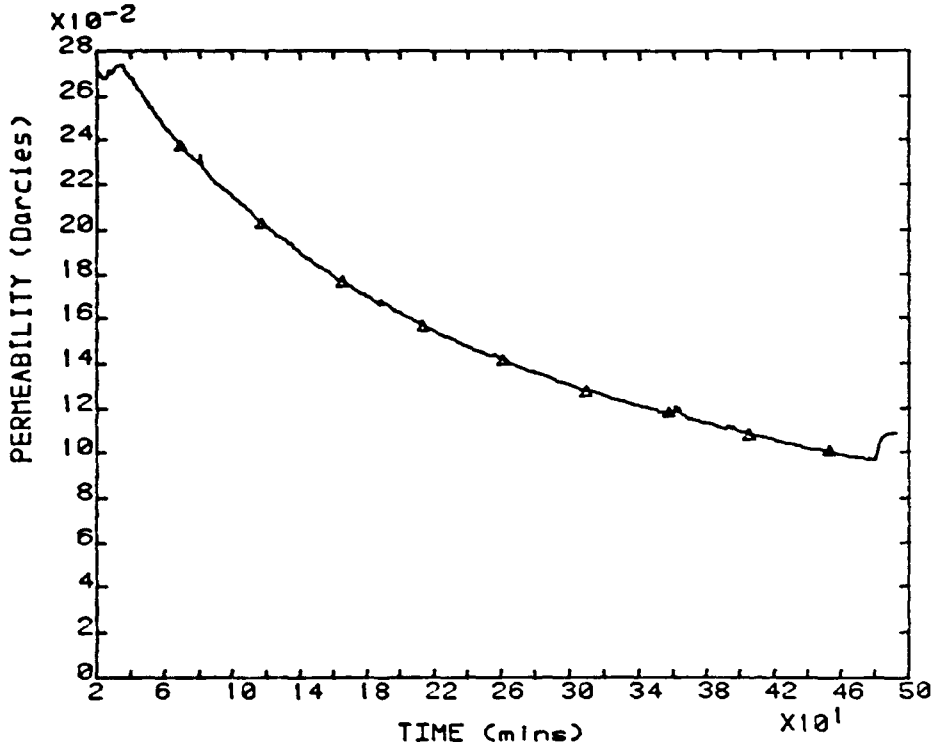

Figure A5.42a EXPERIMENT C247.57.5KK-1S
SECTION PERMEABILITIES SUPERSATURATION = 18.5

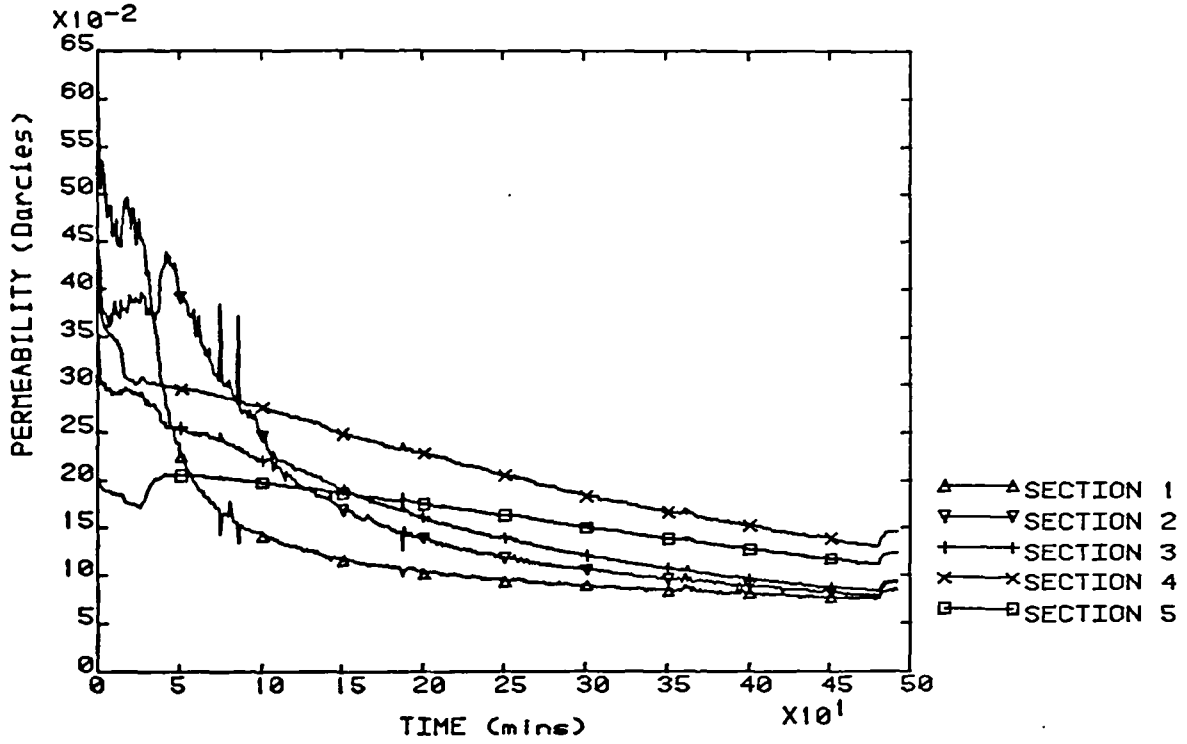

Figure A5.42b EXPERIMENT C247.57.5KK-1S
OVERALL PERMEABILITY SUPERSATURATION = 18.5

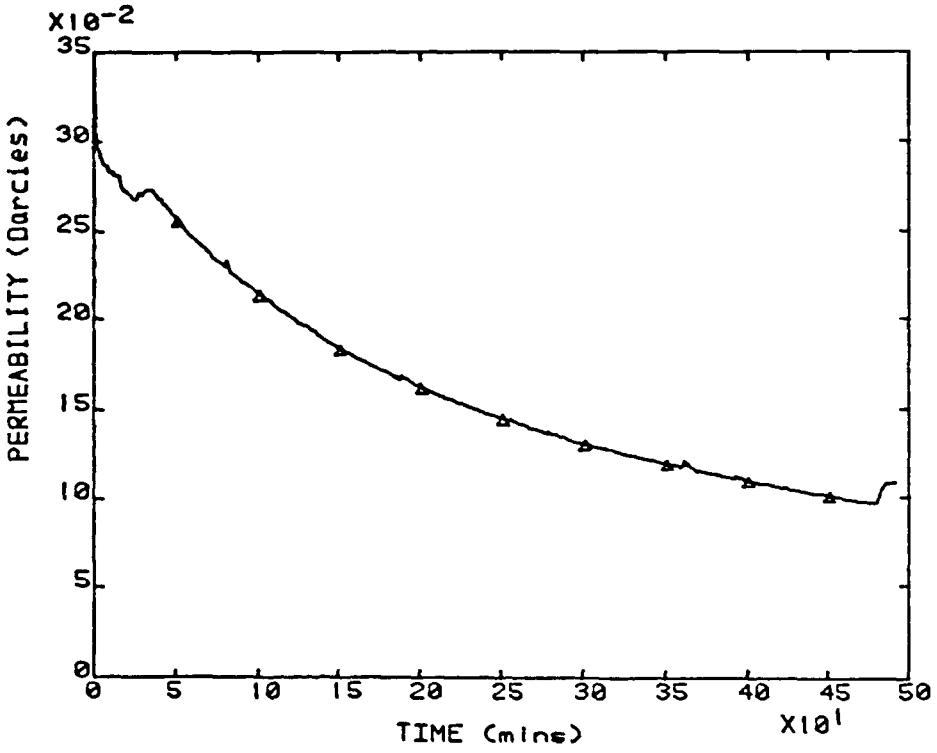

Figure A5.43a SOLUBILITY DATA PREDICTIONS FOR BASO4
WITH BRINE SYSTEM A

TEMPERATURE = 25.0 DEG C PRESSURE = 1.0 BAR

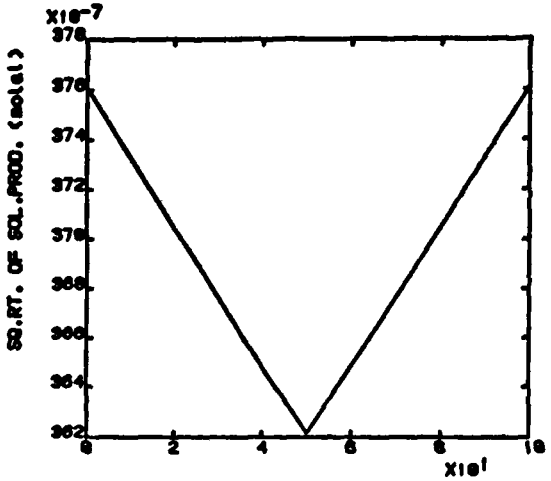

Figure A5.43b SOLUBILITY DATA PREDICTIONS FOR BASO4
WITH BRINE SYSTEM A

TEMPERATURE = 25.0 DEG C PRESSURE = 1.0 BAR

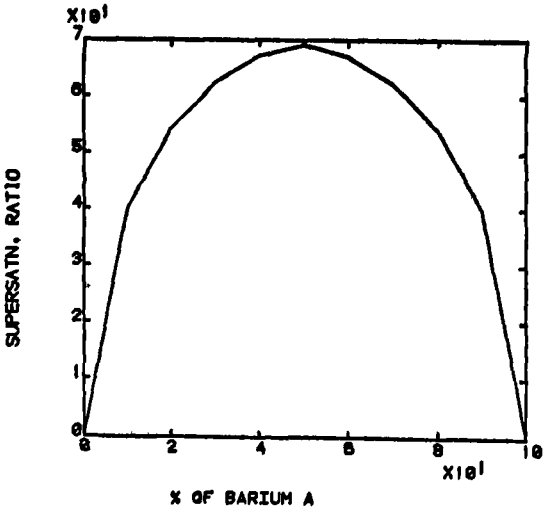

Figure A5.44a SOLUBILITY DATA PREDICTIONS FOR BASO4
WITH BRINE SYSTEM B

TEMPERATURE = 25.0 DEG C PRESSURE = 1.0 BAR

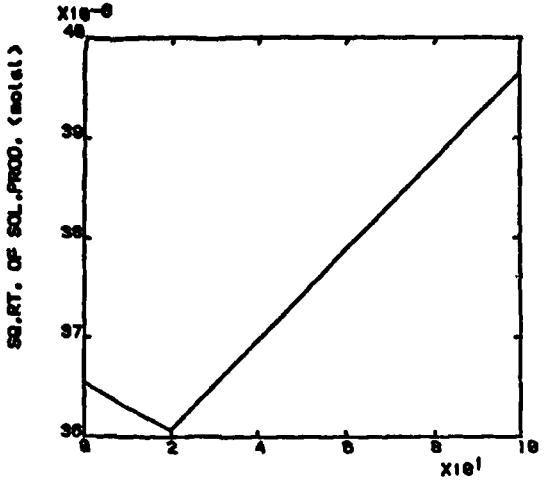

Figure A5.44b SOLUBILITY DATA PREDICTIONS FOR BASO4
WITH BRINE SYSTEM B

TEMPERATURE = 25.0 DEG C PRESSURE = 1.0 BAR

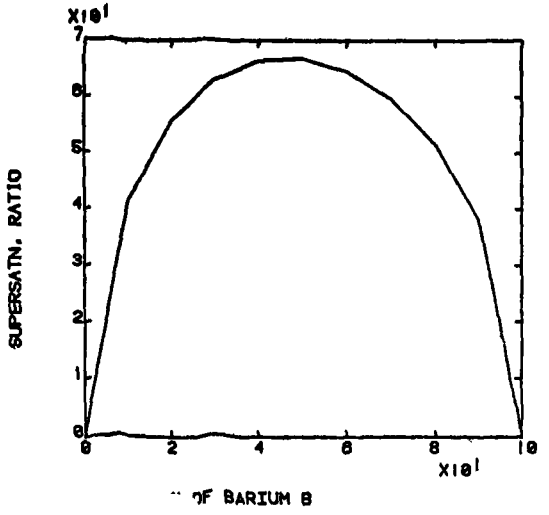

Figure A5 45a SOLUBILITY DATA PREDICTIONS FOR BASO4
WITH BRINE SYSTEM C

TEMPERATURE = 25 0 DEG C PRESSURE = 1 0 BAR

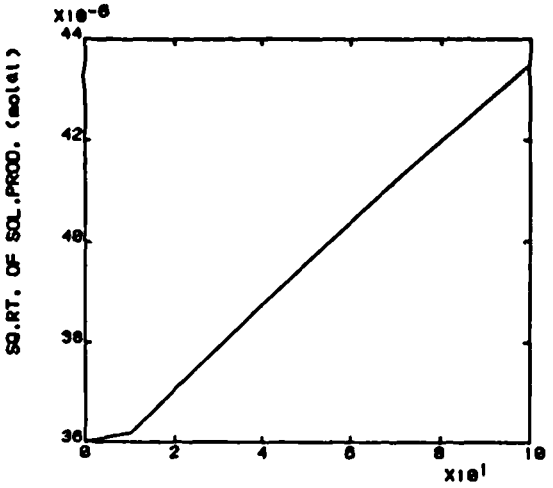

Figure A5 45b SOLUBILITY DATA PREDICTIONS FOR BASO4
WITH BRINE SYSTEM C

TEMPERATURE = 25 0 DEG C PRESSURE = 1 0 BAR

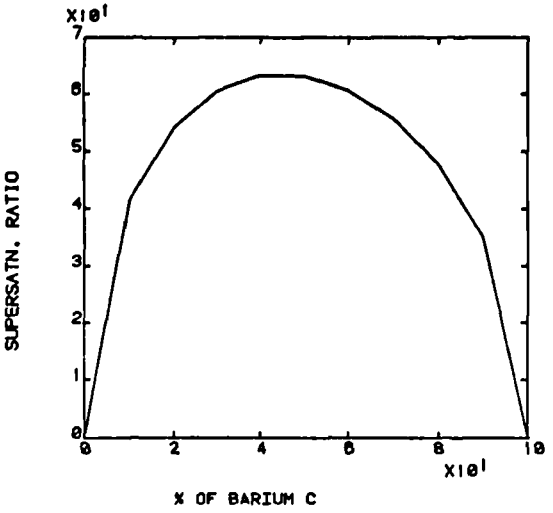

Figure A5 46a SOLUBILITY DATA PREDICTIONS FOR BASO4
WITH BRINE SYSTEM D

TEMPERATURE = 25 0 DEG C PRESSURE = 1 0 BAR

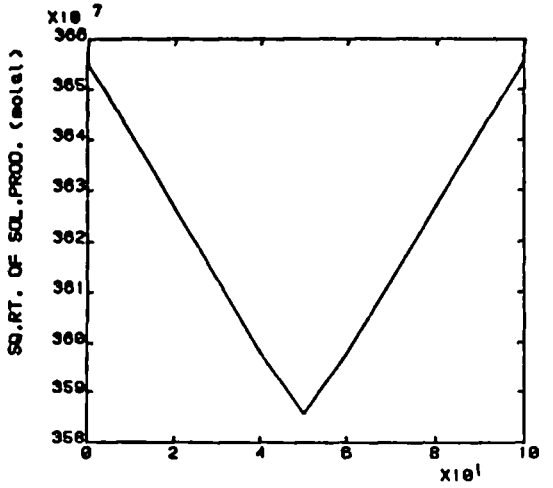

Figure A5 46b SOLUBILITY DATA PREDICTIONS FOR BASO4
WITH BRINE SYSTEM D

TEMPERATURE = 25 0 DEG C PRESSURE = 1 0 BAR

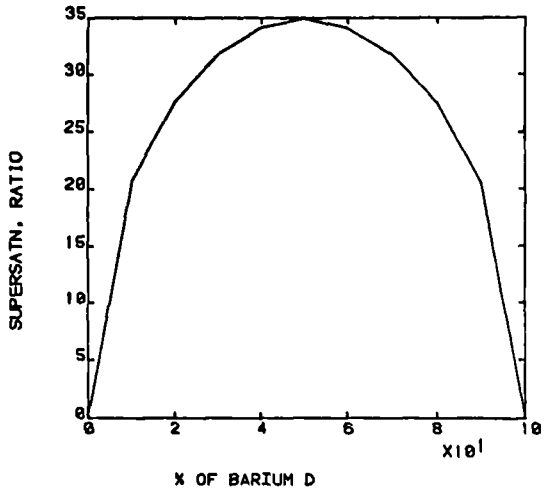

Figure A5.47a SOLUBILITY DATA PREDICTIONS FOR BASO4
WITH BRINE SYSTEM E

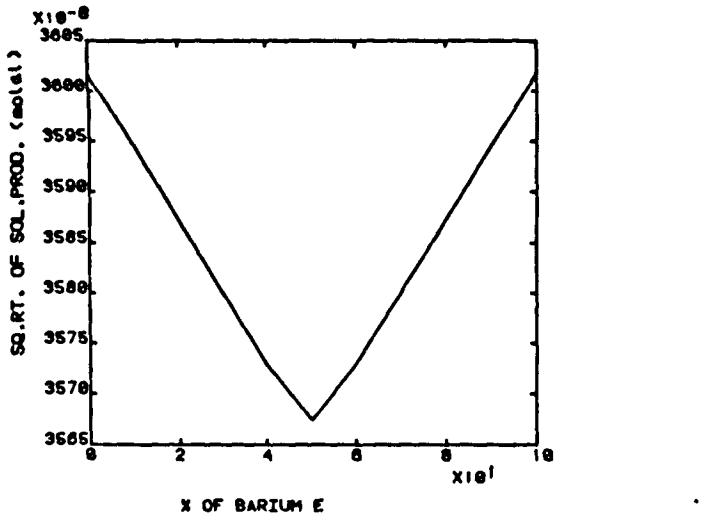

Figure A5.47b SOLUBILITY DATA PREDICTIONS FOR BASO4
WITH BRINE SYSTEM E

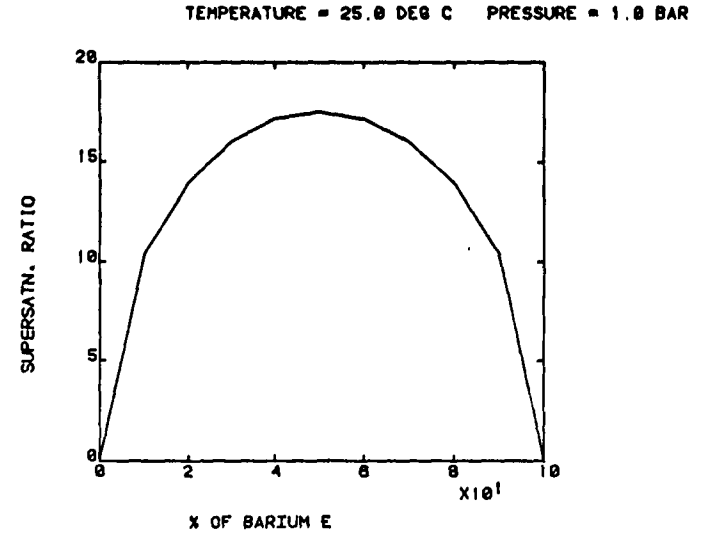

Figure A5.48a SOLUBILITY DATA PREDICTIONS FOR BASO4
WITH BRINE SYSTEM F

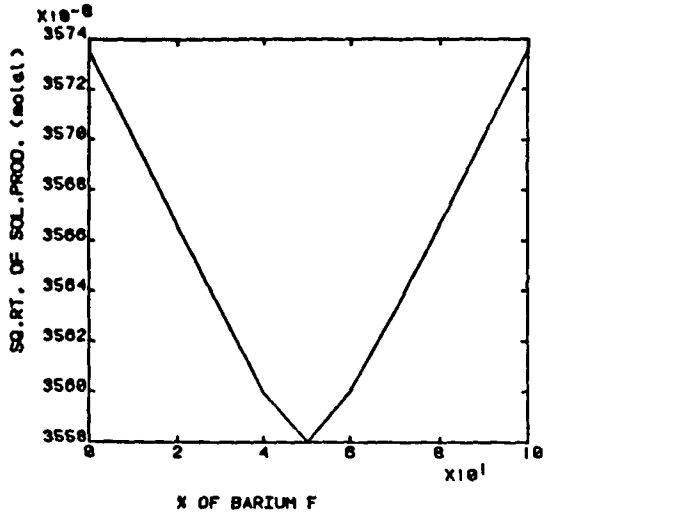

Figure A5.48b SOLUBILITY DATA PREDICTIONS FOR BASO4
WITH BRINE SYSTEM F

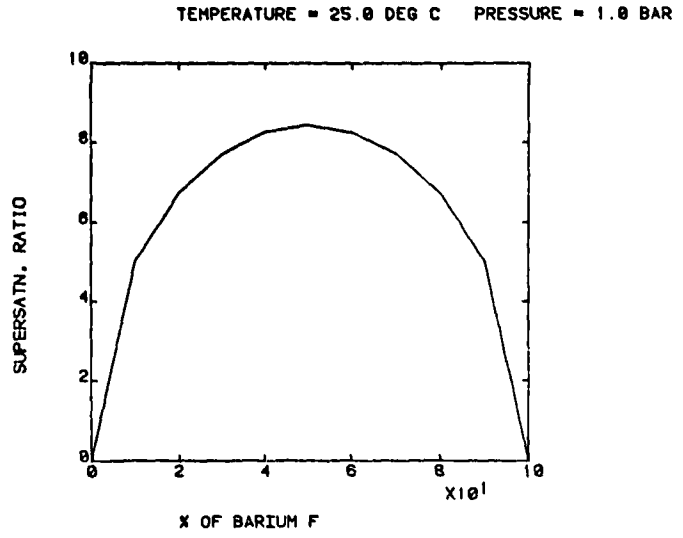

Figure A5.49a SOLUBILITY DATA PREDICTIONS FOR BASO4
WITH BRINE SYSTEM G

TEMPERATURE = 25.0 DEG C PRESSURE = 1.0 BAR

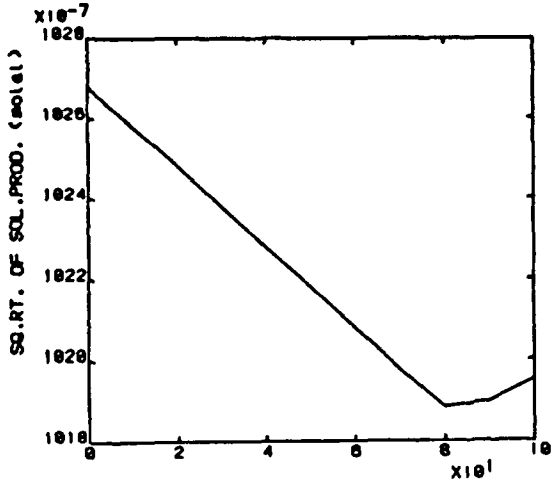

Figure A5.49b SOLUBILITY DATA PREDICTIONS FOR BASO4
WITH BRINE SYSTEM G

TEMPERATURE = 25.0 DEG C PRESSURE = 1.0 BAR

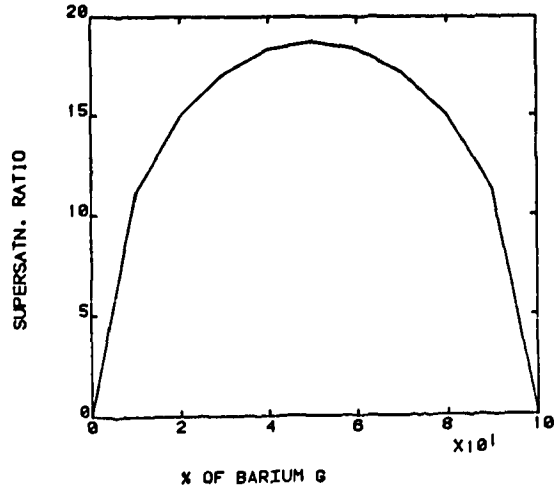

Figure A5.50a SOLUBILITY DATA PREDICTIONS FOR BASO4
WITH BRINE SYSTEM H

TEMPERATURE = 25.0 DEG C PRESSURE = 1.0 BAR

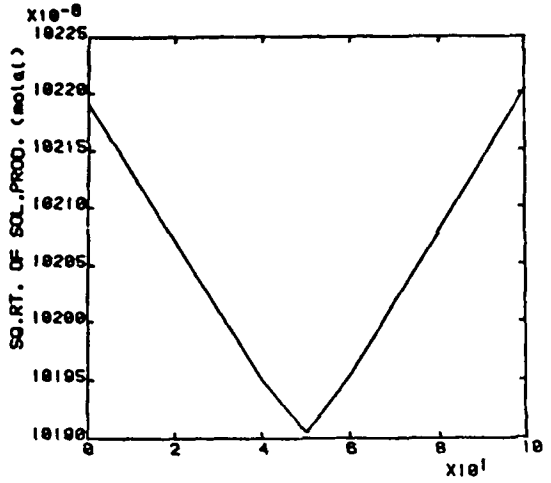

Figure A5.50b SOLUBILITY DATA PREDICTIONS FOR BASO4
WITH BRINE SYSTEM H

TEMPERATURE = 25.0 DEG C PRESSURE = 1.0 BAR

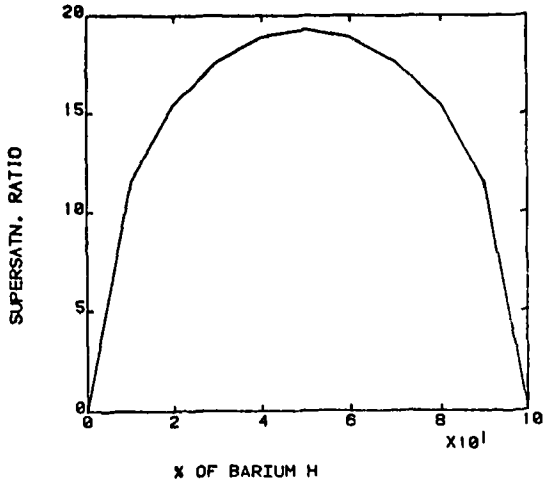

Figure A5.51a SOLUBILITY DATA PREDICTIONS FOR BASO4
WITH BRINE SYSTEM I

TEMPERATURE = 25.0 DEG C PRESSURE = 1.0 BAR

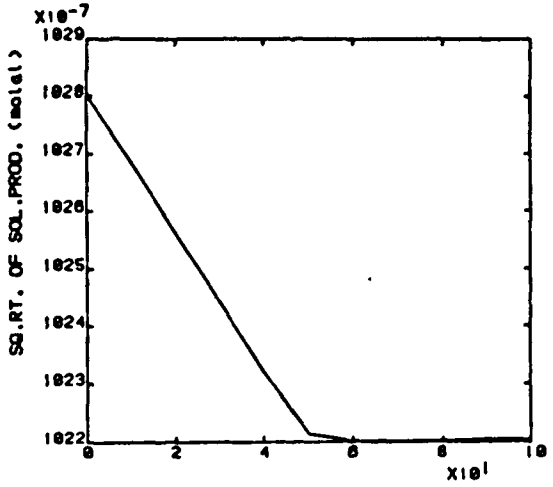

% OF BARIUM I

Figure A5.51b SOLUBILITY DATA PREDICTIONS FOR BASO4
WITH BRINE SYSTEM I

TEMPERATURE = 25.0 DEG C PRESSURE = 1.0 BAR

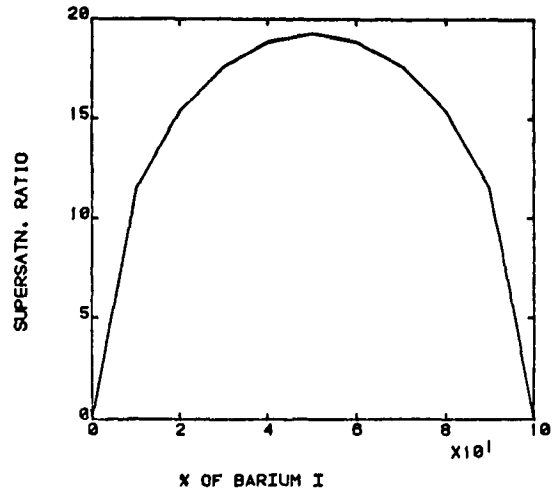

% OF BARIUM I

Figure A5.52a SOLUBILITY DATA PREDICTIONS FOR BASO4
WITH BRINE SYSTEM J

TEMPERATURE = 25.0 DEG C PRESSURE = 1.0 BAR

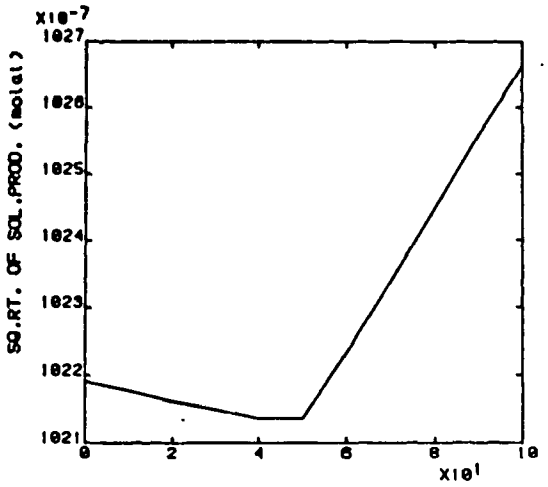

% OF BARIUM J

Figure A5.52b SOLUBILITY DATA PREDICTIONS FOR BASO4
WITH BRINE SYSTEM J

TEMPERATURE = 25.0 DEG C PRESSURE = 1.0 BAR

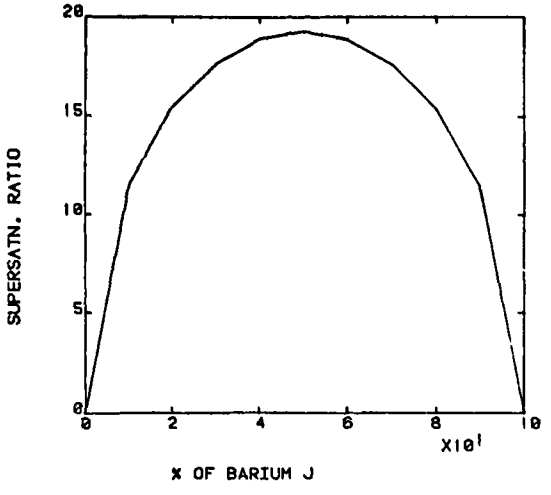

% OF BARIUM J

Figure A5.53a SOLUBILITY DATA PREDICTIONS FOR BASO4
WITH BRINE SYSTEM K

TEMPERATURE = 25.0 DEG C PRESSURE = 1.0 BAR

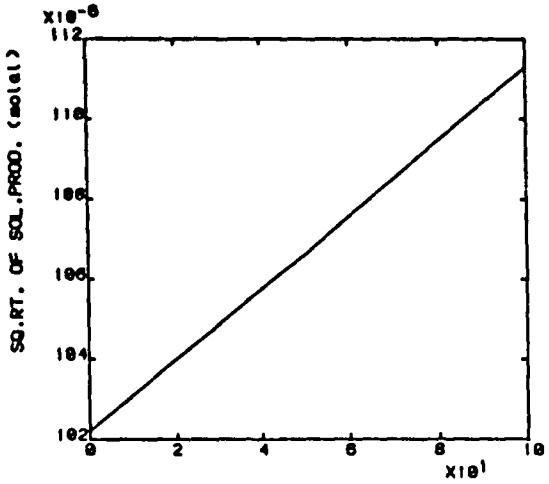

Figure A5.53b SOLUBILITY DATA PREDICTIONS FOR BASO4
WITH BRINE SYSTEM K

TEMPERATURE = 25.0 DEG C PRESSURE = 1.0 BAR

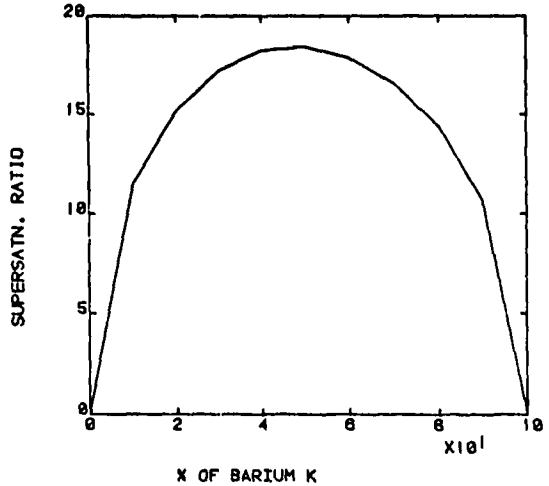

APPENDIX A6.1 THE NETWORK MODEL COORDINATE AND NUMBERING SYSTEMS

The Coordinate System and Grid Block Representation of the Network

The structure of the network model and the method of reference to any particular node or capillary was based on a system of coordinates. The coordinate system had three axes: i; j and k. The i axis lay along the length of the network while the j and k axes lay along the network's breadth and height respectively. The dimensions of the network were given in terms of these three axes.

For the sake of the coordinate system and for physical visualisation purposes, each node or capillary in the network was considered to occupy one grid block. It should be remembered that although nodes were considered in this way for the purposes of identifying them and their location, as far as the model was concerned they had no volume. Any grid block that was not either a node or a capillary was considered to be part of the solid rock matrix.

As an example of this method of representing the network, figure A6.1 shows the network, of overall dimensions 5,5,5, used as example in chapter 3. Figure A6.1 shows a three dimensional representation of the system of capillaries that made up the network and how this was interpreted in the coordinate system by five cross-sections through the i axis. Note that as the inlet and oulet faces contained only nodes, it was not necessary to include them in the coordinate system.

In the coordinate representation of the model the capillaries were of square cross-section and were bounded on all sides by solid rock matrix except at either end where they met cubic nodes. There were two types of cross-section through the i axis, those that contained nodes linked by capillaries and those that contained capillaries alone. These two types of cross-section had to be taken into account when

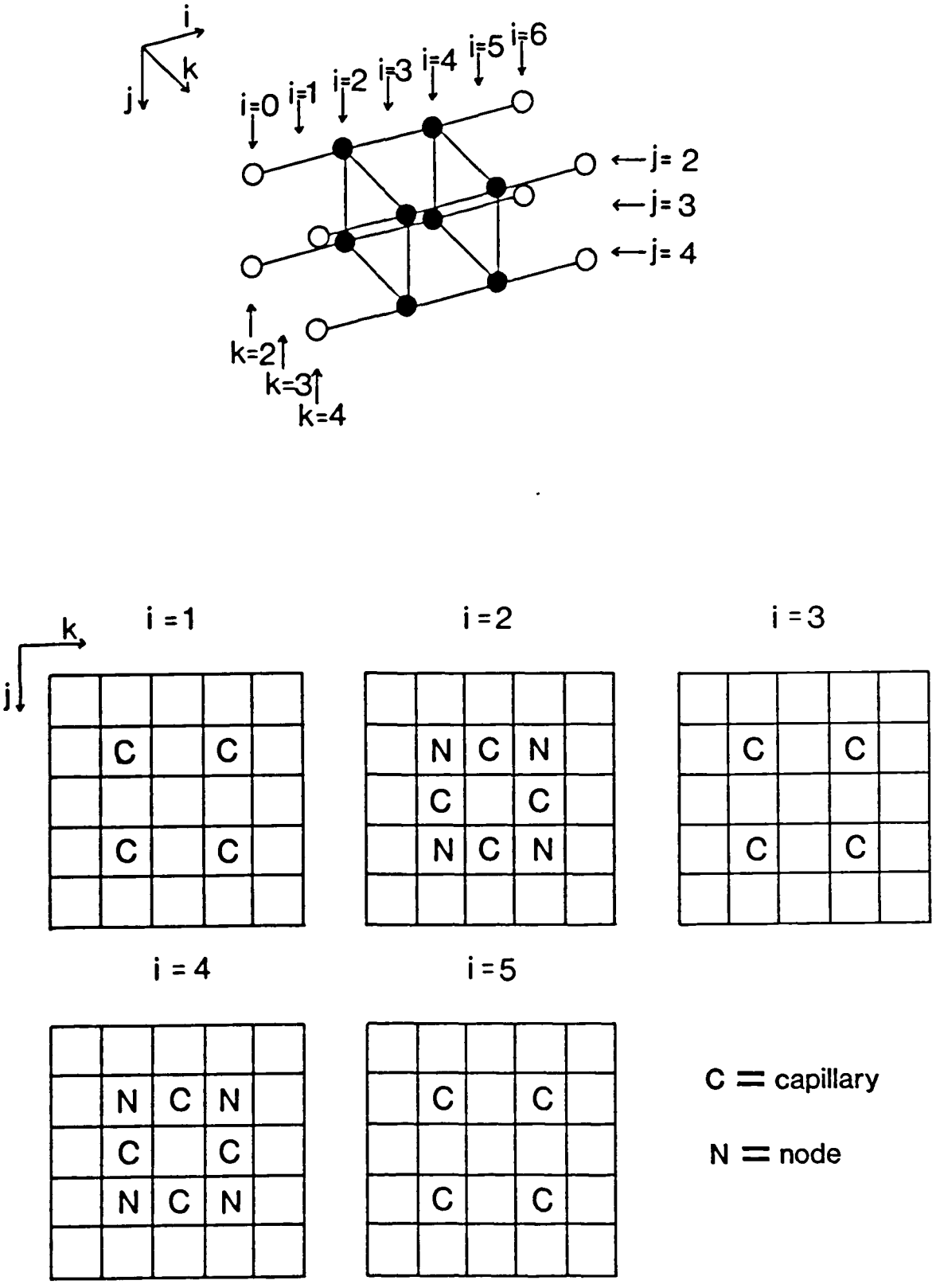

Figure A6.1 Network model coordinate system

calculating the number of nodes and capillaries in the network. When the network is viewed in the coordinate system, the origins of the overall dimensions of 5,5,5 become obvious. Note that the dimensions of the network must always be odd.

The Capillary and Node Numbering System

In the network model part of the simulation programme, data relatimg to the capillaries was stored in three-dimensional arrays of the same overall dimensions as the network. The number of rock matrix and node blocks shown in the coordinate system in figure A6.1 demonstrates how wasteful of computer memory space this form of storage was. In the rest of the simulation programme, nodes and capillaries were referred to by number. The numbering system followed a set of rules that were the same for both nodes and capillaries.

The numbering system worked by cross-section through the i axis, starting with the cross-section containing the inlet face, which was not actually part of the coordinate system but could be considered to be at i=0. The nodes and capillaries were numbered separately, line by line along the j axis. When all nodes and capillaries in a particular cross-section had been numbered the count moved on to the next cross-section. Figure A6.2 shows the result of the numbering technique for nodes and capillaries.

Equations for calculating the number of nodes and capillaries in the network and for calculating the number of any node from its coordinates are given below. It was never necessary to calculate the number of a capillary from its coordinates.

$$N_{node} = \frac{(i_{max}-1)(j_{max}-1)(k_{max}-1)}{8} + \frac{(j_{max}-1)(k_{max}-1)}{2} \quad \ldots (A6.1)$$

$$C_{node} = \frac{i\,(j_{max}-1)(k_{max}-1)}{8} + \frac{(j-2)(k_{max}-1)}{4} + \frac{k}{2} \quad \ldots (A6.2)$$

$$N_{cap} = \frac{(i_{max}+1)(j_{max}-1)(k_{max}-1)}{8} +$$

$$\frac{(i_{max}-1)}{2} \quad \frac{(j_{max}-1)(k_{max}-3)}{4} + \frac{(j_{max}-3)(k_{max}-1)}{4} \quad \ldots (A6.3)$$

where: N_{node} = number of nodes in network

C_{node} = number of node under consideration

N_{cap} = number of capillaries in network

i_{max} = length of network along i axis

j_{max} = breadth of network along j axis

k_{max} = height of network along k axis

i,j,k = coordinate of node under consideration

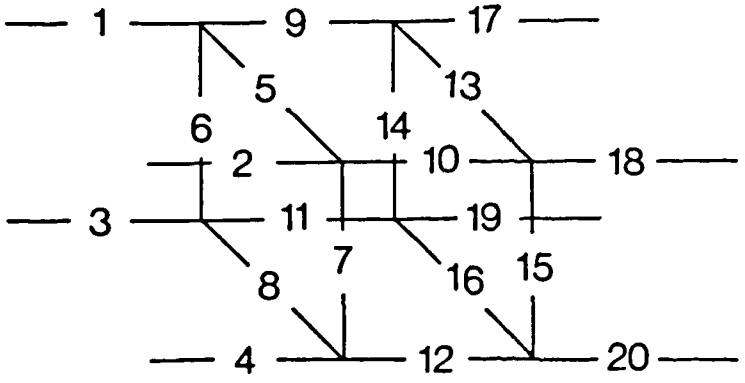

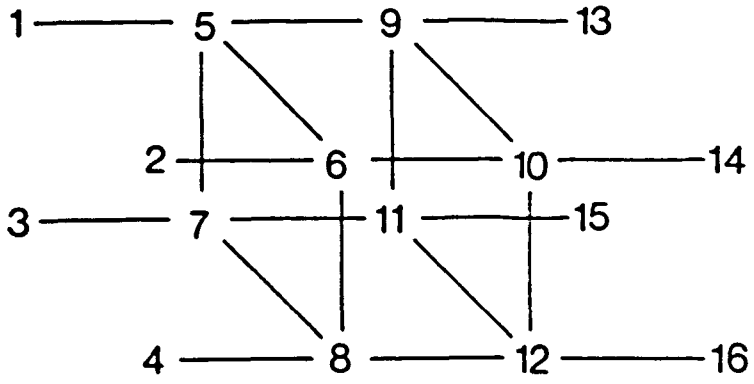

Figure A6.2 Network model capillary and node numbering systems

APPENDIX A6.2 FURTHER DOCUMENTATION FOR SCALING NETWORK MODEL PROGRAMME

A6.2.1 Introduction

This appendix provides some, all-be-it limited, documentation for the model described in this thesis. The various options and parameters in the programme are referred to by the variable name used in the programme listing.

This appendix is split into several sections, which discuss separately the various parts of the model, namely: the network model of a porous medium; the calculation or specification of supersaturation and the simulation of scale growth within the network model.

A6.2.2 Control of the Network Model

The procedures followed by the network model are adequately described in chapters 3 and 6. This section describes the control of the network model in greater detail. Control of the network model may be split into three parts. Firstly, the overall sizing of the model; secondly, the generation of the capillary throat diameters and lengths and lastly, the calculation of flowrates and pressures.

Overall sizing of the model

The model of a core was made up of a number of networks (defined by ISECT). Each network was of a size defined by the maximium coordinates IMAX, JMAX, KMAX. All these sizing parameters were

supplied to the model in its input data.

Generation of capillary throat diameters

The network model generation subroutine, NETGEN, had three methods of generating the capillary throat sizes. The simplest method was to set all the throat sizes to be equal to a size given by the variable DIAMED in the input data. This technique was useful for testing various aspects of the model as the results could be more easily predicted.

The second method used a 25% median deviation distribution to constrain the throat sizes. This distribution was based around a throat size defined by DIAMED with a maximum size of DIAMAX, both supplied in the input data.

The third method was that described in chapter 3 which generated a pore size distribution constrained by an experimental capillary pressure curve. The experimental capillary pressure curve was digitised for the model using NPOSD points. The saturation values were stored in array SATN and corresponding pore throat sizes (in μm) from the capillary pressure curve were stored in array POSD. The pore throat sizes were supplied as input data, the saturations were generated within the programme.

The selection of the capillary size distribution was controlled by the variable IDIST, set in the input data. The possible values of IDIST are given below.

IDIST	DISTRIBUTION
1	capillary pressure curve
2	unidiameter
3	25% median deviation

Solution of the Sparse Matrix of Nodal Summation Equations

In the model used in this work the sparse matrix of the nodal summation equations was solved using the MA28 library of subroutines from the Harwell library available on the IBM system at the SERC Rutherford Appleton Laboratories. The majority of the modelling work was performed on this IBM system. The MA28 library used a variant of Gaussian elimination for sparse systems to solve the equations in the model.

A6.2.3 Control of Supersaturation Generation within the Model

There were two options available in the model for specifying the level of supersaturation entering the first network. The simplest method, which was used throughout the model tests described in this work, was to merely set the inlet supersaturation, SSIN, to whatever was the desired value. For the purposes of the calculations in the rest of the model, it was also necessary to supply values for the square-root of the solubility product, SOL, and the concentration excess of the scaling anion over the scaling cation, CEX (c_{ex} in equation 3.24), for the brine flowing through the network.

Alternatively, all these parameters could be calculated within the model using the set of solubility prediction subroutines, VICKI, originally written by Pucknell[35], but with some corrections and modifications by the current author. For the solubility prediction system the programme must be supplied with the compositions of the two brines, in terms of ionic concentrations, and the fraction (RMIX) of the first specified brine in the final brine mix. Also required are the temperature (TC) (°C) and pressure (P) (bar) conditions of the brine mix.

The intersection mixing option that controls the passage of supersaturation from one network section of the model core to the next, as described in subsection 6.3.3, was selected in the input data by setting the flag NSOPT. If NSOPT was set to zero, the outlet flows from one network were mixed to calculate the inlet supersaturation for the next network. If NSOPT was set to 1, the flows from outlet nodes on one network were passed to corresponding inlet nodes on the next network.

A6.2.4 Control of Scale Growth in the Network Model

For the calculation of supersaturations throughout the model, the reaction rate constant, KREAC (k in equation 3.17) (mol/lm^{2}s), was specified in the input data. For the calculation of scale volumes the length of the time steps, TPER (seconds), was required. The number of time steps used in the model was controlled by the value of the variable ITIME. The weighting factors for the distribution of scale within the capillaries were stored in the variables DIS1, DIS2 and DIS3 for the entry wide end, throat and exit wide end respectively. All these parameters were supplied in the input data to the programme.

The calculation of the surface area term, s in equation 3.17, was made separately for each capillary in the network. The adjustments to the magnitude of this term for the tests described in chapter 6, were made by applying a factor to the calculation in the programme.

A6.2.5 Diagnostic Data from the Model

The model could supply data on most aspects of its operation. For most purposes, much of this was not required. The amount of data

provided by the model was controlled by a variable ILVL, set in the input data to the programme. Increasing the value of ILVL provided more and more detailed information as can be seen from table A37.

The model also had its own set of error messages for indicating any malfunction due to incorrect setting of input data or failure of any calculation procedure. A number describing the error condition was stored in the variable IFAIL. All the error conditions caused IFAIL to become negative, which, when detected, would cause immediate termination of the model. The error conditions and the associated values of IFAIL are given in table A38.

Table A37 Diagnostic data produced by the model for various values of ILVL

ILVL	DIAGNOSTICS PRODUCED
0	Only basic permeability data
1	Table of pore size frequencies and simulated mercury saturation data for each section (not produced if ILVL = 9)
2	Pressures at nodes
4	Outlet supersaturations and volumes of scale for each capillary
5	Capillary flowrates, throat diameters and lengths
9	As for ILVL = 1 but for whole of simulated core

All values of ILVL cause the indicated diagnostics to be produced as well as those for all lower values of ILVL.

Table A38. Values assigned to variable IFAIL when an error is encountered

IFAIL	SOURCE OF ERROR
-1	Subroutine SOLVER
-3	Subroutine BOUND
-9	Subroutine NETSOL

REFERENCES

1 Ayad, N.A. and El-Hadidi, S.M.: "Water Treatment and Injection System in UMM Shaif Field Offshore Abu Dhabi", SPE 7764 presented at SPE MIddle East Oil Technical Conference, Manama, Bahrain, 25-29 March (1979).

2 Bernard, G.G.: "Effect of Reactions Between Interstitial and Injected Waters On Permeability of Rocks", Producers Monthly (Dec. 1955), p.26-32.

3 Bernard, G.G.: "Effect of Reactions Between Interstitial and Injected Waters On Permeability of Reservoir Rocks", Illinois State Geological Survey Bulletin, 80, (1957), p.98-114.

4 Bertero, L., Chierici, G.L., Gottardi, G., Mesini, E. and Mormino, G.: "Chemical Equilibrium Models: Their Use in Simulating the Injection of Incompatible Waters", SPE 14126 presented at SPE International Meeting on Petroleum Engineering, Beijing, China, 17-20 March (1986).

5 Boyle, M.J. and Mitchell, R.W.: "Scale Inhibition Problems Associated with North Sea Oil Production", SPE 8164 presented at Offshore Europe Conference, Aberdeen, Scotland, 3-7 September (1979).

6 Case, L.C.: "Water Problems in Oil Production: An Operators Manual", The Petroleum Publishing Co., Tulsa, Oklahoma, (1970).

7 Cowan, J.C.: and Weintritt, D.J.: "Water-Formed Scale Deposits", Gulf Publishing Co., Houston, Texas, (1976).

8 Dana, E.S.: "Dana's System of Mineralogy", 6th edition, John Wiley and Sons, New York, (1892).

9 Deer, W.A., Howie, R.A. and Zussman, J.: "An Introduction to the Rock Forming Minerals", Longman Group Ltd., London, (1966).

10 Earlougher, R.C. and Love, W.W.: "Sequestering Agents for Prevention of Scale Deposition in Oil Wells", Journal of Petroleum Technology, (April 1957), p.17-20.

11 Fatt, I.: "The Network Model of Porous Media: III. Dynamic Properties of Networks with Tube Radius Distribution", Petroleum Transactions, AIME, 207, (1956), p.164-181.

12 Fielder, M. and Hughes, C.T.: "Downhole Scale Control in the Thistle Field", presented at Royal Society of Chemistry Chemicals in the Oil Industry Conference, Manchester, England, 26-27 March (1985).

13 Fischer, R.B.: "Precipitation of Barium Sulfate - Investigation by Electron Microscopy", Analytical Chemistry, 23, No. 11, (1951), p.1667-1671.

14 Fischer, R.B. and Rhinehammer, T.B.: "Rapid Precipitation of Barium Sulfate", Analytical Chemistry, 25, No. 10, (1953), p.1544-1548.

15 Gardner, G.L. and Nancollas, G.H.: "Crystal Growth in Aqueous Solution at Elevated Temperatures. Barium Sulfate Growth Kinetics", Journal of Physical Chemistry, 87, No. 23, (1983), p.4699-4703.

16 Golshan, H.: "Development and Application of Stochastic Pore Structure Models", Ph.D. Thesis, Victoria University of Manchester, (1979).

17 Goulding, P.S.: "Progress Report - Oilfield Scale", Dept. Petroleum Engineering, Heriot-Watt University, Scotland, (Dec 1985).

18 Personal communication.

19 Greig, A.C., Dent, J. and Hellings, G.: "Scale Inhibitor Testing - An Evaluation of Some Laboratory Procedures", presented at Royal Society of Chemistry Chemicals in the Oil Industry Conference, Manchester, England, 26-27 March (1985).

20 Hamilton, W.R., Woolley, A.R. and Bishop, A.C.: "The Hamlyn Guide to Minerals, Rocks and Fossils", Hamlyn Publishing Group Ltd., London, (1974).

21 Hourston, K.E.: "Scale Prediction, Prevention and Removal, with Reference to the South Brae Reservoir", M.Eng. Project Report, Dept. Petroleum Engineering, Heriot-Watt University, Scotland, (1985).

22 Khelil, C., Harouaka, A. and Delhoume, A.: "Water Injection in Algeria - Problems and Solutions", SPE 7762 presented at SPE Middle East Oil Technical Conference, Manama, Bahrain, 25-29 March (1979).

23 Laird, R.W. and Cogbill, A.F.: "Incompatible Waters Can Plug Oil Sands", World Oil, (May 1958), p.188-190.

24 Liu, S.T., Nancollas, G.H. and Gasiecki, E.A.: "Scanning Electron Microscopic and Kinetic Studies of the Crystallization and Dissolution of Barium Sulfate Crystals", Journal of Crystal Growth, 33, (1976), p.11-20.

25 Mealor, D. and Townshend, A.: "Homogeneous Nucleation of Some Sparingly Soluble Salts", Talanta, 13, (1966), p.1069-1074.

26 Miles, L.: "New Well Treatment Inhibits Scale", Oil and Gas Journal, 8 June (1970), p.97-99.

27 Mitchell, R.W.: "The Forties Field Sea-Water Injection System", Journal of Petroleum Technology, (June 1978), p.877-884.

28 Nancollas, G.H.: "Oilfield Scale. Physical Chemical Studies of its Formation and Prevention", presented at Royal Society of Chemistry Chemicals in the Oil Industry Conference, Manchester, England, 26-27 March (1985).

29 Nancollas, G.H. and Liu, S.T.: "Crystal Growth and Dissolution of Barium Sulfate", Society of Petroleum Engineers Journal, (Dec. 1975), p.509-516.

30 Nancollas, G.H. and Purdie, N.: "Crystallization of Barium Sulphate in Aqueous Solution", Transactions of the Faraday Society, 59, (1963), p.735-740.

31 Nielsen, A.E.: "Kinetics of Precipitation", Pergamon Press, Oxford, (1964).

32 Ogletree, J.O. and Overly, R.J.: "Sea-Water and Subsurface-Water Injection in West Delta Block 73 Waterflood Operations", Journal of Petroleum Technology, (June 1977), p.623-628.

33 Okada, S. and Magari, S.: "Morphology of Barium Sulfate as Seen through Electron Microscopy", Analytical Chemistry, 27, No. 9, (1955).

34 Ostroff, A.G.: "Compatibility of Waters for Secondary Recovery", Producers Monthly, (March 1963), p.2-9.

35 Pucknell, J.K.: "Oilfield Scale: An Investigation of the Mechanisms of Formation and Prevention and the Development of Methods by which its Occurrence can be Predicted", Ph.D. Thesis, Heriot-Watt University, Scotland, (1983).

36 Personal communication.

37 Read, P.A. and Ringen, J.K.: "The Use of Laboratory Tests to Evaluate Scaling Problems During Water Injection", SPE 10593 presented at SPE Sixth International Symposium on Oilfield and Geothermal Chemistry, Dallas, Texas, 25-27 January (1982).

38 Personal communication.

39 Scott, G.C.: "Methods of Predicting Impairment and Injectivity Decline for Homogeneous Sandstone Reservoirs", M.Eng. Project Report, Dept. Petroleum Engineering, Heriot-Watt University, Scotland, (1984).

40 Scott-Will, A.G.: "Reaction and Flow of Carbonated Brines through Calcareous Sandstones: A Study Under Oil Reservoir Conditions", Ph.D. Thesis, Heriot-Watt University, Scotland, (1985).

41 Simm, I.: "Operating the Scaling Rig at Elevated Temperatures", Filenote IS/3, Dept. Petroleum Engineering, Heriot-Watt University, Scotland, (March 1983).

42 Simm, I.: "Formation Damage Due to Barium Sulphate Scale and its Removal", M.Eng. Project Report, Dept. Petroleum Engineering, Heriot-Watt University, Scotland, (1984).

43 Smith, A.L.: "Radioactive Scale Formation", presented at Royal Society of Chemistry Chemicals in the Oil Industry Conference, Manchester, England, 26-27 March (1985).

44 Somerville, J.E.: "The Use of Matrices in the Calculation of Flow Within a Capillary Network Model", Filenote JS/3, Dept. Petroleum Engineering, Heriot-Watt University, Scotland, (June 1981).

45 Somerville, J.E.: "Pore Size Distribution and Permeability Modelling", Filenote JS/4, Dept. Petroleum Engineering, Heriot-Watt University, Scotland, (March 1982).

46 Suito, E. and Takiyama, K.: "Formation and Aging of Precipitates. I. Electron Microscopic Studies of the Formation of Barium Sulfate Precipitate", Bulletin of the Chemical Society of Japan, 27, No. 3, (1954), p.121-125.

47 Swanson, B.F.: "A Simple Correlation Between Permeability and Mercury Capillary Pressures", Journal of Petroleum Technology, 33, (1981), p.2498-2504.

48 Takiyama, K.: "Formation and Aging of Precipitates. XII. Studies on Types of Crystal Growth of Barium Sulfate by Dissolution in Water", Bulletin of the Chemical Society of Japan, 32, No. 5, (1959), p.442-445.

49 Tanner, R.N. and Wittingham, K.P.: "Scale Control During Waterflooding Operations: A Field Appraisal of Inhibitor Requirements and Performance", SPE 14127 presented at SPE International Meeting on Petroleum Engineering, Beijing, China, 17-20 March (1986).

50 Todd, A.C., Somerville, J.E. and Graham Scott: "The Application of Depth Formation Damage Measurements in Predicting Water Injectivity Decline", SPE 12498 presented at the Formation Damage Control Symposium, Bakersfield, CA, 13-14 February (1984).

51 Vetter, O.J.G.: "How Barium Sulfate is Formed: An Interpretation", Journal of Petroleum Technology, (Dec. 1975), p.1515-1523.

52 Vetter, O.J.G., Kandarpa, V. and Harouaka, A,: "Prediction of Scale Problems Due to Injection of Incompatible Waters", Journal of Petroleum Technology, (Feb 1982), p.273-284.

53 Personal communication.

54 Horikoshi, E.: "Volcanic Activity Related to the Formation of the Kuroko-type Deposits in the Kosaka District, Japan", Mineralium Deposita (Berlin), 4, (1969), p.321-345.